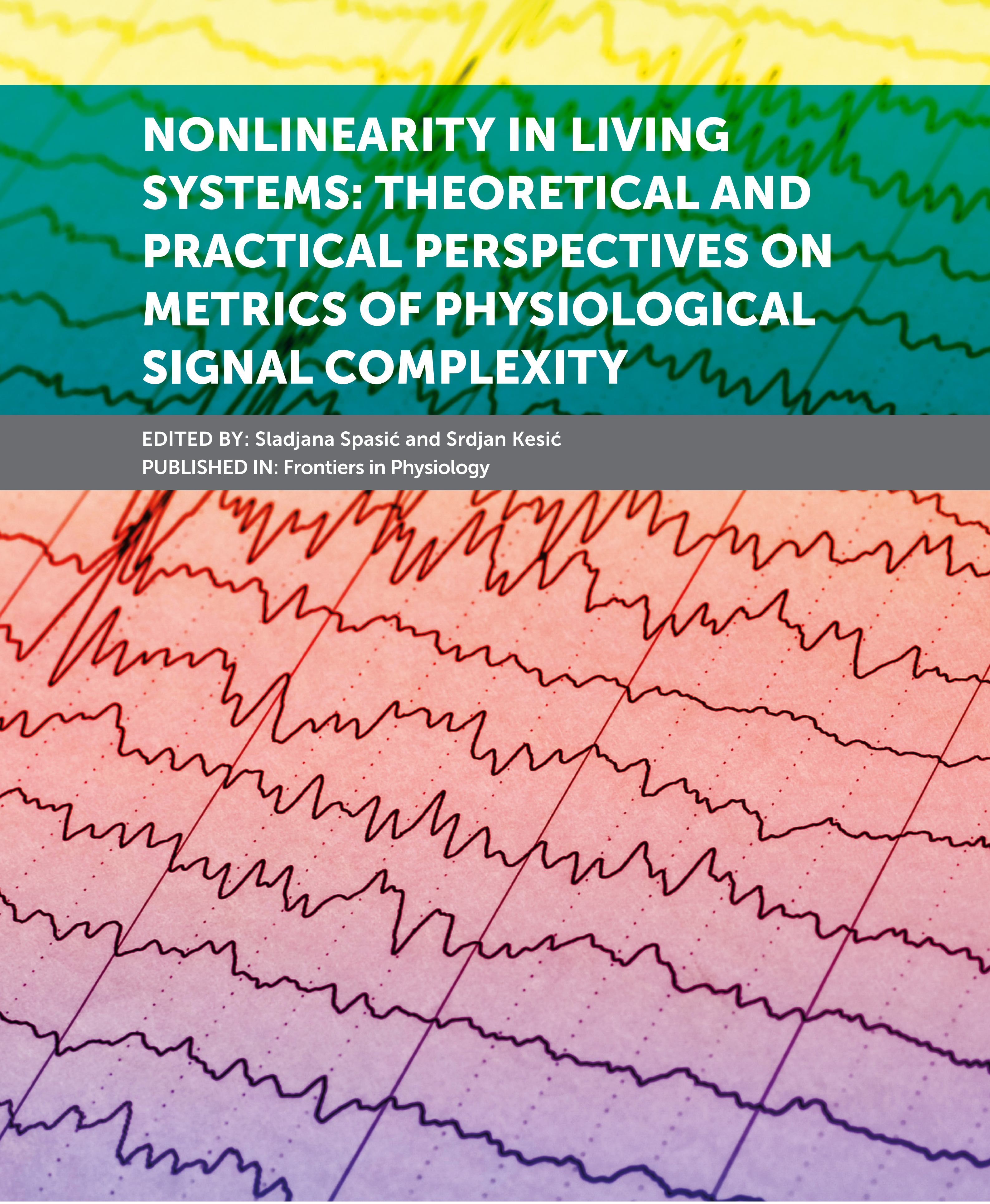

NONLINEARITY IN LIVING SYSTEMS: THEORETICAL AND PRACTICAL PERSPECTIVES ON METRICS OF PHYSIOLOGICAL SIGNAL COMPLEXITY

EDITED BY: Sladjana Spasić and Srdjan Kesić
PUBLISHED IN: Frontiers in Physiology

frontiers Research Topics

Frontiers Copyright Statement

© Copyright 2007-2019 Frontiers Media SA. All rights reserved.

All content included on this site, such as text, graphics, logos, button icons, images, video/audio clips, downloads, data compilations and software, is the property of or is licensed to Frontiers Media SA ("Frontiers") or its licensees and/or subcontractors. The copyright in the text of individual articles is the property of their respective authors, subject to a license granted to Frontiers.

The compilation of articles constituting this e-book, wherever published, as well as the compilation of all other content on this site, is the exclusive property of Frontiers. For the conditions for downloading and copying of e-books from Frontiers' website, please see the Terms for Website Use. If purchasing Frontiers e-books from other websites or sources, the conditions of the website concerned apply.

Images and graphics not forming part of user-contributed materials may not be downloaded or copied without permission.

Individual articles may be downloaded and reproduced in accordance with the principles of the CC-BY licence subject to any copyright or other notices. They may not be re-sold as an e-book.

As author or other contributor you grant a CC-BY licence to others to reproduce your articles, including any graphics and third-party materials supplied by you, in accordance with the Conditions for Website Use and subject to any copyright notices which you include in connection with your articles and materials.

All copyright, and all rights therein, are protected by national and international copyright laws.

The above represents a summary only. For the full conditions see the Conditions for Authors and the Conditions for Website Use.

ISSN 1664-8714
ISBN 978-2-88945-894-3
DOI 10.3389/978-2-88945-894-3

About Frontiers

Frontiers is more than just an open-access publisher of scholarly articles: it is a pioneering approach to the world of academia, radically improving the way scholarly research is managed. The grand vision of Frontiers is a world where all people have an equal opportunity to seek, share and generate knowledge. Frontiers provides immediate and permanent online open access to all its publications, but this alone is not enough to realize our grand goals.

Frontiers Journal Series

The Frontiers Journal Series is a multi-tier and interdisciplinary set of open-access, online journals, promising a paradigm shift from the current review, selection and dissemination processes in academic publishing. All Frontiers journals are driven by researchers for researchers; therefore, they constitute a service to the scholarly community. At the same time, the Frontiers Journal Series operates on a revolutionary invention, the tiered publishing system, initially addressing specific communities of scholars, and gradually climbing up to broader public understanding, thus serving the interests of the lay society, too.

Dedication to Quality

Each Frontiers article is a landmark of the highest quality, thanks to genuinely collaborative interactions between authors and review editors, who include some of the world's best academicians. Research must be certified by peers before entering a stream of knowledge that may eventually reach the public - and shape society; therefore, Frontiers only applies the most rigorous and unbiased reviews.
Frontiers revolutionizes research publishing by freely delivering the most outstanding research, evaluated with no bias from both the academic and social point of view. By applying the most advanced information technologies, Frontiers is catapulting scholarly publishing into a new generation.

What are Frontiers Research Topics?

Frontiers Research Topics are very popular trademarks of the Frontiers Journals Series: they are collections of at least ten articles, all centered on a particular subject. With their unique mix of varied contributions from Original Research to Review Articles, Frontiers Research Topics unify the most influential researchers, the latest key findings and historical advances in a hot research area! Find out more on how to host your own Frontiers Research Topic or contribute to one as an author by contacting the Frontiers Editorial Office: researchtopics@frontiersin.org

NONLINEARITY IN LIVING SYSTEMS: THEORETICAL AND PRACTICAL PERSPECTIVES ON METRICS OF PHYSIOLOGICAL SIGNAL COMPLEXITY

Topic Editors:
Sladjana Spasić, University of Belgrade, Singidunum University, Serbia
Srdjan Kesić, University of Belgrade, Serbia

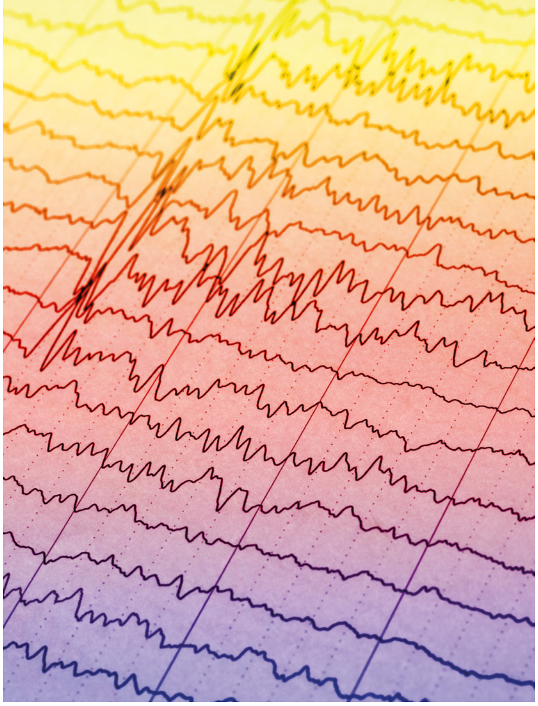

Image: Chaikom/Shutterstock.com

The biological basis of physiological signals is incredibly complex. While many types of research certainly appreciate molecular, cellular and systems approach to unravel overall biological complexity, in the recent decades the interest for mathematical and computational characterization of structural and functional basis underlying biological phenomena gain wide popularity among scientists. Nowadays, we witnessed wide range applications of nonlinear quantitative analysis that produced measures such as fractal dimension, power-law scaling, Hurst exponent, Lyapunov exponent, approximate entropy, sample entropy, Lempel–Ziv complexity, as well as other metrics for predictions of onset and progression of many pathological conditions, especially in the central nervous systems (CNS). In this Research Topic, we seek to bring together the recent practical and theoretical advances in the development and application of nonlinear methods or narrower fractal-based methods for characterizing the complex physiological systems at multiple levels of the organization. We will discuss the use of various complexity measures and appropriate parameters for characterizing the variety of physiological signals up to the systems level. There are multiple aims in this topic. The recent advancement in the application of nonlinear methods for both normal and pathological physiological conditions is the first. The second aim is to emphasize the more recent successful attempt to apply these methods across animal species. Finally, a comprehensive understanding of advantages and disadvantages of each method, especially between its mathematical assumptions and real-world applicability, can help to find out what is at stake regarding the above aims and to direct us toward the more fruitful application of nonlinear measures and statistics in physiology and biology in general.

Citation: Spasić, S., Kesić, S., eds. (2019). Nonlinearity in Living Systems: Theoretical and Practical Perspectives on Metrics of Physiological Signal Complexity. Lausanne: Frontiers Media. doi: 10.3389/978-2-88945-894-3

Table of Contents

I. THEORETICAL AND METHODOLOGICAL APPROACHES

II. NONLINEAR ANALYSIS OF ELECTROENCEPHALOGRAM AND HEART RATE VARIABILITY

III. OTHER APPLICATIONS OF NONLINEAR AND LINEAR MEASURES

frontiers in Physiology

EDITORIAL
published: 29 March 2019
doi: 10.3389/fphys.2019.00298

Editorial: Nonlinearity in Living Systems: Theoretical and Practical Perspectives on Metrics of Physiological Signal Complexity

Sladjana Z. Spasić [1,2] and Srdjan Kesić [3]*

[1] Department of Life Sciences, Institute for Multidisciplinary Research, University of Belgrade, Belgrade, Serbia, [2] Faculty of Informatics and Computing, Singidunum University, Belgrade, Serbia, [3] Department of Neurophysiology, Institute for Biological Research "Siniša Stanković", University of Belgrade, Belgrade, Serbia

Keywords: fractal physiology, non-linearity, electroencephalograph, hearth beat, fractal dimension, non-linear measures, disease

Editorial on the Research Topic

Nonlinearity in Living Systems: Theoretical and Practical Perspectives on Metrics of Physiological Signal Complexity

Despite the extraordinary development of physiology in recent decades, we still struggle to understand the multilevel organization and functional integration in complex biological systems (Goldberger et al., 2002; West, 2010). In this respect, the use of non-linear descriptors and models in physiology is becoming an essential part of current and future efforts to understand complex biological systems in both health and disease (Goldberger et al., 2002). Nonetheless, non-linear-based methods have been utilized in solving many fascinating problems in different subfields of physiology and pathophysiology.

In this Research Topic, we present original research articles, reviews and new hypotheses that extend our knowledge and understanding of fractal physiology and its interdisciplinary nature. Many of physiological researches in recent decades has focused on quantitative analysis, characterization of dynamics across time scales, and ultimately control of functional physiological networks, especially in the central and peripheral nervous system (West, 2010; França et al., 2018). Also, one of the greatest challenges of fractal physiology is to elucidate the fractal and non-linear mechanisms involved in the generation and allometric control of complex physiological networks, for which we know that they are a product of several different and interacting temporal scales (Goldberger et al., 2002; West, 2010; França et al., 2018). Therefore, it would not be wrong to emphasize that the future of physiology lies in finding ways for applying existing non-linear measures, developing new ones, and setting new hypotheses aimed at understanding the variability of physiological time series in health and disease. In this respect, Bohara et al. provide a new hypothesis with valuable theoretical insight into the relationship between crucial events (1/f noise) and the wave-like nature of the brain processes. The results of this paper confirm an important role of crucial events in the dynamics of the brain; they provide theoretical tools necessary to understand the joint action of crucial events and periodicity, which can be helpful in better understanding of cognitive processes. von Wegner proposed an information-theoretic approach to numerically determine the Markov order of discrete processes defined over a finite space. This approach uses a combination of autoinformation and partial autoinformation to deal with Markov and non-Markov processes with known stochastic properties and can be used for discrete transformation of electroencephalograph (EEG) data sets as well.

OPEN ACCESS

Edited and reviewed by:
Bruce J. West,
United States Army Research Laboratory, United States

****Correspondence:***
Sladjana Z. Spasić
sladjana@imsi.rs;
sladjana@imsi.bg.ac.rs

Specialty section:
This article was submitted to Fractal Physiology, a section of the journal Frontiers in Physiology

Received: *07 February 2019*
Accepted: *06 March 2019*
Published: *29 March 2019*

Citation:
Spasić SZ and Kesić S (2019) Editorial: Nonlinearity in Living Systems: Theoretical and Practical Perspectives on Metrics of Physiological Signal Complexity. Front. Physiol. 10:298. doi: 10.3389/fphys.2019.00298

Many of the contributions highlight the non-linear behavior of various components of an organism ("vertical" component of complexity) from the cellular to tissue and organ levels work together to maintain complex physiological networks. Among the multiplicity of non-linear measures, Higuchi fractal dimension (HFD), used alone or in combination with other measures, once again proves to be a valuable and important source of new information about neuronal networks underlying time scale invariant EEG dynamics. In that regard, Croce et al. used HFD and detrended fluctuation analysis (DFA) to investigate circadian rhythms in fractal features of EEG signals. These authors showed that HFD can be useful for monitoring circadian fluctuations of fractal features of EEG at rest in both eyes closed and eyes open conditions. Päeske et al. employed a set of non-linear measures such as HFD, Katz fractal dimension (KFD), Lempel-Ziv complexity (LZC), sample entropy (SampEn), and synchronization likelihood (SL) to estimate the impact of the strong cyclic signal component on the result of surrogate data method in the case of resting EEG signals (80 healthy human subjects) and the impact of segment length on this method. The authors have found that in the case of the signals with non-monotonic spectrum and strong dominant frequency, the correct use of surrogate data method requires the signal length comprising of full periods of the spectrum dominant frequency. This study once more highlights the importance of correct selection of EEG signal segment length for the surrogate data method to estimate non-linearity. Lebiecka et al. showed that HFD may be a useful marker for evaluation of the repetitive transcranial magnetic stimulation (rTMS) effectiveness and the therapy progress as well as for group differentiation between major depression disorder (MDD) and bipolar disorder (BP), or between responders and non-responders. In this research topic, the significance of HFD as a non-linear measure for different time series including electrocardiograph (ECG) signals has been confirmed. For instance, Gomolka et al. performed HFD analysis of heart rate variability (HRV) in order to assess the autonomic nervous system (ANS) sympathetic and parasympathetic activity in healthy and diabetic individuals. They concluded that HFD may be used for assessment of percutaneous auricular vagus nerve stimulation (pVNS) on ANS, to provide stimulation feedback for online regulation of therapy in a fast and robust way. Furthermore, Ahammer et al. simultaneously used video recordings and electrode registration of potentials to characterize beat to beat variability of cardiac tissue in control conditions and during acetylcholine stimulation. By using variation analyses of video recordings with two distinguished non-linear measures, SampEn and HFD, these authors showed that high-speed video camera technique might represent a non-invasive tool that allows long-lasting recordings for detecting variations in beating dynamics during varying conditions.

The use of other non-linear measures and their specific combinations also occupy a significant place in this research topic. Thus, Liang et al. employed DFA combined with surrogate data method to measure the long-range temporal correlations (LRTCs) of the EEG signals of patients with the minimal conscious state after the spinal cord stimulation (SCS). Authors concluded that the brain activities at low-frequency oscillations, particularly in the frontal and occipital regions, were improved by SCS. By using cross recurrence quantification analysis (cRQA) of the coupling of the gaze and postural sway to the motion of a visual stimulus, Haworth and Stergiou showed that chaos is an invariant and beneficial feature of biological motion, a feature which may be critical for immediate and robust coordination of the self with the environment and other environmental agents. In a similar manner, Andreo et al. applied Box-counting FD as well Minkowski-Bouligand FD measure of dynamic changes in the center of mass during a set movement that indicated real-time processing effects during a balance task associated with the type of taping used to enhance postural stability. Hwang et al. applied stabilogram diffusion analysis and showed that amplification of low-frequency errors improves force control by shifting relative significance of feedforward and feedback processes. Lucas et al. combined Shannon entropy, wavelets, mean bending energy in order to devise automated determination of foot type. Their research suggests that automated wavelet-based foot type classification of 2D binary images of the plantar surface of the foot is comparable to current state-of-the-art methods providing a cost and time effective tool suitable for clinical diagnostics. In their study Solé-Casals at al. proposed a methodology for extracting of handwriting features using the discrete Fourier transform (DFT) and derive an algorithm in order to discriminate between control and subjects with essential tremor (ET). Authors showed that the radius and residues of XY positions of an Archimedes' spiral, could be used to detect ET with a performance of almost 85 and 96%. The results indicated that it is possible to detect ET from controls using a reduced set of features, which makes this method feasible for implementation in the portable form of the device and on the web network. Ibáñez-Molina et al. used Lempel-Ziv complexity (LZC) and Multiscale LZC to reveal EEG multiscale complexity in schizophrenia patients during picture naming. In addition to showing that patients and controls showed a different pattern of brain complexity depending on their cognitive state (at rest or under cognitive challenge), these authors once more demonstrated that non-linear approaches to EEG signal analysis can help to characterize brain dysfunction in schizophrenia.

Two original papers dealt with the correlation between the neurodegenerative process underlying cognitive impairment and retinal vascular complexity. Cabrera DeBuc et al. used information dimension, correlation dimension, FD measured by box counting method for quantification the correlation between the retinal vascular complexity and neurodegenerative changes in patients with cognitive impairment (CI). This paper showed that there are multimodal retinal markers that may be sensitive to CI decline, suggesting that retinal geometric vascular and functional parameters might be associated with physiological changes in the retina due to CI. In a similar manner, Kostic et al. illustrated that the FD of the foveal vessel arborization could provide useful information to identify early morphological changes in the retina of patients with type 2 diabetes mellitus. Despite the significant progress in the development and application of non-linear methodology in biomedical research, there is still room for the use of linear methods in the analysis of electrophysiological signals. In that respect, Jalilifar et al. have evaluated antiepileptogenic effects of low-frequency stimulation (LFS) before or after kindling using spectral power analysis (theta/alpha ratio) of EEG signals.

The development of automated systems that can predict the course of the disease is one of the greatest challenges of modern pathophysiology that can provide better outcomes of medical interventions. In recent times, there is an increasing interest in adaptive neuro-fuzzy inference systems (ANFIS) and their application to non-linear dynamical systems in health and disease. Accordingly, Yadollahpour et al. have developed ANFIS based medical decision support system to predict chronic kidney disease progression.

The "horizontal" component of complexity is also not neglected in this topic. In that regard, Eguiraun et al. proposed a non-linear analysis and Shannon entropy to characterize the relationship of the constituted complex entities with other complex entities (interactions between individuals of *European seabass*). Finally, the topic includes the review of measures and metrics of biological systems. Kasum et al. summarize and reviews different mathematical and informational approaches to biological systems, providing an interesting overview of the complex relationship between experimental biomedical research on one hand and computational science and mathematics on other.

Although a common thread runs between them, each article in this research topic proposes distinctive applications of non-linear methodology in physiology and deserves attention in its own right. Together, they illustrate the importance and vitality of fractal research in physiology and medicine. Whether through an effort to improve our understanding of crucial events as an important process of self-organization; consideration of how best to exploit and combine non-linear measures; extension of applications of these measures to new physiological and pathological conditions, the authors here develop engaging proposals for investigating "horizontal" and "vertical" components of complexity in biological systems.

AUTHOR CONTRIBUTIONS

All authors listed have made a substantial, direct and intellectual contribution to the work, and approved it for publication.

ACKNOWLEDGMENTS

We acknowledge the support provided by Projects No. 173027 and No. 173045 funded by the Ministry of Education, Science, and Technological Development of the Republic of Serbia. We thank all researchers who participated in this research topic, as well as the reviewers on their contribution to the quality of published articles.

REFERENCES

França, L. G. S., Miranda, J. G. V., Leite, M., Sharma, N. K., Walker, M. C., Lemieux, L., et al. (2018). Fractal and multifractal properties of electrographic recordings of human brain activity: toward its use as a signal feature for machine learning in clinical applications. *Front. Physiol.* 9:1767 doi: 10.3389/fphys.2018.01767

Goldberger, A. L., Amaral, L. A., Hausdorff, J. M., Ivanov, P. C., Peng, C. K., and Stanley, and, H. E. (2002). Fractal dynamics in physiology: alterations with disease and aging. *Proc. Natl. Acad. Sci. U.S.A.* 99(Suppl. 1), 2466–2472. doi: 10.1073/pnas.012579499

West, B. J. (2010). Fractal physiology and the fractional calculus: a perspective. *Front. Physiol.* 1:12. doi: 10.3389/fphys.2010.00012

Conflict of Interest Statement: The authors declare that the research was conducted in the absence of any commercial or financial relationships that could be construed as a potential conflict of interest.

Copyright © 2019 Spasić and Kesić. This is an open-access article distributed under the terms of the Creative Commons Attribution License (CC BY). The use, distribution or reproduction in other forums is permitted, provided the original author(s) and the copyright owner(s) are credited and that the original publication in this journal is cited, in accordance with accepted academic practice. No use, distribution or reproduction is permitted which does not comply with these terms.

frontiers
in Physiology

HYPOTHESIS AND THEORY
published: 29 August 2018
doi: 10.3389/fphys.2018.01174

Bridging Waves and Crucial Events in the Dynamics of the Brain

Gyanendra Bohara[1]*, *Bruce J. West*[2] *and Paolo Grigolini*[1]

[1] *Center for Nonlinear Science, University of North Texas, Denton, TX, United States,* [2] *Information Science Directorate, Army Research Office, Durham, NC, United States*

Earlier research work on the dynamics of the brain, disclosing the existence of crucial events, is revisited for the purpose of making the action of crucial events, responsible for the $1/f$ −noise in the brain, compatible with the wave-like nature of the brain processes. We review the relevant neurophysiological literature to make clear that crucial events are generated by criticality. We also show that although criticality generates a strong deviation from the regular wave-like behavior, under the form of Rapid Transition Processes, the brain dynamics also host crucial events in regions of nearly coherent oscillations, thereby making many crucial events virtually invisible. Furthermore, the anomalous scaling generated by the crucial events can be established with high accuracy by means of direct analysis of raw data, suggested by a theoretical perspective not requiring the crucial events to yield a visible physical effect. The latter follows from the fact that periodicity, waves and crucial events are the consequences of a spontaneous process of self-organization. We obtain three main results: (a) the important role of crucial events is confirmed and established with greater accuracy than previously; (b) we demonstrate the theoretical tools necessary to understand the joint action of crucial events and periodicity; (c) we argue that the results of this paper can be used to shed light on the nature of this important process of self-organization, thereby contributing to the understanding of cognition.

Keywords: brain waves, crucial events, periodicity, 1/f spectrum, coherence

OPEN ACCESS

Edited by:
Srdjan Kesić,
University of Belgrade, Serbia

Reviewed by:
Andrew A. Fingelkurts,
BM-Science, Finland
Sebastian Wallot,
Max-Planck-Institut für Empirische Ästhetik, Germany

***Correspondence:**
Gyanendra Bohara
gyanendrabohara@my.unt.edu

Specialty section:
This article was submitted to Fractal Physiology, a section of the journal Frontiers in Physiology

Received: *20 May 2018*
Accepted: *06 August 2018*
Published: *29 August 2018*

Citation:
Bohara G, West BJ and Grigolini P (2018) Bridging Waves and Crucial Events in the Dynamics of the Brain. Front. Physiol. 9:1174. doi: 10.3389/fphys.2018.01174

1. INTRODUCTION

Following the dynamics of the brain is a challenging issue that has forced researchers to go beyond applying the conventional forms of non-equilibrium statistical physics (Papo, 2013) and is expected to contribute to reshaping the emerging field of complex networks as well (Papo et al., 2014). The dynamics of the brain and of biological processes in general, are characterized by homeodynamics (Yates, 1994), thereby implying that the analysis of biological dynamics ought to be done taking into account that it is typically driven by rhythms and waves.

A parallel line of inquiry has recently been developed that focuses on the connection between the dynamics of the brain and the phenomenon of criticality (Aburn et al., 2012; Tagliazucchi et al., 2012; Boonstra et al., 2013). Criticality in the brain is a subject widely discussed in the neurophysiology literature, as reviewed in the recent paper (Cocchi et al., 2017) and is a term adopted by physicists to denote, for instance, the spontaneous magnetization of a material below the Curie temperature. At the critical temperature T_C where this transition occurs, a long-range correlation between the thermally disordered spins occurs. It is widely thought that an analogous condition is fulfilled by brain dynamics with the consequence of strongly correlating the functionality of different physical regions of the brain. This connection between brain dynamics and phase transition processes at criticality led the present investigators to focus on the concept of crucial events.

For context, let us briefly consider how the concept of crucial events was introduced in neurophysiology. Contoyiannis and Diakonos (Contoyiannis and Diakonos, 2000) studied a 3-dimensional Ising model at criticality and proved it to be the generator of Type I intermittency. In the sequel (Contoyiannis et al., 2002) they pointed out that this connection with Type I intermittency can be formally expressed through a waiting-time probability density function (PDF) $\psi(\tau)$, with a dominant inverse power law (IPL) structure, with IPL index μ. This PDF is exponentially truncated at long times. Using the intermittency language (Manneville and Pomeau, 1979; Pomeau and Manneville, 1980) a laminar region is interpreted as a quiet zone between short regimes of rapid erratic activity. The durations of different laminar regions are uncorrelated and the turbulent processes separating consecutive laminar regions are the crucial events studied in this paper. The discovery of crucial events in the field of turbulence (Manneville and Pomeau, 1979; Pomeau and Manneville, 1980) had deep consequences in statistical physics. In fact, if the IPL index μ of $\psi(\tau)$ is smaller than 3, the process hosting the crucial events is not ergodic. On the other hand , the statistical analysis of molecular diffusion in biological cells (Metzler et al., 2014) shows that these processes are not ergodic, since they host crucial events. This leads to the inequality $\mu < 3$ as being an important condition for the definition of crucial events. It has to be stressed that ergodicity breakdown seems to be a general property of biological processes (Grigolini, 2015), not limited to the specific case of molecular diffusion in biological cells.

Returning to neurophysiology, we can make the conjecture that crucial events in the EEGs are signaled by abrupt transitions from regular to a fast irregular behavior, Rapid Transition Processes (RTPs). Allegrini et al. (2010) searched for these events in the brain of healthy patients using a technique for identification of RTPs in the brain activity proposed by brothers Fingelkurts and co-workers (Fingelkurts, 1998; Fingelkurts and Fingelkurts, 2005, 2006, 2008, 2015; Kaplan et al., 2005). After detecting them, Allegrini et al. (2010) proved that, as expected, the RTPs host crucial events.

On the basis of earlier remarks, crucial events are defined in terms of their statistical properties as follows. The time intervals between consecutive crucial events are described by the waiting-time PDF $\psi(\tau)$ having an IPL structure

$$\psi(\tau) \propto \frac{1}{\tau^{\mu}}, \tag{1}$$

with the IPL index μ in the interval

$$1 < \mu < 3. \tag{2}$$

From the earlier arguments, furthermore, it is clear that the crucial events are renewal and consequently the times τ_i should not be correlated. If a sequence of crucial events are defined by the time intervals τ_1,τ_2,τ_3,... then the time-average correlation function is a Kronecker delta function where the time average is indicated by an overbar

$$C(t) = \frac{\sum_{|i-j|=t} \overline{(\tau_i - \overline{\tau})\left(\tau_j - \overline{\tau}\right)}}{\sum_i \overline{(\tau_i - \overline{\tau})^2}}. \tag{3}$$

This correlation function is properly normalized, thereby yielding $C(0) = 1$, and in the case of genuine renewal events should satisfy the condition $C(t) = 0$ for $t > 0$. This renewal property can also be expressed by the assumption that the probability of occurrence of both τ_i and τ_j, $\Pi(\tau_i, \tau_j)$, when $i \neq j$ is given by,

$$\Pi(\tau_i, \tau_j) = P(\tau_i)P(\tau_j), \tag{4}$$

where $P(\tau_i)$ and $P(\tau_j)$ are the probability of occurrence of τ_i and τ_j, respectively.

Allegrini et al. (2010) following the line of thoughts illustrated in this Introduction conjectured that these crucial events are a signature of criticality and addressed the important tasks of detecting them from the observation of EEG time series (Coles and Rugg, 1995). The criticality hypothesis is in line with the views of many other researchers (Levina et al., 2007, 2009; Haimovici et al., 2013). In conclusion, the widely shared idea that the brain operates at criticality led to the discovery that crucial events act on the brain. This important conclusion left open two important problems, hereby illustrated. Their solutions are the main results of this paper.

1.1. First Problem

It is not yet clear what kind of criticality generates crucial events, either that determined by externally tuning a control parameter (Ising-like), or that achieved spontaneously through the internal system dynamics, i.e., self-organized criticality (SOC), is expected to afford a sufficient theoretical picture. We discuss the open issue of the proper form of criticality to use to increase our understanding of the brain dynamics in sections 5 and 6.

Here we stress that the research lines of this paper are determined by the recent form of self-organization called self-organized temporal criticality (SOTC) (Mahmoodi et al., 2017, 2018a,b; Mahmoodi et al., to be submitted). This form of criticality has been proposed for the purpose of establishing a new view of the field of Evolutionary Game Theory. The authors of this field explain the emergence of cooperation, in spite of the incentive for the single individual to cheat, and are looking for the spontaneous emergence of the global cognition that cooperation generates more social benefits, and consequently more benefits for the single individuals. SOTC shows that this cognition emerges naturally from a social interaction where the degree of social attention, which is related in some way to the control parameter of the ordinary approaches to phase transitions, is changed by the single individuals and it increases or decreases according to whether their overall social benefit increases or decreases.

1.2. Second Problem

The second problem left unsettled by the results of Allegrini et al. (2010) is how to make crucial events compatible with homeodynamics (Yates, 1994). Although SOTC has a sociological origin, it can also be applied to neurophysiological processes and more generally to biological processes satisfying the principle of homeodynamics. In this case the single units are oscillators that adjust their interactions with other units so as to maximize the reciprocal synchronization (Mahmoodi et al., to be submitted). This extension of SOTC yielding the emergence of global periodicity makes it difficult to make analytical predictions. Recent work (Lambert et al., to be submitted) bypasses this difficulty: it is a promising way to take homeodynamics into account so as to make periodic behavior compatible with crucial events, replacing extensive computations with analytical equations. This theoretical approach establishes a connection between coherence and criticality-induced crucial events, and was recently used (Tuladhar et al., 2018) to evaluate the influence of meditation on brain dynamics (Tuladhar et al., 2018) by means of the statistical analysis of the heart rate variability time series of these subjects.

The main result of the present paper is establishing an approach that simultaneously detects the statistical properties of crucial events and a connection with the wave-like nature of brain dynamics. The adoption of the RTP method is very attractive but, as shown in section 2, its adoption does not make it possible for us to measure the complexity of brain dynamics directly and in addition requires a filtering process. Herein we propose a technique of analysis of EEG time series data not requiring the detection of RTPs, and that leads to the detection of scaling directly from raw data. We show that the resulting scaling is identical to that obtained in earlier work using RTP's. More importantly, the present technique helps establish a bridge between EEG waves (di Santo et al., 2018) and crucial events. In fact, as shown in section 3, this bridge is expected to lead us to understand more about what form of criticality to apply to study the dynamics of the brain.

1.3. Outline of the Paper

In section 2 we review the procedure adopted to detect RTP events. We devote section 3 to an intuitive introduction to the process of self-organization combining periodicity and crucial events and in section 4 we analyze the spectrum of one EEG to point out the interesting qualitative agreement with the predictions of section 3 . In section 5 we illustrate a technique of detection of crucial events that facilitates the analysis of EEG time series. Finally, in section 6 we draw some conclusions and present plans for future work.

2. DETECTION OF RAPID TRANSITION EVENTS

As mentioned earlier, the efficacy of the RTP method in the study of brain dynamics has been established by the brothers Fingelkurts and co-workers (Fingelkurts, 1998; Fingelkurts and Fingelkurts, 2005, 2006, 2008, 2015; Kaplan et al., 2005). The connection between RTPs and crucial events has been demonstrated by Allegrini et al. (2010). However, for the sake of clarity we sketch here the approach adopted by the latter authors to obtain crucial events from RTPs, to emphasize the importance of recovering the same results for detecting the same scaling, using a very different technique. We base our analysis on data derived from Fingelkurts (1998), which are available in physionet.org Fingelkurts and Fingelkurts (2005).

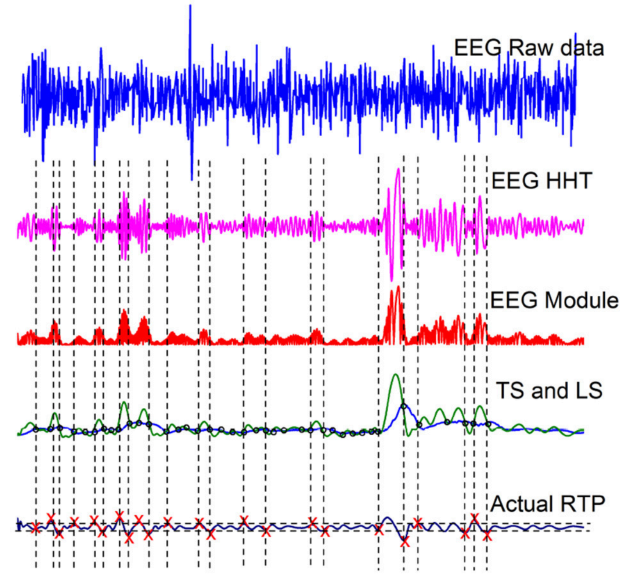

FIGURE 1 | Illustration of the RTP procedure of Kaplan et al. (2005).

These EEG time series data have been filtered between 0.15-28 Hz and the sampling rate (F_s) is 2048 Hz. We select one healthy subject, from the dataset, and the top panel of **Figure 1** shows the raw data of this subject. The second panel displays one intrinsic mode function, obtained adopting the method of Hilbert-Huang Transformation (HHT) illustrated in Huang and Wu (2008). The HHT method decomposes the original EEG signal into many intrinsic mode functions, with different structures. We select a structure with a kind of sausage-like pattern suggested by the theoretical results of (Bologna et al., 2010). They proved that a set of infinitely many three-state oscillators, cooperatively interacting with an interaction parameter K, at criticality generate a coherent non-harmonic oscillation. When the number of oscillators is finite the regular non-harmonic oscillations generate a sausage-like structure similar to the second panel of **Figure 1**. In section 6.1 we make additional remarks on the criticality-induced sausage-like structure.

The third panel from the top of **Figure 1** is the modulus of the data depicted in the second panel. The green curve in the fourth panel is the envelope of the curve of the third panel, called a Testing Sequence (TS). The blue curve in the fourth panel is the Level Sequence (LS) obtained from the TS by means of a running-average smoothing. Finally, the red crosses in panel five denote crucial events.

Note that this procedure for finding the crucial events is not sufficiently accurate to be restricted to detecting only renewal events. It is known that the events revealed by this analysis are a mixture of crucial events and ordinary Poisson events (Allegrini et al., 2010). However, the presence of Poisson events does not prevent us from detecting the anomalous scaling generated by the crucial events. The desired scaling is detected in the following way. The authors of Grigolini et al. (2001) use the detected events to generate a diffusion process $x(t)$ by means of the rule that the random walker jumps ahead when an event, either crucial or Poisson, occurs. The scaling generated by the Poisson events has a power-law index $\delta = 0.5$, whereas the scaling power-law index δ of the crucial events is given by the important relation

$$\delta = \frac{1}{\mu - 1}. \tag{5}$$

Note that the latter scaling dominates asymptotically in the time due to Equation (5) resulting in $\delta > 0.5$ when the condition $2 < \mu < 3$ applies (Grigolini et al., 2001). When $1 < \mu < 2$ crucial events yield the scaling $\delta = (\mu - 1)$, but the EEG time series studied in this paper and the subordination theory of section 3, adopted to explain their complexity, show that we need to focus on $\mu > 2$.

To be explicit, since in this paper as far as the scaling detection is concerned, we adopt the same procedure as that proposed by Grigolini et al. (2001), we generate a fluctuation $\xi(t)$ holding the value 1 when an event, either crucial or Poisson, occurs, and the vanishing value when no event occurs. The diffusion variable $x(t)$ is obtained from the following equation of motion

$$\frac{d}{dt}x = \xi(t). \tag{6}$$

Using a moving window of size t, we generate a PDF $p(x, t)$ and the Shannon information entropy

$$S(t) = -\int_{-\infty}^{+\infty} dx p(x, t) ln[p(x, t)]. \tag{7}$$

The PDF constructed from the diffusion process has the scaling form

$$p(x, t) = \frac{1}{t^{\delta}} F\left(\frac{x}{t^{\delta}}\right). \tag{8}$$

Then inserting Equation (8) into Equation (7), after some algebra yields

$$S(t) = A + \delta ln(t), \tag{9}$$

where A is the entropy constant

$$A \equiv -\int_{-\infty}^{+\infty} dy F(y) ln[F(y)]. \tag{10}$$

To make this treatment compatible with the subsequently discussed arguments about intermediate asymptotics, we rewrite Equation (9) in the following way

$$S(t) = C + \delta(t) ln(t), \tag{11}$$

where C denotes a constant that may differ from A, when, as we find herein, the proper complexity scaling emerges only in the region of *intermediate asymptotics*.

It is important to stress that a significant advance of the theoretical justification of Equation (11) based on an extension of the theory of SOC, incorporating complexity in the time domain, is called SOTC (Mahmoodi et al., 2017, 2018a,b). This new theory provides a rationale for the crucial IPL index μ. In fact, according to SOTC the processes of spontaneous self-organization, in general, and especially those behind the statistical analysis used herein, namely physiological processes, naturally evolves to a state generating the crucial events defined in section 1. These events manifest scaling in the intermediate time domain, called intermediate asymptotics (Goldenfeld, 1992; Barenblatt, 1996). As a consequence of temporal complexity emerging in the intermediate time scale, $S(t)$ is not a straight line when expressed as a function of $ln(t)$. As shown in **Figure 2**, entropy is a straight line in the intermediate time region and its slope is used to define the statistics of crucial events occurring within that region through the IPL index μ, established by Equation (5). This data analysis technique has been labeled the diffusion entropy approach (DEA).

To explain using an intuitive interpretation the intermediate asymptotics, we notice that the short-time region corresponds to the time scale where the self-organization is not yet perceived by the interacting units. According to SOTC (Mahmoodi et al., 2017), the intermediate time scale with temporal complexity becomes more and more extended as the number of units cooperatively interacting increases. However, the fluctuation intensity becomes smaller and the long-time scale is a sort of Poisson shoulder that, however, does not affect the communication efficiency of the complex system, since that efficiency is determined by the intermediate time region. The exponential truncation favors the transmission of information, because the flexibility of the complex system's response to the environment requires that the system explore a sufficiently high number of crucial events (*free-will states*) to adapt itself to the external influence. It has the effect of making the mean value of the time interval between consecutive crucial events finite, even in the case $\mu < 2$. We remind the reader that the theoretical mean time between crucial events is $< \tau > \propto 1/(\mu - 2)$, if $\mu > 2$ and it is divergent if $\mu < 2$ and the IPL PDF is not truncated.

The events generated by SOTC are renewal, which explains adopting Equation (5) for the connection between δ and μ, which is based in fact on the renewal assumption (Grigolini et al., 2001). We see from **Figure 2** that the subject examined with DEA procedure yields $\mu = 2.2$.

It is convenient to stress the fact that the choice of the RTP method, illustrated in **Figure 1**, has been motivated by the intuitive assumption that crucial events have physical effects. With reference to the second panel from the top of **Figure 1**, an event may be located in the short-time region of weak fluctuations separating the ending of one sausage from the beginning of another. Actually, the theoretical approach outlined in section 3 suggests that many more crucial events exist, thereby leading to a scaling method evaluation resting on a much larger

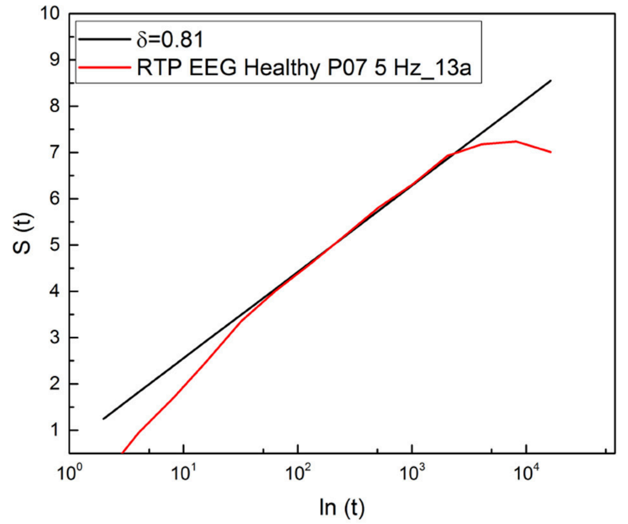

FIGURE 2 | Detection of the scaling δ applying DEA to the diffusion process generated by a random walker making a jump ahead when a crucial event occurs.

number of crucial events, even if, as in the case of the earlier mentioned method by the brothers Fingelkurts and co-workers (Fingelkurts, 1998; Fingelkurts and Fingelkurts, 2005, 2006, 2008, 2015; Kaplan et al., 2005), not all the events adopted to generate the diffusion process analyzed with DEA, are crucial.

3. SUBORDINATION

Establishing the statistics of the crucial events manifest in EEG time series by means of the detection of RTP, unfortunately, does not help us to build a bridge between the wavelike nature of EEG time series and crucial events. To establish the theoretical connection between the periodicity of EEG time series and crucial events, we adopt the SOTC model of units with an individual periodicity, for instance the SOTC model (Mahmoodi et al., 2017) as applied to the Kuramoto model (Kuramoto, 1975). This computationally demanding approach, however, has not yet been converted into an analytical approach for bridging the gap between waves and crucial events. We believe that the theoretical remarks of this section are a fair account of this form of SOTC.

The research work done in the recent past on the brain with the help of the RTP method led Allegrini et al. (2009) to conclude that the crucial events are characterized by values of μ very close to $\mu = 2$, according to the prescription

$$S(\omega) \propto \frac{1}{\omega^{3-\mu}}. \qquad (12)$$

The derivation of this spectrum was done by other researchers (Margolin and Barkai, 2006; Lukovic and Grigolini, 2008), who assumed that the time regions between consecutive crucial events are filled with either $+1's$ or $-1's$, values generated by a coin tossing algorithm. However, no direct evaluation of the EEG spectrum was done. Herein we see that if the EEG spectrum is evaluated, the frequency region for $\omega \rightarrow 0$ is affected by strong fluctuations making it difficult to assess the IPL property of Equation (12). However, we are able to shed light into the overall structure of the spectrum and we argue that this is compatible with Equation (12).

To establish a bridge between crucial events and periodicity, as done by Ascolani et al. (2009), we make an extension of the well known Continuous Time Random Walk (CTRW) (Montroll and Weiss, 1965; Sokolov, 2000; Shlesinger, 2017). The subordination to a coherent process with frequency Ω is a mathematically simple way of simulating a genuine process of self-organization. We have a clock, the hands of which move clockwise with frequency Ω from noon to noon, making T_{RR} clicks with the time interval Δt between one click and the next. Thus,

$$\Omega = \frac{2\pi}{T_{RR}\Delta t}. \qquad (13)$$

The crucial events, some of which have been detected by Allegrini et al. (2010) through the search of RTP, are imbedded into this regular motion, by assuming that the time interval between consecutive clicks is derived from a waiting-time PDF $\psi(\tau)$ with the temporal complexity of Equation (1). The explicit analytical form of $\psi(\tau)$ is

$$\psi(\tau) = (\mu - 1)\frac{T^{\mu-1}}{(\tau + T)^{\mu}}, \qquad (14)$$

corresponding to the survival probability

$$\Psi(\tau) = \left(\frac{T}{\tau + T}\right)^{\mu-1}. \qquad (15)$$

The parameter T serves the purpose of properly defining the short-time scale and setting the normalization condition $\Psi(0) = 1$. The temporal complexity becomes important at times $\tau \gg T$.

This procedure of infusing the original perfect coherence of the clock with complex randomness establishes a bridge between waves and crucial events. This has the effect of turning the frequency Ω into an effective frequency Ω_{eff}, thereby modeling a process of self-organization of interacting oscillators, each of which is characterized by its own frequency, into a collective homeodynamic process.

According to the theoretical treatment of Lambert et al. (to be submitted), the effective frequency is, valid for $\mu > 2$,

$$\Omega_{eff} = \frac{\Omega(\mu - 2)}{T}. \qquad (16)$$

This theoretical prediction suggests, in agreement with **Figure 3**, that the frequency peak is evident for $\mu > 2$ and that, in addition, it also depends on the parameter T of the waiting-time PDF $\psi(\tau)$ of Equation (14). This property is used in section 4 to shed light into the meaning of the HHT components of the method adopted to detect RTP events Huang and Wu (2008). In the range $\mu > 2$, when both the first and second moment of τ are finite, $\Omega_{eff} = \Omega$ (Lambert et al., to be submitted).

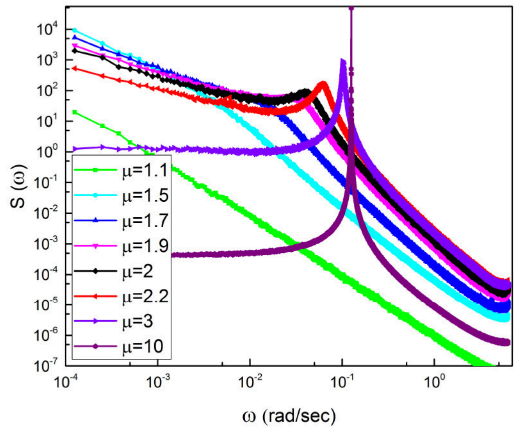

FIGURE 3 | Power Spectra obtained averaging over 300 trajectories with numerical parameters $T = 0.5$ and the regular oscillation before subordination has the frequency $\Omega = 0.77$. The inlay denotes the calculations for IPL indices spanning a range from 1.1 to 10.

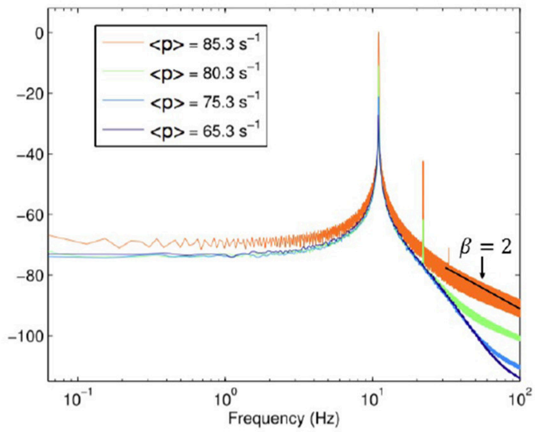

FIGURE 4 | Power Spectra derived with permission from Aburn et al. (2012) under the terms of the Creative Commons Attribution License http://creativecommons.org/licenses/by/3.0/.<p>denotestheneuronfiringrate.

This illustration of subordination makes it evident that crucial events are not only at the border between consecutive pieces of the sausage but the oscillatory-like behavior within a sausage hosts crucial events. It is surprising that the same conclusion has been achieved by the Fingelkurts brothers (Fingelkurts and Fingelkurts, 2005) who wrote "By varying the parameters of this technique it is possible to obtain the segments corresponding to a more or less detailed structure of the EEG/EMG. Therefore, there are prospects for the description of the structural EEG/EMG organization as a hierarchy of segmental descriptions on different time-scales. We make the conjecture that this may have the effect of establishing a correlation between the non-crucial events, thereby contributing a significant theoretical advance on the issue of cognition, and the effects of meditation on the dynamics of the brain (Tuladhar et al., 2018). This observation suggests that it should be possible to design a method of statistical analysis for extracting information from a larger set of crucial events even if they remain invisible.

Figure 3 illustrates spectra generated by surrogate sequences obtained using the subordination method with $\Delta t = 1$. We keep the frequency Ω fixed and change the IPL index μ. We note that a spectrum consists of three parts. There exists a peak corresponding to the effective frequency Ω_{eff} that shifts to the right upon decreasing μ and disappears for $\mu < 2$. At the left of the Ω_{eff} peak the slope of the spectrum β is determined to be

$$\beta = 3 - \mu. \tag{17}$$

We see that the spectrum becomes flat at $\mu = 3$ and remains flat for higher values of μ, as clearly shown in **Figure 3**.

Note that due to the average of many realizations, which is not possible with real EEG time series, the region of low frequency is regular and is not affected by the fluctuations that would appear when evaluating the spectrum with only one time series. For this reason, the adoption of surrogate time series makes it possible for us to prove that, as expected, subordination is compatible with the emergence of $1/f$ −noise in the ideal case $\mu = 2$.

Let us now discuss the spectra depicted in **Figure 4**, which was obtained by Aburn et al. (2012) by approaching the Hopf supercritical bifurcation in order to better understanding the alpha rhythm of human EEG time series. We note that this spectrum is similar to those of **Figure 3** when $\mu \geq 3$. In other words, this theory does not involve crucial events. It is interesting to notice that for values of ω larger than the peak frequency, the spectrum depicted in **Figure 4** yields the slope $\beta = 2$. The comparison between **Figures 3**, **4** indicates that subordination creates a bridge between periodicity and crucial events, while making the high-frequency region identical to that of a spectrum with no crucial events.

When $\mu < 3$ there exists a close connection between periodicity and complexity, as indicated in **Figure 3** showing that the position of the periodicity bump is very sensitive to the temporal complexity.

4. SPECTRA FROM RAW DATA

In this section we discuss the spectrum generated by real EEG time series fluctuations as shown in **Figure 5**. We see that the region of low frequencies is very erratic, due to the fact that, as mentioned earlier, the use of only one time series makes it impossible to generate a smooth curve. There exists an indication of a frequency bump, generated by periodicity, and for frequencies larger than this bump the slope $\beta = 2$ is rediscovered. This real spectrum depends on a wide swath of frequencies.

To stress the multi-frequency nature of the real spectrum, again using the HHT method (Huang and Wu, 2008) we evaluate six intrinsic mode functions of the EEG raw data corresponding to the spectrum of **Figure 5**. These different components of the whole signal correspond to six different frequencies of decreasing value. They are the frequencies: 26.84; 18.97 hz, 10.59 hz; 5.406 hz and 2.438 hz and 1.031 hz, which are shown in **Figure 6**.

In **Figure 7** we use the subordination prescription described in section 3, with Δt given by an inverse sampling frequency of real data ($\Delta t = \frac{1}{2048} sec$) to generate surrogate spectra, helping to clarify the meaning of the different spectra in **Figure 6**. We assign to the monochromatic frequency 62 hz with six different values of the parameters T, mimicking the dominant frequencies of the six HHT components illustrated in **Figure 6**. The real spectrum of **Figure 5** is interpreted as a superposition of the spectra illustrated in **Figure 7**. In fact all these spectra share the property $\beta = 3 - \mu$ in the low frequency region and the property $\beta = 2$ in the high frequency regions and intermediate region where the change of slope occurs is significantly broader than in the monochromatic case.

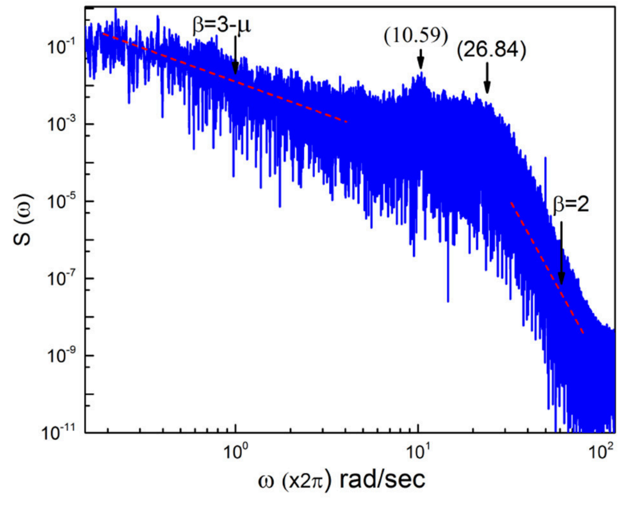

FIGURE 5 | Power Spectrum obtained from raw EEG time series data.

5. METHOD OF STRIPES

The stripe method was originally adopted to detect the scaling of crucial events hosted by heartbeats (Allegrini et al., 2002) and was not used in the case of EEG time series in all likelihood because of the lack of a proper theoretical understanding of the connection between crucial events and periodicity. The same method was more recently applied by Bohara et al. (2017) to establish a connection between the occurrence of crucial events and multifractality.

In section 3 we used an intuitive illustration of the process of self-organization, based on subordination that affords theoretical support for the adoption of the method of stripes. The central idea is that the RTP method detects only a small fraction of crucial events, whereas real EEG time series and subordination theory with them, host a much larger number of crucial events, even if they remain invisible.

Figure 8 shows how the method of stripes works. As is well known (Coles and Rugg, 1995), an EEG time series captures Event Related Potentials (ERPs) which, in turn, measures the rate of firing neurons. The method divides the vertical axis into many

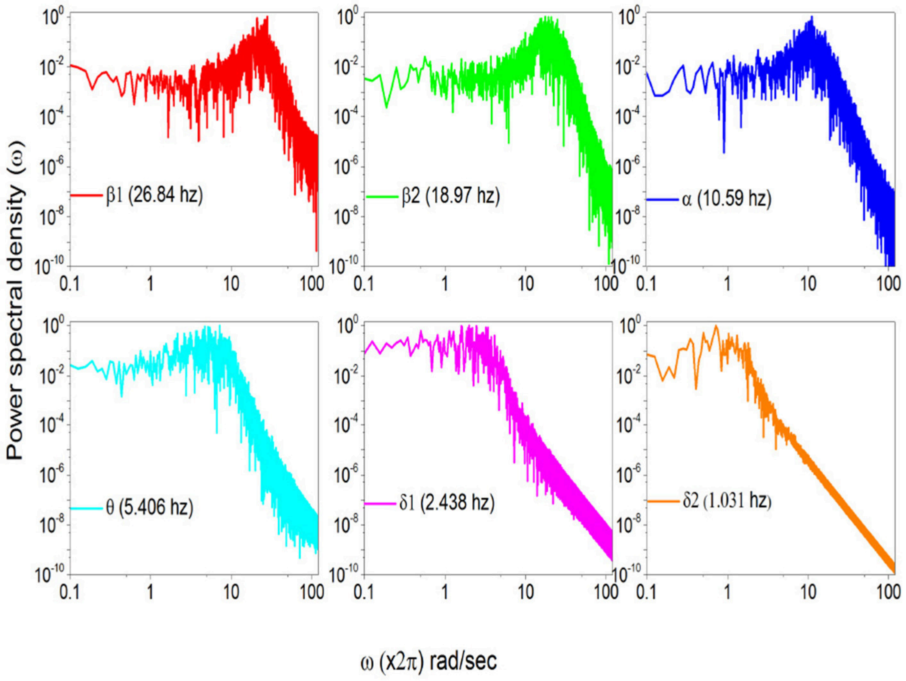

FIGURE 6 | Power Spectra of the same subject with different HHT frequency components.

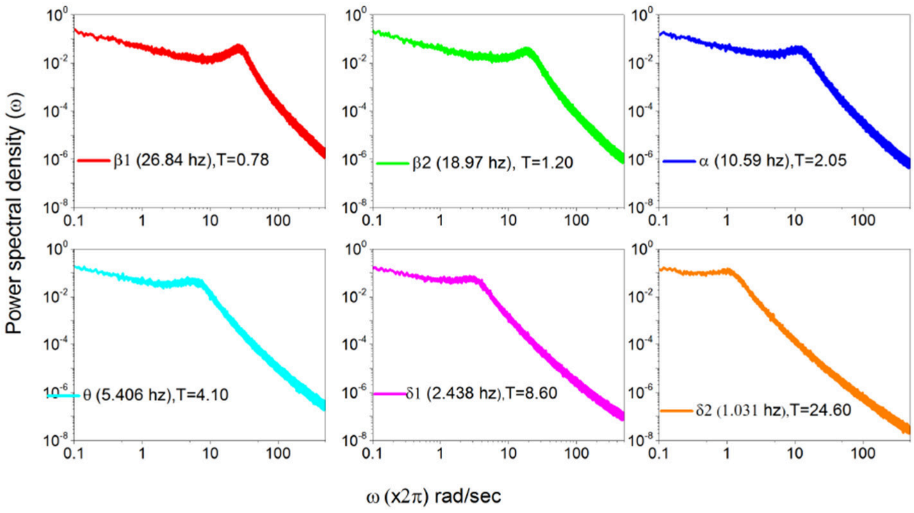

FIGURE 7 | Power Spectra generated using the data recorded in **Figure 6** according to subordination of section 3.

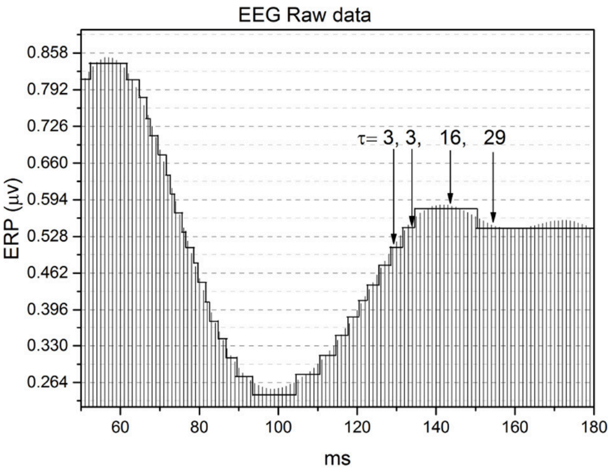

FIGURE 8 | Illustration of the method of the stripes. The size of stripes is $\Delta E = 1/30\ \mu$v.

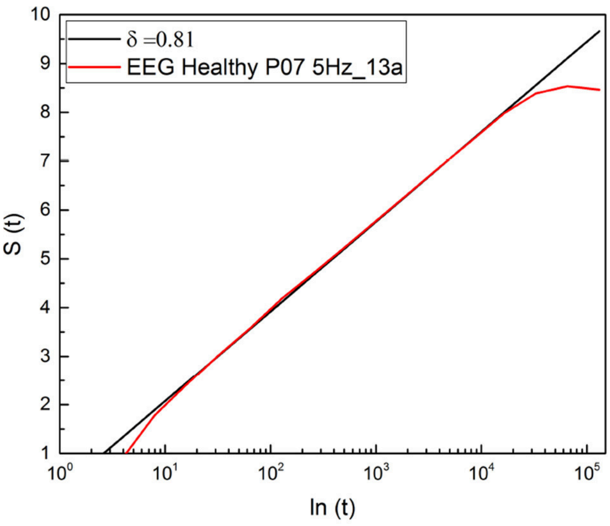

FIGURE 9 | DEA applied to the diffusion process generated by the stripe-crossing events.

stripes of size ΔE, here assumed to have the value $\Delta E = 1/30$ μv, and we record the times at which the raw signal crosses the line separating two adjacent stripes. The level of the stripe is determined by the number of neuron firings at a given time, and we record for how long that firing rate remains constant.

The change from one firing rate to another is an event. Of course this event is not necessarily a crucial event. As a consequence, the time interval between consecutive events cannot be used to define the important parameter μ. This lack of precision in determining the occurrence of crucial events applies also to the RTP method. Let us call N_T the total number of events detected, N_c the total number of (unknown) crucial events and N_{nc} the total number of non-crucial, possibly Poisson events. The intermediate asymptotics, revealing the complex scaling δ of Equation (5), begins earlier upon increase of the ratio

$$r_c \equiv \frac{N_c}{N_T}. \tag{18}$$

In both cases, the adoption of the DEA method is essential. In fact, after recording events with the method of stripes, as done with the method of RTP, we adopt the prescription of Grigolini et al. (2001). We again turn the sequence of detected events, either crucial or not, into a diffusion signal $x(t)$ by making the random walker jump ahead by a fixed quantity, equal to 1. As pointed out in section 2, the non-crucial events generates a diffusion process with scaling $\delta = 0.5$ and the crucial events, on the contrary, generate the scaling index of Equation (5) that for $\mu > 2$ is larger than 1/2, thereby making it possible for DEA to establish the correct scaling of Equation (5) at long times.

The result illustrated in **Figure 9** shows that the scaling detected with this method is virtually identical to the result obtained with the use of RTP method. In both cases the complex scaling of Equation (5) appears in the intermediate time regime, but it appears that the present method is more accurate, since the slope covers three decades of scale, see **Figure 9**, while the RTP method is limited to only two decades (**Figure 2**). This is a clear indication that the method of stripes makes the ratio r_c of Equation (18) significantly larger than the RTP method.

6. CONCLUDING REMARKS

The adoption of the RTP method makes it easy to establish the non-local nature of the brain criticality (Allegrini et al., 2010). This is a consequence of the fact that it is sufficient to count how many electrodes undergo RTP's at the same times. However, the detailed illustration in section 2 shows that the procedure to establish the occurrence of an RTP is not straightforward and we conjecture that it may be replaced by the adoption of a cross-correlation function between the EEG time series generated by different electrodes. But this remains to be verified.

6.1. Self-Organized Temporal Criticality(SOTC)

The sausage-like structure of the model studied by Bologna et al. (2010) has a surprising similarity to the second panel from the top of **Figure 1**. This is not accidental. In fact, the theory adopted by (Bologna et al., 2010) is a phase transition obtained by the control parameter K taking on the critical value $K = 1.5$. At criticality the oscillators are no longer independent of one another and as a result of highly correlated motion they generate a regular non-harmonic oscillation.

The SOTC is a new form of self-organization studied by Mahmoodi et al. (2017, 2018b), which establishes a significant difference between critical slowing down and temporal complexity. In the case of a conventional form of criticality, where the control parameter is finely tuned so as to generate phase transition (Beig et al., 2015) the two forms of complexity can be mistakenly judged to be equivalent. When a system at criticality is assigned a distribution different from the equilibrium distribution, the system is expected to relax back toward equilibrium with infinitely slow motion (critical slowing down). When the number of units is finite the mean field fluctuates around the mean value and the time interval between consecutive origin re-crossings, temporal complexity, may be as slow as critical slowing down (Beig et al., 2015).

In the case of SOTC the time necessary to evolve toward the condition of temporal criticality is finite (Mahmoodi et al., 2017, 2018b). In the special case studied by Bologna et al. (2010), another form of criticality generated by the fine tuning of the control parameter, but combining crucial events with periodicity, the mean field does not have regular oscillations: the intensity of these oscillations and their frequency are modulated in time generating the sausage-like structure of the second panel from the top of **Figure 1**. SOTC of a set of cooperating oscillators is expected to spontaneously lead to the same qualitative results. Subordination theory affords a simple way of mimicking this process of organization, introducing *ad hoc* the crucial events, which actually are the results of a spontaneous self-organization.

The processes of phase transitions are characterized by IPL PDFs with indices expressing the universality of criticality. The construction of renormalization group theory made it possible to determine without a detailed knowledge of the micro-interactions of the system, the scaling nature of phase transitions. In the case of the brain the micro-units, whose dynamics depart from the erratic behavior of independent units to collective behavior at criticality, are neurons. However, in spite of the frequent use of the term SOC these models rest on tuning a control parameter to a critical value that establishes global properties making the micro-dynamics unimportant in favor the macro-dynamics of criticality. If a neuron fires all the neurons linked to it makes a step ahead toward the firing level. Criticality is a condition generated by a suitable value of the control parameter that establishes a complex dynamics characterized by temporal complexity, namely, the crucial events defined in section 1. An interesting example of “Self-organized criticality” is given by Levina et al. (2009). They propose a very interesting model generating super-criticality and sub-criticality as well as criticality, a puzzling result because we expect that a process of self-organization may lead only to criticality. We make the conjecture that SOTC may realize this wide set of condition depending on how the process of self-organization is realized.

6.2. Future Research Work

The results of this paper suggest promising directions to establish homeodynamics as a form of genuinely spontaneous organization. SOTC (Mahmoodi et al., 2017) affords the prescription to turn a set of independent Poisson units, fluctuating between the values $\xi = 1$ and $\xi = -1$, into a self-organized system, thereby yielding, with a finite number of units, temporal complexity and crucial events. It is important to stress that, as shown by Mahmoodi et al. (2017), SOTC is a generator of complexity in line with the important concept of *intermediate asymptotics* of Barenblatt (Goldenfeld, 1992; Barenblatt, 1996). This is made evident in **Figures 2**, **9**. The deviation of the scaling in both the short-time and long-time regions from the complex prediction of Equation (5) is not due to the numerical inaccuracy of DEA. Rather it is a surprising benefit of this technique of analysis that does not rely on the evaluation of the second moment of the PDF $p(x, l)$ of Equation (8), but is a direct consequence of the general scaling behavior of the PDF. Not only is the PDF not forced to be Gaussian, its exact function form is not important.

These remarks lead us to conclude that the subordination theory used in this paper is an appropriate way to mimic the self-organization of units characterized by periodicity, as manifest in their spectra.

The comments we make in section 3 on the surprising agreement between the physical meaning of SOTC and the architectonic structures of Fingelkurts and Fingelkurts (2005) deserves further study. In our view, the interesting review paper (Fingelrkurts et al., 2012) provides directions on how to approach the challenging problem of cognition especially if it is supplemented by the contribution that emotion is expected to afford to it (Tuladhar et al., 2018), presumably through the proper action that meditation and emotion may exert on the non-crucial events.

ETHICS STATEMENT

We base our analysis on data derived from Matran-Fernandez and Polo (2017), which are available in physionet.org Goldberger et al. (2000). Matran-Fernandez and Polo (2017) has the following information. The study received the approval from the Ethics Committee of the University of Essex, and consent was obtained from all participants in written form prior to the beginning of the experiment. Recruitment of volunteers was performed via advertising through the University of Essex's mailing lists in February-March 2013. Only participants above 18 years old were considered for the experiment. Moreover, given the high presentation rates that are used in the RSVP protocol, participants were also screened for any personal or family history of epilepsy. No other exclusion criteria were used. Using these criteria, no participants were excluded from the experiment. All participants completed the experiment and were included in the analysis. No power analysis was performed to calculate sample size.

AUTHOR CONTRIBUTIONS

All authors listed have made a substantial, direct and intellectual contribution to the work, and approved it for publication.

ACKNOWLEDGMENTS

The authors thank Welch and ARO for financial support through Grant No. B-1577 and W911NF- 15-1-0245, respectively.

REFERENCES

Aburn, M. J., Holmes, C. A., Roberts, J. A., Boonstra, T. W., and Breakspear, M. (2012). Critical fluctuations in cortical models near instability. *Front. Physiol.* 3:331. doi: 10.3389/fphys.2012.00331

Allegrini, P., Grigolini, P., Hamilton, P., Palatella, L., and Raffaelli, G. (2002). Memory beyond memory in heart beating, a sign of a health physiological condition. *Phys. Rev. E* 65:041926. doi: 10.1103/PhysRevE.65.041926

Allegrini, P., Menicucci, D., Bedini, R., Fronzoni, L., Gemignani, A., Grigolini, P. et al. (2009). Spontaneous brain activity as a source of ideal 1/f noise. *Phys. Rev. E* 80:061914. doi: 10.1103/PhysRevE.80.061914

Allegrini, P., Menicucci, D., Bedini, R., Gemignani, A., and Paradisi, P. (2010). Complex intermittency blurred by noise: theory and application to neural dynamics. *Phys. Rev. E* 82:015103 R. doi: 10.1103/PhysRevE.82.015103

Allegrini, P., Paradisi, P., Menicucci, D., and Gemignani, A. (2010). Fractal complexity in spontaneous EEG metastable-state transitions: new vistas on integrated neural dynamics. *Front. Physiol.* 1:128. doi: 10.3389/fphys.2010.00128

Ascolani, G., Bologna, M., Grigolini, P. (2009). Subordination to periodic processes and synchronization. *Physica A* 388:2727. doi: 10.1016/j.physa.2009.03.025

Barenblatt, G. I. (1996). *Scaling, Self-Similarity, and Intermediate Asymptotics*. Cambridge: Cambridge University Press.

Beig, M. T., Svenkeson, A., Bologna, M., West, B. J., Grigolini, P. (2015). Critical slowing down in networks generating temporal complexity. *Phys. Rev.* 91:012907. doi: 10.1103/PhysRevE.91.012907

Bohara, G., Lambert, D., West, B. J., and Grigolini, P. (2017). Crucial events, randomness, and multifractality in heartbeats. *Phys. Rev. E* 96:062216. doi: 10.1103/PhysRevE.96.062216

Bologna, M., Geneston, E., Grigolini, P., Turalska, M., and Lukovic, M. (2010). "Coherence and complexity," in *Decision Making,* ed P. Grigolini and B. J. West (Singapore: World Scientific), 119–134. doi: 10.1142/9789814365826_0007

Boonstra, T. W., He, B. J., and Daffertshofer, A. (2013). Scale-free dynamics and critical phenomena in cortical activity. *Front. Physiol.* 4:79. doi: 10.3389/fphys.2013.00079

Cocchi, L., Gollo, L. G., Zalesky, A., and Breakspear, M. (2017). Criticality in the brain: a synthesis of neurobiology, models and cognition. *Progr. Neurobiol.* 158:132. doi: 10.1016/j.pneurobio.2017.07.002

Coles, M. G. H., and Rugg, M. D. (1995). "Event-related brain potentials: an introduction," in *Electrophysiology of the Mind. Event-related Potentials and Cognition*, eds M. Rugg and M. Coles (Oxford: Oxford University Press), 1–26.

Contoyiannis, Y. F., and Diakonos, F. K. (2000). Criticality and intermittency in the order parameter space. *Phys. Lett. A* 268:286. doi: 10.1016/S0375-9601(00)00180-8

Contoyiannis, Y. F., Diakonos, F. K., and Malakis, A. (2002). Intermittent dynamics of critical fluctuations. *Phys. Rev. Lett.* 89:035701. doi: 10.1103/PhysRevLett.89.035701

di Santo, S. Villegas, P., Burioni, R., and Muñoz, M. A. (2018).Landau-Ginzburg theory of cortex dynamics: Scale-free avalanches emerge at the edge of synchronization. *Proc. Natl. Acad. Sci. U.S.A.* 115:E1356. doi: 10.1073/pnas.1712989115

Fingelkurts, A. A. (1998). *Time-spatial organization of the human EEG segmental structure* Ph.D. Dissertation, Russian Federation, MSU, Moscow.

Fingelkurts, A. A., and Fingelkurts, A. A. (2005). "Mapping of the brain operational architectonics" in *Focus on Brain Mapping Research*, ed F. J. Chen (Hauppague, NY: Nova Science Publishers, Inc.), 59–98.

Fingelkurts, A. A., and Fingelkurts, A. A. (2006). Timing in cognition and EEG brain dynamics: discreteness versus continuity. *Cogn. Process.* 7:135. doi: 10.1007/s10339-006-0035-0

Fingelkurts, A. A., and Fingelkurts, A. A. (2008). Brain-mind operational architectonics imaging: technical and methodological aspects. *Open Neuroimaging J.* 2:73. doi: 10.2174/1874440000802010073

Fingelkurts, A. A., and Fingelkurts, A. A. (2015). Operational architectonics methodology for EEG analysis: theory and results. *Neuromethods* 91:1. doi: 10.1007/7657_2013_60

Fingelrkurts, A. A., Fingelkurts, A. A. and Neves, C. F. H. (2012). "Machine" consciousness and "artificial" thought: an operational architectonics model guided approach. *Brain Res.* 1428:80. doi: 10.1016/j.brainres.2010.11.079

Goldberger, A. L., Amaral, L. A. N., Glass, L., Hausdorff, J. M., Ivanov, P. C., Mark, R. G., et al. (2000). Stanley, physioBank, physioToolkit, and physioNet: components of a new research resource for complex physiologic signals. *Circulation* 101:e215–e220. doi: 10.1161/01.CIR.101.23.e215

Goldenfeld, N. (1992). *Lectures on Phase Transitions and the Renormalization Group*. Reading, MA: Addison-Wesley Publishing Company.

Grigolini, P. (2015). Emergence of biological complexity: criticality, renewal and memory. *Chaos Solitons Fractals* 81:575. doi: 10.1016/j.chaos.2015.07.025

Grigolini, P., Palatella, G., and Raffaelli, G. (2001). Asymmetric anomalous diffusion: an efficient way to detect memory in time series. *Fractals* 9:439. doi: 10.1142/S0218348X01000865

Haimovici, A., Tagliazucchi, E., Balenzuela, P., and Chialvo, D. R. (2013). Brain organization into resting state networks emerges at criticality on a model of the human con-nectome. *Phys. Rev. Lett.* 110:178101. doi: 10.1103/PhysRevLett.110.178101

Huang, N. E., and Wu, Z. (2008) A review on Hilbert-Huang transform: method and its applications to geophysical studies. *Rev. Geophys. Wiley Online Lib.* 46:2. doi: 10.1029/2007RG000228

Kaplan, A. Y., Fingelkurts, A. A., Fingelkurts, A. A., Borisov, B. S., and Darkhovsky, B. S. (2005). Nonstationary nature of the brain activity as revealed by EEG/MEG: methodological, practical and conceptual challenges. *Signal Proces* 85:2190. doi: 10.1016/j.sigpro.2005.07.010

Kuramoto, Y. (1975). Self-entrainment of a population of coupled non-linear oscillators, in *International Symposium on Mathematical Problems in Theoretical Physics* (Berlin;Heidelberg: Springer).

Levina, A., Herrmann, J. M., and Geisel, T. (2007). Dynamical synapses causing self-organized criticality in neural networks. *Nature Phys.* 3, 857–860. doi: 10.1038/nphys758

Levina, A., Herrmann, J. M., and Geisel, T. (2009). Phase transitions towards criticality in a neural system with adaptive interactions. *Phys. Rev. Lett.* 102:118110. doi: 10.1103/PhysRevLett.102.118110

Lukovic, M., and Grigolini, P. (2008). Power spectra for both interrupted and perennial aging processes. *J. Chem. Phys.* 129:184102. doi: 10.1063/1.3006051

Mahmoodi, K., Grigolini, P., and West, B. J. (2018a). On social sensitivity to either zealot or independent minorities. *Chaos Solitons Fractals* 110:185. doi: 10.1016/j.chaos.2018.03.028

Mahmoodi, K., West, B. J., and Grigolini, P. (2017). Self-organizing complex networks: individual versus global rules. *Front. Physiol.* 8:478. doi: 10.3389/fphys.2017.00478

Mahmoodi, K., West, B. J., and Grigolini, P. (2018b). Self-organized temporal criticality: bottom-up resilience versus top-down vulnerability. *Complexity* 2018:8139058. doi: 10.1155/2018/8139058

Manneville, P., and Pomeau, Y. (1979). Intermittency and Lorenz model. *Phys. Lett. A* 75:1. doi: 10.1016/0375-9601(79)90255-X

Margolin, G., and Barkai, E. (2006). Nonergodicity of a time series obeying Lévy statistics. *J. Stat. Phys.* 122:137. doi: 10.1007/s10955-005-8076-9

Matran-Fernandez, A., and Polo, R. (2017). Towards the automated localization of targets in rapid image-sifting by collaborative brain-computer interfaces. *PLoS ONE* 12:178498. doi: 10.1371/journal.pone.0178498

Metzler, R., Jeon, J.-H., Cherstvya, A. G., and Barkai, E. (2014). Anomalous diffusion models and their properties: nonstationarity, non-ergodicity, and ageing at the centenary of single particle tracking. *Phys. Chem. Chem. Phys.* 16:24128. doi: 10.1039/C4CP03465A

Montroll, E., and Weiss, G. H. (1965). Random walks on lattices. II. *J. Math. Phys.* 6:167. doi: 10.1063/1.1704269

Papo, D. (2013). Time scales in cognitive neuroscience. *Front. Physiol.* 4:86 . doi: 10.3389/fphys.2013.00086

Papo, D., Zanin, M., Pineda-Pardo, J. A., Boccaletti, S., and Buldú, J. M. (2014). Functional brain networks: great expectations, hard times and the big leap forward. *Phil. Trans. R. Soc. B* 369:20130525. doi: 10.1098/rstb.2013.0525

Pomeau, Y., and Manneville, P. (1980). Intermittent transition to turbulence in dissipative dynamical system. *Commun. Math. Phys.* 74:189. doi: 10.1007/BF01197757

Shlesinger, M. (2017). Origins and applications of the Montroll- Weiss continuous time random walk. *Eur. Phys. J. B.* 90:93. doi: 10.1140/epjb/e2017-80008-9

Sokolov, I. M. (2000). Lévy Flights from a continuous-time process. *Phys. Rev. E* 63:011104. doi: 10.1103/PhysRevE.63.011104

Tagliazucchi, E., Balenzuela, P. D. Fraiman, D. R., and Chialvo, A. (2012). Criticality in large-scale brain fMRI dynamics unveiled by a novel point process analysis. *Front. Physiol.* 3:15. doi: 10.3389/fphys.2012.00015

Tuladhar, R., Bohara, G., Grigolini, P., and West, B. J. (2018) Meditation-induced coherence and crucial events. *Front. Physiol.* 9:626. doi: 10.3389/fphys.2018.00626

Yates, F. E. (1994). Order and complexity in dynamical systems: homeodynamics as a generalized mechanics for biology. *Math. Comput. Model.* 19:49. doi: 10.1016/0895-7177(94)90189-9

Conflict of Interest Statement: The authors declare that the research was conducted in the absence of any commercial or financial relationships that could be construed as a potential conflict of interest.

Copyright © 2018 Bohara, West and Grigolini. This is an open-access article distributed under the terms of the Creative Commons Attribution License (CC BY). The use, distribution or reproduction in other forums is permitted, provided the original author(s) and the copyright owner(s) are credited and that the original publication in this journal is cited, in accordance with accepted academic practice. No use, distribution or reproduction is permitted which does not comply with these terms.

frontiers
in Physiology

ORIGINAL RESEARCH
published: 04 December 2018
doi: 10.3389/fphys.2018.01707

Measures and Metrics of Biological Signals

Obrad Kasum[1], *Aleksandar Perović*[1,2]* *and Aleksandar Jovanović*[1]

[1] *Group for Intelligent Systems (GIS), Faculty of Mathematics, University of Belgrade, Belgrade, Serbia,* [2] *Faculty of Transport and Traffic Engineering, University of Belgrade, Belgrade, Serbia*

The concept of biological signals is becoming broader. Some of the challenges are: searching for inner and structural characteristics; selecting appropriate modeling to enhance perceived properties in the signals; extracting the representative components, identifying their mathematical correspondents; and performing necessary transformations in order to obtain form for subtle analysis, comparisons, derived recognition, and classification. There is that unique moment when we correspond the adequate mathematical structures to the observed phenomena. It allows application of various mathematical constructs, transformations and reconstructions. Finally, comparisons and classifications of the newly observed phenomena often lead to enrichment of the existing models with some additional structurality. For a specialized context the modeling takes place in a suitable set of mathematical representations of the same kind, a set of models M, where the mentioned transformations take place. They are used for determination of structures **M**, where mathematical finalization processes are preformed. Normalized representations of the initial content are measured in order to determine the key invariants (characterizing characteristics). Then, comparisons are preformed for specialized or targeted purposes. The process converges to the measures and distance measurements in the space **M**. Thus, we are dealing with measure and metric spaces, gaining opportunities that have not been initially available. Obviously, the different aspects in the research or diagnostics will demand specific spaces. In our practice we faced a large variety of problems in analysis of biological signals with very rich palette of measures and metrics. Even when a unique phenomena are observed for slightly different aspects of their characteristics, the corresponding measurements differ, or are refinements of the initial structures. Certain criteria need to be fulfilled. Namely, characterization and semantic stability. The small changes in the structures have to induce the small changes in measures and metrics. We offer a collection of the models that we have been involved in, together with the problems we met and their solutions, with representative visualizations.

Keywords: measures of biological signals, metrics on biological signals, complexity, dimension, similarity

OPEN ACCESS

Edited by:
Sladjana Z. Spasić,
University of Belgrade, Serbia

Reviewed by:
Fred Hasselman,
Radboud University Nijmegen,
Netherlands
Zoran M. Nikolic,
University of Belgrade, Serbia
Ion Andronache,
University of Bucharest, Romania

****Correspondence:***
Aleksandar Perović
pera@sf.bg.ac.rs

Specialty section:
This article was submitted to
Fractal Physiology,
a section of the journal
Frontiers in Physiology

Received: *14 June 2018*
Accepted: *13 November 2018*
Published: *04 December 2018*

Citation:
Kasum O, Perović A and Jovanović A
(2018) Measures and Metrics of
Biological Signals.
Front. Physiol. 9:1707.
doi: 10.3389/fphys.2018.01707

INTRODUCTION

A biological signal is any mapping (change) of a biological quantity/content into the corresponding set (codomain), with the purpose to represent the particular process in a form suitable for studying, monitoring, determination of functional connections (relations, dependence) between the studied quantity and its relevant constituents.

The change in biological quantities can have particular significance and lead to discovering of deep processes hidden from the direct (e.g., visual) observations. Long ago, it was discovered that biological organisms function through a sequence of interconnected processes-results of action of systems and subsystems within a hierarchically organized functions.

Hence, it is prudent to formally define a biological signal as a function of the form $f : D \rightarrow M$ that maps the initial set of biological phenomena (states, conditions, etc.) D into the corresponding codomain M of measurement data. For example, such signals are the usual home or clinical measurement of the body temperature, arterial pressure or atmospheric pressure, performed sporadically or at regular intervals. The purpose is to determine their current values, and to monitor their change in time in order to identify the presence of pathology, or to control the side effects of introduced drugs that may have negative impact on systems regulating vital functions.

Certain biological phenomena such as body temperature or blood pressure are analog. The number of erythrocytes, or the number of bacteria per space unit are examples of digital signals, but with a large number of units. The corresponding measuring procedures are designed to obtain the suitable approximations within some finite scale. For example, the body temperature of a living human is scaled by the degrees in Celsius, with $\min = 35^{\circ}C$ and $\max = 42^{\circ}C$. Similarly, the blood pressure is scaled by a height in millimeters of Hg in a capillary tube, while the number of erythrocytes is scaled in thousands per space unit etc. The basic concepts about analog and digital quantities can be found in textbooks (Attenborough, 2003; Werde and Spiegel, 2010; Hsu, 2014).

On the other hand, measurements are performed in order to assess the presence or the absence of a property/pathology. As such, they are composed with the additional binary scale (absence, presence), ternary scale (absence, presence, strong presence), and so on. Some phenomena require more complex structures involving indications of inner dependences, usually represented by multigraphs.

Regardless of the form of the performed measurements, the modern computers are at such technical level that allows implementation of various numerical and symbolic algorithms related to acquisition, representation, analysis and transformation/manipulation of biological signals. Hence, the modern representation of biological signals use mathematical structures (numerical or abstract) suitable for digitization, exact representation, deeper insights and finally, classification. In the very rich variety of biological signals, here we focus on some mathematical representation and operation aspects involving broad range of applications, thus illustrating the rich abundance of phenomena and their mathematical treatment, rather than trying to have more complete approach, which needs much larger space and more complex method coverage.

Automated acquisition and processing of biological signals has opened the possibility of elimination of subjectivity in validation and interpretation of a measurement. At the same time, digitization has enabled application of the large mathematical apparatus, making possible nontrivial transformations of the initial content. The large number of scientific breakthroughs that are made in this way has established the new, highly prominent scientific discipline involving broad mathematical modeling and their computer implementations.

Developing some systems for operation with biological signals, in our group GIS (Group for Intelligent Systems), we have implemented systems for digital upgrades of the existing analog research and clinical equipment for the measurement of e.g., arterial pressure, ECG, EEG, specific neurology, ultrasound, NMR, and digital microscopy signals. Those systems have enabled digital acquisition of the various types of related signals, including biometric parameters like voice and fingerprints, acquisition of various molecular biology signals like chromosomes and genetic sequences. We have also implemented tools for representation, visualization, manipulation and transformation of signals and integrated it with the CCD computerized microscopy.

In particular, developed software solutions include: signal monitoring, acquisition and real time analysis (the first version was implemented in 1994); image acquisition and analysis (1994); image spectroscopy (1995), photomorphology (1995–1998), color combine fluorescent microscopy (1997–1998); automatized karyotyping involving object recognition, normalization, and classification (1997).

As mentioned above, before implementation, all measurements and analyses were performed manually by direct observation. The improvement in efficiency and precision was immediately observed by the involved researches. Developed solutions have been in use for almost two decades at more than 20 research laboratories at the University of Belgrade, Lomonosov state university at Moscow, and UC Berkeley, see (Jovanović, 2001; Jovanović et al., 2014).

In addition, we have also developed hardware for those laboratories including CCD microscopes, computerized EEG, ECG, CTG, acoustic RT spectroscopes, equipment for recording of magnetic field attenuation etc. (see Jovanović, 2001; Jovanović et al., 2014).

Those systems have enabled precise measurements, significant reduction of errors previously made by subjective visual detection of important features, nontrivial numerical, algebraic, geometrical, topological, and visual transformations of the acquired signals and integration with other related computerized systems. In particular, images displayed at **Figures 1**, **2**, **4**, **7–9**, **12** and **21** were produced by the mentioned software for signal acquisition, processing and visualization.

In last few decades we are witnessing impressive developments of technologies and methods implemented in biological signals. More powerful instrument perception is progressing together with more powerful and more sophisticated methods.

BASICS

A biological signal, coded in computer as a digital function, is usually a finite approximation of an analog signal. Consequently, sampling resolution should be sufficient in order to provide a quality acquisition, enabling detection, extraction, recognition, and normalization of important features in signals and adequate comparison with etalons. Moreover, the successful implementation of mentioned procedures can be further enriched to fully or highly automated systems for classification,

FIGURE 1 | A mammal acoustic signal.

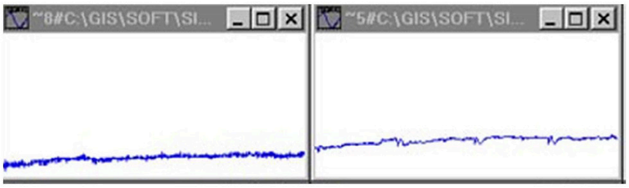

FIGURE 2 | Arterial pressure signals with implanted transducers (rats) (Jovanović, 2001; Jovanović et al., 2014).

reasoning, and decision making. This aim is the essential improvement of the previously achieved insights.

The older (we can say classical) methods, that are usually simple, do not necessarily lead to simplifications, though they are often ballasted with certain semantic limits. On the other hand, the more modern and sophisticated methods do not necessarily improve our knowledge. In the case of careless application, they might lead to false understanding with broader poor consequences. Some of issues related to methods for computation of Granger causality were discussed in (Kasum et al., 2015).

The application of Mathematics and Statistics require permanent criticism and scrutiny, especially in the points where these are connected to non-mathematical semantics. The proper mix of simple and complex modeling could offer substantial advantages.

The initial signal usually requires preprocessing involving different types of normalizations. The standard examples are:

- Filtering of electrophysiological signals;
- Filtering of microscopic optic signals and certain preprocessing operations, e.g., determination of contours of microscopic objects or their nonlinear transformations, or determination of contours of spectrogram features.

Discrete and continual counting measures normalized to the real unit interval are the most prominent measures present in expression of the observed statistical dependences, statistical analysis of the experimental data, probabilistic estimations on finite domains, or on more abstract mathematical structures.

Biomedical statistical analysis involves comparison with the control group, computation of the relevant statistics (e.g., mean, variance, correlation coefficient, $p-$value, $F-$ statistics etc.), determination of the regression curves (so called curve fitting) and so on. Statistics has proved to be a very important and powerful mathematical method in biological experimentation, indispensable in the contemporary research and scientific publishing. Conceptual correspondence between the initial measurement and their statistical interpretation always require additional observation and unbiased critical analysis of the initially proposed connections between the natural semantics of the studied phenomena and the constructed mathematical (statistical) model. The following examples will illustrate main issues with semantic stability in the above connection. For basic concepts about statistics we refer the reader to the textbook (Spiegel and Stephens, 2018).

Example 2.1 A simple sinusoidal oscillation $y = f(x)$ around c on the interval $[a, b]$ will be by the application of the standard signal energy measure $\int_a^b f(x)\,dx$ identified with its mean value, which is the constant function $y = c$ (**Figure 6**.)

As a consequence of the integration, any additional information that the initial signal carry will be lost. ☐

Example 2.2 Consider the signal $y = f(x)$ defined by

$$\begin{aligned} f(x) &= 440 \cdot 1_{[0,1)}(x) + 528 \cdot 1_{[1,2)}(x) + 660 \cdot 1_{[2,3)}(x) \\ &\quad + 528 \cdot 1_{[3,4)}(x) + 440 \cdot 1_{[4,5]}(x) \end{aligned}$$

for $0 \leq x \leq 5$. Its average energy $\int_0^5 f(x)dx$ is adequately represented by its mean value $y = 519.2$ (see **Figure 10**).

However, the above signal can be interpreted as a producing the equal length tunes a, c_1, e_1, c_1, a (frequencies on the y axis, A-minor chord), while the corresponding mean 519.2, is atonal and does not have any meaningful connection with the played melody.

METHOD

Complexity Issues

While dealing with simple signals, with simple changes in time, the direct simple representation/visualization is often satisfactory. However, the study of subtler details and processes, and integration of system insight, requires increased complexity. The modern research demands, with invisible important features, higher complexity in representations, and involved structures. This is the point of departure from the simple and simplest representations and measurements, thus opening room for more complex functions and structures and consequently, for more complex measures and operations on these structures. It is very difficult to determine what would be the upper bound for complexity of mathematical structures when dealing with biological signals. Especially now when everybody is aware that neurological signals are directly related to the processing of sensory information and system control in all variety of situations. As an illustration, we refer the reader to the concept of Granger causality that has been extensively used in neuroscience, see (Granger, 1969, 1980; Granger and Morris, 1976; Geweke, 1982, 1984; Kaminski and Blinowska, 1991; Sameshima and Baccala, 1999; Baccalá and Sameshima, 2001a; Baccala and Sameshima, 2001b; Kaminski et al., 2001; Brovelli et al., 2004; Babiloni et al., 2005, 2007; Wang et al., 2007; Blinowska, 2008, 2011; Kuś et al., 2008; Takahashi et al., 2008; Blinowska et al., 2010; Brzezicka et al., 2011; Kasum et al., 2015).

Moreover, and much more important, biological signals like DNA sequences are information bearing structures (even more, they are knowledge bases) and should be treated as such. The particular DNA molecule should be also studied by its set of consequences, not solely by its morphological properties. It seems

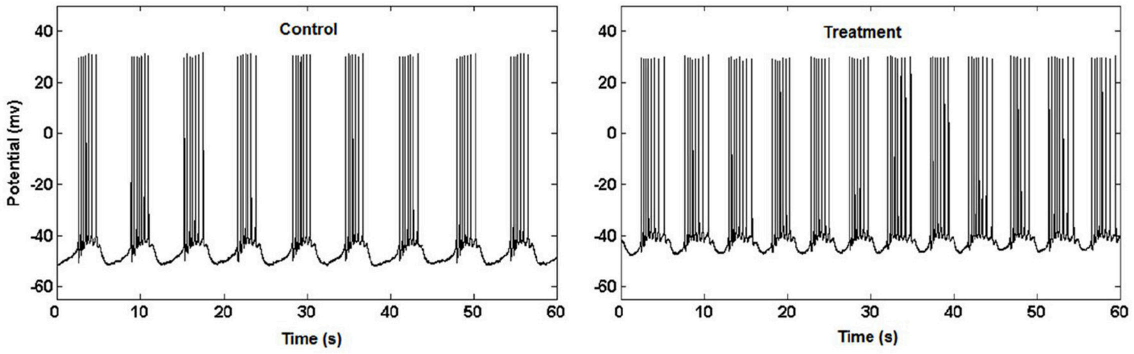

FIGURE 3 | Garden snail neuron activity (Kesić et al., 2014).

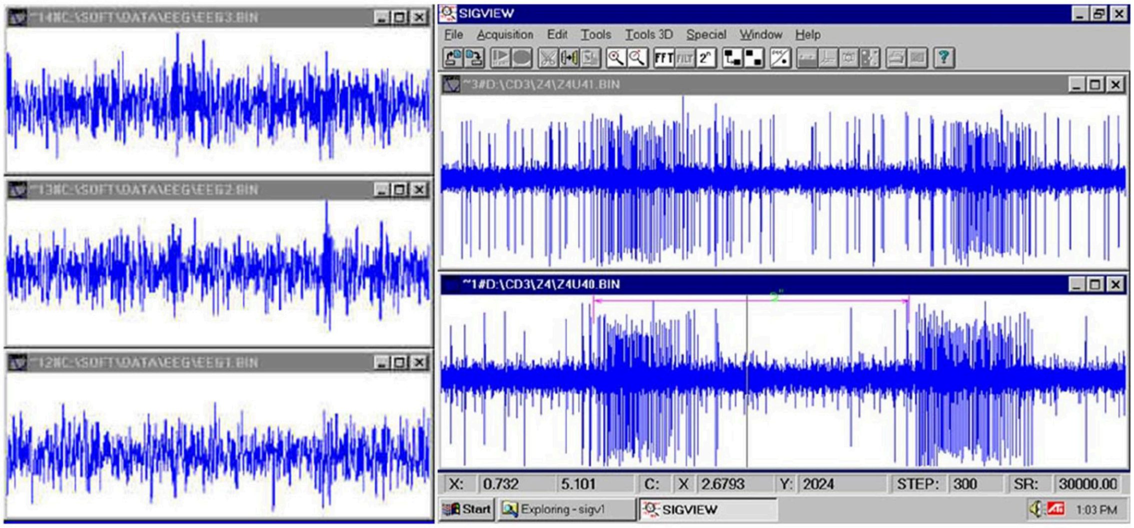

FIGURE 4 | (Left): fast EEG; **(Right)**: very fast firing of a neuron (Jovanović, 2001; Jovanović et al., 2014).

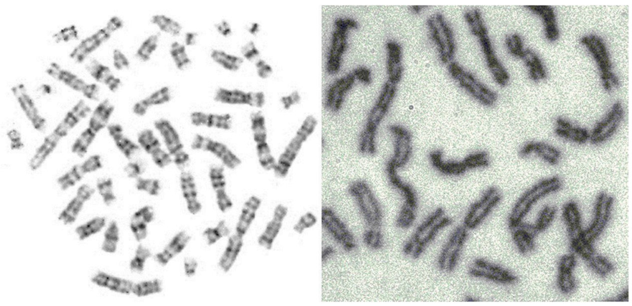

FIGURE 5 | Mitosis-two chromosome distributions (Jovanović, 2001; Jovanović et al., 2014).

prudent to involve the entire data science and a significant part of mathematical logic into foundations of biology.

For example, propositions "today is Tuesday" and "it is not true that today is not Tuesday" have the same meaning, but syntactically are quite different. In terms of Euclidean metrics (the main tool for the similarity estimation), they are quite distant. Thus, the syntactical similarity can be quite different form the more important, semantic similarity. The syntax similarity only works properly if applied on objects in normal form (a concept similar to disjunctive or conjunctive normal form in propositional logic).

Back to DNA, we may ask the following questions:

- Is there a normal form of a DNA sequence?
- If the answer is positive, are the DNA molecules always in the normal form?
- What are the properties of the "gene to protein" relation?
- Can we produce an axiom system and derivation rules (i.e., logic) for the synthesis of proteins?

It is not our attention to dispute the well-established use of the Hilbert space formalism in acquisition of biological signals. However, it cannot be the sole mathematical apparatus used in biology, since it offers nothing about consequence relations and

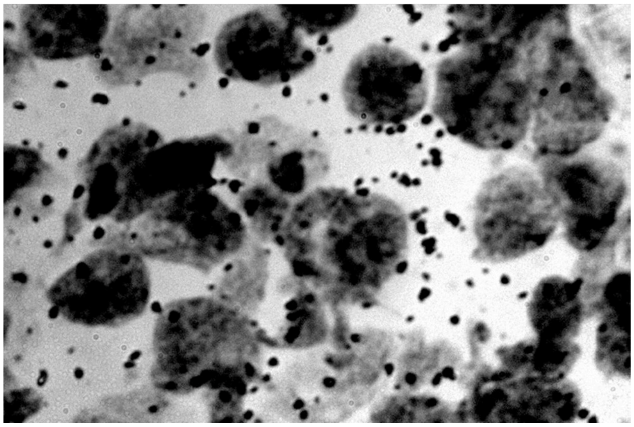

FIGURE 6 | RNA dots related to the neuron nucleus (rats) (Jovanović, 2001; Jovanović et al., 2014).

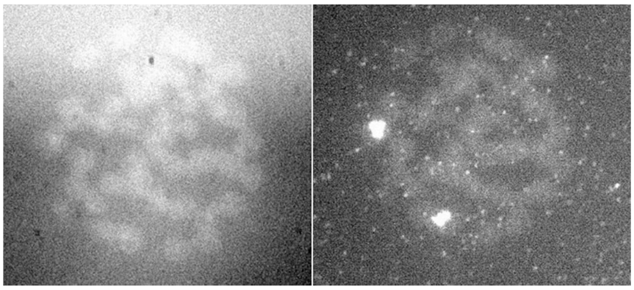

FIGURE 7 | FISH signal of the same preparation in two different wavelengths (Jovanović, 2001; Jovanović et al., 2014).

deduction in general. It seems prudent to involve some other mathematical disciplines related to automated reasoning. For the reader unfamiliar with the basic concepts of mathematical logic we refer to (Mendelson, 1997).

This is why more complex methods are finding applications and are well emancipated in the processing of biological signals. Here we shortly summarize some elements with their relevant properties that are already in broader use.

Measures and Metrics

Where there are measurements, immediately there are measures. The signal processing techniques involve application of different kind of measures: counting cardinality, probabilistic, vector valued (non-monotonic), common Euclidean geometry measures, special probabilistic Boolean ($\{0, 1\}$-valued) filters (those emerge in situations when deciding if an object has certain property or not) and so on. Usually, the sets occurring in experiments are fairly simple in the sense that they can be adequately approximated by finite sets, or by finite Boolean combinations of intervals and points. As such, they can be rather directly and easily measured. Original entities/objects are corresponded to their mathematical representations. Then obviously, a question arises: to what extent are the representations of a certain kind of entities similar/identical, which we resolve obviously with certain distance measurements-metrics between individual representations. Thus representations, no matter how simple or complex, become points in the space of representations and distance measurements directly determine similarity of originals.

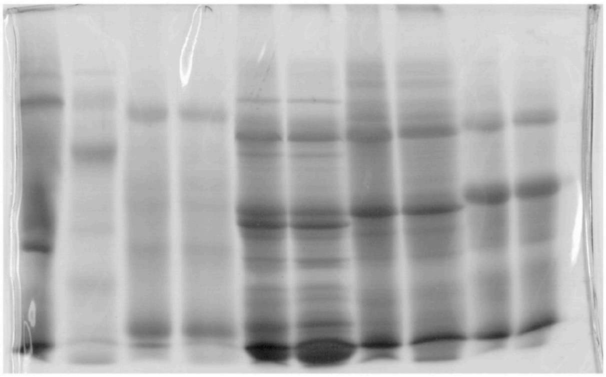

FIGURE 8 | Gel used in molecular biology (Jovanović, 2001; Jovanović et al., 2014).

However, one should always be aware of the underlying measure algebra, particularly when dealing with probability measures. The main cause of so called probability paradoxes is absence of the precise determination of the underlying measure algebra, i.e., the absence of the precise definition of the set of events that can be measured with the given probability function. For readers unfamiliar with the basic probabilistic concepts we refer textbooks (Attenborough, 2003; Spiegel and Stephens, 2018).

One of the subjects of the contemporary research is the study of the impact of quantum phenomena on complex biological formations, starting from large molecules, to large systems like brain and related biological phenomena e.g., consciousness. Along this line has emerged the awareness of the necessity of precise description and understanding of signals that are more complex and structures, which leads to utilization of more complex sets (events) and measures on them.

An example of this kind would be determination of the geometric probability for the set with fractal or rather complex boundary. Fractals have become broadly present in Biology in representation of biological functions and characterization of their complexity. Functions are sets; events in a probability are sets.

Another example of more complex measures involves Boolean measures on the set of natural numbers $\mathbb{N}$ induced by nontrivial filters and their total extensions.

The first measurements of the more complex curves and geometric objects were performed with the discovery and application of the infinitesimal calculus. The definite integral $\int_a^b f(x)\,dx$ of a positive function f on $[a, b]$ returns the surface area of the corresponding curved trapezium bounded with lines $y = 0$, $x = a$, $x = b$, and $y = f(x)$.

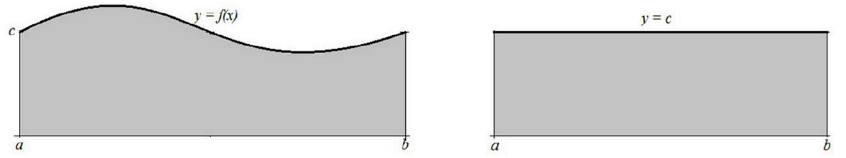

FIGURE 9 | Integral computation.

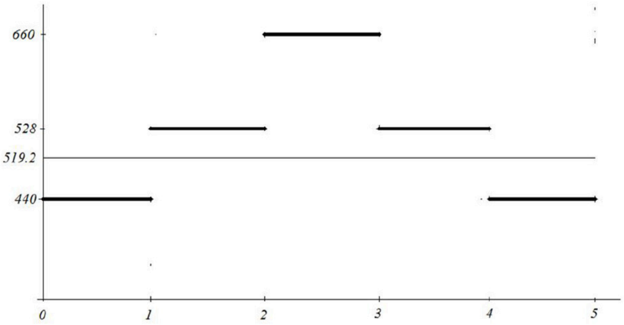

FIGURE 10 | Simple calculation of the mean and its semantics.

Development of calculus has brought the methods for integration of more complex functions, e.g., functions with countably many jump discontinuities and functions with essential discontinuities. The abstract concept of an integral has been finally shaped with Lebesgue's theory of measure and integration.

Starting with the basic geometric measures arising from Euclidean metrics (length of a straight line, area of a rectangle, volume of a cube); the measure of more complex sets is determined by application of the $\sigma-$additivity property:

$$\mu\left(\bigcup_{n=0}^{\infty} A_n\right) = \sum_{n=0}^{\infty} \mu\left(A_n\right)$$

for pairwise disjoint sets A_n, $n\in \mathbb{N}$,
For example, let

$$A = \bigcup_{n=0}^{\infty}\left[n, n+\frac{1}{2^n}\right].$$

Since

$$\left[n, n+\frac{1}{2^n}\right] \cap \left[m, m+\frac{1}{2^m}\right] = \varnothing$$

for $m \neq n$, and $\mu\left(\left[n, n+\frac{1}{2^n}\right]\right) = \frac{1}{2^n}$, we obtain that

$$\mu\left(A\right) = \sum_{n=0}^{\infty} \frac{1}{2^n} = 1.$$

The main feature of the zero−measure sets. Precisely, if E is a set of the positive measure, Z is a zero−measure set (i.e., $\mu\left(Z\right) = 0$), then for any Lebesgue integrable function f, the following is true:

$$\int_E f\left(x\right) d\mu = \int_{E\smallsetminus Z} f\left(x\right) d\mu.$$

This was a significant improvement of the Riemann integral.

The modern understanding of a probability is as a normed measure on a probability space. More precisely, probability space is a triple $(\Omega, \mathcal{A}, P)$, where Ω is a nonempty set of elementary events, $\mathcal{A}$ is a $\sigma-$complete subalgebra of the powerset algebra $\mathcal{P}\left(\Omega\right)$, and $P\colon \mathcal{A} \to [0, 1]$ is a $\sigma-$additive function such that $P\left(\Omega\right) = 1$. In particular, P is total *if* $\mathcal{A} = \mathcal{P}\left(\Omega\right)$. These notions can be similarly defined for any other kind of measure.

The additivity *add* $\left(\mu\right)$ *of* a measure μ is defined as the smallest cardinal number κ such that there is a family $Z = \{Z_i : i \in \kappa\}$ satisfying the following two properties:

- $\mu\left(Z_i\right) = 0$ for all $i \in \kappa$;
- $\mu\left(\bigcup_{i\in\kappa} Z_i\right) > 0$.

Some examples:

1. Calculating area of the curved trapezium;
2. Calculating area of the figure whose boundary has finitely many stepped discontinuities;
3. Calculating area of the figure whose boundary has countably many stepped discontinuities;
4. Calculating geometric probability of the set with simple boundary;
5. Calculating geometric probability of the set with fractal boundary (e.g., Weierstrass function).

Note that *add* $\left(\mu\right) = \omega$ means that μ is $k-$additive for all finite k. Measures of various additivity are investigated in theory and used in practice, when additivity can be arbitrary large.

The notions of metrics and measure play important part in modeling of similarity. In the study of information bearing structures, most notably formal deductive systems, it is often easier to define measure than metrics. For example, a consistent propositional theory (set of formulas) T naturally induces the corresponding binary measure μ_T on Lindenbaum algebra LA by

$$\mu_T\left([\phi]\right) = \begin{cases} 1, & T \vdash \phi \\ 0, & T \nvdash \phi \end{cases}$$

Here ϕ is a propositional formula and $[\phi] = \{\psi : \vdash \psi \leftrightarrow \phi\}$.

One of the most common ways to generate metrics from a given measure μ is to measure symmetric difference:

$$d\left(A, B\right) = \mu\left(A \triangle B\right).$$

The obtained metrics d do not satisfy condition $d\left(A, B\right) = 0 \Rightarrow A = B$, so it is a pseudo-metrics.

Dimension

The most commonly known meaning of the notion of dimension is that it is the cardinal number of any basis of the given vector space. For example, dimension of the Euclidean space $\mathbb{R}^n$ is, as expected, equal to n. Recall that two vector spaces over the same field are isomorphic if and only if they have equal dimensions. This theorem establishes dimension of the vector space as its most important characteristics.

Another important concept of dimension is topological dimension. We shall omit a rather cumbersome technical definition, and try to illustrate the concept in the case of charts. A $k-$dimensional chart in $\mathbb{R}^n$ for $k < n$ is any subset of $\mathbb{R}^n$ of the form

$$M = \{(x_1\left(t_1, \ldots, t_k\right), \ldots, x_n\left(t_1, \ldots, t_k\right)) : \left(t_1, \ldots, t_k\right) \in I_1 \times \ldots \times I_k\},$$

where each $I_i \subseteq \mathbb{R}$ is an interval and each $x_i : I_1 \times \ldots \times I_k \rightarrow \mathbb{R}$ is a smooth function. For example, a sphere with radius $R = 5$ and center at origin is represented by the chart

$$S = \left\{(5\cos\left(s\right)\cos\left(t\right), 5\sin\left(s\right)\cos\left(t\right), 5\sin\left(t\right)) : 0 \leq s < 2\pi, -\frac{\pi}{2} \leq t \leq \frac{\pi}{2}\right\}.$$

Generally, a plain curve can be intuitively described as the set of the form

$$s = \left\{\left(x(t), y\left(t\right) : t \in I\right\},$$

where I is an interval. However, various conceptual problems emerge when the additional conditions on coordinate functions $x(t)$ and $y(t)$ are omitted. This was explicitly shown by Weierstrass, Dirichlet, Peano, Hilbert, Sierpinski, and others, who constructed quite exotic functions. Some of them are continuous and nowhere differentiable (Weierstrass functions, Koch triangle etc.), space filling (Peano curve is a continuous surjection of the segment $[0, 1]$ onto the square $[0, 1] \times [0, 1]$) and so on. The basic concepts of calculus can be found in textbooks (Attenborough, 2003; Werde and Spiegel, 2010; Hsu, 2014; Spiegel and Stephens, 2018).

Note that if l is a graph of a Weierstrass function, then, every two points on it are, measured along l, at infinite length. The same is true for fractal curves.

Higuchi fractal dimension procedure became popular with the expanding applications on biological, especially neurological signals. It has been used alone or in combination with other signal analysis techniques in the revealing complexity patterns in the single neuron activity as well as in EEG/ECoG signals that originate from complex neuronal networks in different physiological and pathophysiological conditions (Kesić and Spasić, 2016).

Example 3.3.1 (Higuchi fractal dimension) In (Kesić et al., 2014) authors use Mean of the empirical *HFD* distribution to investigate the changes in the complexity of snail Br neuron activity after the treatment application. *HFD* measure allows fast computational tracking of variations in signals and in this study has been used in combination with the normalized mean of the empirical *HFD* distribution because the signal of Br neuron activity is non-stationary (**Figure 3**). This study, among other factors, showed that the normalized mean of empirical *HFD* distribution method is a significant mathematical invariant in monitoring the effects of different treatments on modulation of bursting neuronal activity.

On **Figure 11** is shown typical electrophysiological activity of garden snail Br neuron (60 s) and corresponding Higuchi's fractal dimension (HFD) values in control condition (left column) and after treatment application (right column). Mean of empirical FD distribution of the group in control condition and after treatment application behaves as the mathematical invariant characterizing system modulation.

In 1918 Felix Hausdorff introduced a generalization of the notion of topological dimension in order to classify objects with fractal boundaries.

Definition 3.3.2. (Hausdorff measure) Let $\left(X, d\right)$ be a metric space and let $\lambda \geq 0$. The Hausdorff measure $H^\lambda : \mathcal{P}\left(X\right) \rightarrow [0, +\infty]$ is defined by

$$H^\lambda\left(S\right) = \sup_{\delta > 0} \inf \left\{\sum_{n=0}^{\infty} d\left(U_n\right)^\lambda : S \subseteq \bigcup_{n=0}^{\infty} U_n \wedge \left(\forall n \in \mathbb{N}\right) d\left(U_n\right) < \delta\right\}. \square$$

The connection between Hausdorff measure and Lebesgue measure is rather strong, as it is stated by the following theorem.

Theorem 3.3.3 Suppose that $E \subseteq \mathbb{R}^n$ is a Borel set and that μ_n is the Lebesgue measure on $\mathbb{R}^n$. Then,

$$\mu_n\left(E\right) = \frac{\pi^{\frac{n}{2}}}{2^n \Gamma\left(\frac{n}{2} + 1\right)} H^n\left(E\right). \square$$

Now the Hausdorff dimension is defined by

$$\dim_H(S) = \inf\left\{\lambda \geq 0 : H^\lambda\left(S\right) = 0\right\}.$$

A consequence Theorem 3.3.2 is the fact that topological dimension of any smooth manifold M is equal to its Hausdorff dimension $\dim_H\left(M\right)$. In particular:

- $\dim_H(D^n) = n$, where $D^n = \{\boldsymbol{x} \in \mathbb{R}^n : \|\boldsymbol{x}\| \leq 1\}$ is the n $-$ dimensional unit ball in $\mathbb{R}^n$;
- $\dim_H([0, 1]^n) = n$;
- $\dim_H(\{\boldsymbol{x}\}) = 0$ for any $\boldsymbol{x} \in \mathbb{R}^n$;
- $\dim_H([0, 1] \times \{0\}) = 1$.

The more interesting examples are related to various fractals.

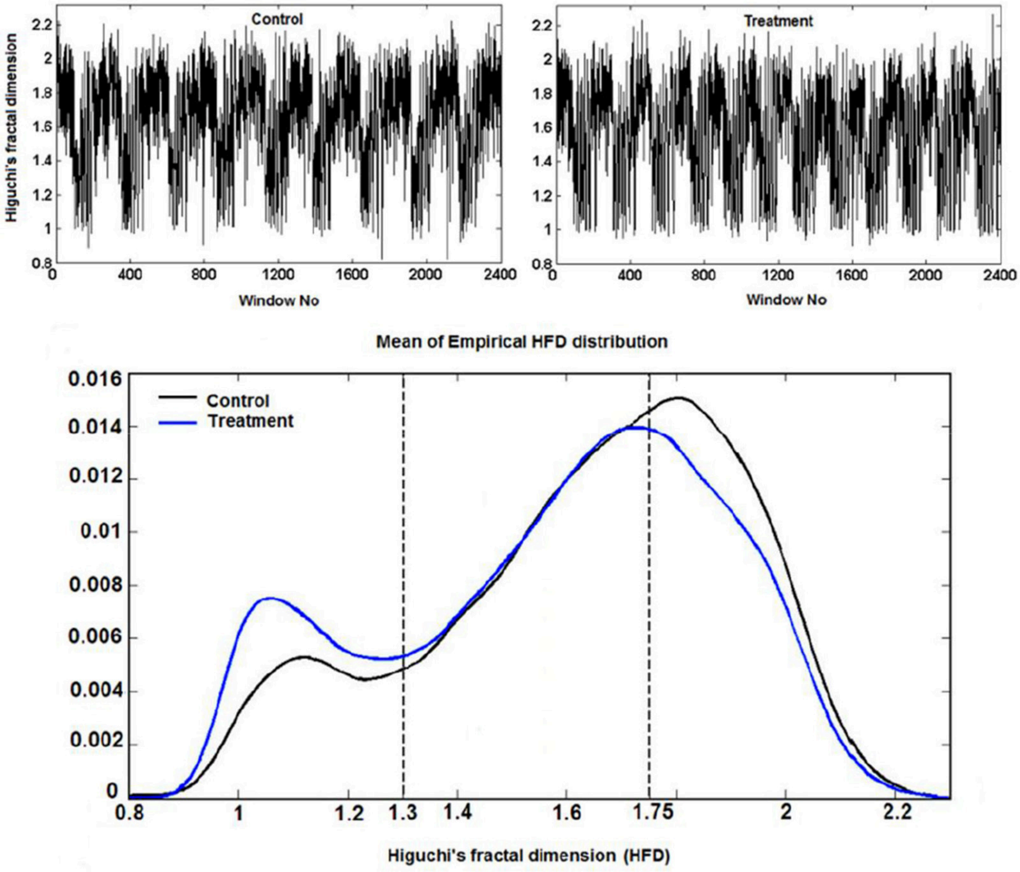

FIGURE 11 | Higuchi's fractal dimension (Kesić et al., 2014).

FIGURE 12 | Construction of Cantor set.

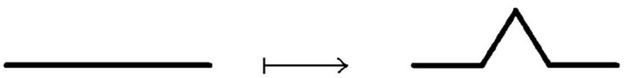

FIGURE 13 | Construction of Koch line.

Example 3.3.4 (Cantor set) Arguably, the most important fractal construction method was given by Georg Cantor with his iterative construction of the nowhere dense subset of the real unit interval that is equipotent with the unit interval (i.e., has the same cardinal number). In particular, Cantor set C is defined by

$$C = \bigcap_{n=1}^{\infty} \bigcup_{k=0}^{3^{n-1}-1} \left(\left[\frac{k}{3^{n-1}}, \frac{3k+1}{3^n} \right] \cup \left[\frac{3k+2}{3^n}, \frac{k+1}{3^{n-1}} \right] \right).$$

The intuitive definition goes as follows:

- Start with $C_0 = [0, 1]$;
- Remove the middle third from C_0. More precisely, $C_1 = C_0 \setminus \left(\frac{1}{3}, \frac{2}{3}\right)$. Note that $C_1 = \left[0, \frac{1}{3}\right] \cup \left[\frac{2}{3}, 1\right]$;
- Repeat the above procedure on each closed subinterval. For example, $C_2 = \left[0, \frac{1}{9}\right] \cup \left[\frac{2}{9}, \frac{1}{3}\right] \cup \left[\frac{2}{3}, \frac{5}{9}\right] \cup \left[\frac{8}{9}, 1\right]$;

$$C = \bigcap_{n=0}^{\infty} C_n.$$

The corresponding Hausdorff dimension of the Cantor set is given by

$$\dim_H(C) = \log_3(2)\,. \ \square$$

Example 3.3.5 (Cantor comb)

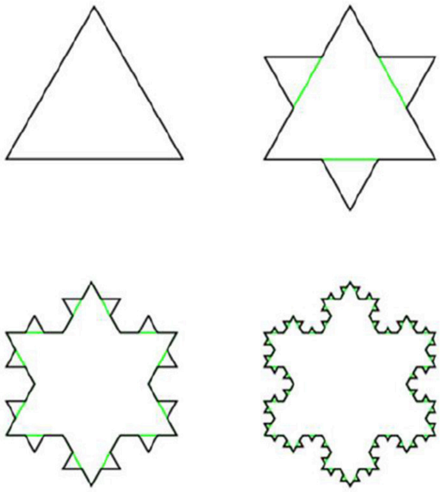

FIGURE 14 | Construction of Koch snowflake.

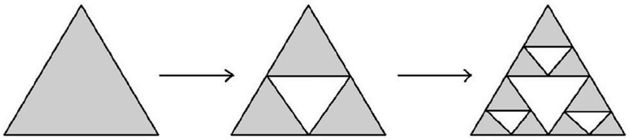

FIGURE 15 | Construction of Sierpinski triangle.

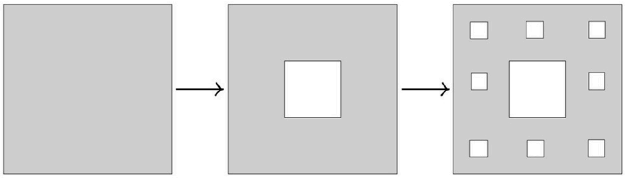

FIGURE 16 | Construction of Sierpinski carpet.

The Cantor comb is the set $CC = C \times [0,1]$. The corresponding Hausdorf dimension is calculated as follows:

$$\dim_H(CC) = \dim_H(C) + \dim_H([0,1]) = \log_3(2) + 1. \ \square$$

Example 3.3.6 (Koch line and Koch snowflake) A Koch line is a planar fractal .whose iterative construction is a modification of the construction of the Cantor set. Instead of deleting the middle segment, over it is constructed equilateral triangle, then its base is removed, as shown on **Figure 13**.

This procedure is repeated ad infinitum. Similarly, Koch snowflake is constructed from the equilateral triangle by transformation of its edges into Koch lines, as shown on **Figure 14**.

The Hausdorff dimension of both Koch line and Koch snowflake is equal to $\log_3(4)$.

Example 3.3.7 (Sierpinski triangle and Sierpinski carpet) Another modification of Cantor's iterative fractal construction was introduced by Sierpinski. The corresponding transformations are shown on **Figures 15**, **16**.

The Hausdorff dimension of Sierpinski triangle is equal to $\log_2(3)$, while the Hausdorff dimension of Sierpinski carpet is equal to $\log_3(8)$. $\square$

Boundary-Interior Index

One of the natural questions involving metric characteristics of a given subset of a metric space is to compare measures of sets and their boundaries. A motivation can be found in classical problems of finding a figure with fixed type of boundary (or fixed measure) with maximal or minimal area or volume. An example of this kind is finding a figure of maximal area whose boundary has the fixed length *l*.

Definition 3.4.1 Let A be a measurable set in $\mathbb{R}^n$. We define the boundary-interior index (BI) of A by

$$\mathrm{bi}\,(A) = \begin{cases} \frac{\mu_{n-1}(\partial A)}{\mu_n(A)}, & \text{if division is possible} \\ \left(\mu_{n-1}(\partial A), \mu_n(A)\right), & \text{otherwise} \end{cases}. \ \square$$

In the following examples we shall calculate BI for several important sets illustrating characteristic cases.

Example 3.4.2 (BI of a circle) Let S be a circle of radius R. Then,

$$\mathrm{bi}\,(S) = \frac{\mu_1(\partial S)}{\mu_2(S)} = \frac{2R\pi}{R^2\pi} = \frac{2}{R}.$$

Moreover, circumference $l = \mu_1(\partial S)$ and radius R are connected by the well-known equation $l = 2R\pi$, so in terms of circumference l we can express the BI of a circle by $\mathrm{bi}\,(S) = \frac{4\pi}{l}$ $\square$

Example 3.4.3 (BI of $n-$dimensional ball) Let $D^n_{\boldsymbol{a},R} = \{\boldsymbol{x} \in \mathbb{R}^n : \|\boldsymbol{a} - \boldsymbol{x}\| \leq R\}$ be the $n-$dimensional ball with center $\boldsymbol{a}$ and radius R. Since $\mu_n\left(D^n_{\boldsymbol{a},R}\right) = \frac{2\pi^{n/2}}{n\Gamma(\frac{n}{2})}R^{n-1}$ and $\mu_n\left(\partial D^n_{\boldsymbol{a},R}\right) = \frac{2\pi^{n/2}}{\Gamma(\frac{n}{2})}R^{n-1}$, it follows that $\mathrm{bi}\left(D^n_{\boldsymbol{a},R}\right) = \frac{n}{R}$. $\square$

Example 3.4.4 (BI of $n-$dimensional cube) Let $A = [0,a]^n$ where $a > 0$. Clearly, $\mu_n(A) = a^n$. On the other hand, $\mu_{n-1}(\partial A) = 2na^{n-1}$. Thus, $\mathrm{bi}\,(A) = \frac{2n}{a}$. $\square$

Example 3.4.5 Let H be the area in Euclidean plane $\mathbb{R}^2$ bounded with $y = 0$, $x = 1$ and $xy = 1$. Then,

$$\mu_1(\partial H) = \int_1^\infty \frac{\sqrt{x^4+1}}{x^2}dx \geq \int_1^\infty dx = +\infty$$

and

$$\mu_2(H) = \int_1^\infty \frac{dx}{x} = +\infty.$$

Hence, $\mathrm{bi}\,(H) = (\infty, \infty)$

On the other hand, let T be the region in Euclidean space $\mathbb{R}^3$ that is formed by rotation of H along the x axis. Then,

$$\mu_2(T) = 2\pi + 2\pi \int_1^{\infty} \frac{\sqrt{x^4+1}}{x^3} dx \geq 2\pi + 2\pi \int_1^{\infty} \frac{dx}{x} = +\infty,$$

and

$$\mu_3(T) = \pi \int_1^{\infty} \frac{dx}{x^2} = \pi.$$

Thus, $\mathrm{bi}(T) = (\infty, \pi)$. □

Example 3.4.6 (BI of Koch snowflake KS) Let KS_n be the figure obtained in the $n-$th iteration of the construction of the Koch snowflake. Then, $\mu_1(\partial KS_n) = 3\left(\frac{4}{3}\right)^n$ and $\mu_2(KS_n) = \frac{3\sqrt{3}}{16}\left(\frac{4}{9}\right)^n$ for $n > 0$ and $\mu_2(KS_0) = \frac{\sqrt{3}}{4}$, so

$$\mu_{n-1}(KS) = 3 \lim_{n\to\infty} \left(\frac{4}{3}\right)^n = +\infty$$

and

$$\mu_n(KS) = \frac{\sqrt{3}}{4} + \frac{3\sqrt{3}}{16} \sum_{n=1}^{\infty} \left(\frac{4}{9}\right)^n = \frac{2\sqrt{3}}{5}.$$

Thus, $\mathrm{bi}(KS) = \left(\infty, \frac{2\sqrt{3}}{5}\right)$. If the length of the base of the equilateral triangle KS_0 is equal to $a > 0$, then $\mathrm{bi}(KS) = \left(\infty, \frac{2a^2\sqrt{3}}{5}\right)$. □

Example 3.4.7 (BI of Sierpinski triangle ST and Sierpinski carpet SC) Similarly as in the previous example, let ST_n be the figure obtained in the $n-$th iteration of the construction of Sierpinski triangle. It is not difficult to see that $\mu_1(\partial ST_n) = 3a\left(\frac{3}{2}\right)^n$ and $\mu_2(ST_n) = \frac{a^2\sqrt{3}}{4}\left(\frac{3}{4}\right)^n$, so

$$\mu_1(ST) = \lim_{n\to\infty} 3a\left(\frac{3}{2}\right)^n = +\infty$$

and

$$\mu_2(ST) = \lim_{n\to\infty} \frac{a^2\sqrt{3}}{4}\left(\frac{3}{4}\right)^n = 0.$$

Thus, $\mathrm{bi}(ST) = (\infty, 0)$. Here $a > 0$ is the length of the base of the initial equilateral triangle ST_0.

In the case of Sierpinski carpet, $\mu_2(SC_n) = a^2\left(\frac{8}{9}\right)^n$ and $\mu_1(\partial SC_n) = \frac{a}{2}\left(\frac{8}{3}\right)^n$, so similarly as in the case of Sierpinski triangle we obtain that $\mathrm{bi}(SC) = (\infty, 0)$ □

Example 3.4.8 (BI of Cantor comb CC) Let $CC = C \times [0,1]$ be the Cantor comb and let CC_n be the figure obtained in the n-th iteration of its construction. Since $\mu_1(C) = 0$ and Fubiuni theorem is true for the Lebesgue integral, $\mu_2(D) = 0$.

On the other hand, $\mu_1(CC_n) = 2^{n+1}\frac{3^n+1}{3^n}$, so $\mu_1(CC) = +\infty$. It follows that BI has the same value as in the case of Sierpinski triangle and Sierpinski carpet, i.e., $\mathrm{bi}(CC) = (\infty, 0)$. Note that for any $A \subseteq \mathbb{R}^2$ of positive measure disjoint to CC, the set $B = A \cup CC$ satisfies condition $\mathrm{bi}(B) = \left(\infty, \mu_2(A)\right)$.

On the other hand, boundary of Cantor comb contains $2^{\aleph_0}$ disjoint copies of the segment $[0,1]$, so, its rectification produces a very long line: a concatenation of $2^{\aleph_0}$ copies of $[0,1]$. Clearly, it cannot be represented by a real number, which opens possibility of facilitating some other types of orderings, e.g., Suslin lines. □

Example 3.4.9 (BI of Cantor set C) It is well known that $\mu_1(C) = 0$. Furthermore, $\mu_0(C) = |C| = 2^{\aleph_0}$, so $\mathrm{bi}(C) = \left(2^{\aleph_0}, 0\right)$. For readers unfamiliar with the basic concepts of set theory we refer to the textbook (Jech, 2006).

The case $\mathrm{bi}(A) = (0, a)$ for $a \in (0, +\infty)$ is not possible. Indeed, $\mu_{n-1}(\partial A) = 0$ implies that the topological dimension of A satisfies condition $\dim(\partial A) \leq n-2$, hence either interior or exterior of A is empty. Consequently, $\mu_n(A) = 0$ (case $int(A) = \varnothing$) or $\mu_n(A) = \infty$ (case $ext(A) = \varnothing$).

With respect to objects in $\mathbb{R}^n$ for $n > 1$ with fractal boundaries, BI behaves like a filter: for fractal ∂A, it is either $\mu_{n-1}(\partial A) = 0$ or $\mu_{n-1}(\partial A) = \infty$.

When there is a need to calculate energy under fractal curve, or further integrate it as with spectrograms, we immediately switch to the 2D or 3D objects with complex-fractal boundary.

Chromosomes

The early image processing initiated the efficient algorithms to penetrate images (Haralick et al., 1973). Extracting objects and operating with them toward desired aims demanded more, e.g., (Vukosavic et al., 2001; Cermak et al., 2016). Every analysis of chromosomes begins with identification of single chromosomes and continues with matching of homolog couples using specific banding patterns, thus reaching the basic karyotyping. The careful visual inspection of small objects in direct observation on photography was the only operation made in genetics for decades. This was seriously extended with CCD microscopy (Jovanović, 2001), when chromosomes became available for mathematical modeling and unprecedented detailed analysis. The gain was lost of subjectivity present in earlier direct visual observations (as illustrated on the **Figures 17–20**).

Genetic content is well ordered within chromosomes, with individual genes located at specific positions, organizing chromosomal coordinate system. Chromosomal (karyotype) classification reached in importance since any change, small or smaller is related to most important life aspects of the studied organism.

The methods and techniques applied in these analyses are expanding at an accelerated rate. Besides karyotyping and its comparisons with the developing standards toward the localization and classification of the individual genes, identification of irregular chromosomes with backtracking of the genetic material forming them, as well as the localization of hardly perceptible (small) fractures and their extraction and further analysis, have been in the research focus (Jovanović et al., 2014).

In the formation of microscopic preparations of chromosomes, they get bent forms randomly. The images (patterns) of light absorption correspond to the absorption intensity two-argument functions are 3D manifolds with

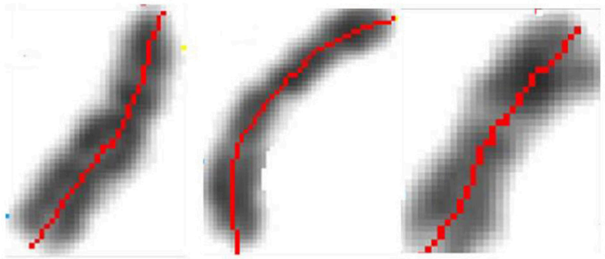

FIGURE 17 | Identification of the central meridian-line of a chromosome before normalization-"rectification," the feature preparation for the metric-comparison (Jovanović, 2001; Jovanović et al., 2014).

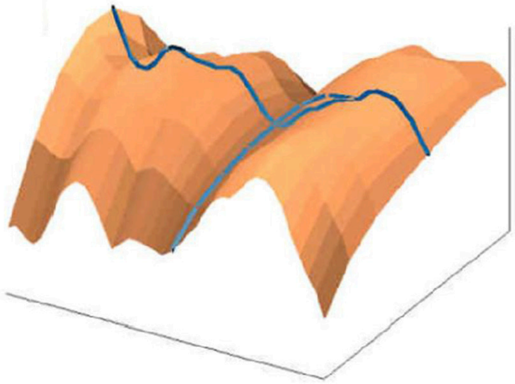

FIGURE 18 | Normalized chromosomal structure detail in chromosomal coordinate system (Jovanović, 2001; Jovanović et al., 2014).

characterizing distribution of convex and concave parts (dark and light segments).

The longitudinal distortions bending, unless negligible make direct geometric analysis and comparison hard or non-reasonable.

What initially remains is the investigation of algebraic and topologic invariants of the representing manifolds. Following with multitude of single chromosome shapes we are forced to operate with this representations collected into large sets which is a serious complication. In this preliminary part of chromosomal analysis we recommended a rather simple controlled normalization procedure, as follows (Jovanović et al., 2010).

After the initial contour definition, we form the original chromosomal coordinate system with the orthogonal section lines on the central meridian line. This determines the initial geodesics and the corresponding metrics. By preserving of this central meridian in its original length, using Euclidean distance (which departs substantially from digital-pixel wise distance), rectifying it and positioning the orthogonal lines in the original points, we obtain the receiving Euclidean coordinate network (mesh). This mesh is used to map the original pixels into the receiving orthogonal mesh.

The inflections of the meridian will demand interpolation of pixels in the receiving network, and they correspond to the convex side. The concave-symmetric part will demand pixel fusions in the receiving image, which is the rectified chromosome. Such normalization is very suitable for applications of metrics in order to determine the degree of chromosome similarity with other compared chromosomes, leading rather straight to classification. Thus, rectifying-normalization is intended to produce image of the studied chromosome, as it would be if the chromosome did not have any inflections in the preparation production.

Clearly, smaller inflection enables more precise rectification of the particular chromosome. In cases when the inflection angle induces substantial detail damage, the rectification procedure can be frozen at each desirable angle, thus preserving important image sections, or, extend necessarily the chromosome length.

The alternative procedure is to generate narrow longitudinal bands concentric to the original curved meridian. Those bands should contain the smaller features that are undesirably distorted in the above normalization of the whole chromosome, and rectify only the selected narrow band. This approach will reduce the above disadvantage to negligible.

Once normalized, chromosomal images are well positioned over the simple rectangular domain. Obviously, the algebraic-topological invariants in the original chromosomes are now algebraic-geometric invariants, in the (almost) orthogonal chromosomal coordinate system.

In the early nineties, zooming the chromosome into the chip diagonal, we managed to obtain close to 100 k pixel per chromosome resolution. Now with pixels reduced hundredfold, the number of pixels per chromosome increases proportionally, offering high resolution orthogonal chromosomal systems. The consequence is significant improvement of accessible details within the observed genetic structures. Once when the real chromosome 3D high resolution images become reality, we will deal with the 3D chromosomal orthogonal cylindrical geometry, with appropriate metrics.

In this way, the original chromosome manifold $MCh_i\left(x,y\right)$ converts to the normalized manifold $M_i\left(x,y\right)$. In order to determine chromosomal invariants we determine the following two corresponding sets

$$\overline{M}max_i = \left\{\left(x,y\right) : \frac{\partial}{\partial x}M_i\left(x,y\right) = 0 \text{ and } M_i\left(x,y\right) \text{ is local max}\right\}$$

and

$$\overline{M}min_i = \left\{\left(x,y\right) : \frac{\partial}{\partial x}M_i\left(x,y\right) = 0 \text{ and } M_i\left(x,y\right) \text{ is local min}\right\},$$

assuming that the central meridian is collinear with the $x-$axis. The absorption bands tend to form parallel reefs, which will result in certain accumulations along some orthogonal lines on the meridian line. When projected to the meridian (for $y = 0$), they will converge to narrow bands. As representatives of these bands, we take their midpoints and collect them into sets (vectors) Max_i.

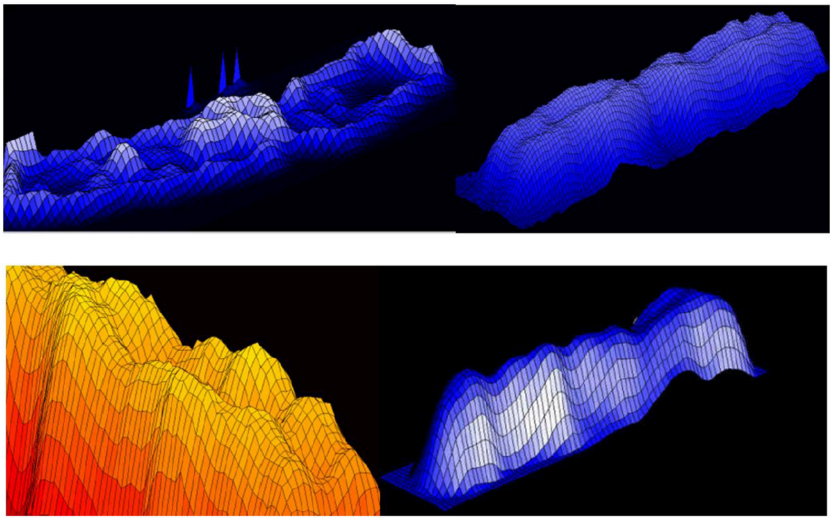

FIGURE 19 | 3D representation of absorption in chromosomes; top left, non-normalized –example, the lowest chromosome from **Figure 5**; the other examples are normalized (Jovanović, 2001; Jovanović et al., 2014).

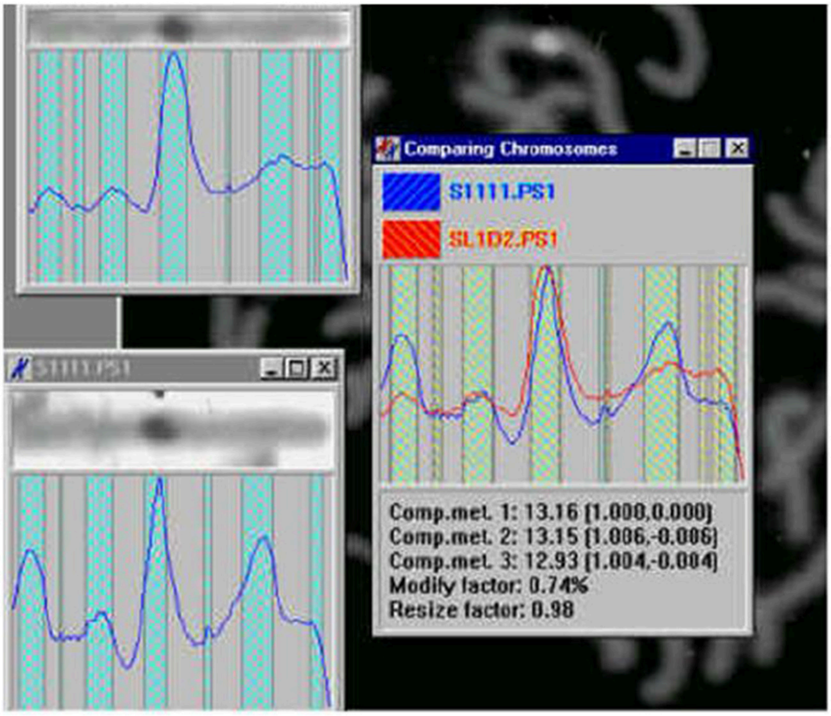

```
Comp.met. 1: 13.16 [1.000,0.000]
Comp.met. 2: 13.15 [1.006,-0.006]
Comp.met. 3: 12.93 [1.004,-0.004]
Modify factor: 0.74%
Resize factor: 0.98
```

FIGURE 20 | Chromosome measurement, comparison and classification (Jovanović, 2001; Jovanović et al., 2014).

Similarly form Min_i for the minimums. In this way we can use Max_i as a single simple chromosomal invariant and define measures on such representations which would indicate the level of chromosome similarity and provide general classification. Then for two representation vectors Max_i and Max_j we can define the metrics by

$$d\left(Max_i, Max_j\right) = \sum_{k=1}^{n} \left|x_{i,k} - x_{j,k}\right| (^*)$$

The alternative is to calculate the relative distances of nonzero coordinates of Max_i and Max_j and use these vectors in the metric

(*). For the alternative purposes we apply more or less refined metrics based on Euclidean metrics, e.g., less refined for global comparisons, more refined for detail inspections.

Earlier we defined some normalized and fuzzy metrics using simplified chromosomal representations. If more detailed and more precise similarity measurement is needed, for the representing set Max_i we can take all local extreme structures, instead of the point-wise projections on the meridian lines (thus, 2D structures).

Other complementary structural study of images of chromosomes is supporting operations on chromosomes with multiple FISH signals, and detection of very small features on chromosomes, see (Jovanović et al., 2014), which would include small structural changes and localization of individual genes in the chromosomal coordinate system.

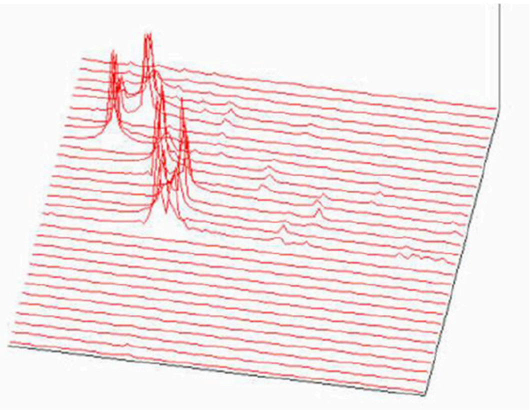

FIGURE 21 | FFT spectrogram as a part of the acoustic melody recognition (Jovanović, 2001; Jovanović et al., 2014).

FOURIER SPECTROSCOPY

Infinite dimensional function spaces, in particular Hilbert spaces, have become a natural mathematical background for signal processing. A Hilbert space H is a normed vector space with a scalar product $\langle\ ,\ \rangle$ which is also complete, i.e., each Cauchy sequence in H is convergent.

A countable Fourier basis of H is any subset $B = \{\boldsymbol{b}_n\ : n\in \mathbb{N}\}$ of H with the following properties:

- $\langle \boldsymbol{b}_n, \boldsymbol{b}_n\rangle = 1$ for all $n\in \mathbb{N}$;
- $\langle \boldsymbol{b}_i, \boldsymbol{b}_j\rangle = 0$ for $i \neq j$;
- $\boldsymbol{x} = \sum_{n=0}^{\infty} \langle \boldsymbol{b}_n, \boldsymbol{x}\rangle\, \boldsymbol{b}_n$, for all $\boldsymbol{x} \in H$.

The number $\hat{\boldsymbol{x}}_n = \langle \boldsymbol{b}_n, \boldsymbol{x}\rangle$ is called the n-th coordinate of $\boldsymbol{x}$ in the basis B. Moreover, the first two properties say that B is an orthonormal system of vectors, while the last property says that each vector can be expanded in Fourier series. Moreover, coefficients $\hat{\boldsymbol{x}}_n$ are uniquely determined in the following sense: $\boldsymbol{x} = \sum_{n=0}^{\infty} a_n \boldsymbol{b}_n \Longrightarrow (\forall n\in \mathbb{N})\ a_n = \hat{\boldsymbol{x}}_n$.

A number of semantic distortions and complications occur if the system B is not orthonormal, and have serious impact on the validity of the spectroscopic analysis. In (Blinowska, 2008) authors developed a system of base functions that is neither orthogonal, nor normed, unintentionally opening a serious question of the exact meaning of the observed harmonics. More precisely, beside the regular harmonics, such spectroscopy always induces virtual harmonics and do not preserve projections. In particular, projections of certain signal components often do not carry the same meaning as in the regular case, in fact they become meaningless.

Note that Fourier basis can be uncountable. However, the number of the nonzero coordinates is at most countable, which is the statement of the classical theorem that is stated below:

Theorem 4.1. Suppose that $B = \{\boldsymbol{b}_i : i \in I\}$ is any Fourier basis of the Hilbert space H and that $\boldsymbol{x} \in H$. Then the set $\left\{i \in I : \hat{\boldsymbol{x}}_i \neq 0\right\}$ is at most countable. □

In signal processing, the standard Hilbert space is the completion of the space of continuous functions on the closed interval $[-\pi, \pi]$. Recall that the scalar product is defined by

$$\langle \boldsymbol{x}, \boldsymbol{y}\rangle = \int_{-\pi}^{\pi} \boldsymbol{x}(t)\, \boldsymbol{y}(t)\, dt.$$

The corresponding standard Fourier basis B is defined by

$$B = \left\{\frac{1}{\sqrt{2\pi}}, \frac{\cos(t)}{\sqrt{\pi}}, \frac{\sin(t)}{\sqrt{\pi}}, \frac{\cos(2t)}{\sqrt{\pi}}, \frac{\sin(2t)}{\sqrt{\pi}}, \frac{\cos(3t)}{\sqrt{\pi}}, \frac{\sin(3t)}{\sqrt{\pi}}, \ldots\right\}.$$

Discrete Fourier transform and the fast Fourier transform (FFT) are the most common and most popular methods for the expansion of the numerical vector $\boldsymbol{x}(t)$ in the standard Fourier basis. Starting from its development in late sixties, it has founded a quite remarkable application in signal processing. In particular, it has enabled discovery of the efficient method for determination of periodic components of the given signal. The usual preprocessing involves various normalization techniques that ensure semantic stability. Readers unfamiliar with the basic concepts of the Fourier spectroscopy we refer to (Attenborough, 2003; Hsu, 2014).

One of the main assumptions is that a given signal $\boldsymbol{x}(t)$ is stationary, or relative stationary on the observed time interval L, i.e., that $\boldsymbol{x}(t)$ do not have significant changes for $t \in L$. It is often a case that authors present and analyze single FFT spectra, without any consideration of signal dynamics. If the signal contains multiple frequency components, say disjoint on the time axis but all within the domain L of the performed FFT, then the present frequency components will be detected without time resolution.

Consequently, in order to isolate and extract disjoint periodic component of a signal, it is necessary to successively perform the FFT with a t time slide at each iteration and the corresponding shortening of the initial signal. Note that this procedure requires appropriate sample rate and resolution.

For instance, performing FFT for the signal from the Example 2.2 with $L \geq 5$, we can detect all frequency components 440, 528 and 660, but without time separation, i.e., they will appear simultaneously. However, performing five FFT's with time sliding $\Delta t = 1$ five times, each time at the interval $\left[k-1, k-1+\Delta t\right]$, we shall obtain five spectra, each of them containing exactly one of the frequency components.

Furthermore, reducing L to 0.5 and Δt to 0.1 will produce 45 spectra each of them with a single frequency components, or two at the switch zones. In this way, we have approached the criterion of spectral stability and obtained time spectra—a spectrogram with separated tones and melodies within the signal, with the more precise determination of the basic frequencies, intensities, and duration of its components, conditions present in the change of frequency components. This provides a more complete insight into dynamics of a signal.

In particular, with a spectrogram with 50 equidistant spectra we can compensate possibly or certainly erroneous insight and understanding of circumstances induced by analysis of single spectra. Applying some interventions on Fourier spectrograms, e.g., (Jovanović et al., 2010; Spasić et al., 2010), it is possible to achieve very sharp time resolution of the present frequency components and their realistic magnitudes.

The example on **Figure 22** (Culić and Šaponjić, 1998; Japundzic-Zigon, 1998, 2001; Japundzic-Zigon et al., 2004) with hemorrhage offers insight into the effects of different substances on AP, the modulators of AP regulating system. Different approaches are available for single sort of experiment. For example presence/absence of major frequency features and their relative relationship, like frequency shifts and power ratios. The low frequency range LF and high frequency-HF, at the middle of frequency interval are essential features in these experimentation, yielding spectrogram characterizations of investigated physiology, which converge to the binary measure form- Y/N, filters, if/when, for example, distinguishing between control, and experimental group, as in the experiment in **Figure 23**, distinguishing spectral morphology of normal-control state and modulated spectrogram after administration of scopolamine methyl nitrate.

Some other issues are related to semantics of the signal processing by Fourier spectroscopy, see Spasić et al. (2010). Here we shall emphasize the following two important moments. A good time spectrogram can contain features significant for the studied process. Such content often require higher order spectroscopy, with or without the preprocessing involving normalization and application of various measurement, (see Jovanović et al., 2010; Perović et al., 2013).

Secondly, if the spectrogram contains small, hardly detectible, or imperceptible components in some cases they can be detected and extracted by application of the specific methods developed for the image processing. Some of them are applied for the analysis and detection of small features in chromosomes (e.g., Bradski, 1998; Bouguet, 2000; Welch and Bishop, 2004).

We can conclude that measures applied in various classification problems have better semantic correspondence with the reality when used on sufficiently resolute spectrograms or on their features. Furthermore, it is clear that all relevant measures will involve similar invariants-features, with high context dependence.

Specific situations often change the approach for choice of the adequate measure for the complexity of features. In the case of chromosomes, the Euclidean geometry is replaced by the local chromosomal geometry induced by the corresponding geodesics (contours, meridians). In spectroscopy, possible measures will focus on some of the following.

- Position of dominant lines;
- Dispersion;
- Second order FFT performed on extracted features;
- Counting/comparing of picks within certain frequency range with the threshold ε;
- Binary $0-1$ measures defined by filters and maximal filters, for example connected to the position of higher harmonics.

Additional treatment of measures on spectra and spectrograms in more general settings is given and discussed in the next section.

BRAIN CONNECTIVITY MEASURES

The EEG resolution (the number of electrodes on the scull) has exceeded 2^8 points more than a decade. Higher density of electrodes-signals for EEG will increase with technology development, and is expected to reach thousands soon.

The relationship of different signals within integrated neurological functions received significant attention in the last few decades. The focus was mainly on the problem of modeling brain connectivity. Developed models have led to the broad range of applications in numerous experimental laboratories, contributing to the rich discourses of fundamental importance in neuroscience.

Clearly, as every processing in the brain involves certain signal processes in the brain, any investigation of neurological signals almost certainly faces the most complex kind of signals. It is also well known that a highly complex system behavior mimics highly chaotic random systems.

For this reason, the successful modeling of stock market trends by Cleave Granger in late sixties and early seventies (Granger, 1969, 1980; Granger and Morris, 1976), soon after found application in the modeling of brain processes, namely brain connectivity.

The initial Granger causality model improved by Geweke which for vector variables has a form

$$\boldsymbol{x}(t) = \sum_{j=1}^{p} \boldsymbol{A}\left(j\right) \boldsymbol{x}\left(t-j\right) + \boldsymbol{E}(t),$$

where $\boldsymbol{x}(t) = (x_1(t), \ldots, x_n(t))$ is a vector of variables, $\boldsymbol{A}\left(j\right), j = 1, \ldots, p$ is a coefficient matrix defining variable contributions at step $t-j$, $\boldsymbol{E}(t)$ are prediction errors. In terms of frequency, Geweke in (Geweke, 1982, 1984) defined the causality model by

$$\boldsymbol{x}(\lambda) = \boldsymbol{A}^{-1}(\lambda)\,\boldsymbol{E}(\lambda) = \boldsymbol{H}(\lambda)\,\boldsymbol{E}(\lambda),$$

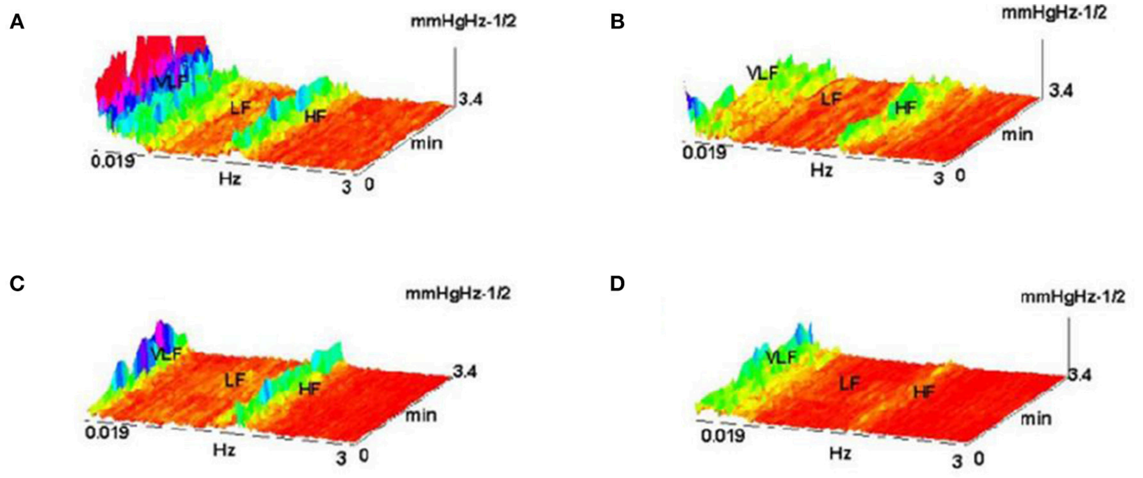

FIGURE 22 | Shown are FFT spectrograms of arterial pressure –AP in hemorrhage experiments, exhibiting the actions of AP modulators present in the AP regulation (system antagonists: renin angiotensin, of sympathetic nervous system and vasopressin). **(A)** hemorrhage 10%; **(B)** hemorrhage 10% pretreated with captopril; **(C)** the same, pretreatment withy phentolamin; **(D)** pretreatment with the substance V2255 (Jovanović, 2001; Jovanović et al., 2014).

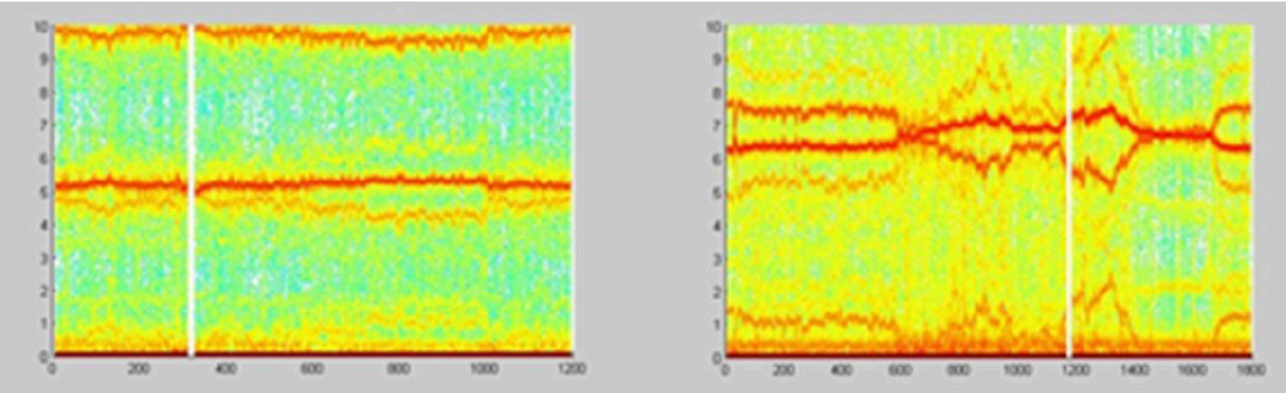

FIGURE 23 | Spectrograms showing the normal AP state and the spectrogram changes and regular feature destructions after administration of scopolamine methyl nitrate (Jovanović, 2001; Jovanović et al., 2014).

where

$$\boldsymbol{A}(\lambda) = -\sum_{j=0}^{p} \boldsymbol{A}(j) e^{-2i\pi\lambda j},$$

$\boldsymbol{A}(0) = \boldsymbol{I}$ and $\boldsymbol{H}(\lambda)$ is the system transfer matrix. Then he defined the measure of linear causality of two vectors of variables $\boldsymbol{x}$ and $\boldsymbol{y}$ at frequency λ by

$$f_{y\to x}(\lambda) = \ln\left(\frac{|\boldsymbol{S}_{xx}(\lambda)|}{\left|\boldsymbol{H}_{xx}(\lambda)\,\boldsymbol{\Sigma}_2(\lambda)\,\boldsymbol{H}^{*}_{xx}(\lambda)\right|}\right).$$

Here $\boldsymbol{H}^{*}_{xx}(\lambda)$ is the Hermitian transpose of $\boldsymbol{H}_{xx}(\lambda)$, $|\,|$ denotes determinant and $\boldsymbol{S}_{xx}(\lambda)$ is the upper left block of the spectral density matrix $\boldsymbol{S}(\lambda)$ defined by

$$\boldsymbol{S}(\lambda) = \begin{bmatrix} \boldsymbol{S}_{xx}(\lambda) & \boldsymbol{S}^{*}_{yx}(\lambda) \\ \boldsymbol{S}_{yx}(\lambda) & \boldsymbol{S}_{yy}(\lambda) \end{bmatrix} = \boldsymbol{H}(\lambda)\,\boldsymbol{\Sigma}_2(\lambda)\,\boldsymbol{H}^{*}(\lambda),$$

$$\boldsymbol{H}(\lambda) = \begin{bmatrix} \boldsymbol{H}_{xx}(\lambda) & \boldsymbol{H}_{xy}(\lambda) \\ \boldsymbol{H}_{yx}(\lambda) & \boldsymbol{H}_{yy}(\lambda) \end{bmatrix}.$$

Finally, $\boldsymbol{\Sigma}_2(\lambda)$ is the matrix of error variance.

The idea of Geweke that directed causality between the two nodes i and j of the graph consisting of precisely located electrodes-signals needs to be analyzed frequency wise was a substantial improvement, which was followed by other brain modeling teams, some of which received major attention and spread broadly.

In the implementations the major connectivity measures are estimating:

- Connectivity between two nodes i and j;

- Direction of connectivity between *i* and *j*;
- Intensity of connectivity between *i* and *j*. (1)

All of this properties are integrated into a single measure, while generally neglecting the frequency λ at which causality is constructed, replacing it with the maximum over a frequency interval Λ.

Following Geweke, Kaminski, and Blinowska introduced a modification called direct transfer function, defined by

$$DTF_{ij}(\lambda) = \frac{\left|\boldsymbol{H}_{ij}(\lambda)\right|}{\sqrt{\sum_{k=1}^{n}\left|\boldsymbol{H}_{ik}\right|^2}},$$

measuring causality from *j* to *i* at frequency λ. Initially they started with non-normalized form of DTF using the expression of Geweke (Kaminski and Blinowska, 1991; Kaminski et al., 2001).

Sameshima and Bacala proposed somewhat different approach in modifying Geweke measure (Sameshima and Baccala, 1999; Baccalá and Sameshima, 2001a; Baccala and Sameshima, 2001b), with their partial directed coherence, measuring influence of signal at the node *i* to the signal at the node *j* at frequency λ, formally defined by

$$PDC_{ij}(\lambda) = \pi_{ij}(\lambda) = \frac{\boldsymbol{A}_{ij}(\lambda)}{\sqrt{\boldsymbol{a}_j^*(\lambda)\,\mathbf{a}_j(\lambda)}}.$$

Here $\boldsymbol{A}_{ij}(\lambda)$ is the i,j-th entry of $\boldsymbol{A}(\lambda)$, $\boldsymbol{a}_j(\lambda)$ is the j-th column of $\boldsymbol{A}(\lambda)$ and $\boldsymbol{a}_j^*(\lambda)$ is the Hermitian transpose of $\mathbf{a}_j(\lambda)$.

Earlier, they also introduced the direct coherence measure with the intention to estimate direct connectivity between nodes *i* and *j* at frequency λ. It was defined by

$$DC_{ij}(\lambda) = \frac{\sigma_{jj}\boldsymbol{H}_{ij}(\lambda)}{\sqrt{\sum_{k=1}^{n}\sigma_{kk}^2\left|\boldsymbol{H}_{ik}(\lambda)\right|^2}}.$$

More recently Sameshima and Baccala introduced information PDC and DTF (Takahashi et al., 2010), for which they claimed to measure the information flow from the signal at the node *j* to the signal at the node *i* by

$$iPDC_{ij}(\lambda) = \overline{\boldsymbol{A}}_{ij}(\lambda)\,\sigma_{ii}^{-1/2}\left(\overline{\boldsymbol{a}}_j^*(\lambda)\,\boldsymbol{\Sigma}_{\boldsymbol{w}}^{-1}\overline{\boldsymbol{a}}_j(\lambda)\right)^{-1/2}$$

and

$$iDTF_{ij}(\lambda) = \overline{\boldsymbol{H}}_{ij}(\lambda)\,\rho_{jj}^{\frac{1}{2}}\left(\overline{\boldsymbol{h}}_j^*(\lambda)\,\boldsymbol{\Sigma}_{\boldsymbol{w}}^{-1}\overline{\boldsymbol{h}}_j(\lambda)\right)^{-\frac{1}{2}}.$$

Here $\boldsymbol{\Sigma}_{\boldsymbol{w}}=\mathbb{E}\left(\boldsymbol{w}(n)\,\boldsymbol{w}^T(n)\right)$ is a positive definite covariance matrix of the so called zero mean wide stationary process $\boldsymbol{w}(n)$, and ρ_{jj} is the variance of the so called partialized innovation process $\zeta_j(n)$ defined by $\zeta_j(n) = w_j(n) - \mathbb{E}(w_j(n)/\{w_l(n) : l \neq j\})$.

Let us mention that numerous experimental teams used the above measures in their discoveries where the above measures reached highest popularity in the formation and formulation of the key conclusions and results, including further modifications (Brovelli et al., 2004; Babiloni et al., 2005, 2007; Schelter et al., 2005; Chen et al., 2006; Singh et al., 2007; Wang et al., 2007).

In (Kasum et al., 2015) we undertook a thorough analysis of these approaches studying all tiny details in the computation and comparison of these measures on the authors data sets, discovering certain inconsistencies and problems involving these measures which substantially compromise their application in some important issues (Kuś et al., 2008; Takahashi et al., 2008; Blinowska et al., 2010; Blinowska, 2011; Brzezicka et al., 2011).

Presenting three qualities (1) integrally, we are neglecting differences in their importance and masking the most important aspect—being connected. For this reason, we proposed their separated analysis with certain additions, which can result in the different insight of the local inconsistency in the above methods. This is briefly shown on the **Figure 24** for a reduced small subset of the system involving 20 × 20 graphs.

On the left diagram is shown connectivity difference between the two measures with corrected statistical zero value. The right diagram contains the same connectivity difference between the two connectivity measures after the natural harmonization of the two experimental zeroes. The consequence is the loss of the connectivity difference in the example illustrating by the authors of PDC the difference and the advantages of their method. Manipulating with different values of statistical zero, one can reach arbitrarily desirable conclusions. Since, we earlier have shown that the DTF is exposing abundant connectivity, when almost everything is connected (D. Adams axiom), now the same will be true for PDC as well, only if sensitivity is sufficiently adjusted, not as far as in the original measure comparisons (Sameshima and Baccala, 1999).

Some alternative approaches were suggested by other research teams (Kroger et al., 2006; Watkins et al., 2006; Jovanović and Perović, 2007; Liu et al., 2007; Aoyama et al., 2009; Klonowski et al., 2009).

On the other hand, we introduced the concept of weak connectivity (Kasum et al., 2015), which might be essential in some processes and might remain hardly noticeable or even imperceptible for the current methods. We offer some alternative methods for detection of such phenomena. One of them is rather simple and goes as follows.

For a set *E* of signals we say that there is connectivity of *E* at frequency λ if

$$\overline{\pi}_E(\lambda) = \prod_{f\in E} PS\left(f\right)(\lambda) \neq 0.$$

Here $PS(f)$ is the power spectrum of f, $PS\left(f\right)(\lambda)$ is the λ-th coordinate of $PS(f)$, and $\prod$ is the coordinate-wise product.

The use of *E* with multiple signals instead of binary *E* might enhance some hardly noticeable periodic components which are present in the whole group of signals. Then, we can say that *E* is connected if $\overline{\pi}_E \neq \boldsymbol{0}$, i.e., if $\overline{\pi}_E(\lambda) \neq 0$ for some λ.

Besides the above considerations, we also recommended the connectivity being considered over the time interval *T*, rather than at a single point in *T*. The intention is to obtain insights

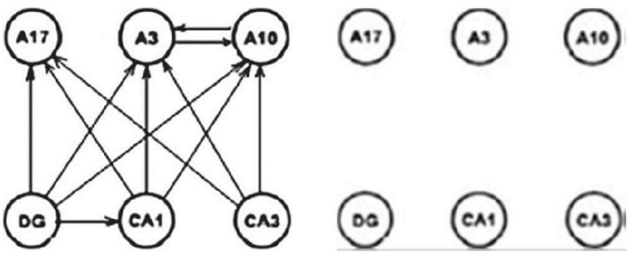

FIGURE 24 | Connectivity difference between DTF and PDC (Kasum et al., 2015).

in the time dynamics of connectivity. In this way the usual connectivity directed graphs, after some adaptations, can be substituted with their integration over time. Consequently, this will produce dynamic graph movies instead of single directed graphs, analogous to the spectra—spectrogram integration.

For the power spectra product of the initial time point t we can integrate $\pi_E(\lambda) = \pi_E(\lambda, t)$ over $t \in T$ and $\lambda \in \Lambda$ to obtain

$$\pi_E(\lambda, T) = \int_{t \in T} \pi_E(\lambda, t)\, dt$$

and

$$\pi_E(\lambda, \Lambda) = \int_{\lambda \in \Lambda} \pi_E(\lambda, t)\, d\lambda$$

as connectivity measures over the time interval T and the frequency interval Λ.

Other methods to establish connectivity on these higher structures are available. Once connectivity between the sets of signals is established, we might consider other two properties: the connectivity direction and intensity.

DISCUSSION

Biological research, centered on biological signals is in explosive expansion, with neurological contents leading in complexity. With 100 B (Billion) neurons and some its exponent of neuronal connections, the individual brain, as an information processing system responsible for all knowledge accumulated in history, plus a lot of other behavior, exceeds by far the complexity of the whole Internet processing, with all rich parallelism and powerful computational nuclei.

The unknown complexity of individual working brain is far out of reach of our understanding yet. Certainly, it is the most powerful function humanity met in history. Numerous of the processes are multi valued, certain processes binary, dispersed over a range of frequencies. It is the hardest possible approach to learn the unknown functionality from the hardware and individual signal sources. With the simple personal computer it would be a very hard way to reach understanding of software system controls involved, especially all the components of the operating system.

Yet, there are already conferences and discoveries related to the operation of human consciousness, which was until very recently a "nonscientific category." The approach of parallel investigation of multitude of tasks is promising, as some of the issues are being resolved from multiple projections. The number of combined teams of scientists engaged in brain research is growing, engaging significant resources, which might prove useful.

Mathematical methods briefly discussed here and much more are a product of the brain, thus having its representation and life within the brain much before it is used in brain modeling. Thinking in this way we could be sure all of Mathematics so far applied in biological signals is anything but too complex, as we never experienced the situation when very complex is completely described by very simple.

Nevertheless, we should mention some issues that will be faced sooner in much simpler environments like Quantum Physics and Cosmology. People usually consider Mathematics as a tool set sitting on the shelves, ready to be applied by whomever in whatever capacity and fragments of its developed contents, with all time growing complexity, as natural scientists and engineers are learning more of Mathematics. And this is good, as Mathematics is a public property. The history teaches us that it is hard to guarantee, even for the most abstract parts, that any of discovered Mathematics will never be needed by application. This is the only security for the future of Mathematical funding.

With the growing complexity of the applied mathematical concepts, we are approaching some serious issues of foundations of Mathematics. Before that, let us mention that the symbol ∞ does not represent infinity uniquely since Cantor's discoveries in 1873, when he showed that arithmetical and geometric infinity, i.e., natural numbers and real line are different infinite quantities. As a consequence, infinity has been scaled in terms of pairwise different cardinal numbers. However, the size of this scale is enormous; it cannot be coded by any set. This was the creation of Set theory, and the beginning of the studies of foundations of Mathematics, which is probably never ending.

When dealing with simplest measurements and simplest Euclidean measures we think that everything can be measured. One can only imagine the disappointment of Lebesgue who developed the beautiful completion of measure and integration, when Vitali find a rather simple set on the real line which is not Lebesgue-measurable. In fact there are $2^{\aleph_0}$ Lebesgue-measurable sets, while there are $2^{2^{\aleph_0}}$ subsets of $\mathbb{R}$.

The existence of immeasurable sets is highly counterintuitive. These sets cannot be sketched, they are totally amorphous. Sets with fractal boundaries can be seen as a bridge toward the intuitive visualization of immeasurable sets.

From earlier examples, namely, from Lobachevski discovery of non-Euclidean geometries, in twenties of 19th century, which was against all believes of the nature of Geometry, after he showed equiconsistency of the first non-Euclidean Geometry with the anciently perfectly founded Euclidean Geometry which we still learn in the schools, we learned that Mathematical theories, packed around their axioms can be at the same level of logical certainty, while obviously impossible mixed together since with colliding axioms.

And within very short time-a few decades, that discovery gave rise to the huge developments in Geometry, immediately picked up by the most prestigious theoretical physicists as proper Cosmometry (Geometry of the Universe, or its specific parts, e.g., environments of black holes). Concerning the issues related to all measures, we have to say that numerous depend on the axiomatics for Mathematics which is the defining Geometry of the Universe of Mathematics. And there are alternatives combining a smaller set of fundamental axioms and their weaker or stronger versions.

Without entering a discussion that does not belong here, let us just say that AC (Axiom of Choice) is very much needed in the foundations of Mathematics, but there are alternatives. AC implies that Lebesgue measure is not total. However, it implies that there are numerous mentioned measures that are total. Banach proved that there is a total extension of Lebesgue measure which is countably-additive, while, as the Solovay theorem shows (Solovay, 1970, 1971; Pap, 2002), the existence of a total countably-additive extensions of the Lebesgue measure is equconsistent to a very strong property. Some of the functions close to the above-examined fractals are complex enough to open the fundamental issues (for a survey on recent developments in Measure theory see e.g., Pap, 2002).

On the other hand, we can stay on the flat Earth and deal only with short approximation of the phenomena, avoiding entering the zone of the complex Mathematics and its fundamental issues. Yet, as proved by Goedel, we cannot escape the hot issues even remaining only in Arithmetic, nor in any theory containing its copy (like Geometry).

Other Approaches

Our aim was not to deliver a comprehensive overview of the all metrics and measurements involved in the contemporary biological studies. We have been focused primarily on our work. However, it is prudent to at least mention some of the important topics that are missed here.

The first is related to methods for fractal analysis developed initially for the fractal dimension of observed time series from human physiology and performance. We refer the reader to (Holden et al., 2013).

The second is related to measurement of self-affine structures and a spectrum of scaling parameters. An example of this kind is the detrended fluctuation analysis presented in (Kantelhardt et al., 2002).

The third is related to the recurrence quantification analysis based on the Taken's theorem. For more information we refer the reader to (Webber and Marwan, 2015).

The fourth is related to properties such as ergodicity, anomalous diffusion and multiplicative interactions presented in (Molenaar, 2004; Hasselman, 2013).

The fifth and the final is related to application of non-commutative probabilities presented in (Brovelli et al., 2004; Busemeyer and Bruza, 2012).

AUTHOR CONTRIBUTIONS

OK has written the initial draft of sections Measures and Metrics, Dimension, and Boundary-interior index; AJ has written the initial draft of sections Basics, Complexity Issues, Chromosomes, and Fourier spectroscopy (together with AP). AJ and AP have written the initial drafts of Introduction and Discussion. All authors have participated in revision and proofreading of the present version of the manuscript.

ACKNOWLEDGMENTS

Images at **Figures 3**, **11** are courtesy of Sladjana Spasić, for which we are indebted. The remaining images are property of GIS.

REFERENCES

Aoyama, A., Honda, S., and Takeda, T. (2009). Magnetoencephalographic study of auditory feature analysis associated with visually based prediction. *Int. J. Bioelectromagn.* 11, 144–148.

Attenborough, M. (2003). *Mathematics for Electrical Engineering and Computing*. Newnes.

Babiloni, F., Cincotti, F., Marciani, M., Salinari, S., Astolfi, L., Tocci, A., et al. (2007). The estimation of cortical activity for brain-computer interface: applications in a domotic context. *Comp. Intellig. Neurosci.* 2007:91651. doi: 10.1155/2007/91651

Babiloni, F., Mattia, D., Basilisco, A., Astolfi, L., Cincotti, F., Ding, L., et al. (2005). "Improved estimation of human cortical activity and connectivity with the multimodal integration of neuroelectric and hemodynamic data related to motor and cognitive tasks," in *27^{th} Annual International Conference of the IEEE Engineering in Medicine and Biology Society*. IEEE Engineering in Medicine and Biology Society, 5888–5891.

Baccalá, L., and Sameshima, K. (2001a). Partial directed coherence: a new concept in neural structure determination. *Biol. Cybern*. 84, 463–474. doi: 10.1007/PL00007990

Baccala, L., and Sameshima, K. (2001b). "Chapter 3:Overcoming the limitations of correlation analysis for many simultaneously processed neural structures," in *Progress in Brain Research, Vol 130*, ed, M. A. L. Nicolelis, (Elsevier).

Blinowska, K. (2008). Methods for localization of time-frequency specific activity and estimation of information transfer in brain. *Int. J. Bioelectromagn.* 10, 2–16.

Blinowska, K. (2011). Review of the methods of determination of directed connectivity from multichannel data. *Med. Biol. Eng. Comput*. 49, 521–529. doi: 10.1007/s11517-011-0739-x

Blinowska, K., Kus, R., Kaminski, M., and Janiszewska, J. (2010). Transmission of brain activity during cognitive task. *Brain Topogr*. 23, 205–213. doi: 10.1007/s10548-010-0137-y

Bouguet, J. (2000). *Pyramidal Implementation of the Lucas Kanade Feature Tracker*. Available online at: Preprint, http://robots.stanford.edu/cs223b04/algo_affine_tracking.pdf

Bradski, G. (1998). *Computer Vision Tracking for Use in a Perceptual User Interface*. Available online at: Preprint, http://www.cse.psu.edu/\simrcollins/CSE598G/papers/camshift.pdf

Brovelli, A., Ding, M., Ledberg, A., Chen, Y., Nakamura, R., and Bressler, S. (2004). Beta oscillations in a large-scale sensorimotor cortical network: directional influences revealed by Granger causality. *Proc. Natl. Acad. Sci. U.S.A.* 101, 9849–9854. doi: 10.1073/pnas.0308538101

Brzezicka, A., Kaminski, M., Kaminski, J., and Blinowska, K. (2011). Information transfer during a transitive reasoning task. *Brain Topogr*. 24, 1–8. doi: 10.1007/s10548-010-0158-6

Busemeyer, J., and Bruza, P. (2012). *Quantum Models of Cognition and Decision*. Cambridge University Press.

Cermak, S., Kosicek, M., Mladenovic-Djordjevic, A., Smiljanic, K., Kanazir, S., and Hecimovic, S. (2016). Loss of cathepsin B and L leads to lysosomal dysfunction. NPC-like cholesterol sequestration and accumulation of the key Alzheimer's proteins. *PLOS ONE*. 11:e0167428. doi: 10.1371/journal.pone.0167428

Chen, Y., Bressler, S. L., and Ding, M. (2006). Frequency decomposition of conditional Granger causality and application to multivariate neural field potential data. *J. Neurosci. Methods* 150, 228–237. doi: 10.1016/j.jneumeth.2005.06.011

Culić, M., and Šaponjić, J. (1998). Methodological approaches in understanding the cerebellar motor and nonmotor functions. *Jugoslav. Physiol. Pharmacol. Acta* 3, 11–20.

Geweke, J. (1982). Measurement of linear dependence and feedback between multiple time series. *J. Am. Stat. Assoc.* 77, 304–313.

Geweke, J. (1984). Measures of conditional linear dependence and feedback between time series. *J. Am. Stat. Assoc.* 79, 907–915.

Granger, C. (1969). Investigating causal relations by econometric models and cross-spectral methods. *Econometrica* 37, 424–438.

Granger, C. (1980). Testing for causality: a personal viewpoint. *J. Econ. Dynam. Cont.* 2, 329–352.

Granger, C., and Morris, M. (1976). Time series modeling and interpretation. *J. R. Stat. Soc. Ser. A* 139, 246–257.

Haralick, R., Shanmugam, K., and Dinstein, I. (1973). Textural features for image classification. *IEEE Trans. Syst. Man Cybern.* 3, 610–621.

Hasselman, F. (2013). When the blind curve is finite: dimension estimation and model inference based on empirical waveforms. *Front. Physiol.* 4:75. doi: 10.3389/fphys.2013.00075

Holden, J. G., Riley, M. A., Gao, J., and Torre, K. (2013). Fractal analyses: statistical and methodological innovations and best practices. *Front. Physiol.* 4:97. doi: 10.3389/fphys.2013.00097

Hsu, H. (2014). *Signals and Systems*. Schaum's outlines series, McGraw-Hill.

Japundzic-Zigon, N. (1998). Physiological mechanisms in regulation of blood pressure fast frequency variations. *Clin. Exp. Hyperten.* 20, 359–388.

Japundzic-Zigon, N. (2001). Effects of nonpeptide V1a and V2 antagonists on blood pressure fast oscillations in conscious rats. *Clin. Exp. Hyperten.* 23, 277–292. doi: 10.1081/CEH-100102667

Japundzic-Zigon, N., Milutinović, S., and Jovanović, A. (2004). Effects of nonpeptide and selective V1 and V2 antagonists on blood pressure short-term variability in spontaneously hypertensive rats. *J. Pharmacol. Sci.* 95, 47–55. doi: 10.1254/jphs.95.47

Jech, T. (2006). *Set Theory*. Springer.

Jovanović, A. (2001). Research in the group for intelligent systems at Belgrade University, problems and results (Russian). *Intelek. Sistemi* 6, 163–182.

Jovanović, A., Kasum, O., Perić, N., and Perović, A. (2014). "Enhancing microscopic imaging for better object and structural detection, insight and classification," in Microscopy: *Advances* in *Scientific Research* and *Education*, FORMATEX Microscopy *Series* N6, VOL. 2, ed, A. Mendez-Vilas.

Jovanović, A., and Perović, A. (2007). Brain computer interfaces - some technical remarks. *Int. J. Bioelectromag.* 9, 91–102. doi: 10.1016/j.specom.2010.01.001

Jovanović, A., Perović, A., Klonowski, W., Duch, W., Djordjević, Z., and Spasic, S. (2010). Detection of structural features in biological signals. *J. Signal Process. Syst.* 60, 115–129. doi: 10.1007/s11265-009-0407-7

Kaminski, M., Ding, M., Truccolo, W., and Bressler, S. (2001). Evaluating causal relations in neural systems: Granger causality, directed transfer function and statistical assessment of significance. *Biol. Cybern.* 85, 145–157. doi: 10.1007/s004220000235

Kaminski, M. J., and Blinowska, K. J. (1991). A new method of the description of the information flow in the brain structures. *Biol Cybern.* 65, 203–210. doi: 10.1007/BF00198091

Kantelhardt, J., Zschiegner, S., Koscielny-Bunde, E., Bunde, A., Halvin, S., and Stanley, E. (2002). *Multifractal Detrended Fluctuation Analysis of Nonstationary Time Series*. arXiv:physics/020207v1.

Kasum, O., Dolicanin, E., Perović, A., and Jovanović, A. (2015). Brain connectivity extended and expanded. *EPJ Nonlin. Biomed. Phys.* 3, 4. doi: 10.1140/epjnbp/s40366-015-0019-z

Kesić, S., Nikolić, L. J., Savić, A., Janać, B., and Spasić, S. (2014). kes2. *Gen. Physiol. Biophys.* 33, 335–344. doi: 10.4149/gpb_2014010

Kesić, S., and Spasić, S. (2016). Application of Higuchi's fractal dimension from basic to clinical neurophysiology: a review. *Comp. Methods Prog. Biomed.* 133, 55–70. doi: 10.1016/j.cmpb.2016.05.014

Klonowski, W., Duch, W., Perović, A., and Jovanović, A. (2009). Some computational aspects of the brain computer interfaces based on inner music. *Comp. Intelligen. Neurosci.* 2009:950403. doi: 10.1155/2009/950403

Kroger, J., Elliott, L., Wong, T., Lakey Dang, J. H., and George, J. (2006). "Detecting mental commands in high frequency EEG: faster brain-machine interfaces," in *Proceedings of the 2006 Biomedical Engineering Society Annual Meeting*, Chicago.

Kuś, R., J Blinowska, K., Kaminski, M., and Basinska-Starzycka, A. (2008). Transmission of information during continuous attention test. *Acta Neurobiol. Exp.* 68, 103–112.

Liu, L., Arfanakis, K., and Ioannides, A. (2007). Visual field influences functional connectivity pattern in a face affect recognition task. *Int. J. Bioelectromagn.* 9, 245–248.

Mendelson, E. (1997). *Introduction to Mathematical Logic*. Chapman & Hall.

Molenaar, P. (2004). A manifesto on psychology as idiographic science: bringing the person back into scientific psychology, this time forever. *Measurement* 2, 201–218. doi: 10.1207/s15366359mea0204_1

Pap, E. (Ed.) (2002). *Handbook of Measure Theory*. Elsevier.

Perović, A., Dordevic, Z., Paskota, M., Takači, A., and Jovanović, A. (2013). Automatic recognition of features in spectrograms based on some image analysis methods. *Acta Polytechn. Hungarica* 10, 153–172.

Sameshima, K., and Baccala, L. (1999). Using partial directed coherence to describe a neuronal assembly interactions. *J. Neurosci. Methods* 94, 93–103.

Schelter, B., Winterhalder, M., Eichler, M., Peifer, M., Hellwig, B., Guschlbauer, B., et al. (2005). Testing for directed influences among neural signals using partial directed coherence. *J. Neurosci. Methods* 152, 210–219. doi: 10.1016/j.jneumeth.2005.09.001

Singh, H., Li, Q., Hines, E., and Stocks, N. (2007). Classification and feature extraction strategies for multi channel multi trial BCI data. *Int. J. Bioelectromagn.* 9, 233–236.

Solovay, R. (1970). A model of Set theory in which every set of reals is Lebesgue measurable. *Ann. Math.* 92, 1–56.

Solovay, R. (1971). Real-valued measurable cardinals. axiomatic set theory. *Proc. Symp. Pure Math.* 13, 397–428.

Spasić, S., Perović, A., Klonowski, W., Djordjević, Z., Duch, W., and Jovanović, A. (2010). Forensics of features in the spectra of biological signals. *Int. J. Bioelectromagn.* 12, 62–75.

Spiegel, M., and Stephens, L. (2018). *Statistics*. Schaum's outlines series, McGraw-Hill.

Takahashi, D., Baccalá, L., and Sameshima, K. (2008). Partial directed coherence asymptotics for VAR processes of infinite order. *Int. J. Bioelectromagn.* 10, 31–36.

Takahashi, D. Y., Baccalá, L., and Sameshima, K. (2010). Information theoretic interpretation of frequency domain connectivity measures. *Biol. Cybern.* 103, 463–469. doi: 10.1007/s00422-010-0410-x

Vukosavic, S., Ruzdijic, S., Veskov, R., Rakic, L., and Kanazir, S. (2001). Differential effects of amphetamine and phencyclidine on the expression of growth-associated protein GAP-43. *Neurosci. Res.* 40, 133–140. doi: 10.1016/S0168-0102(01)00222-X

Wang, X., Chen, Y., Bressler, S. L., and Ding, M. (2007). Granger causality between multiple interdependent neurobiological time series: blockwise versus pairwise methods. *Int. J. Neur. Syst.* 17, 71–78. doi: 10.1142/S0129065707000944

Watkins, C., Kroger, J., Kwong, N., Elliott, L., and George, J. (2006). "Exploring high-frequency EEG as a faster medium of brain-machine communication," in *Proceedings Institute of Biological Engineering 2006 Annual Meeting*, Tucson.

Webber, C., and Marwan, N. (editors) (2015). *Recurrence Quantification Analysis: Theory and Best Practices*. Springer.

Welch, G., and Bishop, G. (2004). *An Introduction to the Kalman Filter*. Chapter Hill: University of North Carolina at Chapter Hill.

Werde, R., and Spiegel, M. (2010). *Advanced Calculus*. Schaum's outlines series, McGraw-Hill.

Conflict of Interest Statement: The authors declare that the research was conducted in the absence of any commercial or financial relationships that could be construed as a potential conflict of interest.

The handling editor declared a shared affiliation, though no other collaboration, with the authors at time of review.

The reviewer ZMN declared a shared affiliation, with no collaboration, with the authors to the handling editor at time of review.

Copyright © 2018 Kasum, Perović and Jovanović. This is an open-access article distributed under the terms of the Creative Commons Attribution License (CC BY). The use, distribution or reproduction in other forums is permitted, provided the original author(s) and the copyright owner(s) are credited and that the original publication in this journal is cited, in accordance with accepted academic practice. No use, distribution or reproduction is permitted which does not comply with these terms.

frontiers in Physiology

METHODS
published: 11 October 2018
doi: 10.3389/fphys.2018.01382

Partial Autoinformation to Characterize Symbolic Sequences

Frederic von Wegner[1,2]*

[1] Epilepsy Center Rhein-Main, Goethe University Frankfurt, Frankfurt am Main, Germany, [2] Department of Neurology and Brain Imaging Center, Goethe University Frankfurt, Frankfurt am Main, Germany

An information-theoretic approach to numerically determine the Markov order of discrete stochastic processes defined over a finite state space is introduced. To measure statistical dependencies between different time points of symbolic time series, two information-theoretic measures are proposed. The first measure is time-lagged mutual information between the random variables X_n and X_{n+k}, representing the values of the process at time points n and $n+k$, respectively. The measure will be termed autoinformation, in analogy to the autocorrelation function for metric time series, but using Shannon entropy rather than linear correlation. This measure is complemented by the conditional mutual information between X_n and X_{n+k}, removing the influence of the intermediate values $X_{n+k-1}, \ldots, X_{n+1}$. The second measure is termed partial autoinformation, in analogy to the partial autocorrelation function (PACF) in metric time series analysis. Mathematical relations with known quantities such as the entropy rate and active information storage are established. Both measures are applied to a number of examples, ranging from theoretical Markov and non-Markov processes with known stochastic properties, to models from statistical physics, and finally, to a discrete transform of an EEG data set. The combination of autoinformation and partial autoinformation yields important insights into the temporal structure of the data in all test cases. For first- and higher-order Markov processes, partial autoinformation correctly identifies the order parameter, but also suggests extended, non-Markovian effects in the examples that lack the Markov property. For three hidden Markov models (HMMs), the underlying Markov order is found. The combination of both quantities may be used as an early step in the analysis of experimental, non-metric time series and can be employed to discover higher-order Markov dependencies, non-Markovianity and periodicities in symbolic time series.

Keywords: EEG microstates, information theory, entropy, mutual information, Markovianity, stationarity

OPEN ACCESS

Edited by:
Srdjan Kesić,
University of Belgrade, Serbia

Reviewed by:
Hussein M. Yahia,
Institut National de Recherche en Informatique et en Automatique (INRIA), France
Luca Faes,
Università degli Studi di Palermo, Italy

***Correspondence:**
Frederic von Wegner
vonWegner@med.uni-frankfurt.de

Specialty section:
This article was submitted to Fractal Physiology, a section of the journal Frontiers in Physiology

Received: *30 May 2018*
Accepted: *11 September 2018*
Published: *11 October 2018*

Citation:
von Wegner F (2018) Partial Autoinformation to Characterize Symbolic Sequences. Front. Physiol. 9:1382. doi: 10.3389/fphys.2018.01382

1. INTRODUCTION AND BACKGROUND

Information theory occupies a central role in time series analysis. The concept of entropy provides numerous important connections to statistical physics and thermodynamics, often useful in the interpretation of the results (Kullback, 1959; Cover and Thomas, 2006). Despite the large number of available measures, there is no generally accepted systematic procedure for the analysis of symbolic time series, although collections of theory and methods are readily available (Daw et al., 2003; Mézard and Montanari, 2009). In metric time series analysis however, a hierarchical set of analyses and tests has been established by Box and Jenkins (Box and Jenkins, 1976). The seminal work by these authors deals with autoregressive and moving average processes, some of the most prominent Markov processes across many fields of science (Häggström, 2002). The result is a standardized procedure for analyzing continuous valued, discrete time stochastic processes (Box and Jenkins, 1976). The procedure addresses the impressive complexity of possible stochastic processes by combining semi-quantitative, visual analysis steps with a number of rigorous statistical test procedures. The first step in Box-Jenkins analysis is the visual and statistical assessment of the autocorrelation function (ACF) and the partial autocorrelation function (PACF) of the data. In particular, the order of purely autoregressive processes can be directly deduced from the PACF coefficients. For a p-th order autoregressive process, it can be shown that PACF coefficients for time lags larger than p are equal to zero, within statistical limits.

Information-theoretical time series analysis is closely linked to the theory of Markov processes, as Markov processes are defined via their temporal dependencies. The elemental case is a first-order Markov process $(X_n)_{n\in\mathbb{Z}}$, for which the transition $X_n \rightarrow X_{n+1}$ depends on the current state X_n only. Due to this property, first-order Markov processes are termed memory-less, as their past does not influence transitions to future states. Markov processes of order M generalize this property and have transition probabilities defined by M past states $(X_n, \ldots, X_{n-M+1})$, thus representing finite memory effects of the time series. Using information-theoretical methods, memory effects and temporal dependencies can be quantified. A more formal treatment of Markov processes follows in the Materials and Methods section, after introducing the necessary notation.

To assess the Markov property of a time series, and to identify the Markov order of an empirical symbol sequence, classical statistics derives a number of tests as detailed in the Materials and Methods section (Hoel, 1954; Anderson and Goodman, 1957; Goodman, 1958; Billingsley, 1961; Kullback et al., 1962).We recently used the tests developed in (Kullback et al., 1962) to characterize electroencephalographic (EEG) data transformed into a symbolic time series termed microstate sequences (von Wegner and Laufs, 2018). Using time-lagged mutual information, we could show that the symbolic four-state sequences still retain periodic features of the underlying continuous EEG signal (von Wegner et al., 2017, 2018). The aim of the present article is to introduce partial autoinformation as a measure that is complementary to the time-lagged mutual information function, in the same sense that the PACF complements the autocorrelation function in classical time series analysis of continuous random variables. In the past, we have used the term autoinformation function (AIF) for time-lagged mutual information, in analogy with the autocorrelation function (ACF) of classical time series analysis (von Wegner et al., 2017). To continue the analogy, the newly introduced measure will be termed partial autoinformation function (PAIF), because it answers the same question about the information content of a symbolic time series as the partial autocorrelation function (PACF) does about correlations. The new measure is derived based on the analogy with the PACF and theoretical connections with well-known functionals such as the entropy rate and active information storage are established. Next, we apply the AIF/PAIF approach to a number of symbolic time series ranging from Markov and non-Markov model data with known properties to simulated data representing physical systems (Ising model, abstract ion channel model) and experimental EEG microstate data. Finally, limitations and possible applications are discussed for larger state spaces and finite samples.

2. MATERIAL AND METHODS

2.1. Autoregressive Processes

To illustrate the motivation for this study, an exemplary autoregressive process is used to explain the principles of time series analysis with the (partial) autocorrelation approach. Autoregressive (AR) processes model time series of continuous random variables in discrete time (Box and Jenkins, 1976). The p-th order or AR(p) process models the dependency of X_n on its past via a linear combination of the p values preceding X_n:

$$X_n = \phi_1 X_{n-1} + \ldots + \phi_p X_{n-p} + \varepsilon_n \tag{1}$$

where $\phi_1, \ldots, \phi_p$ are called the autoregression coefficients and ε_n represents identically and independently distributed (iid) Gaussian noise.

The linear dependencies created by Equation (1) can be quantified by the time autocorrelation function (ACF). The ACF coefficients ρ_k of a stationary stochastic process X_n are defined as:

$$\rho_k = C\left(X_{n+k}, X_n\right) \tag{2}$$

where $C(X, Y) = \sum_i \frac{(X_i-\mu_X)(Y_i-\mu_Y)}{\sigma_X \sigma_Y}$ denotes Pearson's correlation coefficient. The ACF coefficients describe the linear correlation between process values at two different time steps X_n and X_{n+k}, without taking into account the effect of the intermediate time steps $X_{n+k-1}, \ldots, X_{n+1}$. However, X_n could be correlated with X_{n+k} directly, independent of the intermediate values, or the correlation between X_n and X_{n+k} could be conveyed via the intermediate values and vanish when conditioned on these intermediates. To distinguish these cases, the PACF performs a multivariate regression of X_{n+k} on all values $X_{n+k-1}, \ldots, X_n$ and finally records the conditioned or partial correlation between X_n and X_{n+k}, removing the effect of the intermediate values:

$$\varphi_{kk} = C\left(X_{n+k}, X_n \mid X_{n+k-1}, \ldots, X_{n+1}\right). \tag{3}$$

Continuous-valued, discrete time AR processes can be systematically assessed using the combination of the autocorrelation function and the PACF (Box and Jenkins, 1976).

We here present an example using a third-order autoregressive process that is parametrized by:

$$X_n = 0.85X_{n-1} - 0.2X_{n-2} + 0.1X_{n-3} + \varepsilon_n \tag{4}$$

with AR coefficients $\phi_1 = 0.85$, $\phi_2 = -0.2$ and $\phi_3 = 0.1$. **Figure 1** shows the ACF/PACF analysis of a simulated sample path ($N = 10^5$ samples). The left panel, **Figure 1A** shows the exponentially decaying ACF. Though the analytical form of the ACF can be expressed in terms of the three AR coefficients, visual analysis does not allow to deduce the order of the AR process or the magnitude of the coefficients. The right panel, **Figure 1B** shows the PACF whose zero-lag coefficient $\varphi_{00} = 1$, by definition. The following three values φ_{11-33} directly reflect the relative magnitude and sign of the AR coefficients ϕ_{1-3}. Thus, through PACF analysis, the AR(3) structure of the process can be conjectured from visual analysis already. In practice, the statistical significance of each coefficient can also be assessed quantitatively. In **Figure 1**, confidence intervals ($\alpha = 0.05$) are shown in blue.

The classical Box-Jenkins approach to time series analysis considers the magnitude of ACF and PACF coefficients to guess the statistical structure of the data (Box and Jenkins, 1976). For a pure autoregressive process of order p, the PACF coefficients φ_{kk} vanish for $k > p$. In case of a pure moving average process, the expected value of the ACF coefficients ρ_k are zero for $k > p$. For mixed (ARMA) processes, the model orders cannot be determined visually. Although the pure AR model order can be deduced from the decay of the PACF, and the PACF coefficients φ_{kk} can be expressed in terms of the AR coefficients ϕ_k, the exact value of the AR coefficients ϕ_k cannot be derived visually, with the exception of a few simple low-order cases.

2.2. Information Theory

Information theory is rooted in mathematical statistics and uses entropy as one of its main concepts (Kullback, 1959). Entropy characterizes the shape of probability distributions and thereby, the amount of uncertainty or surprise associated with samples generated from the distribution. This section summarizes the concepts and definitions needed to derive the PAIF, more extensive treatments can be found in classical and more recent monographs (Kullback, 1959; Cover and Thomas, 2006; Mézard and Montanari, 2009). Connections of the PAIF with other information-theoretical quantities are derived in the first paragraph of the Results section. Logarithms are computed as $\log_2$, such that all information-theoretical quantities are measured in bits.

We here consider stochastic processes $(X_n)_{n \in \mathbb{Z}}$, i.e., sequences of random variables X_n, where each X_n takes values in some finite alphabet of L different symbols $S = \{s_0, \ldots, s_{L-1}\}$. In practice, we deal with finite samples of the underlying process, $(X_n)_{n=0,\ldots,N-1}$. In the following, contiguous data blocks starting from index n, and covering the past k values of the process, $\left(X_n, X_{n-1}, \ldots X_{n-k+1}\right)$ will be termed k-histories and are written as

$$\mathbf{X}_n^{(k)} = \left(X_n, X_{n-1}, \ldots X_{n-k+1}\right). \tag{5}$$

Denoting a specific realization of the random variable X_i as x_i, the joint probability distribution of k-histories is given by

$$P(\mathbf{X}_n^{(k)}) = \Pr\left(X_n = x_n, X_{n-1} = x_{n-1}, \ldots X_{n-k+1} = x_{n-k+1}\right).$$

where $x_i \in S$, for all $i = n-k+1, \ldots, n$. In the following, the compact notation $P(\mathbf{X}_n^{(k)})$ will be used.

The information content of a random variable X with possible values $x_i \in S$ and associated probabilities $P(X =$

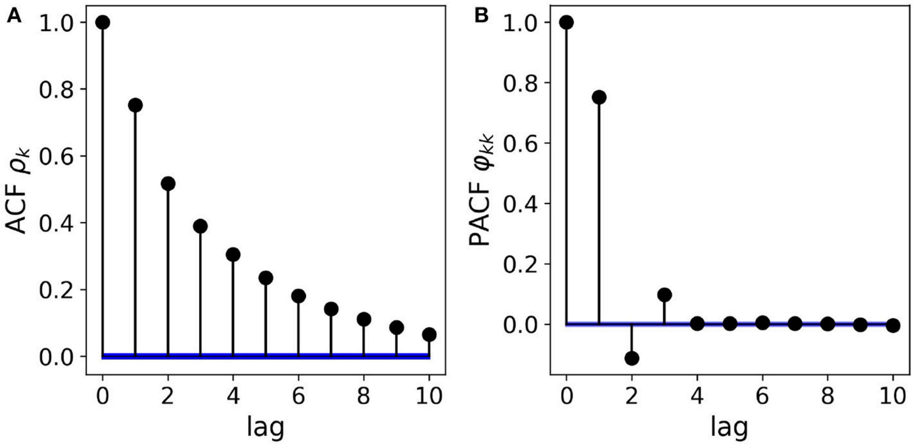

FIGURE 1 | Partial autocorrelation analysis of a real-valued autoregressive process. **(A)** The AR(3) structure of the data cannot be deduced visually from the shape of the ACF, though the exponential decay can be parametrized exactly by the three AR coefficients. **(B)** Removing the effect of intermediate values, the PACF coefficients directly reflect the AR(3) structure as well as the magnitude and sign of the AR coefficients. Confidence intervals ($\alpha = 0.05$) for the absence of correlations are shown in blue.

$x_i) = p_i$ is measured by the **Shannon entropy** $H(X) = -\sum_i p_i \log p_i$ (Kullback, 1959). The information content of the joint distribution representing the k-history $\mathbf{X}_n^{(k)}$ is measured by the **joint entropy**, which is defined as (Kullback, 1959; Cover and Thomas, 2006):

$$H_X(n,k) := H(\mathbf{X}_n^{(k)}) \tag{6}$$

$$= -\sum_{\mathbf{X}_n^{(k)}} P(\mathbf{X}_n^{(k)}) \log P(\mathbf{X}_n^{(k)}) \tag{7}$$

where the sum runs over all possible values of $X_n = x_n, \ldots, X_{n-k+1} = x_{n-k+1}$. The expression $H_X(n,k)$ contains the time parameter n, such that the expression for $H_X(n,k)$ can be used even in the case of non-stationary processes, whose statistical properties may depend on n. Under time-stationary conditions, the entropy is obtained by averaging over all time points and the resulting entropy will be abbreviated

$$H_k = \langle H_X(n,k) \rangle_n$$

where $\langle \cdot \rangle_n$ denotes time averaging.

Adding information about the value of another random variable Y reduces the uncertainty about X, in case X and Y are statistically dependent. If X and Y are independent, the entropy of X does not change with the additional information about Y. To measure the influence of Y on X, **conditional entropy** is defined as $H(X \mid Y) = H(X,Y) - H(Y)$. In the following, two conditional entropy terms will be used.

The first term is a finite approximation to the entropy rate of the stochastic process X. The **entropy rate** h_X of a process quantifies the amount of surprise about the next symbol X_{n+1} emitted by the process, given knowledge about its past values $\mathbf{X}_n^{(k)}$. The theoretical or analytical value h_X is defined via an infinitely long history

$$h_X = \lim_{k \to \infty} H(X_{n+1} \mid \mathbf{X}_n^{(k)}).$$

When working with finite experimental data samples, the entropy rate has to be estimated from finite k-histories (Runge et al., 2012; Barnett and Seth, 2015; Faes et al., 2015; Xiong et al., 2017):

$$h_X(n,k) = H(X_{n+1} \mid \mathbf{X}_n^{(k)}). \tag{8}$$

Using the definition of conditional entropy, $h_X(n,k)$ can be computed from joint entropies as:

$$h_X(n,k) = H(X_{n+1}, \mathbf{X}_n^{(k)}) - H(\mathbf{X}_n^{(k)}) \tag{9}$$

$$= H(\mathbf{X}_{n+1}^{(k+1)}) - H(\mathbf{X}_n^{(k)}). \tag{10}$$

Following the notation used for Shannon entropy, the time-stationary expression for the entropy rate will be denoted $h_k = \langle h_X(n,k) \rangle_n$.

The second conditional entropy term used is the **two-point conditional entropy** $H(X_{n+k} \mid X_n)$, that measures the amount of information about X_{n+k} contained in X_n.

Next, **mutual information** between two random variables is defined as $I(X;Y) = H(X) - H(X \mid Y)$ and measures the information shared between both variables. Mutual information will be used to compute two quantities that are useful in characterizing symbol sequences.

First, **active information storage (AIS)** (Lizier et al., 2012) is complementary to the entropy rate. While the entropy rate measures how much information (or surprise) is contained in X_{n+1}, despite knowledge of its k-history $\mathbf{X}_n^{(k)}$, AIS measures the amount of common (or shared) information between X_{n+1} and its k-history. The active information storage term for a history of length k is defined as

$$a_X(n,k) = I(X_{n+1}; \mathbf{X}_n^{(k)}) \tag{11}$$

and the stationary expression is $a_k = \langle a_X(n,k) \rangle_n$.

For computational implementation, active information storage is decomposed into joint entropy terms:

$$\begin{aligned} I(X_{n+1}; \mathbf{X}_n^{(k)}) &= H(X_{n+1}) - H(X_{n+1} \mid \mathbf{X}_n^{(k)}) \\ &= H(X_{n+1}) + H(\mathbf{X}_n^{(k)}) - H(X_{n+1}, \mathbf{X}_n^{(k)}) \\ &= H(X_{n+1}) + H(\mathbf{X}_n^{(k)}) - H(\mathbf{X}_{n+1}^{(k+1)}). \end{aligned}$$

The second mutual information term used is $I(X_{n+1}; X_k)$, and yields an estimate of the statistical dependency between the random variables X_n and X_{n+k}. In a recent publication, we used the term **autoinformation function (AIF)** to denote the set of time-lagged mutual information terms computed for a number of time lags (von Wegner et al., 2017). The name AIF was derived from the formal analogy with the autocorrelation function (ACF) for metric time series. We defined the AIF coefficient at time lag k as:

$$\alpha_X(n,k) = I(X_{n+k}; X_n) \tag{12}$$

$$= H(X_{n+k}) - H(X_{n+k} \mid X_n) \tag{13}$$

$$= H(X_{n+k}) + H(X_n) - H(X_{n+k}, X_n) \tag{14}$$

and the stationary term is $\alpha_k = \langle \alpha_X(n,k) \rangle_n$. Rather than using linear correlation to measure the dependency between two time points, as the ACF does, the AIF employs mutual information between the random variables at time points n and $n+k$. The measure is symmetric, i.e., $I(X_n; X_{n+k}) = I(X_{n+k}; X_n)$ and therefore does not contain directional information. In analogy to the autocorrelation function, division of all coefficients by $\alpha_X(n,0)$ normalizes the AIF to $\alpha_X(n,0) = 1$. The computational cost is independent of the time lag k, as all entropies are computed from one-dimensional ($H(X_{n+k})$, $H(X_n)$) and two-dimensional ($H(X_{n+k}, X_n)$) distributions.

Finally, the definition of partial autoinformation, the central concept of this work, is based on the concept of **conditional mutual information** which includes a third random variable

Z, on which the mutual information between X and Y is conditioned:

$$I(X;\, Y \mid Z) = H(X \mid Z) - H(X \mid Y, Z). \tag{15}$$

The information-theoretical match for the PACF should estimate the two-point dependency between X_n and X_{n+k}, while removing the influence of the intermediate variables $\mathbf{X}^{(k-1)}_{n+k-1} = (X_{n+k-1}, \ldots, X_{n+1})$. This is achieved by computing the conditional mutual information (Equation 15) between X_n and X_{n+k}, given $\mathbf{X}^{(k-1)}_{n+k-1}$.

We therefore define the PAIF coefficient $\pi_X(n,k)$ at time lag k as:

$$\begin{aligned}\pi_X(n,k) &= I(X_{n+k};\, X_n \mid X_{n+k-1} \ldots X_{n+1}) && (16)\\ &= I(X_{n+k};\, X_n \mid \mathbf{X}^{(k-1)}_{n+k-1}). && (17)\end{aligned}$$

Using the definition of conditional mutual information in terms of conditional entropies, and the expression of conditional entropy in terms of joint entropies, the computation of $\pi_X(n,k)$ can be reduced to the estimation of joint entropies:

$$\begin{aligned}\pi_X(n,k) \;&=\; H(X_{n+k} \mid \mathbf{X}^{(k-1)}_{n+k-1}) - H(X_{n+k} \mid \mathbf{X}^{(k-1)}_{n+k-1}, X_n) && (18)\\ &=\; H(X_{n+k}, \mathbf{X}^{(k-1)}_{n+k-1}) - H(\mathbf{X}^{(k-1)}_{n+k-1}) - H(X_{n+k}, \mathbf{X}^{(k)}_{n+k-1})\\ &\quad + H(\mathbf{X}^{(k)}_{n+k-1}) && (19)\\ &=\; H(\mathbf{X}^{(k)}_{n+k}) - H(\mathbf{X}^{(k-1)}_{n+k-1}) - H(\mathbf{X}^{(k+1)}_{n+k}) + H(\mathbf{X}^{(k)}_{n+k-1}). && (20)\end{aligned}$$

The stationary expression is

$$\begin{aligned}\pi_k &= h_{k-1} - h_k\\ &= -H_{k-1} + 2H_k - H_{k+1}.\end{aligned}$$

For the first two coefficients $\pi_X(n,0)$ and $\pi_X(n,1)$, there are no intermediate values $\mathbf{X}^{(k-1)}_{n+k-1}$ to condition on. Analogous to the PACF algorithm, we set $\pi_X(n,0) = \alpha_X(n,0)$ and $\pi_X(n,1) = \alpha_X(n,1)$. The computational load increases exponentially with history length k, as the discrete joint distribution $P(\mathbf{X}^{(k-1)}_{n+k-1})$ over L labels has L^{k-1} elements.

The computation of the quantity of interest, the PAIF coefficients, is visualized in **Figure 2**. Above, the relationships between the quantities discussed here are shown as an information diagram, a special form of a Venn diagram. AIF coefficients are represented by the intersection of the two dark gray circles which represent $H(X_{n+k})$ and $H(X_n)$, respectively. In the scheme below, where each element of the time series X_n is visualized as a square box, the AIF coefficients represent the shared information between X_{n+k} and X_n, without taking into account the effects of $\mathbf{X}^{(k-1)}_{n+k-1}$ (light gray areas in the information diagram above and the symbolic sequence below). The PAIF corresponds to the part of $I(X_{n+k}; X_n)$ that does not intersect with the lower circle, representing the intermediate values $H(\mathbf{X}^{(k-1)}_{n+k-1})$. The area that represents the PAIF is shown in dark blue in the information scheme.

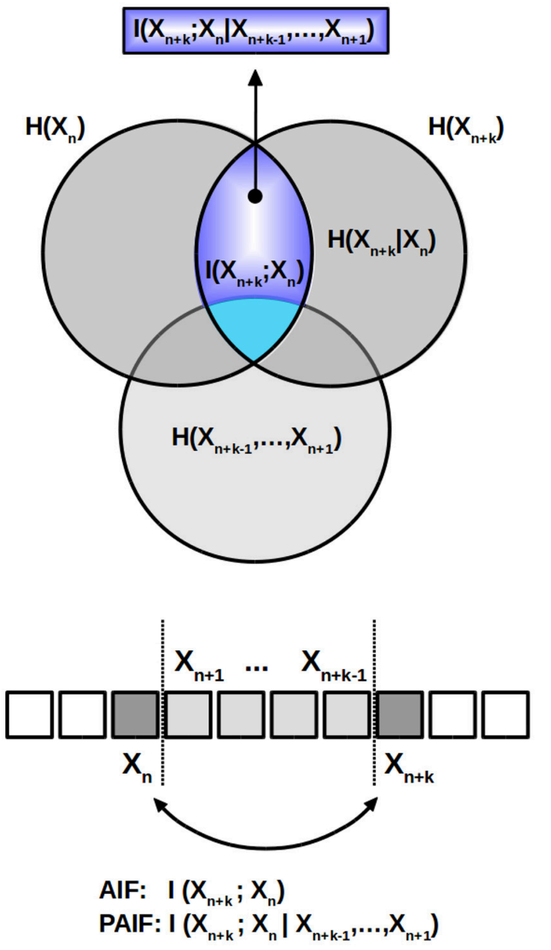

FIGURE 2 | AIF/PAIF analysis. The information diagram above illustrates the partition of the total data entropy. The intersection of the two dark gray circles, representing H_n and H_{n+k}, respectively, corresponds to the AIF coefficient $I(X_{n+k}; X_n)$ (light blue area). It measures the shared information between the time points n and $n + k$, while ignoring the intermediate variables. The PAIF coefficients are represented by the dark blue sub-area of $I(X_{n+k}; X_n)$ that results from excluding all elements that belong to the intermediate values $H(X_{n+k-1}, \ldots, X_{n+1})$, shown in light gray color in the Venn diagram and the symbolic time series below.

2.3. Markovianity Tests

A discrete Markov process $(X_n)_{n\in\mathbb{Z}}$ of order M is defined via the property

$$P(X_{n+1} \mid \mathbf{X}^{(M+k)}_n) = P(X_{n+1} \mid \mathbf{X}^{(M)}_n) \tag{21}$$

for all positive integers $k \geq 0$. In words, the transition probabilities from X_n to the state X_{n+1} depend on the M-history of X_n, whereas inclusion of more values from the process' past, beyond X_{n-M+1}, does not convey further information about the transition probabilities.

General tests for the Markov property of low orders have been introduced in the 1950s and further tests for many special cases are still being developed today. Early works used analytical expressions for the distribution of symbol counts, given a certain Markov structure, and developed likelihood ratio tests for the cases of known (Bartlett, 1951) and unknown (Hoel, 1954) transition probabilities. Further developments included χ^2 tests for hypotheses about the time-stationarity of transition probabilities, direct comparisons of different Markov orders (Anderson and Goodman, 1957; Goodman, 1958), as well as parameter estimation methods and tests for continuous time Markov processes (Billingsley, 1961). Using close relationships between χ^2 statistics and information-theoretical expressions, test statistics based on Kullback-Leibler metrics were summarized as a monograph and in a practice-oriented article containing many numerical examples by Kullback (Kullback, 1959; Kullback et al., 1962). Further approaches include the application of the Akaike information criterion to optimize the order estimate for a discrete Markov chain (Tong, 1975) as well as data compression oriented algorithms (Merhav et al., 1989) and extensive surrogate data tests (Pethel and Hahs, 2014). The results of the PAIF method developed here is compared to the Markov order test presented in van der Heyden et al. (1998). The latter test compares finite entropy rate estimates ($h_X(n,k)$) of the data to be tested with surrogate statistics obtained from M-order Markov surrogates with the same transition probabilities $P(X_{n+1} \mid \mathbf{X}_n^{(M)})$ as the data. The algorithm for the computation of the surrogates is given in detail in (van der Heyden et al., 1998) and is summarized in the following section 2.4. This test will be termed conditional entropy test. In this article, surrogate statistics for each test data set are computed from $n = 100$ surrogate sequences for each Markov order $M = 0, \ldots, 5$. The Markov order identified by the conditional entropy test is taken to be the value M for which all $h_X(n,k)$ lie within the $\alpha = 0.05$ confidence interval defined by the surrogates.

We recently published our Python implementation of the Markovianity tests of order 0-2 as well as symmetry and stationarity tests as given in Kullback et al. (1962), in article form (von Wegner and Laufs, 2018), and as open-source code. Although the code is part of an algorithm to process EEG microstate sequences, the tests can be exported and applied generically.

2.4. Markov Surrogate Data

A Markov process of order M is also defined via its transition probabilities $P(X_{n+1} \mid \mathbf{X}_n^{(M)})$, where the probability to go into state X_{n+1} is conditioned on the M-history $\mathbf{X}_n^{(M)}$. To synthesize a Markov process of order M, using the same transition probabilities as the underlying experimental time series (X_n), the empirical M-order transition matrix is estimated first. To this end, all contiguous tuples of length $(M+1)$ taken from the time series, i.e., tuples of the form $(X_{n-M+1}, \ldots, X_n, X_{n+1})$ are considered. The maximum likelihood estimate for the transition probability $P(X_{n+1} \mid \mathbf{X}_n^{(M)})$ based on this sample is given by

$$\hat{p}_{ML}(X_{n+1} \mid \mathbf{X}_n^{(M)}) = \frac{\#(X_{n+1}, \mathbf{X}_n^{(M)})}{\#(\mathbf{X}_n^{(M)})}$$

where $\#(\cdot)$ denotes the number of times a specific outcome occurs in the empirical sequence (X_n) (Anderson and Goodman, 1957; van der Heyden et al., 1998). For instance, $\#(\mathbf{X}_n^{(M)})$ is the number of realizations $(X_n = x_n, \ldots, X_{n-M+1} = x_{n-M+1})$. While counting the tuples, the joint distribution of $\mathbf{X}_n^{(M)}$ is recorded at the same time.

Following van der Heyden et al. (1998), the first M values of each surrogate Markov sequence are initialized with a sample from the joint distribution $\mathbf{X}_n^{(M)}$. From there, we have a M-history $\mathbf{X}_n^{(M)}$ for every subsequent value X_{n+1}. The value of X_{n+1} is chosen according to the transition probabilities $\hat{p}_{ML}(X_{n+1} \mid \mathbf{X}_n^{(M)})$ and the given M-history. Given a specific M-history $\mathbf{X}_n^{(M)}$, there are L transition probabilities $q_0, \ldots, q_{L-1}$, where $q_i = \hat{p}_{ML}(X_{n+1} = s_i \mid \mathbf{X}_n^{(M)})$. The distribution of the state $X_{n+1} = s_i$ is sampled correctly using a pseudo-random number r, uniformly distributed on the unit interval, $r \sim \mathcal{U}_{[0,1]}$, and the condition $\sum_{l=0}^{i-1} q_l \leq r < \sum_{l=0}^{i}$.

We recently published a Python implementation for first-order Markov surrogates in the open-source package described in von Wegner and Laufs (2018), and have included the M-order Markov surrogates in the Github repository associated with this paper.

2.5. The Two-State Markov Process

The general concepts introduced above are easily applied to a two-state, first-order Markov process that can be written as

$$A \underset{q}{\overset{p}{\rightleftharpoons}} B$$

with transition rates p and q. The self-transition rate for $A \rightarrow A$ is $1-p$, and the rate of $B \rightarrow B$ is $1-q$. The complete transition matrix T reads

$$T = \begin{pmatrix} 1-p & p \\ q & 1-q \end{pmatrix}$$

and has eigenvalues $\lambda_0 = 1$ and $\lambda_1 = 1-(p+q)$. The eigenvalue $\lambda_0 = 1$ is assured by the Perron-Frobenius theorem as T is a stochastic matrix, i.e., $\sum_j T_{ij} = 1$ for all i. The normalized positive eigenvector to λ_0 is the equilibrium or stationary distribution p_{st} of the process,

$$p_{\text{st}} = \left(\frac{q}{p+q}, \frac{p}{p+q} \right).$$

We set $p_A = \frac{q}{p+q}$ and $p_B = \frac{p}{p+q}$. With the auxiliary functions $\varphi, \psi : [0,1] \rightarrow \mathbb{R}$ defined as $\varphi(x) = -x \log x$ and $\psi(x) = \varphi(x) + \varphi(1-x)$, the analytical quantities H_{pq}, h_{pq} and a_{pq} for the 2-state first-order Markov process acquire a very simple form.

The Shannon entropy of the 2-state Markov process is

$$\begin{aligned} H_{pq} &= -p_A \log p_A - p_B \log p_B \\ &= \varphi(p_A) + \varphi(1-p_A) \\ &= \psi(p_A). \end{aligned}$$

Due to the Markov property, the entropy rate is $h_{pq} = H(X_{n+1} \mid X_n)$ and evaluates to

$$h_{pq} = -p_A \left[(1-p)\log(1-p) + p\log p\right] - p_B \left[q\log q + (1-q)\log(1-q)\right] = p_A\psi(p) + p_B\psi(q).$$

The Markov property reduces the full expression for information storage $I(X_{n+1}; \mathbf{X}_n^{(k)})$ to $a_{pq} = I(X_{n+1}; X_n)$:

$$\begin{aligned} a_{pq} &= -p_A \log p_A - p_B \log p_B \\ &\quad + p_A \left[(1-p)\log(1-p) + p\log p\right] + p_B \left[q\log q + (1-q)\log(1-q)\right] \\ &= \psi(p_A) - p_A\psi(p) - p_B\psi(q). \end{aligned}$$

The total entropy is conserved between active information storage and the entropy rate:

$$H_{pq} = a_{pq} + h_{pq}. \tag{22}$$

To validate the proposed approach, these analytical results will later be compared with numerical results of a hidden Markov process classified as first-order Markovian by the PAIF method.

2.6. Higher-Order Markov Processes

To test the properties of the PAIF, two higher-order Markov processes with known properties are synthesized.

The first process is a third-order Markov process denoted $MC_{1..M=3}$, with transition probabilities that depend on $\mathbf{X}_n^{(M=3)}$. Given L states, there are L^M possible M-histories preceding X_{n+1}, such that $P(X_{n+1} \mid \mathbf{X}_n^{(M)})$ in matrix form has shape (L^M, L). The specific transition probabilities are random numbers fulfilling $\sum_j P(X_{n+1} = s_j \mid \mathbf{X}_n^{(M)}) = 1$ for all M-histories $\mathbf{X}_n^{(M)}$. Sample paths are generated using the method described in section 2.4.

The second process will be termed $MC_{M=3}$ and is constructed in such a way that the $X_n \rightarrow X_{n+1}$ transition only depends on X_{n-2}. Like the first process, this process can also be classified as third-order Markovian ($M = 3$), with the particular property that the influence of X_n and X_{n-1} vanishes.

2.7. Hidden Markov Processes

A more general class of discrete processes is represented by probabilistic finite state machines (Crutchfield and Young, 1989), which implement hidden Markov models (HMMs). Hidden Markov models generate sequences of symbols defined over a set of observable states that correspond to our measurements. The observable symbols are emitted by a set of hidden states that follow a Markov process, usually of first order. Each hidden state emits the observable symbols according to its own probability distribution defined over the observable set. It is important to note that the sequence of emitted symbols does not necessarily follow a Markov law.

2.7.1. Even Process

The even process is a non-Markov process with two hidden states ($\{A, B\}$) and two observables ($\{0, 1\}$). The process scheme is visualized in **Figure 4A**. The process can emit arbitrarily long sequences of zeros by repeated self-transitions of the hidden state $A \rightarrow A$. With probability $p = 0.5$, the state A can switch to B and hereby emit a 1, which is followed by another 1 with probability $p = 1$. Thus, ones are always generated in pairs, i.e., in blocks of even length. The procedure generates dependencies that in theory reach into the infinite past and can therefore not be reduced to a Markov process.

2.7.2. Golden Mean Process

Two different implementations of the Golden-mean process are used. First, a 2-state first-order Markovian implementation using two hidden states ($\{A, B\}$) and two observable states ($\{0, 1\}$) (Ara et al., 2016), and second, a fourth-order Markov implementation using seven hidden ($\{A-G\}$) and two observable states ($\{0, 1\}$) (Mahoney et al., 2016). The scheme of the 2-state process (**Figure 4B**) is structurally similar to the even process, but dynamically different. Ones are never emitted repeatedly, i.e., they are always preceded and followed by a zero, in contrast to the even process. The 7-state golden mean process is a so-called R, k-Markov process with Markov order $R = 4$ and cryptic order $k = 3$, in our case (Mahoney et al., 2016).

2.8. Ising Model Data

The Ising model is a widely used discrete model from statistical physics (Hohenberg and Halperin, 1977). The model describes the ferromagnetic interaction of elementary spin variables, with two possible values ± 1, as a function of temperature and the coupling coefficients between spins. The model can be realized with different geometries and in many cases, shows a phase transition at a critical temperature. We use a 2D square lattice geometry ($L = 50$) and run the system for 10^6 time steps. Sample paths are generated by Monte Carlo simulation using a standard Gibbs sampling scheme (Bortz et al., 1975).

2.9. Simulated Ion Channel Data

The dynamics of a simple ion channel with one open and one closed state is modeled as a motion of a particle in the double-well potential $V(x) = -\frac{a}{2}x^2 + \frac{b}{4}x^4$, which shows two stable local minima at $x_{1,2} = \pm\sqrt{\frac{a}{b}}$ and one unstable local maximum at $x_0 = 0$ (Liebovitch and Czegledy, 1992; von Wegner et al., 2014). The system is excited by thermal noise, as implemented by iid Gaussian pseudo-random numbers ξ_n. The system is described by von Wegner et al. (2014)

$$X_{n+1} = X_n + (aX_n - bX_n^3)dt + \xi_n \tag{23}$$

and integrated with an Euler scheme and $\mathrm{dt} = 10^{-3}$.

2.10. EEG Microstate Sequences

A resting state EEG data set from a 21 year old, healthy right-handed female during wakeful rest was selected and analyzed. The data set is part of a larger database for which we have reported the detailed pre-processing pipeline before (von Wegner et al., 2016, 2017). The 30 channel EEG raw data was sampled at 5 kHz using the standard $10-10$ electrode configuration, band-pass filtered to the $1-30$ Hz range using a zero-phase Butterworth filter with a slope of 24 dB/octave, down-sampled to 250 Hz and re-referenced to an average reference. Written informed consent was obtained from the subject and the study was approved by the ethics committee of the Goethe University, Frankfurt, Germany. EEG microstates were identified using the first four principal components (PCA analysis) of the data set and the symbolic microstate sequence was obtained by competitively fitting the microstate maps back into the EEG data set as detailed in (von Wegner et al., 2016, 2017).

3. RESULTS

3.1. Theoretical Results: Relations Between Measures

Using the time index $n+k$ as a reference, the partial autoinformation coefficients $\pi_X(n,k) = I(X_{n+k}; X_n \mid \mathbf{X}^{(k-1)}_{n+k-1})$ can be related to the entropy rate $h_X(n+k-1,k) = H(X_{n+k} \mid \mathbf{X}^{(k)}_{n+k-1})$ and to active information storage $a_X(n+k-1,k) = I(X_{n+k}; \mathbf{X}^{(k)}_{n+k-1})$ as follows.

The entropy rate $h_X(n+k-1,k)$ can be written as the difference of two joint entropies of different lengths (Equation 9), $h_X(n+k-1,k) = H(\mathbf{X}^{(k+1)}_{n+k}) - H(\mathbf{X}^{(k)}_{n+k-1})$.

Next, active information storage can be expressed as the difference of a joint entropy and the entropy rate:

$$\begin{aligned} a_X(n+k-1,k) &= I(X_{n+k}; \mathbf{X}^{(k)}_{n+k-1}) \\ &= H(X_{n+k}) - H(X_{n+k} \mid \mathbf{X}^{(k)}_{n+k-1}) \\ &= H(X_{n+k}) - h_X(n+k-1,k). \end{aligned}$$

In the stationary case, we have

$$H_1 = a_k + h_k. \tag{24}$$

Similar to the case presented for the 2-state Markov process, it is observed that also in the general case, the entropy $H(X_{n+k})$ is conserved, being the sum of active information storage and the entropy rate. In words, the information about the future state X_{n+k} is the sum of the actively stored information from time step n up to time step $n+k-1$, and the entropy rate between time steps $n+k-1$ to $n+k$.

Finally, the PAIF coefficient $\pi_X(n,k)$ can be written as the difference of entropy rates for different history lengths:

$$\begin{aligned} \pi_X(n,k) &= I(X_{n+k}; X_n \mid \mathbf{X}^{(k-1)}_{n+k-1}) \\ &= H(X_{n+k} \mid \mathbf{X}^{(k-1)}_{n+k-1}) - H(X_{n+k} \mid \mathbf{X}^{(k)}_{n+k-1}) \\ &= h_X(n+k-1,k-1) - h_X(n+k-1,k). \end{aligned}$$

Alternatively, $\pi_X(n,k)$ can also be decomposed into a difference of AIS terms for two different history lengths:

$$\begin{aligned} \pi_X(n,k) &= I(X_{n+k}; X_n \mid \mathbf{X}^{(k-1)}_{n+k-1}) \\ &= H(X_{n+k} \mid \mathbf{X}^{(k-1)}_{n+k-1}) - H(X_{n+k} \mid \mathbf{X}^{(k-1)}_{n+k-1}, X_n) \\ &= H(X_{n+k} \mid \mathbf{X}^{(k-1)}_{n+k-1}) - H(X_{n+k} \mid \mathbf{X}^{(k)}_{n+k-1}) \\ &= H(X_{n+k}) - H(X_{n+k} \mid \mathbf{X}^{(k)}_{n+k-1}) - \big[H(X_{n+k}) \\ &\quad - H(X_{n+k} \mid \mathbf{X}^{(k-1)}_{n+k-1}) \big] \\ &= I(X_{n+k}; \mathbf{X}^{(k)}_{n+k-1}) - I(X_{n+k}; \mathbf{X}^{(k-1)}_{n+k-1}) \\ &= a_X(n+k-1,k) - a_X(n+k-1,k-1). \end{aligned}$$

Going from line 3 to line 4, we simply added and subtracted $H(X_{n+k})$. In words, the PAIF at time lag k is the difference between two AIF terms with history lengths k and $k-1$, respectively.

The results can be summarized in a more compact form using the stationary expressions:

$$\begin{aligned} \pi_k &= a_k - a_{k-1} \qquad (25) \\ &= h_{k-1} - h_k. \qquad (26) \end{aligned}$$

For stationary Markov processes, the joint Shannon entropy H_k exists and the k-order entropy rate estimates h_k converge in the limit of $k \to \infty$ (Cover and Thomas, 2006). Using Equation 24, it follows that the AIS coefficients a_k also converge. Thus, $\lim_{k\to\infty} a_k - a_{k-1} = 0$ and $\lim_{k\to\infty} h_{k-1} - h_k = 0$. Using Equation 25, we deduce that the PACF coefficients π_k also vanish in the large k limit:

$$\lim_{k\to\infty} \pi_k = 0.$$

3.1.1. Markovianity

Using the Markov property defined in Equation 21, it is straightforward to prove that for a stationary Markov process of order M, the PAIF coefficients vanish ($\pi_X(n,k) = 0$) for $k > M$:

$$\begin{aligned} \pi_X(n,k) &= I(X_{n+k}; X_n \mid \mathbf{X}^{(k-1)}_{n+k-1}) \\ &= H(X_{n+k} \mid \mathbf{X}^{(k-1)}_{n+k-1}) - H(X_{n+k} \mid \mathbf{X}^{(k)}_{n+k-1}) \\ &= h_{k-1} - h_k \\ &= h_M - h_M \\ &= 0. \end{aligned}$$

Let the first- and second-order finite differences of an arbitrary discrete function f_k of integer parameter k be defined as $\delta_k f_k = f_k - f_{k-1}$, and $\delta_k^2 f_k = f_{k+1} - 2f_k + f_{k-1}$, then we get

$$\begin{aligned} \pi_k &= h_{k-1} - h_k \\ &= -\delta_k\, h_k \\ &= -\delta_k^2\, H_k. \end{aligned}$$

Thus, the Markovianity test proposed in (van der Heyden et al., 1998) addresses a sequence of entropy rates h_k, for different history lengths k, which is the negative first-order difference of the sequence of Shannon entropies H_k. PAIF analysis uses the second-order difference of the sequence of Shannon entropies $\pi_k = -\delta_k^2 \ H_k$. The advantage of the PAIF analysis is the visual exploration of the coefficients, that are equal to zero for $k > M$, exactly like in visual PACF diagnostics for metric time series.

3.2. Higher-Order Markov Processes

The results for the two third-order Markov processes are shown in **Figures 3A–D**. The AIF and PAIF for the third-order Markov processes $MC_{1...M=3}$ is shown in **Figures 3A,B**, respectively. The shape of the AIF does not reveal the third-order dependencies by visual inspection. The PAIF, however, clearly reflects the construction of the process, showing significant PAIF coefficients only up to time lag $k = 3$.

For the second process, $MC_{M=3}$, the entropy dynamics can already be estimated by visual inspection of the AIF, which shows a clear periodicity (**Figure 3C**). Significant PAIF coefficients only occur at time lags that are multiples of the Markov order, $M = 3$. The PAIF (**Figure 3D**) however, demonstrates the Markov structure of the process in a single significant coefficient π_3.

Kullback's Markovianity tests of order 0-2 rejected the Markovian null hypotheses for both processes, as expected for Markov processes of order three, by construction. The conditional entropy test correctly identified the Markov order $M = 3$ in both cases.

Confidence intervals ($\alpha = 0.05$) constructed from uncorrelated surrogate time series are shown in blue. Due to their small magnitude, they visually appear as lines.

3.3. Hidden Markov Models

Figure 4 shows the results obtained from HMM data. First, the non-Markovian even process is analyzed. To the right of the HMM scheme, **Figure 4A** shows the PAIF of a single sample path of length $n = 10^6$. The inset shows that for all tested time lags the PAIF coefficients lie above the iid confidence interval (blue lines). Thus, PAIF analysis suggests that we are observing a non-Markov process with extended memory effects.

Figure 4B shows the PAIF of the 2-state golden mean process. The PAIF has two significant coefficients π_0, π_1 and decays to zero for all other time lags. The PAIF thus classifies the process correctly as a first-order Markov process, despite the hidden Markov implementation. Due to the Markov property, the process can also be represented by a transition matrix and

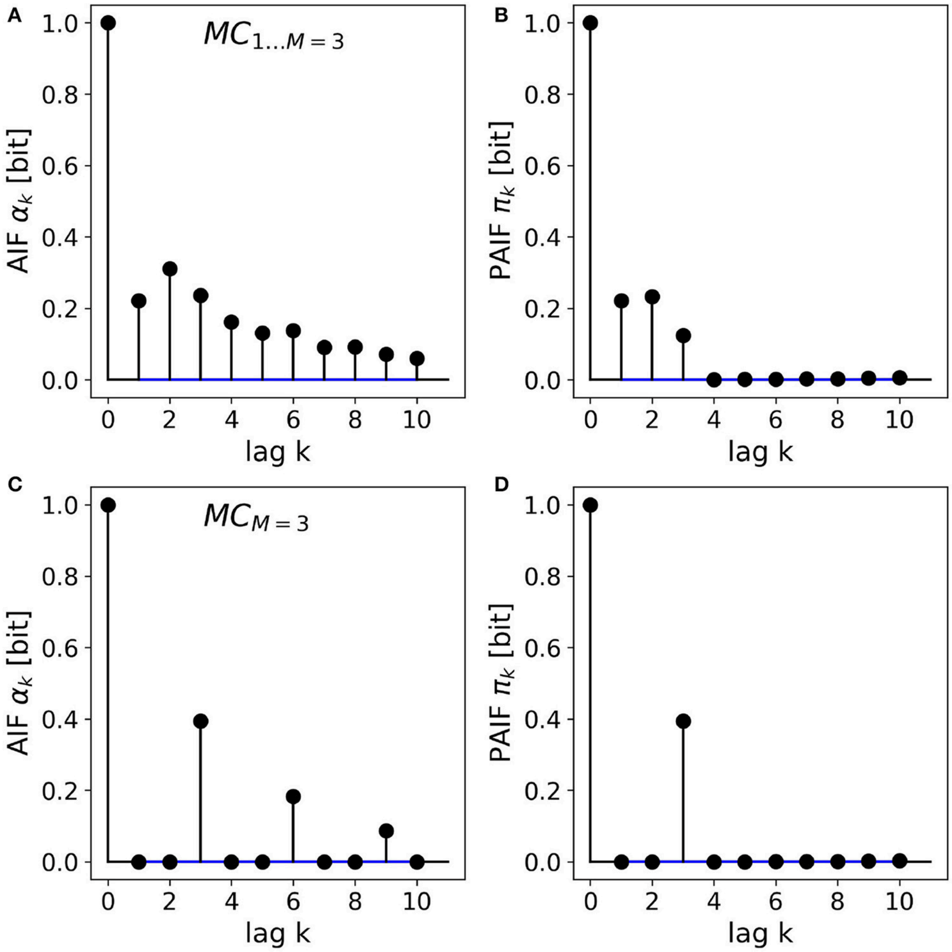

FIGURE 3 | AIF/PAIF analysis of two third-order Markov process samples. **(A)** The AIF of the $MC_{1...M=3}$ process slowly decays toward zero and does not reveal the Markov order of the process. **(B)** The PAIF of $MC_{1...M=3}$ shows a cutoff after $k = 3$ coefficients, in accordance with the nominal Markov order. **(C)** The AIF of the $MC_{M=3}$ process has period 3 and thus hints at the memory structure of the process. **(D)** The PAIF of the $MC_{M=3}$ process clearly identifies the Markov order of the process by a distinct peak at the time lag corresponding to the correct model order $M = k = 3$.

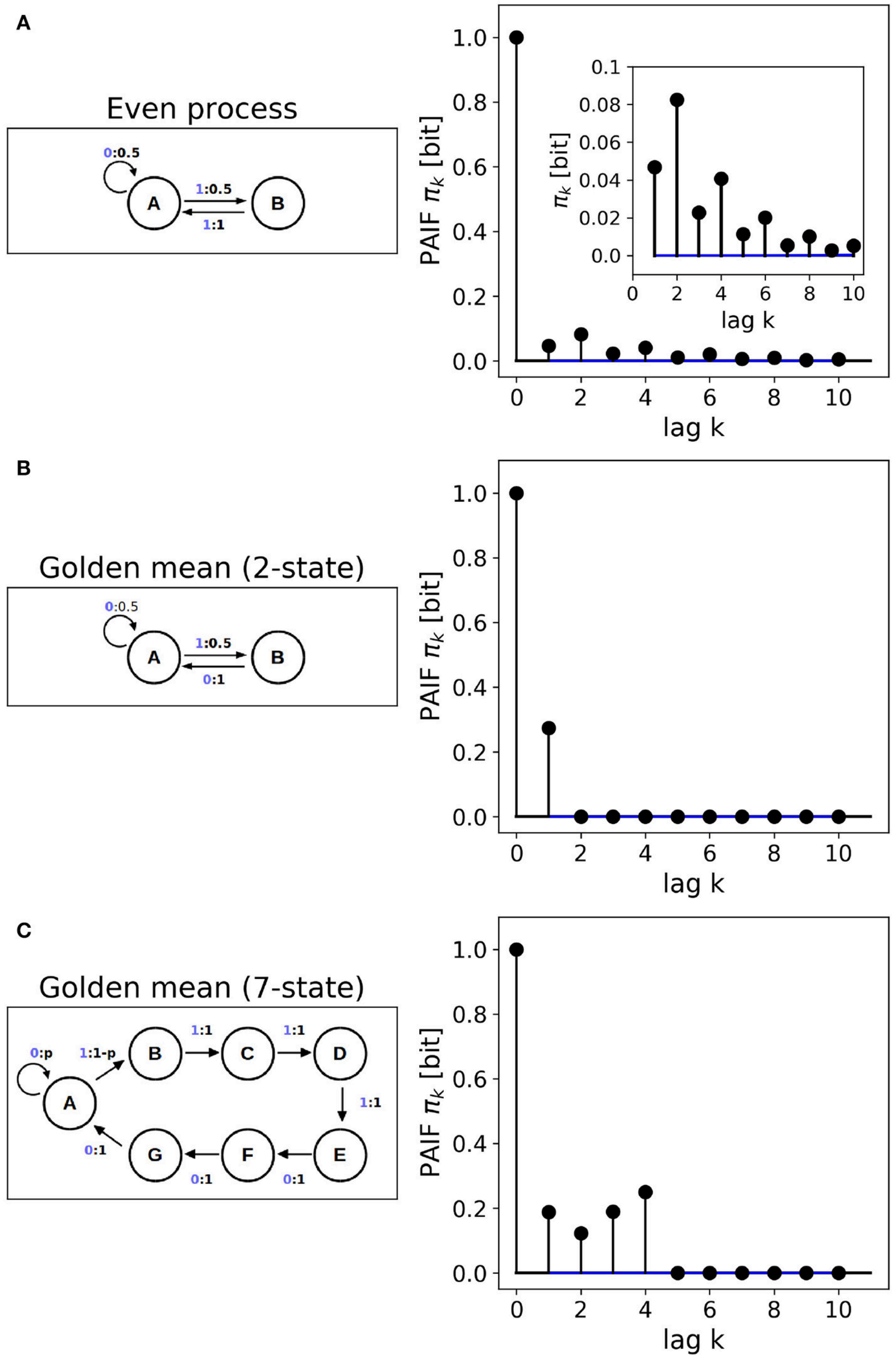

FIGURE 4 | Finite state machines. **(A)** Non-Markovian even process, Markov order $M = \infty$. **(B)** 2-state implementation of the golden-mean process, Markov order $M = 1$. **(C)** 7-state implementation of the golden-mean process, Markov order $M = 4$. The Markov orders are correctly identified by the PAIF approach.

an equilibrium distribution. The associated transition matrix T is

$$T = \begin{pmatrix} \frac{1}{2} & \frac{1}{2} \\ 1 & 0 \end{pmatrix}$$

with stationary distribution $p_{\mathrm{st}} = [\frac{2}{3}, \frac{1}{3}]$. Using these quantities, the theoretical results from Section 2.5 can be applied. Using finite histories ($k = 2 \dots 10$), entropy conservation (Equation 24) is fulfilled with a maximum error of 7.25×10^{-4}, where the error was calculated as $\frac{H_1 - h_k - a_k}{H_1}$. Based on this analysis, the Shannon

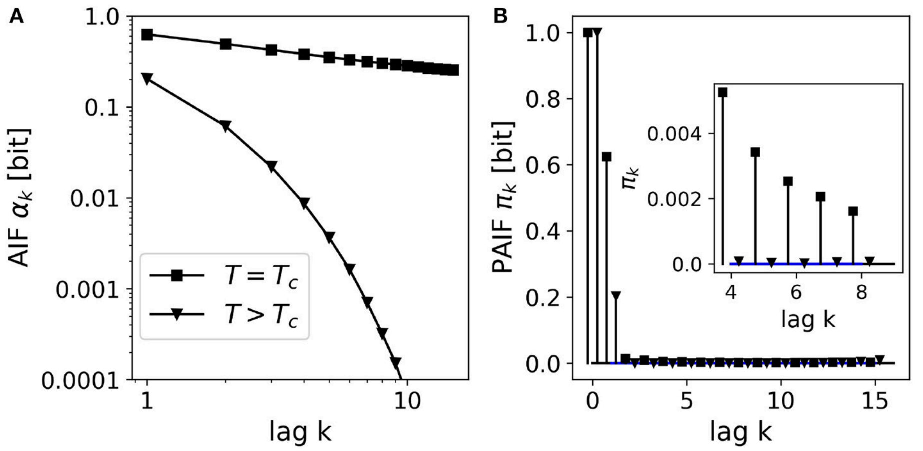

FIGURE 5 | AIF/PAIF analysis of 2D-Ising model data: Results for single lattice site time series ($n = 10^6$ samples) at two temperatures are shown, close to the critical temperature $T_C \approx 2.27$ (black squares), and at a higher temperature far from the critical point, $T = 5.00$ (black triangles). **(A)** The AIF is shown in log-log coordinates to better visualize the qualitative difference between the power-law decay (linear in log-log coordinates) at the critical temperature ($T = T_C$), and the exponential decay at higher temperatures ($T = 3.00$). **(B)** The PAIF for both temperatures illustrates a dominant coefficient π_1. However, the inset shows significant positive PAIF coefficients and thus, non-Markovian behavior close at the critical temperature (squares).

entropy of a single symbol is $H_1 = 0.919$ bit, and consists of an entropy rate of $h_X = 0.669$ bit and active information storage of $a_X = 0.253$ bit.

The 7-state HMM of the golden mean process is analyzed in **Figure 4C**. The fourth-order Markov structure of the implementation is clearly reflected by the PAIF that shows four positive coefficients. The PAIF captures the correct Markov order although the model contains seven hidden states and emits two observable symbols.

Kullback's Markovianity tests of order 0–2 correctly classified the 2-state golden mean process as first-order Markovian. The p-values for orders 0-2 were $p_0 = 0.000$, $p_1 = 0.697$, and $p = 0.990$, respectively. For the non-Markovian even process and the fourth-order Markovian 7-state golden mean process, low-order (0-2) Markovianity was correctly rejected. The conditional entropy test correctly identified the Markov properties of all three processes, i.e., found first- and fourth-order properties for the 2-state and 7-state golden mean processes, respectively, and an order $M > 5$ for the even process.

3.4. The Ising Model

We simulated an Ising model on a 2D lattice (50 × 50 elements) at two temperatures, (i) around the critical temperature $T_c = \frac{2}{1+\sqrt{2}} \approx 2.27$, and (ii) at a higher temperature $T = 5.00$. From statistical physics, it is known that the system's autocorrelation function shows a slow, power-law decay at the critical point, and an exponential decay far from the critical point where dynamics are dominated by thermal fluctuations. AIF/PAIF analysis was performed on time series of 10^6 samples of a randomly selected lattice site. The results are shown in **Figure 5**.

In contrast to the other figures in this manuscript, the AIF in **Figure 5A** is shown in log-log coordinates, to better visualize the difference between exponential and power-law behavior. The AIF at the critical point T_c shows an almost linear behavior in log-log coordinates (black squares), indicating very slow relaxation dynamics, as expected. For the higher temperature, far from the critical point ($T = 5.0$, black triangles), however, we observe a quickly decaying autoinformation trace, in accordance with results from classical time series analysis. **Figure 5B** shows the PAIF in linear coordinates, as in all other figures. It is observed that in both cases, $T = T_c, T = 5.0$, the PAIF profiles seem to be similar. We find two positive PAIF coefficients π_0, π_1, and significantly smaller PAIF coefficients for larger time lags. The inset, however, shows that at the critical temperature (squares), the PAIF coefficients lie above the confidence interval, demonstrating non-Markovian, long-range memory effects where the system undergoes a phase transition.

3.5. Simulated Ion-Channel Data

Simplified ion channel dynamics were generated by integration of Equation 23, representing the motion of a particle in a bistable potential, for instance an ion channel with two metastable states corresponding to the open (O) and close (C) state, respectively. To obtain a symbolic time series of O- and C-states, the continuous variable X_n is thresholded at a value of zero. Thereby, all positive values $X_n > 0$ are assigned to the open state (O), and all negative values ($X_n < 0$) are mapped to the close state. The AIF/PAIF analysis of the thresholded signal simulating electrophysiological ion channel data is shown in **Figure 6**. We observe a slowly decaying AIF (**Figure 6A**) without any information about the Markov order of the signal. The PAIF profile shows large coefficients π_0 and π_1, followed by vanishing PAIF coefficients for $k > 1$. Though Markovian dynamics are expected for the continuous dynamics, it is not obvious that the Markov property could be detected after thresholding.

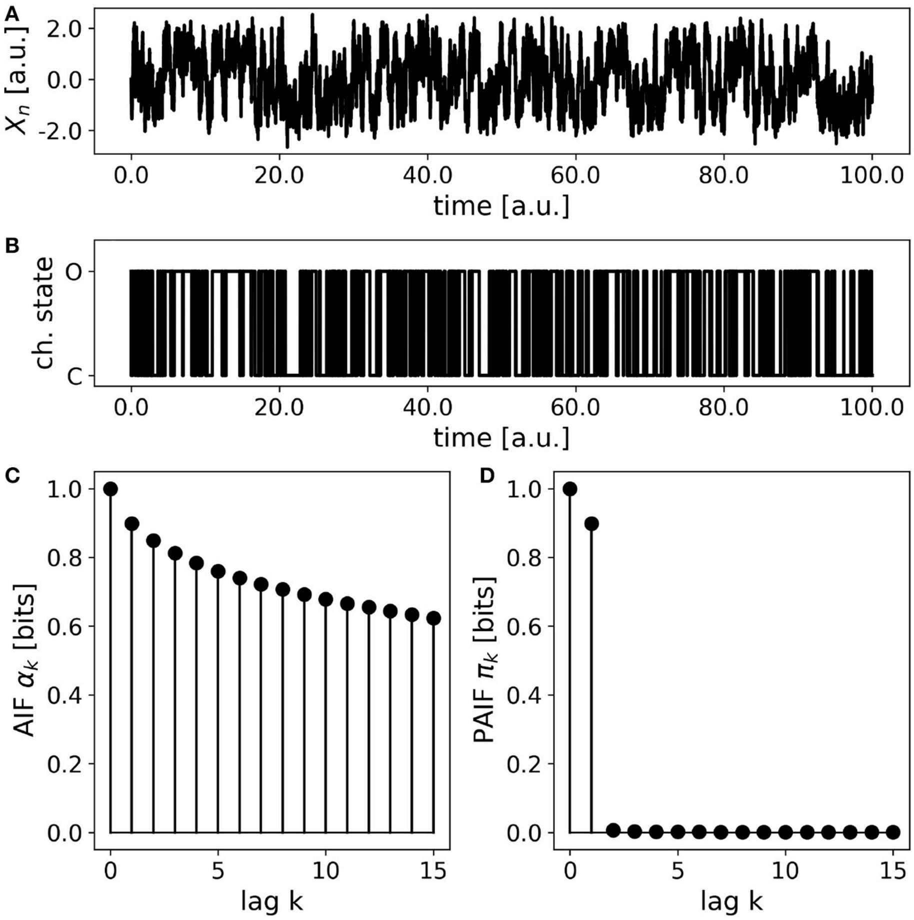

FIGURE 6 | Simulated ion channel data. **(A)** A continuous stochastic process X_n is obtained from a simulation of a double-well potential. A bistable behavior resembling ion channel recordings is observed. **(B)** Thresholding the continuous variable X_n into an open state (O, $X_n > 0$) and a close state (C, $X_n < 0$) yields a symbolic, binary process. **(C)** The AIF of the binary process shows a slow decay without revealing the Markov order of the process. **(D)** The PAIF suggests first-order Markov dynamics by vanishing PAIF coefficients π_k for $k > 1$.

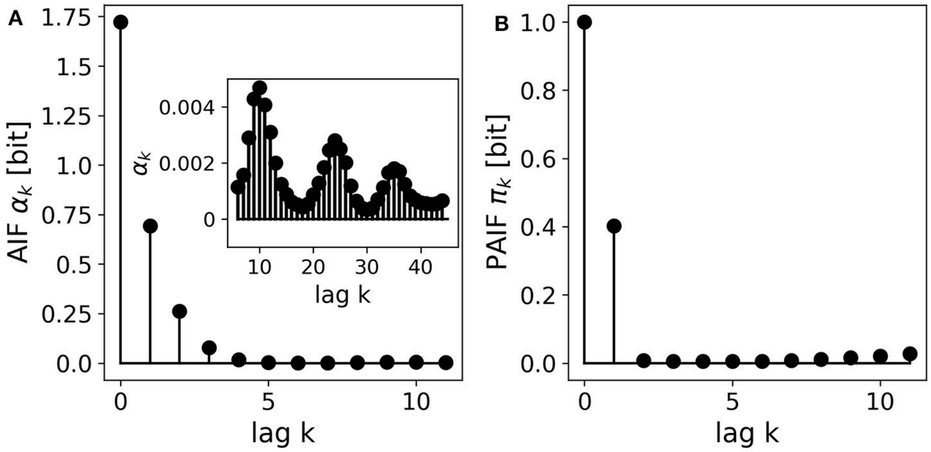

FIGURE 7 | A 4-state resting state EEG microstate sequence. **(A)** The AIF shows a monotonous decay for smaller time lags $k < 10$. The inset shows the AIF for larger time lags ($k_{max} = 50$) and reveals periodicities that could not be predicted at shorter time scales. **(B)** The PAIF indicates a mainly first-order Markovian structure but does not allow the computation of time lags as large as the AIF due to the exponentially growing size of the associated distributions.

3.6. EEG Microstate Sequences

The EEG microstate sequence shows a more complex behavior than the other presented examples. **Figure 7A** shows the AIF of the 4-state sequence, which seems to decay monotonously. The inset shows further information for longer time lags up to $k = 40$. We observe several periodic peaks at these time lags, an effect that we have discussed in detail in a recent publication (von Wegner et al., 2017). The PAIF in **Figure 7B** shows a dominant coefficient π_1. This finding suggests a mainly first-order Markov mechanism, and does not hint at the periodic behavior found in the AIF. Moreover, we observe increasing PAIF coefficients for larger time lags ($k > 8$). This effect is caused by finite joint entropy estimates, which suffer from an insufficient sample size, given the history length k, and the size of the state space, here $L = 4$.

4. DISCUSSION

In the present article, an information-theoretical approach for the early diagnostic steps in symbolic time series analysis is established. In close analogy to classical time series analysis of continuous-valued random variables, a combined approach using two different measures that estimate the dependency between two time points is used. While autoinformation measures the statistical dependence between X_n and X_{n+k} directly, partial autoinformation removes the influence of the segment between both time points. The names AIF and PAIF were chosen to represent the close connection with the ACF/PACF approach. We have recently used the AIF to characterize stochastic processes and experimental EEG data (von Wegner et al., 2017, 2018), and the underlying functional can be found under the name of time-lagged mutual information in the literature. Partial autoinformation, however, is not found in the literature, to the best of the author's knowledge. Close connections to the entropy rate and the active information storage of the process, two well-studied information-theoretical quantities (Cover and Thomas, 2006; Lizier et al., 2012), are found and detailed. In particular, the newly introduced PAIF can be expressed either as the difference of two entropy rates with history lengths $k - 1$ and k, respectively, or as the difference of two active information storage terms with different history lengths. These relationships also assure that the PAIF coefficients approach zero in the large k limit.

The ability of the PAIF to identify the order of a stationary Markov process is shown analytically by re-writing the PAIF in terms of conditional entropies. A short proof shows that the PAIF coefficients of a stationary Markov process of order M are zero ($\pi_k = 0$) for $k > M$. The practical performance of the method is validated numerically, using test data with known Markov orders, and by comparison with the results of two other tests (Kullback et al., 1962; van der Heyden et al., 1998). All test examples used in this article are correctly classified by the PAIF approach, in the same way the PACF performs for continuous autoregressive processes. A close relationship between the PAIF and the conditional entropy test (van der Heyden et al., 1998) is established by re-writing both in terms of joint entropies H_k. We found that while the conditional entropy test addresses the first-order discrete difference of H_k with respect to k, the PAIF actually tests the corresponding second-order discrete derivative. This completes the goal of establishing an information-theoretical tool analogous to classical PACF analysis.

Our experimental data examples also reveal some important limitations of the approach. The PAIF coefficients for the 4-state EEG microstate sequence ($n = 153,225$ samples) increase for time lags above approximately $k > 8$. Comparison with Markov surrogate samples shows that this increase is due to the limited sample size, and is not a feature of the EEG data set (data not shown). The effect is easily understood by a simple numerical example. If for the same data set, we wanted to compute the PAIF coefficients for the same time lags as used in the AIF (**Figure 7**), joint probability distributions with L^k bins will occur. Thus, to extend the PAIF analysis of a $L = 4$-state process to $k = 50$, distributions with $4^{50} > 10^{30}$ elements have to be estimated, clearly exceeding the length of the data sample numerous times. The example also shows that this is an intrinsic limitation of the approach, as it always occurs for information-theoretical quantities involving joint entropies, and is not specific to the PAIF introduced here.

Finally, the present article exclusively deals with discrete stochastic processes. Future investigations should include the corresponding quantities for continuous random variables, and Gaussian processes in particular. For example, it has been shown in the past that for Gaussian random variables, Granger causality is equivalent to transfer entropy (Barnett et al., 2009). By analogy, it can be conjectured that the PAIF and PACF approaches are likely to be related, if not equivalent, for Gaussian processes.

It will be interesting to see further applications of the presented approach to theoretical and experimental data and to investigate further theoretical connections to other quantities already in use.

AUTHOR CONTRIBUTIONS

FvW designed the study, performed all presented analyses, and wrote the manuscript.

FUNDING

This work was funded by the Bundesministerium für Bildung und Forschung (grant 01 EV 0703) and LOEWE Neuronale Koordination Forschungsschwerpunkt Frankfurt (NeFF) as well as by the LOEWE program CePTER.

ACKNOWLEDGMENTS

The author thanks Helmut Laufs for permission to use the EEG data set used in this article. The author also thanks the Reviewers for valuable input and suggestions, in particular the work by van der Heyden et al.

REFERENCES

Anderson, T. W., and Goodman, L. A. (1957). Statistical inference about Markov chains. *Ann. Math. Stat.* 28, 89–110.

Ara, P. M., James, R. G., and Crutchfield, J. P. (2016). Elusive present: hidden past and future dependency and why we build models. *Phys. Rev. E Stat. Nonlinear Soft Matter Phys.* 93:022143. doi: 10.1103/PhysRevE.93.022143

Barnett, L., Barrett, A. B., and Seth, A. K. (2009). Granger causality and transfer entropy are equivalent for Gaussian variables. *Phys. Rev. E Stat. Nonlinear Soft Matter Phys.* 103:238701. doi: 10.1103/PhysRevLett.103.238701

Barnett, L., and Seth, A. K. (2015). Granger causality for state-space models. *Phys. Rev. E Stat. Nonlinear Soft Matter Phys.* 91:040101. doi: 10.1103/PhysRevE.91.040101

Bartlett, M. S. (1951). The frequency goodness of fit test for probability chains. *Math. Proc. Cambridge Philos. Soc.* 47, 86–95.

Billingsley, P. (1961). Statistical methods in Markov chains. *Ann. Math. Stat.* 32, 12–40.

Bortz, A. B., Kalos, M. H., and Lebowitz, J. L. (1975). A new algorithm for Monte Carlo simulation of Ising spin systems. *J. Comput. Phys.* 17, 10–18.

Box, G. E. P., and Jenkins, G. M. (1976). *Time Series Analysis: Forecasting and Control*. Holden-Day. Hoboken, NJ: Wiley.

Cover, T. M. and Thomas, J. A. (2006). *Elements of Information Theory*. New York, NY: Wiley-Interscience.

Crutchfield, J. P. and Young, K. (1989). Inferring statistical complexity. *Phys. Rev. Lett.* 63, 105–108.

Daw, C. S., Finney, C. E. A., and Tracy, E. R. (2003). A review of symbolic analysis of experimental data. *Rev. Sci. Instrum.* 74, 915–930. doi: 10.1063/1.1531823

Faes, L., Porta, A., and Nollo, G. (2015). Information decomposition in bivariate systems: theory and application to cardiorespiratory dynamics. *Entropy* 17, 277–303. doi: 10.3390/e17010277

Goodman, L. A. (1958). Exact probabilities and asymptotic relationships for some statistics from m-th order Markov chains. *Ann. Math. Stat.* 29, 476–490.

Häggström, O. (2002). *Finite Markov Chains and Algorithmic Applications*. Cambridge, UK: Cambridge University Press.

Hoel, P. G. (1954). A test for Markoff chains. *Biometrika* 41, 430–433.

Hohenberg, P. C., and Halperin, B. I. (1977). Theory of dynamic critical phenomena. *Rev. Mod. Phys.* 49, 435–479.

Kullback, S. (1959). *Information Theory and Statistics*. Mineola, NY: Dover Publications, Inc.

Kullback, S., Kupperman, M., and Ku, H. H. (1962). Tests for contingency tables and Markov chains. *Technometrics* 4, 573–608.

Liebovitch, L. S., and Czegledy, F. P. (1992). A model of ion channel kinetics based on deterministic, chaotic motion in a potential with two local minima. *Ann. Biomed. Eng.* 20, 517–531.

Lizier, J. T., Prokopenko, M., and Zomaya, A. Y. (2012). Local measures of information storage in complex distributed computation. *Inform. Sci.* 208, 39–54. doi: 10.1016/j.ins.2012.04.016

Mahoney, J. R., Aghamohammadi, C., and Crutchfield, J. P. (2016). Occam's quantum strop: synchronizing and compressing classical cryptic processes via a quantum channel. *Sci. Rep.* 6:20495. doi: 10.1038/srep20495

Merhav, N., Gutman, M., and Ziv, J. (1989). On the estimation of the order of a markov chain and universal data compression. *IEEE Trans. Info Theor.* 35, 1014–1019.

Mézard, M. and Montanari, A. (2009). *Information, Physics, and Computation*. Oxford University Press, Oxford, UK.

Pethel, S. D., and Hahs, D. W. (2014). Exact significance test for Markov order. *Phys. D* 269, 42–47. doi: 10.1016/j.physd.2013.11.014

Runge, J., Heitzig, J., Petoukhov, V., and Kurths, J. (2012). Escaping the curse of dimensionality in estimating multivariate transfer entropy. *Phys. Rev. Lett.* 108:258701. doi: 10.1103/PhysRevLett.108.258701

Tong, H. (1975). Determination of the order of a markov chain by akaike's information criterion. *J. Appl. Probabil.* 12, 488–497.

van der Heyden, M. J., Diks, C. G. C., Hoekstra, B. P. T., and DeGoede, J. (1998). Testing the order of discrete markov chains using surrogate data. *Phys. D* 117, 299–313.

von Wegner, F., and Laufs, H. (2018). Information-theoretical analysis of EEG microstate sequences in Python. *Front. Neuroinform.* 10:30. doi: 10.3389/fninf.2018.00030

von Wegner, F., Laufs, H., and Tagliazucchi, E. (2018). Mutual information identifies spurious Hurst phenomena in resting state EEG and fMRI data. *Phys. Rev. E Stat. Nonlinear Soft Matter Phys.* 97:022415. doi: 10.1103/PhysRevE.97.022415

von Wegner, F., Tagliazucchi, E., Brodbeck, V., and Laufs, H. (2016). Analytical and empirical fluctuation functions of the EEG microstate random walk - short-range vs. long-range correlations. *Neuroimage* 141, 442–451. doi: 10.1016/j.neuroimage.2016.07.050

von Wegner, F., Tagliazucchi, E., and Laufs, H. (2017). Information-theoretical analysis of resting state EEG microstate sequences - non-Markovity, non-stationarity and periodicities. *Neuroimage* 158, 99–111. doi: 10.1016/j.neuroimage.2017.06.062

von Wegner, F., Wieder, N., and Fink, R. H. A. (2014). Microdomain calcium fluctuations as a colored noise process. *Front. Genet.* 5:376. doi: 10.3389/fgene.2014.00376

Xiong, W., Faes, L., and Ivanov, P. C. (2017). Entropy measures, entropy estimators, and their performance in quantifying complex dynamics: effects of artifacts, nonstationarity, and long-range correlations. *Phys. Rev. E Stat. Nonlinear Soft Matter Phys.* 95:062114. doi: 10.1103/PhysRevE.95.062114

Conflict of Interest Statement: The author declares that the research was conducted in the absence of any commercial or financial relationships that could be construed as a potential conflict of interest.

Copyright © 2018 von Wegner. This is an open-access article distributed under the terms of the Creative Commons Attribution License (CC BY). The use, distribution or reproduction in other forums is permitted, provided the original author(s) and the copyright owner(s) are credited and that the original publication in this journal is cited, in accordance with accepted academic practice. No use, distribution or reproduction is permitted which does not comply with these terms.

frontiers in Physiology

ORIGINAL RESEARCH
published: 12 November 2018
doi: 10.3389/fphys.2018.01567

Circadian Rhythms in Fractal Features of EEG Signals

Pierpaolo Croce[1], *Angelica Quercia*[1], *Sergio Costa*[1] *and Filippo Zappasodi*[1,2]*

[1] *Department of Neuroscience, Imaging and Clinical Sciences, G. d'Annunzio University, Chieti, Italy,* [2] *Institute for Advanced Biomedical Imaging, G. d'Annunzio University, Chieti, Italy*

Time-of-day modulations affect both performance on a wide range of cognitive tasks and electrical activity of the brain, as recorded by electroencephalography (EEG). The aim of this work was to identify fluctuations of fractal properties of EEG time series due to circadian rhythms. In twenty-one healthy volunteers (all males, age between 20 and 30 years, chronotype: neutral type) high density EEG recordings at rest in open and closed eyes conditions were acquired in 4 times of the day (8.00 a.m., 11.30 a.m., 2.30 p.m., 7.00 p.m.). A vigilance task (Psychomotor Vigilance Test, PVT) was also performed. Detrended fluctuation Analysis (DFA) of envelope of alpha, beta and theta rhythms was performed, as well as Highuchi fractal dimension (HFD) of the whole band EEG. Our results evidenced circadian fluctuations of fractal features of EEG at rest in both eyes closed and eyes open conditions. Lower values of DFA exponent were found in the time T1 in closed eyes condition, likely effect of the sleep inertia. An alpha DFA exponent reduction was found also in central sensory-motor areas at time T3, the day time in which the sleepiness can be present. In eyes open condition, HFD lowered during the day. In eyes closed condition, an HFD increase was observed in central and frontal regions at time T2, the time in which alertness reaches its maximum and homeostatic sleep pressure is low. Complexity and the persistence of temporal correlations of brain rhythms change during daytime, parallel to changes in alertness and performance.

Keywords: detrended fluctuation analyses, higuchi fractal dimension, circadian rhythm, amsterdam resting-state questionnaire (ARSQ), electroencephalography

OPEN ACCESS

Edited by:
Srdjan Kesić,
University of Belgrade, Serbia

Reviewed by:
John G. Holden,
University of Cincinnati, United States
Ahmet Ademoglu,
Boğaziçi University, Turkey

****Correspondence:***
Filippo Zappasodi
filippo.zappasodi@unich.it

Specialty section:
This article was submitted to Fractal Physiology, a section of the journal Frontiers in Physiology

Received: *01 August 2018*
Accepted: *18 October 2018*
Published: *12 November 2018*

Citation:
Croce P, Quercia A, Costa S and Zappasodi F (2018) Circadian Rhythms in Fractal Features of EEG Signals. Front. Physiol. 9:1567. doi: 10.3389/fphys.2018.01567

INTRODUCTION

According to the traditional model of control, physiological systems self-regulate their activity to preserve steadiness by reducing fluctuations around a homeostatic equilibrium point. Differently from this view, a wide bulk of evidence has recently been provided that several physiological time signals exhibit intrinsic fractal fluctuations (Goldberger et al., 2002; Stam, 2005). Indeed, heartbeat, respiration, gait rhythm, dynamics of neurotransmitter release, electromyography, brain activity reveal similar temporal patterns over multiple time scales (Hausdorff et al., 2001; Meyer and Stiedl, 2003; Fadel et al., 2004; Leao et al., 2005; Stam, 2005; Swie et al., 2005; He et al., 2007, 2010; Milstein et al., 2009; Scafetta et al., 2009; Zappasodi et al., 2015). An object exhibits fractal properties if similar details can be observed on different scales (Mandelbrot, 1983; Voss, 1988; Feder, 2013). These properties come up from nonlinear feedback interactions between mechanisms operating on multiple scales, sign of high integrity and adaptability of the whole system (Di Ieva et al., 2014). Also, a time process $X(t)$ can display fractal properties if it possesses a scale-invariant structure over time and statistical similarity emerges at different time scales of its dynamics. For this process a self-affinity behavior can be retrieved (Barabasi and Albert, 1999), as $X(ct) = c^H X(t)$. The estimation of the scaling exponent H, the Hurst exponent (Feder, 2013), has been found to be particularly attractive for describing the brain dynamics. Indeed, the amplitude modulation of oscillations of neuronal pools dynamics, revealed by electrophysiological techniques as electroencephalography (EEG) or magnetoencephalography (MEG), reveal long-term spatiotemporal structure in a temporal range from few seconds to tenth of minutes in resting state conditions at both eyes closed and eyes open (Linkenkaer-Hansen et al., 2001). The de-trended fluctuation analysis (DFA) is a widely-used method for the detection of long-range correlations in time series. Indeed, amplitude fluctuations of alpha, beta, and theta oscillations obey a power-law scaling behavior.

The fractal behavior of a time series has been linked to its "complexity," that can be seen as the amount of information required to describe the time series (Mandelbrot, 1985). The concept of "complexity" refers to a highly structured temporal structure observed in the brain signal in an intermediate situation between pure randomness, like in white noise, and the absence of variability (constancy or pure periodicity), both conditions evidenced as non-physiological states (Di Ieva et al., 2014; Zappasodi et al., 2014; Smits et al., 2016). Since the existence of long term correlation is no guarantee of complexity, the complexity of a time series can be directly evaluated by its fractal dimension (Mandelbrot, 1985). Indeed, this measure quantifies the complexity and the self-similarity of a time series. The algorithm proposed by Higuchi (Higuchi fractal dimension, HFD, Higuchi, 1988) has been successfully directly applied to EEG signals to evidence modulation of complexity in different physiological conditions, as well as alterations in pathologies (for a review see Kesić and Spasić, 2016).

Fractal dimension and Hurst exponent quantify different properties: while the first is a local property, measuring the "roughness" of a signal (i.e., a "mild" or "wild" randomness), the latter quantifies a global characteristic, i.e., the long-memory dependence (long-range correlation) of the time series. For self-affine processes, where fractal properties can be retrieved, the local properties are reflected in the global one. Therefore, fractal dimension and Hurst exponent are linked.

Although the fractal properties have been recently described in brain time series both in health and disease, the neurophysiological mechanisms of fractal regulation are unknown. Recently the circadian pacemaker (suprachiasmatic nucleus) has been described to play a crucial role in generating fractal patterns in behavioral activity and heart rate at long time scales, and modulates their fluctuations at short time scales (Pittman-Polletta et al., 2013). Indeed, in humans, temporal fluctuations in physiological parameters and behavioral performance, on a wide range of cognitive functions, vary over the 24-h light-dark cycle. This cycle is driven by two interacting processes: the homeostatic sleep pressure (process S), which increases with time spent awake, and the circadian pacemaker (process C), a nearly 24-h endogenous process that drives at specific times of the day wakefulness and sleep (Borbély, 1982; Cajochen and Dijk, 2003; Rogers et al., 2003; Dijk and von Schantz, 2005; Cajochen et al., 2010). The circadian and homeostatic processes interact to provide stable levels of vigilance/alertness and cognitive performance during daytime (16-h) of normal wakefulness, when the circadian timing system fights the wake-dependent (or homeostatic) arousal decline. Indeed, alertness reaches its maxima during the early morning, when homeostatic sleep pressure is low, whereas decreases at its lowest level during the evening hours, when homeostatic sleep pressure is high (Van Dongen et al., 2003), even if exist a mid-afternoon window of sleep propensity (from ∼14:00 to ∼16:00) and an alertness window in the early evening hours from ∼19:00 to ∼22:00 (Lavie, 1989; Johnson, 1990). However, individual chronotype, namely "diurnal preference" in the timing of daily activities (Horne and Ostberg, 1976) under the control of the circadian clock (Roenneberg et al., 2007), influences peaks and troughs in alertness and performance. Hence, some people are more alert and perform better in the morning, whereas others in the evening, an effect referred to as the "synchrony effect" (May and Hasher, 1998) depending on individual chronotype.

In awake adults, data collected by sleep deprivation protocol and forced desynchrony protocol (i.e., sleep–wake cycle induced to uncouple from endogenous circadian rhythm) showed that both factors (process C and process S) contribute to a frequency-specific variation of EEG activity (Finelli et al., 2000; Cajochen and Dijk, 2003; Marzano et al., 2010). Moreover, resting waking EEG recordings are considered as an objective measure of alertness levels (Strijkstra et al., 2003). Specifically, an increase of EEG power density in the theta (4–8 Hz) and alpha (8–12 Hz) frequency range across prolonged periods of wakefulness has been associated with a decline of alertness and sleepiness (Drapeau and Carrier, 2004). In a recent EEG study, Meisel et al. (2017) reported a decline in long term correlation in alpha band as sleep deprivation progresses. Moreover, HFD has been applied to detect behavioral microsleep (Peiris et al., 2006) and changes from awake to drowsy states (Bojić et al., 2010; Pavithra et al., 2014).

The aim of this work was to identify fluctuations of fractal properties of EEG time series due to circadian rhythms. To this aim, high density EEG was collected in 4 different times of the day in both closed and open eyes conditions. Given the exploratory aspect of this study, we did not aim to differentiate the sleep pressure from endogenous factors, as usually done by using sleep deprivation or forced de-synchrony protocols but investigate if modulation of fractal properties over different day times can be retrieved in EEG at rest in physiological conditions.

METHODS

Subjects

Twenty-one healthy volunteers (all males, age 23.6 ± 1.7) participated to the study. To avoid any kind of sleep debt and alterations of the sleep-wake cycle all selected participants reported no history of sleep, medical or psychiatric disorders and a good sleep quality (sleep schedule of 7-8 h/night), as assessed by self-rating questionnaires (Vignatelli et al., 2003; Violani et al., 2004). Moreover, in all participants, chronotype has been investigated by the Morningness Eveningness Questionnaire

(MEQ, Horne and Ostberg, 1976), that assesses chronotype based on diurnal preferences (e.g., preferred time of day to perform physical and mental work; Horne and Ostberg, 1976). With this questionnaire, chronotype is categorized as a score (range:16–86), with high numbers corresponding to morning types (59 and above), low numbers corresponding to evening types (41 and below), and numbers between 42 and 58 corresponding to intermediate types. All selected participants had an intermediate chronotype (mean and standard deviation 53 ± 4). Exclusion criteria included shift workers, athletes and participants that had traveled crossing time zones in the 3 months before the study. The protocol was approved by the local Ethical Committee. All subjects gave written informed consent in accordance with the Declaration of Helsinki.

Experimental Procedure

For one week before the experiment, participants were asked to maintain a regular sleep-wake schedule. The night before the experiment, participants were asked to go to bed at their usual bedtime and to wake up at ∼ 7:00 a.m. The quality of the sleep was checked by a wrist-worn actigraph (wActiSleep+, ActiGraph, Pensacola, FL, ActiGraph). A Sleep Efficiency >85% was required, to avoid any kind of sleep debt. These data were analyzed with Actilife (v.6.7.1, Actigraph[1], Pensacola, FL), using a sleep/wake detection validated algorithm (Cole et al., 1992; Sadeh et al., 1994). Bed and rise times from the sleep diaries helped to frame the time in bed during which actigraphy data were analyzed.

The day of the experiment high density EEG recordings were acquired in 4 times of the day (T1: 8.00 a.m., T2: 11.30 a.m., T3: 2.30 p.m., T4: 7.00 p.m.) in 2 conditions: 10 min of eyes open and 10 min of eyes closed. The 2 conditions were randomized across subjects and times. The four times were chosen on the basis of well-known peaks of levels of vigilance/alertness and cognitive performance during daytime. Indeed, T0 correspond to the time were sleep inertia may be present (Jewett et al., 1999), in T2 alertness reaches its maxima and homeostatic sleep pressure is low, T3 is a mid-afternoon window of sleep propensity and in T4 homeostatic sleep pressure is high, but alertness is high (Lavie, 1989; Jewett et al., 1999; Van Dongen et al., 2003).

During the recordings, subjects were sitting on a comfortable armchair in a low light room and, in the eyes open condition, fixed a cross on a screen. Soon after both closed and open eyes recordings, participants were asked to complete the Amsterdam Resting-State Questionnaire (ARSQ). The questionnaire was presented on a screen and consisted of 55 statements about the feelings and thoughts experienced during the 10 min rest. For each statement, a 5-points rate from completely disagree to completely agree was used. Questions were grouped into 10 factors: Discontinuity of Mind, Theory of Mind, Self, Planning, Sleepiness, Comfort, Somatic Awareness, Health Concern, Visual Thought, and Verbal Thought (Diaz et al., 2013). Finally, a 10 min vigilance task (Psychomotor Vigilance Test, PVT; (Dinges and Powell, 1985) was done. Subjects were asked to fix a monitor with a red rectangular box and press a button when a counter appeared to the screen. The response stopped the counter and was required to be delivered as soon as possible. The period between the end of the counter and the begin of the following stimulus was randomly distributed between 2 and 10 s. To quantify the performance, the following parameters were extracted for each time (Basner and Dinges, 2011): number of lapses (i.e., number of responses >500 ms), number of false starts (i.e., response shorter than 100 ms), response speed (i.e., mean of the inverse of reaction times).

The EEG activity was recorded by a 128-channel system (Electrical Geodesic). The impedances were kept below 100 kΩ. EEG data were sampled at 250 Hz and collected for off line processing.

Data Analysis

Data were visually inspected to exclude saturated epochs of EEG signals from further analysis. A semi-automatic procedure, based on Independent Component Analysis (Barbati et al., 2004), was applied to identify and remove ocular, cardiac, and muscular artifacts. Signals were down-sampled to 125 Hz and re-referenced to the common average. Noisy channels were excluded and replaced by spline interpolation.

Band Power

The Power Spectral Density (PSD) was estimated for each EEG channel by means of the Welch procedure (Hamming windowing of 8 s, resulting in a frequency resolution of 0.125 Hz, 50% overlap). For each EEG channel and both conditions, band powers were obtained by the sum of the power spectrum in each frequency band normalized by the number of frequency bins. The considered frequency bands were: alpha (from 8 to 13 Hz), beta (from 15 to 25 Hz), and theta (from 4 to 7.5 Hz).

Detrended Fluctuation Analysis

The DFA was applied to analyze the scale-free decay of temporal correlations in the amplitude envelope of brain rhythms. Peng et al. (1994) introduced this method to quantify long-range temporal correlation with less strict assumptions about the signal stationarity. The method quantifies the detrended fluctuations F(n) of the envelope at different time scales n. Firstly, each EEG signal was band-pass filtered in theta (4–7.5 Hz), alpha (8–13 Hz), or beta (15–25 Hz) band (**Figures 1A,B**). A Finite Impulse Response filter set to 2 cycles of the lowest frequency was used (filter order: 62 for theta, 31 for alpha, 16 for beta band). The envelope of the band-passed signals was computed by the modulus of its analytic signal, obtained by Hilbert transform. The cumulative sum y of the envelope x was then calculated:

$$y\left(k\right) = \sum_{i=1}^{k} \left| x\left(i\right) - < x > \right|$$

Where, $<x>$ denotes the mean of the envelope x. By applying scaling analysis to $y(k)$ no a priori assumptions about the signal stationarity is required (Hardstone et al., 2012).

The cumulative sum was then partitioned into N_s windows of length s (j = 1, 2, ... N_s). For each window, the local trend was

---

[1] ActiGraph. Available online at: https://www.actigraphcorp.com/ (Accessed July 24, 2018).

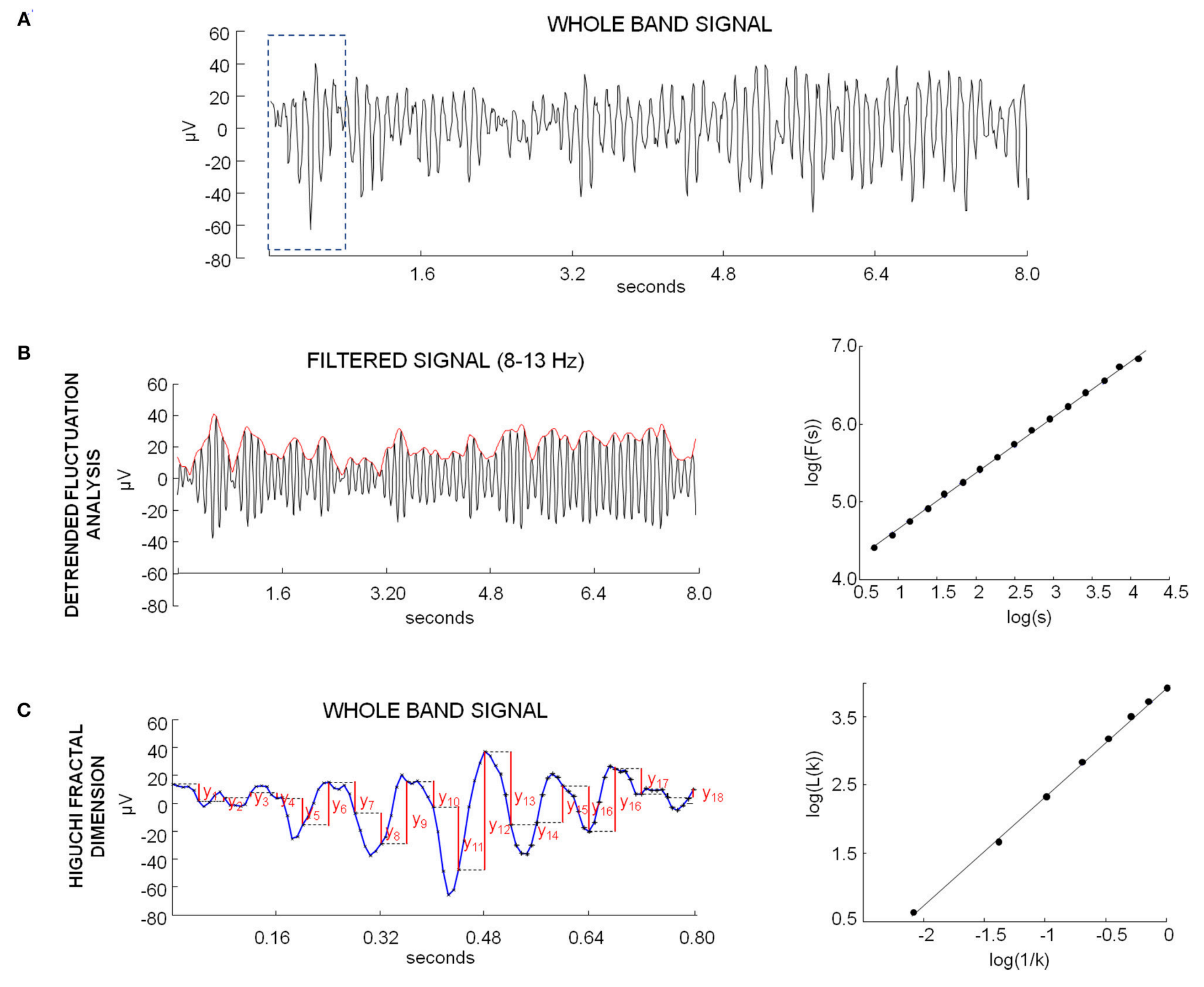

FIGURE 1 | (A) Example of whole band EEG signal of one occipital channel in eyes closed condition. **(B)** Example of DFA calculation. Left: signal shown in **(A)** filtered in alpha band (black) and envelope obtained by modulus of analytic signal (red). Right: plot on logarithmic axes of the mean fluctuation per windows size, obtained from cumulative sum of alpha envelope, against the window size (expressed in seconds). The DFA exponent is the slope of the best-fit line. **(C)** Example of HFD calculation. Left: example sequence determination on the portion of EEG signal in the dotted box in A for the length calculation of x_k^m, with k = 5. The values are calculated as follows: $|x(m+ik) - x(m+(i-1)k)|$, for i = 1,2,3,... 18. The length of the curve $L(k)$ is evaluated as average over m of these values. Right: plot of *log*($L(k)$) against *log*(1/k), for k = 1,.. kmax (kmax = 8). The curve is said to have fractal dimension β if $L(k) \sim k^{-\beta}$.

calculated by a least-square line fitting procedure (Kantelhardt et al., 2002). If $x_{j,s}(i)$ is the ordinate of the fitting line of the j-th segment of length s at time bin i ($i = 1,2,\ldots s$), the fluctuation of the j-th segment of length s, i.e., the root-mean-square deviation from the trend, was calculated as:

$$RMS_j^s = \frac{1}{2}\sum_{i=1}^{s}\left\{x\left[(j-1)\,s+i\right] - x_{j,s}(i)\right\}^2$$

To obtain the fluctuation function, for each scale s the average of the root mean square deviation from the trend was obtained (Kantelhardt et al., 2002):

$$F\,(s) = \sqrt{\frac{1}{N_s}\sum_{j=1}^{S} RMS_j^s}$$

The scaling behavior of the fluctuation function can be obtained by the log-log plot of $F(s)$ over s (**Figure 1B**). If a long-range power-law correlation exists, the following relationship holds:

$$F(s) \sim s^H$$

and the plot is a line, with slope equal to H, the DFA exponent or Hurst exponent (Feder, 2013).

The inclusion of very short windows in the fitting range of the fluctuation function introduces correlation between neighboring samples of the signal. For this reason, we applied the procedure presented in Hardstone et al. (2012) to estimate the effect of narrow-band filtering in DFA values for theta, alpha and beta bands. Briefly, for each band 1000 realizations of white noise were generated and band-pass filtered. On each signal, the amplitude envelope was extracted, DFA performed and the lowest fitting time window estimated from the log-log plot of scale against fluctuation function. The investigated scale ranges from 0.1 s to 100 s. Since for a white-noise signal a DFA exponent of 0.5 is expected, the lowest fitting time window was chosen as the value of the scale after that the trend line of the fluctuation function has a slope of 0.5. Based on obtained results, we found a lowest fitting time window of 2 s for alpha band, of about 1.4 s for beta band and of 4 s for theta band. Therefore, we estimated DFA exponent with a scale in a range of 2 s to 1 min for alpha and beta band and of 4 s to 1 min for theta band.

Higuchi Fractal Dimension

For both conditions and in each time, HFD values of each EEG channel were computed for the whole band signal (i.e., signal filtered between 1 and 40 Hz). As a global measure of HFD, all HFD values obtained for the single channels were averaged.

Fractal dimension is considered as a measure of complexity of a curve. For time series representing this curve, HFD ranges from 1 for deterministic constant functions to 2 for white noise. The algorithm proposed by Higuchi was used (Higuchi, 1988; Accardo et al., 1997). Briefly, the algorithm directly estimates the mean length of the curve $L(k)$ through a measure unit of a segment of k samples. From any given time series of N samples: $x(1)$, $x(2)$, ... $x(N)$, k new time series with initial time sample m and time step k are derived as:

$$x_k^m: \quad x(m), x(m+k), x(m+2k), \ldots x\left(m + int\left(\frac{N-m}{k}\right)k\right)$$

The length of each curve x_k^m is calculated as follows (**Figure 1C**):

$$L_m(k) = \frac{1}{k}\left[\frac{N-1}{int\left(\frac{N-m}{k}\right)k}\left(\sum_{i=1}^{int\left(\frac{N-m}{k}\right)} \left|x(m+ik) - x(m+(i-1)k)\right|\right)\right]$$

For each k, the length of the curve $L(k)$ is evaluated as:

$$L(k) = \frac{1}{k}\sum_{m=1}^{k} L_m(k)$$

The calculation of the curve length $L(k)$ is repeated for k from *1* to k_{max}. The curve is said to have fractal dimension β if:

$$L(k) \sim k^{-\beta}$$

In this case the plot of $log(L(k))$ against $log(k)$ should fall on a straight line with slope equal to $-\beta$, so HFD can be obtained by a least-squares linear best-fitting procedure (**Figure 1C**).

Since HFD is highly dependent on the value of K_{max}, this parameter has a crucial role in HFD estimation. In our knowledge, the studies addressing this issue tested different values directly on their data (for a review see the Appendix A in Kesić and Spasić, 2016). For this reason, according to previous studies (Zappasodi et al., 2014, 2015), a value of $k_{max} = 8$ was applied to the whole-band EEG with a sampling frequency of 125 Hz.

Statistical Analysis

The aim of the statistical analysis was to test if differences across times were present in the non-linear fractality measures depending on the condition (eyes open or closed). Firstly, the topographies of both Hurst exponent and HFD were obtained separately for each band in all the 4 times and the 2 conditions. For each subject, each time and each condition, in the topographical maps the channels of maximum amplitude have been chosen and the channels around the maxima with values exceeding the 90% of maximum have been individuated. Clusters of electrodes have been obtained by conjunctions of these groups of electrodes. The mean Hurst exponent and HFD values over these channels were considered for further analysis. Repeated measure Analyses of Variance (ANOVAs) were separately performed for Hurst exponent and HFD. A 4 X 2 X N design was applied, with Time (T1, T2, T3, T4), Conditions (eyes open, eyes closed) and Region (N maxima individuated on the topographies) as within-subject factors. Greenhouse-Geisser correction has been applied if the sphericity assumption was not valid. *Post-hoc* paired samples *t*-tests were carried out to assess significant differences among times. *Post-hoc* comparisons were FDR corrected.

DFA exponent values could depend on band power. Indeed, estimates of DFA exponent can be biased toward lower values when amplitude of the rhythm reduces, and signal-to-noise ratio increases and vice-versa toward higher values when amplitude increases. Therefore, Spearman's correlations between DFA exponent and corresponding band powers were calculated to evidence positive correlations. Moreover, the same ANOVA design of DFA and HFD was applied on band powers, by considering regions with the same channels used for the fractal measures.

Finally, to verify if band power of rest EEG or non-linear measures (DFA exponents or HFD) predict ARSQ factors, multiple regression analysis was separately performed on each ARSQ factor, considered as dependent variables of the model. Values of each time and both conditions were considered together (4 times X 2 conditions X 20 subjects, resulting in 160 variables). Independent variables were all the band powers, DFA exponents and HFD values in the considered regions. Times and conditions were also included in the model as categorical variables.

RESULTS

The mean topographies of DFA exponent of alpha and beta bands and of HFD were similar across the four times, with the maximal values in specific regions, depending on condition. In alpha band, maximal values were located in occipito-parietal and frontal regions, in particular in eyes closed condition, while in eyes open condition maxima of DFA exponents were also observed in bilateral sensorimotor regions (C3 and C4 of the 10–20 international system, **Figure 2**). In beta band, the posterior maximum of DFA exponents in eyes closed and central areas in eyes open condition were found approximately on the same electrodes of alpha band. The mean topographies of HFD values showed maxima in central sensorimotor regions and minima in parieto-occipital and frontal regions. A maximum of HFD was observed in the temporo-parietal electrodes of left hemisphere (T5 and TP9) in eyes open condition. Channels around the maxima of the posterior, frontal, and bilateral central areas were chosen to average DFA exponents in alpha and beta bands (**Figure 2**) for the ANOVA design. The same channels were chosen for HFD values, with in additions channels around the left temporo-parietal maximum. In theta band, no specific topographies of DFA exponents over the 4 times were observed. Therefore, to assess whether DFA exponents changed over times, a global DFA theta value was calculated for each subject and both condition as the mean over all EEG channels.

Detrended Fluctuation Analysis

Fifth, ninety-fifth percentile of Hurst exponent values ranged from 0.57 to 0.86 in alpha band (mean ± standard deviation across subjects and times: 0.73 ± 0.09 and 0.69 ± 0.08, respectively for closed and open eyes), from 0.57 to 0.85 in beta band (0.72 ± 0.09 and 0.67 ± 0.07, respectively for closed and open eyes), and from 0.53 to 0.74 in theta band (0.62 ± 0.06 and 0.60 ± 0.07, respectively for closed and open eyes). All mean DFA values were significantly different from 0.5, the DFA exponent value of uncorrelated white noise (one-sample *t*-test $p < 0.0001$ for each band, region, and condition).

In alpha band, repeated measures ANOVA with *Time* (four levels: T1, T2, T3, and T4), *Condition* (two levels: Eyes Closed, Eyes Open), and *Region* (three levels: posterior, central, frontal) as within-subject factors showed significant main effects of *Time* [$F_{(3, 60)} = 3.492$; $p = 0.021$] and *Condition* [$F_{(1, 20)} = 5.808$; $p = 0.026$], as well as significant *Condition*Time* [$F_{(3, 60)} = 4.183$; $p = 0.009$], and *Condition*Region* [$F_{(1.5, 29.8)} = 4.218$; $p = 0.034$] interaction effects, but not significant main effect of *Region* ($p = 0.301$) and interactions *Region*Time* ($p = 0.101$) and *Condition*Region*Time* ($p = 0.718$). Looking at the alpha DFA exponent over time (**Figure 3**), we noticed that at T1 no differences were observed between conditions in all regions. The marked differences were present only at time T2, T3, and T4 for occipital regions and T2 and T4 for frontal and central regions, as assessed by paired *t*-test between eyes closed and eyes open conditions ($p < 0.05$, FDR corrected, **Figure 3**). Moreover, while in open eyes condition no difference among DFA exponent in the different times was found, in closed eyes condition DFA exponent values at time T1 was lower than values at other times in occipital and frontal regions (paired sample *t*-test between T1 and the other times consistently $p < 0.05$, FDR corrected). In central regions, only differences between T1 and T2 and between T1 and T4 were observed.

In beta band, repeated measures ANOVA with *Time*, *Condition,* and *Region* as within-subject factors showed significant main effects of *Time* [$F_{(3, 60)} = 4.128$; $p = 0.010$], *Condition* [$F_{(1, 20)} = 14.319$; $p = 0.001$], *Region* [$F_{(2, 40)} = 9.433$; $p < 0.001$] as well as significant *Condition*Region* [$F_{(1.3, 27.0)} = 4.222$; $p = 0.039$] and *Region*Time* [$F_{(6, 120)} = 2.234$; $p = 0.044$] interaction effects. No significant interactions *Condition*Time* was found [$F_{(3, 60)} = 2.526$; $p = 0.066$] and *Condition*Region*Time* ($p = 0.374$). Also, in this band, DFA exponent values in the eyes open conditions did not differ over time. On the contrary, in closed eyes condition, T1 values were lower than values at other times in all regions ($p < 0.05$ consistently, FDR corrected). Differences between the conditions were observed in all regions at T2, T3, and T4 ($p < 0.05$, FDR corrected).

Finally, Repeated measures ANOVA on theta DFA values with *Time* and *Condition* showed only a significance of the main effect *Time* [$F_{(3, 60)} = 4.669$; $p = 0.005$]. The lack of Condition effect ($p = 0.155$), or interaction *Time*Condition* ($p = 0.428$), indicated that in the 4 times the theta DFA exponents were not different between open closed and eyes conditions. *Post-hoc t*-test indicated a difference between T1 vs. T3 and T1 vs. T4 ($p < 0.05$, **Figure 3**).

Higuchi Fractal Dimension

Fifth, ninety-fifth percentile of HFD values ranged from 1.44 to 1.69 (mean ± standard deviation across subjects and times: 1.54 ± 0.08 and 1.59 ± 0.08, respectively for closed and open eyes).

Repeated measures ANOVA with *Time*, *Condition,* and *Region* (four levels: posterior, central, frontal, left temporo-parietal) as within-subject factors showed significant main effects of *Condition* [$F_{(1, 20)} = 21.193$; $p < 0.001$] and *Region* [$F_{(3, 60)} = 19.608$; $p < 0.001$], as well as significant *Condition*Time* [$F_{(3, 60)} = 7.280$; $p < 0.001$], *Region*Time* [$F_{(5.0, 100.6)} = 2.933$; $p = 0.016$] interaction effects, but not significant main effect of *Time* [$F_{(3, 60)} = 2.319$; $p = 0.084$], and interactions *Region*Condition* ($p = 0.405$) and *Condition*Region*Time* ($p = 0.932$). In parieto-occipital and central regions differences between open and closed eyes conditions were observed in T1, T2, and T3 times ($p < 0.05$), with eyes open HFD values higher than eyes closed HFD values. This difference was also present in all times in left temporo-parietal regions and at times T1 and T3 in frontal regions. Moreover, while in central regions eyes open HFD values did not significantly changed over times, in the other condition a reduction was observed over time (**Figure 4**). In eyes closed condition, an increase at T2 and T4 with respect to T1 and T3 were observed in central regions and the T1 values were lower than the values at the other times in frontal regions (**Figure 4**).

Band Power

Repeated measures ANOVA with *Time*, Condition, and Region on alpha band power values revealed significant main effects of *Condition* [$F_{(1, 20)} = 28.764$; $p < 0.001$], *Region* [$F_{(3, 60)} = 64.231$; $p < 0.001$], and *Time* [$F_{(3, 60)} = 4.874$; $p = 0.004$]. The first 2 main effects confirmed that alpha power in closed eyes condition were higher than in eyes open condition and that alpha power was higher in parieto-occipital regions. The lack of interactions *Time*Condition* ($p = 0.574$), *Time*Regions* ($p = 0.311$), *Time*Condition*Regions* ($p = 0.549$) and the presence of the main effect *Time*, confirmed that during the

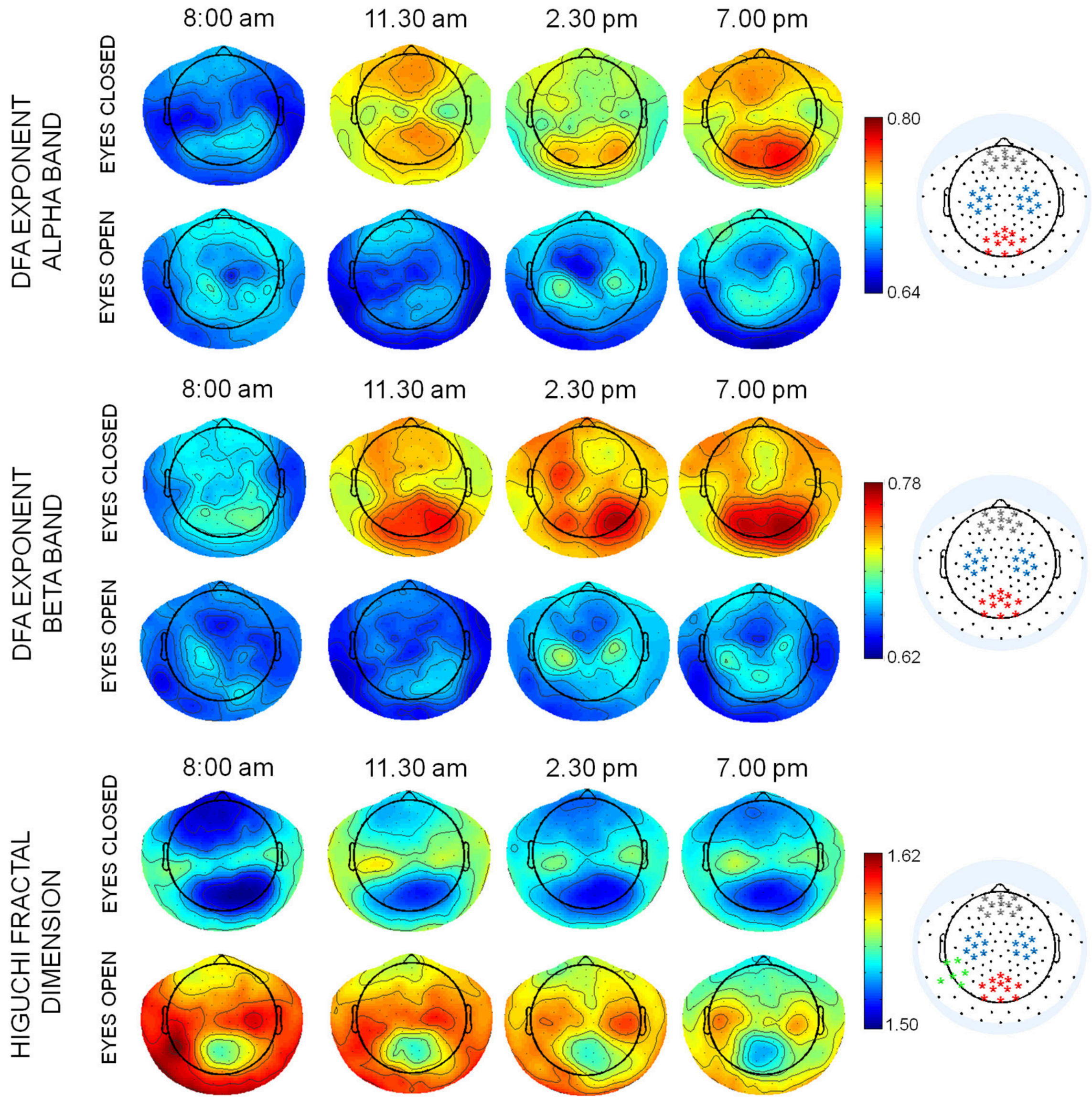

FIGURE 2 | Mean topographies of DFA exponents in alpha and beta bands and of HFD values in eyes closed and open conditions in the 4 times T1: 8:00 am; T2: 11:30 am, T3: 2:30 pm; T4: 7:00 pm. The selection of channels used for averaging the DFA and HFD values are displayed on the right (red: posterior parieto-occipital region; blue: central sensorymotor regions; gray: frontal region; green: left temporo-parietal region).

day the alpha power uniformly changed in all the considered groups of electrodes (mean and standard error over conditions and regions: 6.29 ± 0.10 at T1, 6.38 ± 0.09 at T2, 6.40 ± 0.09 at T3, 6.42 ± 0.10 at T4). In particular, *post hoc* tests showed that the difference was significant only between T1 and T4 ($p = 0.036$ Bonferroni corrected). The same results were found in beta band: the main significant effects *Condition* [$F_{(1,\,20)} = 8.062$; $p = 0.010$], *Region* [$F_{(3,\,60)} = 49.261$; $p < 0.001$], and *Time* [$F_{(3,\,60)} = 8.643$; $p < 0.001$] and the lack of interactions ($p > 0.1$) confirmed a similar increase of power (5.50 ± 0.07 at T1, 5.60 ± 0.07 at T2, 5.62 ± 0.07 at T3, 5.63 ± 0.07 at T4). *Post hoc* tests showed differences of beta band at T1 vs. T2 ($p = 0.009$), at T1 vs. T3 ($p = 0.029$), at T1 vs. T4 ($p = 0.007$). Finally, repeated measures ANOVA with *Time* and *Condition* on theta band power showed only a significant main effect of *Time* [$F_{(3,\,60)} = 3.492$; $p = 7.834$]. Also, for this band, T1 values were different by T2, T3, and T4 ($p = 0.042$, $p = 0.018$ and $p = 0.011$, respectively; mean and standard over conditions: 5.99 ± 0.08 at T1, 6.11 ± 0.08 at T2, 6.15 ± 0.08 at T3, 6.16 ± 0.07 at T4).

In closed eyes condition, no correlations between DFA exponent and band powers were observed for alpha and beta bands. A positive correlation was found for theta band. On the contrary, positive correlations were found between all the band powers and DFA exponent in all bands in eyes open condition (**Table 1**).

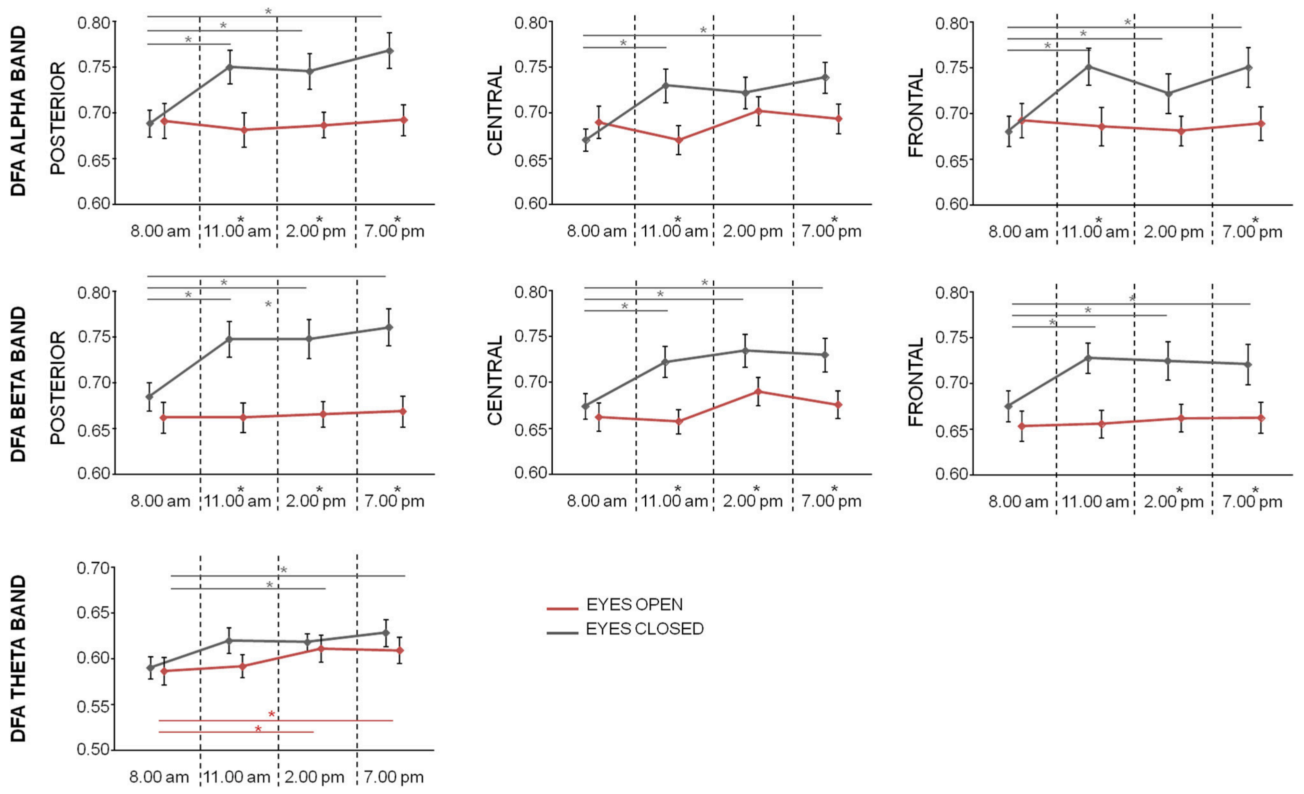

FIGURE 3 | Mean (bars indicate standard error of mean) of DFA exponent values in the different regions for alpha, beta, and theta bands at the 4 times in closed eyes (gray) and open eyes (red) conditions. Significances of the paired *t*-test between times are shown (gray for closed eyes and red for open eyes; $^{*}p < 0.05$, FDR corrected). The difference between eyes closed and eyes open conditions at one time is evidenced by a star as apex of corresponding time.

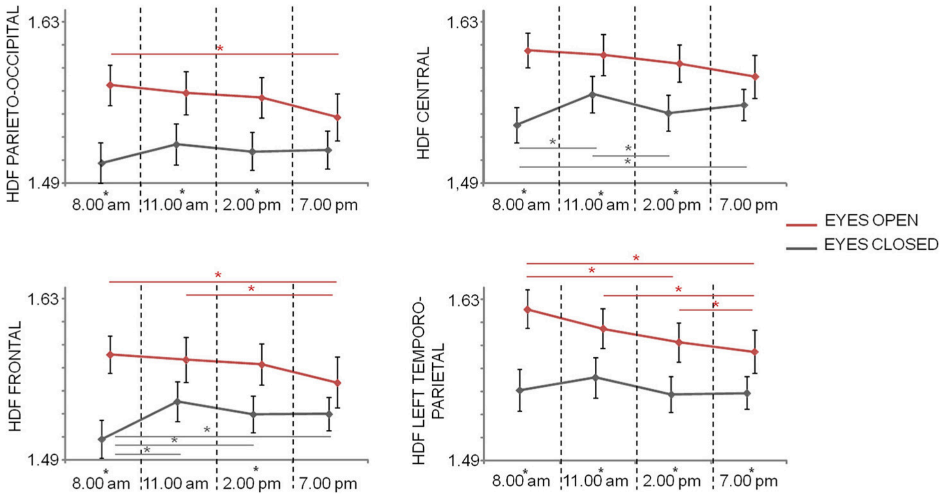

FIGURE 4 | Mean and standard error of HFD values in the different regions at the 4 times in closed eyes (gray) and open eyes (red) conditions. Significances of the paired *t*-test between times are shown (gray for closed eyes and red for open eyes; $^{*}p < 0.05$, FDR corrected). The difference between eyes closed and eyes open conditions at one time is evidenced by a star as apex of corresponding time.

Psychomotor Vigilance Test

The numbers of lapses and false starts did not change over time and was lower or equal to 1 for each conditions and subject. Repeated measure ANOVA design on response speed indicated a significant *Time* effect. Indeed, T4 speed was higher than T1 ($p = 0.012$, Bonferroni corrected) and tended to be higher also than the T3 speed ($p = 0.085$). Mean (standard deviation) values of response speed were (in s^{-1}): 3.574 ± 0.231 at T1; 3.639 ± 0.387 at T2; 3.568 ± 0.330 at T3; 3.678± 0.288 at T4.

Amsterdam Resting-State Questionnaire

Repeated measure ANOVA with *Time* and *Condition* as within subject factors separately applied to ARSQ factors, revealed significant effects only for *Sleepiness* and *Somatic Awareness*. In particular, in Sleepiness a significant effect of the main factor *Time* [$F_{(3, 54)} = 4.992$; $p = 0.004$] and an interaction *Condition*Time* [$F_{(3, 54)} = 3.101$; $p = 0.034$] were found, but not the main effect of *Condition* ($p = 0.877$). *Post-hoc* tests revealed that, while no differences in times were found in open eyes condition (mean values ± standard deviation for T1, T2, T3, and T4: 1.67 ± 0.20; 2.13 ± 0.25; 2.22 ± 0.26; 1.88 ± 0.22), T1 scores were lower than the scores at the other times in eyes closed condition (T1: 1.27 ± 0.19; T2: 2.02 ± 0.26; T3: 2.26 ± 0.25; T4: 2.19 ± 0.25, paired-sample *t*-test T1 vs. T2, $p = 0.009$; T1 vs. T3, $p = 0.006$; T1 vs. T4, $p = 0.010$, Bonferroni corrected). For Somatic Awareness, only the significance of the main factor *Time* was found [$F_{(3, 54)} = 3.661$; $p = 0.009$] and neither *Condition* ($p = 0.475$) nor the interaction *Condition*Time* ($p = 0.862$) resulted significant. *Post-hoc* tests revealed a difference only between T1 and T4 times ($p = 0.050$, mean scores between the 2 conditions: 2.14 ± 0.14; 1.98 ± 0.16; 1.85 ± 0.15; 1.69 ± 0.18 at the 4 times).

Relationship Between Spectral and Fractal Features With ARSQ Factors

As shown in **Table 2**, different spectral and fractal features entered the regression model, predicting factors of ARSQ. Up to the 27% of the variance was explained (minimum 9% for *Sleepiness*, maximum 27% for *Somatic Awareness*). A positive sign of the estimated coefficients indicates a positive relationship between the spectral/fractal variables and the ARSQ factors, i.e., the higher the power band or fractal measure, the higher the score of ARSQ. A negative sign indicated the opposite. No variables entered the model for the *Comfort* factor.

TABLE 1 | Rho (*p*-values in italics, not corrected for multiple comparisons) of Spearman's correlations between DFA exponents and band powers in eyes closed and eyes open conditions.

	Eyes Closed	Eyes Open
Posterior alpha	0.111	0.462
	0.374	*<0.001*
Central alpha	0.115	0.422
	0.310	*<0.001*
Frontal alpha	0.079	0.478
	0.486	*<0.001*
Posterior beta	0.184	0.352
	0.102	*<0.001*
Central beta	0.188	0.421
	0.094	*<0.001*
Frontal beta	0.194	0.425
	0.085	*<0.001*
Theta	0.455	0.684
	<0.001	*<0.001*

TABLE 2 | Regression models with ARSQ factors as dependent variables and spectral/fractal features as independent variables.

Dependent variables	Independent variables	Estimated coefficients	*R*-values	ANOVA
Discontinuity of Mind	Left temp Beta Pow	−1.157		$F_{(3, 154)} = 11.369$; $p < 0.001$
	Theta Pow	0.776	0.425	
	Central DFA exp - alpha	1.428		
Theory of Mind	Left temp Beta Pow	−1.326	0.438	$F_{(2, 155)} = 18.434$; $p < 0.001$
	Theta Pow	0.603		
Self	Frontal HFD	2.970		
	Central Beta Pow	−1.121	0.475	$F_{(3, 154)} = 14.973$; $p < 0.001$
	Posterior Beta Pow	0.651		
Planning	Central Beta Pow	−0.796		
	Posterior Beta Pow	1.297	0.406	$F_{(3, 154)} = 10.154$; $p < 0.001$
	Left temp Beta Pow	−1.013		
Sleepiness	Central DFA exp – beta	3.005	0.308	$F_{(2, 155)} = 8.108$; $p < 0.001$
	Time	0.157		
Comfort	No variables entered			
Somatic Awareness	Frontal DFA exp - alpha	−0.755		
	Posterior Alpha Pow	−0.178	0.524	$F_{(5, 152)} = 11.537$; $p < 0.001$
	Posterior HFD	9.829		
	Frontal HFD	−6.298		
	Time	−0.103		
Health Concern	Central HFD	1.854		
	Frontal DFA exp—alpha	−1.463	0.350	$F_{(3, 154)} = 7.182$; $p < 0.001$
	Condition	−0.216		
Visual Thought	Left temp Beta Pow	−0.937		$F_{(3, 154)} = 8.200$; $p < 0.001$
	Theta Pow	2.101	0.372	
	Central Beta Pow	−1.345		
Verbal Thought	Left temp Beta Pow	−2.051		$F_{(3, 154)} = 14.853$; $p < 0.001$
	Central HFD	−3.007	0.473	
	Theta Pow	1.058		

Times and conditions were included as categorical variables.

DISCUSSION

Our results evidenced circadian modulations of fractal features of EEG at rest in both eyes closed and eyes open conditions. The investigated fractal characteristics were long term memory of amplitude modulation of alpha, beta, and theta rhythms in a time range from few seconds to 1 min, as assessed by Hurst exponent estimated by Detrended Fluctuation Analysis, and global complexity, as assessed by Higuchi Fractal Dimension.

According to previous results (Linkenkaer-Hansen et al., 2001; Nikulin and Brismar, 2004, 2005), in our study scaling exponent values (approximately between 0.6 and 0.8) indicated the presence of long range temporal correlation of neuronal oscillations in alpha, beta and theta bands. The presence of high long-term correlation indicates a more temporally structured amplitude modulation of the neuronal rhythms, building up through neural local interactions until they extend throughout the whole system (Linkenkaer-Hansen et al., 2001). It is not yet understood if the less temporally uncorrelated modulation of the rhythm is a sign of a reduced functionality of the brain areas. It has been suggested that the temporal correlations of amplitude modulation of oscillations on time scales of seconds to tens of seconds may be important for the temporal integrity of cognition, since a reduction of scaling exponent is related to several neurological impairments and diseases (Hausdorff et al., 2001; Parish et al., 2004; Linkenkaer-Hansen et al., 2005; Montez et al., 2009). Moreover, a more whitened state, characterized by a lower scaling exponent, has been found to lead more often to percept destabilization (Sangiuliano Intra et al., 2018).

Topography of DFA exponents confirmed a scalp distribution coherent with the physiological distribution of cortical rhythms, in posterior occipital-parietal, central sensory-motor, and frontal regions. This distribution indicates a topographical specialization of brain areas. Indeed, all cortical circuits accumulate information over time to continuously use past information to process the incoming one. As shown in an electrocardiographic study (Hasson et al., 2015), the timescale of accumulation, linked to the scaling exponent, changes hierarchically from short processing timescale, typical of sensory regions, to higher-order regions, which show typically long processing timescales.

No differences in eyes open conditions over day times were observed in our data. On the contrary, lower values of DFA in both alpha and beta bands were observed in eyes closed condition in the first time, between 8.00 and 9.00 a.m. In this line, the significantly lower values of DFA exponent we found in the time T1 may be the expression of a lowered arousal, causing a decrement in cognitive performances in the first hours of the morning, due to effects of the sleep inertia (Jewett et al., 1999; Ferrara and De Gennaro, 2000). This reduction in T1 was observed only in closed eyes condition, in which it is likely that arousal levels were lower. In line with this interpretation, we found that the PVT performance was lower in the time T1, suggesting a reduced vigilance in this time. A reduction in beta activity upon awakening has been previously found in EEG recording as sign of sleep inertia (Marzano et al., 2011). Interestingly, an alpha scaling exponent reduction was found also in central sensory-motor areas at time T3 in closed eyes condition. In our data, the maximum of mean values of sleepiness factor in the ARSQ, also if not reaching significance, was reached in the T3 time. These results may be interpreted as a reduced functionality in the day time in which the sleepiness can be present (Jewett et al., 1999).

In a recent EEG study, Meisel et al. (2017) found in a sustained wakefulness protocols, a decline of scaling exponent in alpha band as sleep deprivation progresses, apparently contrary to our finding of a DFA exponent increase during the day. However, the aims of this study were different from ours, as subjects were sleep deprived. We tried to keep the physiological conditions as ecological as possible: subjects were outside the laboratory between 2 consecutive measures, the light exposure was natural, and, under the supervision of an experimenter, they were in their habitual environment. The differences between the 2 studies may be caused also by individual variation in the circadian influence on fractal neural activity control (21 subjects in our study, 7 subjects in Meisel et al., 2017).

As previously pointed out (Kantelhardt et al., 2002; Hardstone et al., 2012), power amplitude could bias the values of DFA exponent, since low amplitude could be associated to low signal to noise ratio, and scaling exponent could be reduced toward values more similar to scaling exponent of white noise. On the contrary, high amplitude, resulting in high signal to noise ratio, could bias toward higher values of DFA exponents. For this reason, we investigated also the effect of time on power bands. We found both in eyes open and eyes closed conditions, an increase in all bands over time. However, the lack of correlation between DFA exponent values and alpha and beta band powers in eyes closed condition confirmed that our results on DFA exponents are not due to the increase of band power. On the contrary, in theta band, no difference between eyes closed and eyes open condition was found and a similar trend between scaling exponent and power was evidenced. Since a high correlation between the scaling exponent and the theta power was found, we cannot exclude that the results in theta band may be biased by the power changes over time.

Our results in band power are in accordance to previous studies. In protocols with 40 h sustained wakefulness, theta band exhibited a minimum ∼1 h after the onset of melatonin secretion and alpha band activity showed a minimum close to the body temperature minimum (Aeschbach et al., 1999), therefore minima of daily theta and alpha activity were found in the first hours of the morning. In these studies, both circadian effects and endogenous processes interact. In contrast, in forced desynchronized paradigms, where subjects were kept several days in an environment free of time cues with an artificial dim light, the circadian rhythm of plasma melatonin desynchronized and the contribution of circadian phase (process C) can be separated by the elapsed time awake effects (process S). In this situation, effects on EEG band power in wakefulness of both processes have been described (Cajochen et al., 2002). Specifically, circadian oscillations of theta, alpha, and beta bands have been found, with increase during the daytime and decrease during the biological night hours. Minimum of beta and theta activity was in correspondence of the onset of melatonin secretion, located in fronto-central derivation, and the minimum of alpha activity in posterior and frontal regions was close to the peak of melatonin rhythm (Cajochen et al., 2002). Our findings in band power are in line with these results, since an increase during the day was observed, with minima in the first T1 time. Wake-dependent variations in desynchronized protocols are more pronounced in frontal regions, with an increase of beta band. A reduction of alpha activity with elapsed time awake was also observed (Cajochen et al., 2002; for a review see Cajochen and Dijk, 2003).

Our data showed changes during the daytime also on HFD in a spatial-dependent modality, depending on condition (eyes closed or open). Indeed, in eyes open condition, fractal dimension lowered during the day, in particular in occipital, frontal, and temporo-parietal regions. In eyes closed condition, an HFD increase was observed at time T2 in central and frontal regions. Decrease of complexity over time during the day in the open eyes condition may be interpreted as a circadian modulation of efficiency of neural activity parallel to changes in arousal and cognitive performance (Wright et al., 2012). In line with this interpretation, an increase of complexity in central and frontal areas was found at T2, the time in which alertness reaches its maximum and homeostatic sleep pressure is low.

The fluctuations over daytime of fractal features we observed, tend to implicate that the complexity of brain electrical activity cannot be entirely described by a single scaling exponent. This may suggest a multi-fractal nature of brain dynamics. Indeed, previous studies evidenced multi-fractal nature of the human sleep EEG activity (Ma et al., 2006; Weiss et al., 2009, 2011), and showed that multifractality might be an adequate approach for compact modeling of brain activities and a useful pattern classification technique to distinguish among different brain states during sleep (Weiss et al., 2011; Zorick and Mandelkern, 2013). Future studies with an extensive characterization and a detailed topographic analysis of EEG multi-fractal features in awake human EEG are needed to systematically address this point.

A direct causal influence of circadian rhythm to scaling properties cannot be supported by our data. Indeed, scaling would be the result of stochastically perturbed oscillatory entrapment across a broad range of times scales (Bak et al., 1987; Turcotte, 1999), and circadian rhythms could come out from a background of stochastically fluctuating biological processes at different temporal scales. From a theoretical perspective, this view would overturn the more intuitive notion that very regular biological oscillations regulate physiology, and regulate also scaling, in favor of the idea that scaling itself is the background model for the dynamics of physiological time series and thus also for their fluctuations at different time scales. In this context, we can hypothesize that homeostatic sleep pressure, together with other endogenous and exogenous physiological factors (Muto et al., 2016), contribute to brain dynamics, characterized by a fractal, or even better multi-fractal, behavior. As a result, daily fluctuations of scale exponents and complexity can be found in brain dynamics.

The question arises as to whether fractal dimension and Hurst exponent provide additional information to spectral features in describing the rest conditions. Previous studies reported evidence that variation in spectral and fractal feature of EEG can be linked to retroactive self-reports of subjective experiences at rest (Knyazev, 2013; Diaz et al., 2016). Even if with an exploratory purpose, we separately performed a regression analysis for each factor of ARSQ, considered as dependent variable, and with fractal dimension, scaling exponents and band powers as independent variables. We found that not only spectral features, but also fractal characteristics entered the model to explain up to the 20% of the variance. These relationships are suggestive of the ability of fractal features to summarize the neuronal activity in terms of temporal structuring or complexity in relation to cognition or behavior. In particular, reduction of left temporo-parietal or central beta power and increase of theta activity was linked to higher scores of several ARSQ factors, underling the role of beta desynchronization/theta synchronization of these rhythms in several cognitive domains (Engel and Fries, 2010). Positive signs of the estimated coefficients of the regression models were found for beta DFA exponents and HFD values. This finding indicates that increase in complexity in specific areas or a greater persistence of temporal correlations in alpha or beta bands predict higher score of specific ARQS factor. A negative coefficient was found only for frontal alpha DFA exponent in Somatic Awareness and Health Concern. Irrmischer et al. (2018) found an increase of Somatic Awareness during meditation and a decrease of alpha scaling exponent most pronounced above parietal, central, and frontal regions, but also a decrease in Health Concern was found. A direct link between ARSQ factor and spectral or fractal features is beyond the aim of this work. The interesting finding here is that our results underline the fact that spectral features cannot be considered alone in explaining highly non-linear phenomena and that fractal characteristics of the signal have *per se* physiological meaning.

Even if growing evidence has accumulated that circadian rhythm dysregulation not only is a risk factor for metabolic and cardiovascular diseases (Broussard and Van Cauter, 2016; Morris et al., 2016), but also contributes to neurodegenerative processes (Musiek et al., 2015), little attention has been paid to circadian rhythm modulations of brain dynamics in real clinical settings. Our data add evidence of circadian modulation in spectral and fractal features in healthy subjects. These results can help to characterize factors of intra-individual variability in describing brain dynamics and to personalize interventions or therapies in clinical applications. Indeed, if complexity of neuronal dynamics and long-term correlation of brain rhythms, factors related to the modality of neuronal responses to incoming input or sensory plasticity (Palva and Palva, 2011; Palva et al., 2013), changes during the daytime, it would be expected that the correct information on the time of the day when the individual state optimizes the individual response could be utilized to indicate the correct timing for a therapeutic or rehabilitative intervention. Therefore, the characterization of fractal phenomena can provide new psychophysical models (Zueva, 2015). In this direction, future studies are needed to underline alteration of circadian modulation of fractal features in neurological or psychiatric diseases, as well as to understand the link between fractal features, brain functions and behavior.

In conclusion, in our study differences in fractal features of rest EEG activity during the 4 daily times have been evidenced. Complexity and the persistence of temporal correlations of brain rhythms changes during daytime, parallel to changes in alertness and performance. The characterization of circadian modulations of fractal features may in future provide important information to build meaningful physiological models. Further studies under condition known to induce desynchrony amongst circadian oscillators are needed to disentangle the effects of circadian endogenous factors and homeostatic sleep pressure.

AUTHOR CONTRIBUTIONS

PC, AQ, SC, and FZ designed the study, interpreted the data, and wrote the manuscript. PC and FZ carried out the experiments. PC, SC, and FZ analyzed the data. All of the authors participated in drafting the work and agreed on the final version of the manuscript.

ACKNOWLEDGMENTS

Authors would like to thank Mauro Treddenti and Giandomenico Bisaccia for assistance in EEG recordings.

REFERENCES

Accardo, A., Affinito, M., Carrozzi, M., and Bouquet, F. (1997). Use of the fractal dimension for the analysis of electroencephalographic time series. *Biol Cybern* 77, 339–350. doi: 10.1007/s004220050394

Aeschbach, D., Matthews, J. R., Postolache, T. T., Jackson, M. A., Giesen, H. A., and Wehr, T. A. (1999). Two circadian rhythms in the human electroencephalogram during wakefulness. *Am. J. Physiol.* 277, R1771–1779.

Bak, P., Tang, C., and Wiesenfeld, K. (1987). Self-organized criticality: an explanation of 1/f noise. *Phys. Rev. Lett.* 59, 381–382.

Barabasi, A. -L., and Albert, R. (1999). Emergence of scaling in random networks. *Science* 286, 509–512. doi: 10.1126/science.286.5439.509

Barbati, G., Porcaro, C., Zappasodi, F., Rossini, P. M., and Tecchio, F. (2004). Optimization of an independent omponent analysis approach for artifact identification and removal in magnetoencephalographic signals. *Clin. Neurophysiol.* 115, 1220–1232. doi: 10.1016/j.clinph.2003.12.015

Basner, M., and Dinges, D. F. (2011). Maximizing sensitivity of the psychomotor vigilance test (PVT) to sleep loss. *Sleep* 34, 581–591. doi: 10.1093/sleep/34.5.581

Bojić, T., Vuckovic, A., and Kalauzi, A. (2010). Modeling EEG fractal dimension changes in wake and drowsy states in humans–a preliminary study. *J. Theor. Biol.* 262, 214–222. doi: 10.1016/j.jtbi.2009.10.001

Borbély, A. A. (1982). A two process model of sleep regulation. *Hum. Neurobiol.* 1, 195–204.

Broussard, J. L., and Van Cauter, E. (2016). Disturbances of sleep and circadian rhythms: novel risk factors for obesity. *Curr. Opin. Endocrinol. Diabetes Obes.* 23, 353–359. doi: 10.1097/MED.0000000000000276

Cajochen, C., Chellappa, S., and Schmidt, C. (2010). What keeps us awake?-the role of clocks and hourglasses, light, and melatonin. *Int. Rev. Neurobiol.* 93, 57–90. doi: 10.1016/S0074-7742(10)93003-1

Cajochen, C., and Dijk, D. -J. (2003). Electroencephalographic activity during wakefulness, rapid eye movement and non-rapid eye movement sleep in humans: comparison of their circadian and homeostatic modulation. *Sleep Biol. Rhythms* 1, 85–95. doi: 10.1046/j.1446-9235.2003.00041.x

Cajochen, C., Wyatt, J. K., Czeisler, C. A., and Dijk, D. J. (2002). Separation of circadian and wake duration-dependent modulation of EEG activation during wakefulness. *Neuroscience* 114, 1047–1060. doi: 10.1016/S0306-4522(02)00209-9

Cole, R. J., Kripke, D. F., Gruen, W., Mullaney, D. J., and Gillin, J. C. (1992). Automatic sleep/wake identification from wrist activity. *Sleep* 15, 461–469.

Di Ieva, A., Grizzi, F., Jelinek, H., Pellionisz, A. J., and Losa, G. A. (2014). Fractals in the neurosciences, part i: general principles and basic neurosciences. *Neuroscientist* 20, 403–417. doi: 10.1177/1073858413513927

Diaz, B. A., Hardstone, R., Mansvelder, H. D., Van Someren, E. J. W., and Linkenkaer-Hansen, K. (2016). Resting-state subjective experience and EEG biomarkers are associated with sleep-onset latency. *Front. Psychol.* 7:492. doi: 10.3389/fpsyg.2016.00492

Diaz, B. A., Van Der Sluis, S., Moens, S., Benjamins, J. S., Migliorati, F., Stoffers, D., et al. (2013). The Amsterdam resting-state questionnaire reveals multiple phenotypes of resting-state cognition. *Front. Hum. Neurosci.* 7:446. doi: 10.3389/fnhum.2013.00446

Dijk, D.-J., and von Schantz, M. (2005). Timing and consolidation of human sleep, wakefulness, and performance by a symphony of oscillators. *J. Biol. Rhythms* 20, 279–290. doi: 10.1177/0748730405278292

Dinges, D. F., and Powell, J. W. (1985). Microcomputer analyses of performance on a portable, simple visual RT task during sustained operations. *Behav. Res. Methods Instr. Comput.* 17, 652–655. doi: 10.3758/BF03200977

Drapeau, C., and Carrier, J. (2004). Fluctuation of waking electroencephalogram and subjective alertness during a 25-hour sleep-deprivation episode in young and middle-aged subjects. *Sleep* 27, 55–60. doi: 10.1093/sleep/27.1.55

Engel, A. K., and Fries, P. (2010). Beta-band oscillations–signalling the status quo? *Curr. Opin. Neurobiol.* 20, 156–165. doi: 10.1016/j.conb.2010.02.015

Fadel, P. J., Barman, S. M., Phillips, S. W., and Gebber, G. L. (2004). Fractal fluctuations in human respiration. *J. Appl. Physiol.* 97, 2056–2064. doi: 10.1152/japplphysiol.00657.2004

Feder, J. (2013). *Fractals*. New York, NY: Springer Science & Business Media.

Ferrara, M., and De Gennaro, G. (2000). The sleep intertia phenomenonduring the sleep-wake transition: theoretical and operational issues. *Aviat. Space Environ. Med.* 71, 843–848.

Finelli, L. A., Baumann, H., Borbély, A. A., and Achermann, P. (2000). Dual electroencephalogram markers of human sleep homeostasis: correlation between theta activity in waking and slow-wave activity in sleep. *Neuroscience* 101, 523–529. doi: 10.1016/S0306-4522(00)00409-7

Goldberger, A. L., Amaral, L. A. N., Hausdorff, J. M., Ivanov, P. C., Peng, C.-K., and Stanley, H. E. (2002). Fractal dynamics in physiology: alterations with disease and aging. *Proc. Natl. Acad. Sci. U.S.A.* 99(Suppl. 1), 2466–2472. doi: 10.1073/pnas.012579499

Hardstone, R., Poil, S.-S., Schiavone, G., Jansen, R., Nikulin, V. V., Mansvelder, H. D., et al. (2012). Detrended fluctuation analysis: a scale-free view on neuronal oscillations. *Front. Physiol.* 3:450. doi: 10.3389/fphys.2012.00450

Hasson, U., Chen, J., and Honey, C. J. (2015). Hierarchical process memory: memory as an integral component of information processing. *Trends Cogn. Sci.* 19, 304–313. doi: 10.1016/j.tics.2015.04.006

Hausdorff, J. M., Ashkenazy, Y., Peng, C. -K., Ivanov, P. C., Stanley, H. E., and Goldberger, A. L. (2001). When human walking becomes random walking: fractal analysis and modeling of gait rhythm fluctuations. *Physica A* 302, 138–147. doi: 10.1016/S0378-4371(01)00460-5

He, B. J., Snyder, A. Z., Vincent, J. L., Epstein, A., Shulman, G. L., and Corbetta, M. (2007). Breakdown of functional connectivity in frontoparietal networks underlies behavioral deficits in spatial neglect. *Neuron* 53, 905–918. doi: 10.1016/j.neuron.2007.02.013

He, B. J., Zempel, J. M., Snyder, A. Z., and Raichle, M. E. (2010). The temporal structures and functional significance of scale-free brain activity. *Neuron* 66, 353–369. doi: 10.1016/j.neuron.2010.04.020

Higuchi, T. (1988). Approach to an irregular time series on the basis of the fractal theory. *Physica D* 31, 277–283. doi: 10.1016/0167-2789(88)90081-4

Horne, J. A., and Ostberg, O. (1976). A self-assessment questionnaire to determine morningness-eveningness in human circadian rhythms. *Int. J. Chronobiol.* 4, 97–110.

Irrmischer, M., Poil, S. -S., Mansvelder, H. D., Intra, F. S., and Linkenkaer-Hansen, K. (2018). Strong long-range temporal correlations of beta/gamma oscillations are associated with poor sustained visual attention performance. *Eur. J. Neurosc.* 48, 2674–2683. doi: 10.1111/ejn.13672

Jewett, M. E., Wyatt, J. K., Ritz-De Cecco, A., Khalsa, S. B., Dijk, D. J., and Czeisler, C. A. (1999). Time course of sleep inertia dissipation in human performance and alertness. *J. Sleep Res.* 8, 1–8.

Johnson, M. (1990). Sleep and alertness: chronobiological, behavioral, and medical aspects of napping. *J. Neurol. Neurosurg. Psychiatry* 53:92.

Kantelhardt, J. W., Zschiegner, S. A., Koscielny-Bunde, E., Havlin, S., Bunde, A., and Stanley, H. E. (2002). Multifractal detrended fluctuation analysis of nonstationary time series. *Physica A* 316, 87–114. doi: 10.1016/S0378-4371(02)01383-3

Kesić, S., and Spasić, S. Z. (2016). Application of Higuchi's fractal dimension from basic to clinical neurophysiology: a review. *Comput. Methods Programs Biomed.* 133, 55–70. doi: 10.1016/j.cmpb.2016.05.014

Knyazev, G. G. (2013). EEG correlates of self-referential processing. *Front. Hum. Neurosci.* 7:264. doi: 10.3389/fnhum.2013.00264

Lavie, P. (1989). Ultradian rhythms in arousal-the problem of masking. *Chronobiol. Int.* 6, 21–28. doi: 10.3109/07420528909059139

Leao, R. N., Leao, F. N., and Walmsley, B. (2005). Non-random nature of spontaneous mIPSCs in mouse auditory brainstem neurons revealed by recurrence quantification analysis. *Proc. Biol. Sci.* 272, 2551–2559. doi: 10.1098/rspb.2005.3258

Linkenkaer-Hansen, K., Monto, S., Rytsälä, H., Suominen, K., Isometsä, E., and Kähkönen, S. (2005). Breakdown of long-range temporal correlations in theta oscillations in patients with major depressive disorder. *J. Neurosci.* 25, 10131–10137. doi: 10.1523/JNEUROSCI.3244-05.2005

Linkenkaer-Hansen, K., Nikouline, V. V., Palva, J. M., and Ilmoniemi, R. J. (2001). Long-range temporal correlations and scaling behavior in human brain oscillations. *J. Neurosci.* 21, 1370–1377. doi: 10.1523/JNEUROSCI.21-04-01370.2001

Ma, Q. L., Ning, X. B., Wang, J., and Bian, C. H. (2006). A new measure to characterize multifractality of sleep electroencephalogram. *Chin Sci Bull* 51, 3059–3064. doi: 10.1007/s11434-006-2213-y

Mandelbrot, B. B. (1983). *The Fractal Geometry of Nature 1997*. New York, NY: Henry Holt and Co.

Mandelbrot, B. B. (1985). Self-affine fractals and fractal dimension. *Phys. Scr.* 32:257. doi: 10.1088/0031-8949/32/4/001

Marzano, C., Ferrara, M., Curcio, G., and De Gennaro, L. (2010). The effects of sleep deprivation in humans: topographical electroencephalogram changes in non-rapid eye movement (NREM) sleep versus REM sleep. *J. Sleep Res.* 19, 260–268. doi: 10.1111/j.1365-2869.2009.00776.x

Marzano, C., Ferrara, M., Moroni, F., and De Gennaro, L. (2011). Electroencephalographic sleep inertia of the awakening brain. *Neuroscience* 176, 308–317. doi: 10.1016/j.neuroscience.2010.12.014

May, C. P., and Hasher, L. (1998). Synchrony effects in inhibitory control over thought and action. *J. Exp. Psychol. Hum. Percept. Perform*. 24, 363–379.

Meisel, C., Bailey, K., Achermann, P., and Plenz, D. (2017). Decline of long-range temporal correlations in the human brain during sustained wakefulness. *Sci Rep* 7:11825. doi: 10.1038/s41598-017-12140-w

Meyer, M., and Stiedl, O. (2003). Self-affine fractal variability of human heartbeat interval dynamics in health and disease. *Eur. J. Appl. Physiol.* 90, 305–316. doi: 10.1007/s00421-003-0915-2

Milstein, J., Mormann, F., Fried, I., and Koch, C. (2009). Neuronal shot noise and brownian 1/f2 behavior in the local field potential. *PLoS ONE* 4:e4338. doi: 10.1371/journal.pone.0004338

Montez, T., Poil, S. -S., Jones, B. F., Manshanden, I., Verbunt, J. P. A., Dijk, B. W., et al. (2009). Altered temporal correlations in parietal alpha and prefrontal theta oscillations in early-stage Alzheimer disease. *Proc. Natl. Acad. Sci. U.S.A.* 106, 1614–1619. doi: 10.1073/pnas.0811699106

Morris, C. J., Purvis, T. E., Hu, K., and Scheer, F. A. (2016). Circadian misalignment increases cardiovascular disease risk factors in humans. *Proc. Natl. Acad. Sci. U.S.A.* 113, E1402–E1411. doi: 10.1073/pnas.1516953113

Musiek, E. S., Xiong, D. D., and Holtzman, D. M. (2015). Sleep, circadian rhythms, and the pathogenesis of Alzheimer disease. *Exp. Mol. Med.* 47:e148. doi: 10.1038/emm.2014.121

Muto, V., Jaspar, M., Meyer, C., Kussé, C., Chellappa, S. L., Degueldre, C., et al. (2016). Local modulation of human brain responses by circadian rhythmicity and sleep debt. *Science* 353, 687–690. doi: 10.1126/science.aad2993

Nikulin, V. V., and Brismar, T. (2004). Long-range temporal correlations in alpha and beta oscillations: effect of arousal level and test-retest reliability. *Clin. Neurophysiol.* 115, 1896–1908. doi: 10.1016/j.clinph.2004.03.019

Nikulin, V. V., and Brismar, T. (2005). Long-range temporal correlations in electroencephalographic oscillations: Relation to topography, frequency band, age and gender. *Neuroscience* 130, 549–558. doi: 10.1016/j.neuroscience.2004.10.007

Palva, J. M., and Palva, S. (2011). Roles of multiscale brain activity fluctuations in shaping the variability and dynamics of psychophysical performance. *Prog. Brain Res.* 193, 335–350. doi: 10.1016/B978-0-444-53839-0.00022-3

Palva, J. M., Zhigalov, A., Hirvonen, J., Korhonen, O., Linkenkaer-Hansen, K., and Palva, S. (2013). Neuronal long-range temporal correlations and avalanche dynamics are correlated with behavioral scaling laws. *Proc. Natl. Acad. Sci. U.S.A.* 110, 3585–3590. doi: 10.1073/pnas.1216855110

Parish, L. M., Worrell, G. A., Cranstoun, S. D., Stead, S. M., Pennell, P., and Litt, B. (2004). Long-range temporal correlations in epileptogenic and non-epileptogenic human hippocampus. *Neuroscience* 125, 1069–1076. doi: 10.1016/j.neuroscience.2004.03.002

Pavithra, M., NiranjanaKrupa, B., Sasidharan, A., Kutty, B. M., and Lakkannavar, M. (2014). "Fractal dimension for drowsiness detection in brainwaves," in *Proceedings of 2014 International Conference on Contemporary Computing and Informatics, IC3I 2014* (Mysore), 757–761.

Peiris, M. R., Jones, R. D., Davidson, P. R., and Bones, P. J. (2006). Detecting behavioral microsleeps from EEG power spectra. *Conf. Proc. IEEE Eng. Med. Biol. Soc.* 1, 5723–5726. doi: 10.1109/IEMBS.2006.260411

Peng, C. K., Buldyrev, S. V., Havlin, S., Simons, M., Stanley, H. E., and Goldberger, A. L. (1994). Mosaic organization of DNA nucleotides. *Phys. Rev. E. Stat. Phys.* 49:1685.

Pittman-Polletta, B. R., Scheer, F. A. J. L., Butler, M. P., Shea, S. A., and Hu, K. (2013). The role of the circadian system in fractal neurophysiological control. *Biol. Rev. Camb. Philos. Soc.* 88, 873–894. doi: 10.1111/brv.12032

Roenneberg, T., Kuehnle, T., Juda, M., Kantermann, T., Allebrandt, K., Gordijn, M., et al. (2007). Epidemiology of the human circadian clock. *Sleep Med. Rev.* 11, 429–438. doi: 10.1016/j.smrv.2007.07.005

Rogers, N. L., Dorrian, J., and Dinges, D. F. (2003). Sleep, waking and neurobehavioural performance. *Front. Biosci.* 8, s1056–1067.

Sadeh, A., Sharkey, K. M., and Carskadon, M. A. (1994). Activity-based sleep-wake identification: an empirical test of methodological issues. *Sleep* 17, 201–207.

Sangiuliano Intra, F., Avramiea, A. E., Irrmischer, M., Poil, S. S., Mansvelder, H. D., and Linkenkaer-Hansen, K. (2018). Long-range temporal correlation in alpha oscillations stabilize perception of ambiguous visual stimuli. *Front. Hum. Neurosci.* 12:159. doi: 10.3389/fnhum.2018.00159

Scafetta, N., Marchi, D., and West, B. J. (2009). Understanding the complexity of human gait dynamics. *Chaos* 19:026108. doi: 10.1063/1.3143035

Smits, F. M., Porcaro, C., Cottone, C., Cancelli, A., Rossini, P. M., and Tecchio, F. (2016). Electroencephalographic Fractal Dimension in Healthy Ageing and Alzheimer's Disease. *PLoS ONE* 11:e0149587. doi: 10.1371/journal.pone.0149587

Stam, C. J. (2005). Nonlinear dynamical analysis of EEG and MEG: review of an emerging field. *Clin. Neurophysiol.* 116, 2266–2301. doi: 10.1016/j.clinph.2005.06.011

Strijkstra, A. M., Beersma, D. G. M., Drayer, B., Halbesma, N., and Daan, S. (2003). Subjective sleepiness correlates negatively with global alpha (8-12 Hz) and positively with central frontal theta (4-8 Hz) frequencies in the human resting awake electroencephalogram. *Neurosci. Lett.* 340, 17–20. doi: 10.1016/S0304-3940(03)00033-8

Swie, Y. W., Sakamoto, K., and Shimizu, Y. (2005). Chaotic analysis of electromyography signal at low back and lower limb muscles during forward bending posture. *Electromyogr. Clin. Neurophysiol.* 45, 329–342.

Turcotte, D. L. (1999). Self-organized criticality. *Report Prog. Phys.* 62, 1377–1429.

Van Dongen, H. P. A., Maislin, G., Mullington, J. M., and Dinges, D. F. (2003). The cumulative cost of additional wakefulness: dose-response effects on neurobehavioral functions and sleep physiology from chronic sleep restriction and total sleep deprivation. *Sleep* 26, 117–126.

Vignatelli, L., Plazzi, G., Barbato, A., Ferini-Strambi, L., Manni, R., Pompei, F., et al. (2003). Italian version of the Epworth sleepiness scale: external validity. *Neurol. Sci.* 23, 295–300. doi: 10.1007/s100720300004

Violani, C., Devoto, A., Lucidi, F., Lombardo, C., and Russo, P. M. (2004). Validity of a short insomnia questionnaire: the SDQ. *Brain Res. Bull.* 63, 415–421. doi: 10.1016/j.brainresbull.2003.06.002

Voss, R. F. (1988). "Fractals in nature: from characterization to simulation," in *The Science of Fractal Images* (New York, NY: Springer-Verlag), 21–70.

Weiss, B., Clemens, Z., Bódizs, R., and Halász, P. (2011). Comparison of fractal and power spectral EEG features: effects of topography and sleep stages. *Brain Res. Bull* 84, 359–375. doi: 10.1016/j.brainresbull.2010.12.005

Weiss, B., Clemens, Z., Bódizs, R., Vágó Z., and Halász, P. (2009). Spatio-temporal analysis of monofractal and multifractal properties of the human sleep EEG. *J. Neurosci. Meth.* 185, 116–124. doi: 10.1016/j.jneumeth.2009.07.027

Wright, K. P., Lowry, C. A., and LeBourgeois, M. K. (2012). Circadian and wakefulness-sleep modulation of cognition in humans. *Front. Mol. Neurosci.* 5:50. doi: 10.3389/fnmol.2012.00050

Zappasodi, F., Marzetti, L., Olejarczyk, E., Tecchio, F., and Pizzella, V. (2015). Age-related changes in electroencephalographic signal complexity. *PLoS ONE* 10:e0141995. doi: 10.1371/journal.pone.0141995

Zappasodi, F., Olejarczyk, E., Marzetti, L., Assenza, G., Pizzella, V., and Tecchio, F. (2014). Fractal dimension of EEG activity senses neuronal impairment in acute stroke. *PLoS ONE* 9:e100199. doi: 10.1371/journal.pone.0100199

Zorick, T., and Mandelkern, M. A. (2013). Multifractal detrended fluctuation analysis of human EEG: preliminary investigation and comparison with the wavelet transform modulus maxima technique. *PLoS ONE* 8:e68360. doi: 10.1371/journal.pone.0068360

Zueva, M. V. (2015). Fractality of sensations and the brain health: the theory linking neurodegenerative disorder with distortion of spatial and temporal scale-invariance and fractal complexity of the visible world. *Front. Aging Neurosci.* 7:135. doi: 10.3389/fnagi.2015.00135

Conflict of Interest Statement: The authors declare that the research was conducted in the absence of any commercial or financial relationships that could be construed as a potential conflict of interest.

Copyright © 2018 Croce, Quercia, Costa and Zappasodi. This is an open-access article distributed under the terms of the Creative Commons Attribution License (CC BY). The use, distribution or reproduction in other forums is permitted, provided the original author(s) and the copyright owner(s) are credited and that the original publication in this journal is cited, in accordance with accepted academic practice. No use, distribution or reproduction is permitted which does not comply with these terms.

ORIGINAL RESEARCH
published: 27 September 2018
doi: 10.3389/fphys.2018.01350

Surrogate Data Method Requires End-Matched Segmentation of Electroencephalographic Signals to Estimate Non-linearity

Laura Päeske[1], Maie Bachmann[1], Toomas Põld[1,2], Sara Pereira Mendes de Oliveira[3], Jaanus Lass[1], Jaan Raik[4] and Hiie Hinrikus[1]*

[1] *Centre of Biomedical Engineering, Department of Health Technologies, Tallinn University of Technology, Tallinn, Estonia,* [2] *Qvalitas Medical Centre, Tallinn, Estonia,* [3] *Department of Electrical and Computer Engineering, Faculty of Engineering, University of Porto, Porto, Portugal,* [4] *Department of Computer Systems, Tallinn University of Technology, Tallinn, Estonia*

The aim of the study is to clarify the impact of the strong cyclic signal component on the results of surrogate data method in the case of resting electroencephalographic (EEG) signals. In addition, the impact of segment length is analyzed. Different non-linear measures (fractality, complexity, etc.) of neural signals have been demonstrated to be useful to infer the non-linearity of brain functioning from EEG. The surrogate data method is often applied to test whether or not the non-linear structure can be captured from the data. In addition, a growing number of studies are using surrogate data method to determine the statistical threshold of connectivity values in network analysis. Current study focuses on the conventional segmentation of EEG signals, which could lead to false results of surrogate data method. More specifically, the necessity to use end-matched segments that contain an integer number of dominant frequency periods is studied. EEG recordings from 80 healthy volunteers during eyes-closed resting state were analyzed using multivariate surrogate data method. The artificial surrogate data were generated by shuffling the phase spectra of original signals. The null hypothesis that time series were generated by a linear process was rejected by statistically comparing the non-linear statistics calculated for original and surrogate data sets. Five discriminating statistics were used as non-linear estimators: Higuchi fractal dimension (HFD), Katz fractal dimension (KFD), Lempel-Ziv complexity (LZC), sample entropy (SampEn) and synchronization likelihood (SL). The results indicate that the number of segments evaluated as non-linear differs in the case of various non-linear measures and changes with the segment length. The main conclusion is that the dependence on the deviation of the segment length from full periods of dominant EEG frequency has non-monotonic character and causes misleading results in the evaluation of non-linearity. Therefore, in the case of the signals with non-monotonic spectrum and strong dominant frequency, the correct use of surrogate data method requires the signal length comprising of full periods of the spectrum dominant frequency. The study is important to understand the influence of incorrect selection of EEG signal segment length for surrogate data method to estimate non-linearity.

Keywords: EEG, dominant frequency, alpha frequency, surrogate data, Fourier transform, segment length

OPEN ACCESS

Edited by:
Sladjana Z. Spasić,
University of Belgrade, Serbia

Reviewed by:
Gonzalo Marcelo Ramírez-Avila,
Universidad Mayor de San Andrés,
Bolivia
Chunhua Bian,
Nanjing University, China

***Correspondence:**
Laura Päeske
laura.paeske@ttu.ee

Specialty section:
This article was submitted to
Fractal Physiology,
a section of the journal
Frontiers in Physiology

Received: *31 May 2018*
Accepted: *06 September 2018*
Published: *27 September 2018*

Citation:
Päeske L, Bachmann M, Põld T, de Oliveira SPM, Lass J, Raik J and Hinrikus H (2018) Surrogate Data Method Requires End-Matched Segmentation of Electroencephalographic Signals to Estimate Non-linearity. Front. Physiol. 9:1350. doi: 10.3389/fphys.2018.01350

INTRODUCTION

Non-linear dynamics is the most appropriate way to describe complex physiological systems and is therefore widely used in biomedical applications. During last decades, the interest in the theory of non-linear dynamics has increased due to raising interest in brain functioning and the necessity to understand complex dynamics of the underlying processes (Hornero et al., 2009; Rodríguez-Bermudez and Garcíıa Laencin, 2015).

The brain is assumed to function as a self-organizing complex network of interacting dynamical non-linear subsystems. Despite some cellular processes may be random and characterized by probability functions, the neural systems may exhibit rather chaotic non-linear nature. Large networks of interconnected neurons behave as self-organized large systems with local non-linear interactions (Hornero et al., 2009). The question, whether EEG signals should be looked at as a non-linear deterministic process or a linear stochastic one, is still open. Therefore, before analyzing EEG signals by non-linear methods, it is required to assess whether the non-linearity exists in the data. In case non-linearity is present, the non-linear dynamics theory could also characterize the intrinsic nature of EEG, helping to understand its dynamics, underlying brain processes and search for its physiological significance, without losing or ignoring important information (Natarajan et al., 2004). The presence of non-linearity can be confirmed by hypothesis testing.

Theiler et al. (1992) described a statistical approach for identifying non-linearity in a time series, through the surrogate data method. A surrogate data is generated from the original data by shuffling the phase spectra. Null hypothesis that data were generated by a linear process is tested by comparing non-linear statistic calculated for original and surrogate data. If the value for original data is significantly different, the null hypothesis can be rejected and non-linearity concluded. The probability that the surrogate data test will reject null hypothesis depends on the non-linear statistic used (Spasic, 2010).

Surrogate data method is widely used on EEG signals for testing the null hypothesis of linearity. There are two main purposes for surrogate data testing. The first purpose is to test whether the chosen non-linear measure captures non-linear structure in the data, which cannot be detected with spectral density function (Breakspear and Terry, 2002; Natarajan et al., 2004; Spasic, 2010; Bae et al., 2017; Orgo et al., 2017). If the data does not have any non-linear structure, a linear method could be used instead. The second purpose is to determine the statistical threshold of connectivity values in network analysis (Dimitriadis et al., 2015, 2017; Olejarczyk et al., 2017), which is being used by a growing number of studies with the method of surrogate data. However, some factors can cause misleading results for EEG signal linearity estimation. Surrogate data testing for a linear stochastic system can indicate false non-linearity in case the process is non-stationary (Timmer, 1998). A specific problem has been identified that false detection of non-linearity may occur in case the data are strongly cyclic (Stam et al., 1998; Small and Tse, 2002). The problem arises when the length of the analyzed signal segment deviates from the multiple full periods of the cyclic component in the signal.

Electroencephalographic (EEG) signal has a strong alpha frequency component in the frequency range between 9 and 11 Hz. This rhythm is most pronounced in occipital region, but is also present in central, temporal or even frontal regions. Alpha rhythm is best revealed during eyes-closed resting state. Therefore, it might be expected that due to the strong cyclic alpha component of the resting eyes-closed signal, the surrogate data method may give false results.

The aim of the study is to clarify the impact of the strong cyclic signal component on the results of surrogate data method in the case of EEG signals. In addition, the impact of segment length is analyzed. For this reason, the degree of non-linearity was found in eyes-closed resting EEG signal depending on the analyzed segment length and deviation from full period of the dominant cyclic component. Five discriminating statistics were used as non-linear estimators: Higuchi fractal dimension (HFD), Katz fractal dimension (KFD), Lempel-Ziv complexity (LZC), sample entropy (SampEn), and synchronization likelihood (SL).

MATERIALS AND METHODS

Subjects

Eighty healthy volunteers (38 female and 42 male) aged 37.0 ± 14.5 years participated in the study. The experiments were approved by the Tallinn Medical Research Ethics Committee and were conducted in accordance with the Declaration of Helsinki. All subjects signed an informed consent.

EEG Recordings

The EEG was recorded using Neuroscan Synamps2 acquisition system (Compumedics, Charlotte, NC, United States) from 30 electrodes, positioned according to the extended international 10–20 system. The sampling frequency was 1,000 Hz. Linked mastoids were used as a reference and electrode impedances were kept below 10 kΩ. EEG was recorded for 6 min, during which subjects were lying in a relaxed position with their eyes closed.

Surrogate Data

Multivariate surrogate data method is used to test whether data were generated by a non-linear process (Theiler et al., 1992; Prichard and Theiler, 1994). The null-hypotheses that data were generated by a linear process and therefore data can be fully explained by a linear model, is set. Surrogate data is generated from original data. If the non-linear statistic calculated for original data significantly differs from the non-linear statistic calculated for surrogate data, null-hypothesis is rejected and non-linearity is detected.

Surrogate data is calculated from time series according to the algorithm by Prichard and Theiler (1994). Fourier transform is applied and the phase of each frequency component is independently rotated by a random degree between $(0, 2\pi)$. After that, inverse Fourier transform is performed. As a result, the power spectrum and the autocorrelation function of the time series is preserved. For multivariate time series, a fixed random sequence is used to alter the phase of each frequency, ensuring linear correlations between simultaneously recorded time series.

To determine whether the value of the non-linear statistic for the original data set significantly differs from the non-linear statistics for the surrogate data, z-test is used (Breakspear and Terry, 2002):

$$Z = \frac{Q_{data} - mean\left(Q_{surrogate}\right)}{std\left(Q_{surrogate}\right)} \tag{1}$$

where Q_{data} is the non-linear statistic calculated for the original data set, $mean\ (Q_{surrogate})$ is the mean and $std\ (Q_{surrogate})$ is the standard deviation of linear statistics calculated for the surrogate data. In the current study, surrogate data was calculated 20 times for each data segment and the significance level of $p < 0.05$ was used. Under the null hypothesis, z-statistic is normally distributed and when $|Z| > 1.96$ for a two-tailed test, the null hypothesis can be rejected. For data analysis, we calculated the degree of non-linearity (DEG), which we define as the percentage of segments where the null hypothesis was rejected and non-linearity was detected:

$$DEG = \frac{n_{sign}}{n} \cdot 100\% \tag{2}$$

where n is the number of segments and n_{sign} is the number of segments, where $|Z| > 1.96$.

Non-linear Statistics

The measures for estimation of non-linearity were selected based on two main criteria. Firstly, whereas different estimators detect various aspects of non-linearity, the applied measures should describe one of the specific features of the signals: self-similarity, dimension-based morphology, complexity, irregularity or functional connectivity. Secondly, less time-consuming methods currently widely used in EEG analysis should be represented. As a result, five non-linear methods were selected: HFD, KFD, LZC, SampEn, and SL. HFD and KFD are fractal dimension methods, LZC is a measure of complexity and SampEn is a measure of irregularity. As connectivity between neurons and synchronization of their spiking play crucial role in the brain functioning, functional connectivity measure SL, although computationally time consuming, was also selected.

The HFD evaluates the complexity and self-similarity of time series (Higuchi, 1988). It is calculated directly in the time domain, making it a simple and fast method. The HFD with a parameter $k_{max} = 8$ was calculated according to the algorithm presented by Higuchi (1988).

The KFD obtains fractal dimension based on morphology, measuring the roughness of the time series (Katz, 1988). The KFD is the ratio of the length of the curve (sum of distances between two successive points), divided by the maximum distance of any point under consideration from the first point. In other words, the ratio of the total length to the straight line corresponding to the maximum distance from the first point. In addition, a scaling factor, an average of the distances between two successive points is used.

Higuchi's and Katz fractal dimensions are the most common methods of estimating the fractal dimension of EEG signals directly in the time domain. Despite both, HFD and KFD describe the fractal dimension of EEG waveform, the behavior of the measures is different. HFD has been suggested being the most accurate, whereas KFD yields the most consistent results regarding discrimination between brain functional states (Esteller et al., 2001). Therefore, both are applied in this study.

The LZC evaluates the randomness of finite sequences (Lempel and Ziv, 1976). First, the EEG signal is transformed into a finite symbol sequence, according to a chosen threshold. Next, the sequence of symbols is analyzed from left to right. The LZC counts the number of times a new pattern is encountered and its recurrence rate for the given sequence. LZC is simple to calculate and does not need long data segments. Larger LZC values correspond to signals that are more complex. Still, the LZC strongly depends on the signal bandwidth (Kalev et al., 2015). In the current study, median value of the sequence was selected as threshold, as it is capable of coping with outliers. Next, the data was binarized (two symbols) according to the threshold. Due to artifact free sequences, selecting between median or mean is not expected to change the outcome considerably.

The SampEn measures the signal irregularity (Richman and Moorman, 2000). Signals that are more irregular give larger SampEn values. The method is quite independent of the signal length. It is suitable for analyzing short and noisy time series. The SampEn is the negative natural logarithm of the conditional probability that two sequences similar for $m = 2$ points remain similar at the next point. Parameters for the SampEn were chosen according to recommendations from previous studies (Richman and Moorman, 2000; Lake and Moorman, 2010): the embedding dimension $m = 2$ and the tolerance $r = 0.2\ SD$, where SD is the standard deviation of the sample.

The SL is a non-linear measure of functional connectivity (Stam and Van Dijk, 2002). The SL estimates dynamical interdependencies between simultaneously recorded time series using Takens' theorem (Takens, 1981) of reconstructing EEG signals into state space. The calculation of the SL is more thoroughly explained in the article by Stam and Van Dijk (2002). The SL parameters were calculated according to the formulas presented in the paper by Montez et al. (2006) with respect to the time-frequency content of the signal. Therefore, the following parameters were used: the embedding lag $L = 7$, the embedding dimension $m = 136$, the number of recurrences $n_{rec} = 10$, the fraction of recurrences $p_{ref} = 0.01$, window $W_1 = 2000$ and window $W_2 = 2999$. Such selection of the parameters ensures that the time-frequency characteristics of the signals are fully taken into account. Therefore, small alterations in these parameters are not expected to change the results of surrogate data method significantly.

Data Processing

Data processing was done in MATLAB (The Math-works, Inc.) using signal processing toolbox. Signals were digitally filtered (1–45 Hz) using zero-phase Butterworth filter and re-referenced according to the reference electrode standardization technique (REST) (Yao, 2001). Signals were divided into 5.3-s segments. Data were visually inspected and segments with artifacts were not analyzed.

Surrogate data method makes an assumption of stationarity. We conducted two stationarity tests: the Kwiatkowski–Phillips–Schmidt–Shin (KPSS) and the Phillips–Perron (PP) test and no non-stationarity was detected.

Dependence on the Segment Length Increment for Alpha Component

The aim of the current section was to determine how DEG depends on the segment length increment. For that purpose, the length of the segment was gradually incremented from an integer number of alpha periods by 2 ms. Therefore, the length of each segment was determined as:

$$l = kT + \Delta t, \Delta t = 0, 2, 4, \ldots, 108\, ms, \quad (3)$$

where k is an integer, T is the period of alpha frequency component and Δt is the segment length increment. The first segment was approximately 5 s, starting and ending at the alpha peak amplitude ($\Delta t = 0$) – consisting of an integer number of alpha periods. Therefore, the exact length of the first segment depended on the alpha period. The second segment started at the same position as the first one, but ended 2 ms later ($\Delta t = 2$). Finally, the length of the last segment ($\Delta t = 108$) was approximately 5.1 s. For most subjects, the length of the last segment corresponds to $l = (k + 1)T$ – again an integer number of alpha periods. As there were 62 data segments for a subject, we repeated the incrementation procedure for each of the 62 data segments and DEG was calculated according to formula (2) for each $\Delta t = 0, 2, 4, \ldots, 108$ ms, where $n = 62$.

Alpha peaks were found by zero-phase filtering signals into alpha frequency band (7.5–13 Hz) using Butterworth filter and peaks were indicated by local maxima. The channel O1 was chosen for processing, because of the highest average alpha power. After finding positions of alpha peaks in channel O1, whole frequency band (1–45 Hz) was used for calculating DEG. The dependence on Δt was found for five different non-linear parameters: HFD, KFD, LZC, SampEn and SL. As SL is calculated between two channels, O1 and O2 were used.

Dependence on Channel

In different channels, the amount of alpha power, the strong cyclic component, differs. This component is most pronounced in occipital region, but is also present in other regions. To analyze the dependence on the EEG channel, three channels were chosen according to average mean alpha power: O1 with the highest alpha power, C3 with average alpha power and T7 with the lowest alpha power. In addition to O1, analysis for C3 and T7 were conducted in accordance to 2.5.1, whereas HFD was used as a non-linear measure.

Dependence on the Segment Length Increment for Different Frequency Components

It is well known that alpha is the dominant frequency during eyes-closed resting state EEG recordings, especially in posterior areas. However, it is important to clarify, whether the surrogate data method is also affected by the cyclic component of other EEG frequency bands. For that purpose, the analysis in 2.5.1 was repeated using HFD, but the segments beginning and the segment length increment have been matched to the following frequencies: delta (1–1.5 Hz; $\Delta t = 0, 20, \ldots, 1000$), theta (4–8 Hz; $\Delta t = 0, 3, \ldots, 126$) and beta (13–30 Hz; $\Delta t = 0, 1, \ldots, 46$). For better comparison, the results for alpha component (7.5–13 Hz; $\Delta t = 0, 2, \ldots, 108$) are also presented.

Dependence on Segment Length

While incrementing the segment by Δt, the overall segment length was almost the same, between 5 and 5.1 s. To analyze the dependence on the segment length, the data were divided into substantially different segment lengths: around 5, 10, 15, and 20 s. Each segment started from alpha peak and ended with alpha peak, consisting of an integer number of alpha periods. Each subject had 10 segments of each segment length, whereas $n = 10$ in formula (2). DEG was calculated for each subject and segment.

Data Processing

The observations of DEG were obtained for each subject. The dependence on the Δt and the segment length were statistically evaluated using one-way analysis of variance (ANOVA) with the significance level of $p < 0.05$. To correct for the problem of multiple comparisons, Bonferroni correction was used by adjusting the p-value $p = p/m$, where m is the number of comparisons.

RESULTS

Average DEG values for end-matched segments according to alpha frequency ($\Delta t = 0$) are presented in **Table 1**. The percentage of segments where non-linearity was detected varies significantly depending on the non-linear measure. KFD indicated the highest degree of non-linearity: the KFD value was significantly changed in 99% of segments, while LZC revealed non-linearity only in 0.4% of the segments.

Dependence on the Segment Length Increment for Alpha Component

The calculated DEG values for HFD, KFD, LZC, SampEn and SL in alpha frequency band are presented in **Supplementary Datasets 1–5**. We conducted ANOVA to analyze whether the segment length increment Δt influences the results of surrogate data method. ANOVA ($p < 0.05/5$) yielded statistically significant results for every non-linear statistic that indicated non-linearity ($DEG > 5\%$): HFD DEG (**Figure 1B**), KFD DEG (**Figure 1D**) and SampEn DEG (**Figure 1H**). For example, when $\Delta t = 0$, then HFD DEG was 46.1%, but $\Delta t = 50$ (corresponding to half alpha period)

TABLE 1 | The degree of non-linearity at alpha peak.

	DEG, %
HFD	46.1
KFD	99.1
LZC	0.4
SampEn	81.5
SL	3.9

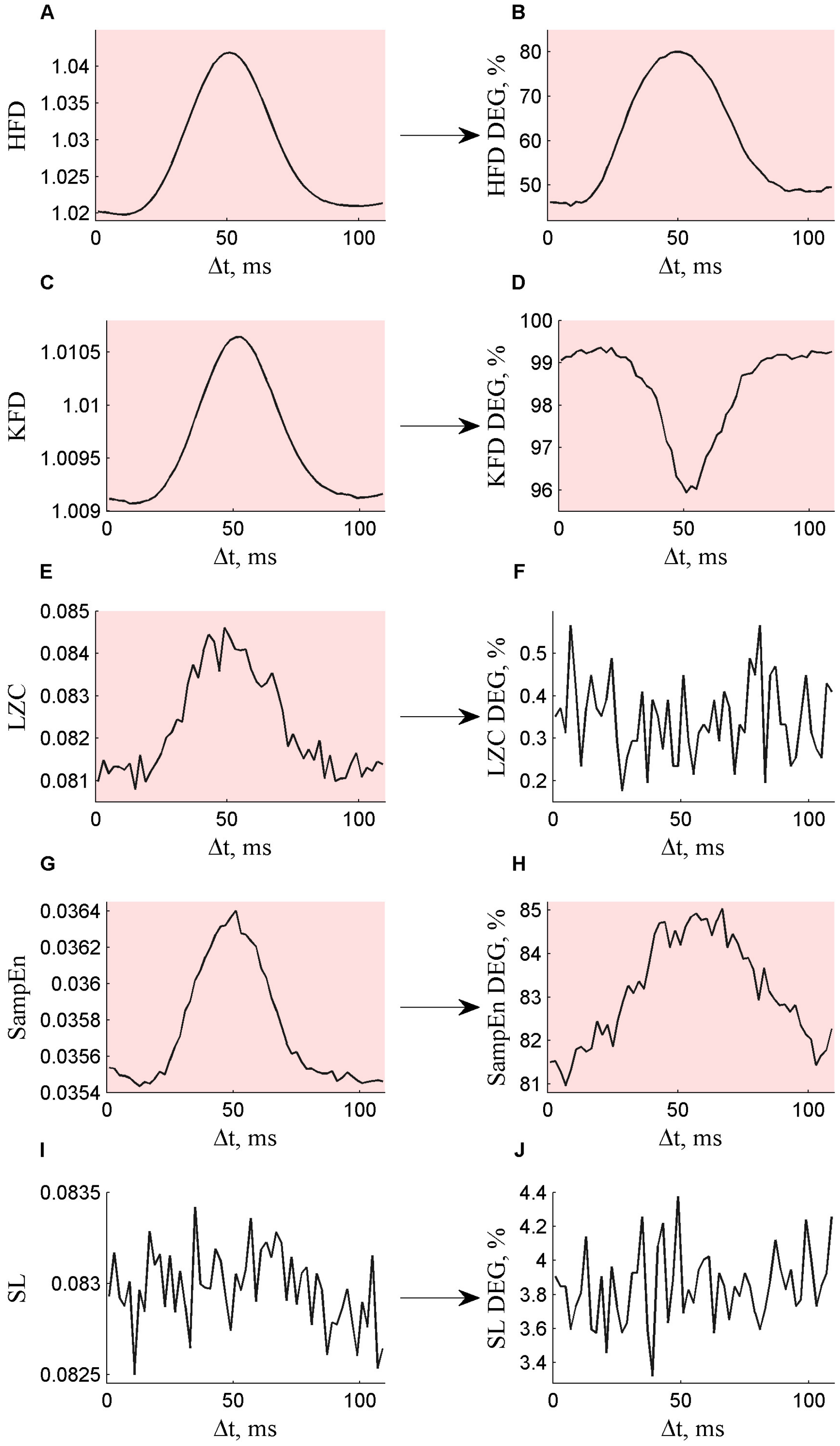

FIGURE 1 | Non-linear measures **(A)** HFD, **(C)** KFD, **(E)** LZC, **(G)** SampEn, and **(I)** SL calculated for surrogate data depending on the segment length increment Δt are presented on the left. The degree of non-linearity DEG depending on the segment length increment Δt for **(B)** HFD DEG, **(D)** KFD DEG, **(F)** LZC DEG, **(H)** SampEn DEG, and **(J)** SL DEG are presented on the right. Statistically significant results are indicated with a pink background.

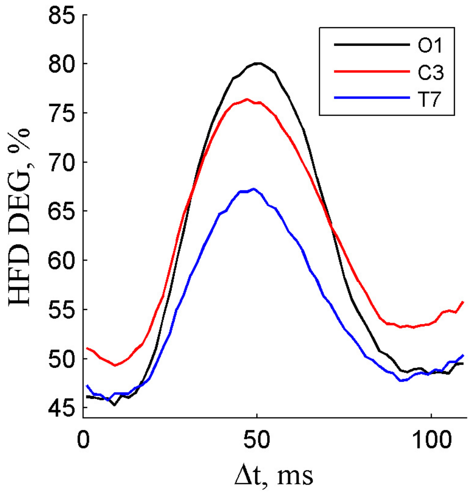

FIGURE 2 | The degree of non-linearity DEG depending on the segment length increment Δt for alpha component in channels O1, C3, and T7.

resulted in HFD DEG 80.0%. LZC DEG (**Figure 1F**) and SL DEG (**Figure 1J**) did not depend on the Δt.

In order to understand the DEG results presented in **Figure 1**, we can consider the values of non-linear measures calculated for original and surrogate data, according to which DEG was calculated. Incrementing the segment length to $\Delta t = 50$ increased the values calculated for surrogate data for all five non-linear measures, but the increase was statistically significant only for HFD (**Figure 1A**), KFD (**Figure 1C**), LZC (**Figure 1E**), and SampEn (**Figure 1G**). Since HFD and SampEn calculated for surrogate data were significantly increased compared to the values calculated for original data, this resulted in an increase also in DEG (**Figures 1B,H**). However, KDF for surrogate data was significantly decreased compared to KFD for original data, resulting in a decrease in DEG (**Figure 1D**). Although LZC calculated for surrogate data was also influenced by segment length increment (**Figure 1E**), LZC was similar for original and surrogate data, yielding low DEG values, resilient to segment length increment (**Figure 1F**).

Dependence on Channel

The calculated HFD DEG values for channels O1, C3 and T7 are presented in **Supplementary Datasets 1, 6, 7**. According to ANOVA ($p < 0.05/3$), HFD depended on the Δt for all studied channels. The deflection in DEG was the largest in channel O1, followed by C3 and T7 (**Figure 2**). These results are in accordance with the amount of spectral alpha power in those channels.

Dependence on the Segment Length Increment for Different Frequency Components

The calculated HFD DEG values for delta, theta, alpha and beta frequency components are presented in **Supplementary Datasets 1, 8–10**. According to ANOVA ($p < 0.05/4$), HFD depended on every calculated cyclic component (**Figure 3**). The difference between maximum and minimum DEG for different Δt was the largest for alpha component (80.0% – 45.3% = 34.7%), followed by theta (63.9% — 51.4% = 12.5%), delta (61.1%—51.1% = 10.0%), and beta component (60.6% — 51.6% = 9.1%).

Dependence on Segment Length

The influence of segment length ($\Delta t = 0$) on DEG was investigated for five non-linear measures: HFD, KFD, LZC, SampEn, and SL (**Supplementary Dataset 11**). The results are presented in **Table 2**. According to ANOVA ($p < 0.05/20$), DEG depended on the segment length for HFD, SampEn, and SL (marked with * in **Table 2**). The results for 5-s segments are slightly different from the results in **Table 1**, because smaller number of segments were used.

DISCUSSION

The aim of the study was to clarify the impact of the strong cyclic EEG signal component on the results of surrogate data method

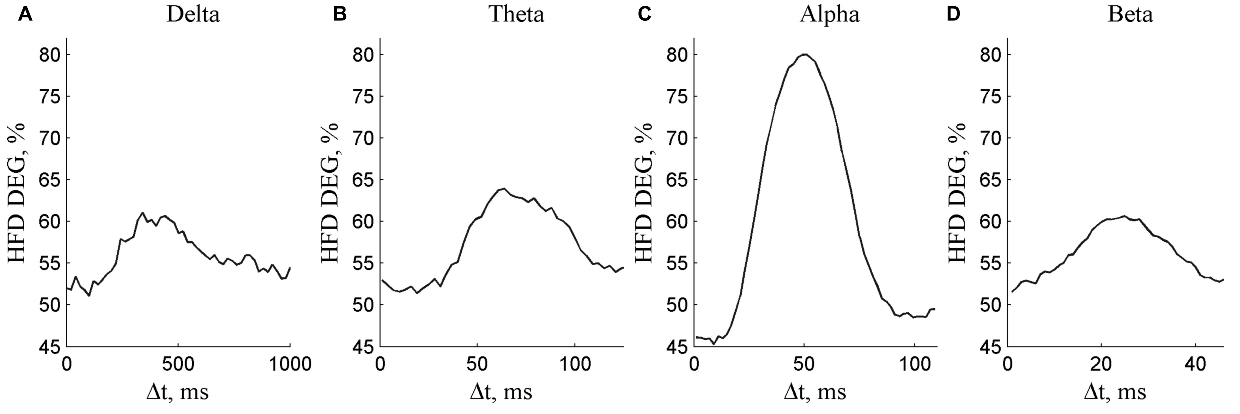

FIGURE 3 | The degree of non-linearity DEG depending on the segment length increment Δt for **(A)** delta, **(B)** theta, **(C)** alpha, and **(D)** beta frequency components.

TABLE 2 | The degree of non-linearity at different segment lengths (*$p < 0.05$).

	DEG, %			
Segment length	**5 s**	**10 s**	**15 s**	**20 s**
HFD	45.7*	41.0*	36.4*	34.0*
KFD	99.9	100	100	100
LZC	0.4	0.6	0.2	0.4
SampEn	82.0*	95.4*	98.5*	99.4*
SL	4.4*	6.5*	7.0*	9.1*

by Theiler et al. (1992). In addition, the impact of segment length was analyzed. The major finding of the study was that if the EEG segment does not contain an integer number of full alpha periods, the values calculated for surrogate data may be significantly altered, resulting in a false rejection of linearity. To the best of our knowledge, similar results have not been reported earlier.

Previous studies have shown that false detection of non-linearity may occur when the data are strongly cyclic (Stam et al., 1998; Small and Tse, 2002). However, the influence of this problem on EEG signals was not previously known. Although surrogate data method is widely used for EEG analysis (Breakspear and Terry, 2002; Natarajan et al., 2004; Spasic, 2010; Dimitriadis et al., 2015, 2017; Bae et al., 2017; Olejarczyk et al., 2017), the cyclic behavior of dominant frequency component is not considered in segmentation. The current study shows the importance of segmenting data according to the alpha component for eyes-closed resting state EEG.

Our results demonstrate remarkable non-monotonic changes in the degree of non-linearity of EEG signals with the fine tuning of the segment length within a period of dominant EEG signal frequency for every non-linear statistic that indicated non-linearity (DEG > 5%): HFD (**Figure 1B**), KFD (**Figure 1D**), and SampEn (**Figure 1H**). The changes in the degree of non-linearity are caused by the changes in the non-linear measures calculated for surrogate data (**Figures 1A,C,G**), whereas the measures calculated for original data have no remarkable dependence on so small alteration of segment length. The impact of segment length tuning on the results of surrogate data method is maximal when the segment length contains an odd number of half-periods of the dominant frequency (**Figure 1**). The phenomenon can be explained by spectral leakage in the discrete Fourier transform while deriving the surrogates, as discrete Fourier transform assumes periodic signals. Thornhill (2005) showed that even a small spectral component other than that at the dominant frequency could be interpreted as non-linearity and causes false detection of non-linearity for sine waves. However, they showed that pseudoperiodic data with weaker cyclic behavior were more robust to small end-mismatches. These results are in accordance with the results in the current study. Moreover, the current study proves that the cyclic behavior of EEG has a strong influence on non-linear measures calculated for surrogate data for large end-mismatch.

Two measures, LZC (**Figure 1F**) and SL (**Figure 1J**), did not detect significant non-linearity (DEG < 5%). In the case of LZC, the possible reason is that the measure is highly sensitive to low frequency EEG component in binarization due to its high amplitude values. The non-linearity, if contained in the low amplitude high frequency activity, gets overlooked in the process of binarization and is not detected by the measure. SL did not detect non-linear coupling, indicating that SL does not necessarily give significantly more information compared to similar linear functional connectivity measures.

The level of alterations caused by fine tuning within a period of dominant frequency differs at different non-linear discrimination measures. The degree of linearity changes about two-fold with HFD, is much lower with KDF and SampEn and becomes insignificant with LZC and SL. The different impact of fine tuning of segment length within a period of dominant frequency can be explained by different sensitivity of various non-linear measures to a small additional spectral component introduced by the deviation of the segment length from a full period. The problem can be solved by selecting the start and end of the segment by matching the period of the strong cyclic component. A segment end-matching can be performed by selecting a segment length equal to integer number of full periods of the dominant frequency (Stam et al., 1998). In addition, Small et al. (2001) suggested an alternative surrogate data method: pseudo-periodic surrogate (PPS) algorithm. However, PPS is not applicable to data where the non-linearity of interest is distortion of the periodic waveform (Thornhill, 2005).

The dependence of the degree of non-linearity on the segment length increment from full alpha periods has the maximal value for alpha frequency component (**Figure 3**). The alteration of the degree of non-linearity with the dominant frequencies in delta, theta or beta bands are less critical. The possible reason is the structure of EEG signal with a dominant alpha frequency. The minimum DEG value in **Figure 3** is the smallest for alpha frequency component. These results show that the synchronization of the fine tuning of the segment length should be performed with the dominant frequency component to decrease the amount of false positive surrogate data results.

The dependence of the degree of non-linearity on the segment length increment from full period of dominant EEG frequency is evident in various EEG channels (**Figure 2**). As expected, the impact is stronger in the EEG channels with higher alpha content (O) and weaker in channels with lower alpha content (T). The influence of segment end-mismatch on other channels also mostly depends on the spectral alpha power and lies between the obtained results of O1 and T7 (**Figure 2**). The results may also be influenced by an additional strong frequency component (channel C3 in **Figure 2**), but the dominant frequency component should be taken into account in segment end-matching.

The degree of linearity estimated at an integer number of alpha periods (**Tables 1**, **2**) shows that the degree of non-linearity varies for different non-linear measures. Different sensitivity to surrogate data method has also been reported by other author (Spasic, 2010) when comparing HFD and third order correlation. Our results suggest that HFD, KFD, and SampEn were more sensitive to non-linearity, while SL and LZC values changed significantly in less than 5% of segments for 5-s segments. In this case, SL has been calculated between O1 and O2 channels.

The results can vary for different channel pairs, but Orgo et al. (2017) found that for SL 5-s segments, the average degree of non-linearity over all channel pairs was similar to that in our current study (6.1% compared to our 4.4%). In addition, the degree of non-linearity estimated in the current study is close to the results reported by Breakspear and Terry (2002), who detected statistically significant evidence of non-linear interactions in 4.8% of the 2.048-s segments of eyes-closed resting state EEG.

The findings presented in **Table 2**, indicating changed non-linearity with increased segment length, are in principle in accordance with the results reported by other research groups (Olbrich et al., 2003; Sun et al., 2012; Orgo et al., 2017). Olbrich et al. (2003) have reported the dependence of rejection of the null hypothesis between natural and surrogate data in sleep EEG on the length of the analyzed segment. They suggested that the increase of evaluated non-linearity with the segment length might occur because of the increasing non-stationarity of the longer time series. In the current study, KPSS and PP test did not reveal any non-stationarity. Sun et al. (2012) have made a conclusion that the length of signal segment for analysis of 3–16 periods is sufficient for detecting non-linearity in the case of EEG phase synchronization. However, in the current study we showed that the results of evaluation of non-linearity vary even with the segment lengths of more than 100 periods. Orgo et al. (2017) were the first to compare the degree of EEG non-linear coupling in different frequency bands and segment lengths, during eyes-closed resting state. Their results showed that the degree of non-linear coupling increased with the length of the segment, and it was most dominant in total, alpha, beta and theta frequency bands.

CONCLUSION

The results of the performed study show that the selection of a proper segment length in evaluating non-linearity of EEG signals with surrogate data method is critical to assure the reliability of evaluation. The results of performed calculations demonstrate that false rejection of linearity occurred with surrogate data method when an EEG segment did not contain an integer number of full alpha periods using HFD, KFD, or sample entropy. LZC and SL did not detect significant non-linearity and were therefore not influenced by segment end-mismatch. The major novel finding is that the correct estimation of non-linearity with surrogate data method requires a segment length comprising of full periods of the spectrum's dominant frequency component. In addition, the degree of non-linearity estimated with HFD, sample entropy and synchronization likelihood significantly changed with the segment length.

DATA AVAILABILITY STATEMENT

The datasets analyzed in this study can be found as a xlsx file in the supplement.

AUTHOR CONTRIBUTIONS

LP and MB designed the study and conducted EEG recordings. LP processed the data. LP, MB, and HH analyzed and interpreted the results and wrote the manuscript. TP, SdO, JL, and JR contributed to discussion of results and writing the manuscript. All authors revised and approved the final manuscript.

FUNDING

This study was partly financially supported by the Estonian Ministry of Education and Research under institutional research financing IUT 19-2, by the higher education scholarship in the growth areas of smart specialization and by the Estonian Centre of Excellence in IT (EXCITE) 2014-2020.4.01.15-0018 funded by the European Regional Development Fund.

SUPPLEMENTARY MATERIAL

The Supplementary Material for this article can be found online at: https://www.frontiersin.org/articles/10.3389/fphys.2018.01350/full#supplementary-material

REFERENCES

Bae, Y., Yoo, B. W., Lee, J. C., and Kim, H. C. (2017). Automated network analysis to measure brain effective connectivity estimated from EEG data of patients with alcoholism. *Physiol. Meas.* 38, 759–773. doi: 10.1088/1361-6579/aa6b4c

Breakspear, M., and Terry, J. R. (2002). Detection and description of non-linear interdependence in normal multichannel human EEG data. *Clin. Neurophysiol.* 113, 735–753. doi: 10.1016/S1388-2457(02)00051-2

Dimitriadis, S. I., Salis, C., Tarnanas, I., and Linden, D. E. (2017). Topological filtering of dynamic functional brain networks unfolds informative chronnectomics: a novel data-driven thresholding scheme based on orthogonal minimal spanning trees (OMSTs). *Front. Neuroinform.* 11:28. doi: 10.3389/fninf.2017.00028

Dimitriadis, S. I., Zouridakis, G., Rezaie, R., Babajani-Feremi, A., and Papanicolaou, A. C. (2015). Functional connectivity changes detected with magnetoencephalography after mild traumatic brain injury. *NeuroImage Clin.* 9, 519–531. doi: 10.1016/j.nicl.2015.09.011

Esteller, R., Vachtsevanos, G., Echauz, J., and Litt, B. A. (2001). Comparison of waveform fractal dimension algorithms. *IEEE Trans. Circuits Syst. Fund. Theory Appl.* 48, 177–183. doi: 10.1109/81.904882

Higuchi, T. (1988). Approach to an irregular time series on the basis of the fractal theory. *Phys. D* 31, 277–283. doi: 10.1016/0167-2789(88)90081-4

Hornero, R., Abásolo, D., Escudero, J., and Gómez, C. (2009). Nonlinear analysis of electroencephalogram and magnetoencephalogram recordings in patients with Alzheimer's disease. *Philos. Trans. Math. Phys. Eng. Sci.* 367, 317–336. doi: 10.1098/rsta.2008.0197

Kalev, K., Bachmann, M., Orgo, L., Lass, J., and Hinrikus, H. (2015). "Lempel-Ziv and multiscale lempel-ziv complexity in depression," in *Conference Proceedins of the IEEE Engineering Medicine Biology Society* (New York, NY: IEEE), 4158–4161. doi: 10.1109/EMBC.2015.7319310

Katz, M. J. (1988). Fractals and the analysis of waveforms. *Comput. Biol. Med.* 18, 145–156. doi: 10.1016/0010-4825(88)90041-8

Lake, D. E., and Moorman, R. (2010). Accurate estimation of entropy in very short physiological time series: the problem of atrial fibrillation detection in implanted ventricular devices. *Am. J. Physiol. Heart Circ. Physiol.* 300:1. doi: 10.1152/ajpheart.00561

Lempel, A., and Ziv, J. (1976). On the complexity of finite sequences. *IEEE Trans. Inf. Theory* 22, 75–81. doi: 10.1109/TIT.1976.1055501

Montez, T., Linkenkaer-Hansen, K., van Dijk, B. W., and Stam, C. J. (2006). Synchronization likelihood with explicit time-frequency priors. *Neuroimage* 33, 1117–1125. doi: 10.1016/j.neuroimage.2006.06.066

Natarajan, K., Acharya, U. R., Alias, F., Tiboleng, T., and Puthusserypady, S. K. (2004). Nonlinear analysis of EEG signals at different mental states. *BioMedical Eng. Online* 3:7. doi: 10.1186/1475-925X-3-7

Olbrich, E., Achermann, P., and Meier, P. F. (2003). Dynamics of human sleep EEG. *Neurocomputing* 5, 857–862. doi: 10.1016/S0925-2312(02)00816-0

Olejarczyk, E., Marzetti, L., Pizzella, V., and Zappasodi, F. (2017). Comparison of connectivity analyses for resting state EEG data. *J. Neural Eng.* 14, 3. doi: 10.1088/1741-2552/aa6401

Orgo, L., Bachmann, M., Kalev, K., Järvelaid, M., Raik, J., and Hinrikus, H. (2017). Dependence of the EEG nonlinear coupling on the frequency bands and the segment lengths. *IFMBE Proc.* 65, 799–802. doi: 10.1007/978-981-10-5122-7_200

Prichard, D., and Theiler, J. (1994). Generating surrogate data for time series with several simultaneously measured variables. *Phys. Rev. Lett.* 73, 951–954. doi: 10.1103/PhysRevLett.73.951

Richman, J. S., and Moorman, J. R. (2000). Physiological time-series analysis using approximate entropy and sample entropy. *Am. J. Physiol. Heart Circ. Physiol.* 278, H2039–H2049. doi: 10.1152/ajpheart.2000.278.6.H2039

Rodríguez-Bermudez, G., and Garcíıa Laencin, P. J. (2015). Analysis of EEG signals using nonlinear dynamics and chaos: a review. *Appl. Math. Inf. Sci.* 9, 1–13. doi: 10.12785/amis/090512

Small, M., and Tse, C. K. (2002). Applying the method of surrogate data to cyclic time series. *Phys. D* 164, 187–201. doi: 10.1016/S0167-2789(02)00382-2

Small, M., Yu, D., and Harrison, R. G. (2001). Surrogate test for pseudoperiodic time series data. *Phys. Rev. Lett.* 87:18. doi: 10.1103/PhysRevLett.87.188101

Spasic, S. (2010). Surrogate data test for nonlinearity of the rat cerebellar electrocorticogram in the model of brain injury. *Sig. Process.* 90, 3015–3025. doi: 10.1016/j.sigpro.2010.04.005

Stam, C. J., Pijn, J. P. M., and Pritchard, W. S. (1998). Reliable detection of nonlinearity in experimental time series with strong periodic components. *Phys. D* 112, 361–380. doi: 10.1016/S0167-2789(97)00183-8

Stam, C. J., and Van Dijk, B. W. (2002). Synchronization likelihood: an unbiased measure of generalized synchronization in multivariate data sets. *Phys. D* 163, 236–251. doi: 10.1016/S0167-2789(01)00386-4

Sun, J., Hong, X., and Tong, S. (2012). Phase synchronization analysis of eeg signals: an evaluation based on surrogate tests. *IEEE Trans. Biomed. Eng.* 59, 2254–2263. doi: 10.1109/TBME.2012.2199490

Takens, F. (1981). "Detecting strange attractors in turbulence," in *Lecture Notes in Mathematics*, eds D. A. Rand and L. -S. Young (Berlin: Springer), 366–381. doi: 10.1007/BFb0091924

Theiler, J., Eubank, S., Longtin, A., Galdrikian, B., and Farmer, J. D. (1992). Testing for nonlinearity in time series: the method of surrogate data. *Phys. D* 58, 77–94. doi: 10.1016/0167-2789(92)90102-S

Thornhill, N. F. (2005). Finding the source of nonlinearity in a process with plant-wide oscillation. *IEEE Trans. Control Syst. Technol.* 13, 434–443. doi: 10.1109/TCST.2004.839570

Timmer, J. (1998). Power of surrogate data testing with respect to nonstationarity. *Phys. Rev. E.* 58, 5153–5156. doi: 10.1103/PhysRevE.58.5153

Yao, D. (2001). A method to standardize a reference of scalp EEG recordings to a point at infinity. *Physiol. Meas.* 22, 693–711. doi: 10.1088/0967-3334/22/4/305

Conflict of Interest Statement: The authors declare that the research was conducted in the absence of any commercial or financial relationships that could be construed as a potential conflict of interest.

Copyright © 2018 Päeske, Bachmann, Põld, de Oliveira, Lass, Raik and Hinrikus. This is an open-access article distributed under the terms of the Creative Commons Attribution License (CC BY). The use, distribution or reproduction in other forums is permitted, provided the original author(s) and the copyright owner(s) are credited and that the original publication in this journal is cited, in accordance with accepted academic practice. No use, distribution or reproduction is permitted which does not comply with these terms.

frontiers
in Physiology

ORIGINAL RESEARCH
published: 28 September 2018
doi: 10.3389/fphys.2018.01385

Complexity Analysis of EEG Data in Persons With Depression Subjected to Transcranial Magnetic Stimulation

Karolina Lebiecka[1,2], Urszula Zuchowicz[1,2], Agata Wozniak-Kwasniewska[3,4†], David Szekely[3,4,5†], Elzbieta Olejarczyk[2*] and Olivier David[3,4]

[1] Department of Automatics and Biomedical Engineering, AGH University of Science and Technology, Kraków, Poland, [2] Nalecz Institute of Biocybernetics and Biomedical Engineering, Polish Academy of Sciences, Warsaw, Poland, [3] U1216, Inserm, Grenoble, France, [4] Grenoble Institut des Neurosciences, Université Grenoble Alpes, Grenoble, France, [5] Service de Psychiatrie, Centre Hospitalier Universitaire Grenoble Alpes, Grenoble, France

Aim: The aim of this work was to study the neurophysiological effect of repetitive transcranial magnetic stimulation (rTMS) applied to the left dorsolateral prefrontal cortex (DLPFC) in 8 patients with major depression disorder (MDD) and 10 patients with bipolar disorder (BP), considering separately responders and non-responders to rTMS therapy in each of both groups.

Methods: The Higuchi's Fractal Dimension (FD) was analyzed from 64-channels EEG signals in five physiological frequency bands and every channel separately. Changes of FD were analyzed before and after 1st, 10th, and 20th session of rTMS.

Results: Some differences in response to the rTMS therapy was found across individual groups. In MDD responders, FD decreased in all bands after longer stimulation (20th session). Whereas, in BP non-responders, FD decreased after 1st session in all bands as well as after 10th session in lower frequencies (delta and theta). In MDD non-responders and BP responders FD increased at the beginning of the therapy (1st and 10th session, respectively), but the final FD value did not changed in comparison to the initial FD value, except the FD decrease for theta band in BP responders. Comparison between groups showed a higher FD in MDD responders than in MDD non-responders in every band before as well as after stimulation. In contrast to MDD patients, FD was lower in BP responders than in BP non-responders in higher frequency bands (alpha, beta, and gamma) in both conditions as well as in lower frequency bands (delta and theta) after stimulation. Comparing both groups of responders, FD was lower in MDD than in BP in every band, except alpha. In case of non-responders, FD was higher in BP than in MDD in all bands in both conditions.

Conclusion: The results showed that FD may be useful marker for evaluation of the rTMS effectiveness and the therapy progress as well as for group differentiation between MDD and BP or between responders and non-responders. The changes of FD under the influence of rTMS allow to unambiguously conclude whether the effect of stimulation is positive or negative as well as allow to evaluate an optimal time of rTMS.

Keywords: EEG, repetitive transcranial magnetic stimulation, complexity, Higuchi fractal dimension, major depression disorder, bipolar disorder, depression

OPEN ACCESS

Edited by:
Sladjana Z. Spasić,
University of Belgrade, Serbia

Reviewed by:
Arcady A. Putilov,
Institute of Molecular Biology and Biophysics (RAS), Russia
Ronny P. Bartsch,
Bar-Ilan University, Israel

****Correspondence:***
Elzbieta Olejarczyk
eolejarczyk@ibib.waw.pl

†Present address:
Agata Wozniak-Kwasniewska,
SynapCell SAS, Saint-Ismier, France
David Szekely,
Service de Psychiatrie, Centre Hospitalier Princesse Grace, Monte Carlo, Monaco

Specialty section:
This article was submitted to Fractal Physiology,
a section of the journal Frontiers in Physiology

Received: *29 June 2018*
Accepted: *11 September 2018*
Published: *28 September 2018*

Citation:
Lebiecka K, Zuchowicz U, Wozniak-Kwasniewska A, Szekely D, Olejarczyk E and David O (2018) Complexity Analysis of EEG Data in Persons With Depression Subjected to Transcranial Magnetic Stimulation. Front. Physiol. 9:1385.
doi: 10.3389/fphys.2018.01385

INTRODUCTION

Major depressive disorder (MDD) is a mood disorder that causes a persistent feeling of sadness and loss of interest (Sadock et al., 2003; Hersen and Rosqvist, 2008; American Psychiatric Association, 2013; WHO, 2017). While, bipolar disorder (BD), called manic depression, is a mental health condition that causes extreme mood swings that include periods of abnormally elevated mood (mania or hypomania) and lows (depression) (Anderson et al., 2012; American Psychiatric Association, 2013; WHO, 2017). The causes of depression are divided into two main types: (1) endogenous – resulting from abnormal functioning of the central nervous system (CNS) at the cellular or protein level, and these are biological causes e.g., following the production of monoamines – neurotransmitters, such as serotonin, noradrenaline or dopamine, disruption of the serotonin and associated enzymes transport, formation of inflammatory processes in the limbic system of the brain; (2) exogenous – activating or being a "self-dependent" causes of depression, e.g., somatic diseases such as hormonal disorders, cancer, surgical procedures, incurable and chronic diseases, deficiencies of B group vitamins, CNS diseases such as multiple sclerosis, Alzheimer's disease, Parkinson's disease, Huntington's chorea, cerebrovascular diseases (especially temporal lobe and frontal lobe), the use of certain drugs and psychoactive substances (Kramer, 2002).

Not all patients suffering from depression respond to the pharmacological treatment. It was demonstrated, that only less than one third of depression patients reach remission after 12 weeks of initial antidepressant treatment (Trivedi et al., 2006), while another 30% of MDD patients are eventually diagnosed with drug treatment resistant disorder (Fitzgerald et al., 2003; Bewernick and Schlaepfer, 2015; Silverstein et al., 2015). In such drug-resistant cases other therapeutic approaches are needed. Numerous studies have shown that repetitive transcranial magnetic stimulation (rTMS) produced significant clinical effects in patients with various neurological and psychiatric disorders, in particularly in depression (Pascual-Leone et al., 1996; Rossi et al., 2009; Rossi, 2013; Lefaucheur et al., 2014). rTMS can be regarded as an adjunctive therapy to the usual pharmacotherapy with the aim of improving or accelerating the efficacy of these treatments by changing brain activity patterns and promoting cortical plasticity (Friston, 1996; Draganski and Kherif, 2013; Dukart et al., 2014). rTMS is usually applied over the dorsolateral prefrontal cortex (DLPFC), which was proven to be clinically effective in resistant depression therapy (Fitzgerald et al., 2003; Avery et al., 2006; O'Reardon et al., 2007; Concerto et al., 2015; Blumberger et al., 2016; Kito et al., 2016; Health Quality Ontario (2016); Filipcic et al., 2017; Teng et al., 2017). The use of two frequencies are recommended to change the local cortical activity: low frequency (LF) rTMS at 1 Hz to reduce neural excitability, and high frequency (HF) rTMS at 10 Hz to enhance neural excitability (Siebner and Rothwell, 2003; Lefaucheur et al., 2014). Considering asymmetry in frontal cortex activity in patients with drug resistant depression, HF rTMS is applied to the left DLPFC, while LF rTMS is targeted to the right DLPFC (Klein et al., 1999; George et al., 2000; Speer et al., 2000). The effectiveness of therapy depends on other factors also. The main experimental factors that introduced variability in reported rTMS effects are the pulse parameters (Arai et al., 2005; Taylor and Loo, 2007; Classen and Stefan, 2008), the different ways of targeting the DLPFC between experimenters and the different anatomy of the underlying gyri between subjects (Thielscher et al., 2011). The rate of responders increases significantly when the number of sessions is greater than 10, the total number of stimuli per session is greater than 1000, and the stimulation intensity is greater than 100% of the resting motor threshold (Gershon et al., 2003; Berlim et al., 2013; Lefaucheur et al., 2014). A minimum of 10 sessions in 1–2 weeks is usually carried out. The duration of the effect was rarely described and no study assessed the long-term effects of rTMS (Lefaucheur et al., 2014).

Considering high temporal resolution of EEG, its low price and easy application, this technique was used very widely to study both the nature of psychiatric disorders and the effect of rTMS. Many investigators have studied the relation between the therapeutic effect of rTMS in depression and spectral power dynamics of various EEG bands (Pozzi et al., 1993; Kwon et al., 1996; Griskova et al., 2007; Spronk et al., 2008; Valiulis et al., 2012; Woźniak-Kwaśniewska et al., 2015), however, these results were not consistent. Moreover, earlier studies demonstrated that EEG complexity analysis using Higuchi's fractal dimension (FD) can be successfully used in many clinical applications (Klonowski et al., 2000, 2002, 2004, 2005, 2006; Olejarczyk, 2007, 2011; Olejarczyk et al., 2009; Zappasodi et al., 2014, 2015; Cottone et al., 2016, 2017). Some authors applied the FD to compare the complexity of EEG signals in patients with depression and in healthy controls (Bahrami et al., 2005; Ahmadlou et al., 2012; Bachmann et al., 2013, 2018; Akar et al., 2015). All these studies showed a higher FD in both groups of patients with depression (MDD and BP), which would suggest that FD could be a good marker of the rTMS therapy effectiveness. Taking into account the results of these studies, we expected that FD would decrease under the influence of rTMS.

Despite the increasing use of rTMS in drug resistant depression treatment, its exact therapeutic mechanism still remains unknown. The effects of stimulation vary significantly between the studies and individuals. Some drug resistant patients respond well to rTMS treatment, while others remain unaffected. New markers are still needed for more effective patient selection and evaluation of rTMS therapy progress.

The aim of this work was to evaluate the effectiveness of the rTMS applied to the left DLPFC in both groups of patients (MDD and BP). For this purpose, the Higuchi's Fractal Dimension (FD), were analyzed using high-density EEG signals. The differences between MDD and BP patients as well as between patients responding positively and patients not responding to rTMS therapy in each of these groups separately, were studied. The impact of rTMS was evaluated in individual groups of patients for whole frequency range as well as for every band separately. The topographical differences were also considered. Finally, the dependence of these results on duration of stimulation was studied.

MATERIALS AND METHODS

Subjects

This study reuses the data presented in (Woźniak-Kwaśniewska et al., 2015), which contains additional details on the recording conditions. The EEG data were collected in Psychiatry Department of Grenoble University Hospital, after approval by the local ethical committee (ID RCB: 2011-A00114-37). All participants gave a written informed consent.

Two groups of right-handed patients who met Diagnostic and Statistical Manual of Mental Disorder 4th ed. (DSM-IV) criteria for Major Depressive Episode (American Psychiatric Association, 2000), were examined: 10 patients (6 females, age range 32–69, mean 48.7 ± 12.6) suffering from BP and 8 patients (6 females, age range 44–64, mean 52.1 ± 7.8) suffering from MDD. Each of these groups were also divided into responders and non-responders (**Table 1**).

The inclusion criterion was no response to pharmacological treatment of depression using a minimum of two distinctly different classes of antidepressant medications for actual depressive episode (appropriate doses and duration) occurring at the time of enrolment or earlier. Exclusion criteria were: age under 18 years, drug abuse, current comorbid major mental disorders assessed by clinical examination, neurological illness or convulsive disorders, and previous electroconvulsive therapy. All patients were on a range of medications. For bipolar patients, mood stabilizer medication has been unmodified for at least 2 weeks prior to the entry in the study, and remained unchanged throughout the course of the study. No benzodiazepines were administered 2 weeks before and during rTMS treatment. For MDD patients, pre-treatment with an antidepressant and/or mood stabilizer medication has been unmodified for at least 4 weeks prior to the entry in the study, and remained unchanged throughout the course of the study. Only cyanemazine and hydroxyzine were tolerated during the study.

TABLE 1 | Clinical characteristic of the participants.

		Number of patients	Age	Illness duration
MDD	Response	4	53,3 ± 5,8	10.3 ± 6.1
	Non-response	4	51,5 ± 7.5	10,3 ± 5.7
BP	Response	6	49 ± 13	14.8 ± 9.5
	Non-response	4	50 ± 10	24 ± 8.7
	Total	18	48 ± 9.7	15,1 ± 9,6

Demographics characteristics (gender and age) and clinical characteristics (illness and episode duration, depression severity) were evaluated for each patient using Montgomery Asberg Depression Rate Scale (MADRS) (Montgomery and Asberg, 1979), 13-item Beck Depression Inventory (BDI-Short Form) (Collet and Cottraux, 1986; Bouvard et al., 1992, Beck et al., 1996) and Clinical Global Impression (CGI). For bipolar patients, maniac or mixed symptoms were evaluated with Young Mania Rating Scale (YMRS) (Young et al., 1978). All patients were assessed at inclusion, before the first EEG recording and after each 5 rTMS sessions by the same senior psychiatrist (David Szekely). The response to rTMS treatment was defined as at least 50% reduction of the baseline MADRS scores. Patients were qualified as remitters when MADRS score was less than 8. If YMRS was more than 15, at inclusion or during the course of rTMS treatment, patients were excluded from the trial. The absolute changes in MADRS scores between baseline and the end of rTMS (4 weeks after the first evaluation) were used to calculate clinical improvement.

The standard clinical protocol recommended at Grenoble University Hospital was applied. The patients were subjected to rTMS of the left DLPFC over a period of 4 weeks. The rTMS therapy consisted of 20 sessions, with 2000 pulses per session continuously applied at 120% motor threshold. The 64-channel EEG signals were recording immediately before and after the 1st, 10th and 20th session, with FCz as the reference electrode. During the EEG acquisition patients were seated in a reclining armchair with neck and back supported with a pillow, arms relaxed and eyes closed.

EEG Registration and Preprocessing

Fifteen-minutes resting state with eyes closed pre- and post-rTMS recording, without artifacts were analyzed. EEG data pre-processing was performed using EEGlab and SPM8 tools available in MATLAB software. First EEG data were resampled at 250 Hz and band-pass filtered between 0.5 and 45 Hz. Such prepared data were reviewed for large muscle artifacts and non-stereotypical artifacts. Moreover, the mean of each data channel was removed before the application of an Independent Component Analysis (ICA), which is a method that allows to separate source signals from a multivariate measured signals assuming that the source signals are independent

TABLE 2 | The results of ANOVA analysis for factor CONDITION (before and after stimulation) in four groups of patients (BP_non-responders, BP_responders, MDD_non-responders, MDD_responders).

Group	ANOVA results		Mean ± Std	
	F-value	*p*-value	before	after
BP_non-responders	$F(1{,}6930) = 75{,}397$	$P < 0{,}0001$	1.562 ± 0.001	1.579 ± 0.001
BP_responders	$F(1{,}9450) = 11{,}930$	$P = 0.0006$	1.543 ± 0.001	1.536 ± 0.001
MDD_non-responders	$F(1, 5040) = 0.683$	$P = 0.409$	1.459 ± 0.001	1.457 ± 0.001
MDD_responders	$F(1{,}6930) = 59{,}239$	$P < 0.00001$	1.518 ± 0.002	1.544 ± 0.002

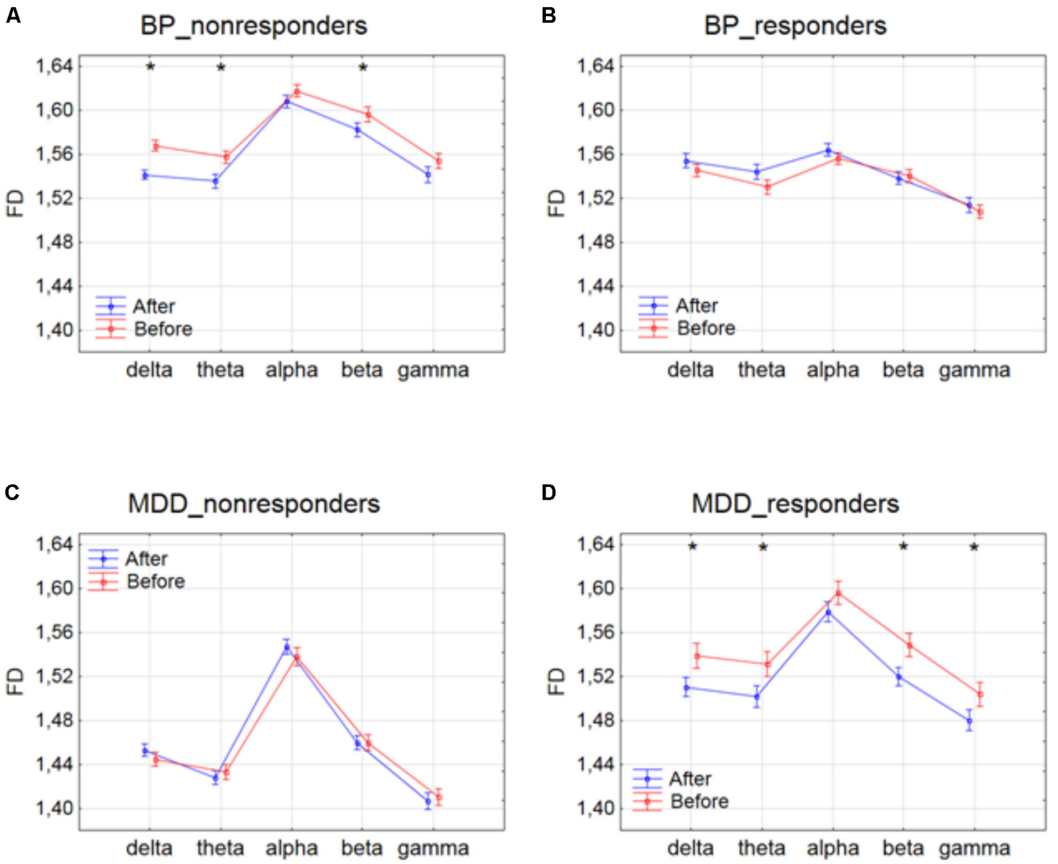

FIGURE 1 | Higuchi fractal dimension for BP_non-responders **(A)**, BP_responders **(B)**, MDD_non-responders **(C)** and MDD_responders **(D)** before and after stimulation in each of frequency bands. The interaction between factors CONDITION and BAND (all three sessions were included). Significant differences between conditions for the individual frequency bands, evaluated by *post hoc* Tukey HSD test, were marked with asterisks.

and non-Gaussian. For example, we can use ICA to remove electrooculographic (EOG) or electrocardiographic (ECG) artifacts from EEG signals (Arad et al., 2018). First 10 min of artifacts-free signals were selected to further analysis. These signals were segmented into 20 s successive epochs, which means that each 10 min recording was divided into 30 epochs. The EEG signals were analyzed in whole band as well as in five frequency bands (delta: 1–3 Hz, theta: 4–7 Hz, alpha: 8–12 Hz, beta: 13–30 Hz, gamma: 30–45 Hz) separately.

Higuchi Fractal Dimension

A fractal dimension (FD) is a measure of signal complexity. The term "fractal" was first introduced in 1975 by Mandelbrot and was described as a set of points that when looked at smaller scales, resembles the whole set. There are many available algorithms to calculate FD, one of them is Higuchi's fractal dimension (HFD), which is defined in time domain. FD value is always between 1 (for deterministic curves) and 2 (for stochastic signals) (Higuchi, 1988).

The signal is represented by a sequence X(1), X(2), . . ., X(N), where N is the total number of samples in the epoch. From the given epoch k new sub-epochs ${X_m}^k$ are defined as:

$$X_{\mathrm{m}}^{\mathrm{k}} : X(m), X(m+k), \ldots, X\left(m + int\left(\frac{N-m}{k}\right)k\right),$$
$$m = 1, 2, \ldots, k,$$

where m – initial time, k – interval time.

For each of the sub-epochs ${X_m}^k$, the average length $L_m(k)$ is computed as:

$$L_{\mathrm{m}}^{\mathrm{k}} = \frac{1}{k}\left[\sum_{\mathrm{i=1,int}\left(\frac{\mathrm{N-m}}{\mathrm{k}}\right)}^{\mathrm{k}} |X(m+ik) - X(m+(i-1)k| \frac{N-1}{int\left(\frac{N-m}{k}\right)}\right]$$

where N is the total number of signal samples, $\frac{N-1}{int\left(\frac{N-m}{k}\right)}$ is a normalization factor.

The length of the segment L(k) for the time interval k is computed as the mean of the k values, for m = 1, 2,. . ., k, that is:

$$L(k) = \frac{1}{k}\sum_{\mathrm{m=1}}^{\mathrm{k}} L_{\mathrm{m}}(k)$$

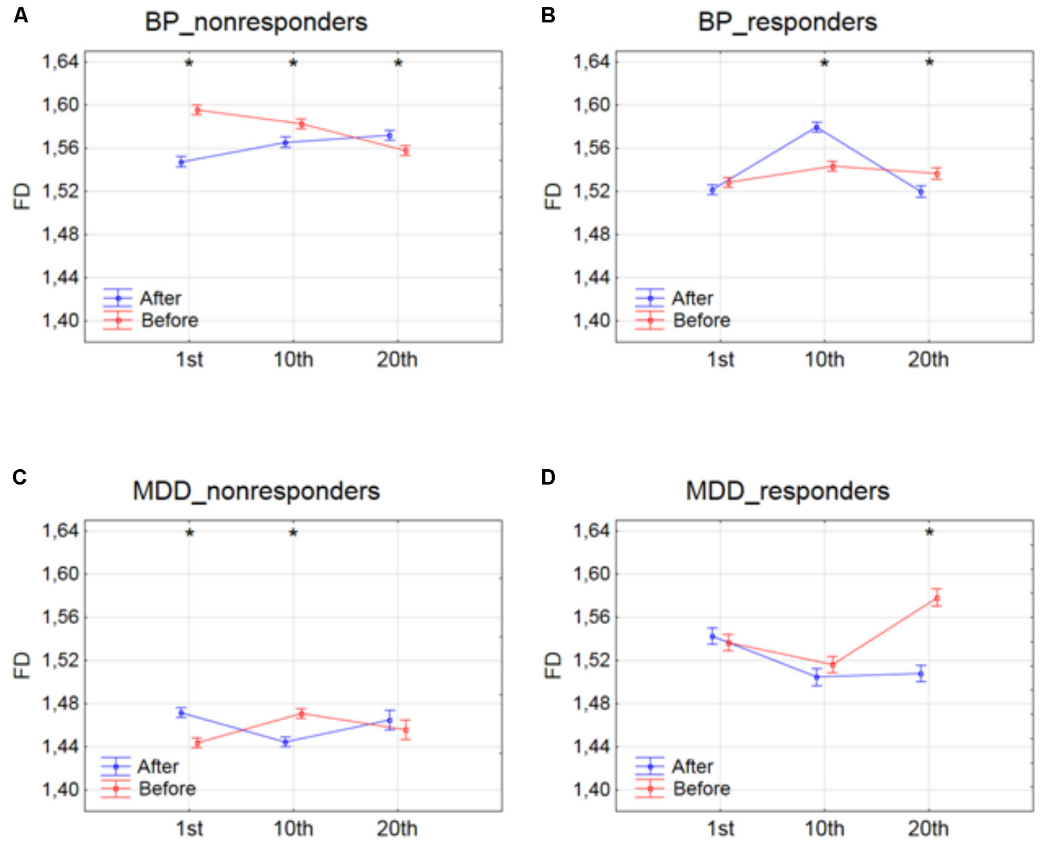

FIGURE 2 | Higuchi fractal dimension for BP_non-responders **(A)**, BP_responders **(B)**, MDD_non-responders **(C)** and MDD_responders **(D)** before and after stimulation in successive sessions (1st, 10th, and 20th session). The interaction between factors CONDITION and SESSION (all frequency bands were included). Significant differences between conditions for the individual sessions, evaluated by *post hoc* Tukey HSD test, were marked with asterisks.

The curve L(k) has a fractal dimension D_f :

$$L(k) \sim k^{-D_f}$$

The calculation is repeated for k values ranging from 1 to $k_{\max}$. In this work, $k_{\max}$ was equal 16. The fractal dimension was calculated as the slope of the line being the linear regression coefficient determined by the least squares method.

$$l\eta L(k) \sim D_f l\eta \frac{1}{k}$$

Statistical Analysis

The analysis of variance (ANOVA) with factors: CONDITION (pre- and post-rTMS), GROUP (BP_non-responders, BP_responders, MDD_non-responders, MDD_responders), BAND (delta, theta, alpha, beta, gamma), CHANNEL (1–63), SESSION (session 1st, 10th and 20th) was performed for FD.

In case of significant effects, *post hoc* tests (Tukey HSD) were performed. The statistical threshold was set at $p < 0.05$, with correction for multiple comparisons by controlling the family wise error (FWE).

RESULTS

The Higuchi fractal dimension was investigated for each of the electrodes in both individual frequency bands (delta, theta, alpha, beta and gamma) as well as in the entire frequency range (0.5–45 Hz).

Differences Between Conditions After and Before Stimulation

First, the three-way ANOVA with factors CONDITION, BAND and CHANNEL was performed to evaluate the effect of rTMS therapy in four groups of patients (BP_non-responders, BP_responders, MDD_non-responders, MDD_responders).

The differences between conditions, before and after stimulation (factor CONDITION), were found in groups: BP_non-responders, BP_responders and MDD_responders (c.f. **Table 2**).

The differences between conditions, before and after stimulation, for the individual frequency bands: delta, theta, alpha, beta and gamma in each of four groups are shown in **Figure 1**. The interaction between factors CONDITION and BAND was significant only for BP_non-responders group [$F(4,6930) = 2.627$; $p = 0.033$]. Significant differences between

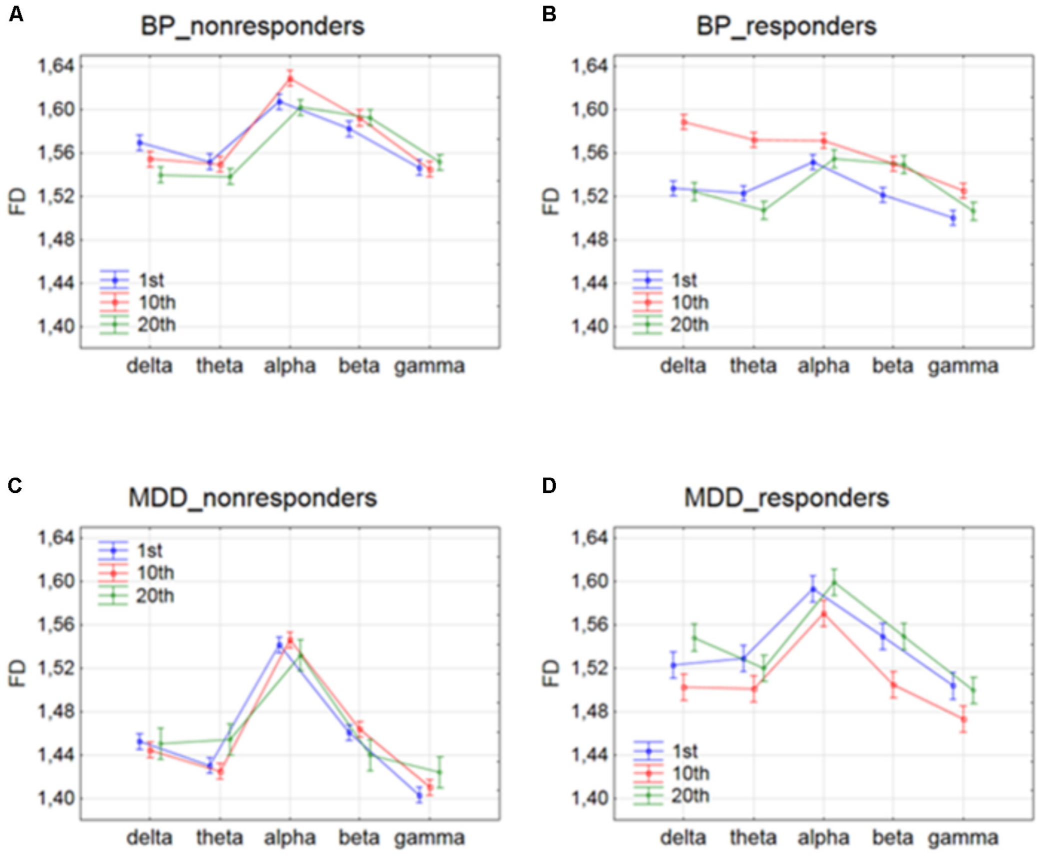

FIGURE 3 | Higuchi fractal dimension for BP_non-responders **(A)**, BP_responders **(B)**, MDD_non-responders **(C)** and MDD_responders **(D)** in five frequency bands. Comparison of results between 1st and 10th, 1st and 20th, and 10th and 20th session. The interaction between factors BAND and SESSION (both conditions were included).

conditions for the individual frequency bands, evaluated by *post hoc* Tukey HSD test, were marked with asterisks (c.f. **Figure 1**). For BP_non-responders group the decrease in FD value after stimulation was found mainly in delta, theta and beta bands (**Figure 1A**). No significant FD differences after stimulation were observed in any of the frequency bands in BP_responders and MDD_non-responders (**Figures 1B,C**). For MDD _responders lower values of FD were found after stimulation for each of frequency bands, except alpha band (**Figure 1D**). No significant topographical differences were found between conditions (factors: CONDITION x CHANNEL and CONDITION x BAND x CHANNEL) (c.f. **Supplementary Figure S1**). FD changed similarly in the whole brain. Thus, the factor CHANNEL has not been considered in the further analysis described in subsections 3.2 and 3.3.

Changes Across Consecutive Sessions

Next, the three-way ANOVA with factors: SESSION, CONDITION and BAND was applied in four groups separately to study the influence of stimulation time on the effect of rTMS therapy. Changes in FD values were analyzed before and after the 1st, 10th and 20th session of rTMS stimulation.

The effect of interaction between factors SESSION and CONDITION was illustrated in **Figure 2**. Significant differences between conditions for every session, evaluated by *post hoc* Tukey HSD test, were marked with asterisks (c.f. **Figure 2**). In BP_non-responders, the FD value significantly decreased after 1st session (**Figure 2A**). Afterward, the FD value started to return to its previous state but slightly decreased again after 10th session. Then, after the 20th session a significant increase of the FD occurred reaching the same level as after the 10th session. In BP_responders, FD value did not change after the 1st session. Afterward, the FD value increased in the second session. However, in the 20th session FD came back to the initial level (**Figure 2B**). In MDD_non-responders, the FD value significantly increased after 1st session (**Figure 2C**) but after 10th session the FD value decreased again reaching the initial level. The FD value did not change after the 20th session. The final FD value after the last session was slightly higher than at the beginning of therapy (**Figure 2C**). The MDD_responders group did not react to the therapy after 1st and 10th session. Nevertheless, after 20th session, the FD value significantly decreased after stimulation (**Figure 2D**).

The effect of interaction between factors SESSION and BAND was shown in **Figure 3**. For BP_non-responders group, the FD

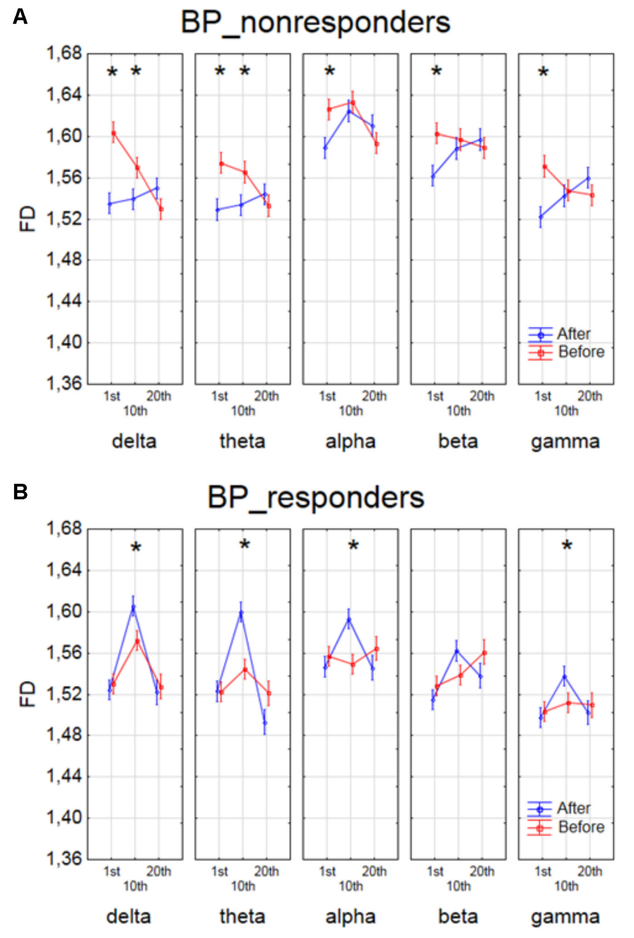

FIGURE 4 | Higuchi fractal dimension for BP_non-responders group **(A)** and for BP_responders group **(B)** for each band separately, showing changes in FD values before and after 1st, 10th and 20th session. The interaction between factors CONDITION, BAND and SESSION (separately for every group of BP patients). Significant differences between conditions for the individual sessions and bands, evaluated by *post hoc* Tukey HSD test, were marked with asterisks.

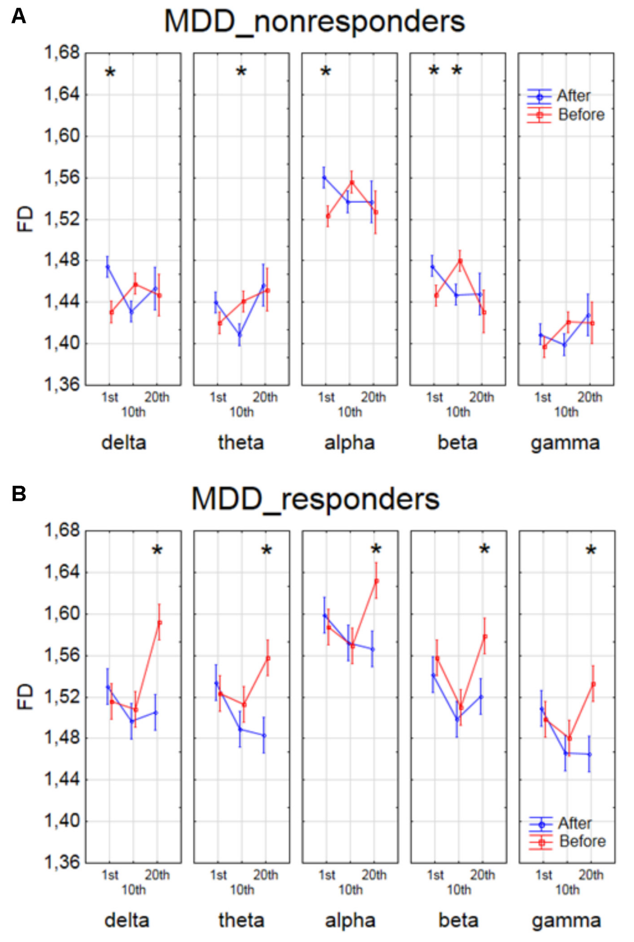

FIGURE 5 | Higuchi fractal dimension for MDD_non-responders group **(A)** and for MDD_responders group **(B)** for each band separately, showing changes in FD values before and after 1st, 10th and 20th session. The interaction between factors CONDITION, BAND and SESSION (separately for every group of MDD patients). Significant differences between conditions for the individual sessions and bands, evaluated by *post hoc* Tukey HSD test, were marked with asterisks.

value decreased for delta band and increased for beta band only between 1st and 20th session (c.f. **Figure 3A**). The FD for alpha band increased after 1st session but then returned to the previous level after 10th session. For MDD_non-responders group, FD values increased for theta band only between 10th and 20th session (c.f. **Figure 3C**). For BP_responders, FD values increased between 1st and 10th session in each of five frequency bands, but then decreased below the initial level in the 20th session in delta, theta, alpha and gamma bands (c. f. **Figure 3B**). For beta band, the value of FD remained unchanged between 10th and 20th session. For MDD_responders, decrease of FD value was found in higher frequency bands (beta and gamma) between 1st and 10th session (c.f. **Figure 3D**). However, between 10th and 20th session FD value increased again in these bands reaching the previous level. For delta band, the value of FD increased between 10th and 20th session.

The effect of interaction between factors SESSION, CONDITION and BAND was shown in four groups of patients in **Figures 4**, **5**. The analysis for BP_non-responders in each of five frequency bands showed a significant decrease of FD value after 1st session and a decrease of low frequency bands (delta and theta) after 10th session (**Figure 4A**). The analysis for BP_responders showed a significant increase of FD value in each of five frequency bands, except beta band, after the 10th session, followed by decrease of FD value after 20th session for all bands, reaching lower level than before 1st session (**Figure 4B**). For MDD_non-responders group the significant increase of the FD values was found after 1st session in delta, alpha and beta bands, and after 10th session in theta and beta bands (**Figure 5A**). For each frequency band, the final FD value did not changed significantly after 20th session in comparison to the FD value before 1st session. For MDD_responders, no significant differences after 1st and 10th sessions were found

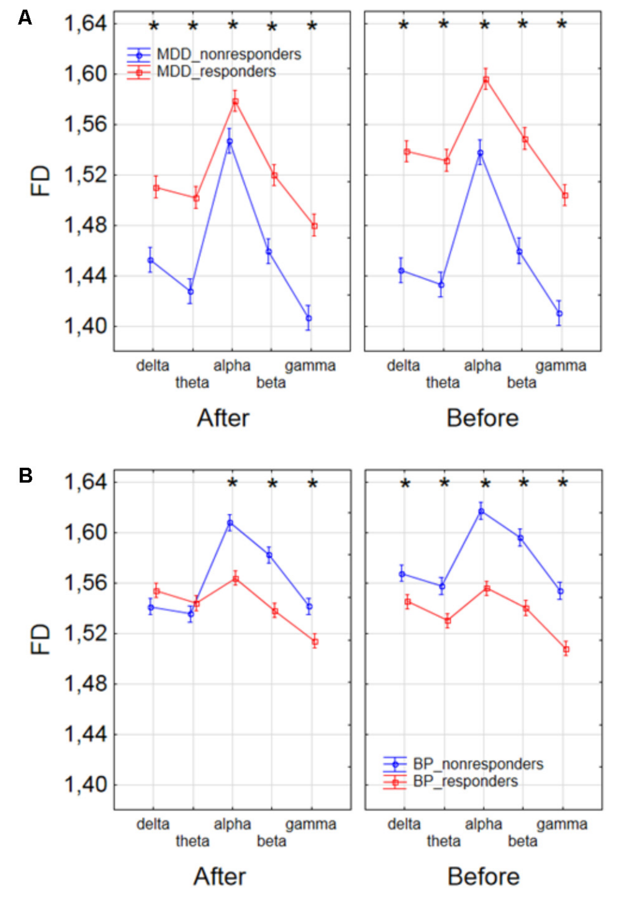

FIGURE 6 | Comparison of FD value between MDD_non-responders and MDD_responders groups **(A)** and between BP_non-responders and BP_responders groups **(B)** in each frequency band separately, for condition before and after session. The interaction between factors CONDITION, BAND, and GROUP (comparison between responders and non-responders separately in groups of MDD and BP patients). Significant differences between both groups for the individual frequency bands and conditions, evaluated by *post hoc* Tukey HSD test, were marked with asterisks.

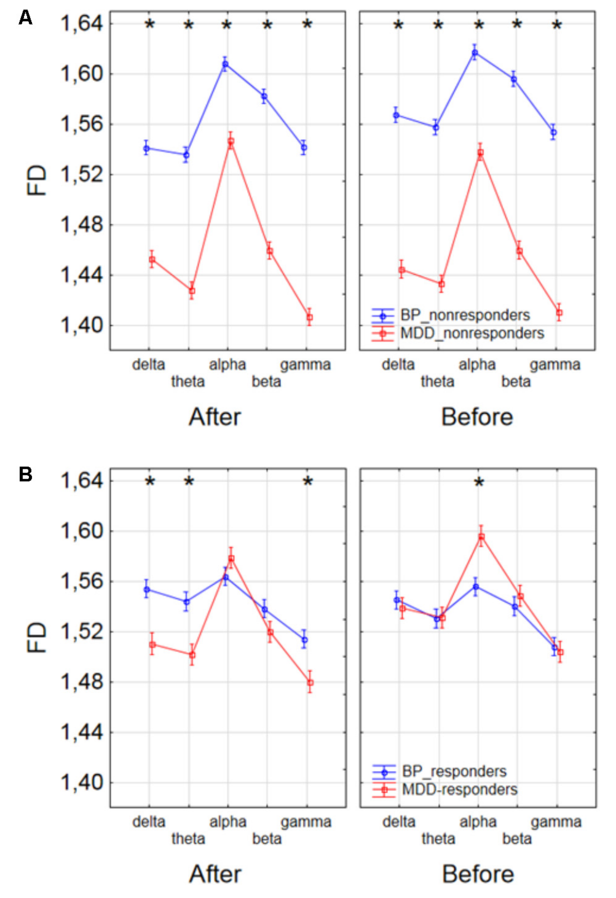

FIGURE 7 | Comparison of FD value between BP_non-responders and MDD_non-responders groups **(A)** and between BP_responders and MDD_responders groups **(B)** in each frequency band separately, for condition before and after session. The interaction between factors CONDITION, BAND and GROUP (comparison between groups of MDD and BP patients separately for responders and non-responders). Significant differences between both groups for the individual frequency bands and conditions, evaluated by *post hoc* Tukey HSD test, were marked with asterisks.

(**Figure 5B**). The effectiveness of the therapy appeared only after the 20th session. The significant decrease of FD value was noted after the 20th session in each of five frequency bands.

Differences Between Groups of Patients

Finally, to find the differences between groups of patients, the three-way ANOVA with factors: GROUP, CONDITION and BAND was performed. The following groups of patients were compared: MDD-responders vs. MDD-non-responders; BP-responders vs. BP-non-responders; MDD-responders vs. BP-responders, and MDD-non-responders vs. BP-non-responders. In MDD_responders higher value of FD was found for each of frequency bands in comparison to MDD_non-responders before as well as after stimulation. For both of groups the highest value of FD was observed for alpha band. The significant decrease of FD value in each frequency band can be observed for MDD_responders group also (compare red lines in right panel with left panel in **Figure 6A**). FD values were lower in BP_responders than in BP_non-responders for higher frequencies (alpha, beta, and gamma bands) after and also before the stimulation (**Figure 6B**). Whereas, for delta and theta band FD was lower only before the stimulation. The significant differences between MDD_non-responders and BP_non-responders were found for each frequency band. The lower FD values were observed in MDD_non-responders for both conditions, after and before the stimulation (**Figure 7A**). The results of the comparison of FD value between BP_responders and MDD_responders were statistically significant for delta, theta and gamma bands after the stimulation. The FD was lower for these bands in group of MDD_responders. Before the stimulation only differences in alpha band were statistically significant. The FD value was higher for MDD_responders. For other frequency bands no significant differences were found between these groups (**Figure 7B**).

DISCUSSION

The analysis of FD confirmed the effectiveness of rTMS therapy in MDD and BP. Bahrami et al. (2005) and Bachmann et al. (2013, 2018) found that FD in BP patients was higher than FD in healthy controls. Thus, we expected that FD would decrease in BP after stimulation. The patients from group of BP_responders reacted negatively to the therapy in the 10th session, but the change was not permanent (**Figure 4B**). Changes of FD showed an unfavorable reaction in the initial phase of therapy, but finally, the therapy was effective because the FD values after the 20th session were lower for each of five frequency bands than before the 1st session (c. f. **Figure 4B**), what was expected. This may mean that patients suffering from BP need longer therapy to be effective the stimulation. However, further studies are required to confirm these results.

In MDD_responders, FD decreased in each of frequency bands after 20th session (c.f. **Figure 5B**). This result is in line with the conclusions of other authors (Ahmadlou et al., 2012; Bachmann et al., 2013, 2018; Akar et al., 2015). The authors found the higher FD values in the MDD group in beta and gamma bands in the frontal lobe, than in the control group, that means the decrease of FD after stimulation is desirable in this group of patients.

In MDD_non-responders, the response to rTMS was opposite to the expected one at the beginning of the therapy. However, the final FD value did not changed significantly in comparison to the initial FD value.

In BP_non-responders the decrease in FD value after 1st session was found in each of five frequency bands as well as a decrease of low frequency bands (delta and theta) after 10th session (**Figure 4A**). No significant changes were observed in the last session. Thus, it can mean that the patients from the BP_non-responders group reacted positively to a shorter rTMS therapy.

Our results of the analysis of Higuchi fractal dimensions showed that rTMS stimulation can be an effective therapy in patients with MDD and bipolar disorder, however, some differences in response to the therapy across individual groups were found.

CONCLUSION

In this paper, the impact of rTMS on the complexity of EEG evaluated by FD was studied for the first time. We demonstrated that the complexity analysis of EEG data in persons with depression subjected to rTMS allowed to find the differences between conditions (before and after stimulation) and between individual groups of patients (MDD and BP, responders and non-responders) as well as to evaluate the impact of time stimulation on these results. The results of other authors (Bahrami et al., 2005; Ahmadlou et al., 2012; Bachmann et al., 2013, 2018; Akar et al., 2015) showed that FD is higher in both groups of patients with depression (MDD and BP) than in healthy controls. Thus, FD can be a good marker of rTMS efficiency because its changes allow to unambiguously conclude whether the effect of stimulation is positive or negative as well as allow to evaluate an optimal time of rTMS. Nevertheless, this study has some limitations. A bigger number of patients in each group as well as group of healthy controls should be examined in the future studies to confirm these preliminary but promising results.

Moreover, the FD is only one of many measures of the complexity of EEG signal. The complexity can be infer by studying of interactions between signals. The interactions between the EEG signals can be evaluated by different connectivity measures and indices based on graph theory (Olejarczyk et al., 2017a,b; Olejarczyk and Jernajczyk, 2017). Recently, a new field of Network Physiology has been developed (Bartsch et al., 2015; Liu et al., 2015; Ivanov et al., 2016). Its objective is an investigation of interactions not only within the brain but also between the brain and other organs by the analysis of signals from different non-linear dynamic systems in the human organism. This field indicates new directions for future research.

ETHICS STATEMENT

This study was carried out in accordance with the recommendations of Ethics Committee of the Grenoble University Hospital with written informed consent from all subjects.

DATA AVAILABILITY STATEMENT

The datasets for this manuscript are not publicly available because of Grenoble University Hospital policy. Requests to access the datasets should be directed to Prof. Olivier David, email: Olivier.David@inserm.fr.

AUTHOR CONTRIBUTIONS

KL analyzed the EEG data and wrote the manuscript. UZ preprocessed the EEG data. EO conceived the work, supervised the EEG data analysis, and wrote the manuscript. AW-K acquired the EEG data. DS recruited the patients and designed the trial. OD designed the trial, interpreted the EEG data, and critically reviewed the manuscript.

SUPPLEMENTARY MATERIAL

The Supplementary Material for this article can be found online at: https://www.frontiersin.org/articles/10.3389/fphys.2018.01385/full#supplementary-material

REFERENCES

Ahmadlou, M., Adeli, H., and Adeli, A. (2012). Fractality analysis of frontal brain in major depressive disorder. *Int. J. Psychophysiol.* 85, 206–211. doi: 10.1016/j.ijpsycho.2012.05.001

Akar, S. A., Kara, S., Agambayev, S., and Bilgic, V. (2015). Nonlinear analysis of EEGs of patients with major depression during different emotional states. *Comput. Biol Med.* 67, 49–60. doi: doi:10.1016/j.compbiomed.2015.09.019

American Psychiatric Association [APA] ((2013). *Diagnostic and Statistical Manual of Mental Disorders*, 5th Edn. Arlington, TX: American Psychiatric Publishing. doi: 10.1176/appi.books.9780890425596

American Psychiatric Association [APA] (2000). *Diagnostic and Statistical Manual of Mental Disorders*. Washington, DC: American Psychiatric Association.

Anderson, I. M., Haddad, P. M., and Scott, J. (2012). Bipolar disorder. *BMJ* 345:e8508. doi: 10.1136/bmj.e8508

Arad, E., Bartsch, R. P., Kantelhardt, J. W., and Plotnik, M. (2018). Performance-based approach for movement artifact removal from electroencephalographic data recorded during locomotion. *PLoS One* 13:e0197153. doi: 10.1371/journal.pone.0197153

Arai, N., Okabe, S., Furubayashi, T., Terao, Y., Yuasa, K., and Ugawa, Y. (2005). Comparison between short train, monophasic and biphasic repetitive transcranial magnetic stimulation (rTMS) of the human motor cortex. *Clin. Neurophysiol.* 116, 605–613. doi: 10.1016/j.clinph.2004.09.020

Avery, D. H., Holtzheimer, P. E. III., and Fawaz, W. (2006). A controlled study of repetitive transcranial magnetic stimulation in medication-resistant major depression. *Biol. Psychiatry* 59, 187–184. doi: 10.1016/j.biopsych.2005.07.003

Bachmann, M., Lass, J., Suhhova, A., and Hinrikus, H. (2013). Spectral asymmetry and Higuchi's fractal dimension measures of depression electroencephalogram. *Comput. Math. Methods Med.* 2013:251638. doi: 10.1155/2013/251638

Bachmann, M., Paeske, L., Kalev, K., Aarma, K., Lehtmets, A., Oopik, P., et al. (2018). Methods for classifying depression in single channel EEG using linear and nonlinear signal analysis. *Comput. Methods Programs Biomed.* 155, 11–17. doi: 10.1016/j.cmpb.2017.11.023

Bahrami, B., Seyedsadjadi, R., Babadi, B., and Noroozian, M. (2005). Brain complexity increases in mania. *Neuroreport* 16, 187–191. doi: 10.1097/00001756-200502080-00025

Bartsch, R. P., Liu, K. K. L., Bashan, A., and Ivanov, P. C. (2015). Network physiology: how organ systems dynamically interact. *PLoS One* 10:e0142143. doi: 10.1371/journal.pone.0142143

Beck, A. T., Steer, R. A., Ball, R., and Ranieri, W. (1996). Comparison of beck depression inventories-IA and -II in psychiatric outpatients. *J. Pers. Assess.* 67, 588–597. doi: 10.1207/s15327752jpa6703_13

Berlim, M. T., Van den Eynde, F., and Daskalakis, Z. J. (2013). Clinically meaningful efficacy and acceptability of low-frequency repetitive transcranial magnetic stimulation (rTMS) for treating primary major depression: a meta-analysis of randomized, double-blind and sham-controlled trials. *Neuropsychopharmacology* 38, 543–551. doi: 10.1038/npp.2012.237

Bewernick, B., and Schlaepfer, T. E. (2015). Update on neuromodulation for treatment-resistant depression. *F1000Research* 4:F1000FacultyRev-1389. doi: 10.12688/f1000research.6633.1

Blumberger, D. M., Maller, J. J., Thomson, L., Mulsant, B. H., Rajji, T. K., Maher, M., et al. (2016). Unilateral and bilateral MRI-targeted repetitive transcranial magnetic stimulation for treatment-resistant depression: a randomized controlled study. *J. Psychiatry Neurosci.* 41, E58–E66. doi: 10.1503/jpn.150265

Bouvard, M., Charles, S., Guerin, J., Aimard, G., and Cottraux, J. (1992). Study of Beck's hopelessness scale. Validation and factor analysis. *Encephale* 18, 237–240.

Classen, J., and Stefan, K. (2008). "Changes in TMS measures induced by repetitive TMS," in *The Oxford Handbook of Transcranial Stimulation*, eds C. M. Epstein, E. M. Wassermann, and U. Ziemann (Oxford: Oxford University Press), 185–200.

Collet, L., and Cottraux, J. (1986). The shortened beck depression inventory (13 items). Study of the concurrent validity with the Hamilton scale and Widlocher's retardation scale. *Encephale* 12, 77–79.

Concerto, C., Lanza, G., Cantone, M., Ferri, R., Pennisi, G., Bella, R., et al. (2015). Repetitive transcranial magnetic stimulation in patients with drug-resistant major depression: a six-month clinical follow-up study. *Int. J. Psychiatry Clin. Pract.* 19, 252–258. doi: 10.3109/13651501.2015.1084329

Cottone, C., Porcaro, C., Cancelli, A., Olejarczyk, E., Salustri, C., and Tecchio, F. (2016). Cortical parcellation based on local neuronal electrical activity. *Clin. Neurophysiol.* 127, e18–e132. doi: 10.1016/j.clinph.2015.11.252

Cottone, C., Porcaro, C., Cancelli, A., Olejarczyk, E., Salustri, C., and Tecchio, F. (2017). Neuronal electrical ongoing activity as a signature of cortical areas. *Brain Struct. Funct.* 222, 2115–2126. doi: 10.1007/s00429-016-1328-4

Draganski, B., and Kherif, F. (2013). In vivo assessment of use-dependent brain plasticity–beyond the "one trick pony" imaging strategy. *Neuroimage* 73, 255–259. doi: 10.1016/j.neuroimage.2012.08.058

Dukart, J., Regen, F., Kherif, F., Colla, M., Bajbouj, M., Heuser, I., et al. (2014). Electroconvulsive therapy-induced brain plasticity determines therapeutic outcome in mood disorders. *Proc. Natl. Acad. Sci. U.S.A.* 111, 1156–1161. doi: 10.1073/pnas.1321399111

Filipcic, I., Milovac, Z., Sucic, S., Gajsak, T., Filipcic, I. S., Ivezic, E., et al. (2017). Efficacy, safety and tolerability of augmentative rTMS in treatment of major depressive disorder (MDD): a prospective cohort study in Croatia. *Psychiat. Danub.* 29, 31–38. doi: 10.24869/psyd.2017.31

Fitzgerald, P. B., Brown, T. L., and Marston, N. A. (2003). Transcranial magnetic stimulation in the treatment of depression: a double-blind, placebo-controlled trial. *Arch. Gen. Psychiatry* 60, 1002–1008. doi: 10.1001/archpsyc.60.9.1002

Friston, K. J. (1996). Theoretical neurobiology and schizophrenia. *Br. Med. Bull.* 52, 644–655. doi: 10.1093/oxfordjournals.bmb.a011573

George, M. S., Nahas, Z., Molloy, M., Speer, A. M., Oliver, N. C., Li, X. B., et al. (2000). A controlled trial of daily left prefrontal cortex TMS for treating depression. *Biol. Psychiatry* 48, 962–970. doi: 10.1016/S0006-3223(00)01048-9

Gershon, A. A., Dannon, P. N., and Grunhaus, L. (2003). Transcranial magnetic stimulation in the treatment of depression. *Am. J. Psychiatry* 160, 835–845. doi: 10.1176/appi.ajp.160.5.835

Griskova, I., Ruksenas, O., Dapsys, K., Herpertz, S., and Höppner, J. (2007). The effects of 10 Hz repetitive transcranial magnetic stimulation on resting EEG power spectrum in healthy subjects. *Neurosci. Lett.* 419, 162–167. doi: 10.1016/j.neulet.2007.04.030

Health Quality Ontario (2016). Repetitive transcranial magnetic stimulation for treatment-resistant depression: a systematic review and meta-analysis of randomized controlled trials. *Ont. Health Technol. Assess. Ser.* 16, 1–66.

Hersen, M., and Rosqvist, J. (2008). *Handbook of Psychological Assessment, Case Conceptualization, and Treatment: Adults*, Vol. 1. Hoboken, NJ: John Wiley & Sons, 32.

Higuchi, T. (1988). Approach to an irregular time series on the basis of the fractal theory. *Physica D* 31, 277–283. doi: 10.1016/0167-2789(88)90081-4

Ivanov, P. C. H., Liu, K. K. L., and Bartsch, R. P. (2016). Focus on the emerging new fields of network physiology and network medicine. *New J. Phys.* 18:100201. doi: 10.1111/ede.12187

Kito, S., Hasegawa, T., Takamiya, A., Noda, T., Nakagome, K., Higuchi, T., et al. (2016). Transcranial magnetic stimulation modulates resting EEG functional connectivity between the left dorsolateral prefrontal cortex and limbic regions in medicated patients with treatment-resistant depression. *J. Neuropsychiatry Clin. Neurosci.* 29, 155–159. doi: 10.1176/appi.neuropsych.15120419

Klein, E., Kreinin, I., Chistyakov, A., Koren, D., Mecz, L., Marmur, S., et al. (1999). Therapeutic efficacy of right prefrontal slow repetitive transcranial magnetic stimulation in major depression: a double-blind controlled study. *Arch. Gen. Psychiatry* 56, 315–320. doi: 10.1001/archpsyc.56.4.315

Klonowski, W., Olejarczyk, E., and Stepien, R. (2000). Nonlinear dynamics of EEG-signal reveals influence of magnetic field on the brain. *Conf. Proc. IEEE Eng. Med. Biol. Soc.* 22, 2955–2958.

Klonowski, W., Olejarczyk, E., and Stepien, R. (2002). Complexity of EEG-signal in time domain – Possible biomedical application. *AIP Conf. Proc.* 622, 155–160. doi: 10.1063/1.1487530

Klonowski, W., Olejarczyk, E., and Stepien, R. (2005). "Sleep EEG analysis using higuchi's fractal dimension," in *Proceedings of the International Symposium on Nonlinear Theory and its Applications NOLTA2005*, Bruges, 222–225.

Klonowski, W., Olejarczyk, E., Stepien, R., Jalowiecki, P., and Rudner, R. (2006). "Monitoring the depth of anaesthesia using fractal complexity method," in *Complexus Mundi. Emergent Patterns in Nature*, ed. M. N. Novak (Singapore: World Scientific), 333–342. doi: 10.1142/9789812774217_0031

Klonowski, W., Olejarczyk, E., Stepien, R., and Szelenberger, W. (2004). Complexity of Polysomnogram signals. *WSEAS Conf.* 3, 1290–1294.

Kramer, T. A. M. (2002). Endogenous versus exogenous: still not the issue. *Med. Gen. Med.* 4. Available at: http://www.medscape.com/viewarticle/418269

Kwon, J. S., Youn, T., and Jung, H. Y. (1996). Right hemisphere abnormalities in major depression: quantitative electroencephalographic findings before and after treatment. *J. Affect. Disord.* 40, 169–173. doi: 10.1016/0165-0327(96)00057-2

Lefaucheur, J. P., Andre-Obadia, N., Antal, A., Ayache, S. S., Baeken, C., Benninger, D. H., et al. (2014). Evidence-based guidelines on the therapeutic use of repetitive transcranial magnetic stimulation (rTMS). *Clin. Neurophysiol.* 125, 2150–2206. doi: 10.1016/j.clinph.2014.05.021

Liu, K. K., Bartsch, R. P., Lin, A., Mantegna, R. N., and Ivanov, P. C. H. (2015). Plasticity of brain wave network interactions and evolution across physiologic states. *Front. Neural Circuits* 9:62. doi: 10.3389/fncir.2015.00062

Montgomery, S. A., and Asberg, M. (1979). A new depression scale designed to be sensitive to change. *Br. J. Psychiatry* 134, 382–389. doi: 10.1192/bjp.134.4.382

Olejarczyk, E. (2007). "Application of fractal dimension method of functional MRI time-series to limbic dysregulation in anxiety study," in *Procedings of the 29th Annual International Conference of the IEEE Engineering in Medicine and Biology Society*, (Lyon: IEEE), 3408–3410.

Olejarczyk, E. (2011). *Fractal Dimension in Time Domain—Application in EEG-Signal Analysis Classification and Application of Fractals*. New York, NY: Nova Science Publishers, 161–185.

Olejarczyk, E., Bogucki, P., and Sobieszek, A. (2017a). The EEG split alpha peak: phenomenological origins and methodological aspects of detection and evaluation. *Front. Neurosci.* 11:506. doi: 10.3389/fnins.2017.00506

Olejarczyk, E., and Jernajczyk, W. (2017). Graph-based analysis of brain connectivity in schizophrenia. *PLoS One* 12:e0188629. doi: 10.1371/journal.pone.0188629

Olejarczyk, E., Marzetti, L., Zappasodi, F., and Pizzella, V. (2017b). Comparison of connectivity analyses methods in EEG during resting state. *J. Neural Eng.* 14:036017. doi: 10.1088/1741-2552/aa6401

Olejarczyk, E., Sobieszek, A., Rudner, R., Marciniak, R., Wartak, M., Stasiowski, M., et al. (2009). Evaluation of the EEG-signal during volatile anaesthesia: methodological approach. *Biocybern. Biomed. Eng.* 29, 3–28.

O'Reardon, J. P., Solvason, H. B., Janicak, P. G., Sampson, S., Isenberg, K. E., Nahas, Z., et al. (2007). Efficacy and safety of transcranial magnetic stimulation in the acute treatment of major depression: a multisite randomized controlled trial. *Biol. Psychiatry* 62, 1208–1216. doi: 10.1016/j.biopsych.2007.01.018

Pascual-Leone, A., Rubio, B., Pallardo, F., and Catala, M. D. (1996). Rapid-rate transcranial magnetic stimulation of left dorsolateral prefrontal cortex in drug-resistant depression. *Lancet* 348, 233–237. doi: 10.1016/S0140-6736(96)01219-6

Pozzi, D., Golimstock, A., Migliorelli, R., Tesón, A., García, H., and Starkstein, S. (1993). Quantified electroencephalographic correlates of depression in Alzheimer's disease. *Biol. Psychiatry* 34, 386–391. doi: 10.1016/0006-3223(93)90183-E

Rossi, S. (2013). "Safety of transcranial magnetic stimulation: with a note on regulatory aspects," in *Transcranial Brain Stimulation*, eds C. Miniussi, W. Paulus, and P. M. Rossini (Boca Raton, FL: CRC Press), 415–426.

Rossi, S., Hallett, M., Rossini, P. M., and Pascual-Leone, A. (2009). Safety of TMS Consensus Group. Safety, ethical considerations, and application guidelines for the use of transcranial magnetic stimulation in clinical practice and research. *Clin. Neurophysiol.* 120, 2008–2039. doi: 10.1016/j.clinph.2009.08.016

Sadock, V. A., Sadock, B. J., and Kaplan, H. I. (2003). *Kaplan & Sadock's Synopsis of Psychiatry: Behavioral Sciences/Clinical Psychiatry*. Philadelphia, PA: Lippincott Williams & Wilkins.

Siebner, H. R., and Rothwell, J. (2003). Transcranial magnetic stimulation: new insights into representational cortical plasticity. *Exp. Brain Res.* 148, 1–16. doi: 10.1007/s00221-002-1234-2

Silverstein, W. K., Noda, Y., Barr, M. S., Vila-Rodriguez, F., Rajji, T. K., Fitzgerald, P. B., et al. (2015). Neurobiological predictors of response to dorsolateral prefrontal cortex repetitive transcranial magnetic stimulation in depression: a systematic review. *Depress. Anxiety* 32, 871–891. doi: 10.1002/da.22424

Speer, A. M., Kimbrell, T. A., Wassermann, E. M., Repella, J. D., Willis, M. W., Herscovitch, P., et al. (2000). Opposite effects of high and low frequency rTMS on regional brain activity in depressed patients. *Biol. Psychiatry* 48, 1133–1141. doi: 10.1016/S0006-3223(00)01065-9

Spronk, D., Arns, M., Bootsma, A., van, Ruth R, and Fitzgerald, P. B. (2008). Long-term effects of left frontal rTMS on EEG and ERPs in patients with depression. *Clin. EEG Neurosci.* 39, 118–124. doi: 10.1177/155005940803900305

Taylor, J. L., and Loo, C. K. (2007). Stimulus waveform influences the efficacy of repetitive transcranial magnetic stimulation. *J. Affect. Disord.* 97, 271–276. doi: 10.1016/j.jad.2006.06.027

Teng, S., Guo, Z., Peng, H., Xing, G., Chen, H., He, B., et al. (2017). High-frequency repetitive transcranial magnetic stimulation over the left DLPFC for major depression: session-dependent efficacy: a meta-analysis. *Eur. Psychiatry* 41, 75–84. doi: 10.1016/j.eurpsy.2016.11.002

Thielscher, A., Opitz, A., and Windhoff, M. (2011). Impact of the gyral geometry on the electric field induced by transcranial magnetic stimulation. *Neuroimage* 54, 234–243. doi: 10.1016/j.neuroimage.2010.07.061

Trivedi, M. H., Fava, M., and Wisniewski, S. R. (2006). Medication augmentation after the failure of SSRIs for depression. *N. Eng. J. Med.* 354, 1243–1252. doi: 10.1056/NEJMoa052964

Valiulis, V., Gerulskis, G., Dapšys, K., Vištartaite, G., Šiurkute, A., and Maèiulis, V. (2012). Electrophysiological differences between high and low frequency rTMS protocols in depression treatment. *Acta Neurobiol. Exp.* 72, 283–295.

WHO (2017). *Depression and Other Common Mental Disorders: Global Health Estimates*. Geneva: World Health Organization.

Woźniak-Kwaśniewska, A., Szekely, D., Harquel, S., Bougerol, T., and David, O. (2015). Resting electroencephalographic correlates of the clinical response to repetitive transcranial magnetic stimulation: A preliminary comparison between unipolar and bipolar depression. *J. Affect. Disord.* 183, 15–21. doi: 10.1016/j.jad.2015.04.029

Young, R. C., Biggs, J. T., Ziegler, V. E., and Meyer, D. A. (1978). A rating scale for mania: reliability, validity and sensitivity. *Br. J. Psychiatry* 133, 429–435. doi: 10.1192/bjp.133.5.429

Zappasodi, F., Marzetti, L., Olejarczyk, E., Tecchio, F., and Pizzella, V. (2015). Age-related changes in electroencephalographic signal complexity. *PLoS One* 10:e0141995. doi: 10.1371/journal.pone.0141995

Zappasodi, F., Olejarczyk, E., Marzetti, L., Assenza, G., Pizzella, V., and Tecchio, F. (2014). Fractal dimension of EEG activity senses neuronal impairment in acute stroke. *PLoS One* 9:e100199. doi: 10.1371/journal.pone.0100199

Conflict of Interest Statement: The authors declare that the research was conducted in the absence of any commercial or financial relationships that could be construed as a potential conflict of interest.

Copyright © 2018 Lebiecka, Zuchowicz, Wozniak-Kwasniewska, Szekely, Olejarczyk and David. This is an open-access article distributed under the terms of the Creative Commons Attribution License (CC BY). The use, distribution or reproduction in other forums is permitted, provided the original author(s) and the copyright owner(s) are credited and that the original publication in this journal is cited, in accordance with accepted academic practice. No use, distribution or reproduction is permitted which does not comply with these terms.

frontiers in Physiology

ORIGINAL RESEARCH
published: 07 September 2018
doi: 10.3389/fphys.2018.01213

EEG Multiscale Complexity in Schizophrenia During Picture Naming

Antonio J. Ibáñez-Molina[1], Vanessa Lozano[2], María. F. Soriano[3], José. I. Aznarte[3], Carlos J. Gómez-Ariza[1] and M. T. Bajo[2]*

[1] Department of Psychology, University of Jaén, Jaén, Spain, [2] Department of Experimental Psychology, University of Granada, Granada, Spain, [3] Hospital San Agustín, Jaén, Spain

Introduction: Patients with schizophrenia show cognitive deficits that are evident both behaviourally and with EEG recordings. Recent studies have suggested that non-linear analyses of EEG might more adequately reflect the complex, irregular, non-stationary behavior of neural processes than more traditional ERP measures. Non-linear analyses have been mainly applied to EEGs from patients at rest, whereas differences in complexity might be more evident during task performance.

Objective: We aimed to investigate changes in non-linear brain dynamics of patients with schizophrenia during cognitive processing.

Method: 18 patients and 17 matched healthy controls were asked to name pictures. EEG data were collected at rest and while they were performing a naming task. EEGs were analyzed with the classical Lempel-Ziv Complexity (LZC) and with the Multiscale LZC. Electrodes were grouped in seven regions of interest (ROI).

Results: As expected, controls had fewer naming errors than patients. Regarding EEG complexity, the interaction between Group, Task and ROI indicated that patients showed higher complexity values in right frontal regions only at rest, where no differences in complexity between patients and controls were found during the naming task. EEG complexity increased from rest to task in controls in left temporal-parietal regions, while no changes from rest to task were observed in patients. Finally, differences in complexity between patients and controls depended on the frequency bands: higher values of complexity in patients at rest were only observed in fast bands, indicating greater heterogeneity in patients in local dynamics of neuronal assemblies.

Conclusion: Consistent with previous studies, schizophrenic patients showed higher complexity than controls in frontal regions at rest. Interestingly, we found different modulations of brain complexity during a simple cognitive task between patients and controls. These data can be interpreted as indicating schizophrenia-related failures to adapt brain functioning to the task, which is reflected in poorer behavioral performance.

OPEN ACCESS

Edited by:
Sladjana Z. Spasić,
University of Belgrade, Serbia

Reviewed by:
Miles A. Whittington,
University of York, United Kingdom
Marzieh Zare,
Institute for Research in Fundamental Sciences (IPM), Iran

****Correspondence:***
Antonio J. Ibáñez-Molina
aibanez@ujaen.es;
anjoibanez@gmail.com

Specialty section:
This article was submitted to Fractal Physiology, a section of the journal Frontiers in Physiology

Received: *29 May 2018*
Accepted: *13 August 2018*
Published: *07 September 2018*

Citation:
Ibáñez-Molina AJ, Lozano V, Soriano MF, Aznarte JI, Gómez-Ariza CJ and Bajo MT (2018) EEG Multiscale Complexity in Schizophrenia During Picture Naming. Front. Physiol. 9:1213. doi: 10.3389/fphys.2018.01213

Highlights:

- We measured classical and multiscale Lempel-Ziv Complexity (LZC_N and MLZC) of the EEG signal of patients with schizophrenia and controls at rest and while performing a cognitive task.
- We found that patients and controls showed a different pattern of brain complexity depending on their cognitive state (at rest or under cognitive challenge).
- Our results illustrate the value of the MLZC in the characterization of the pattern of brain complexity in schizophrenia on function of frequency bands.
- Nonlinear methodologies of EEG analysis can help to characterize brain dysfunction in schizophrenia.

Keywords: schizophrenia, EEG, non-linear analysis, multiscale lempel-ziv complexity, naming task

INTRODUCTION

Patients with schizophrenia suffer from cognitive impairments in a wide number of domains that include attention, language, working memory, episodic and semantic memory (Heinrichs and Zakzanis, 1998; Addington et al., 2003). However, many studies have shown evidence that the cognitive deficit that underlies schizophrenia is not generalized, but specific to some functions (e.g., semantic memory, working memory) (Cohen and Servan-Schreiber, 1992; Goldman-Rakic, 1994; Kerns and Berenbaum, 2002; Jonides and Nee, 2005). In addition, there have been many attempts to specify the brain dysfunctions related to the specific cognitive deficits by analyzing EEG signals. Electrophysiological studies have traditionally used methodologies of linear analyses, such as Event-Related Potentials (ERP) or power analysis (Kiang et al., 2007; Hughes et al., 2012). The absence of abnormalities of the raw EEG in patients with schizophrenia has led researchers to study quantitative parameters of EEG (QEEG). Spectral and coherence analyses of EEG are commonly used in the studies of QEEG abnormalities in schizophrenia (see Hughes and John, 1999).

Recently, new approaches to the study of EEG signals have been developed from non-linear system theories that can be helpful to understand brain dysfunctions associated with schizophrenia. Non-linear measures might render more adequate to reflect the complex, irregular and non-stationary behavior of neural processes. Some have suggested that non-linear approaches may be more powerful than classical lineal analyses to relate brain patterns of activation to cognition (e.g., Pereda et al., 2005; Klonowsky, 2009). EEG signals are the result of the non-linear combination of electrical activity generated by interacting oscillators from the cerebral cortex and other biological sources such as muscles. Consequently, the EEG signals have complex non-linear structures when looking at them in the time dimension. Most non-linear analyses have tried to quantify the complexity of EEG signals and to relate it to functional aspects of the neural networks. Thus, EEG complexity has been related to the integrity of neural connectivity, and with the number of distinct generators contributing to a given EEG signal (e.g., Lutzenberger et al., 1995). Hence, the more complex the signal is, the wider the distribution of cortical activation related to it (e.g., Mölle et al., 1999). Complexity is also related to the synchrony of oscillations of the generators. Synchronization between oscillators has been proposed as a general mechanism for information exchange within neural circuits (e.g., Engel et al., 2001; Fries, 2005). In general, it has been shown that synchrony is negatively related to complexity (Escudero et al., 2015; Ghanbari et al., 2015). While this relationship is far from being perfect (Ibáñez-Molina et al., 2018), highly synchronized signals (e.g., epileptic seizures) give rise to low complexity values (Radhakrishnan and Gangadhar, 1998). In sum, and although the exact meaning of complexity is still a matter of debate, complexity seems to be related to a number of variables: connectivity of neural networks, number of oscillators involved in the generation of signals, and synchrony of oscillations. Hence, for a given cognitive function, complexity reflects key functional aspects of the underlying neural sources. In general, high levels of complexity in the EEG recording indicate that the neural generators of the signal tend to be widely distributed and desynchronized. On the contrary, a low level of complexity indicates that the neural generators tend to be local and/or synchronized.

A number of complexity measures have been developed, some of which [the correlation dimension (D2), the Lyapunov exponent (L1), the Lempel-Ziv complexity (LZC), and the multiscale entropy analysis (MSE)] have been applied to EEGs from psychiatric patients (Sohn et al., 2010; Fernández et al., 2011; Bachiller et al., 2014). However, there are important differences among these methods. Thus, for example, while D2 and L1 are chaos-based estimates of complexity, LZC is based on algorithmic complexity, and MSE quantifies entropy over multiple time scales. More relevant, D2 and L1 require a large amount of EEG data, whereas LZC and the MSE are suitable for short and non-stationary time series.

Most of these measures quantify the degree of randomness or degrees of freedom of a system. Indeed, at a conceptual level, complexity has been often interpreted as irregularity, unpredictability, desynchrony or randomness (see Stam, 2005, for a review). However, it has been pointed out that complexity should not be equated to randomness, but to an intermediate state between randomness and order (Tononi and Edelman, 1998; Stam, 2005; Yang and Tsai, 2013). Yang and Tsai (2013) have proposed that brain complexity underlies the behavioral ability to adapt to the constantly changing environment. From this view, an abnormal brain complexity would give rise to either highly ordered or highly random behavioral patterns. Both regular and random patterns can be indicative of pathology and represent a deviation from complexity (Goldberger et al., 2002; Yang et al., 2015). This idea is supported by evidence showing lower values of brain complexity in some disorders (e.g., Alzheimer's disease, Stam et al., 2009), whereas higher values of complexity are found in other disorders (i.e., schizophrenia) or during normal aging (Yang and Tsai, 2013).

Over the last years non-linear analyses have proven their utility to detect changes in brain complexity in some mental disorders (Yang and Tsai, 2013), with most studies focused on schizophrenia. (Fernández et al., 2011; Fernández et al., 2013). Some of these studies have found that patients with schizophrenia exhibit higher complexity than healthy controls in their EEG signals (Li et al., 2008; Takahashi et al., 2010; Fernández et al., 2011), although decreased complexity values have also been reported (Hoffmann et al., 1996; Lee et al., 2001; Akar et al., 2016). These apparently inconsistent findings might be explained by a number of confounding variables, such as the nature of the complexity estimates employed or the condition under which patients are tested (e.g., rest, closed eyes or active processing). Additionally, a relevant issue is that complexity is modulated by age. While complexity increases with age in healthy people, the opposite trend has been observed in patients with a mental disorder (Fernández et al., 2011; Méndez et al., 2012).

In a recent review, Fernández et al. (2013) proposed that three main variables seem to modulate EEG complexity in schizophrenia: medication, age, and symptomatology. Thus, increased complexity in schizophrenia is found in those studies that include young patients without medication and with a predominance of positive symptoms. In a previous study (Fernández et al., 2011), these authors reported increased complexity in patients with schizophrenia compared with a control group. However, whereas complexity positively correlated with age in the control group, patients with schizophrenia exhibited the opposite pattern (decreasing complexity with age). With regard to medication, some studies have shown that antipsychotics reduce complexity (as measured with MSE) in patients with schizophrenia (Takahashi et al., 2010), and that antidepressants reduce the usually high values of complexity in depression (Méndez et al., 2012).

Finally, EEG complexity also depends on the recording conditions. Several studies have reported that complexity increases in healthy participants while performing cognitive tasks (arithmetic, visual and reading tasks, see Stam, 2005, for a comprehensive review). On the contrary, Ibáñez-Molina and Iglesias-Parro (2014) have shown that EEG complexity is lower when healthy participants attend to visual or auditory stimuli than when they attend to their own thoughts (mind wandering). Furthermore, whether complexity increases or diminishes with cognitive demands might rely on the specific brain networks involved in the cognitive task.

In schizophrenia, most studies have focused on EEGs from patients at rest (Fernández et al., 2011), though exceptions exist (Kirsch et al., 2000; Li et al., 2008; Bachiller et al., 2014). Kirsch et al. (2000) compared EEG complexity (D2) of patients and controls at rest and while performing the continuous performance test (CPT). While they did not find differences between the two groups in the resting state condition, control participants showed a decrease in complexity when performing the cognitive task that was not observed in patients. According to the authors of the study, the healthy controls, but not the patients, were able to adjust their brain functioning to the task demands. However, because they recorded EEG from a unique electrode (in the Cz site), they were not able to explore changes in complexity on different brain regions under cognitive processing. Li et al. (2008) compared LZC of the EEG from patients with schizophrenia and depression with that of controls at rest and while performing a mental arithmetic task. Patients with schizophrenia showed higher LZC than controls at most electrodes. Both groups exhibited a decreased LZC during the task, although this decrease was smaller in the control group. More recently, Bachiller et al. (2014) compared spectral entropy (SE) between a resting condition and a task condition (auditory odd-ball task) in patients with schizophrenia and controls. SE quantifies the degree of disorder in a signal. They found that controls showed a decrease in entropy when performing the cognitive task, compared to rest, at parietal and central brain regions, whereas patients showed a reliable lower decrease than controls. Similar to Kirsch et al. (2000), Bachiller et al. (2014) failed to find differences in brain complexity between patients and controls in the resting state condition. On the contrary, Carlino et al. (2012) found a significant increase in EEG complexity (D2) during "active" conditions (eyes open, counting forward and counting backward conditions) compared to an eyes-closed resting condition, but only in the control group. At rest, however, the authors found greater complexity in patients than in controls. In sum, the evidence regarding EEG complexity while participants are performing cognitive tasks is mixed. It is possible that differences in the cognitive demands of the tasks, or in the non-linear measures used in different studies, underlie these divergences.

In the present study we aimed to gain further insight into how brain complexity changes under cognitive demands in patients with schizophrenia and healthy controls. To this end, we recorded EEGs from participants with schizophrenia and healthy controls at rest and while they performed a picture naming task. This cognitive task was selected for two reasons. First, it is a short and easy task wherein participants have to attend and name aloud visually presented stimuli. In addition, and more relevant, the picture-naming task has shown to be useful as a measure of semantic memory impairments in patients with schizophrenia (Soriano et al., 2008), which have been widely reported in this population (Manschreck et al., 1988; Kerns and Berenbaum, 2002). Specifically, here we compared EEG complexity in patients and controls in a resting state condition (seating and with open eyes) and while they were performing the naming task. Complexity was estimated with the classical Lempel-Ziv complexity analysis (LZC_N) and the modified LZC to measure different frequency bands (Ibáñez-Molina et al., 2015). This modified measure was termed Multiscale Lempel-Ziv complexity (MLZC) and we selected it because of its several advantages over other non-linear measures: namely, it can be applied to short time series and non-stationary and noisy signals. In addition, the MLZC measure allows for the exploration of the signal at different time scales. Previous results have shown that the classical LZC neglects rapid components of the EEG signals (Ibáñez-Molina et al., 2015; Kalev et al., 2015). The Multiscale LZC, however, allows for a better characterization of EEG complexity in different frequency bands. Most rapid components of the EEG signals reflect local functional configurations in the cortex, whereas slow oscillations reflect more long-range cortical interactions (Buzsáki and Draguhn, 2004). However, a word of caution is necessary regarding the causal role of fast and slow rhythms, since slow oscillatory activity could reflect the long-range coordination of faster components or the operation of a single mechanism that generates the specific rhythm. Despite this, the MLZC permits a better characterization of the signal in terms of its oscillatory components and, because it is more sensitive to rapid rhythms, it might serve as a more suitable tool to detect local neural interactions than the classical LZC.

Based on previous results (Li et al., 2008; Takahashi et al., 2010; Fernández et al., 2011), we expected to find higher EEG complexity in patients, compared to controls, in the rest condition. We also hypothesized that complexity would vary in healthy controls while performing the naming task. More interesting, and given that patients with schizophrenia usually show poorer performance in naming tasks (Soriano et al., 2008), we aimed to explore whether their EEG complexity was modulated by the fact of performing the cognitive task. Finally, we aimed to examine through the MLZC whether differences in complexity between patients and controls depend on specific components (slow or rapid) of the EEG signal.

MATERIALS AND METHODS

Participants

The patients group was composed of 18 participants attending the Mental Health Day Hospital of the St Agustín Hospital in Linares. In their clinical record, they were diagnosed with schizophrenia, schizophreniform or schizoaffective disorder according to DSM-IV criteria. The patients' diagnosis was confirmed through a clinical interview performed by the psychiatrist or clinical psychologist in charge of the patient. In addition, the Spanish version (Peralta and Cuesta, 1994) of The Positive and Negative Syndrome Scale (PANSS) (Kay et al., 1987) was used to evaluate patients' current clinical state; and some additional demographic information was obtained (see **Table 1**). At the time of testing, all patients were taking antipsychotic medications with good compliance. All the patients were receiving atypical antipsychotics, usually risperidone, olanzapine, or clozapine. Before participating, they were informed of the task and study and asked to sign informed consent forms in accordance with Ethical Committee of the Hospital.

TABLE 1 | Demographic and clinical characteristics of the study sample means (and standard deviations).

	Patients (*n* = 18)	**Control (*n* = 17)**
Age, years	35.26 (8.96)	29.6 (9.42)
Females	3	6
Education	2.39 (0.21)	2.59 (0.22)
Illness duration, years	13.21 (9.47)	–
GAF	45.44 (17)	–
PANNS		
Positive	14.9 (7.9)	–
Negative	17.16 (6)	–
General	34.05 (8.4)	–

**Groups did not differ significantly on any of the demographic characteristics ($p < 0.05$).*

The control group was composed of 17 healthy adult participants. They were recruited from the family members of the clinical and research staff of the Unit. Care was taken that none of the control participants had a history of psychotic disorders, or family members with psychotic disorders. In addition, none of the participants, control or patients, had a history of substance use disorders, neurological illness, head trauma, or mental retardation. There were no significant differences between patients and controls in age or educational level (see **Table 1**).

The number of participants per group was decided on the basis of the sample sizes considered in previous studies using EEG recordings on schizophrenic patients (e.g., Sabeti et al., 2009; Carlino et al., 2012).

Task

Eighty black and white simple pictures were employed as targets. Three additional pictures were used for practice. The pictures were selected from the norms of Puerta-Melguizo et al. (1998). The order of the pairs was randomized. The STIM^2 software was employed to create the task. Each trial consisted of a sequence of stimuli, which appeared in the center of a computer screen. First, a mask was presented for 500 ms and then the picture target was presented for 100 ms, the mask for another 14 ms, and finally a tone that signaled the participant to respond. Thus, responses were delayed, in order to avoid the influence of vocal movements on the EEG recording. Participants were instructed to look at the center of the screen and to name the pictures as soon as they heard the tone. The experimenter registered the participants' responses. The task took about 10 min.

EEG Recording

EEG data were obtained with a 36 Ag/Ag Cl electrodes cap (QuikCap), and they were recorded with a sampling frequency of 1000 Hz (22 bits). EEG was recorded at rest and while the naming task was being performed. Participants were always seated in a chair opposite the computer screen. A Neuroscan SynAmps 32-channel amplifier was used for data acquisition. EEG data were applied a band-pass filter with cut-off frequencies of 1 and 30 Hz. The reference electrode was the left mastoid. The influence of eye movements on the EEG signal was eliminated through ERPlab. Facial movements were recorded through 4 electrodes and segments that included them were eliminated. EEG segments corresponding to errors in the naming task were also excluded from the analysis. Electrodes impedance was maintained below 5 kΩ for all participants. The rest segments were selected from each participant right before the task with a length of 5×10^4 ms. EEG segments from the task of 2×10^3 ms were extracted after the appearance of each trial. They were selected so that the influence of the verbal responses was not included.

Analyses

Behavioral Data

A response was considered an error when the participants stuttered or hesitated in naming the target, or they misnamed or failed to name the target. We compared error percentages in patients and controls. Naming times were not analyzed, since vocal responses were delayed in order to avoid muscle influences on the EEG recording.

Classical LZC and Multiscale LZC

Lempel-Ziv Complexity measures complexity as defined by Kolmogorov (1965); namely, the number of bits of the shortest computer program that can generate the analyzed time series. Thus, LZC tests the randomness of a sequence by searching for patterns in the series (Lempel and Ziv, 1976). Recent studies have presented it as an effective tool in analyzing biomedical signals (Zozor et al., 2005), and in fact it has been widely used to characterize the EEG of several mental and neurological disorders (Nagarajan, 2002; Aboy et al., 2006). For the present study we employed the classical LZC (LZC_N) and the MLZC measure introduced by Ibáñez-Molina et al. (2015). The original LZC measure estimates the complexity of a time series by a binarization process in which the signal is transformed into a binary sequence by using its median as a threshold. It has been shown that this based-on-median binarization neglects fast components of the EEG signals (Ibáñez-Molina et al., 2015). The MLZC can be seen as a generalization of the original LZC because it uses multiple thresholds for binarization. Thresholds are median-based smoothed versions of the original signals. By increasing the width of the window used for the smoothing, the new versions include less and less fast components. Thus, when used as thresholds for binarization they capture the missing fluctuations in the original series. Hence, this procedure allows us to capture signal variations at different time scales that make it possible to obtain a spectrum of complexity ranging from fast to low rhythms. That is, the MLZC considers both temporal and spectral information from the EEG signals and, consequently, it permits the evaluation of the complexity of the different brain rhythms and the detection of complexity variations in a specific oscillatory band. It is also possible to relate a specific threshold of binarization to a particular frequency band on the basis of the sampling rate of the signal, so that the width of the smoothing procedure can be associated with a particular frequency. Thus, for example, to capture a rhythm of 1 Hz with a sampling rate of 1000 Hz, we need at least a smoothing with a window length of 1000 points.

Formally, a 0-1 sequence $\{p(n)\} = s(1), s(2)...s(N)$, was created by comparison of each data point x(n) in the series with its T_d in the following way:

$$s(n) = \begin{cases} 0 \;\; if \;\; x(n) \;\; < T_{\mathrm{d}} \\ 1 \;\; if \;\; x(n) \;\; \geq T_{\mathrm{d}} \end{cases} \tag{1}$$

The first binary sequence was constructed using the median of the entire signal as T_d (T_{dN}). The other binarizations were created using smoothed versions of the signal as T_ds. Each data point x(n) had an unique T_{dw}(n) which was calculated by:

$$\begin{aligned} T_{\mathrm{dw}}(n) \;&=\; median\;\left(x\left(n - \frac{w_{\mathrm{k}}-1}{2}\right), \ldots., x(n), \ldots, \right. \\ &\qquad \left. x\left(n + \frac{w_{\mathrm{k}}-1}{2}\right)\right), \\ n \;&= 1 + \frac{w_{\mathrm{k}}-1}{2}, \ldots.., N - \frac{w_{\mathrm{k}}-1}{2} \end{aligned} \tag{2}$$

where W = [w_k,. . .,w_m], k = 1,. . .,m is the vector that contains window lengths of the smoothing procedure.

In order to obtain the LZC spectrum of all $\{x(n)\}$, each P_{w}(n) was explored according to the following steps:

(a) EEG segments were analyzed using segments of 2×10^3 ms and averaged for each experimental condition. In the rest condition, long segments (5×10^4 ms) were analyzed using a moving window procedure. The moving window length was 2×10^3 ms with an overlap of 2×10^2 ms. In the task condition, EEG segments were time locked to stimulus onset for each trial. Hence, at task, a total of 80 segments of 2×10^3 ms were analyzed for each participant and then averaged to obtain a final value of MLZC.

(b) LZC was calculated for each window by means of a complexity counter C_{w}(n). During a left to right scan of a given binary sequence, C_{w}(n) increased by one unit every

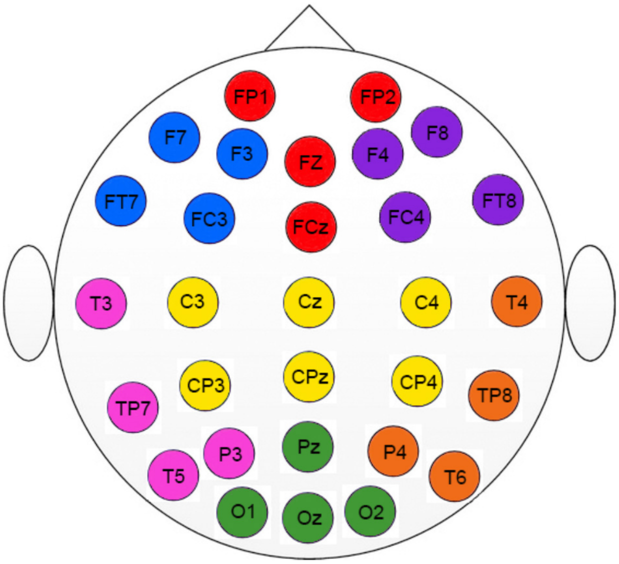

FIGURE 1 | Regions of interest used in the study (ROI). Colors indicate the electrodes for each specific ROI. Left frontal (blue); Frontal (red); Right frontal (purple); Left temporal-parietal (pink); Central (yellow); Right temporal-parietal (orange); Parietal-occipital (green).

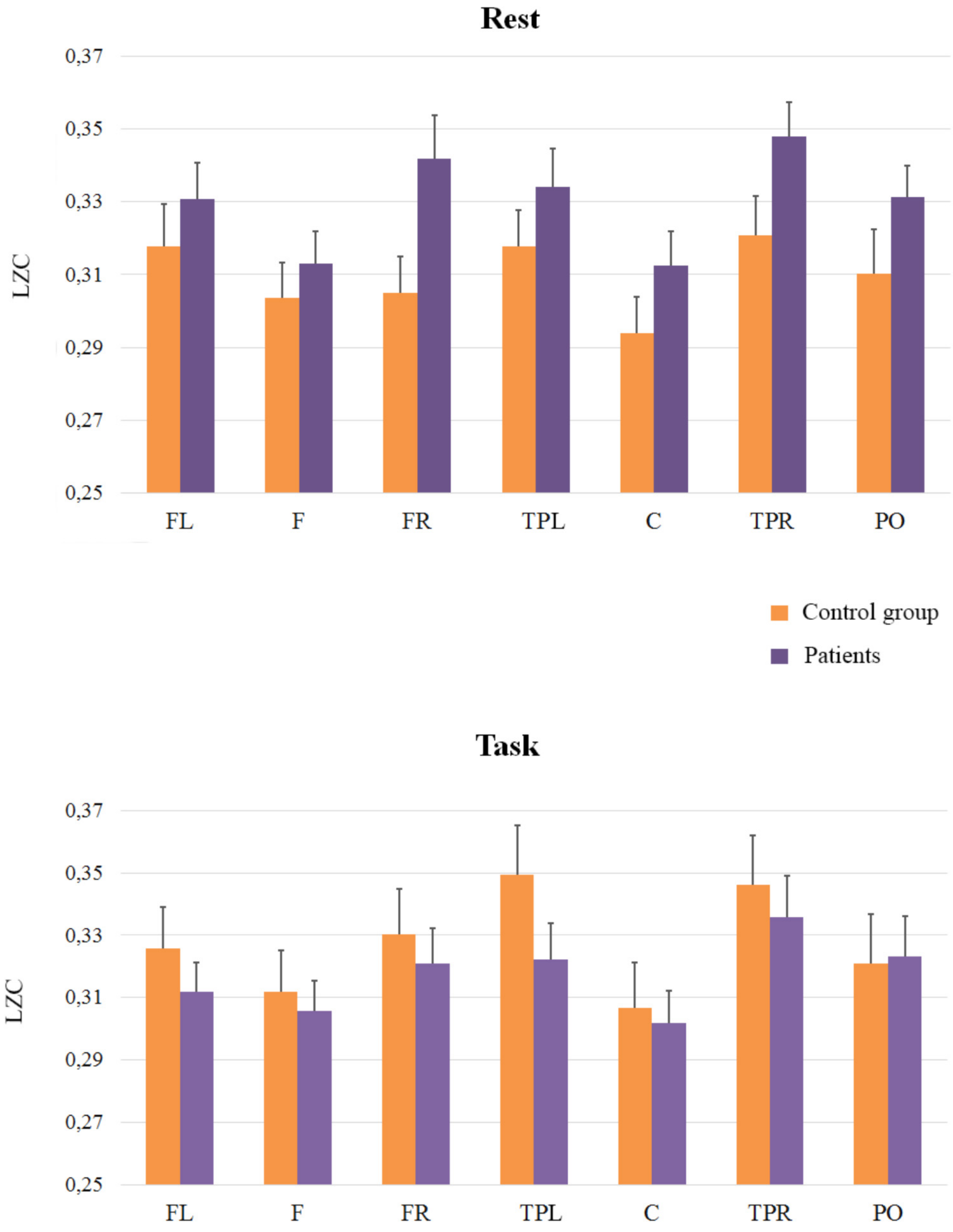

FIGURE 2 | Means and SE (error bars) of Classical LZC for each ROI. Labels in the x-axis indicate each ROI: Left frontal (LF); Frontal (F); Right frontal (RF); Left temporal-parietal (TPL); Central (C); Right temporal-parietal (TPR); Parietal-occipital (PO).

time a new subsequence of consecutive characters was encountered.

(c) Each LZC_w was obtained when $C_w(n)$ values were normalized with

$$LZC = \frac{C_w(n)}{\frac{n}{\log_2 n}} \quad (3)$$

where the sub index w indicates the window length of the smoothing that produced $P_w(n)$. Note that LZC_N will refer to the median based LZC.

(d) The final LZC_w value of each signal was calculated by the average of all values obtained with the moving window procedure.

RESULTS

Analyses of the behavioral accuracy data indicated that patients committed more errors (10%, *SD* = 7.1) than controls (6%, *SD* = 3.4), though the effect only approached to statistical significance [$F(1,33) = 7.47$; $MSE = 73.73$; $p = 0.07$].

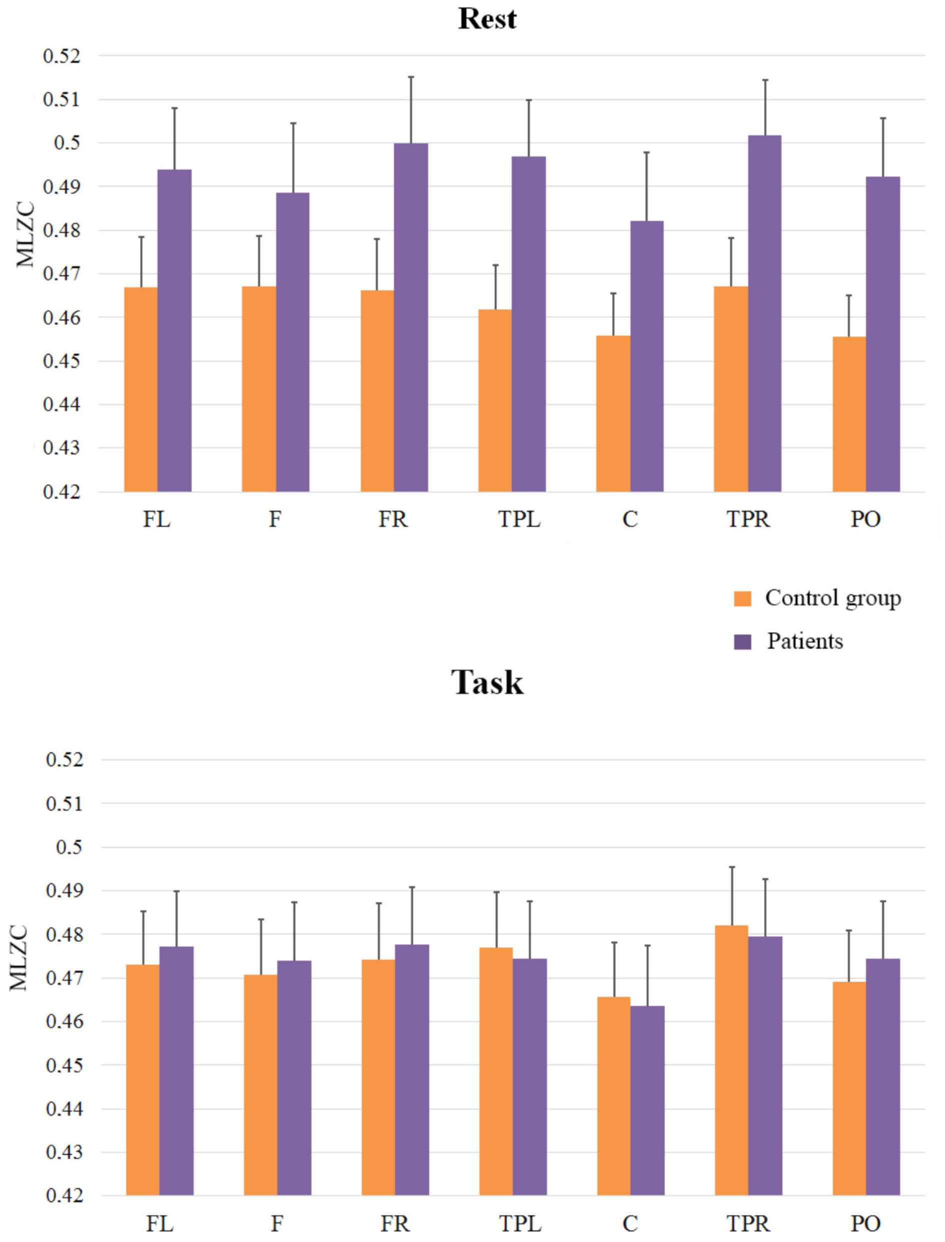

FIGURE 3 | Means and SE (error bars) of fast rhythms MLZC for each ROI. Labels in the x-axis indicate each ROI: Left frontal (LF); Frontal (F); Right frontal (RF); Left temporal-parietal (TPL); Central (C); Right temporal-parietal (TPR); Parietal-occipital (PO).

Regarding electrophysiological data, electrodes were grouped in seven Regions Of Interest (ROI, see **Figure 1**). We conducted three mixed ANOVAs with Group as the between participants factor, and Cognitive State (rest vs. task) and ROI (1: left frontal 2: frontal 3: right frontal 4: left temporal-parietal 5: central 6: right temporal-parietal 7: parietal-occipital, see **Figure 1**), as within-participant variables. Each ANOVA was conducted on a specific range of scales. The first analysis was performed on the classical LZC_N measure (see **Figure 2**). The results of this analysis showed a reliable main effect of ROI, [$F(6,198) = 13.43$; $MSE = 0.001$; $p < 0.01$]; complexity was significantly lower in medial Central and Frontal regions than it was in the rest of regions. The effect of group did not reach statistical significance ($F < 1$). However, more importantly, we found a significant Group × Cognitive State × ROI interaction [$F(6,198) = 2.18$; $MSE = 0.0003$; $p < 0.05$]. In order to examine this second-order interaction, we analyzed separately the effects of ROI and Cognitive State in each group. We found a reliable ROI × Cognitive State interaction in the control group [$F(6,96) = 26.9$; $MSE = 0.0008$; $p < 0.05$], which showed that control participants exhibited greater complexity in Left-Temporal-Parietal regions while performing the task than at

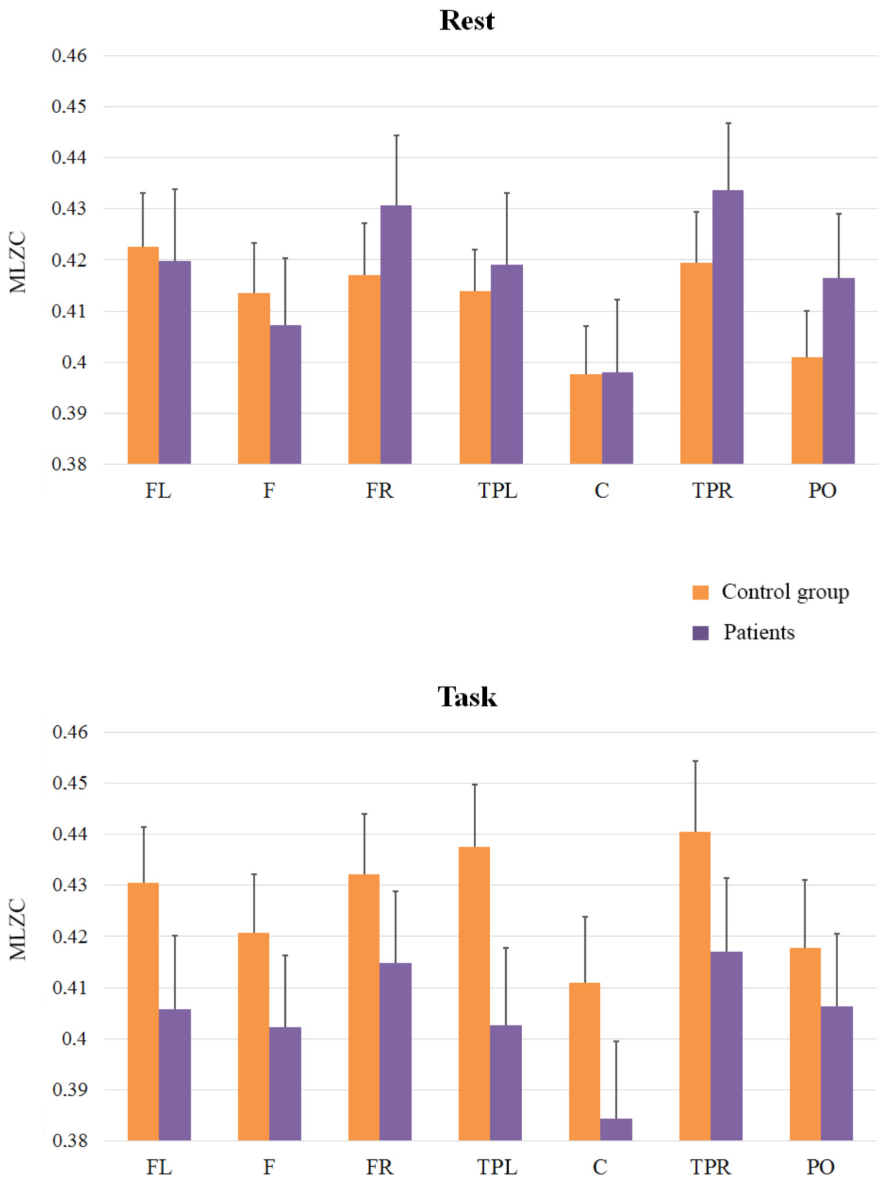

FIGURE 4 | Means and SE (error bars) of slow rhythms MLZC for each ROI. Labels in the x-axis indicate each ROI: Left frontal (LF); Frontal (F); Right frontal (RF); Left temporal-parietal (TPL); Central (C); Right temporal-parietal (TPR); Parietal-occipital (PO).

rest, [$F(1,33) = 6.12$; $MSE = 0.001$, $p < .05$]. On the contrary, the ROI x Cognitive State interaction did not reach statistical significance in patients ($F < 1$): there were no significant differences in complexity between rest and task in the patients group.

In addition, we compared the groups at rest and during task performance: planed comparisons showed that in the rest condition complexity was higher in patients than in controls in Right-Frontal [($F(1,33) = 5.53$; $MSE = 0.002$; $p < 0.05$)] and in Right-Temporal-Parietal regions, even though this latter effect was statistically marginal, [$F(1,33) = 3.53$; $MSE = 0.002$; $p = 0.06$]. During task performance, however, there were no significant differences between patients and controls ($F < 1$).

The second ANOVA was carried out to investigate the complexity of the signals in scales ranging from LZC_{21} to LZC_{101} (frequency bands > 10 Hz), since we aimed to evaluate the complexity predominantly associated with fast rhythms and low amplitudes (See **Figure 3**). As in the previous analysis, the main effect of ROI was reliable [$F(6,198) = 7.25$; $MSE = 0.0003$; $p < 0.051$], and it reflected that complexity was lower in Central Region than in the rest of regions. The effect of Group [$F(1,33) = 1.22$; $MSE = 0.0257$; $p = 0.28$] and the interactions between ROI and Group ($F < 1$), and Cognitive State and Group [$F(1,33) = 2.1$; $MSE = 0.0127$; $p = 0.16$] did not reach significance, but the interaction of Group × Cognitive State x ROI, $F(6,198) = 2.1$; $MSE = 0.0001$;

$p = 0.05$ did. In order to examine this second-order interaction, we analyzed the effects of ROI and Cognitive State in each group. Again, we found a significant ROI × Cognitive State interaction in the control group [$F(6,96) = 2.8$, $MSE = 0.0002$; $p < 0.05$], while the ROI × Cognitive State interaction was not significant in the patients group ($F < 1$). In addition, planned comparisons showed higher levels of complexity in the rest condition for patients than for controls in Left-temporal-parietal [$F(1,33) = 4.41$; $MSE = 0.002$; $p < 0.05$], and Right-temporal-parietal [$F(1,33) = 4.13$; $MSE = 0.002$; $p = 0.05$] sites, while no effects were found in the task condition (all $ps > 0.5$).

The third analysis (see **Figure 4**) was applied to scales from LZC_{121} to LZC_{201} to explore slow rhythms (frequency bands in an approximate range of 5–8 Hz). It revealed a main effect of ROI [$F(6,198) = 15.95$; $MSE = 0.0004$; $p < 0.01$] and a similar pattern of complexity across regions to that found in previous analyses; The effect of Group ($F < 1$), and the interactions between ROI and Group [$F(6,198) = 1.80$; $MSE = 0.0004$; $p = 0.10$], and Cognitive State and Group [$F(1,33) = 2.07$; $MSE = 0.0117$; $p = 0.16$] did not reach significance, but the interaction of Group x Cognitive State x ROI was significant [$F(6,198) = 2.19$; $MSE = 0.0002$; $p < 0.05$]. Interestingly, the pattern of results differed from that of the fast scales, indicating that the complexity of EEG signals was similar in patients and in controls in the rest condition ($F < 1$), but complexity in patients tended to be lower than in control participants in the task condition. Although this tendency did not reach statistical significance, it was marginally significant at the central region [$F(1,33) = 3.18$; $MSE = 0.003$; $p = 0.08$].

Finally, and because the ANOVAs failed to capture the rest to task changes in complexity in patients and controls (see **Figures 2**, **4** in nearly all the regions), we explored this general pattern by categorizing the rest vs. task changes as ‘up’ (Task-Rest > 0) or ‘down’ (Task-Rest ≤ 0), and then performing a non-parametric chi-squared test on each region. The results of this analysis (see **Table 2**) revealed that the differences between the groups in complexity changes from rest to task are especially evident in fast rhythms.

TABLE 2 | Non-parametric analyses of complexity changes from Rest to Task in patients vs. controls on each region of interest.

	LZC_N χ^2 (gl = 1), *p*-value	LZC_{21-101} χ^2 (gl = 1), *p*-value	$LZC_{121-201}$ χ^2 (gl = 1), *p*-value
FL	3.54, 0.06	1.37, 0.24	2.44, 0.12
F	4.80, 0.03*	1.37, 0.24	0.77, 0.38
FR	4.80, 0.03*	3.44, 0.06	1.45, 0.23
TPL	0.31, 0.58	3.73, 0.05	1.70, 0.19
C	0.72, 0.39	6.41, 0.01*	3.73, 0.05
TPR	2.62, 0.10	6.56, 0.01*	0.72, 0.39
PO	0.70, 0.40	4.06, 0.04*	2.91, 0.09

**Groups differed significantly in the Task – Rest qualitative variable ($p < 0.05$). Task vs. Rest complexities were characterized by a categorical variable with the value ‘up’ in the case that the transition from rest to task was positive, and the value ‘down’ if the transition was negative. Differences between the control and patients groups were analyzed for each region of interest by χ^2 tests.*

DISCUSSION

EEG complexity is being increasingly used to explore brain dynamics in healthy and pathological states, since complexity indexes might more adequately reflect the complex, irregular, non-stationary behavior of neural processes than more traditional ERP measures. The present work aimed to explore possible differences in EEG complexity between patients with schizophrenia and controls under conditions involving different cognitive demands. Overall, our results showed two important patterns: (1) patients exhibited higher complexity in frontal regions than control participants at rest; and (2) while control participants showed an increment in complexity from rest to task, there were no reliable differences in complexity between rest and task in the patients group.

Regarding the higher complexity in frontal regions for patients at rest, our findings are in accordance with those from most recent studies with patients with features similar to the ones displayed by our patients’ sample. Thus, although there are some divergent results (Li et al., 2008; Takahashi et al., 2010; Fernández et al., 2011; Akar et al., 2016), higher complexity has been mainly observed in young, drug-naive patients with active symptomatology, whereas lower complexity than controls has been observed in studies with medicated chronic patients (Fernández et al., 2013). Because our patients were recruited from a Mental Health Day Hospital, although they were medicated, most of them were young adults with active psychotic symptoms (see **Table 1**). In addition, higher complexity at rest has also been found in other mental disorders such as depression (Méndez et al., 2012), while lower complexity has been found in Alzheimer Disease (AD) (Jeong, 2004; Stam et al., 2009). As we mentioned, higher complexity values would reflect more and more widely distributed neural nodes oscillating at a lower synchrony. Hence, high complexity in schizophrenia (and other severe mental disorders as depression) could be indicative of isolation or disconnection of brain nodes (Friston et al., 1995) as well as disorganization of spiking activity (Takahashi et al., 2010).

The finding of lower complexity in patients with schizophrenia in some of previous studies could be due to the elevated requirements of some measures (classical measures as D2 and L1 require stationary dynamical systems). Distinct tolerance to noise or requirements related to length of time-series are other variables that could explain the lack of agreement in results. In the context of mental disease, Sabeti et al. (2009) compared the discriminative power of several measures and found that Higuchi fractal dimension, Lempel-Ziv complexity and Entropy indexes were the most informative in discriminating between patients with schizophrenia and controls.

The second and more remarkable finding in the present study is that we observed (with the classical LZC_N measure) an increase in EEG complexity in Left-Temporal-Parietal regions during task performance only in controls, with the group of patients showing comparable complexity at rest and during task performance. Although it had been suggested that changes in complexity during cognitive processing might depend on the specific brain regions involved in the task (Elbert et al., 1994), research regarding this modulation has been scarce. In the present study the cognitive task was a visual naming task. Although it might seem low-demanding at first sight, picture naming involves a number of cognitive processes including visual perception, semantic memory and phonological retrieval (Race and Hillis, 2015). Studies employing functional neuroimaging or lesion data converge in the idea that semantic memory is generally dependent on the left hemisphere, specifically on ventral and lateral regions of the posterior temporal lobe (Chao et al., 1999; Hamberger, 2015; Race and Hillis, 2015). The lack of observable changes in brain complexity during the task in patients was also associated with impairment in performance in the naming task in patients. Together, these findings would support the idea that patients encountered difficulties to adapt their brain functioning to the task demands.

In addition, the use of the MLZC provides relevant data regarding differences in complexity between patients and controls in fast and slow components of the EEG. As we mentioned, the classical LZC neglects rapid components of the EEG signals (Ibáñez-Molina et al., 2015; Kalev et al., 2015). In contrast, the Multiscale LZC, allows for a better characterization of EEG complexity in different frequency bands. A study by Yang et al. (2013) has also spotlighted the importance of frequency bands in the estimation of complexity in AD. In this study, they found that increased severity of AD was associated with decreased MSE complexity as measured by short-time scales, but with increased MSE complexity as measured by long-time scales. In a similar vein, Kalev et al. (2015) have shown that MLZC is able to capture differences in complexity between patients with depression and controls in the high frequency scales, whereas the classical LZC did not differentiate between the groups because it underestimated high frequency components of the EEG signal. Our results also illustrate the value of the MLZC in the estimation of complexity in different frequency bands. While the classical LZC estimate indicated that patients exhibited higher values of complexity at rest in some brain regions, separate analyses for rapid and slow scales pointed to a more complex pattern of results. Specifically, patients showed higher values of complexity during rest only for fast rhythms. On the contrary, control participants tended to present higher values of LZ during the task in slow rhythms. Although the functional meaning of these results is not evident to us, they support the idea that complexity should be separately assessed for different rhythms. To fully understand complexity for rapid and slow oscillatory rhythms, there are two aspects to consider: (1) the more complex a signal is, the more variability it exhibits, and (2) while the variability for fast rhythms reflects local functional configurations in the cortex, for slow oscillations complexity captures more long-range cortical interactions (Buzsáki and Draguhn, 2004). Hence, one could speculate that fast oscillations reflecting local dynamics of neuronal assemblies are more heterogeneous for patients at rest. This might result from an irregular by-default functioning at a local level. On the contrary, the higher complexity of the slow rhythms in controls might result from a more flexible establishment and switching between a large variety of long range cortical interactions directed to adapt themselves to the task at hand. Finally, the non-parametric analyses of rest-task changes showed that differences between patients and controls from rest to task were especially evident in fast frequencies, which is in line with the findings by Kalev et al. (2015) in depression. These results could be indicating that differences between patients and controls in cognitive functioning would rely more on local neural configurations than on the dynamics of whole-brain networks. The fact that the non-parametric analyses revealed differences between patients and controls in parietal and occipital electrode locations in fast scales, could be interpreted as reflecting abnormal processing in primary visual areas. This finding is in line with experiments showing that schizophrenic patients exhibit abnormal beta-gamma induced rhythm during visual perception (Uhlhaas et al., 2006; Uhlhaas and Singer, 2010; Grützner et al., 2013). However, we should note that this explanation is tentative and the present results are novel and need replication.

Some limitations of the study need to be considered. First, and most important, the small sample prevented us from analyzing the relationship between demographic and symptomatic characteristics of patients and EEG complexity. As previously mentioned, age and symptomatology influence complexity measures (Fernández et al., 2013). Second, all patients were on antipsychotic treatment, which could have impacted on their EEG patterns. Finally, we evaluated brain complexity of participants while performing a naming task. Cognitive tasks vary in a number of variables: processing system (attention, language, memory...), perceptual domain (visual, auditory. . .), and difficulty, among others. Therefore, it would be highly speculative to extrapolate results from a visual naming task to other cognitive tasks. Future research should address how changes in brain complexity are modulated by cognitive demands.

ETHICS STATEMENT

This study was carried out in accordance with the ethical standards of the research committee of St Agustin Hospital and with the 1964 Helsinki declaration. The protocol was approved by the committee of St Agustin Hospital and all subjects gave written informed consent.

AUTHOR CONTRIBUTIONS

MS, MB, JA, CG-A, and AI-M made a substantial, direct and intellectual contribution to the main hypothesis and design of the experiment. VL and AI-M conducted the experiment and analyzed the EEG data sets. All authors participated in the preparation of the manuscript.

FUNDING

This research was supported by Junta de Andalucía (Biomedical and Health Science Research Project PI-0410-2014 to MS and PI-0386-2016 to S. Iglesias-Parro); and Ministerio de Economía, industria y competitividad (PSI2015-65502-C2-1-P to MB and PSI2015-65502-C2-2-P to CG-A).

REFERENCES

Aboy, M., Hornero, R., Abásolo, D., and Álvarez, D. (2006). Interpretation of the Lempel-Ziv complexity measure in the context of biomedical signal analysis. *IEEE Trans. Biomed. Eng.* 53, 2282–2288. doi: 10.1109/TBME.2006.883696

Addington, J., Brookes, B. L., and Addington, D. (2003). Cognitive functioning in first episode psychosis: initial presentation. *Schizophr. Res.* 62, 59–64. doi: 10.1016/S0920-9964(02)00340-7

Akar, S. A., Kara, S., Latifoğlu, F., and Bilgi, V. (2016). Analysis of the complexity measures in the EEG of schizophrenia patients. *Int. J. Neural Syst.* 26: 1650008. doi: 10.1142/S0129065716500088

Bachiller, A., Díez, A., Suazo, V., Domínguez, C., Ayuso, M., Hornero, R., et al. (2014). Decreased spectral entropy modulation in patients with schizophrenia during a P300 task. *Eur. Arch. Psychiatry Clin. Neurosci.* 264, 533–543. doi: 10.1007/s00406-014-0488-6

Buzsáki, G., and Draguhn, A. (2004). Neuronal oscillations in cortical networks. *Science* 304, 1926–1929. doi: 10.1126/science.1099745

Carlino, E., Sigaudo, M., Pollo, A., Benedetti, F., Mongini, T., Castagna, F., et al. (2012). Nonlinear analysis of electroencephalogram at rest and during cognitive tasks in patients with schizophrenia. *J. Psychiatry Neurosci.* 37, 259–266. doi: 10.1503/jpn.110030

Chao, L. L., Haxby, J. V., and Martin, A. (1999). Attribute-based neural substrates in temporal cortex for perceiving and knowing about objects. *Nat. Neurosci.* 2, 913–919. doi: 10.1038/13217

Cohen, J. D., and Servan-Schreiber, D. (1992). Context, Cortex, and dopamine: a connectionist approach to behavior and biology in schizophrenia. *Psychol. Rev.* 99, 45–77. doi: 10.1037/0033-295X.99.1.45

Elbert, T., Ray, W. J., Kowalik, Z. J., Skinner, J. E., Graf, K. E., and Birbaumer, N. (1994). Chaos and physiology: deterministic chaos in excitable cell assemblies. *Physiol. Rev.* 74, 1–47. doi: 10.1152/physrev.1994.74.1.1

Engel, A. K., Fries, P., and Singer, W. (2001). Dynamic predictions: oscillations and synchrony in top–down processing. *Nat. Rev. Neurosci.* 2, 704–716. doi: 10.1038/35094565

Escudero, J., Ibáñez-Molina, A., and Iglesias-Parro, S. (2015). "Effect of the average delay and mean connectivity of the Kuramoto model on the complexity of the output electroencephalograms," in *Proceedings of the Annual International Conference of the IEEE Engineering in Medicine and Biology Society*, (Piscataway, NJ: IEEE), 7873–7876. doi: 10.1109/EMBC.2015.7320217

Fernández, A., Gómez, C., Homero, R., and López-Ibor, J. J. (2013). Complexity and schizophrenia. *Prog. Neuropsychopharmacol. Biol. Psychiatry* 45, 267–276. doi: 10.1016/j.pnpbp.2012.03.015

Fernández, A., López-Ibor, M. I., Turrero, A., Santos, J. M., Morón, M. D., Hornero, R., et al. (2011). Lempel-Ziv complexity in schizophrenia: a MEG study. *Clin. Neurophysiol.* 122, 2227–2235. doi: 10.1016/j.clinph.2011.04.011

Fries, P. (2005). A mechanism for cognitive dynamics: neuronal communication through neuronal coherence. *Trends Cogn. Sci.* 9, 474–480. doi: 10.1016/j.tics.2005.08.011

Friston, K. J., Tononi, G., Sporns, O., and Edelman, G. M. (1995). Characterising the complexity of neuronal interactions. *Hum. Brain Mapp.* 3, 302–314. doi: 10.1002/hbm.460030405

Ghanbari, Y., Bloy, L., Edgar, J. C., Blaskey, L., Verma, R., and Roberts, T. P. L. (2015). Joint analysis of band-specific functional connectivity and signal complexity in autism. *J. Autism Dev. Disord.* 45, 444–460. doi: 10.1007/s10803-013-1915-7

Goldberger, A. L., Peng, C. K., and Lipsitz, L. A. (2002). What is physiologic complexity and how does it change with aging and disease? *Neurobiol. Aging* 23, 23–26. doi: 10.1016/S0197-4580(01)00266-4

Goldman-Rakic, P. S. (1994). Working memory dysfunction in schizophrenia. *J. Neuropsychiatry Clin. Neurosci.* 6, 348–357. doi: 10.1176/jnp.6.4.348

Grützner, C., Wibral, M., Sun, L., Rivolta, D., Singer, W., Maurer, K., et al. (2013). Deficits in high-(> 60 Hz) gamma-band oscillations during visual processing in schizophrenia. *Front. Hum. Neurosci.* 7:88. doi: 10.3389/fnhum.2013.00088

Hamberger, M. J. (2015). Object naming in epilepsy and epilepsy surgery. *Epilepsy Behav.* 46, 27–33. doi: 10.1016/j.yebeh.2014.12.019

Heinrichs, R. W., and Zakzanis, K. K. (1998). Neurocognitive deficit in schizophrenia: a quantitative review of the evidence. *Neuropsychology* 12, 426–445. doi: 10.1037/0894-4105.12.3.426

Hoffmann, R. E., Buchsbaum, M. S., Jensen, R. V., Guich, S. M., Tsai, K., and Nuechterlein, K. H. (1996). Dimensional complexity of EEG waveforms in neuroleptic-free schizophrenic patients and normal control subjects. *J. Neuropsychiatry Clin. Neurosci.* 8, 436–441. doi: 10.1176/jnp.8.4.436

Hughes, J. R., and John, E. R. (1999). Conventional and quantitative electroencephalography in psychiatry. *J. Neuropsychiatry Clin. Neurosci.* 11, 190–208. doi: 10.1176/jnp.11.2.190

Hughes, M. E., Fulham, W. R., Johnston, P. J., and Michie, P. T. (2012). Stop-signal response inhibition in schizophrenia: behavioural, event-related potential and functional neuroimaging data. *Biol. Psychol.* 89, 220–231. doi: 10.1016/j.biopsycho.2011.10.013

Ibáñez-Molina, A., Iglesias-Parro, S., Soriano, M. F., and Aznarte, J. I. (2015). Multiscale Lempel-ziv complexity for EEG measures. *Clin. Neurophysiol.* 126, 541–548. doi: 10.1016/j.clinph.2014.07.012

Ibáñez-Molina, A. J., and Iglesias-Parro, S. (2014). Fractal characterization of internally and externally generated conscious experiences. *Brain Cogn.* 87, 69–75. doi: 10.1016/j.bandc.2014.03.002

Ibáñez-Molina, A. J., Iglesias-Parro, S., and Escudero, J. (2018). Differential effects of simulated cortical network lesions on synchrony and EEG complexity. *Int. J. Neural Syst.* doi: 10.1142/S0129065718500247 [Epub ahead of print].

Jeong, J. (2004). EEG dynamics in patients with Alzheimer's disease. *Clin. Neurophysiol.* 115, 1490–1505. doi: 10.1016/j.clinph.2004.01.001

Jonides, J., and Nee, D. E. (2005). Assessing dysfunction using refined cognitive methods. *Schizophr. Bull.* 31, 823–829. doi: 10.1093/schbul/sbi053

Kalev, K., Bachmann, M., Orgo, L., Lass, J., and Hinrikus, H. (2015). Lempel-Ziv and multiscale Lempel-Ziv complexity in depression. *Conf. Proc. IEEE Eng. Med. Biol. Soc.* 2015, 4158–4161. doi: 10.1109/EMBC.2015.7319310

Kay, S. R., Fiszbein, A., and Opler, L. A. (1987). The positive and negative syndrome scale PANSS for schizophrenia. *Schizophr. Bull.* 13, 261–276. doi: 10.1093/schbul/13.2.261

Kerns, J. G., and Berenbaum, H. (2002). Cognitive Impairments associated with formal thought disorder in people with schizophrenia. *J. Abnorm. Psychol.* 111, 211–224. doi: 10.1037/0021-843X.111.2.211

Kiang, M., Kutas, M., Light, G. A., and Braff, D. L. (2007). Electrophysiological insights into conceptual disorganization in schizophrenia. *Schizophr. Res.* 92, 225–236. doi: 10.1016/j.schres.2007.02.001

Kirsch, P., Besthorm, C., Klein, S., Rindfleisch, J., and Olbrich, R. (2000). The dimensional complexity of the EEG during cognitive tasks reflects the impaired information processing in schizophrenic patients. *Int. J. Psychophysiol.* 36, 237–246. doi: 10.1016/S0167-8760(00)00077-5

Klonowsky, W. (2009). Everything you wanted to ask about EEG but were afraid to get the right answer. *Nonlinear Biomed. Phys.* 3, 1–5. doi: 10.1186/1753-4631-3-2

Kolmogorov, A. N. (1965). Three approaches to the quantitative definition of information. *Probl. Inf. Transm.* 1, 1–7.

Lee, Y. J., Zhu, Y. S., Xu, Y. H., Shen, M. F., Zhang, H. X., and Thakor, N. V. (2001). Detection of non-linearity in the EEG of schizophrenic patients. *Clin. Neurophysiol.* 112, 1288–1294. doi: 10.1016/S1388-2457(01)00544-2

Lempel, A., and Ziv, J. (1976). On the complexity of finite sequences. *IEEE Trans. Inf. Theory* 22, 75–81. doi: 10.1109/TIT.1976.1055501

Li, Y., Tong, S., Liu, D., Gai, Y., Wang, X., Wang, J., et al. (2008). Abnormal EEG complexity in patients with schizophrenia and depression. *Clin. Neurophysiol.* 119, 1232–1241. doi: 10.1016/j.clinph.2008.01.104

Lutzenberger, W., Preissl, H., and Pulvermüller, F. (1995). Fractal dimension of electroencephalographic time series and underlying brain processes. *Biol. Cybern.* 73, 477–482. doi: 10.1007/BF00201482

Manschreck, T. C., Maher, B. A., Milavetw, J. J., Ames, D., Weisstern, C. C., and Schneyer, M. K. (1988). Semantic priming in thought disordered schizophrenic patients. *Schizophr. Res.* 1, 61–66. doi: 10.1016/0920-9964(88)90041-2

Méndez, M. A., Zuluaga, P., Hornero, R., Gomez, C., Escudero, J., Rodriguez-Palancas, A., et al. (2012). Complexity analysis of spontaneous brain activity: effects of depression and antidepressant treatment. *J. Psychopharmacol.* 26, 636–643. doi: 10.1177/0269881111408966

Mölle, M., Marshall, L., Wolf, B., Fehm, H. L., and Born, J. (1999). EEG complexity and performance measures of creative thinking. *Psychophysiology* 36, 95–104. doi: 10.1017/S0048577299961619

Nagarajan, R. (2002). Quantifying physiological data with Lempel-Ziv complexity - certain issues. *IEEE Trans. Biomed. Eng.* 49, 1371–1373. doi: 10.1109/TBME.2002.804582

Peralta, V., and Cuesta, M. J. (1994). Psychometric properties of the positive and negative syndrome scale PANSS in schizophrenia. *Psychiatry Res.* 53, 31–40. doi: 10.1016/0165-1781(94)90093-0

Pereda, E., Quian Quiroga, R., and Bhattacharya, B. (2005). Nonlinear multivariate analysis of neurophysiological signals. *Prog. Neurobiol.* 77, 1–37. doi: 10.1016/j.pneurobio.2005.10.003

Puerta-Melguizo, M. C., Bajo, M. T., and Gómez-Ariza, C. J. (1998). Competidores semánticos: estudio normativo de un conjunto de 518 pares de conceptos [Semantic Competitors: normative Study of a set of 518 pairs of concepts]. *Psicologica* 19, 321–343.

Race, D. S., and Hillis, A. B. (2015). Naming. Reference module in neuroscience and biobehavioral psychology. *Hum. Brain Mapp.* 3, 455–459. doi: 10.1016/B978-0-12-397025-1.00267-0

Radhakrishnan, N., and Gangadhar, B. N. (1998). Estimating regularity in epileptic seizure time series data—a complexity measure approach. *IEEE Eng. Med. Biol. Mag.* 17, 89–94. doi: 10.1109/51.677174

Sabeti, M., Katebi, S., and Boostani, R. (2009). Entropy and complexity measures for EEG signal classification of schizophrenic and control participants. *Artif. Intell. Med.* 47, 263–274. doi: 10.1016/j.artmed.2009.03.003

Sohn, H., Kim, I., Lee, W., Peterson, B. S., Hong, H., Chae, J. H., et al. (2010). Linear and non-linear EEG analysis of adolescents with attention-deficit/hyperactivity disorder during a cognitive task. *Clin. Neurophysiol.* 121, 1863–1870. doi: 10.1016/j.clinph.2010.04.007

Soriano, M. F., Jiménez, J. F., Román, P., and Bajo, M. T. (2008). Cognitive substrates in semantic memory of formal thought disorder in schizophrenia. *J. Clin. Exp. Neuropsychol.* 30, 70–82. doi: 10.1080/13803390701220011

Stam, C. J. (2005). Nonlinear dynamical analysis of EEG and MEG: review of an emerging field. *Clin. Neurophysiol.* 116, 2266–2301. doi: 10.1016/j.clinph.2005.06.011

Stam, C. J., de Haan, W., Daffertshofer, A., Jones, B. F., Manshanden, I., Walsum, A. M., et al. (2009). Graph theoretical analysis of magnetoencephalographic functional connectivity in Alzheimer's disease. *Brain* 132, 213–224. doi: 10.1093/brain/awn262

Takahashi, T., Cho, R. Y., Mizuno, T., Kikuchi, M., Murata, T., Takahashi, K., et al. (2010). Antipsychotics reverse abnormal EEG complexity in drug-naïve schizophrenia: a multiscale entropy analysis. *Neuroimage* 51, 173–182. doi: 10.1016/j.neuroimage.2010.02.009

Tononi, G., and Edelman, G. M. (1998). Consciousness and complexity. *Science* 282, 1846–1851. doi: 10.1126/science.282.5395.1846

Uhlhaas, P. J., Linden, D. E., Singer, W., Haenschel, C., Lindner, M., Maurer, K., et al. (2006). Dysfunctional long-range coordination of neural activity during Gestalt perception in schizophrenia. *J. Neurosci.* 26, 8168–8175. doi: 10.1523/JNEUROSCI.2002-06.2006

Uhlhaas, P. J., and Singer, W. (2010). Abnormal neural oscillations and synchrony in schizophrenia. *Nat. Rev. Neurosci.* 11, 100–113. doi: 10.1038/nrn2774

Yang, A. C., Hong, C. J., Liou, Y. J., Huang, K. L., Huang, C. C., Liu, M. E., et al. (2015). Decreased resting-state brain activity complexity in schizophrenia characterized by both increased regularity and randomness. *Hum. Brain Mapp.* 36, 2174–2186. doi: 10.1002/hbm.22763

Yang, A. C., and Tsai, S.-J. (2013). Is mental illness complex? From behavior to brain. *Prog. Neuropsychopharmacol. Biol. Psychiatry* 45, 253–257. doi: 10.1016/j.pnpbp.2012.09.015

Yang, A. C., Wang, S.-J., Lai, K.-L., Tsai, C.-F., Yang, C.-J., Hwang, J.-P., et al. (2013). Cognitive and neuropsychiatric correlates of EEG dynamic complexity in patients with Alzheimer's disease. *Prog. Neuropsychopharmacol. Biol. Psychiatry* 47, 52–61. doi: 10.1016/j.pnpbp.2013.07.022

Zozor, S., Ravier, P., and Buttelli, O. (2005). On Lempel-Ziv complexity for multidimensional data analysis. *Physica A* 345, 285–302. doi: 10.1371/journal.pone.0032239

Conflict of Interest Statement: The authors declare that the research was conducted in the absence of any commercial or financial relationships that could be construed as a potential conflict of interest.

Copyright © 2018 Ibáñez-Molina, Lozano, Soriano, Aznarte, Gómez-Ariza and Bajo. This is an open-access article distributed under the terms of the Creative Commons Attribution License (CC BY). The use, distribution or reproduction in other forums is permitted, provided the original author(s) and the copyright owner(s) are credited and that the original publication in this journal is cited, in accordance with accepted academic practice. No use, distribution or reproduction is permitted which does not comply with these terms.

frontiers
in Physiology

ORIGINAL RESEARCH
published: 29 October 2018
doi: 10.3389/fphys.2018.01511

Long-Range Temporal Correlations of Patients in Minimally Conscious State Modulated by Spinal Cord Stimulation

Zhenhu Liang[1], Jiani Li[1], Xiaoyu Xia[2], Yong Wang[1], Xiaoli Li[3], Jianghong He[2] and Yang Bai[4]**

[1] Institute of Electrical Engineering, Yanshan University, Qinhuangdao, China, [2] Department of Neurosurgery, PLA Army General Hospital, Beijing, China, [3] State Key Laboratory of Cognitive Neuroscience and Learning and IDG/McGovern Institute for Brain Research, Beijing Normal University, Beijing, China, [4] Department of Basic Medical Science, School of Medicine, Hangzhou Normal University, Hangzhou, China

Spinal cord stimulation (SCS) has been shown to improve the consciousness levels of patients with disorder of consciousness (DOC). However, the underlying mechanisms of SCS remain poorly understood. This study recorded resting-state electroencephalograms (EEG) from 16 patients with minimally conscious state (MCS), before and after SCS, and investigated the mechanisms of SCS on the neuronal dynamics in MCS patients. Detrended fluctuation analysis (DFA), combined with surrogate data method, was employed to measure the long-range temporal correlations (LRTCs) of the EEG signals. A surrogate data method was utilized to acquire the genuine DFA exponents (GDFAE) reflecting the genuine LRTCs of brain activity. We analyzed the GDFAE in four brain regions (frontal, central, posterior, and occipital) at five EEG frequency bands [delta (1–4 Hz), theta (4–8 Hz), alpha (8–13 Hz), beta (13–30 Hz), and gamma (30–45 Hz)]. The GDFAE values ranged from 0.5 to 1, and showed temporal and spatial variation between the pre-SCS and the post-SCS states. We found that the channels with GDFAE spread wider after SCS. This phenomenon may indicate that more cortical areas were engaged in the information integration after SCS. In addition, the GDFAE values increased significantly in the frontal area at delta, theta, and alpha bands after SCS. At the theta band, a significant increase in GDFAE was observed in the occipital area. No significant change was found at beta or gamma bands in any brain region. These findings show that the enhanced LRTCs after SCS occurred primarily at low-frequency bands in the frontal and occipital regions. As the LRTCs reflect the long-range temporal integration of EEG signals, our results indicate that information integration became more "complex" after SCS. We concluded that the brain activities at low-frequency oscillations, particularly in the frontal and occipital regions, were improved by SCS.

Keywords: spinal cord stimulation, minimally conscious state, electroencephalogram, long-range temporal correlations, detrended fluctuation analysis

OPEN ACCESS

Edited by:
Srdjan Kesić,
University of Belgrade, Serbia

Reviewed by:
Oren Shriki,
Ben-Gurion University of the Negev, Israel
Gonzalo Marcelo Ramírez-Avila,
Universidad Mayor de San Andrés, Bolivia

****Correspondence:***
Jianghong He
he_jianghong@yeah.net
Yang Bai
baiyang@hznu.edu.cn

Specialty section:
This article was submitted to Fractal Physiology, a section of the journal Frontiers in Physiology

Received: *07 May 2018*
Accepted: *08 October 2018*
Published: *29 October 2018*

Citation:
Liang Z, Li J, Xia X, Wang Y, Li X, He J and Bai Y (2018) Long-Range Temporal Correlations of Patients in Minimally Conscious State Modulated by Spinal Cord Stimulation. Front. Physiol. 9:1511. doi: 10.3389/fphys.2018.01511

INTRODUCTION

Disorder of consciousness (DOC) is a state of prolonged altered consciousness (Eapen et al., 2016). Patients with DOC can be subdivided into minimally conscious state (MCS) and vegetative state (VS) according to their behavioral signs of awareness. Patients with MCS show inconsistent, but discernible signs of consciousness such as command-following or other purposeful behaviors (Giacino et al., 2002).

It has been suggested that spinal cord stimulation (SCS) is an effective brain intervention technique for patients with MCS (Georgiopoulos et al., 2010; Mattogno et al., 2017). SCS has several advantages over deep brain stimulation such as its simplicity, its lesser degree of invasiveness, and its programmable parameters (Bai et al., 2017a). To date, the underlying mechanisms of SCS and its effects on neural responsiveness remain poorly understood (Visocchi et al., 2001; Yamamoto et al., 2012). The effects of SCS in MCS patients can be assessed by several electroencephalography (EEG) measurements (Bai et al., 2017a,b) including entropies, detrended fluctuation analysis (DFA) (D'Rozario et al., 2013), neuronal oscillation coupling (Köster et al., 2014), and integrated information based features (Gallimore, 2015). Entropy is an important measure of both the randomness and the disorder of a dynamic system (Carhart-Harris et al., 2014). Both sample entropy and permutation entropy have been shown to be effective at distinguishing states of consciousness (i.e., wakefulness, deep sevoflurane, and isoflurane anesthesia) (Wang et al., 2014; Liang et al., 2015). Approximate entropy has been found to decrease during the transition from wakefulness to sleep. During wakefulness, it has been shown to be higher in adults than in children (Lee et al., 2013). The coupling strength of narrow-band neuronal oscillations in brain networks has also been shown to be correlated with consciousness (Buzsaki and Draguhn, 2004). Previous studies have suggested that the synchronization of neuronal oscillations is correlated with sensory, motor, and cognitive events (Varela et al., 2001; Jacobs and Kahana, 2010). Based on the synchronization phenomenon in neuronal activities, many measures, such as phase-amplitude coupling, coherence, and phase synchronization, have been proposed for consciousness assessment (Liang et al., 2016; Bai et al., 2017b; Pal et al., 2017). Our previous study has suggested that bicoherence, global synchronization (Bai et al., 2017a), as well as global and local networks (Bai et al., 2017b), can be altered by SCS with 70 Hz in MCS patients.

In addition to the features mentioned above, it has also been hypothesized that consciousness emerges from the critical state of brain activity. The hierarchy of long-range temporal correlations (LRTCs) implies the long-term memory of a brain system (Zhang et al., 2018). In the temporo-spatial theory of consciousness (TTC), LRTCs are postulated to be a core mechanism of consciousness (Northoff and Huang, 2017). They exist in "scale-free" systems based on fractal theory (Richard et al., 2012). "Scale-free" systems involve two phenomena: self-similarity and self-affinity. Self-similarity means that a small part of the fractal structure is similar to the entire structure, while self-affinity indicates that the properties of a fractal scale are different along various dimensions (Mandelbrot, 1999). These two phenomena cannot be easily characterized by their respective means and standard deviations (Eke et al., 2000). Therefore, "scale-free" systems can only be measured by the power–law function, with only a mathematical function, without a typical scale (Richard et al., 2012). Accordingly, DFA is widely used to analyze the scale-free time series (Palva et al., 2013) with three correlation properties of the signals: (1) uncorrelated scaling (DFA > 1), correlated scaling ($0.5 <$ DFA < 1), and anti-correlated scaling ($0 <$ DFA < 0.5) (Hu et al., 2001). The correlated scaling ($0.5 <$ DFA < 1), also known as LRTC, indicates long-range temporal dependency characteristics of the time series. Many studies have investigated the LRTCs of the neural signals under general anesthesia (Krzeminski et al., 2017; Zhang et al., 2018), during sleep (Tagliazucchi et al., 2013; Allegrini et al., 2015), and in states of self-consciousness (Huang et al., 2016). These studies have found that the brain dynamics present robust LRTCs during conscious states. Whereas, the LRTCs are disrupted during unconscious states. Given that the LRTCs can reflect complex neural information processing, we hypothesize that the effect of SCS can be measured by LRTCs in the long-range temporal dependency framework. Based on this hypothesis, this study combines the DFA and the surrogate data method to measure the genuine LRTCs. We then investigate the temporo-spatial changes of genuine LRTCs of the EEG signals in MCS patients during SCS.

MATERIALS AND METHODS

Subjects

The eligibility criteria for the subjects were: (1) patients had been diagnosed as MCS by the JFK Coma Recovery Scale-Revised (CRS-R) (Kalmar and Giacino, 2005); (2) patients were in stable clinical states; and (3) there were no confounding complications (e.g., infections). This study was approved by the ethics committee of the PLA Army General Hospital. Informed consent to participate in the study was obtained from legal representatives of the patients.

Data Recording and Preprocessing

EEG recording was conducted at least 3 weeks after the SCS surgical procedure. Treatments other than SCS that could modify neural excitability were avoided during EEG recording. The SCS stimulation protocol follows our previous study (Bai et al., 2017a), summarized as follows: The SCS stimulator (Prime Advanced, Medtronic Inc., Minneapolis, MN, United States) was placed under the anterior chest wall. The stimulation frequency was set at 70 Hz, based on clinical experience. The amplitude and duration of the pulses were 3 V and 210 μs, respectively. The stimulator produced a periodic voltage difference between the two stimulation electrodes, with a duration of 20 min. The electrodes sent pulses to stimulate the specific level of the spinal cord. All subjects were in the supine position, and in a wakeful state, throughout the study. If the subjects showed to be in a sleep state (i.e., prolonged eye closure or sleep waveforms, such as spindles or K-complex waves appearing in the EEG), the study would be paused. The JFK CRS-R arousal facilitation protocol would then be performed to arouse the subjects.

A 10 min EEG was recorded both before and after SCS. A 32-channel EEG cap (BrainAmp 64 MRplus, Brain Products, Germany) with Ag/AgCl electrodes was used for EEG recording. Electrode positioning was based on the international 10–20 electrode placement system, as shown in **Figure 1**. The sampling rate of the system was 1 kHz. A conductive EEG gel was used to remove cutin and oil from subjects' scalps. The electrode–skin impedance of subjects was decreased to less than 5 kΩ before the recording.

The EEG signal preprocessing was conducted with EEGLAB (version 12.0.2.5b) in a MATLAB environment (Version, 2014a, MathWorks Inc.; Natick, MA, United States). Continuous data segments with significant noise were rejected based on visual inspection. The 50 Hz power frequency artifact was removed by the notch filter. The EEG data was filtered into 1–45 Hz and downsampled to 100 Hz using symmetric finite impulse response filters (MATLAB function firls.m) and the MATLAB function *resample.m*, respectively. The relevant components of the artifacts, such as eye movements and muscle activities, were identified and removed by the independent component analysis function in EEGLAB. After pre-processing, the EEG signals were divided into five frequency bands: delta (1–4 Hz), theta (4–8 Hz), alpha (8–13 Hz), beta (13–30 Hz), and gamma (30–45 Hz).

Genuine DFA Exponent (GDFAE)

We combined the DFA and the surrogate data method to evaluate the effect of SCS at different oscillation bands. DFA is a classic measure of the LRTCs of EEG activity (Peng et al., 1995). It quantifies the fluctuations of a time series based on the power-law method. DFA can systematically remove the trend of each order from the data. Thus, it has a robust effect against noise. The surrogate data method has been widely applied to constrain spurious detection in non-linear analysis (Dolan and Spano, 2001). In this study, surrogate data tests were utilized to acquire the GDFAEto reflect the genuine LRTCs of brain activities. The flow chart of the algorithm and the step-by-step results are shown in **Figures 2**, **3**, respectively.

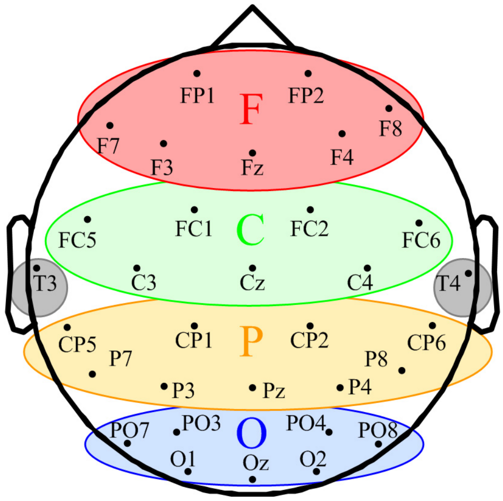

FIGURE 1 | Schematic of space participation of five regions for 32-channel EEG. The seven channels in the red ellipse constituted the frontal region (F). The seven channels in the green ellipse were divided into the central region (C). The yellow ellipse comprised nine channels represents the parietal region (P). The blue ellipse comprised nine channels represents the occipital region (O). T3 and T4 in the gray circles were classified into the temporal region.

The GDFAE can be obtained in three steps. The detailed process is as follows:

Step 1: Calculating the original DFA exponent of the EEG data.

(1) Remove the mean value x_{ave} of the amplitude envelope of the EEG time series $x(t)$ to obtain a series independent of the global linear trend. The cumulative sum of the detrended amplitude $y(k)$ is calculated as:

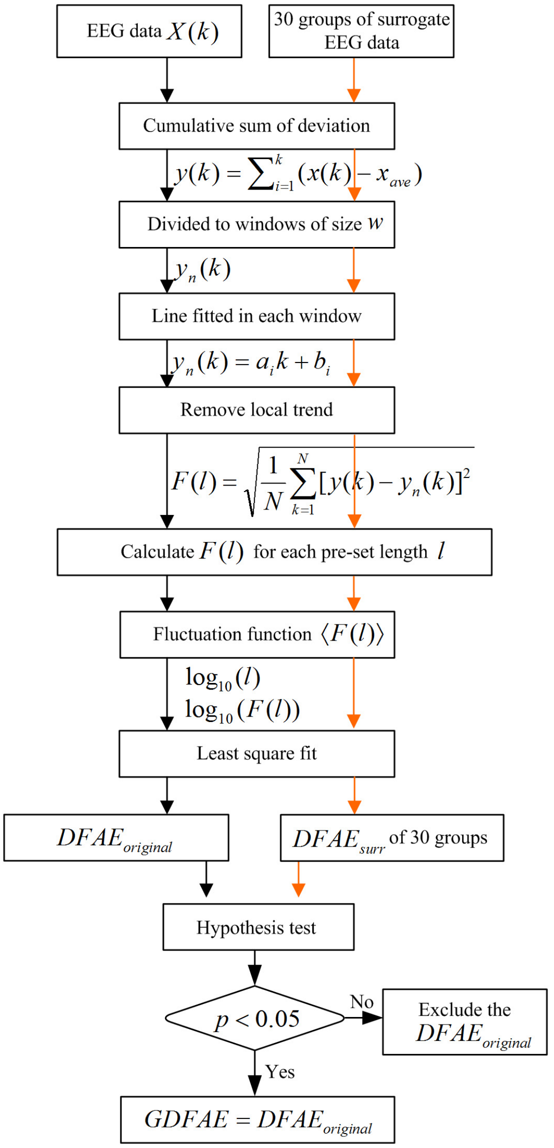

FIGURE 2 | Flow diagram for GDFAE calculation.

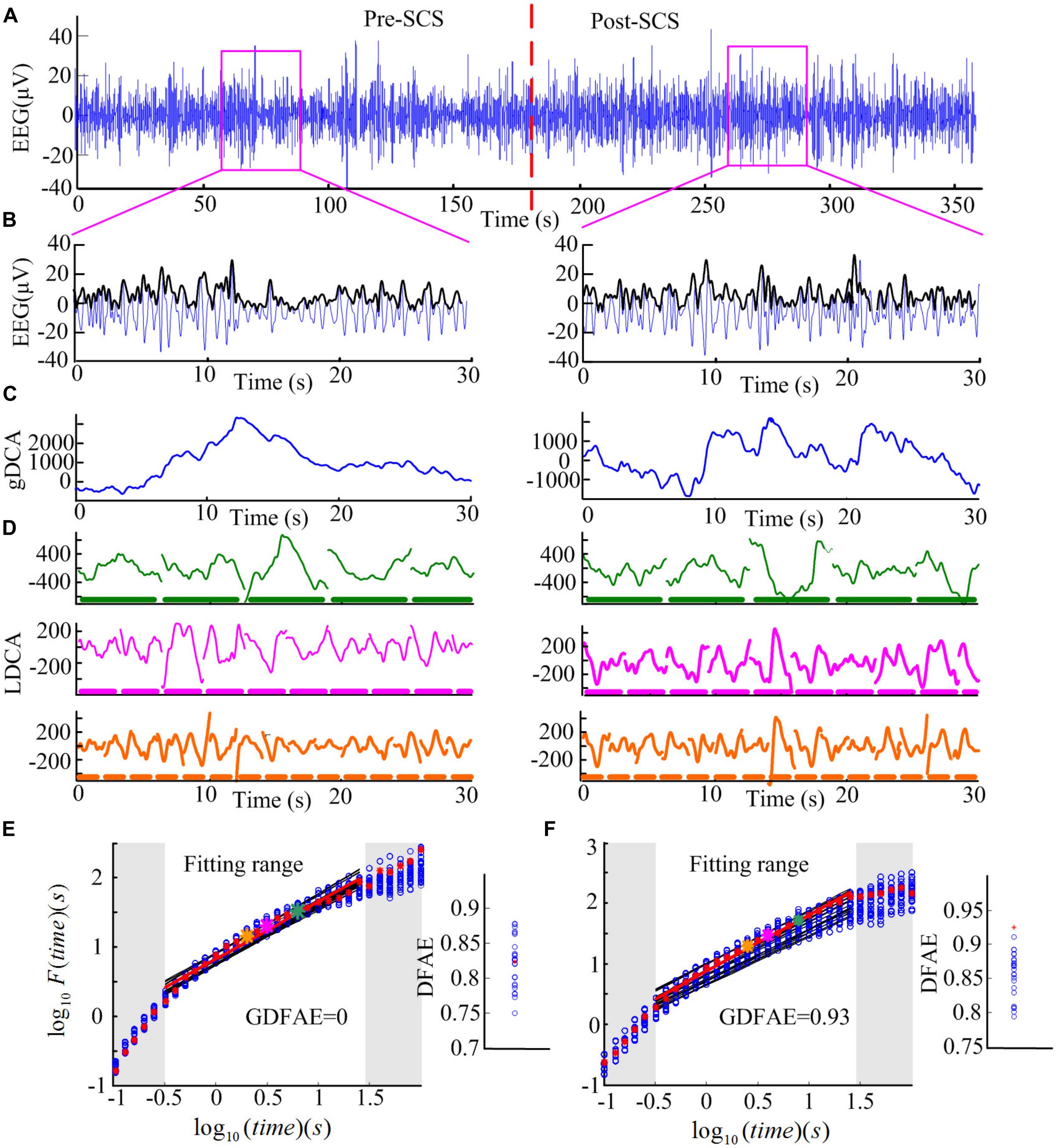

FIGURE 3 | Step-by-step illustration of DFAE calculation. **(A)** Delta band preprocessed EEG signals totaling 6 min (3 min before SCS and 3 min after SCS) from participant No. 2 at channel FP2. The red dash line denotes the SCS. **(B)** Delta band EEG signals of 30 s were extracted from the two states (blue line) and amplitude envelope (black line). **(C)** Detrended cumulative amplitude, without the global linear trend, of both states. **(D)** LDCA of time window of length 6.3 s (top), 3.2 s (middle), and 2.0 s (bottom); the thick dash line parallel to the timeline represents the time windows, the length of each piece on behalf of the length of the time window–green for 6.3 s, pink for 3.2 s, and orange for 2.0 s. **(E)** The fitting of the logarithmic fluctuation function for both real EEG signals and surrogate EEG data performed for the pre-SCS state; red asterisks and hollow blue circles represent the real and the surrogate EEG respectively. The big asterisks correspond to the same color time window in panel **(D)**. The red and black lines are the linear regression fitted lines. To obtain a reliable exponent, the log times (windows) in the gray area were excluded from the linear regression. The windows which are too narrow (in the lower left corner) exhibit inherently steeper scaling, whereas windows too large (i.e., those in the upper right corner) may induce the lacking of data for reliably estimating the variability. The right part is the corresponding slope (*DFAE*) value of the function. The blue circles represent $DFAE_{surr}$ and the red asterisk represents $DFAE_{original}$. This significance test shows that this channel, in this state, is a spurious DFA channel. Thus, the GDFAE = 0. **(F)** The fitting of the logarithmic fluctuation function for the post-SCS state. Similar to panel **(E)**, but the significance test showed that it is a genuine DFA channel in this state (GDFAE = $DFAE_{original}$ = 0.9251).

$y\left(k\right) = \sum_{i=1}^{k}\left[x\left(k\right) - x_{ave}\right]$, where $x_{ave} = \frac{1}{N}\sum_{i=1}^{N} x\left(i\right)$, N indicates the length of $x\left(t\right)$. The new time series $y\left(k\right)$ is called the global detrended cumulative amplitude (gDCA). To clarify the DFA procedure, sequences of 30 s were extracted and calculated for the presentation. The extracted data of 30 s from both states (pink rectangle in **Figure 3A**) and their amplitude envelopes, are shown in **Figure 3B**. The gDCA for both states (pre- and post-SCS) were thus obtained (**Figure 3C**).

(2) The gDCA $y\left(k\right)$ was divided into several non-overlapping subsequences of length l. Each subsequence corresponded to a time window, and the length of the time windows was defined as eight times larger than the filter order and eight times smaller than the recording length (Hardstone et al., 2012). The least squares method (LSM) was applied to fit the trend of each time window as a straight line $y_n\left(k\right) = a_i k + b_i$, where a_i and b_i were the undetermined coefficients. In each time window, $y_n\left(k\right)$ was subtracted from the primary $y\left(k\right)$ to remove the local trend. The fluctuation function $F\left(l\right)$ was quantified as a square deviation function, that is, the average root mean square of the locally detrended cumulative amplitude (LDCA) as follows:

$$F\left(l\right) = \sqrt{\frac{1}{N}\sum_{k=1}^{N}\left[y\left(k\right) - y_n\left(k\right)\right]^2} \tag{1}$$

All fluctuation functions $F\left(l\right)$ of the time windows of different length l were calculated, where l is defined equidistantly on a logarithmic scale. **Figure 3D** shows the LDCA of a time window with lengths of 6.3 s (top), 3.2 s (middle), and 2.0 s (bottom).

(3) The fluctuation function $F\left(l\right)$ and window length l were transformed into a logarithmic coordinate, and LSM was used to estimate the linear trend and slope α of the fitted line. α is also commonly referred to as the Hurst scaling exponent H (Colombo et al., 2016) or the DFA exponent (Krzeminski et al., 2017). The DFA exponent of the original EEG was abbreviated as $DFAE_{original}$. In **Figures 3E,F**, the green, pink, and orange asterisks correspond to the time windows of 6.3, 3.2, and 2.0 s in (D), respectively.

Step 2: Calculating the surrogate data set for the original EEG signals.

First, the real recorded EEG signals $x\left(n\right)$ were transformed into the frequency domain $X\left(k\right)$ by the discrete Fourier transform as follows: $X\left(k\right) = \sum_{n=0}^{N-1} x\left(n\right) e^{-j2\pi kn/N}$. Second, a uniform random sequence $v\left(k\right)$ was produced. The phase spectra of $X\left(k\right)$ was replaced by the random sequence $v\left(k\right)$ with the amplitude spectra of $X\left(k\right)$ remaining unchanged, that is, $S\left(k\right) = \left|X\left(k\right)\right| e^{jv\left(k\right)}$. The existing spurious temporal correlations in the signal were replaced, but the spectrum shape was preserved. Finally, the surrogate data were obtained through the inverse discrete Fourier transform $s\left(n\right) = \frac{1}{N}\sum_{k=0}^{N-1} S\left(k\right) e^{j2\pi kn/N}$(Schreiber and Schmitz, 1996, 2000). For the frequency band of each channel, 30 groups of surrogate data were produced.

Step 3: Obtaining the GDFAE at each frequency band.

The surrogate DFA exponents were calculated for each band and termed $DFAE_{surr}$. The Wilcoxon signed-rank test (*signrank.m*) was applied to eliminate any spurious DFA exponents. The $DFAE_{surr}$ was tested with $DFAE_{original}$. Their difference sequence was tested with the hypothesis that the element in the sequence comes from a distribution with a median of 0. The significance threshold was set to the 95% confidence level. If the null hypothesis was rejected at the 5% level ($p < 0.05$ and $h = 1$), the $DFAE_{original}$ would be different from the distribution of 30. Thus, the $DFAE_{original}$ was the exact GDFAE. Otherwise, the $DFAE_{original}$ would have been considered a spurious LRTC value. This can also be described as follows:

$$GDFAE = \begin{cases} DFAE_{original} : h = 1, p < 0.05 \\ null : otherwise \end{cases} \tag{2}$$

The GDFAE describes the robust correlation characteristics of a time series (Colombo et al., 2016). When $GDFAE$=0.5, the signals are white noise with no autocorrelation. When $GDFAE$=1, the signals are 1/f noise. When $0.5 < GDFAE < 1$, the signals are temporally anti-correlated. When $0.5 < GDFAE < 1$, the recorded EEG signals are positive temporal correlations, that is, LRTCs. Thus, the neural activity at a given time could potentially have been influenced by the neural activities which had occurred several minutes before (Maxim et al., 2005; He, 2011).

Figures 3E,F present the surrogate analysis of two EEG periods. The logarithmic function and the corresponding window length for the real EEG (red asterisks) and the surrogate data (blue circle) are fitted in the red and black lines, respectively. The right part of **Figure 3E** shows the distribution of the DFAE for the real EEG ($DFAE_{original}$) and the surrogate EEG ($DFAE_{surr}$). $DFAE_{original}$ is not distinctly different from the distribution of $DFAE_{surr}$. This indicates that this EEG segment lacks genuine LRTCs (GDFAE = 0). Conversely, **Figure 3F** shows the GDFAE, which has genuine LRTCs.

In the DFA measurement, selecting the size of the windows for linear fitting is crucial (Kantelhardt et al., 2001). If the length of each window is too large, there will not be enough windows for calculation, and the results may be inaccurate. Although this problem can be alleviated by overlapping windows, window length must be no larger than 10% of the signal length (Hardstone et al., 2012). Conversely, if the length of each window is too short, more scaling will be observed in the fluctuation function. With the increasing length of the windows, the scaling behavior will converge asymptotically. The lengths of the windows (l) are represented equidistantly on a logarithmic scale (see in **Figure 3E**). The latter, because of the fluctuation functions $\left[F\left(l\right)\right]$ and the corresponding l, will be transformed into a logarithmic coordinate to obtain slope α. Linear fitting was performed only for windows in which the fluctuation function depicted a straight line to get a reliable exponent α. To eliminate the edge effect, we used an automated process (Fell et al., 2000). First, a histogram of the first derivative for each pair of the adjacent fluctuation data was plotted. Second, the majority of the derivative values were grouped together. Finally, the 90th percentile value of the distribution was chosen as the threshold for fitting (Krzeminski et al., 2017).

Statistical Analysis

This study evaluated the changes in LRTCs after SCS in MCS patients. We analyzed the GDFAE in different brain regions, at different frequency bands, before and after SCS. Considering the multi-factor effects, a three-way repeated analysis of variance (three-way ANOVA; *anovan.m*) was applied to analyze the interactions and the main effects of the three factors: (I) brain states (two levels: pre- and post- SCS), (II) frequency bands (five levels: delta, theta, alpha, beta, and gamma), and (III) brain regions (four levels: frontal, central, parietal, and occipital). After obtaining the interactions and the main effects of the three factors, a *post hoc* test with the Bonferroni correction was used to determine the significant difference of the GDFAE values between the two states in each brain region, at each frequency band.

RESULTS

According to the eligibility criteria, 16 MCS patients were enrolled in this study. Their demographic data and clinical diagnoses are presented in **Table 1**. According to our previous study, the EEG channels were divided into five regions. The frontal region (F): FP1, FP2, Fz, F3, F4, F7, and F8; the central region (C): FC1, FC2, FC5, FC6, Cz, C3, and C4; the parietal region (P): CP1, CP2, CP5, CP6, Pz, P3, P4, P7, and P8 (**Figure 1**); the occipital region (O): PO3, PO4, PO7, PO8, Oz, O1, and O2; the temporal region: T3 and T4. Since the temporal region only included two channels, we excluded the temporal region from the analysis of the changes in LRTCs.

TABLE 1 | Patient demographics.

Subject	CRS-R	Etiology	Post_injury (months)
1	8	Hemorrhage	18
2	9	Hemorrhage	5
3	10	Traumatism	9
4	10	Hemorrhage	12
5	7	Ischemia-hypoxia	4
6	8	Ischemia-hypoxia	3
7	7	Hemorrhage	10
8	9	Traumatism	3
9	7	Hemorrhage	5
10	7	Hemorrhage	4
11	7	Ischemia-hypoxia	3
12	7	Hemorrhage	11
13	10	Ischemia-hypoxia	4
14	8	Traumatism	13
15	8	Ischemia-hypoxia	4
16	9	Hemorrhage	6

CRS-R, coma recovery scale-revised.

The EEG spectra of all channels were calculated to reveal the changes in EEG oscillation after SCS. To illustrate this, **Figure 4** shows the power spectra of one subject in which the power was concentrated at the delta and theta bands. The spectra of the different channels was diverse. The power of the high frequency bands (beta and gamma) increased after SCS in most channels such as FP1, FP2, and F7. In some of the channels, such as FC1, FC2, and CZ, it did not. The color bar was set from −25 to 20 dB to highlight the differences between the two states (pre- and post-SCS). The maximum power differential between the pre-SCS and the post-SCS state was 15 dB.

Then, the $DFAE_{original}$ and $DFAE_{surr}$ of each channel, at each frequency band, were calculated to obtain the GDFAE. If the $DFAE_{original}$ deviated from the distribution of $DFAE_{surr}$, this indicated that the EEG data in this state had genuine LRTCs. **Figure 5** shows the distribution of the genuine and spurious LRTCs at each frequency band for one subject, both before and after SCS. The quantity of genuine LRTCs channels increased after SCS. However, the significant increases in spatial distribution were not consistent for each frequency band. The proportions of genuine LRTC channels at each frequency band are presented in **Table 2**. The results indicate that at all five frequency bands, the spatial distribution of the genuine LRTCs broadened after SCS.

To explore how SCS modulated the LRTCs at different frequency bands, the averaged GDFAE values of the 32 channels for each subject, at each neural oscillation band (delta, theta, alpha, beta, and gamma), were calculated. The descriptive statistics for the averaged GDFAE in the pre-SCS and post-SCS states are presented in **Figure 6**. The mean and standard deviation values in **Figure 6** are listed in **Table 3**. The value of the averaged exponents in both states ranged from 0.5 to 1. The GDFAE values at the delta, theta, and alpha bands were larger than those at the high-frequency bands (i.e., beta and gamma). The mean values of the averaged GDFAE increased significantly in the post-SCS state compared to those from the pre-SCS state, especially at the delta ($p = 0.039$), theta ($p = 0.021$), and alpha ($p = 0.032$) bands. The results of the multiple comparison test are shown in **Figure 6**. Furthermore, the standard deviation of the GDFAE was smaller at the alpha band than it was at the other frequency bands.

To analyze the effect of SCS on different spatial regions, the GDFAE values of the five frequency bands were analyzed (including four brain regions). The *topoplot* function in EEGLAB was applied to obtain a two-dimensional topographical map of the GDFAE value. The spatial distributions of the averaged non-zero GDFAE values of the 16 subjects at each frequency band are presented in **Figure 7**. Non-zero GDFAE values ranged from 0.5 to 1, indicating that the EEG dynamics were presented in the LRTCs. Moreover, the LRTCs were stronger in the post-SCS state at the delta, theta, and alpha frequency bands (**Figure 7**). Lastly, the spatial distribution showed an increase in the frontal and occipital regions.

The GDFAE statistics for all 16 patients are shown as box plots in **Figure 8**. Three-way ANOVA and a multiple comparison

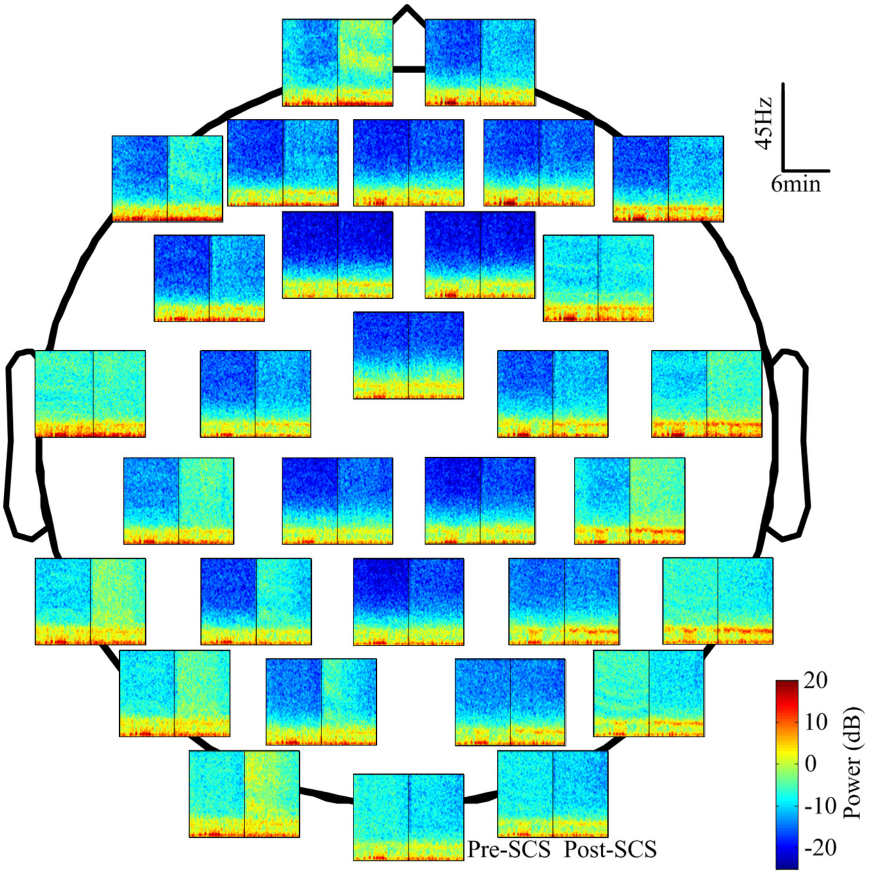

FIGURE 4 | The power spectrum of 32 channels in the corresponding position of one participant (No. 1 in **Table 1**). The spectrum was computed with the short-time Fourier transform with a Hamming window. The blue represents the lower power and the dark red represents the higher power. The black line in each spectrum block represents the interposition of the SCS.

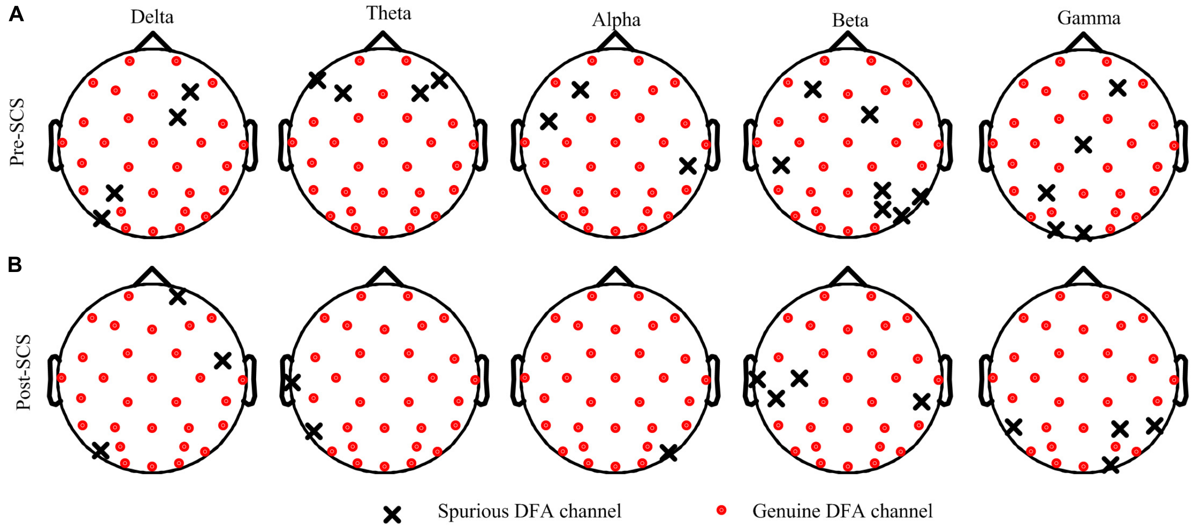

FIGURE 5 | Surrogate data results for one participant (No. 7 in **Table 1**). **(A,B)** are the spatial distribution of the genuine and spurious DFA channels at five frequency bands, at pre- and post-SCS states. The solid red circle represents the genuine DFA channel and the black crosses represent the spurious DFA channel.

TABLE 2 | The proportion of the significant GDFAE in pre- and post-SCS stage, at different frequency bands [Median (min–max)].

	Delta	Theta	Alpha	Beta	Gamma
Pre-SCS	0.91 (0.84–1.00)	0.87 (0.75–0.97)	0.92 (0.91–0.94)	0.92 (0.78–1.00)	0.88 (0.75–1.00)
Post-SCS	0.94 (0.91–1.00)	0.93 (0.72–1.00)	0.93 (0.81–1.00)	0.93 (0.81–1.00)	0.93 (0.88–1.00)

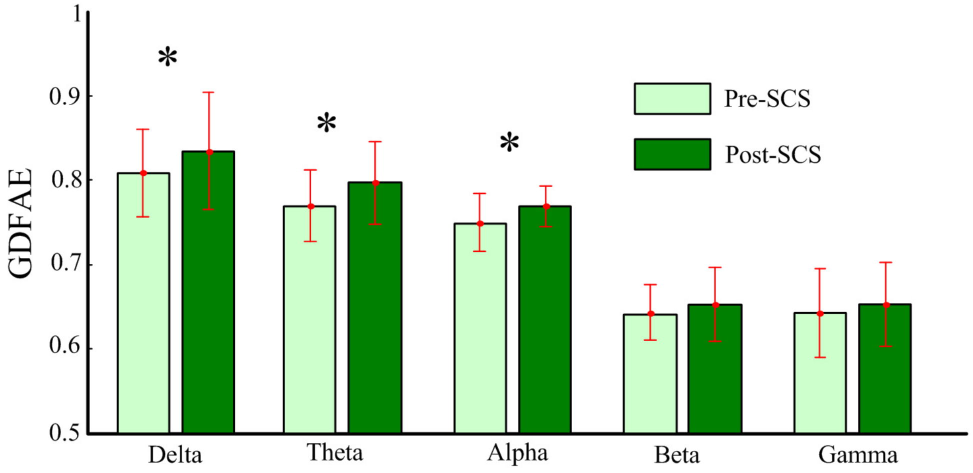

FIGURE 6 | Descriptive statistics for the averaged GDFAE for all patients. This includes the bar (mean) and the error bar (standard deviation) of the averaged GDFAE at five frequency bands, at pre- and post-SCS states. The asterisk denotes a *p*-value less than 0.05 in multiple comparison test, with Bonferroni correction.

TABLE 3 | Descriptive statistics for average GDFAE of each participant in pre- and post-SCS stages, at different frequency bands (mean ± SD).

	Delta	Theta	Alpha	Beta	Gamma
Pre-SCS	0.809 ± 0.052	0.770 ± 0.042	0.750 ± 0.034	0.643 ± 0.033	0.642 ± 0.052
Post-SCS	0.835 ± 0.070	0.797 ± 0.049	0.769 ± 0.024	0.653 ± 0.044	0.653 ± 0.050

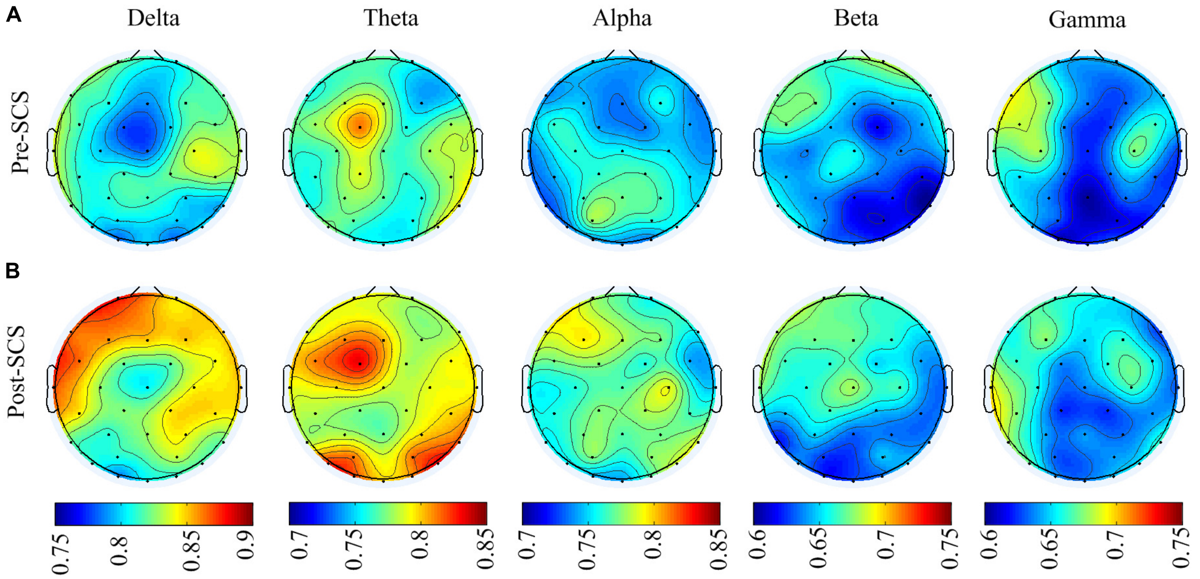

FIGURE 7 | (A) Spatial distribution topographic of the non-zero GDFAE at each frequency band in pre-SCS state. **(B)** Topographic of the post-SCS state.

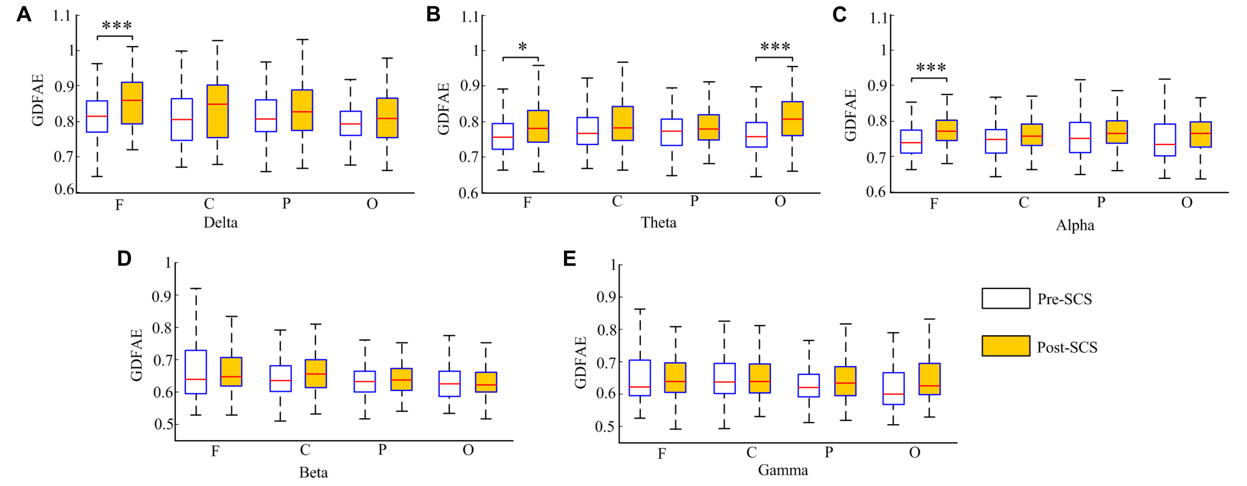

FIGURE 8 | Box plot of the GDFAE for all 16 patients. Each graphic includes both states of all four regions at one frequency band. The symbol "***" denotes a p-value less than 0.001, "**" denotes a p-value less than 0.01, and "*" denotes a p-value less than 0.05.

test (*multcompare.m*) with the Bonferroni correction were used to test significance. The three-way ANOVA analysis showed the interactions and the main effects of the three factors [state (I), frequency band (II), and brain region (III)]. The interactions of I*II and I*III were both significant ($p < 0.001$ and $p < 0.05$, respectively). This indicated that the changes in the GDFAE after SCS were related to the brain regions and frequency bands. In other words, the variation between the pre- and the post-SCS GDFAE in different brain regions or at different frequency bands varied in degree. The main effects of factor I were significant ($p < 0.001$), indicating that the GDFAE values in pre- and post-SCS states were significantly different. A multiple comparison test analyzed the difference between the pre- and post-SCS for the different brain regions and frequency bands. We used the Bonferroni correction for the number of frequency bands and brain regions to account for the repetition of testing. **Figure 8** shows that the GDFAE significantly increased at delta, theta and alpha bands after SCS. At the delta band, the significant increase was in the frontal region ($p < 0.001$). At the theta band, a significant increase was found in the frontal ($p < 0.05$) and occipital regions ($p < 0.001$). A significant increase at the alpha band was also observed in the frontal region ($p < 0.001$). However, no significant increase or decrease was found at the beta or gamma bands in any brain region. The indices in the box plots were not normally distributed (Lilliefors test). Therefore, all indices were expressed as medians (min–max), and are listed in **Table 4**. The p-values of the significance test for the GDFAE statistics are shown in **Table 5**.

DISCUSSION

This study investigated the dynamic brain activity changes in pre- and post-SCS state of MCS patients. The GDFAE was employed to assess the LRTCs of EEG signals, recorded from 16 MCS patients. We analyzed the GDFAE changes in different brain regions, at different frequency bands. The results indicated that the LRTCs in the post-SCS state were more enhanced than those in the pre-SCS state, in some regions and frequency bands. The main findings are as follows: (i) The proportion of the non-zero GDFAE in the post-SCS state was higher than that of the pre-SCS state [i.e., the quantity of channels with GDFAE increased at all frequency bands in the post-SCS state (**Table 2**)]. This indicated that the long-range temporal integration became more widespread after SCS. (ii) The GDFAE value increased after SCS, especially at the lower frequency bands (delta, theta, and alpha). The increased GDFAE suggested that the LRTCs in this neural oscillation had become stronger after SCS. (iii) The LRTCs of the frontal region significantly increased in the post-SCS state at the delta, theta, and alpha frequency bands. The occipital region also showed a significant increase at the alpha band (**Figure 8** and **Table 5**). The dominant enhancement of LRTCs in the frontal region and at the alpha frequency band could provide more evidence for the potential mechanisms of SCS in modulating the brain activities of MCS patients.

This study utilized the DFA method. In addition to DFA, other measures and theories have been proposed to analyze the EEG signals. Among them, entropy is an important non-linear method. Both the fluctuation of the entropy and the DFA exponents of the EEG signals can indicate the complexity of the brain system (Lee et al., 2004; Morabito et al., 2012). However, when applied to pathologic signals, DFA is recommended over entropy due to its capability to discriminate and predict the occurrence of a pathological state (e.g., epileptic seizure) (Cirugeda-Roldán et al., 2012).

According to the DFA methodology, the LRTCs in EEG signals are related to conscious behaviors. The larger fluctuation corresponded to the strengthening of the long-term memory of the underlying neural processes. When the LRTCs are weakened, the information integration tends to break down or decline (Thiery et al., 2018). For example, Krzeminski et al. (2017) found a breakdown in LRTCs at the alpha frequency band during

TABLE 4 | Descriptive statistics for GDFAE in different brain regions in pre- and post-SCS stages, at different frequency bands [Median (min–max)].

	Delta	Theta	Alpha	Beta	Gamma
Pre-F	0.81 (0.77–0.86)	0.76 (0.72–0.80)	0.74 (0.71–0.77)	0.68 (0.60–0.73)	0.62 (0.60–0.70)
Post-F	0.86 (0.79–0.91)	0.78 (0.74–0.83)	0.77 (0.75–0.80)	0.65 (0.62–0.71)	0.64 (0.60–0.70)
Pre-C	0.81 (0.75–0.85)	0.77 (0.74–0.81)	0.75 (0.71–0.78)	0.63 (0.60–0.68)	0.64 (0.60–0.69)
Post-C	0.83 (0.75–0.90)	0.78 (0.75–0.84)	0.76 (0.73–0.79)	0.66 (0.61–0.70)	0.63 (0.60–0.70)
Pre-P	0.81 (0.77–0.86)	0.77 (0.73–0.81)	0.75 (0.71–0.80)	0.60 (0.60–0.68)	0.62 (0.60–0.66)
Post-P	0.83 (0.74–0.89)	0.78 (0.75–0.82)	0.77 (0.74–0.80)	0.64 (0.61–0.67)	0.63 (0.60–0.69)
Pre-O	0.79 (0.76–0.83)	0.76 (0.73–0.80)	0.73 (0.70–0.79)	0.62 (0.59–0.66)	0.60 (0.57–0.67)
Post-O	0.81 (0.76–0.87)	0.81 (0.76–0.86)	0.77 (0.73–0.80)	0.62 (0.60–0.66)	0.63 (0.60–0.70)

Pre-F, pre-SCS stage in frontal region; Post-F, post-SCS stage in frontal region; Pre-C, pre-SCS stage in central region; Post-C, post-SCS stage in central region; Pre-P, pre-SCS stage in parietal region; Post-P, post-SCS stage in parietal region; Pre-O, pre-SCS stage in occipital region; Post-O, post-SCS stage in occipital region.

TABLE 5 | *p*-Value of the significance test for the GDFAE statistics in **Figure 8**.

	Delta	Theta	Alpha	Beta	Gamma
F	1.108e-04	0.035	3.149e-05	0.782	1.000
C	0.100	0.275	0.461	0.996	0.937
P	0.442	0.758	0.761	1.000	0.215
O	0.756	2.469e-07	0.178	0.995	0.929

general anesthesia. The DFA exponents decreased from the value associated with wakeful state to that of general anesthesia. The authors hypothesized that the brain activity exhibited robust LRTCs, and thus could be disrupted during general anesthesia. A similar phenomenon has also been observed during sleep with a decrease in long-term memory in the default mode and attention networks (Tagliazucchi et al., 2013). Insomnia has also been found to be related to LRTCs. Individuals who experienced worse sleep quality tended to have stronger LRTCs during wakefulness (Colombo et al., 2016). Furthermore, the LRTCs could be controlled by engaging an intrinsic neuroregulation through a closed-loop neuro-feedback stimulation–the LRTCs were found to be stronger during stimulation (Zhigalov et al., 2016). Based on the studies mentioned above, the fluctuations in the LRTCs were related to neural behaviors. Thus, in our results, the increased LRTCs may indicate that a more "complex" cortical information integration is restored after the SCS. From the perspective of complexity, various studies have shown that loss of consciousness is correlated with a decrease in complexity, such as in general anesthesia (Alonso et al., 2014; Liang et al., 2015; Schartner et al., 2015; Hudetz et al., 2016) and sleep (Priesemann et al., 2013). We concluded that the SCS increases brain dynamics in MCS patients.

After SCS, not only did the value of GDFAE increase, but the non-zero (genuine) proportion of DFA increased as well. To obtain the genuine proportion of DFA, the DFA was combined with the surrogate data method. The crux of the surrogate data method is to eliminate the non-linear correlation by reconstructing the power spectrum while maintaining the same linear feature. The advantage of surrogate data is that it preserves the linear stochastic structure and the amplitude distribution of the original series (Lucio et al., 2012). The two most commonly used algorithms for generating surrogate data are the amplitude-adjusted Fourier transform (AAFT) and the iterated AAFT (Rath and Monetti, 2008). The AAFT is considered a robust surrogate data-generated method and requires less computation than other methods (Pritchard et al., 2010). Using the AAFT, a GDFAE can be achieved that can reflect genuine LRTCs. If the DFAE is not genuine, there will be no LRTCs. Our results showed that the genuine LRTCs are spread more widely after the SCS. Also, more cortical areas were engaged in information integration after the SCS.

The results of this study have also revealed that most of the increased LRTCs occurred at the delta, theta, and alpha frequency bands. This suggests a frequency specificity for the LRTCs in MCS patients. Several other pathological investigations have found that the frequency-specific of LRTCs, such as the theta-band LRTCs, decreases in patients with major depression disorder (Linkenkaer-Hansen et al., 2005). Alpha-band LRTCs have also been shown to decrease in patients with Alzheimer's disease (Montez et al., 2009). In propofol-induced unconsciousness, no frequency-specific LRTCs were observed (Krzeminski et al., 2017). It has been speculated that cross-frequency interactions play a key role in this phenomenon. The temporal dynamic changes at one frequency band may affect other bands, given that the lower frequency oscillations (i.e., delta, theta, and alpha bands) in MCS patients are typically different from those of healthy subjects (Fingelkurts et al., 2012).

The spatial statistics showed that the GDFAE significantly increased in the frontal region at the delta ($p < 0.001$), theta ($p < 0.05$), and alpha ($p < 0.001$) band. The frontal cortex region is responsible for the higher cognitive functions (Frith and Dolan, 1996; María et al., 2010), providing an area for various networks to play out different scenarios (Mesulam, 2002). Yampolsky et al. (2012), suggested that the frontal cortex is vital for awareness and attention. The present study found that the LRTCs increased primarily in the frontal region after SCS, at both the delta and alpha bands. As higher cognitive functions are correlated with the prefrontal region, we hypothesized that SCS could affect these MCS functions by enhancing the temporal integration. The LRTCs also significantly increased in the occipital region at the theta band ($p < 0.001$). It has been suggested that the occipital cortex is involved in language processing (Bedny et al., 2011). Tosoni et al. (2015) have found that the occipital cortex is related to coherent visual motion and responding. Therefore, the significantly enhanced LRTCs in the occipital region after SCS indicate that SCS may impact MCS patients' brain functions, such as language processing and visual functions.

LIMITATIONS

This study has two limitations. First, the GDFAE indices had a range of 0.6–1 (from the pre-SCS to the post-SCS state). Krzeminski et al. (2017) found that the DFA was 0.9 in a wakened state and 0.6 under general anesthesia at the alpha oscillation in electrocorticographic data recordings. In our study, after the SCS, the DFA exponents of some patients passed 0.9, but these patients remained in MCS. We could not confirm whether the high DFA ($>=0.9$) meant that the patients had been conscious after the SCS. However, the relative changes in the GDFAE indices revealed the tendency for change in the complex brain system. Furthermore, an arbitrary quantification based on one parameter to assess the complex brain system is limited. Further studies should consider the multi-dimensional features to analyze the mechanism of the SCS (Kim et al., 2018). The multi-dimensional features should be considered to analyze the mechanism of the SCS in further studies (Kim et al., 2018). Second, as the brain activities of MCS patients have pathological oscillations, the dynamics of the system are different from those in a normal brain. The finding that LRTCs are correlated with consciousness has been established from studies of healthy brain tissue. Similar conclusions should be interpreted cautiously for MCS patients.

CONCLUSION

The SCS showed a strong effect on EEG signals in patients with MCS whose long-range temporal integrations of brain activity had significantly increased (at low-frequency bands) in the frontal and occipital regions. Considering its close relationship with level of consciousness, we suggest that the GDFAE could serve as a new tool to explore the mechanisms of SCS in MCS patients.

AUTHOR CONTRIBUTIONS

ZL, JL, and YB designed this study. ZL collected the important background information. JL performed the statistical analysis. YB and JH carried out the study. YW and XX provided assistance for data acquisition. ZL and JL drafted the manuscript. YB and XL approved the final manuscript.

FUNDING

This research was supported by the National Natural Science Foundation of China (61673333, 61304247, and 81230023) and Natural Science Foundation for Excellent Young Scholars of Hebei Province of China (F2018203281). ZL received support from the China Scholarship Council.

REFERENCES

Allegrini, P., Paradisi, P., Menicucci, D., Laurino, M., Piarulli, A., and Gemignani, A. (2015). Self-organized dynamical complexity in human wakefulness and sleep: different critical brain-activity feedback for conscious and unconscious states. *Phys. Rev. E Stat. Nonlin. Soft Matter Phys.* 92:032808. doi: 10.1103/PhysRevE.92.032808

Alonso, L. M., Proekt, A., Schwartz, T. H., Pryor, K. O., Cecchi, G. A., and Magnasco, M. O. (2014). Dynamical criticality during induction of anesthesia in human ECoG recordings. *Front. Neural Circuits* 8:20. doi: 10.3389/fncir.2014.00020

Bai, Y., Xia, X., Li, X., Wang, Y., Yang, Y., Liu, Y., et al. (2017a). Spinal cord stimulation modulates frontal delta and gamma in patients of minimally consciousness state. *Neuroscience* 346, 247–254. doi: 10.1016/j.neuroscience.2017.01.036

Bai, Y., Xia, X., Liang, Z., Wang, Y., Yang, Y., He, J., et al. (2017b). Frontal connectivity in EEG gamma (30-45 Hz) respond to spinal cord stimulation in minimally conscious state patients. *Front. Cell. Neurosci.* 11:177. doi: 10.3389/fncel.2017.00177

Bedny, M., Pascualleone, A., Dodellfeder, D., Fedorenko, E., and Saxe, R. (2011). Language processing in the occipital cortex of congenitally blind adults. *Proc. Natl. Acad. Sci. U.S.A.* 108, 4429–4434. doi: 10.1073/pnas.1014818108

Buzsaki, G., and Draguhn, A. (2004). Neuronal oscillations in cortical networks. *Science* 304, 1926–1929. doi: 10.1126/science.1099745

Carhart-Harris, R. L., Robert, L., Hellyer, P. J., Murray, S., Amanda, F., Enzo, T., et al. (2014). The entropic brain: a theory of conscious states informed by neuroimaging research with psychedelic drugs. *Front. Hum. Neurosci.* 8:20. doi: 10.3389/fnhum.2014.00020

Cirugeda-Roldán, E. M., Molina-Picó, A., Cuesta-Frau, D., Oltra-Crespo, S., and Miró-Martínez, P. (2012). "Comparative study between sample entropy and detrended fluctuation analysis performance on EEG records under data loss," in *Proceedings of the 34th Annual International Conference of the IEEE Engineering in Medicine and Biology Society*, (San Diego, CA: IEEE), 4233–4236. doi: 10.1109/EMBC.2012.6346901

Colombo, M. A., Wei, Y., Ramautar, J. R., Linkenkaer-Hansen, K., Tagliazucchi, E., and Van Someren, E. J. W. (2016). More severe insomnia complaints in people with stronger long-range temporal correlations in wake resting-state EEG. *Front. Physiol.* 7:576. doi: 10.3389/fphys.2016.00576

Dolan, K. T., and Spano, M. L. (2001). Surrogate for nonlinear time series analysis. *Phys. Rev. E Stat. Nonlin. Soft Matter Phys.* 64:046128. doi: 10.1103/PhysRevE.64.046128

D'Rozario, A. L., Wong, K. K. H., Bartlett, D. J., Marshall, N. S., Dijk, D. J., Kim, J. W., et al. (2013). A new EEG biomarker of neurobehavioural impairment and sleepiness in sleep apnea patients and controls during extended wakefulness. *Clin. Neurophysiol.* 124, 1605–1614. doi: 10.1016/j.clinph.2013.02.022

Eapen, B. C., Georgekutty, J., Subbarao, B., Bavishi, S., and Cifu, D. X. (2016). Disorders of consciousness. *Phys. Med. Rehabil. Clin. N. Am.* 28, 245–258. doi: 10.1016/j.pmr.2016.12.003

Eke, A., Hermán, P., Bassingthwaighte, J. B., Raymond, G. M., Percival, D. B., Cannon, M., et al. (2000). Physiological time series: distinguishing fractal noises from motions. *Pflugers Archiv.* 439, 403–415. doi: 10.1007/s004249900135

Fell, J., Kaplan, A., Darkhovsky, B., and Röschke, J. (2000). EEG analysis with nonlinear deterministic and stochastic methods: a combined strategy. *Acta Neurobiol. Exp.* 60, 87–108.

Fingelkurts, A. A., Fingelkurts, A. A., Bagnato, S., Boccagni, C., and Galardi, G. (2012). EEG oscillatory states as neuro-phenomenology of consciousness as revealed from patients in vegetative and minimally conscious states. *Conscious. Cogn.* 21, 149–169. doi: 10.1016/j.concog.2011.10.004

Frith, C., and Dolan, R. (1996). The role of the prefrontal cortex in higher cognitive functions. *Brain Res. Cogn. Brain Res.* 5, 175–181. doi: 10.1016/S0926-6410(96)00054-7

Gallimore, A. R. (2015). Restructuring consciousness -the psychedelic state in light of integrated information theory. *Front. Hum. Neurosci.* 9:346. doi: 10.3389/fnhum.2015.00346

Georgiopoulos, M., Katsakiori, P., Kefalopoulou, Z., Ellul, J., Chroni, E., and Constantoyannis, C. (2010). Vegetative state and minimally conscious state: a review of the therapeutic interventions. *Stereotact. Funct. Neurosurg.* 88, 199–207. doi: 10.1159/000314354

Giacino, J. T., Ashwal, S., Childs, N., Cranford, R., Jennett, B., Katz, D. I., et al. (2002). The minimally conscious state: definition and diagnostic criteria. *Neurology* 58, 349–353. doi: 10.1212/WNL.58.3.349

Hardstone, R., Poil, S. S., Schiavone, G., Jansen, R., Nikulin, V. V., Mansvelder, H. D., et al. (2012). Detrended fluctuation analysis: a scale-free view on neuronal oscillations. *Front. Physiol.* 3:450. doi: 10.3389/fphys.2012.00450

He, B. J. (2011). Scale-free properties of the functional magnetic resonance imaging signal during rest and task. *J. Neurosci.* 31, 13786–13795. doi: 10.1523/JNEUROSCI.2111-11.2011

Hu, K., Ivanov, P. C., Chen, Z., Carpena, P., and Stanley, H. E. (2001). Effect of trends on detrended fluctuation analysis. *Phys. Rev. E Stat. Nonlin. Soft Matter Phys.* 64:011114. doi: 10.1103/PhysRevE.64.011114

Huang, Z., Obara, N., Davis, H. H. T., Pokorny, J., and Northoff, G. (2016). The temporal structure of resting-state brain activity in the medial prefrontal cortex predicts self-consciousness. *Neuropsychologia* 82, 161–170. doi: 10.1016/j.neuropsychologia.2016.01.025

Hudetz, A. G., Vizuete, J. A., Pillay, S., and Mashour, G. A. (2016). Repertoire of mesoscopic cortical activity is not reduced during anesthesia. *Neuroscience* 339, 402–417. doi: 10.1016/j.neuroscience.2016.10.023

Jacobs, J., and Kahana, M. J. (2010). Direct brain recordings fuel advances in cognitive electrophysiology. *Trends Cogn. Sci.* 14, 162–171. doi: 10.1016/j.tics.2010.01.005

Kalmar, K., and Giacino, J. T. (2005). The JFK coma recovery scale–revised. *Neuropsychol. Rehabil.* 15, 454–460. doi: 10.1080/09602010443000425

Kantelhardt, J. W., Koscielny-Bunde, E., Rego, H. H. A., Havlin, S., and Bunde, A. (2001). Detecting long-range correlations with detrended fluctuation analysis. *Physica A* 295, 441–454. doi: 10.1016/S0378-4371(01)00144-3

Kim, H., Hudetz, A. G., Lee, J., Mashour, G. A., and Lee, U. (2018). Estimating the integrated information measure phi from high-density electroencephalography during states of consciousness in humans. *Front. Hum. Neurosci.* 12:42. doi: 10.3389/fnhum.2018.00042

Köster, M., Friese, U., Schöne, B., Trujillobarreto, N., and Gruber, T. (2014). Theta-gamma coupling during episodic retrieval in the human EEG. *Brain Res.* 1577, 57–68. doi: 10.1016/j.brainres.2014.06.028

Krzeminski, D., Kaminski, M., Marchewka, A., and Bola, M. (2017). Breakdown of long-range temporal correlations in brain oscillations during general anesthesia. *Neuroimage* 159, 146–158. doi: 10.1016/j.neuroimage.2017.07.047

Lee, G. M., Fattinger, S., Mouthon, A. L., Noirhomme, Q., and Huber, R. (2013). Electroencephalogram approximate entropy influenced by both age and sleep. *Front. Neuroinform.* 7:33. doi: 10.3389/fninf.2013.00033

Lee, J.-M., Kim, D.-J., Kim, S. I., Kim, I.-Y., and Suk Park, K. (2004). Nonlinear-analysis of human sleep EEG using detrended fluctuation analysis. *Med. Eng. Phys.* 26, 773–776. doi: 10.1016/j.medengphy.2004.07.002

Liang, Z., Ren, Y., Yan, J., Li, D., Voss, L. J., Sleigh, J. W., et al. (2016). A comparison of different synchronization measures in electroencephalogram during propofol anesthesia. *J. Clin. Monit. Comput.* 30, 451–466. doi: 10.1007/s10877-015-9738-z

Liang, Z., Wang, Y., Sun, X., Li, D., Voss, L. J., Sleigh, J. W., et al. (2015). EEG entropy measures in anesthesia. *Front. Comput. Neurosci.* 9:16. doi: 10.3389/fncom.2015.00016

Linkenkaer-Hansen, K., Monto, S., Rytsala, H., Suominen, K., Isometsa, E., and Kahkonen, S. (2005). Breakdown of long-range temporal correlations in theta oscillations in patients with major depressive disorder. *J. Neurosci.* 25, 10131–10137. doi: 10.1523/JNEUROSCI.3244-05.2005

Lucio, J. H., Valdés, R., and Rodríguez, L. R. (2012). Improvements to surrogate data methods for nonstationary time series. *Phys. Rev. E Stat. Nonlin. Soft Matter Phys.* 85:056202. doi: 10.1103/PhysRevE.85.056202

Mandelbrot, B. B. (1999). *Multifractals and 1/f Noise Wild Self-Affinity in Physics (1963–1976)*. Berlin: Springer. doi: 10.1007/978-1-4612-2150-0

María, R., Alice, P., Russell, T., Alexandra, W., Teresa, T., Nagui, A., et al. (2010). Executive function and fluid intelligence after frontal lobe lesions. *Brain* 133, 234–247. doi: 10.1093/brain/awp269

Mattogno, P. P., Barbagallo, G., Iacopino, G., Pappalardo, G., La Rocca, G., Signorelli, F., et al. (2017). Recovery from chronic diseases of consciousness: state of the art in neuromodulation for persistent vegetative state and minimally conscious state. *Acta Neurochir. Suppl.* 124, 19–25. doi: 10.1007/978-3-319-39546-3_4

Maxim, V., Sendur, L., Fadili, J., Suckling, J., Gould, R., Howard, R., et al. (2005). Fractional Gaussian noise, functional MRI and Alzheimer's disease. *Neuroimage* 25, 141–158. doi: 10.1016/j.neuroimage.2004.10.044

Mesulam, M. M. (2002). "The human frontal lobes: transcending the default mode through contingent encoding," in *Principles of Frontal Lobe Function*, eds D. T. Stuss and R. T. Knight (New York, NY: Oxford University Press), 8–30.

Montez, T., Poil, S.-S., Jones, B. F., Manshanden, I., Verbunt, J. P., Van Dijk, B. W., et al. (2009). Altered temporal correlations in parietal alpha and prefrontal theta oscillations in early-stage Alzheimer disease. *Proc. Natl. Acad. Sci. U.S.A.* 106, 1614–1619. doi: 10.1073/pnas.0811699106

Morabito, F. C., Labate, D., Foresta, F. L., Bramanti, A., Morabito, G., and Palamara, I. (2012). Multivariate multi-scale permutation entropy for complexity analysis of Alzheimer's disease EEG. *Entropy* 14, 1186–1202. doi: 10.3390/e14071186

Northoff, G., and Huang, Z. (2017). How do the brain's time and space mediate consciousness and its different dimensions? Temporo-spatial theory of consciousness (TTC). *Neurosci. Biobehav. Rev.* 80, 630–645. doi: 10.1016/j.neubiorev.2017.07.013

Pal, D., Silverstein, B. H., Sharba, L., Li, D., Hambrecht-Wiedbusch, V. S., Hudetz, A. G., et al. (2017). Propofol, sevoflurane, and ketamine induce a reversible increase in delta-gamma and theta-gamma phase-amplitude coupling in frontal cortex of rat. *Front. Syst. Neurosci.* 11:41. doi: 10.3389/fnsys.2017.00041

Palva, J. M., Zhigalov, A., Hirvonen, J., Korhonen, O., Linkenkaerhansen, K., and Palva, S. (2013). Neuronal long-range temporal correlations and avalanche dynamics are correlated with behavioral scaling laws. *PNAS* 110, 3585–3590. doi: 10.1073/pnas.1216855110

Peng, C. K., Havlin, S., Stanley, H. E., and Goldberger, A. L. (1995). Quantification of scaling exponents and crossover phenomena in nonstationary heartbeat time series. *Chaos* 5, 82–87. doi: 10.1063/1.166141

Priesemann, V., Valderrama, M., Wibral, M., and Le, V. Q. M. (2013). Neuronal avalanches differ from wakefulness to deep sleep–evidence from intracranial depth recordings in humans. *PLoS Comput. Biol.* 9:e1002985. doi: 10.1371/journal.pcbi.1002985

Pritchard, W. S., Duke, D. W., and Krieble, K. K. (2010). Dimensional analysis of resting human EEG. II: surrogate-data testing indicates nonlinearity but not low-dimensional chaos. *Psychophysiology* 32, 486–491. doi: 10.1111/j.1469-8986.1995.tb02100.x

Rath, C., and Monetti, R. (2008). "Surrogates with random fourier phases," in *Proceedings of the 2008 International Conference Topics on Chaotic Systems: Selected Papers from Chaos*, (Singapore: World Scientific), 274–285.

Richard, H., Simon-Shlomo, P., Giuseppina, S., Rick, J., Nikulin, V. V., Mansvelder, H. D., et al. (2012). Detrended fluctuation analysis: a scale-free view on neuronal oscillations. *Front. Physiol.* 3:450. doi: 10.3389/fphys.2012.00450

Schartner, M., Seth, A., Noirhomme, Q., Boly, M., Bruno, M.-A., Laureys, S., et al. (2015). Complexity of multi-dimensional spontaneous EEG decreases during propofol induced general anaesthesia. *PLoS One* 10:e0133532. doi: 10.1371/journal.pone.0133532

Schreiber, T., and Schmitz, A. (1996). Improved surrogate data for nonlinearity tests. *Phys. Rev. Lett.* 77, 635–638. doi: 10.1103/PhysRevLett.77.635

Schreiber, T., and Schmitz, A. (2000). Surrogate time series. *Physica D* 142, 346–382. doi: 10.1016/S0167-2789(00)00043-9

Tagliazucchi, E., Von Wegner, F., Morzelewski, A., Brodbeck, V., Jahnke, K., and Laufs, H. (2013). Breakdown of long-range temporal dependence in default mode and attention networks during deep sleep. *Proc. Natl. Acad. Sci. U.S.A.* 110, 15419–15424. doi: 10.1073/pnas.1312848110

Thiery, T., Lajnef, T., Combrisson, E., Dehgan, A., Rainville, P., Mashour, G. A., et al. (2018). Long-range temporal correlations in the brain distinguish conscious wakefulness from induced unconsciousness. *Neuroimage* 179, 30–39. doi: 10.1016/j.neuroimage.2018.05.069

Tosoni, A., Pitzalis, S., Committeri, G., Fattori, P., Galletti, C., and Galati, G. (2015). Resting-state connectivity and functional specialization in human medial parieto-occipital cortex. *Brain Struct. Funct.* 220, 3307–3321. doi: 10.1007/s00429-014-0858-x

Varela, F., Lachaux, J.-P., Rodriguez, E., and Martinerie, J. (2001). The brainweb: phase synchronization and large-scale integration. *Nat. Rev. Neurosci.* 2, 229–239. doi: 10.1038/35067550

Visocchi, M., Tartaglione, T., Romani, R., and Meglio, M. (2001). Spinal cord stimulation prevents the effects of combined experimental ischemic and traumatic brain injury. *Stereotact. Funct. Neurosurg.* 76, 276–281. doi: 10.1159/000066731

Wang, Y., Liang, Z., Voss, L. J., Sleigh, J. W., and Li, X. (2014). Multi-scale sample entropy of electroencephalography during sevoflurane anesthesia. *J. Clin. Monit. Comput.* 28, 409–417. doi: 10.1007/s10877-014-9550-1

Yamamoto, T., Katayama, Y., Obuchi, T., Kobayashi, K., Oshima, H., and Fukaya, C. (2012). Spinal cord stimulation for treatment of patients in the minimally conscious state. *Neurol. Med. Chir.* 52, 475–481. doi: 10.2176/nmc.52.475

Yampolsky, C., Hem, S., and Bendersky, D. (2012). Dorsal column stimulator applications. *Surg. Neurol. Int.* 3(Suppl. 4), S275–S289. doi: 10.4103/2152-7806.103019

Zhang, J., Huang, Z., Chen, Y., Ghinda, D., Nikolova, Y., Wu, J., et al. (2018). Breakdown in the temporal and spatial organization of spontaneous brain activity during general anesthesia. *Hum. Brain Mapp.* 39, 2035–2046. doi: 10.1002/hbm.23984

Zhigalov, A., Kaplan, A., and Palva, J. M. (2016). Modulation of critical brain dynamics using closed-loop neurofeedback stimulation. *Clin. Neurophysiol.* 127, 2882–2889. doi: 10.1016/j.clinph.2016.04.028

Conflict of Interest Statement: The authors declare that the research was conducted in the absence of any commercial or financial relationships that could be construed as a potential conflict of interest.

Copyright © 2018 Liang, Li, Xia, Wang, Li, He and Bai. This is an open-access article distributed under the terms of the Creative Commons Attribution License (CC BY). The use, distribution or reproduction in other forums is permitted, provided the original author(s) and the copyright owner(s) are credited and that the original publication in this journal is cited, in accordance with accepted academic practice. No use, distribution or reproduction is permitted which does not comply with these terms.

frontiers in Physiology

ORIGINAL RESEARCH
published: 21 August 2018
doi: 10.3389/fphys.2018.01162

Higuchi Fractal Dimension of Heart Rate Variability During Percutaneous Auricular Vagus Nerve Stimulation in Healthy and Diabetic Subjects

Ryszard S. Gomolka[1]*, Stefan Kampusch*[2]*, Eugenijus Kaniusas*[2]*, Florian Thürk*[2]*, Jozef C. Széles*[3] *and Wlodzimierz Klonowski*[1]***

[1] Nalecz Institute of Biocybernetics and Biomedical Engineering, Polish Academy of Sciences, Warsaw, Poland, [2] Institute of Electrodynamics, Microwave and Circuit Engineering, TU Wien, Vienna, Austria, [3] Division of Vascular Surgery, University Clinic for Surgery, Medical University of Vienna, Vienna, Austria

Analysis of heart rate variability (HRV) can be applied to assess the autonomic nervous system (ANS) sympathetic and parasympathetic activity. Since living systems are non-linear, evaluation of ANS activity is difficult by means of linear methods. We propose to apply the Higuchi fractal dimension (HFD) method for assessment of ANS activity. HFD measures complexity of the HRV signal. We analyzed 45 RR time series of 84 min duration each from nine healthy and five diabetic subjects with clinically confirmed long-term diabetes mellitus type II and with diabetic foot ulcer lasting more than 6 weeks. Based on HRV time series complexity analysis we have shown that HFD: (1) discriminates healthy subjects from patients with diabetes mellitus type II; (2) assesses the impact of percutaneous auricular vagus nerve stimulation (pVNS) on ANS activity in normal and diabetic conditions. Thus, HFD may be used during pVNS treatment, to provide stimulation feedback for on-line regulation of therapy in a fast and robust way.

Keywords: Higuchi fractal dimension, heart rate variability, autonomic nervous system, vagus nerve stimulation, diabetes

OPEN ACCESS

Edited by:
Sladjana Z. Spasić,
University of Belgrade, Serbia

Reviewed by:
Tatiana Dias de Carvalho,
National University of La Matanza, Argentina
Chunhua Bian,
Nanjing University, China

****Correspondence:***
Wlodzimierz Klonowski
wklon@ibib.waw.pl;
wklonowski@gmail.com

Specialty section:
This article was submitted to Fractal Physiology, a section of the journal Frontiers in Physiology

Received: *14 March 2018*
Accepted: *03 August 2018*
Published: *21 August 2018*

Citation:
Gomolka RS, Kampusch S, Kaniusas E, Thürk F, Széles JC and Klonowski W (2018) Higuchi Fractal Dimension of Heart Rate Variability During Percutaneous Auricular Vagus Nerve Stimulation in Healthy and Diabetic Subjects. Front. Physiol. 9:1162. doi: 10.3389/fphys.2018.01162

INTRODUCTION

Analysis of HRV represents a common tool for assessment of autonomic cardiac regulation and provides information about pathophysiological changes in various diseases (Task Force of the European Society of Cardiology the North American Society of Pacing Electrophysiology, 1996; Ashkenazy et al., 1999; Klonowski, 2007; Pierzchalski et al., 2011; Bian et al., 2012; Jiang et al., 2013; Shaffer and Ginsberg, 2017). Based on evaluation of HRV, it was recently suggested that auricular vagus nerve stimulation (VNS) positively influences the ANS by activating its parasympathetic branch (La Marca et al., 2010; Kampusch et al., 2013, 2015a,b) and deactivating its sympathetic branch (Clancy et al., 2014; Murray et al., 2016). Estimation of sympathetic and parasympathetic activity of ANS is necessary for an accurate adjustment of auricular VNS, the task that is difficult to achieve and potentially vulnerable to erroneous interpretation with standard linear methods (Skinner et al., 1992; Yeragani et al., 1993; Wagner and Persson, 1998; Klonowski, 2007; Sharma, 2009; Sassi et al., 2015).

Abbreviations: ANS, autonomic nervous system; HFD, Higuchi fractal dimension; HRV, heart rate variability; pVNS, percutaneous auricular vagus nerve stimulation; SD, standard deviation.

Herein, we propose to apply a HFD algorithm (Higuchi, 1988), for assessment of ANS activity based on HRV. HFD is simple, fast and it is applicable in real-time calculations. In contrary to the linear methods, HFD can be directly applied to HRV series in time domain and it is suitable for short time series analysis, i.e., of 100–200 data points of a non-stationary signal. HFD needs to be provided with only one input parameter $k_{\max}$, specifying a maximal distance between the points compared in the time series. As the HFD measures the complexity of the curve that represents the analyzed signal on a plane, it always attains values between 1 and 2. The value of 1 corresponds to a regular time series (simple curve has Euclidean dimension equal 1) while for Gaussian-type noise HFD may attain different values: 1.5 for Brownian, 1.8 for pink, and 2.0 for white noise (Klonowski, 2007, 2011).

Up to date, the Higuchi algorithm was widely used in analysis of biomedical signals (Skinner et al., 1992; Klonowski, 2007, 2011; Sharma, 2009; West, 2010; Di Ieva et al., 2015; Kesić and Spasić, 2016) but only several papers presented HFD evaluation of HRV (Yeragani et al., 1993; Diosdado et al., 2010; Pierzchalski et al., 2011; Kamath, 2013; Sassi et al., 2015; Kesić and Spasić, 2016; Tavares et al., 2016; Wajnsztejn et al., 2016; Gomes et al., 2017). Hence, the aim of our research was to assess whether, based on HRV time series analysis, HFD would: (1) discriminate healthy subjects from patients with diabetes mellitus type II; (2) assess the impact of pVNS on ANS activity in normal and diabetic conditions.

MATERIALS AND METHODS

Data

We retrospectively analyzed 56 RR time series, of 84 min duration each, from an open-label pilot study registered at ClinicalTrials.gov (no. NCT02098447). The study was approved by the local ethics committee of the Medical University of Vienna (no. 1924/2013) and by the Austrian Agency for Health and Food Safety. The RR time series were recalculated from ECG recordings obtained from nine healthy and five diabetic subjects, aged 40–80 years, with clinically confirmed long-term diabetes mellitus type II, and diabetic foot ulcer (*ulcus cruris*) lasting for more than 6 weeks (**Table 1**). Subject's exclusion criteria were: participation in another clinical trial over the last 5 weeks before the experiment; addiction to substance abuse; autonomous nervous system dysfunction (except diabetic polyneuropathy); medical treatment with vasoactive substances; history of heart arrhythmia or presence of an active implantable device. Women in childbearing age were not included if pregnant or nursing. All diabetic subjects had a history of diabetes in average(SD) of 14(5) years. The ECGs were acquired by means of a MP36 recording system with a three-lead Einthoven II derivation (BIOPAC Systems, Inc., Goleta, CA, United States) and a sampling rate of 1 kHz, for further calculation of heart rate and HRV signals. The measurements were obtained between February 24, 2014 and April 3, 2015. The heart rate was calculated using proprietary MATLAB algorithms with manual control (normal-normal RR series, extrasystoles, and artifacts excluded manually). All subjects gave written informed consent in accordance with the Declaration of Helsinki.

TABLE 1 | Demographic characteristics of healthy and diabetic subjects (*p*-values for differences in age and BMI are given) included in the study (Ref. ClinicalTrials.gov no. NCT02098447).

	Healthy subjects (n = 9)	Diabetic subjects (n = 5)
Sex (male/female)	4/5	4/1
Age (y.o.)	50.7 ± 7.2	53.8 ± 11.1 (p = 0.63)
BMI (kg/m^2)	23.8 ± 3.3	34.6 ± 7.5 (p < 0.001)

Each of the healthy and diabetic subjects underwent four sessions of pVNS mediated via four needle electrodes, with one acting as the reference electrode, in vagally innervated regions of the right auricle (Kampusch et al., 2013, 2015a,b; Kaniusas et al., 2015). Each session consisted of five consecutive phases: B- baseline measurement (10 min), S1- first pVNS (22 min), P1- baseline measurement after the first pVNS (20 min), S2- second pVNS (22 min), P2- baseline measurement after the second pVNS (10 min). All measurements were performed at comparable daytimes.

Eleven out of 56 RR time series were excluded because of significant artifacts. The artifacts were caused by a low quality of the raw data (7 time series) or presence of cardiac arrhythmia in the signal (4 time series). Therefore, further analysis was performed on 45 RR time series (28 for healthy and 17 for diabetics).

In order to standardize the length of the series, every RR record was linearly resampled with 1 Hz. Low frequency of resampling was used to preserve the original characteristics of the signal. Higher sampling frequencies would change the shape of the original RR curve by introducing additional samples and extending the total length of the signal, subsequently affecting the estimation of real HFD values by introduction of low frequencies.

Higuchi Fractal Dimension Algorithm

Calculations were performed by means of an in-house implementation of the HFD algorithm in MATLAB R2016b (The Mathworks Inc., Natick, MA, United States; Academic License, IBBE PAS). HRV signals were analyzed within windows of 100 data points displaced by a 50 consecutive samples across the signal, which resulted in 99 HFD values for each of the RR time series. The window of 100 data points reflected approximately 1.5 min windows in RR time series. Consecutively, every phase in each of the time series consisted of the following number of HFD values: B- 11 HFD values; S1- 25 values; P1- 24 values; S2- 25 values; P2- 14 values.

Estimation of the Optimal $k_{\max}$ Parameter

In order to find an optimal $k_{\max}$ parameter, allowing clear differentiation between healthy and diabetic subjects, the HFD was calculated in all of the 45 RR time series, for $k_{\max}$ ranging from 2 to 50 (**Figure 1**). Calculation for $k_{\max}$ above 50 was not

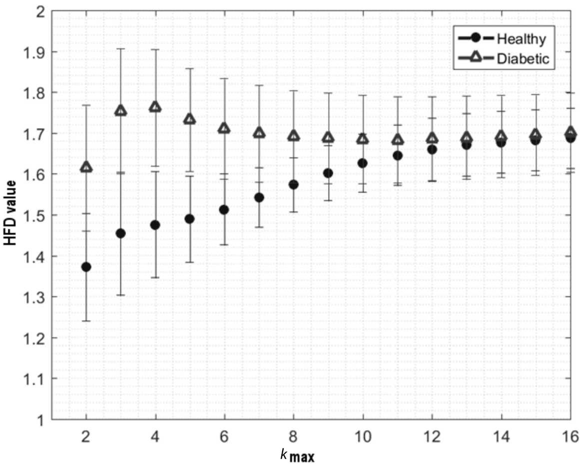

FIGURE 1 | Fluctuation of aggregated average ± SD of HFD values for healthy and diabetic subjects, calculated for $k_{\max}$ parameter from 1 to 16. Clear differentiation between subjects obtained for $k_{\max} = 5$, by means of two-sided Wilcoxon ranksum test ($p < 7.97e{-}25$).

possible due to the window length of 100 samples – maximal distance between compared samples was less than 1/2 of the window length. Optimal $k_{\max}$ was chosen based on a clear separation of the mean of the aggregated HFD values for healthy and diabetic subjects, and on the minimization of the two-sided Wilcoxon ranksum test *p*-value for comparison of medians of the HFD values. Subsequent analyses were performed for HFDs calculated with the chosen parameter $k_{\max} = 5$. (cf. 3.1, **Figure 1**)

Aggregated Distributions of HFD Values – Overall

In each of the RR time series, 99 HFD values were calculated. HFDs aggregated from the time series were tested by Shapiro–Wilk normality test, to confirm non-normal distribution of the values. Afterwards, the aggregated HFD distributions were computed in healthy and diabetics from 2,772 and 1,683 HFD values, respectively. Fifth, 25th, 75th, and 95th percentiles, means, medians, SDs, skewness, and kurtosis were calculated separately in both HFD distributions, for subsequent comparison.

Average HFD Values Across the Time Series

Mean representative vectors of HFDs were calculated in respect to time (t) in healthy and diabetics, for comparison by means of Wilcoxon matched-pairs signed rank test. For visual presentation of the results, the average ±95% confidence intervals of the aggregated HFD values from healthy and diabetics were plotted in function of time. Pearson's linear correlation coefficient was calculated between the average HFDs(t) and the time course of the experiment in both groups. Results were considered significant if correlation exceeded 50% with a *p*-significance value <0.05.

Average HFD Values Within the Experimental Phases

To assess whether the HFDs for healthy and diabetics are changing overtime between B, S1, P1, S2, and P2 phases, average ± SD of aggregated HFD values were calculated for each phase of the time series in each of the subjects separately. As a result, each of the subjects was represented by 5 average ± SD HFD values. Afterward, two-way analysis of variance (ANOVA) was applied to reveal significant differences between the average HFDs in healthy and diabetic groups, in respect to the phase of experiment. Bonferroni's multiple comparison test was used in search of differences between specific phases of the time series. Whiskers-box plots of the aggregated HFDs within the phases were generated for visual representation of the results.

Aggregated Distributions of HFD Within the Experimental Phases

To check whether pVNS changes the shape of HFD distribution overtime, 5th, 25th, 75th, and 95th percentiles, means, medians, SDs, skewness and kurtosis were calculated for the HFD aggregated distributions from B, S1, P1, S2, and P2 phases separately, for subsequent comparison. Afterwards, 10 bins-wide histograms of the aggregated HFD distributions were computed within the phases, for healthy and diabetic subjects separately. To objectively assess the magnitude of the changes caused by pVNS, contrast histograms were calculated as a ratio of difference to sum of bins heights between previously computed histograms for S1

TABLE 2 | Numerical characteristics of HFD aggregated distributions for experimental phases B, S1, P1, S2, P2 in healthy and diabetic subjects.

	Healthy subjects						**Diabetic subjects**					
	Overall	**B**	**S1**	**P1**	**S2**	**P2**	**Overall**	**B**	**S1**	**P1**	**S2**	**P2**
5th percentile	1.29	1.34	1.30	1.28	1.29	1.26	1.42	1.45	1.44	1.37	1.44	1.37
25th percentile	1.38	1.42	1.39	1.37	1.38	1.33	1.60	1.65	1.64	1.59	1.59	1.51
75th percentile	1.59	1.57	1.61	1.59	1.59	1.55	1.85	1.92	1.85	1.83	1.85	1.80
95th percentile	1.76	1.75	1.75	1.76	1.78	1.70	2.00	2.00	1.98	1.98	2.00	1.99
Mean	1.49	1.50	1.51	1.49	1.50	1.45	1.72	1.77	1.74	1.71	1.72	1.65
Median	1.48	1.49	1.49	1.48	1.48	1.43	1.73	1.77	1.76	1.72	1.72	1.63
SD	0.14	0.12	0.14	0.15	0.15	0.15	0.17	0.17	0.16	0.18	0.17	0.19
Skewness	0.42	0.75	0.33	0.42	0.52	0.37	–0.30	–0.64	–0.53	–0.38	–0.12	0.18
Kurtosis	2.80	3.48	2.42	2.48	2.83	3.35	2.44	2.99	2.87	2.59	2.27	2.17

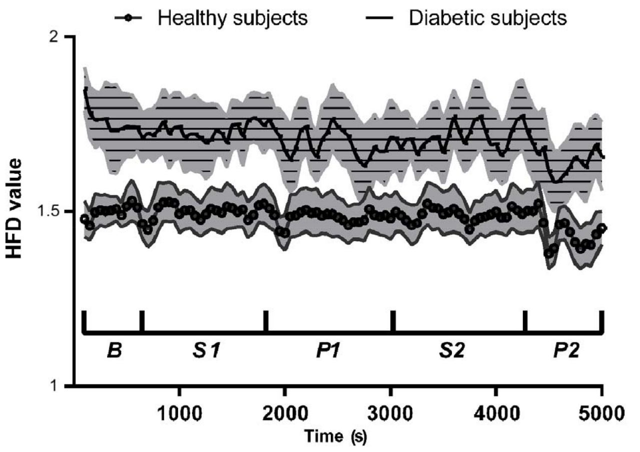

FIGURE 2 | Mean ± 95% confidence intervals of HFD values during the course of experiment, for healthy and diabetic subjects separately.

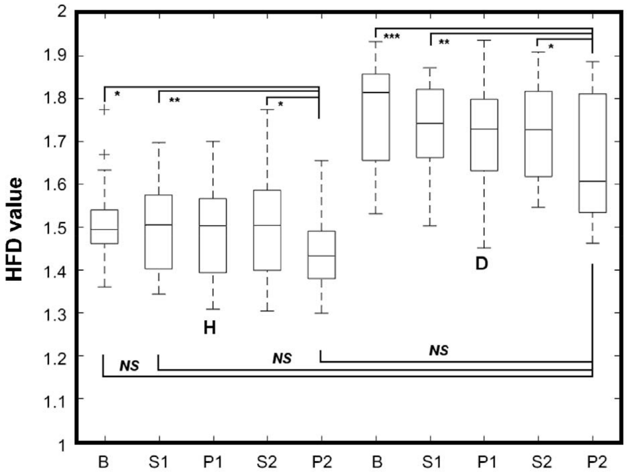

FIGURE 3 | Whiskers-box plot for HFD values aggregated in respect to the phase of experiment, for healthy (H) and diabetic (D) subjects separately. Whiskers represent the range of min-max HFD values. B, S1, P1, S2, P2 – phases of the experiment. *$p < 0.05$; **$p < 0.01$; ***$p < 0.001$.

and B; P1 and S1, S2 and P1, P2 and S2, and P2 and B phases in both groups.

Statistical Analysis

All calculations and statistical analyses were performed by means of MATLAB R2016b.

RESULTS

Estimation of the Optimal $k_{\max}$ Parameter

The aggregated HFD values for healthy and diabetics were found as the most statistically different for $k_{\max} = 5$, by means of a two-sided Wilcoxon ranksum test ($p < 0.001$). Hence, the optimal $k_{\max}$ parameter, allowing clear differentiation between the healthy and diabetes group, was chosen as 5.

Aggregated Distributions of HFD Values – Overall

Shapiro–Wilk normality test revealed that HFD values, aggregated jointly from healthy and diabetic subjects, do not form a normal distribution ($W = 0.9745$, $p < 0.05$). Characteristics of HFD aggregated distributions (i.e., 5th, 25th, 75th, and 95th percentiles, means, medians, SDs, skewness, and kurtosis) are presented in **Table 2**.

Average HFD Values Across the Time Series

Wilcoxon matched-pairs signed rank test revealed statistical differences between the average HFD(t) values in healthy and diabetics ($W = 4{,}950$, 99 pairs, $p < 0.0001$). The mean(median) difference between the groups was 0.226(0.230). Absolute Pearson's linear correlation coefficient between the average HFD(t) values and the time course of experiment was larger in diabetics ($r = -0.56$, $p < 0.0001$), than in healthy ($r = -0.44$, $p = 0.0002$; **Figure 2**).

Average HFD Values Within the Experimental Phases

Two-way ANOVA showed significant differences between the average HFD's from different experimental phases, in healthy and diabetic subjects. The differences were visible between the healthy and diabetic group [$F(1,43) = 60.79$, $p < 0.0001$], and due to the experimental phases [$F(4,172) = 10.80$, $p < 0.0001$]. Bonferroni's multiple comparisons test showed significant differences in mean HFD values between B and P2, S1 and P2, and S2 and P2 phases both in healthy ($p < 0.05$, $p < 0.01$, and $p < 0.05$, respectively) and diabetics ($p < 0.001$, $p < 0.01$, and $p < 0.05$, respectively). The mean HFD values were significantly different between healthy and diabetics in all phases (largest $p < 0.05$) except P2 in diabetic subjects, which was not different from B, S1, and P2 in healthy (**Figure 3**).

Aggregated Distributions of HFD Within the Experiment Phases

Table 2 presents numerical characteristics of HFD aggregated distributions for experimental phases B, S1, P1, S2, P2 (5th, 25th, 75th, and 95th percentiles, means, medians, SDs, skewness and kurtosis) in healthy and diabetic subjects. **Figure 4** shows 10 bins-wide histograms of the aggregated HFD distributions for the phases and **Figure 5** shows contrast histograms for comparison of the distributions between S1 and B; P1 and S1, S2 and P1, P2 and S2, and P2 and B phases, for healthy and diabetics. The characteristics and the histograms were calculated in total from 4,455 HFD values. Overall mean(median) ± SD HFD values were found as 1.49(1.48) ± 0.14 and 1.72(1.73) ± 0.17 for healthy and diabetic subjects, respectively. In diabetic subjects, skewness of aggregated HFD distributions was observed to change from negative (–0.64) to positive (0.18) between the experimental phases (Pearson's correlation coefficient $r = 0.98$;

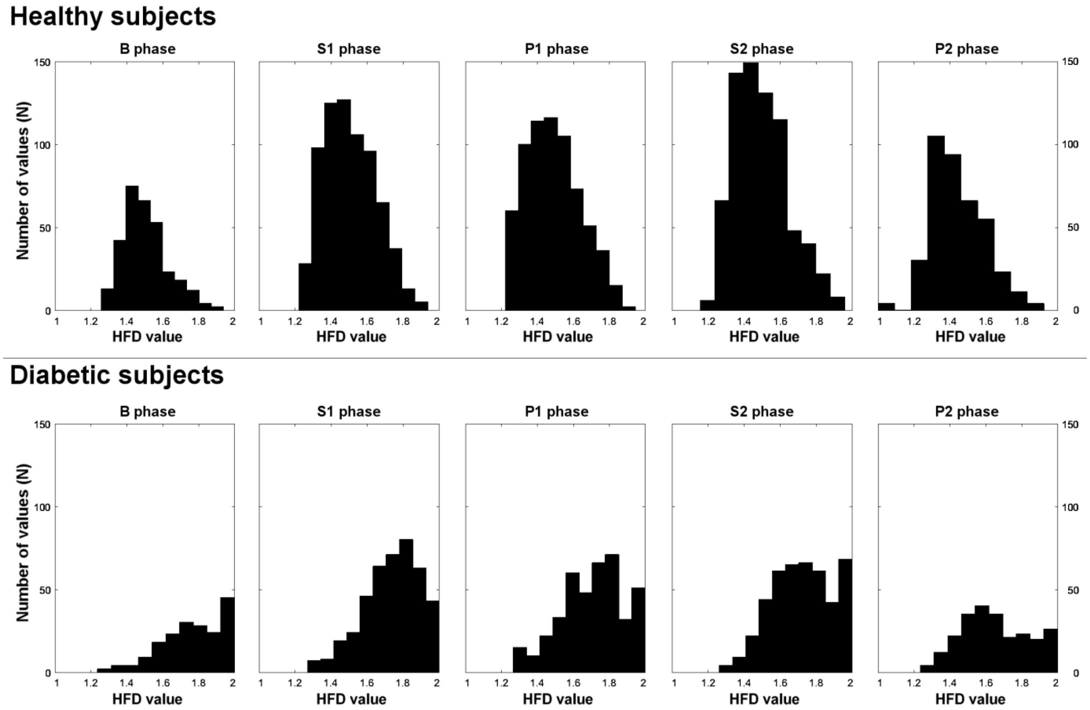

FIGURE 4 | Histograms of aggregated HFD distributions from B, S1, P1, S2, P2 experimental phases, for healthy and diabetic subjects separately.

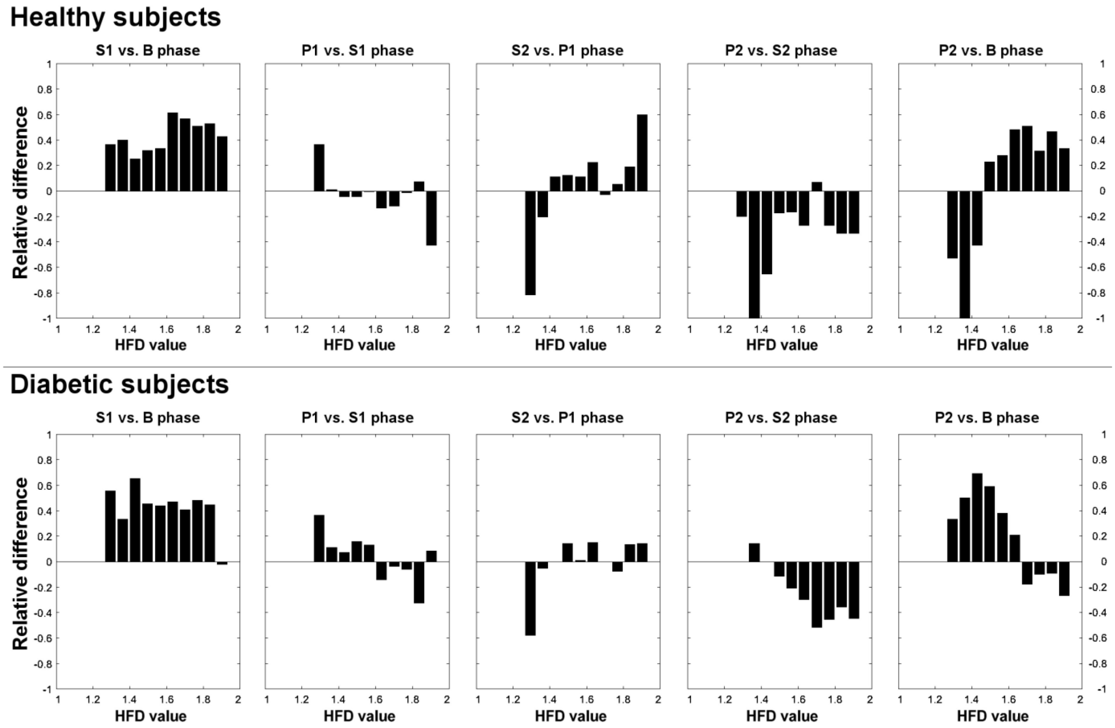

FIGURE 5 | Contrast histograms of HFD distributions for comparison of S1 and B; P1 and S1, S2 and P1, P2 and S2, and P2 and B experimental phases, for healthy and diabetic subjects separately.

$R^2 = 0.96$, $p < 0.01$). The opposite, but not monotonic (and not significantly different from zero slope) effect was observable in the healthy group ($r = 0.54$; $R^2 = 0.29$, $p = 0.35$). Moreover, kurtosis of the distributions was found consistently dropping over the experimental phases only in diabetics.

DISCUSSION

This study advances knowledge in HRV analysis in healthy and diabetic subjects. By means of our implementation of Higuchi's method, overall mean ± SD of aggregated HFD values were found higher for diabetics than for healthy subjects (**Figure 1** and **Table 2**). Significant differences in mean values of HFD aggregated distributions were found between the B, S1, and P2 phases in both groups. It is also worth to highlight that the mean HFD from P2 in diabetics was found not different from that in B, S1, and P2 phases in healthy (**Figure 3**). The results indicate no significant influence of pVNS on mean HFD during or directly after the stimulation in both groups. However, the effect seems to be delayed in time and its overall permanence was more explicit in diabetics than in healthy subjects. Moreover, skewness of the aggregated HFD distributions was rising significantly from negative to positive between the phases in diabetics, while a clear trend was not observable in healthy.

Our findings agree with the changes observed in spectral analysis of the RR time series, like the total power (TP – total variability), high frequency power (HF – parasympathetic activity), low frequency (LF – mixed sympathetic and parasympathetic activity) power, and the LF/HF ratio (sympathovagal balance) in the presented subject population (Kampusch et al., 2015b, unpublished data). TP, HF, LF, and LF/HF significantly differ between healthy and diabetic subjects at baseline and converge due to stimulation. Increases in those parameters could be shown due to stimulation in healthy and diabetics, indicating an increased parasympathetic activity and changed sympathovagal balance, like also observed in HFD analysis here. Further studies are required to understand in detail the interrelation of the evaluated HFD parameters with ANS measures. However, our findings are in accordance with previous reports regarding the HFD or detrended fluctuation analysis (Ashkenazy et al., 1999) of the HRV signal in normal conditions, congestive heart failure and heart transplanted patients (Cerutti et al., 2007), single or multiple lesions stroke (D'Addio et al., 2009), in arrhythmia (Pierzchalski et al., 2011), during meditation (Diosdado et al., 2010; Kamath, 2013), guided breathing exercises (Tavares et al., 2016), in children with ADHD hyperactivity disorder (Wajnsztejn et al., 2016), in healthy subjects immediately after physical exercises (Gomes et al., 2017), or in diabetes (Malpas and Maling, 1990).

Our results indicate a slight pVNS-induced shift of HFD values from assembled close to 2 (chaotic signal) to lower values, in diabetics. The shift was observed mostly for the HFDs above the 50th percentile of distribution and was confirmed by the change in the distribution's skewness and kurtosis (**Table 2** and **Figure 4**). Moreover, a relative increase in HFDs below 1.6 is observable in P2, compared to B in diabetics. The effect is connected with a smaller decrease for HFDs above 1.6 (**Figure 5**). In contrary, pVNS seems to affect the whole distribution of the HFD values equally in healthy. The shape of the HFD distribution was not changed here substantially over the experiment (**Figure 4**), however, a slight increase in the higher HFDs associated with a decrease in HFDs of lower range is observable between P2 and B (**Figure 5**).

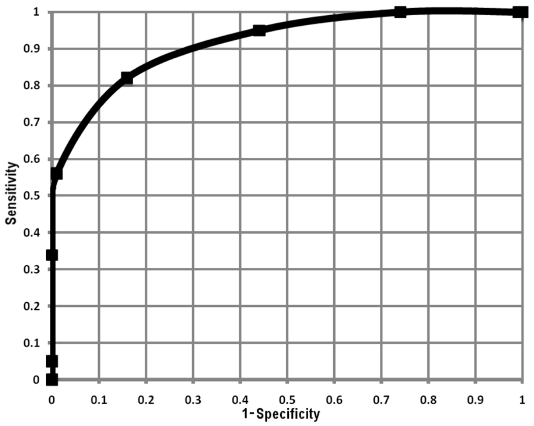

FIGURE 6 | Receiver operating curve calculated from average HFD values within the experimental phases, for each healthy and diabetic subject (in total 140 HFD values for healthy and 85 for diabetic subjects).

As higher HFD values correspond to the presence of higher frequencies in the signals Fourier spectrum (Yeragani et al., 1993; Klonowski et al., 2006) our observations would suggest that pVNS may increase the parasympathetic (see above) and decrease the sympathetic activity of ANS in diabetic conditions, which is in line with (Clancy et al., 2014) for healthy subjects. Such observation implies VNS-induced stabilization of ANS balance in diabetic subjects. It is worth to note that due to neuropathy a lower parasympathetic and lower sympathetic activity is generally observed in diabetes, compared to normal conditions (Task Force of the European Society of Cardiology the North American Society of Pacing Electrophysiology, 1996). Moreover, we found diabetic subjects showing larger SD of HFD values in all of the experimental phases ("more chaotic" RR signal), so pVNS seems to have a "fine-tuning" effect on ANS activity. The effect in healthy is much weaker, since pVNS seems to alter their ANS activity within the range of auto regulation capabilities.

Limitations of our study include the necessary predefinition of the input parameter $k_{\max}$, in advance. Herein, we have experimentally set $k_{\max}$ to 5. Higher $k_{\max}$ values would provide underestimation, while lower provide overestimation of HFD (HFD close to 1 or to 2, respectively). In both situations the distinction between the healthy and diabetic group might be not possible (**Figure 1**). Further, with respect to the included subject groups, a significant difference in BMI of healthy and diabetic subjects (**Table 1**) needs to be considered as a potential co-founding factor when analyzing ANS function. We have performed analysis of HRV time series recalculated from original ECG signals. It was previously shown that HFD may provide similar results when applied to raw data (Pierzchalski et al., 2011).

Hence, it would be worth to compare HFD analysis with spectral analysis performed on the same HRV time series, or to apply both analyses to the original ECG signals from diabetic and healthy subjects. Additionally, physical activity and medication were not documented during the study for diabetic subjects.

Hence, our results indicate that HFD provides high resolution insight into ANS activity during pVNS based on HRV time series analysis. Simplicity of HFD makes the assessment of ANS activity prospectively possible in on-line systems and may bring accuracy (**Figure 6**) to both diagnostic systems and therapeutic closed-loop pVNS systems.

CONCLUSION

We have shown that the HFD assesses the ANS activity and differentiates healthy from diabetic subjects, based on HRV signals. Moreover, HFD provides fast and robust distinction between action of parasympathetic and sympathetic ANS activity. Because of its simplicity, HFD may be easily used in pVNS systems to provide direct stimulation feedback for on-line regulation of therapy. Hence, our results have potential implication for patients' care and technological advancement of pVNS therapy.

AUTHOR CONTRIBUTIONS

RG performed the data analysis and wrote the manuscript. SK and FT performed the data analysis and reviewed the manuscript. EK supervised the data analysis and reviewed the manuscript. JS supplied the data and reviewed the manuscript. WK designed the conception of the work, supervised the data analysis, and reviewed the manuscript.

FUNDING

This research was partially funded by EU COST Action BM1309 "EMF-MED," through "Short Term Scientific Mission" (STSM) grant for RG. SK and EK were funded by the Austrian Research Promotion Agency (Grant No. 853701).

ACKNOWLEDGMENTS

RG and WK acknowledge support by Nalecz Institute of Biocybernetics and Biomedical Engineering, Polish Academy of Sciences through its statutory activity and covering publication costs.

REFERENCES

Ashkenazy, Y., Lewkowicz, M., and Levitan, J. (1999). Discrimination between healthy and sick cardiac autonomic nervous system by detrended heart rate variability analysis. *Fractals* 07, 85–91. doi: 10.1142/S0218348X99000104

Bian, C., Qin, C., Ma, Q. D., and Shen, Q. (2012). Modified permutation-entropy analysis of heartbeat dynamics. *Phys. Rev. E Stat. Nonlin. Soft Matter Phys.* 85(2 Pt 1):021906. doi: 10.1103/PhysRevE.85.021906

Cerutti, S., Esposti, F., Ferrario, M., Sassi, R., and Signorini, M. G. (2007). Long-term invariant parameters obtained from 24-h holter recordings: a comparison between different analysis techniques. *Chaos* 17:15108. doi: 10.1063/1.2437155

Clancy, J. A., Mary, D. A., Witte, K. K., Greenwood, J. P., Deuchars, S. A., and Deuchars, J. (2014). Non-invasive vagus nerve stimulation in healthy humans reduces sympathetic nerve activity. *Brain Stimul.* 7, 871–877. doi: 10.1016/j.brs.2014.07.031

D'Addio, G., Corbi, G., Accardo, A., Russo, G., Ferrara, N., Mazzoleni, M. C., et al. (2009). Fractal behaviour of heart rate variability reflects severity in stroke patients. *Stud. Health Technol. Inform.* 150, 794–798. doi: 10.3233/978-1-60750-044-5-794

Di Ieva, A., Esteban, F. J., and Grizzi, F. (2015). Fractals in the Neurosciences, Part II. *Neuroscientist* 21, 30–43. doi: 10.1177/1073858413513928

Diosdado, A. M., Coyt, G. G., and Uribe, B. M. P. (2010). "Oscillations in the evaluation of fractal dimension of RR intervals time series," in *Proceedings of the 2010 Annual International Conference of the IEEE Engineering in Medicine and Biology* (Piscataway, NJ: IEEE), 4570–4573.

Gomes, R. L., Vanderlei, L. C. M., and Garner, D. M. (2017). Higuchi fractal analysis of heart rate variability is sensitive during recovery from exercise in physically active men. *Med. Express* 4, 1–8. doi: 10.5935/MedicalExpress.2017.03.02

Higuchi, T. (1988). Approach to an irregular time series on the basis of the fractal theory. *Physica D* 31, 277–283. doi: 10.1016/0167-2789(88)90081-4

Jiang, S., Bian, C., Ning, X., and Ma, Q. D. (2013). Visibility graph analysis on heartbeat dynamics of meditation training. *Appl. Phys. Lett.* 102, 253–702. doi: 10.1063/1.4812645

Kamath, C. (2013). Analysis of heart rate variability signal during meditation using deterministic-chaotic quantifiers. *J. Med. Eng. Technol.* 37, 436–448. doi: 10.3109/03091902.2013.828106

Kampusch, S., Kaniusas, E., and Szeles, J. C. (2013). "New approaches in multi-punctual percutaneous stimulation of the auricular vagus nerve," in *Proceedings of the Sixth Annnual International Conference on IEEE/EMBS Neural Engineering*, San Diego, CA.

Kampusch, S., Kaniusas, E., and Széles, J. C. (2015a). Modulation of muscle tone and sympathovagal balance in cervical dystonia using percutaneous stimulation of the auricular vagus nerve. *Artif. Organs* 39, E202–E212. doi: 10.1111/aor.12621

Kampusch, S., Thürk, F., Kaniusas, E., and Széles, J. C. (2015b). "Autonomous nervous system modulation by percutaneous auricular vagus nerve stimulation," in *Proceedings of the 2015 IEEE Sensors Applications Symposium*, Zadar, 79–84.

Kaniusas, E., Kampusch, S., and Széles, J. C. (2015). "Depth profiles of the peripheral blood oxygenation in diabetics and healthy subjects in response to auricular electrical stimulation," in *Proceedings of the 2015 IEEE Sensors Applications Symposium*, Zadar, 11–16.

Kesić, S., and Spasić, S. Z. (2016). Application of higuchi's fractal dimension from basic to clinical neurophysiology: a review. *Comput. Methods Programs* 133, 55–70. doi: 10.1016/j.cmpb.2016.05.014

Klonowski, W. (2007). From conformons to human brains: an informal overview of nonlinear dynamics and its applications in biomedicine. *Nonlinear Biomed. Phys.* 1:5. doi: 10.1186/1753-4631-1-5

Klonowski, W. (2011). Personalized neurological diagnostics from biomedical physicist's point of view and application of new non-linear dynamics methods in biosignal analysis. *Int. J. Biol. Biomed. Eng.* 5, 190–200.

Klonowski, W., Olejarczyk, E., Stepien, R., et al. (2006). "Monitoring the depth of anaesthesia using fractal complexity method," in *Complexus Mundi*, ed. M. Novak Miroslav (Singapore: World Scientific), 333–342.

La Marca R, Nedeljkovic, M., Yuan, L., Maercker, A., and Elhert, U. (2010). Effects of auricular electrical stimulation on vagal activity in healthy men: evidence from a three-armed randomized trial. *Clin. Sci.* 118, 537–546. doi: 10.1042/CS20090264

Malpas, S. C., and Maling, T. J. (1990). Heart-rate variability and cardiac autonomic function in diabetes. *Diabetes Metab. Res. Rev.* 39, 1177–1181. doi: 10.2337/diabetes.39.10.1177

Murray, A. R., Atkinson, L., Mahadi, M. K., Deuchars, S. A., and Deuchars, J. (2016). The strange case of the ear and the heart: the auricular vagus nerve and its influence on cardiac control. *Auton. Neurosci.* 199, 48–53. doi: 10.1016/j.autneu.2016.06.004

Pierzchalski, M., Stepien, R. A., and Stepien, P. (2011). New nonlinear methods of heart rate variability analysis in diagnostics of atrial fibrillation. *Int. J. Biol. Biomed. Eng.* 5, 201–208.

Sassi, R., Cerutti, S., Lombardi, F., Malik, M., Huikuri, H. V., Peng, C. K., et al. (2015). Advances in heart rate variability signal analysis: joint position statement by the e-cardiology ESC working group and the european heart rhythm association co-endorsed by the asia pacific heart rhythm society. *Europace* 17, 1341–1353. doi: 10.1093/europace/euv015

Shaffer, F., and Ginsberg, J. P. (2017). An overview of heart rate variability metrics and norms. *Front. Public Health* 5:258. doi: 10.3389/fpubh.2017.00258

Sharma, V. (2009). Deterministic chaos and fractal complexity in the dynamics of cardiovascular behavior: perspectives on a new frontier. *Open Cardiovasc. Med. J.* 3, 110–123. doi: 10.2174/1874192400903010110

Skinner, J., Molnar, M., Vybiral, T., and Mitra, M. (1992). Application of chaos theory to biology and medicine.itle. *Integr. Physiol. Behav. Sci.* 27, 39–53. doi: 10.1007/BF02691091

Task Force of the European Society of Cardiology the North American Society of Pacing Electrophysiology (1996). Heart rate variability: standards of measurement, physiological interpretation, and clinical use. *Circulation* 93, 1043–1065. doi: 10.1161/01.CIR.93.5.1043-1065

Tavares, B. S., de, Paula Vidigal G, Garner, D. M., Raimundo, R. D., de, Abreu LC, and Valenti, V. E. (2016). Effects of guided breath exercise on complex behaviour of heart rate dynamics. *Clin. Physiol. Funct. Imaging* 37, 1–8. doi: 10.1111/cpf.12347

Wagner, C., and Persson, P. (1998). Chaos in the cardiovascular system: an update. *Cardiovasc. Res.* 40, 257–264. doi: 10.1016/S0008-6363(98)00251-X

Wajnsztejn, R., Carvalho, T. D., De, and Garner, D. M. (2016). Higuchi fractal dimension applied to RR intervals in children with attention deficit hyperactivity disorder. *J. Hum. Growth Dev.* 26, 147–153. doi: 10.7322/jhgd.119256

West, B. J. (2010). Fractal physiology and the fractional calculus: a perspective. *Front. Physiol.* 1:12. doi: 10.3389/fphys.2010.00012

Yeragani, V. K., Srinivasan, K., Vempati, S., Pohl, R., and Balon, R. (1993). Fractal dimension of heart rate time series: an effective measure of autonomic function. *J. Appl. Physiol.* 75, 2429–2438. doi: 10.1152/jappl.1993.75.6.2429

Conflict of Interest Statement: JS, EK, and SK own shares and receive honoraria from SzeleSTIM GmbH.

The remaining authors declare that the research was conducted in the absence of any commercial or financial relationships that could be construed as a potential conflict of interest.

The handling Editor declared a past co-authorship with one of the authors, WK.

Copyright © 2018 Gomolka, Kampusch, Kaniusas, Thürk, Széles and Klonowski. This is an open-access article distributed under the terms of the Creative Commons Attribution License (CC BY). The use, distribution or reproduction in other forums is permitted, provided the original author(s) and the copyright owner(s) are credited and that the original publication in this journal is cited, in accordance with accepted academic practice. No use, distribution or reproduction is permitted which does not comply with these terms.

frontiers
in Physiology

ORIGINAL RESEARCH
published: 18 May 2018
doi: 10.3389/fphys.2018.00546

Sinoatrial Beat to Beat Variability Assessed by Contraction Strength in Addition to the Interbeat Interval

Helmut Ahammer[1]†, Susanne Scheruebel[1]†, Robert Arnold[1], Michael Mayrhofer-Reinhartshuber[1,2], Petra Lang[1], Ádám Dolgos[3], Brigitte Pelzmann[1] and Klaus Zorn-Pauly[1]*

[1] Institute of Biophysics, Medical University of Graz, Graz, Austria, [2] KML Vision OG, Graz, Austria, [3] Institute for eHealth, Graz University of Applied Sciences, Graz, Austria

Beat to beat variability of cardiac tissue or isolated cells is frequently investigated by determining time intervals from electrode measurements in order to compute scale dependent or scale independent parameters. In this study, we utilize high-speed video camera recordings to investigate the variability of intervals as well as mechanical contraction strengths and relative contraction strengths with nonlinear analyses. Additionally, the video setup allowed us simultaneous electrode registrations of extracellular potentials. Sinoatrial node tissue under control and acetylcholine treated conditions was used to perform variability analyses by computing sample entropies and Higuchi dimensions. Beat to beat interval variabilities measured by the two recording techniques correlated very well, and therefore, validated the video analyses for this purpose. Acetylcholine treatment induced a reduction of beating rate and contraction strength, but the impact on interval variability was negligible. Nevertheless, the variability analyses of contraction strengths revealed significant differences in sample entropies and Higuchi dimensions between control and acetylcholine treated tissue. Therefore, the proposed high-speed video camera technique might represent a non-invasive tool that allows long-lasting recordings for detecting variations in beating behavior over a large range of scales.

Keywords: heart rate variability, beat to beat variability, video motion analysis, sinoatrial node, acetylcholine, sample entropy, Higuchi dimension

OPEN ACCESS

Edited by:
Sladjana Z. Spasić,
University of Belgrade, Serbia

Reviewed by:
Danuta Makowiec,
University of Gdansk, Poland
Sebastian Wallot,
Max-Planck-Institut für Empirische Ästhetik, Germany

***Correspondence:**
Helmut Ahammer
helmut.ahammer@medunigraz.at

† Joint first authors.

Specialty section:
This article was submitted to Fractal Physiology, a section of the journal Frontiers in Physiology

Received: *16 February 2018*
Accepted: *27 April 2018*
Published: *18 May 2018*

Citation:
Ahammer H, Scheruebel S, Arnold R, Mayrhofer-Reinhartshuber M, Lang P, Dolgos Á, Pelzmann B and Zorn-Pauly K (2018) Sinoatrial Beat to Beat Variability Assessed by Contraction Strength in Addition to the Interbeat Interval. Front. Physiol. 9:546. doi: 10.3389/fphys.2018.00546

INTRODUCTION

Heart rate variability (HRV) refers to variations in the time intervals between two consecutive heart beats and serves as a diagnostic and prognostic tool for cardiac as well as non-cardiac diseases, e.g., heart failure, aging, Parkinson's disease, diabetes, and sepsis (Goldberger et al., 2002; Devos et al., 2003; Kudat et al., 2016; de Castilho et al., 2017; Elstad et al., 2018; Sessa et al., 2018). These variations are mainly attributed to dynamic changes of neuroendocrine inputs on ion channel activity in the sinoatrial node SAN, but a certain degree of beat to beat variability is inherently present at the level of the isolated heart, within the isolated SAN and also at the level of single sinoatrial pacemaker cells (Lombardi and Stein, 2011; Papaioannou et al., 2013; Yaniv et al., 2014a; Zaniboni et al., 2014).

There is a large number of quantitative algorithms to investigate these interval variations in autorhythmic cardiac tissue, cell clusters, or single cells, including spectral, linear, and nonlinear methods. Power-law behavior of beat to beat intervals *BBIs* analyzed by the power spectral method has been shown for neonatal rat cardiomyocytes in cultured tissue layers measured by microelectrode arrays (Ponard et al., 2007). Long-range correlations were also detected in extracellular electrograms of human embryonic stem cell-derived cardiomyocyte clusters by using again spectral methods (Mandel et al., 2012). Furthermore, fractal-like behavior has been reported for rabbit sinoatrial node tissue and for a small percentage of single sinoatrial node cells by using power law and detrended fluctuation analysis (Yaniv et al., 2014a) and in small clusters of chick embryonic cardiomyocytes (Ahammer et al., 2013). So far, investigations have focused on variabilities in the time domain of both, electrical and contraction signals. The underlying processes are tightly linked via the excitation-contraction-coupling (Eisner et al., 2017) and hence, the time structure of the electrical process substantially shapes not only the frequency of contraction but also its magnitude. Thus, it is reasonable to assume that also the variability of the contraction strength shows long-term correlations.

Therefore, in this study we propose the investigation of contraction strengths and their variabilities additionally to interval variabilities in SAN tissue. In detail, we evaluated beat to beat interval variabilities and beat to beat contraction strength *CS* variabilities of murine atrial preparations that contained the SAN region by means of high-speed camera video recordings. Each image of a video represented a time stamp and contractions of the tissue were recorded as changes in average gray values. Simultaneous measurements of extracellular potentials using a cardiac-near-field electrode validated beat to beat intervals of video recordings. Measurements of the spontaneous activity of tissue samples were performed before and after the administration of acetylcholine ACh, the predominant transmitter of the parasympathetic nervous system. Its effects on atrial tissue are already well investigated and include a decrease in beating rate and force of contraction (Kitazawa et al., 2009).

Our main objectives were to determine the suitability of video recordings to register *BBIs* and *CSs* and to analyze changes of nonlinear measures in the variabilities of these two parameters due to ACh treatment. Sample entropy and Higuchi dimension are popular estimators capturing intrinsic nonlinear patterns in time series of measured signals (Higuchi, 1988; Richman and Moorman, 2000). We hypothesized that ACh significantly affects sample entropies and Higuchi dimensions of *BBI* and *CS* variabilities. To distinguish actual values from white noise, surrogate data series were constructed and analyzed.

In summary, this high-speed camera video recording-technique provides a promising tool to thoroughly investigate beat to beat behavior regarding absolute values of beating rate and contraction strength as well as their variabilities in autorhythmic tissue.

METHODS

Tissue Preparation

Hearts from 22 C57/BL6 wildtype mice (aged 12–20 weeks) of both sexes in equal number were used for this study. The preparation of atria including the intact SAN region was carried out as previously described (Torrente et al., 2015). Briefly, mice were heparinized and anesthetized with ketamine (100 mg/kg) and xylazine (10 mg/kg) and the hearts were quickly removed. The atria including the intact SAN region were dissected from the ventricles and fixed with needles on a silicone ground of an experimental chamber. For this study, an extracted SAN tissue of one mouse represented a single experiment. Therefore, the number of experiments corresponds to the number of mice.

The experimental procedure and number of used animals were approved by the ethics committee of the Federal Ministry of Science, Research and Economy of the Republic of Austria (BMWFW-66.010/0101-WF/V/3b/2016). The experiments were conducted according to the Directive of the European Parliament and of the Council of September 22, 2010 (2010/63/EU).

Video Acquisition

The experimental chamber containing the intact SAN tissue was mounted on the stage of an upright microscope (Olympus, BX51W1, 4x objective, light source TH4-200) and the tissue was superfused with oxygenated standard external solution (containing in mM: NaCl 137, KCl 5.4, $CaCl_2$ 1.8, $MgCl_2$ 1.1, $NaHCO_3$ 2.2, NaH_2PO_4 0.4, HEPES/Na^+ 10, D(+)-glucose 5.6, pH 7.4 adjusted with NaOH) which was kept at a constant temperature of 23°C. Recordings were started 20 min after the onset of superfusion in order to allow the tissue to establish and maintain a stable beating rhythm. Close to the primary pacemaking site of the tissue, a small image region of interest ROI showing distinct contractions was selected for recording. After recording of the first video (Con), acetylcholine (ACh, 3 μmol/L) was added to the perfusion solution and after 5 min superfusion time the second video was recorded. A number of nine tissue samples yielded 18 videos.

Tissue samples under investigation showed a beat to beat interval of about 500 ms (∼2 Hz). In order to measure such intervals, it is necessary to sample the temporal course of the beating with enough data samples per second. The Nyquist-Shannon sampling theorem with a sample rate that is the twofold of the highest frequency in the signal is not applicable, because the content of harmonic frequencies are not of interest. More important is, that the sample rate determines a minimal jitter between consecutive time stamps. This jitter must be small, because it influences the nonlinear analysis including variability measures. For an accuracy of e.g., 1%, a number of 100 data samples is needed between two succeeding beats. Particularly, this would yield a sample rate of 200 Hz. Please note that video acquisitions using standard frame rates of 30 Hz would yield an accuracy of only ∼6.67% for a beating rate of ∼2 Hz. We decided to set the accuracy to 0.2% and consequently a sample rate of 1 kHz was used.

Video recordings of beating tissue samples were taken by using a high-speed camera system (MotionBlitz, GMCLTR1.3CL-SSL, Mikrotron, Germany) and a video camera (EoSens CL, MC1362, Mikrotron). This system implemented a hardware recording unit and therefore, avoided erroneous jitter effects of software trigger events such as e.g., USB camera solutions do usually show. The resolution of the camera was set to 1,280 × 1,024 pixels. A ROI with a pixel size of 160 × 160 was selected to get maximal gray level changes during beating of the tissue. **Figure 1A** shows a sample image.

The size of the ROI was empirically optimized by inspections of the temporal signals gained. Larger ROIs yielded too large and inconvenient video files and smaller ROIs yielded too low signal to noise ratios. Regions with thick tissue layers (trabeculae, crista terminalis) moving into the ROI turned out to yield the highest signal to noise ratios. With a sample rate of 1,000 fps and a recording duration of 5 min, a number of 300,000 single uncompressed images (each of them with 160 × 160 = 25,600 pixels) where taken and stored on hard disk in an avi container format. One avi file needed 21 GB of memory. The Mikrotron system saved the individual images in RGB format although the used camera was a gray value camera. Gray value cameras usually give higher signal to noise ratios than color cameras which is important for high-speed acquisitions with very small exposure times. Thus, images were converted in a first step to 8 bit, lowering the memory demand to 7, 6 GB per video. The whole measuring setup was tested against electrical and optical inferences coming from ambient light sources such as the laboratory light or the microscope light source itself. Fourier analyses of videos capturing a static scene revealed no residual frequency components of power supply frequencies or other additional noise components.

Electrical Recordings

For comparison of video and electrical measurements we carried out 13 separate control experiments in order to simultaneously record video as well as extracellular electrical signals. After positioning of the microscope's objective and choosing a ROI, a cardiac-near-field CNF electrode (Hofer et al., 2006) was placed close to the ROI (**Figure 1A**). This ensured that the electrical and optical measurement sites corresponded in the spatial domain. For evaluation of beat to beat intervals, only one of the four CNF channels was used. Electrical signals were amplified (gain 100), anti aliasing lowpass filtered (4th order Bessel, cutoff frequency 20 kHz) and recorded with custom software (LabVIEW, National Instruments, Austin, Texas) at a sampling rate of 100 kHz (NI USB-6210, National Instruments, Austin, Texas). Signals were digitally filtered (Butterworth lowpass, 4th order, cutoff frequency 1.5 kHz and Butterworth highpass, 4th order, cutoff frequency 1.5 Hz). A sample electrical recording can be seen in **Figure 1B**. Subsequent time stamps of individual beats were computed by setting a threshold well above the noise level to the decreasing slopes of the signal (denoted by red plus signs in **Figure 1B**). For signals with lower signal to noise ratio the same threshold criterion was used in the first temporal derivative of the signal where the steep downslope during electrical activation was more pronounced.

Time Signal Generation From Videos

Time signals of the beating tissues were reconstructed by computing the average gray value $\overline{G}_i$ of each image i of a video which can be seen in **Figure 1C**.

$$\overline{G}_i = \frac{1}{N_P} \sum_{p=1}^{N_P} g_{i,p}, \tag{1}$$

with $g_{i,p}$ the gray value in the range [0, 255] of pixel p in the image i, $i = 1, 2, 3, \ldots, N_I$, N_I the number images in a video ($N_I = 300,000$), and $p = 1, 2, 3, \ldots, N_P$, N_P the number of pixels in an image ($N_P = 25,600$).

This yielded a temporal time signal comprising 300,000 data points with a data compression of (25,600 to 1). The algorithm for finding the time stamps of contractions was designed around finding subsequent local minima (denoted by red plus signs in **Figure 1C**). The original signal was slightly smoothed by applying a moving average filter with 25 data points to improve the shape of the minima and to ensure that minima are right between the adjacent declining and rising slopes. A threshold was set between the doubled noise value of the baseline and the smallest minimum in the video. Further on, only values smaller than that threshold were investigated. Then, a minimum was computed by simply looking for the smallest value between two threshold points. Very rarely a minimum consisted of two neighboring points with exactly the same value in which case the second value was taken as the minimum. Finally, a beat to beat interval *BBI* was defined as the temporal interval between two succeeding minima (beats).

$$BBI_b = t_b - t_{b-1}, \tag{2}$$

with t_b, the absolute time of the beat b (minimum) in a video, $b = 2, 3, \ldots, N_B$, and N_B the number of beats in a video. This algorithm (named PointFinder) was implemented in the software IQM (Kainz et al., 2015) and is available from the authors or from the IQM project page (https://sourceforge.net/projects/iqm/). A sample result of *BBIs* is shown in **Figure 2A**.

The number of data points in such a graph was equal to the number of beats $N_B - 1$ during the recording interval of 5 min and therefore, was not constant from video to video. The sample graph in **Figure 2A** consists of actually 660 data points because the specific tissue sample contracted 661 times in 5 min. Roughly, this reflects another data compression of 450 to 1. Overall the method has a compression rate of about 11.6 million to 1.

On further inspection of **Figure 1C**, it is obvious that not only interbeat intervals can be computed from these local minima. Additionally, the height of a minimum measured from the baseline, which is the horizontal line containing the points of relaxed tissue only, can be computed. Such a height reflects the mechanical contraction strength *CS* of the tissue. Stronger contraction of cells in the tissue yielded a higher light absorption and hence darker images in the video and consequently lower minima in the average graphs such as in **Figure 1C**. We created correlation plots of subsequent height changes vs. subsequent interbeat intervals (actual plots are described in section Correlation of Contraction Strengths and Beat to Beat

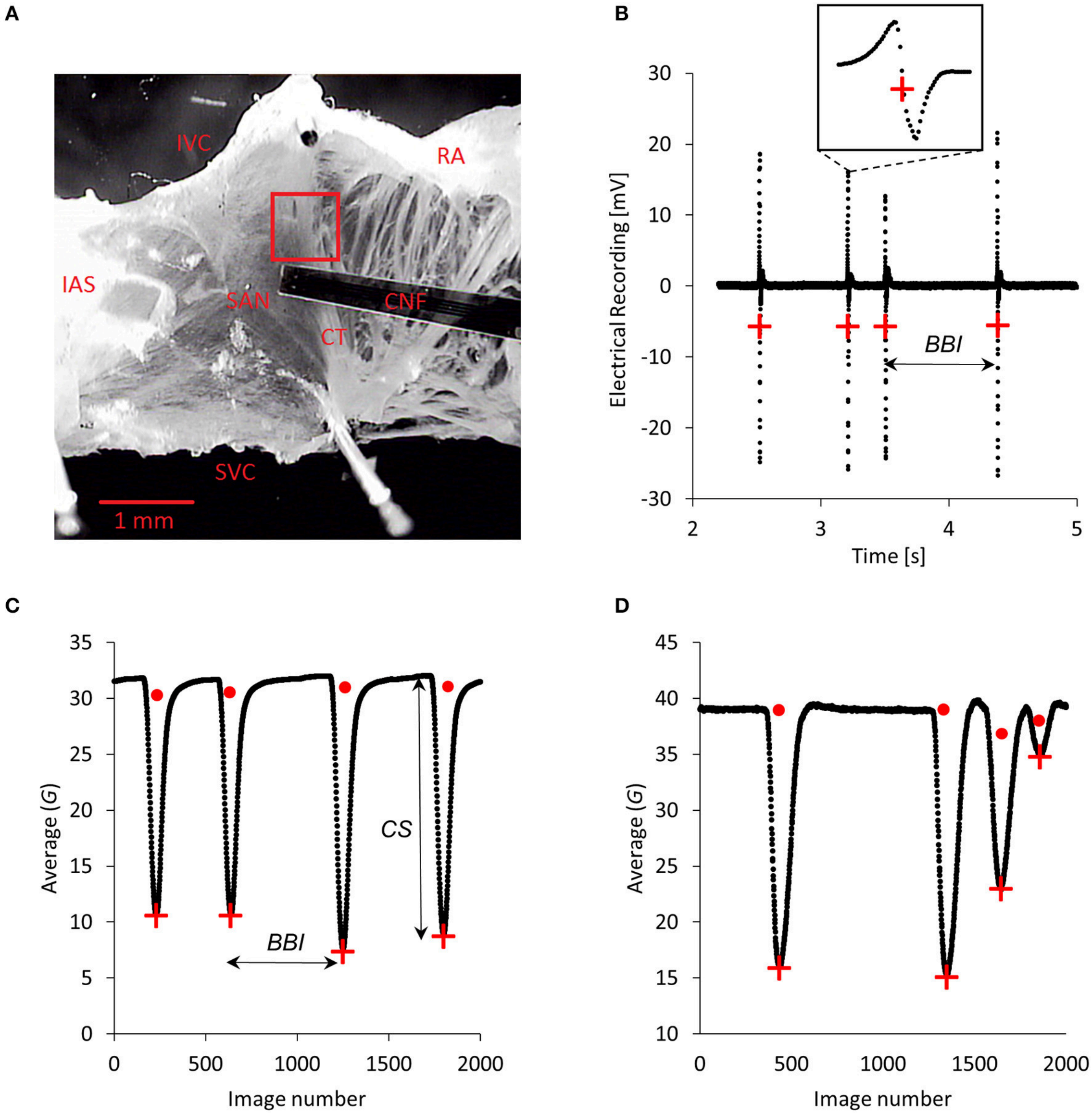

FIGURE 1 | Microscopic sample image and sample recordings. **(A)** Sample image of a tissue preparation including the intact atria and the region of the sinoatrial node SAN. The left atrium cannot be seen in the image. RA, right atrium; CT, crista terminalis; IAS, interatrial septum; IVC, inferior vena cava; SVC, superior vena cava; CNF, cardiac-near-field electrode. The region of interest ROI (red rectangle) with a size of 160 × 160 pixels was set to a region yielding high changes of average gray values. This was usually the case when regions of a thick tissue layer (e.g., trabeculae) moved into the ROI during contractions. **(B)** Sample electrical recording lasting about 4 s (down-sampled to 5 kHz for the graphical representation). Four subsequent beats are depicted and the red plus symbols indicate data points for computing beat to beat intervals *BBIs*. A single beat is zoomed out. **(C)** Sample average gray values $\overline{G}$ according to Equation (1) from about 2,000 (out of 300,000) images. Red plus symbols mark data points that defined the *BBIs* and in addition with the baseline points (red dots) the contraction strengths *CSs*. Interval as well as contraction strength variations are clearly visible for these four contractions. **(D)** Finding correct baseline points is crucial for the determination of the *CSs*. This signal sample shows some beats (red plus symbols) and baseline points (red dots). The first two baseline points were found very well, in contrast to the last two baseline points. Accordingly, *CSs* for these two points cannot be accurately computed.

Intervals). A correlation between these two variables was given in most cases, which is in accordance with previously published data (Torres and Janssen, 2011). Nevertheless, correlations were not perfect and some experiments showed only weak or negative correlations. Consequently, we decided to additionally evaluate variations of contraction strengths.

First, in order to obtain the *CS*, it was necessary to determine the baseline, although it drifted during the time course of 5 min. To avoid drifting and offset errors we computed a separate baseline value for each minimum. The actual baseline value was computed by the median of all points in between the actual minimum and the preceding minimum and thus we obtained

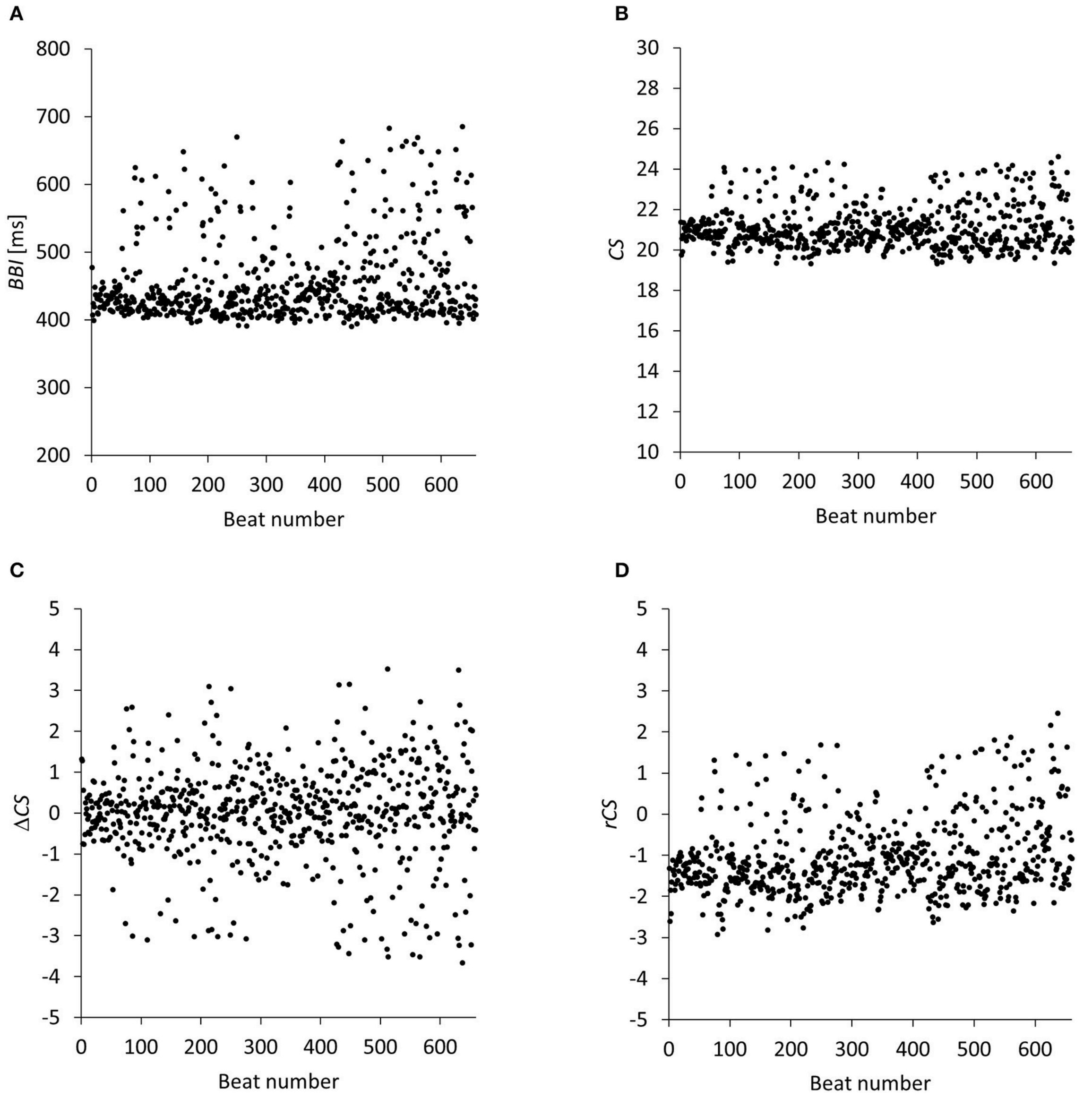

FIGURE 2 | Beat to beat intervals *BBIs* and contraction strengths *CSs*, Δ*CSs*, *rCSs* computed from optical (video) recordings. **(A)** *BBIs* computed according to Equation (2). This tissue sample yielded actually 660 data points (number of beats $N_B = 661$). **(B)** Contraction strengths *CSs* computed according to Equation (3) for the same tissue sample with 660 data points. **(C)** Differences of contraction strengths Δ*CS* computed as the differences of the average gray values $\overline{G}s$ of the beating signal according to Equation (4). **(D)** Relative contraction strengths *rCSs* computed by integration of the Δ*CS* values according to Equation (5).

moving baseline values (for every minimum a separate baseline value, some sample baseline values are depicted graphically in **Figure 1C** with red points). This ensured that baseline drifts, unavoidable during a recording time of 5 min, did not contribute. Consequently, *CS* was computed by

$$CS_b = \left|\overline{G}_b - baseline_b\right|, \tag{3}$$

with CS_b the contraction strength of the beat b, $\overline{G}_b$ the average gray value of the image detected as the "beat image," $baseline_b$ the corresponding baseline value, $b = 1, 2, 3, \ldots, N_B$, and N_B the number of beats in a video. A sample signal can be seen in **Figure 2B**.

Although the signals seemed to be reliable, it turned out that this moving median algorithm produced some variation errors due to residual noise components of the baseline. Additionally, but only occasionally, for one mouse treated with acetylcholine (#5 in **Figure 6**), subsequent contractions showed some consecutively fast repeating bursts instead of full contractions. For such short burst intervals, the median algorithm yielded erroneous baseline values leading to too small *CS* values. A graphical representation of such errors is shown in **Figure 1D**. An alternative algorithm for finding the baseline may be feasible, but we present a convenient way that does not need baseline detection at all.

In this approach we eliminated the baseline (offset), since we actually were interested in variabilities of these temporal signals and not in absolute values. Discrete differentiation of the time signal (average gray values according to Equation (1) and exemplarily depicted in **Figure 1C**) revealed differences of contraction strengths ΔCSs and eliminated the hassle of finding baseline points.

$$\Delta CS_b = \overline{G}_b - \overline{G}_{b-1}, \tag{4}$$

with b = 2,3,. . . , N_B.

Subsequent discrete integration generated back the changing content of the contraction strength signal but without the baseline and was termed relative contraction strength rCS.

$$rCS_b = \Delta CS_b + rCS_{b-1}, \tag{5}$$

with $b = 2, 3, \ldots, N_B$ and $rCS_1 = 0$.

Integration usually gives the anti-derivative plus an unknown constant, which was in our case the baseline (offset). Discrete differentiation followed by integration was actually carried out with software IQM (Kainz et al., 2015) using the mathematics feature for one dimensional signals.

Sample graphs of ΔCS and rCS can be seen in **Figures 2C,D**. *BBI*, *CS* and *rCS* data series for each experiment (Con and ACh treated) are provided as "Data Sheet 1" csv file in the supplement.

Sample Entropy and Higuchi Dimension

Sample entropy *SampEn* and Higuchi dimension D_H are two well-known and successfully applied nonlinear descriptors for time signal variations (Higuchi, 1988; Richman and Moorman, 2000). Approximate entropy *ApEn* is also widely used, but is not suitable for this particular study because the number of beats changed from video to video. *SampEn* is proportional to the conditional probability that a sequence which is similar for m points remains similar for m+1 points. A tolerance distance r is defined so that repetitions must not be exact. Usually, r is defined as a multiple of the standard deviation *SD* of the signal and therefore, *SampEn* is a scale invariant measure (Richman and Moorman, 2000). Self matches are not included.

The discrete time signals $\{x(1), x(2), \ldots, x(N_B)\}$ (x stands for values from *CS* or *rCS* signals) with length N_B were taken and (N_B – m + 1) sequences were created:

$$X_m(i) = [x(i), x(i+1), \ldots, x(i+m-1)]. \tag{6}$$

The parameter m was set to two ($m = 2$). Distances in between these data series were computed using the maximum metric:

$$d\left[X_m(i), X_m(j)\right] = \max_{k=1,2,..,m} \left\{\left|X_m(i+k-1) - X_m(j+k-1)\right|\right\} \tag{7}$$

The normalized sums of distances smaller than the tolerance distance $r = 0.15SD$ were computed for each i, j with $1 \le i,\ j \le N_B - m + 1$ and $i \neq j$:

$$C_i^m(r) = \frac{number\ of\ X_m(j)\ where\ d[X_m(i), X_m(j)] \le r}{N_B - m + 1}. \tag{8}$$

The normalized number of sums can be computed using

$$B^m(r) = \frac{1}{N_B - m} \sum\nolimits_{i=1}^{N_B-m} C_i^m(r). \tag{9}$$

Finally, *SampEn* was computed with

$$SampEn(m, r, N_B) = -\ln\left(\frac{B^{m+1}(r)}{B^m(r)}\right). \tag{10}$$

Higuchi proposed a method to compute the fractal dimension of a signal by using sums of differences with varying inter data point intervals (delays) (Higuchi, 1988). The Higuchi dimension is frequently applied in contemporary neurophysiology and neuropathology (Kesić and Spasić, 2016) and is well known for its accuracy, speed and robustness including high linearities of the double log plots. Phase space reconstructions are not involved and therefore, the number of data points available can be restricted. Initial data points are set to $m = 1$,2,. . . , k with a delay interval $k =$ 1,2,. . . , 30. Following data point series were constructed:

$$S_m(k): x(m), x(m+k), x(m+2k), \ldots,\ x(m + \left\lfloor \frac{N_B - m}{k} \right\rfloor k) \tag{11}$$

The lengths $L_m(k)$ of these series, depending on the initial data points m and k were computed according to:

$$L_m(k) = \frac{1}{k}\left\{\left(\sum\nolimits_{i=1}^{\left\lfloor \frac{N_B-m}{k} \right\rfloor} \left|x(m+ik) - x(m+(i-1)k)\right|\right) \frac{N_B - 1}{\left\lfloor \frac{N_B-m}{k} \right\rfloor k}\right\} \tag{12}$$

The symbol $\lfloor\ \rfloor$ stands for the floor function. For each k, the mean length was determined by

$$L(k) = \frac{1}{k} \sum\nolimits_{m=1}^{k} L_m(k). \tag{13}$$

Finally, a double logarithmic plot of $L(k)$ vs. k was constructed and the slope of a linear regression was used to compute D_H. Values of k above 30 were not used because they introduced noticeable deviations of data points from the linear regression. Signals were processed as they were recorded without editing. Algorithms were implemented in the Software IQM (Kainz et al., 2015) and are available from the authors or from the IQM project page.

Statistics

Statistics was computed with public domain software R, version 3.3.3 and RStudio software version 1.0.136 (RStudio, 2016; R Core Team, 2017). Due to small sample sizes, differences of paired samples were statistically analyzed with a two-sided median test using the R function sintv2 (Wilcox and Rousselet, 2018). This method performs very well in terms of controlling the probability of a Type I error (Wilcox, 2016). Data acquisition via video and electrode setup did not start synchronously (lag of 1–3 beats). Cross correlation (unbiased estimate, MATLAB® R2017b) was used to remove this start dependent asynchronism between the optical and electrical signal. Correlation of *CSs* with *BBIs* was computed using Spearman's rank correlation coefficient r_s. Coefficients of determination R^2 were computed for double log plots to estimate Higuchi dimensions.

Surrogate analysis was performed to provide further evidence of long-range nonlinear correlations in the optically measured signals and to demask possible white noise components indicated by some relatively high *SampEn* and D_H values. Each optically recorded signal was shuffled 50 times using IQM (Kainz et al., 2015). A total number of 5,400 surrogate data series were constructed considering nine SAN tissues, two nonlinear measures (*SampEn*, D_H), two treatments (Con, ACh), three signal types (*BBI*, *CS*, *rCS*), and 50x shuffling. Following evaluation types were carried out:

SurrEval-1: Each individual experimentally gained value was tested against the normally distributed surrogate values applying a two-sided one sample Student's *t*-test.

SurrEval-2: The experimentally gained values were tested against the respective means of the shuffled signals by a two-sided median test using the R function sintv2.

SurrEval-3: The respective means of shuffled control against means of shuffled ACh signals were tested by a two-sided median test using the R function sintv2.

RESULTS

Linear variance measures of the beat to beat interval are dependent on absolute values and are only well suited for linear stochastic processes. Nonlinear signals with random correlations or Random walk like signals can be well investigated with scale independent measures such as the sample entropy *SampEn* or the Higuchi dimension D_H.

Double Log Plots for Higuchi Dimensions

Double log plot linear regressions for estimating the Higuchi dimensions revealed very high coefficients of determination R^2 within a range of [0.959–0.999]. Sample linear regressions can be seen in **Figures 3A,B** for control and ACh treated cases. With this high linearity, the application of the fractal concept seems to be very appropriate and robust. Nevertheless, we found a marginally lower R^2 for some signals (4 out of 18) which was visible as a slight wobbling of data points around the straight line (see a sample graph in **Figure 3B**, blue dots). This occurred for control as well as ACh treated cases. The reason was that the specific signals showed subsequent alternating values which could be interpreted as binary oscillations or negative correlations. Fractal dimensions of period doubling signals cannot be directly calculated, but it is known that periodic components in time series yield distinct and periodic differences in the double log plot (Galvez Coyt et al., 2013).

Correlation of Optically and Electrically Recorded Beat to Beat Intervals

Optically (video) recorded values of *BBIs* correlated very well with electrically recorded values. Representative *BBI* value pairs showing just negligible differences can be seen in **Figure 4A**. A sample regression plot of a whole 5 min recording can be seen in **Figure 4B**. The slopes for all 13 experiments were in the range of [0.977–1.067] and the coefficients of determination R^2 were in the range of [0.984–0.999].

Additionally, we computed sample entropies and Higuchi dimensions for these 13 control samples. Results can be seen in net plots for each individual experiment in **Figure 5A**. Traditional box plots including the data values can be seen in **Figure 5B**.

SampEn values are very close and statistically not different ($p = 0.46$, $df = 12$). For D_H values a *p*-value of 0.05 ($df = 12$)

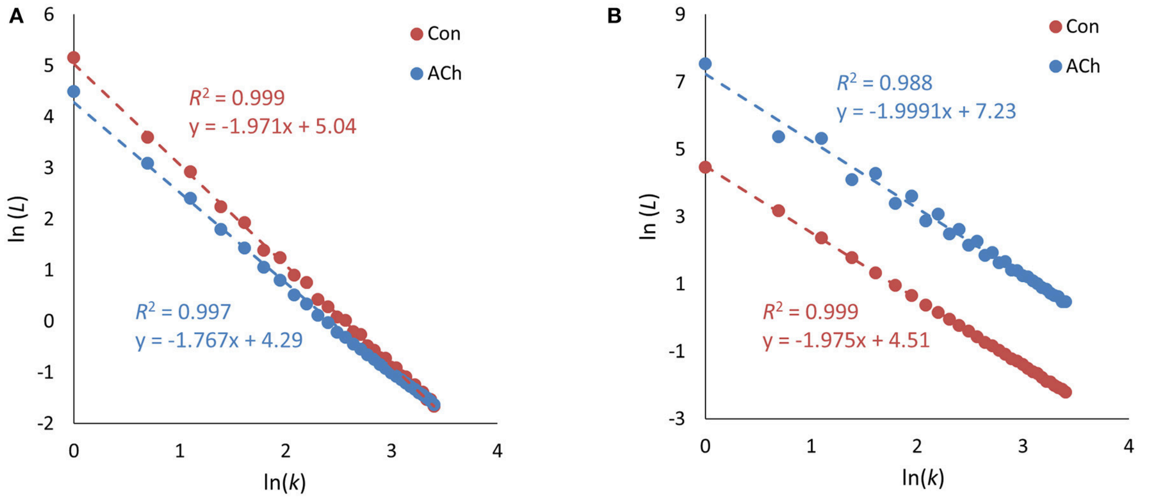

FIGURE 3 | Higuchi dimension D_H double log plots. Data from optical recordings. **(A)** Typical double logarithmic plots of D_H showing very linear regressions for the control and the acetylcholine treated cases. **(B)** Another sample of double logarithmic plots showing occasional deviations from the linear regression, in this particular case for acetylcholine (blue dots).

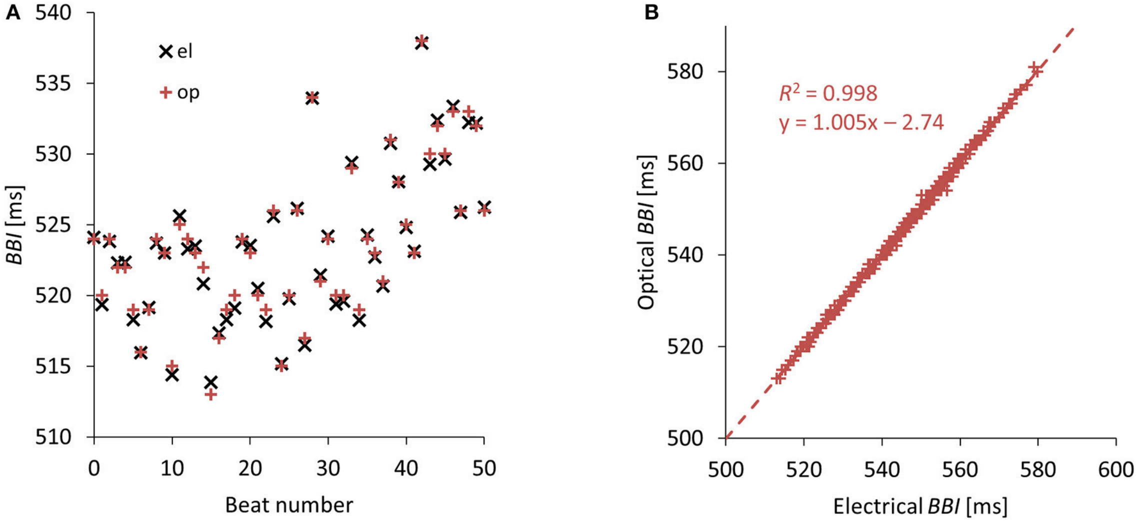

FIGURE 4 | Opto-electrical correlation. **(A)** Some representative beat to beat intervals *BBIs* computed from simultaneously measured electrical and optical (video) recordings. **(B)** Regression of electrically and optically gained *BBIs* from one experiment (i.e., one mouse). The linear slope is very close to one and the coefficient of determination R^2 is very high.

indicates a possible effect. Since the corresponding median difference was very small (only in the third decimal place), we show scatterplots of data point pairs in **Figure 5C**. The minimal deviations from the straight line (no effect) suggest no practical relevance.

Correlation of Contraction Strengths and Beat to Beat Intervals

Scatterplots of *CSs* vs. *BBIs* in milliseconds are shown in **Figure 6**. Control tissue (red) and ACh treated tissue (blue) showed mostly positive correlations. A few correlations are weak and/or negative.

Additionally, scatterplots and correlations of relative contraction strengths *rCSs* vs. *BBIs* were computed. Actual plots are not shown, because the correlations were quite similar compared to **Figure 6**.

Acetylcholine Induced Changes of Beat to Beat Intervals and Contraction Strengths

The median beat to beat interval of the control group was 512 ms and increased to 614 ms after applying ACh. Net and box plots can be seen in **Figure 7** (left column). The significant increase in the beating rate of ∼20% (3 μM ACh) is in line with previously published data (Glukhov et al., 2010).

The median beat to beat contraction strength of the control group was 20.85 and decreased to 13.24 after treatment with ACh. Net- and box plots can be seen in **Figure 7** (right column). The significant decrease of *CS* of ∼37% is in accordance with previously published data (Kitazawa et al., 2009).

Acetylcholine Induced Changes to Sample Entropies and Higuchi Dimensions

Figure 8 depicts net- and box plots of nonlinear measures of *BBIs*. Median values of *SampEn* decrease from 1.58 (Con) to 0.92 (ACh) and are not significantly different ($p = 0.11$, $df = 8$, **Figure 8B**, left column). This is also the case for D_H ($p = 0.97$, $df = 8$, **Figure 8B**, right column) which decreased from 1.98 to 1.97.

SampEn surrogate evaluation according to SurrEval-1 revealed that all experimentally gained values (*BBIs* for Con and ACh) were significantly lower than the shuffled ones with $p < 0.001$, $df = 49$. This agrees with SurrEval-2 showing that all experimental values were also significantly lower than the means of the corresponding shuffled ones with $p < 0.001$, $df = 8$, see **Table 1**. Furthermore, according to SurrEval-3 the means of *SampEn* values for shuffled signals showed no indication for statistical significance between Con and ACh, $p = 0.82$, $df = 8$, see **Figure 8C**.

SurrEval-1 for D_H yielded similar results with $p < 0.001$, $df = 49$, except for some experimental values >2 in the third decimal (two cases for Con and three cases for ACh) where obviously the shuffled values could not further increase. This is well reflected by SurrEval-2 with a borderline $p = 0.05$, $df = 8$ for Con and a non-significant *p*-value for ACh (**Table 1**). As expected, SurrEval-3 reveals no significant difference between the groups Con and ACh, $p = 0.77$, $df = 8$, see **Figure 8C**.

Figure 9 shows net and box plots of nonlinear measures of the proposed *CSs*. Median values for *SampEn* show a significant difference between Con and ACh ($p < 0.001$, $df = 8$), namely a decrease from 1.60 (Con) to 0.72 (ACh) which can been seen in **Figures 9A,B**, left column. Median values for D_H tend to decrease slightly (**Figure 9B**, right column) as indicated by a borderline *p*-value of $p = 0.05$ ($df = 8$). In detail median values decrease from 1.97 (Con) to 1.91 (ACh).

For *SampEn*, all three *CS* surrogate evaluations yielded consistent results regarding nonlinear patterns in the measured signals, since shuffled values were always statistically higher (SurrEval-1: $p < 0.001$, $df = 49$, and SurrEval-2: **Table 1**) and

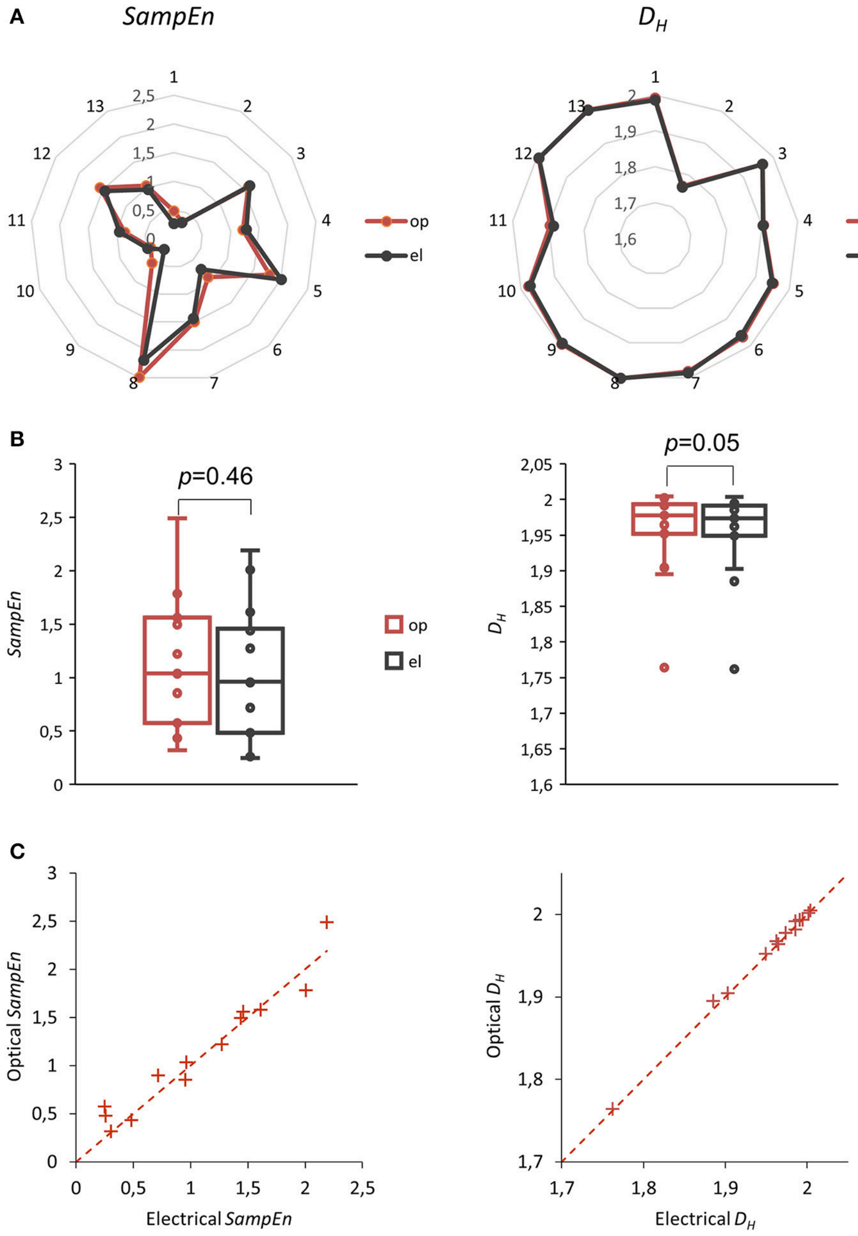

FIGURE 5 | Sample entropy *SampEn* (left column) and Higuchi dimension D_H (right column) of beat to beat intervals *BBIs* determined optically and electrically. **(A)** Net plots showing 13 *SampEn* and D_H values for *BBIs*. **(B)** Box plots of these 13 experiments, *p*-values with $df = 12$, median test. **(C)** Scatterplots of these 13 experiments. Dashed lines represent theoretical correlations with the slope of one.

the difference between Con and ACh vanished compared to the experimental case (SurrEval-3: **Figure 9C**). Now, SurrEval-1 for D_H yielded no exception with $p < 0.001$, $df = 49$ and all three surrogate evaluations are again consistent (SurrEval-2: **Table 1** and SurrEval-3: **Figure 9C**).

Finally, **Figure 10** depicts net and box plots of nonlinear measures of the proposed *rCSs*. For *SampEn*, the decrease and the significance of *rCS* is similar to *CS* with median values from 1.76 (Con) to 0.49 (ACh) and with $p < 0.001$, $df = 8$ (**Figures 10A,B**, left column). The decrease of D_H values is slightly more pronounced for *rCS* compared to *CS* with median values from 1.98 (Con) to 1.91 (ACh) and now exceeds the 95% statistical significance level with $p = 0.03$, $df = 8$ (**Figure 10B**, right column).

Surrogate analyses for *rCs* are again consistent for both, *SampEn* and D_H, indicating nonlinear long-range correlations. Shuffled values are always statistically higher (SurrEval-1: $p < 0.001$, $df = 49$, and SurrEval-2: **Table 1**) and the difference between Con and ACh vanishes compared to the experimental case (SurrEval-3: **Figure 10C**).

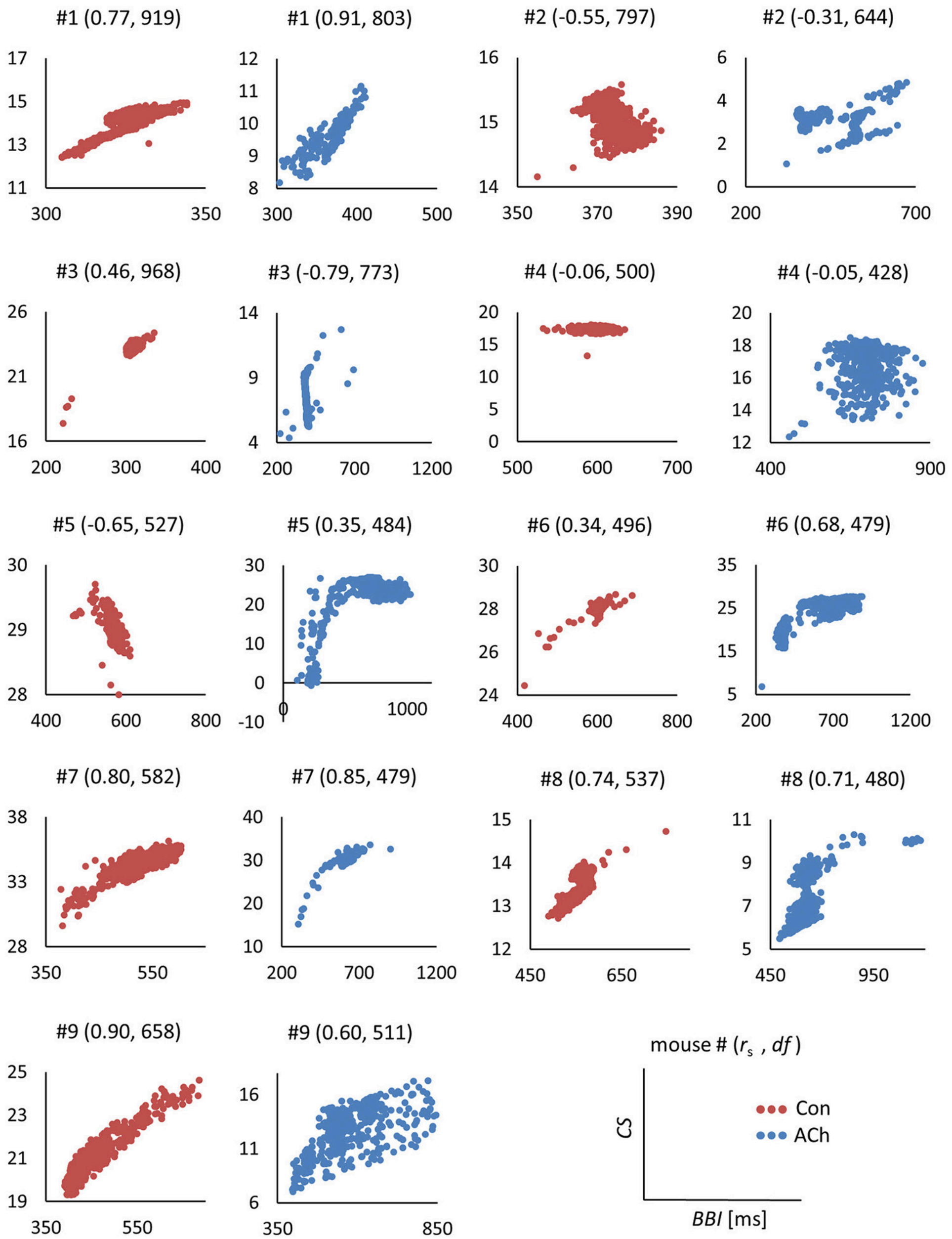

FIGURE 6 | Scatterplots of contraction strengths *CSs* vs. beat to beat intervals *BBIs* in milliseconds. Data from optical recordings. Red dots correspond to control tissue, blue dots to ACh treated tissue. For each individual plot the experiment (mouse) number #, in brackets the actual Spearman's rank correlation coefficient r_S and the degrees of freedom *df* are depicted.

DISCUSSION

Beat to beat intervals are commonly investigated in order to detect nonlinear correlations in time signals. This study proposes an optical method, particularly, a high-speed video technique to detect mechanical contractions of the heart tissue. Usual video recordings with frame rates of about 30 fps or software triggered acquisitions are a convenient way for spectral analyses or computing beating frequencies (Kojima et al., 2006; Chan et al., 2009; Fassina et al., 2011; Hsiao et al., 2013; Ahola et al., 2014). But obviously, video frame rates must be higher for high beating rates (De Luca et al., 2014) or accurate detections of beating events (Stummann et al., 2008). Our high-speed video recordings allowed us to extract beat to beat intervals *BBIs* as well as the contraction strengths *CSs* and the relative contraction strengths *rCSs*, because the average gray value of an image was directly proportional to the mechanical contraction. Variation analyses with two distinguished nonlinear measures, the sample

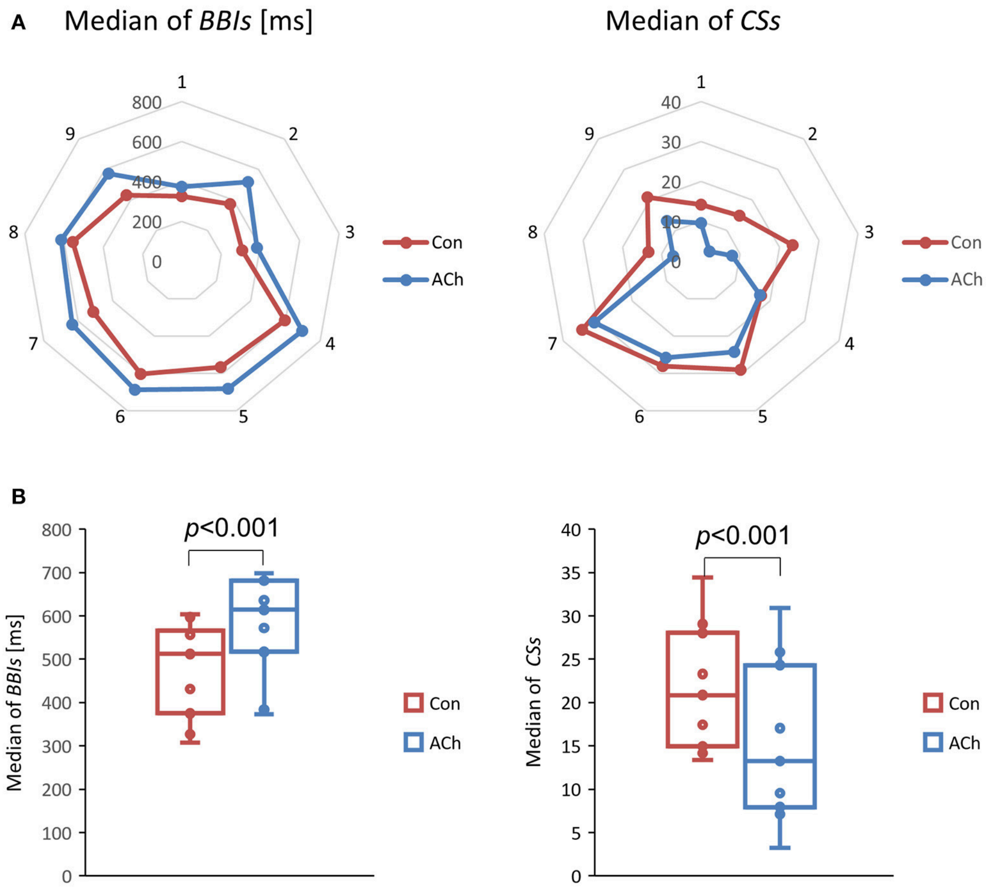

FIGURE 7 | Medians of beat to beat intervals *BBIs* (left column) and contraction strengths *CSs* (right column). Data from optical recordings. The control group is depicted in red and the values for the ACh treated group in blue. **(A)** Net plots of all experiments, showing individual and pairwise values. **(B)** Box plots of all experiments show statistically significant differences between Con and ACh groups, $p < 0{,}001$, $df = 8$, median test.

entropy *SampEn* and the Higuchi dimension D_H, revealed that this video technique is able to produce consistent results for *BBIs* as well as for *CSs* and *rCSs*.

The detection of the baseline (relaxed tissue) may be prone for errors such as measurement noise or optical drifts during the recording and thus, we proposed the second contraction parameter *rCS*. This is basically the varying contraction content of the signal, without the absolute value, drift or offset. *SampEn*, D_H and other scale independent nonlinear measures or fractal dimensions are not dependent on absolute values and consequently, *rCS* is an appropriate and very promising parameter for variance analyses.

To our knowledge, studies of BBV using isolated SAN tissue are very limited. Since no consensus exists to classify possible physiological artifacts (e.g., ectopic beats) in this *in vitro* preparation, we analyzed the original signals without any editing that could lead to a loss of valuable information.

We observed that ACh changed the beating behavior of the sinus node tissue by significantly reducing beating frequency as well as contraction strength, which is in accordance to previously published data (Kitazawa et al., 2009). Application of *SampEn* and D_H, two frequently used nonlinear measures for time signal variations, revealed a significant change of variabilities in the contraction strength but not in the beat to beat interval. The observed reduction of nonlinear measures indicates that the contraction process estimated by *CS* and *rCS* becomes more regular in the SAN tissue after ACh application. The spontaneous activity of pacemaker cells in the SAN tissue is based on two tightly linked clocks referred to as calcium and membrane clock (Lakatta and DiFrancesco, 2009). Both clocks exhibit inherent random components which arise from stochastic opening and closing of transmembrane ion channels (Krogh-Madsen et al., 2017) in the case of the membrane clock and from spontaneous stochastic calcium release via sarcoplasmic ryanodine receptors (Yaniv et al., 2014b) in the case of the calcium clock. The spontaneous calcium release in turn activates the sodium-calcium exchanger thereby triggering the action potential upstroke and subsequently a massive calcium release from sarcoplasmic reticulum, thus coupling excitation with contraction. ACh is an important modulator of SAN beating frequency as well as of contraction strength, particularly in the adjacent atrial tissue (Okada et al., 2013).

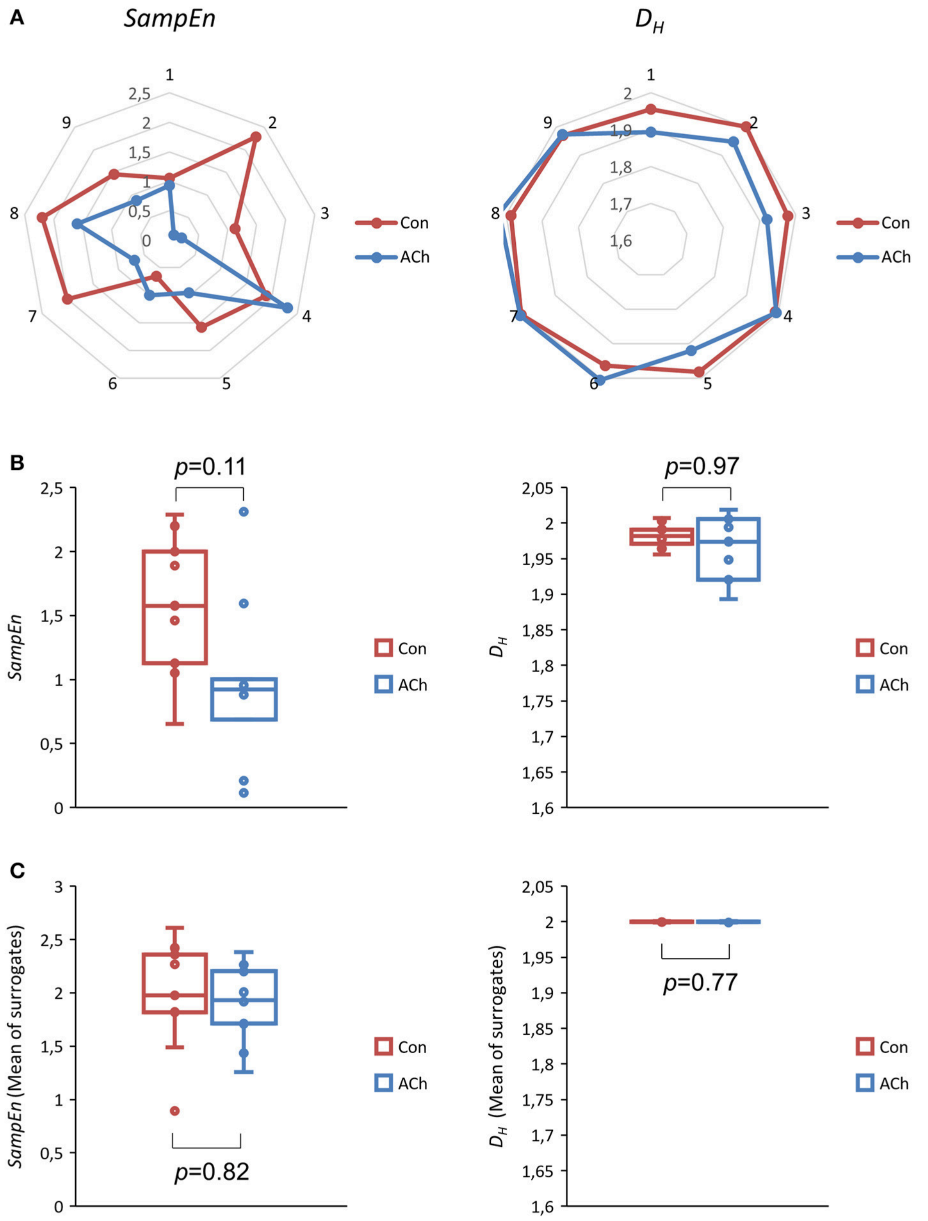

FIGURE 8 | Sample entropy *SampEn* (left column) and Higuchi dimension D_H (right column) of beat to beat intervals *BBIs*. Data from optical recordings. The control group is depicted in red and the ACh treated group in blue. **(A)** Net plots of all experiments, showing individual and pairwise values. **(B)** Box plots of all experiments. Differences are not statistically significant (*SampEn* $p = 0.11$, $df = 8$, D_H $p = 0.97$, $df = 8$, median test). **(C)** Mean *SampEn* and D_H values of shuffled (50x) data series.

TABLE 1 | Median test of sample entropy *SampEn* and Higuchi dimension D_H values from optical recordings against means of 50x shuffled data series according to SurrEval-2.

Nonlinear measure	*BBI* Con	*BBI* ACh	*CS* Con	*CS* ACh	*rCS* Con	*rCS* ACh
SampEn	<0.001(0.36) [0.25, 0.41]	<0.001(1.05) [0.31, 1.32]	<0.001(0.72) [0.23, 1.11]	<0.001(1.50) [1.17, 1.63]	<0.001(0.47) [0.34, 1.05]	<0.001(1.73) [1.25, 2.02]
D_H	0.05(0.02) [0.00, 0.03]	0.27(0.03) [−0.01, 0.08]	<0.001(0.03) [0.01, 0.04]	<0.001(0.09) [0.01, 0.15]	<0.001(0.02) [0.01, 0.08]	<0.001(0.11) [0.02, 0.27]

p-values, median differences and confidence intervals (df = 8) are given for BBI, CS, rCS, and for control and ACh treatment. p-values, (median difference), [confidence interval], median test according to SurrEval-2, df=8.

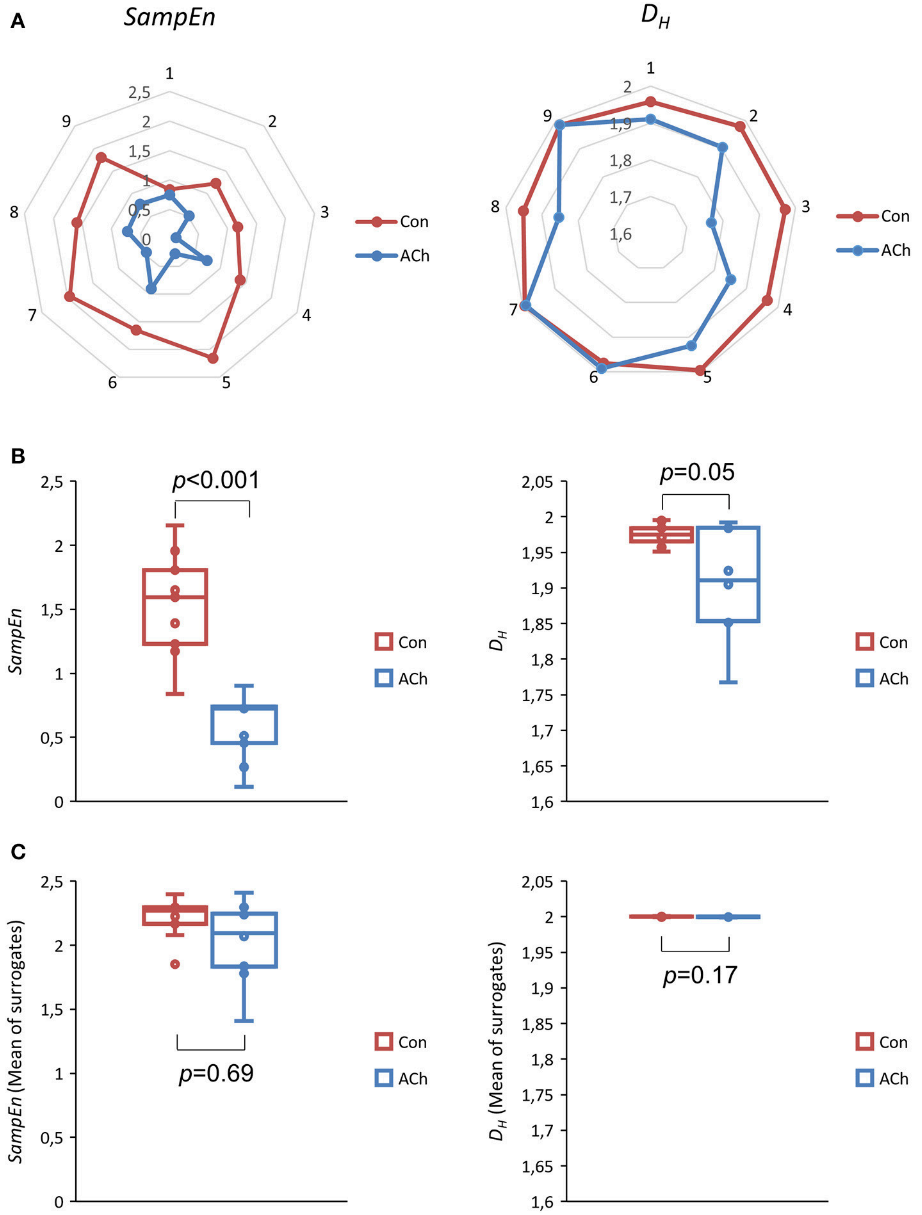

FIGURE 9 | Sample entropy *SampEn* (left column) and Higuchi dimension D_H (right column) of contraction strengths *CSs*. Data from optical recordings. The control group is depicted in red and the ACh treated group in blue. **(A)** Net plots of all experiments, showing individual and pairwise values. **(B)** Box plots of all experiments. The difference in *SampEn* is statistically significant, $p < 0.001$, $df = 8$, median test. The difference in D_H is statistically borderline ($p = 0.05$, $df = 8$). **(C)** Mean *SampEn* and D_H values of shuffled (50x) data series.

Activation of muscarinic receptors by ACh causes multiple effects on the membrane and the calcium clock via G-protein coupled signaling ultimately reducing beating frequency and contractility (Harvey and Belevych, 2003). This is in line with our results. The physiological mechanisms underlying the observed increase in contraction strength regularity by ACh in our study are currently unknown. Theoretically, a reduced randomness in membrane and/or calcium clock as well as in the contraction process itself could account for our observation. It is noteworthy that in our study ACh increases *CS* regularity but not *BBI* regularity. This may be due to the fact that the beating behavior in the time domain is determined solely by sinus node pacemaking, whereas *CS* regularity may also depend on the effect of ACh on atrial tissue present in our preparations.

Studies on ACh effects on SAN cells/tissue using nonlinear measures are very scarce. Yaniv et al (Yaniv et al., 2014a) investigated the beating rate variability at different levels of integration from the heart *in vivo* to single pacemaker cells by linear (coefficient of variation) and nonlinear (approximate

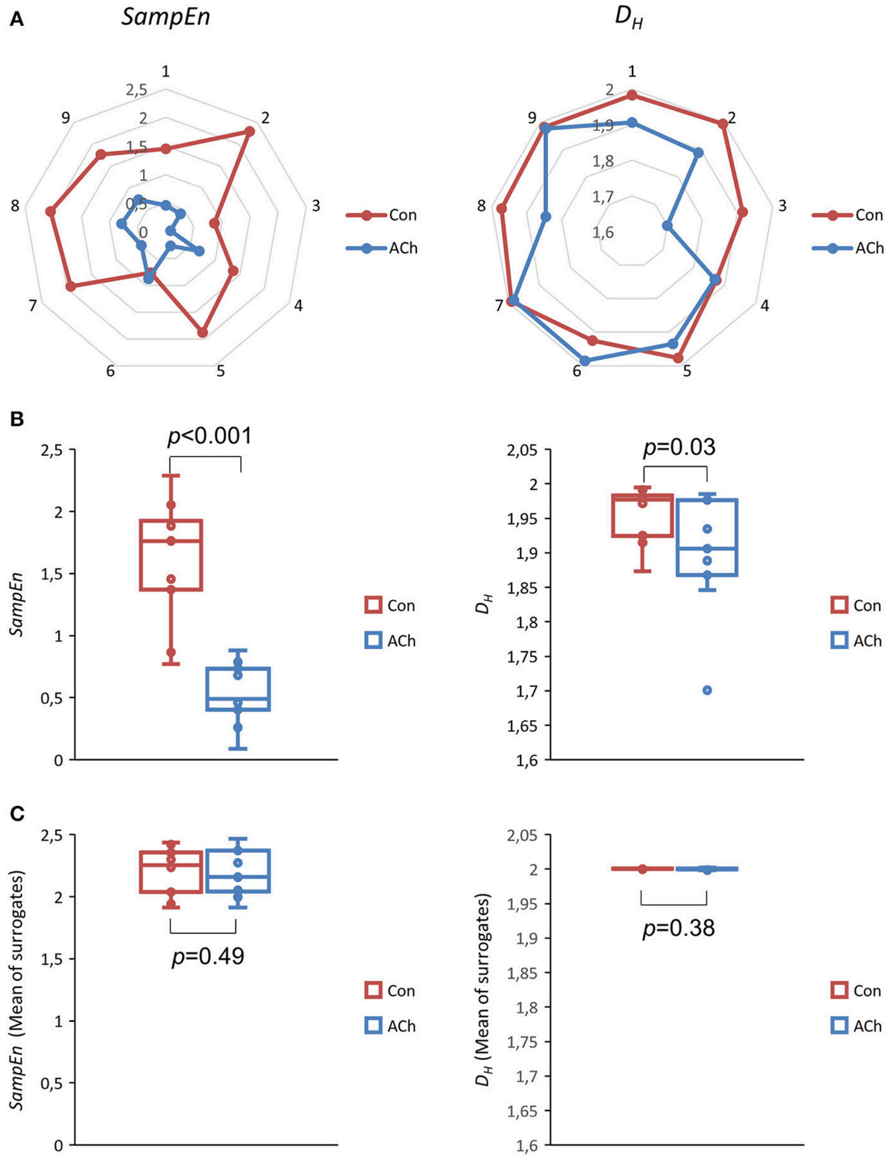

FIGURE 10 | Sample entropy *SampEn* (left column) and Higuchi dimension D_H (right column) of relative contraction strengths *rCSs*. Data from optical recordings. The control group is depicted in red and the ACh treated group in blue. **(A)** Net plots of all experiments, showing individual and pairwise values. **(B)** Box plots of all experiments. The differences in *SampEn* and D_H are statistically significant, $p < 0.001$, $df = 8$ and $p = 0.03$, $df = 8$ respectively, median test. **(C)** Mean *SampEn* and D_H values of shuffled (50x) data series.

entropy, power law and detrended fluctuation analysis) measures. Their results show that beating interval regularity increased in the order *in vivo*, denervated heart, isolated SAN tissue, but decreased again in single pacemaker cells. However, single SAN cells showed fractal-like behavior only to a small percentage. Carbachol, a parasympathomimetic drug, decreased regularity of beating intervals of single SAN cells. Since this group analyzed the effect of parasympathetic stimulation on beating behavior only in the time domain and at the single cell level, a direct comparison to our results does not seem to be reasonable. Clearly, further studies are needed to elucidate the underlying physiological mechanisms of muscarinic stimulation on nonlinear measures in SAN cells/tissue.

Compared to commonly used mechanical force transducer measurements (Kihara and Morgan, 1991; Torres and Janssen, 2011; Koyani et al., 2017), the high-speed video technique used in this study seems to be an appropriate, contact-free tool to quantify changes in contraction strength variability. The SAN preparation represents a very sensitive and fragile tissue which could be easily damaged by hooks or threads of mechanical transducers. Moreover, SAN tissue may not be very suitable for mechanical force measurements because forces developed by the low tissue mass are very small leading to low signal amplitudes and hence low signal to noise ratios. The suggested video method does not provide absolute values of contraction forces. Absolute values are certainly a prerequisite for linear analyses but not for nonlinear investigations of variabilities that are *per se* independent of the absolute value. The electrical and the contractile processes underlying the measured *BBIs* and *CSs* are not reducible to each other, although tightly linked. Thus, the measured video signal provides information about these two distinct processes and consequently allows a more comprehensive characterization compared to frequently used electrode techniques.

For optically computed *SampEn* values, all surrogate evaluations strengthen the experimental findings that long-range correlations are present in *BBI*, *CS,* and *rCS* signals. Shuffled values are always statistically higher compared to experimentally obtained values and the difference between control and ACh treated tissue vanishes compared to the experimental case. Hence, the investigated physiological signals contain inherent nonlinear patterns in the interval and the contraction strength domains, justifying the application of the chosen nonlinear measures. Furthermore, the increase of regularity due to ACh (lower *SampEn* and D_H values) seems to be caused by deterministic and not by random processes.

The surrogate analyses for D_H values agree very well to *SampEn* evaluations, except for *BBI* signals (see **Table 1**). Particularly, some experimental values were already close to two, implicating a high degree of underlying random processes. Obviously, data time series shuffling did not reveal any significant changes. Distinct D_H and *SampEn* surrogate results concerning *BBIs* imply different sensitivities to underlying random and deterministic physiological mechanisms. This may indicate that the Higuchi dimension and not the sample entropy is able to discriminate differences between interval and contraction strength signals, but further investigations are needed to corroborate this assumption. In order to rule out that high D_H values close to two were method specific, we additionally performed a detrended fluctuation analysis DFA (Peng et al., 1994; Goldberger et al., 2002). DFA characterizes white noise with $\alpha = 0.5$ and Brownian noise with $\alpha = 1.5$.The maximal window length was set to 30, comparable to $k = 30$ for D_H. The medians of all control cases including *BBI*, *CS*, and *rCS* ($n = 27$) were 1.98 for D_H and 0.61 for α (DFA) confirming the high degrees of randomness in the signals. Thus, the decreased D_H values under ACh treatment indicate a change from very low correlations to increased long-range correlations and self-affine processes.

Complexity can be defined as the presence of long-range correlations, arising from nonlinear interaction dominated dynamical processes being neither totally regular nor totally irregular (Van Orden et al., 2011). This concept has been successfully applied to discriminate healthy and pathological conditions, where a breakdown of long-term correlations and an according change in fractal dimension has been observed (Goldberger et al., 2002). In our case, SAN tissue preparations show a high degree of irregularity near white noise indicating a low complexity without long-range correlations or self-organizing mechanisms. This may be due to a loss of multiple and interwoven communication pathways and nonlinear dependencies present in the intact heart but not in the tissue preparation. This is supported by ACh as a relevant external stimulus that changes the interaction dominated dynamical system by reducing the degrees of freedom and by introducing long-range correlations, multiplicative interactions and feedback. ACh may be interpreted as a control parameter for the system. Phase transitions or bifurcations, dependent on control parameters exceeding critical values, may also play an important role for our tissue preparation, but at this stage further investigations are necessary to justify such interpretations.

In conclusion, the described technique represents a reliable, easy handling and long-lasting recording method, from which beating rate variabilities and contraction strength variabilities can be assessed.

AUTHOR CONTRIBUTIONS

HA and SS are joint first authors. HA, SS, KZ-P, and BP designed the study. SS and PL dissected SAN tissues from mouse hearts. SS and ÁD carried out video experiments. SS and RA carried out electrical recordings. HA, MM-R, and ÁD developed mathematical algorithms. HA, SS, ÁD, and PL performed video analyses. RA analyzed electrical recordings. KZ-P and HA computed nonlinear parameters and statistical tests. HA, SS, and KZ-P wrote the manuscript. SS, RA, BP, KZ-P, HA, and MM-R revised the manuscript. HA and SS prepared the figures. All authors read and approved the manuscript.

FUNDING

This work was partly supported by research grants from the Austrian National Bank (16435, Anniversary Fund) and the Franz-Lanyar-Foundation (#405) to BP.

DATA AVAILABILITY STATEMENT

BBI, *CS,* and *rCS* data series for each experiment (Con and ACh treated) are provided as csv file in the supplement.

ACKNOWLEDGMENTS

We gratefully thank Dr. Matteo Mangoni and Dr. Pietro Mesirca from the Institut de Génomique Fonctionelle, Montpellier, France, for teaching the preparation technique of sinoatrial node tissue to our group. We thank the reviewers for their valuable suggestions.

SUPPLEMENTARY MATERIAL

The Supplementary Material for this article can be found online at: https://www.frontiersin.org/articles/10.3389/fphys.2018.00546/full#supplementary-material

REFERENCES

Ahammer, H., Scherubel, S., Arnold, R., Zorn-Pauly, K., and Pelzmann, B. (2013). "Beat to beat variability of embryonic chick heart cells under septic conditions: application and evaluation of entropy as well as fractal measures," in *35th Annual International Conference of the IEEE Engineering in Medicine and Biology Society* (Osaka: EMBC), 5566–5569.

Ahola, A., Kiviaho, A. L., Larsson, K., Honkanen, M., Aalto-Setäl,ä, K., and Hyttinen, J. (2014). Video image-based analysis of single human induced pluripotent stem cell derived cardiomyocyte beating dynamics using digital image correlation. *Biomed. Eng. Online* 13:39. doi: 10.1186/1475-925X-13-39

Chan, P. K., Lin, C. C., and Cheng, S. H. (2009). Noninvasive technique for measurement of heartbeat regularity in zebrafish (Danio rerio) embryos. *BMC Biotechnol.* 9:11. doi: 10.1186/1472-6750-9-11

de Castilho, F. M., Ribeiro, A. L. P., da Silva, J. L. P., Nobre, V., and de Sousa, M. R. (2017). Heart rate variability as predictor of mortality in sepsis: a prospective cohort study. *PLoS ONE* 12:e0180060. doi: 10.1371/journal.pone.0180060

De Luca, E., Zaccaria, G. M., Hadhoud, M., Rizzo, G., Ponzini, R., Morbiducci, U., et al. (2014). ZebraBeat: a flexible platform for the analysis of the cardiac rate in zebrafish embryos. *Sci. Rep.* 4:4898. doi: 10.1038/srep04898

Devos, D., Kroumova, M., Bordet, R., Vodougnon, H., Guieu, J. D., Libersa, C., et al. (2003). Heart rate variability and Parkinson's disease severity. *J. Neural Transm.* 110, 997–1011. doi: 10.1007/s00702-003-0016-8

Eisner, D. A., Caldwell, J. L., Kistamás, K., and Trafford, A. W. (2017). Calcium and excitation-contraction coupling in the heart. *Circ. Res.* 121, 181–195. doi: 10.1161/CIRCRESAHA.117.310230

Elstad, M., O'Callaghan, E. L., Smith, A. J., Ben-Tal, A., and Ramchandra, R. (2018). Cardiorespiratory interactions in humans and animals: rhythms for life. *Am. J. Physiol. Heart Circ. Physiol.* doi: 10.1152/ajpheart.00701.2017. [Epub ahead of print].

Fassina, L., Di Grazia, A., Naro, F., Monaco, L., De Angelis, M. G., and Magenes, G. (2011). Video evaluation of the kinematics and dynamics of the beating cardiac syncytium: an alternative to the Langendorff method. *Int. J. Art. Organs* 34, 546–558. doi: 10.5301/IJAO.2011.8510

Galvez Coyt, G., Munoz Diosdado, A., Balderas Lopez, J. A., del Rio Correa, J. L., and Angulo Brown, F. (2013). Higuchi's method applied to the detection of periodic components in time series and its application to seismograms. *Revista Mexic. Fisica S* 59, 1–6.

Glukhov, A. V., Fedorov, V. V., Anderson, M. E., Mohler, P. J., and Efimov, I. R. (2010). Functional anatomy of the murine sinus node: high-resolution optical mapping of ankyrin-B heterozygous mice. *Am. J. Physiol. Heart Circ. Physiol.* 299, H482–H491. doi: 10.1152/ajpheart.00756.2009

Goldberger, A. L., Amaral, L. A., Hausdorff, J. M., Ivanov, P. C. H., Peng, C. K., and Stanley, H. E. (2002). Fractal dynamics in physiology: alterations with disease and aging. *Proc. Natl. Acad. Sci. U.S.A.* 99, 2466–2472. doi: 10.1073/pnas.012579499

Harvey, R. D., and Belevych, A. E. (2003). Muscarinic regulation of cardiac ion channels. *Br. J. Pharmacol.* 139, 1074–1084. doi: 10.1038/sj.bjp.0705338

Higuchi, T. (1988). Approach to an irregular time-series on the basis of the fractal theory. *Physica D* 31, 277–283. doi: 10.1016/0167-2789(88)90081-4

Hofer, E., Keplinger, F., Thurner, T., Wiener, T., Sanchez-Quintana, D., Climent, V., et al. (2006). A new floating sensor array to detect electric near fields of beating heart preparations. *Biosens. Bioelectron.* 21, 2232–2239. doi: 10.1016/j.bios.2005.11.010

Hsiao, C.-W., Bai, M.-Y., Chang, Y., Chung, M.-F., Lee, T.-Y., Wu, C.-T., et al. (2013). Electrical coupling of isolated cardiomyocyte clusters grown on aligned conductive nanofibrous meshes for their synchronized beating. *Biomaterials* 34, 1063–1072. doi: 10.1016/j.biomaterials.2012.10.065

Kainz, P., Mayrhofer-Reinhartshuber, M., and Ahammer, H. (2015). IQM: an extensible and portable open source application for image and signal analysis in java. *PLoS ONE* 10:e0116329. doi: 10.1371/journal.pone.0116329

Kesić, S., and Spasić, S. Z. (2016). Application of Higuchi's fractal dimension from basic to clinical neurophysiology: a review. *Comp. Methods Progr. Biomed.* 133, 55–70. doi: 10.1016/j.cmpb.2016.05.014

Kihara, Y., and Morgan, J. P. (1991). Abnormal Cai2+ handling is the primary cause of mechanical alternans: study in ferret ventricular muscles. *Am. J. Physiol. Heart Circ. Physiol.* 261, H1746–H1755. doi: 10.1152/ajpheart.1991.261.6.H1746

Kitazawa, T., Asakawa, K., Nakamura, T., Teraoka, H., Unno, T., Komori, S., et al. (2009). M3 muscarinic receptors mediate positive inotropic responses in mouse atria: a study with muscarinic receptor knockout mice. *J. Pharmacol. Exp. Ther.* 330, 487–493. doi: 10.1124/jpet.109.153304

Kojima, K., Kaneko, T., and Yasuda, K. (2006). Role of the community effect of cardiomyocyte in the entrainment and reestablishment of stable beating rhythms. *Biochem. Biophys. Res. Commun.* 351, 209–215. doi: 10.1016/j.bbrc.2006.10.037

Koyani, C. N., Kolesnik, E., Wölkart, G., Shrestha, N., Scheruebel, S., Trummer, C., et al. (2017). Dipeptidyl peptidase-4 independent cardiac dysfunction links saxagliptin to heart failure. *Biochem. Pharmacol.* 145, 64–80. doi: 10.1016/j.bcp.2017.08.021

Krogh-Madsen, T., Kold Taylor, L., Skriver, A. D., Schaffer, P., and Guevara, M. R. (2017). Regularity of beating of small clusters of embryonic chick ventricular heart-cells: experiment vs. stochastic single-channel population model. *Chaos* 27:093929. doi: 10.1063/1.5001200

Kudat, H., Akkaya, V., Sozen, A. B., Salman, S., Demirel, S., Ozcan, M., et al. (2016). Heart rate variability in diabetes patients. *J. Int. Med. Res.* 34, 291–296. doi: 10.1177/147323000603400308

Lakatta, E. G., and DiFrancesco, D. (2009). What keeps us ticking: a funny current, a calcium clock, or both? *J. Mol. Cell. Cardiol.* 47, 157–170. doi: 10.1016/j.yjmcc.2009.03.022

Lombardi, F., and Stein, P. K. (2011). Origin of heart rate variability and turbulence: an appraisal of autonomic modulation of cardiovascular function. *Front. Physiol.* 2:95. doi: 10.3389/fphys.2011.00095

Mandel, Y., Weissman, A., Schick, R., Barad, L., Novak, A., Meiry, G., et al. (2012). Human embryonic and induced pluripotent stem cells-derived cardiomyocytes exhibit beat rate variability and power-law behavior. *Circulation* 125, 883–893. doi: 10.1161/CIRCULATIONAHA.111.045146

Okada, M., Noma, C., Yamawaki, H., and Hara, Y. (2013). Negative Inotropic effect of carbachol and interaction between acetylcholine receptor-operated potassium channel (K.ACh Channel) and GTP binding protein in mouse isolated atrium - a novel methodological trial. *J. Vet. Med. Sci.* 75, 377–380. doi: 10.1292/jvms.12-0369

Papaioannou, V. E., Verkerk, A. O., Amin, A. S., and de Bakker, J. M. (2013). Intracardiac origin of heart rate variability, pacemaker funny current and their possible association with critical illness. *Curr. Cardiol. Rev.* 9, 82–96. doi: 10.2174/157340313805076359

Peng, C.-K., Buldyrev, S. V., Havlin, S., Simons, M., Stanley, H. E., and Goldberger, A. L. (1994). Mosaic organization of DNA nucleotides. *Phys. Rev. E Stat. Phys. Plasmas Fluids Relat. Interdisci.p Top.* 49, 1685–1689. doi: 10.1103/PhysRevE.49.1685

Ponard, J. G., Kondratyev, A. A., and Kucera, J. P. (2007). Mechanisms of intrinsic beating variability in cardiac cell cultures and model pacemaker networks. *Biophys. J.* 92, 3734–3752. doi: 10.1529/biophysj.106.091892

R Core Team (2017). *R: A Language and Environment for Statistical Computing.* Vienna: R Core Team.

Richman, J. S., and Moorman, J. R. (2000). Physiological time-series analysis using approximate entropy and sample entropy. *Am. J. Physiol. Heart Circ. Physiol.* 278, H2039–H2049. doi: 10.1152/ajpheart.2000.278.6.H2039

RStudio (2016). *RStudio: Integrated Development for R* (Boston, MA: RStudio Inc.).

Sessa, F., Anna, V., Messina, G., Cibelli, G., Monda, V., Marsala, G., et al. (2018). Heart rate variability as predictive factor for sudden cardiac death. *Aging* 10, 166–177. doi: 10.18632/aging.101386

Stummann, T. C., Wronski, M., Sobanski, T., Kumpfmueller, B., Hareng, L., Bremer, S., et al. (2008). Digital movie analysis for quantification of beating frequencies, chronotropic effects, and beating areas in cardiomyocyte cultures. *ASSAY Drug Dev. Technol.* 6, 375–385. doi: 10.1089/adt.2008.129

Torrente, A. G., Zhang, R., Zaini, A., Giani, J. F., Kang, J., Lamp, S. T., et al. (2015). Burst pacemaker activity of the sinoatrial node in sodium–calcium exchanger knockout mice. *Proc. Natl. Acad. Sci. U.S.A.* 112, 9769–9774. doi: 10.1073/pnas.1505670112

Torres, C. A., and Janssen, P. M. (2011). Contractile strength during variable heart duration is species and preload dependent. *Biomed. Res. Int.* 2011:294204. doi: 10.1155/2011/294204

Van Orden, G., Kloos, H., and Wallot, S. (2011). "Living in the pink: Intentionality, wellbeing, and complexity," in *Philosophy of Complex Systems, Handbook of the Philosophy of Science*, ed Hooker (Amsterdam: Elsevier), 629–672.

Wilcox, R. R., and Rousselet, G. A. (2018). A guide to robust statistical methods in neuroscience. *Curr. Protoc. Neurosci.* 82, 8.42.1–8.42.30. doi: 10.1002/cpns.41

Wilcox, R. R. (2016). *Understanding and Applying Basic Statistical Methods Using R.* Hoboken, NJ: Joh Wiley & Sons.

Yaniv, Y., Ahmet, I., Liu, J., Lyashkov, A. E., Guiriba, T.-R., Okamoto, Y., et al. (2014a). Synchronization of sinoatrial node pacemaker cell clocks and its autonomic modulation impart complexity to heart beating intervals. *Heart Rhythm* 11, 1210–1219. doi: 10.1016/j.hrthm.2014.03.049

Yaniv, Y., Lyashkov, A. E., Sirenko, S., Okamoto, Y., Guiriba, T.-R., Ziman, B. D., et al. (2014b). Stochasticity intrinsic to coupled-clock mechanisms underlies beat-to-beat variability of spontaneous action potential firing in sinoatrial node pacemaker cells. *J. Mol. Cell. Cardiol.* 77, 1–10. doi: 10.1016/j.yjmcc.2014.09.008

Zaniboni, M., Cacciani, F., and Lux, R. L. (2014). Beat-to-beat cycle length variability of spontaneously beating guinea pig sinoatrial cells: relative contributions of the membrane and calcium clocks. *PLoS ONE* 9:e100242. doi: 10.1371/journal.pone.0100242

Conflict of Interest Statement: MM-R was employed by KML vision OG, Graz, Austria. KML vision OG did not sponsor this study.

The other authors declare that the research was conducted in the absence of any commercial or financial relationships that could be construed as a potential conflict of interest.

The handling Editor declared a past co-authorship with one of the authors HA.

Copyright © 2018 Ahammer, Scheruebel, Arnold, Mayrhofer-Reinhartshuber, Lang, Dolgos, Pelzmann and Zorn-Pauly. This is an open-access article distributed under the terms of the Creative Commons Attribution License (CC BY). The use, distribution or reproduction in other forums is permitted, provided the original author(s) and the copyright owner are credited and that the original publication in this journal is cited, in accordance with accepted academic practice. No use, distribution or reproduction is permitted which does not comply with these terms.

frontiers in Physiology

ORIGINAL RESEARCH
published: 11 October 2018
doi: 10.3389/fphys.2018.01441

Orderliness of Visual Stimulus Motion Mediates Sensorimotor Coordination

Joshua Haworth[1,2,3]* **and Nicholas Stergiou**[3,4,5]

[1] Department of Kinesiology, Science and Learning Center, Whittier College, Whittier, CA, United States, [2] Department of Biomechanics, University of Nebraska Omaha, Omaha, NE, United States, [3] Department of Environmental, Agricultural & Occupational Health, College of Public Health, University of Nebraska Medical Center, Omaha, NE, United States, [4] Division of Biomechanics and Research Development, College of Education, University of Nebraska Omaha, Omaha, NE, United States, [5] Department of Biomechanics, University of Nebraska Omaha, Omaha, NE, United States

We explored the coupling of gaze and postural sway to the motion of a visual stimulus, to further understand sensorimotor coordination. Visual stimuli consisted of a horizontally oscillating red dot, moving with periodic (sine), chaotic, or aperiodic (brown noise) temporal structure. Cross Recurrence Quantification Analysis (cRQA) was used to investigate the coupling between each measured signal with the time series of the visual stimulus position. The cRQA parameter of percent determinism indicated similar strength of coupling of gaze with either periodic or chaotic motion structures, yet weaker coupling to aperiodic stimulus motion. The cRQA parameter of Maxline indicated a particular affinity toward chaotic motion. Analysis of postural coupling supports the idea that the complex periodicity of body sway affords interactivity with non-simple environmental dynamics. These results collectively strengthen the argument that chaos is an invariant and beneficial feature of biological motion, a feature which may be critical for immediate and robust coordination of the self with the environment and other environmental agents.

Keywords: biological motion, eye tracking, smooth pursuit, coupled systems, determinism, gaze, posture

OPEN ACCESS

Edited by:
Srdjan Kesić,
University of Belgrade, Serbia

Reviewed by:
Didier Delignieres,
University of Montpellier 1, France
Dimitris Kugiumtzis,
Aristotle University of Thessaloniki,
Greece

****Correspondence:***
Joshua Haworth
joshua.haworth@gmail.com

Specialty section:
This article was submitted to
Fractal Physiology,
a section of the journal
Frontiers in Physiology

Received: *19 March 2018*
Accepted: *21 September 2018*
Published: *11 October 2018*

Citation:
Haworth J and Stergiou N (2018)
Orderliness of Visual Stimulus Motion
Mediates Sensorimotor Coordination.
Front. Physiol. 9:1441.
doi: 10.3389/fphys.2018.01441

INTRODUCTION

Humans exhibit oscillatory dynamics on many time scales, from sleep/wake cycles to breathing to regulation of posture. Even the routine of trips to the grocery must be repeated after some time has passed since the last visit. These are all processes which can be discretized, allowing their iterations to be viewed as single events. In actuality, however, each individual event truly occurs within series, with potentially critical interdependencies between iterations, making each event part of a more general continuity. To ensure success in this complex world, individuals must possess some means by which to coordinate the memories they have about previous events along with predictions about future events, all in line with the real-time 'now' which they are experiencing (Spivey, 2007). Our goal in this paper is to provide in the introduction a contextual motivation for an experiment that explores the role of the complexity of stimulus orderliness as a mediator of sensorimotor coordination, and then through empirical analysis to provide further discussion.

Sejnowski (2010) discussed the propensity of both monkeys and humans to learn optimal strategies in the face of complex problems. Moreover, these behaviors have been replicated in reinforcement based simulations which demonstrate the emergence of solutions given sufficient time to generate experience. This concept is further extended to observations of how children seem to learn so naturally, through simple attempt repetitions and imitation play (Meltzoff et al., 2009). This discovery learning approach has also been discussed by Berthier et al. (2005) where they have demonstrated the efficacy of a fully unsupervised model to generate reaching behavior similar to that which we would expect from a typical human child. In contrast to a supervised model, where 'correct' strategies are instructed, unsupervised models foster the self-discovery of the dynamics of the internal and external environments.

However, it is not just the status of the agent and environment that serve to inform motor strategy development. Thelen and Smith (1994) showed extensively that interaction dynamics serve a large role in the development of motor strategies. Both internal and external constraints can serve to limit our coordination space, reducing the number of potential movement strategies that are available to choose from Todorov and Jordan (2002) extended that variability in movement behavior is ubiquitous, leading further to the conclusion that pre-planned regulations of movement strategies could not possibly be effective. Instead, they demonstrate that it is through real-time feedback (and its optimal control) that purposeful actions are realized. Such a control process should afford easy consideration to even the most complex of experienced dynamics. Albeit, extensive practice might yet be necessary in order to 'learn' the most effective uses of such feedback. We see here a fundamental shift in what it takes to excel in the world, from a strategy of *learn the right way* to *learn the right coordination*. This paradigm shift could have massive impact on how we continue to organize learning environments.

In light of this new perspective, it becomes clear that the quality of experience is one of utmost importance. Here, we do not mean the 'goodliness' type of quality, but instead refer to factors of organization of the experience within space and time; essentially, the 'orderliness' of the learning experience. Sprott (2013) has shown that the inclusion of chaotic dynamics is specifically beneficial to learning in artificial neural networks, suggesting that the benefit of chaos is its core nature of deterministic variability. This flexibility affords the exploration of many combinations of degrees of freedom (potential strategies), while maintaining structural similarity that can be revisited in future iterations of practice. This point echoes the arguments of many others in describing important aspects of play en route to a successful motor repertoire (Siegler, 1996; Adolph and Joh, 2009; Siegler et al., 2010). The suggestion that we may utilize chaos as a means to optimize our learning strategies is quite an interesting notion. This is especially true in light of other recent work describing the general inherence of chaos (and complexity) in the optimization of human behaviors, including movements (Haworth et al., 2013). Further work by Ali et al. (2007) affirmed this idea of inherent chaos in human movement by showing that algorithms for automated motion tracking are more proficient at capturing biological motion when they are set to attend to chaotic motion structures.

The notion of chaos is extendible even to the domain of humanoid movement behavior. Schaal (2007), discussed the role of behavioral variance in helping to make the actions of robots more human-like in order to lead to greater social tolerance. Interestingly, people seem to be quite sensitive to the apparent rigidity of robots. Something about the disproportionate predictability of a robot's motions, relative to a typical person's, makes it a generally unnatural and uneasy visual experience. The assertion that optimum dynamics should include some factor of variance (i.e., from chaos) is certainly interesting, and apparently also quite practical. Duran et al. (2007a,b, 2008) showed that it is possible to develop real-time, dynamic smooth pursuit behavior in robotic systems, using a coupled chaotic systems approach. This tracking behavior is readily responsive to known and novel objects, and their motion trajectories. Moreover in this approach, vision is shown to be sufficient to inform the self-organization of the motion of the postural coordination necessary for object tracking; i.e., neck muscle activations. However, much is yet to be discovered in this domain of sensorimotor connectivity, particularly with regard to the vast expanse of interaction dynamics that are necessary for success in the world.

It should be noted here, that not all environments are actually ultimately complex. Often, either by natural order or imposed organization, we find ourselves operating in a circumstance which is out and out routine. Other times, we may find our operations to be within an environment which truly has no organizational process to it, whatsoever. That which is truly remarkable is that our ability to organize our own behavior is almost ubiquitously robust against these environmental variances. Continued cooperation between human movement scientists and roboticists would surely be mutually beneficial, heading toward elegant descriptions of the way by which persons and machines can interact with environments that range across periodic, through chaotic, even toward completely random orders. As human movement scientists, we make the assertion that an individual's primary means toward 'success' is through effective coordination of their actions within the organization of the world. This requires competency in the production of purposeful movements, but even more so a competency in determining the dynamics of the world within which those actions are to take place.

Several modern techniques have emerged that offer quantitative strategies for assessing qualities of synchronicity between connected systems. Connectivity analysis is often used to study rhythmic neuronal interactions to identify inter-areal synchronization within the brain using techniques such as conditional Granger causality index and partial transfer entropy (Bastos and Schoffelen, 2016). In the fields of action perception and ecological psychology, cross recurrence quantification (cRQA) has been used extensively to elucidate human behavior coupling between two persons or between a person and an environmental stimulus. Common applications include evaluation of social interactions (Richardson et al., 2008; Fusaroli et al., 2014; Davis et al., 2017), conversational dynamics (Dale and Spivey, 2005, 2006), head motions during conversation (Paxton and Dale, 2017), postural coordination (Shockley et al., 2003; Shockley, 2005; King et al., 2012), and eye movements (Richardson and Dale, 2005; Richardson et al., 2007), as well as posture and gaze response to visual stimulus motion complexity (Haworth et al., 2015, 2016).

Thus, we seek in the current work to better understand human-environment interaction by testing the role of the complexity of stimulus orderliness as a mediator of sensorimotor coordination. We sought to find a better understanding through this experiment of the sensitivity and responsiveness of human vision and posture, in response to rhythmic, chaotic, and random motion. Our analysis utilizes percent determinism and maxline outcomes from cross recurrence quantification to evaluate qualities of coupling between each of these systems, as these have been shown previously to uncover interesting aspects of engagement dynamics (Haworth et al., 2015, 2016). We intend to conclude with the assertion that persons are able to observe and respond to a full spectrum of motion dynamics, maintaining particular affinity for chaos.

MATERIALS AND METHODS

Participants and Procedures

Fourteen healthy young adults (4 male and 10 female, age 29.8 ± 10.5 y, height 1.638 ± 0.1 m, and weight 67 ± 14.2 kg) each participated in a single individual session for data collection. Synchronous eye movement and standing posture recordings were taken while a moving point-light stimulus was displayed on a large monitor in front of the participant. FaceLab 4.5 (Seeing Machines, Acton, MA, United States) eye-tracking equipment was used to track eye movements. An AMTI force platform (Advanced Mechanical Technology Inc., OR6-7, with MSA-6 amplifier) was used to record center of pressure (the projection of the body's center of mass onto the surface) throughout each trial. Trials were managed through custom software designed in LabView (National Instruments, Austin, TX, United States), including software synchronization of the data from the eye-tracker and the force platform, as well as the display of the visual stimulus. All data was collected at 50 Hz, as this was the highest common frequency available amongst the set of equipment. Additionally, 50 Hz sampling provides 20 ms resolution of each measured behavior, which is sufficient to observe the dynamics of both postural sway and smooth pursuit eye movements. We purposefully steered away from stimulus oscillation velocity/frequency that could provoke saccade or rapid postural perturbation.

The displayed stimulus (a red dot, 25 pixel radius) was presented on a 55″ 1920 × 1200 pixel LCD monitor, moving according to a predefined motion trajectory (sine, chaos, and brown noise) with an update in position occurring at a rate of 50 Hz. Trials lasted for 5 min each to ensure the capture of adequate lengths of data, with condition order randomized for each participant. Participants were given the instruction to stand quietly and attend to the motion of the stimulus until the end of the trial, as indicated by the investigator. Room lights were dimmed, and conversation was held to a minimum throughout each trial. However, participants were allowed to speak and move about freely in the time between conditions. Grid markings on the surface of the force platform were used to realign the feet to ensure a similar stance between each condition. **Figure 1** provides a diagram of the setup. Informed consent was obtained prior to all experimental procedures, as approved by the University of Nebraska Medical Center Institutional Review Board.

Stimulus Presentation

Stimulus motion animations were constructed such that the position of the stimulus was updated at 50 Hz (above perceptive threshold of object motion), with each new point defined to follow one of three main signal structures; sine, chaos, and brown noise. These particular signals were selected, as they span

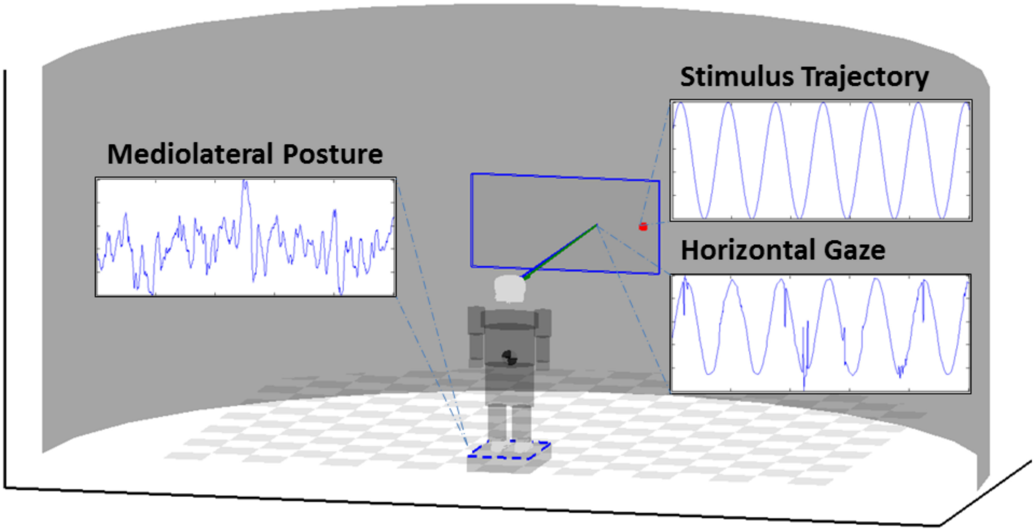

FIGURE 1 | Diagram of the experimental setup. Participants stood atop a force platform in comfortable, self-selected stance. Eye-tracking equipment is affixed to the monitor stand, and positioned to capture gaze response during stimulus presentation. Example time series shown are from the Sine condition.

the domain of 'orderliness.' Sine exhibits perfectly redundant order, brown noise exhibits stochastic or non-redundant order, with chaos exhibiting a dynamic and deterministic mixture of redundancy and non-redundancy.

Each signal is comprised of 15,000 data points updating at 50 Hz, to provide 5 min of continuous stimulus motion. Stimulus time series were constructed using embedded and custom algorithms in Matlab (MathWorks, Natick, MA, United States) and saved in data files on the computer. These data series were accessed and displayed through the main Labview application during each trial. The sine signal was generated using the sin() function in Matlab. Single sinusoidal motion represents the simplest oscillation, such as a frictionless clock pendulum, expressing perfect redundancy. The chaos signal was produced from a model of the motion of a double pendulum, which has recently been shown to successfully model the dynamics of human posture (Suzuki et al., 2012). The free rotations of a two segment linkage are sufficient to afford chaotic dynamics (Shinbrot et al., 1992), which appear in the hip strategies expressed by their model. The *x*-axis position of the distal segment of our custom model was extracted and used to produce the chaos signal. Surrogate testing via phase randomization (Theiler et al., 1992) was used to further the confidence that the generated signal exhibited chaotic dynamics. The brown noise signal was generated by the iterative addition of a random perturbation to the original point position. White noise truly represents purely stochastic nature; however, it would be impossible to follow such a structure with smooth pursuit eye movements. Smooth pursuit requires continuity in the motion of the tracked object. Brown noise in essence is the integral of white noise; maintaining the stochastic nature, while also presenting sufficient continuity to be tracked by smooth pursuit eye movements. Although contentious, human posture has previously been touted to express Brownian motion (Collins and Deluca, 1994); lending confidence to our approach that the Brown Noise stimulus is available for integration in sensorimotor coordination. This spectrum of particular signals provides us with an access to investigate how individuals might manage their gaze and posture in coordination to various motions; particularly on the aspect of orderliness.

Data Processing

Gaze and postural data were recorded at 50 Hz, throughout the entire 5 min duration of stimulus condition presentation. Gaze data was recorded as the on-screen pixel coordinate at which the participant was looking at each time point throughout the trial. Center of pressure was recorded as the measure of posture. For both signals, only the horizontal component of motion was further considered, as the stimulus signal was set to move only in the horizontal direction. To avoid the influence of novelty, the first ten seconds of data was eliminated. Only the subsequent 2 min of data were further processed, to reduce the possibility that fatigue might interfere with the quality of the analyses. Cross recurrence quantification analysis (cRQA) was used to assess coupling of gaze (Gaze) and posture (COP) to the stimulus, separately, as well as between gaze and posture to gauge sensorimotor coupling (SensMot). Metrics of SensMot provide additional novelty to this work, as it provides a first effort toward a 'direct' assessment of the continuous relationship between gaze and posture during an attention driven smooth pursuit task.

Outcome metrics from cRQA were calculated using custom Matlab software (MathWorks, Natick, MA, United States) adapted from those provided by the Perceptual-Motor Dynamics Laboratory at the University of Cincinnati, are described in further detail below (Shockley et al., 2002; Shockley, 2005). Prior to conducting cRQA, gaze data was pre-processed to remove zero (0) values that were recorded during collection from a small number of files; much smaller than 0.01% of data in each file. These data were registered by the eye-tracking software during samplings when the eyes were unable to be imaged for position analysis. This occurred in our case, when persons had an exceptionally long blink. These values were removed from the time series, and replaced using a 5th order cubic spline (Matlab, *interp1* function).

Cross Recurrence Quantification Analysis

Webber and Zbilut (1994) developed recurrence quantification analysis to assess the structure of the temporal evolution of a behavior through the associated measured time series. This process includes embedding a time series into its respective multi-dimensional phase space (Takens, 1981), creating a recurrence matrix (recurrence plot), and then applying various pattern matching algorithms to uncover the underlying dynamics. Later, Zbilut et al. (1998) expanded this technique to include applying these pattern matching approaches to recurrence matrices generated from two separate time series embedded in similarly dimensional phase space. This approach proved useful for uncovering mutual dynamics between the two time series, and has since been used to describe coupled oscillators in many various disciplines, including the coordination of chaotic oscillators (Shockley et al., 2002). Particularly of interest to the current work are the applications of cRQA to discover metrics of coordination of coupled biological rhythms (Richardson and Dale, 2005; Richardson et al., 2008).

In order to conduct cRQA, each time series must be unfolded into a similar multi-dimensional phase space. This is accomplished using parameters of delay and embedding dimension, which are calculated from average mutual information (AMI; Fraser and Swinney, 1986) and False Nearest Neighbors (FNN; Abarbanel, 1996) algorithms. We used values of 22 and 10, respectively, as these were the group averages after passing each dataset through the above algorithms.

In order to achieve outcome data that was both representative of the time series' dynamics, and yet also reasonably comparable, we chose to set a fixed recurrence value instead of radius value; as has been previously suggested (Shockley, 2005). Otherwise, we found that the determinism saturated, and no effective interpretations could be made of the recurrence plots (which by the eye, clearly showed differences; see **Figure 2**, bottom row). We set percent recurrence at 5%, such that we would subsequently evaluate recurrent lines under parameters that are more similar across the three stimulus conditions. Minline represents the shortest duration (in data points) within which the two signals are sequentially recurrent that will be considered in

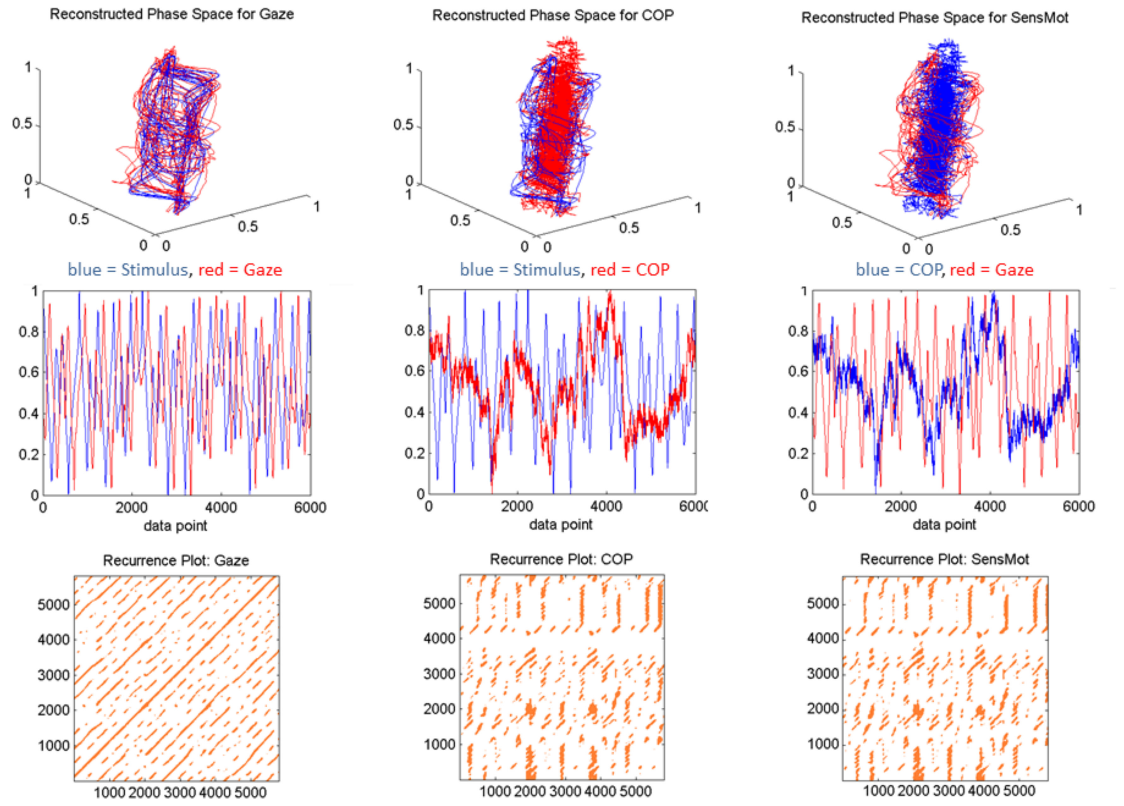

FIGURE 2 | Sample data from a single, representative participant in response to the chaotic stimulus motion. The first three viewable dimensions of the two signals are shown in the first row, with the single-dimensional measured signal in the middle row. The bottom row shows the recurrence plot which indicates the points of coordination, across trial duration, in phase space. This order is repeated for each of Gaze, COP, and SensMot in separate columns as labeled. All data are presented unit normalized spatially and from index value 0 through 6000, corresponding to 2 min of trial duration at 50 Hz.

subsequent computations. Minline was set in our experiment to 25, representing duration of 0.5 s as a minimum threshold to be considered as a recurrent line. This value was chosen based on the logic that smooth pursuit and saccadic eye movements can both occur in shorter time spans, but the saccades would not last longer. Additionally, early runs of sampled data suggested that this value would provide more stable and comparable outcome measures across the three conditions.

Outcome measures from cRQA to be considered here include percent determinism and maxline. These outcomes each provide a unique description of the dynamics available from the cross recurrence plot as they have previously been shown to elucidate dynamical coordination in tasks similar to those used in the current experiment (Shockley et al., 2002, 2003; Richardson et al., 2008). Percent determinism is the ratio of recurrent points that form lines, divided by the total number of recurrent points; reported from 0 to 100%. If every point of recurrence between the two signals is part of a bout of continuous coordination (minimum of 25 points to form a line), percent determinism would report as 100%. It is possible that none of the recurrent points are part of a continuous coordination (line), in which case percent determinism would report as 0%. Maxline is the length of the longest line formed by recurrent points, expressing the extent of coupling between the two signals; reported in number of data points. Larger values of maxline indicate longer bouts of continuous coordination between the compared behaviors. Data is collected at 50 Hz, so each increment of 50 data points for maxline represents 1 s of signal coordination.

Statistical Analysis

Separate one-way, repeated measures ANOVAs (within subject; comparing periodic, chaotic, random conditions) were conducted to test percent determinism and maxline across these three stimulus conditions; for each of Gaze, COP, and SensMot. *Post hoc*, dependent *t*-tests were used to identify where differences occurred. Statistical tests were conducted using IBM SPSS Statistics software (IBM Corporation, Armonk, NY, United States, Version 18), with an alpha set at 0.05.

RESULTS

Results are reported below, separately for each of Gaze, COP, and SensMot. A graphical view of the results can be found in **Figure 3**, with a listing of the pairwise *t*-values in **Table 1**. Additional analyses were conducted, with

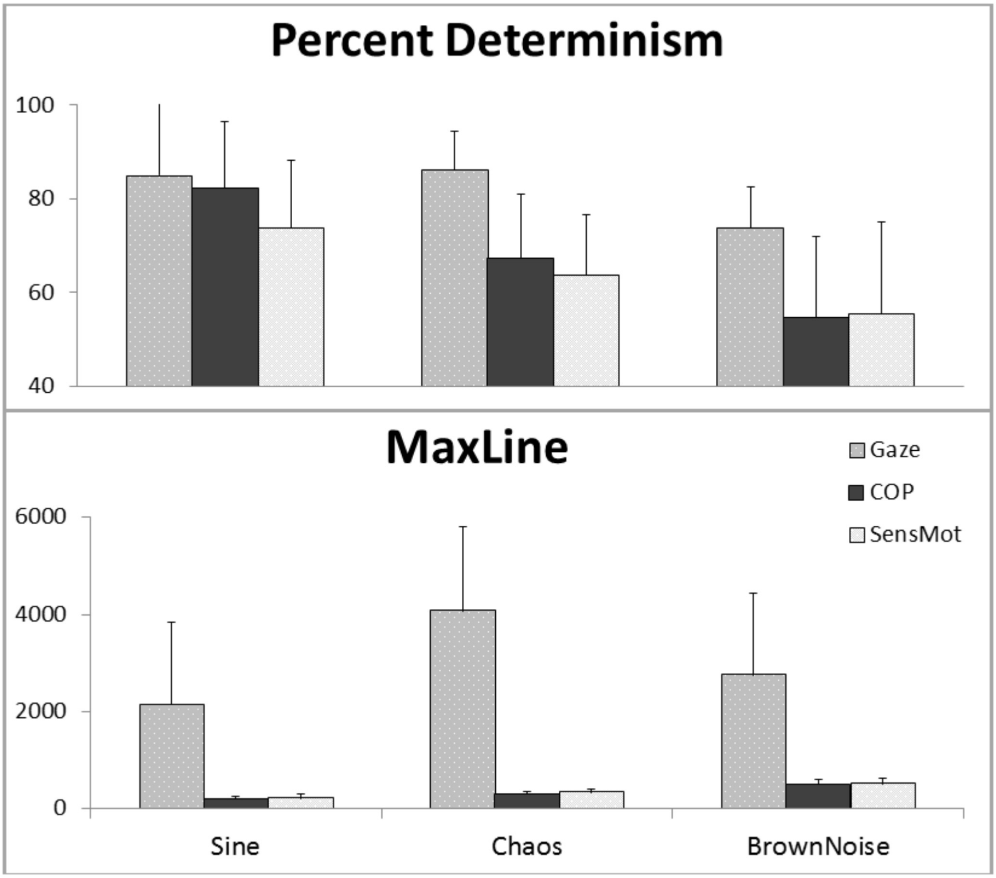

FIGURE 3 | Results of cRQA, showing coupling for Gaze and COP to stimulus motion (Gaze and COP, separately) and in relation to one another (SensMot), across three types of stimulus motion.

proximal parameterizations to those reported, in order to verify the robustness of the findings. In each case, similar results and trends were found as those reported here.

Gaze

The one way ANOVA for percent determinism resulted in significant differences ($p < 0.001$). The *post hoc* analysis (**Table 1**) showed that percent determinism was similar for Gaze in response to the Sine and Chaos signals, but was lesser in response to Brown Noise in comparison to the Sine or Chaos signal. For maxline, ANOVA again found significant differences ($p = 0.04$). *Post hoc* analysis showed maxline of Gaze was largest during the Chaos condition, indicating significantly longer bouts of coordination with Chaos than with either Sine or Brown Noise signals.

TABLE 1 | Mean values of the group ($n = 14$) for each outcome measure, under each stimulus condition.

Stimulus signal	Gaze	*T*-tests		COP	*T*-tests		SensMot	*T*-tests	
Percent Recurrence									
Sine	**85**	Sine · Chaos	0.3371	**82.3**	Sine · Chaos	0.0049*	**73.8**	Sine · Chaos	0.0315*
Chaos	**86.2**	Chaos · Brown	0.0000*	**67.4**	Chaos · Brown	0.0000*	**63.7**	Chaos · Brown	0.0119*
Brown Noise	**73.8**	Brown · Sine	0.0026*	**54.7**	Brown · Sine	0.0003*	**55.4**	Brown · Sine	0.0116*
MaxLine									
Sine	**2137**	Sine · Chaos	0.0005*	**208**	Sine · Chaos	0.0002*	**217**	Sine · Chaos	0.0004*
Chaos	**4071**	Chaos · Brown	0.0305*	**308**	Chaos · Brown	0.0000*	**333**	Chaos · Brown	0.0001*
Brown Noise	**2741**	Brown · Sine	0.2134	**499**	Brown · Sine	0.0000*	**511**	Brown · Sine	0.0000*

*Values in bold indicate the mean of the group for each measure (percent recurrence or maxline) of each behavior (Gaze, COP, or SensMot) in response to each stimulus type (Sine, Chaos, or Brown Noise). T-tests were conducted pairwise, as indicated, with a threshold at *$p < 0.05$ for significance.*

COP and SensMot

The one way ANOVA for percent determinism resulted in significant differences for both COP ($p < 0.001$) and SensMot ($p = 0.004$). *Post hoc* analysis (**Table 1**) showed similar patterns of response to the three conditions for COP and SensMot. Rates of coordination were highest in response to the Sine signal, and lowest in response to the Brown Noise signal. For maxline, significant differences were found for both COP ($p < 0.001$) and SensMot ($p < 0.001$). Again, *post hoc* analysis (**Table 1**) showed similar patterns for COP and SensMot. Shorter duration coordination was found in response to the Sine signal, while longer duration coordination was found in response to the Brown Noise signal.

DISCUSSION

We found that our results support the assertion that persons are able to observe and respond to a full spectrum of motion dynamics. Percent determinism shows that gaze had similar propensity to track Sine and Chaos, indicating an ability to maintain coupling with these signals throughout the trial. Gaze in response to Brown Noise had a significantly lower percent determinism, suggesting a weaker coupling with this motion structure. It is worth noting, though, that above 70% determinism does indicate an ability to coordinate with the random signal, yet in contrast with the other motion structures tends to not couple as strongly. Our question here is whether this reduced coupling to randomness is representative of a system limitation, or the demonstration of preference. Regardless, these results suggest that gaze behavior is proficient in response to a variety of motion structures, and is robust to motion variation of chaotic order. Actually, in looking at maxline data, it appears that persons expressed a particular affinity for chaotic motion.

Maxline represents the longest duration (in data points) within which the two signals are sequentially recurrent. With regard to gaze behavior, we contend that this measure stands as a proxy for the attention span, or ability combined with interest, to maintain stimulus following. Our results indicate that the tendency for coupling is highest in the chaos condition, and similar for the sine and brown noise conditions. In fact, persons coupled with chaos for nearly twice the duration of either of the alternatives. Recall also, the inherency of chaos in biological animacy (Haworth et al., 2013). In turn, these data may lend new insight to how we might understand the interpersonal coordination that has been described previously (Shockley et al., 2003, 2009).

Further, and as suggested above, we feel that the result of gaze maxline being the highest during the chaos condition is very much tied to attention. This interpretation is certainly a bit speculative, as we did not test or measure anything directly explicating attention as an outcome or as a mechanism. However, it is an interesting and reasonable interpretation. Coordinating gaze to the stimulus motion affords continued accrual of information which could be used to predict its future position. In the case of the Sine stimulus, the repetitive nature of the motion trajectory dispels the benefit of highly coupled gaze. It is just a simple periodic rhythm, identifiable in a short viewing period. Following a prediction of periodicity would require only intermittent viewing to confirm the prediction, and continue as such. This interpretation helps to clarify the higher percent determinism value that we found in response to the Sine stimulus. This may represent the viewer continuing to 'come back' to a coordination state in order to verify the constancy of the periodicity assumption that was drawn after a few cycles.

In the case of Gaze response to the Brown Noise stimulus, two unresolvable possibilities exist; either the gaze coupling is so difficult that it cannot be maintained for such longer durations, or the information gained from coupling is poor enough to dispel interest in the continuation of coupling. Although we cannot make a certain conclusion, we look to the gaze behavior in response to the sine motion and our previous interpretation. In that case, the percent determinism was high while the maxline was reduced, suggesting that an intermittent attention strategy had been adopted. In the Brown Noise condition, both metrics were depressed. We take this to indicate a generally reduced attention to this particular signal structure. We thus conclude that the high maxline in the chaos condition indicates a behavior of preference, and not one of limited ability under the other two conditions. In other words, there seems to be a motivation for sustained attention to the chaotic motion structure, which we speculate is based from an implicit awareness of its utility. Ward and West (1998) found that persons were able to learn the underlying dynamic of a particular chaotic process, and then proceed to generate number sequences which contain that dynamic. Considering this along with evidence of the invariance of chaos in biological motion (Ali et al., 2007; Haworth et al., 2013) highlights the value of our observed ability to coordinate with such complex motion structures.

Interestingly, with regard to COP, percent determinism decreased across each of the three conditions. More consistent coupling was found to the Sine signal, while less consistent coupling was found to the Brown Noise signal. It is possible that this is an effect of the inherent redundancy of the stimulus motion signal, itself. Postural coordination with a less redundant signal (Brown Noise) would likely result in less consistently recurrent behavioral patterns. However, the observed trend is actually opposite when we look at maxline, which indicates longest duration couplings to the Brown Noise signal and the shortest to the Sine signal. Given that the two metrics are independent of one another; this inverse relationship is not typically seen in this type of analysis. Thus, we believe it to be a behavioral and not a computational phenomenon. For a more complete understanding, we should consider the natural rhythmicity of posture. All accounts report postural sway to exhibit at least 'noisy' sinusoidal motion (Jeka and Kiemel, 2004).

However, reports also describe posture to demonstrate Brownian motion (Collins and Deluca, 1994); and more recently, posture has been modeled to contain inherent chaotic structure (Suzuki et al., 2012). Without trying to resolve which of these accounts is more accurate, we highlight that each of them presents the case that human posture requires a more complicated model than simple sinusoidal rhythmicity. Given this, our results come into better focus in suggesting that posture coordinates more so with non-rigidly periodic motion structures.

Analysis of SensMot results in the same pattern of behaviors as was found for COP. Several interpretations appear with respect to these results. One is that the coordination of gaze to stimulus motion was sufficiently high that we would not expect dramatically different coordination of posture to stimulus and gaze. Unfortunately, this deflates somewhat the additive value of SensMot to a study which already compares gaze and posture separately. However our results do support its use as a stand-alone metric of sensorimotor coordination, which could cut data preparation and processing time in half without significant loss of information. Separately, given the similarity of results between the COP and SensMot, we speculate that the postural dynamics seem to govern the outcomes of SensMot coordination. This seems to be a bit unexpected, as the assumed information flow of the experience is from the motion of the stimulus, through the sensation/perception of its motion, to the resultant reorganization of posture. It is curious how postural dynamics could weigh more heavily in the coordination of eye and body movement if they are at the end of the information flow. Possibly, postural dynamics do have some regulative influence on the nature of sensorimotor coordination. Further research could explore the temporal resolution of the identified coordination patterns, and seek to provide additional clarity to this interpretation.

CONCLUSION

Our results corroborate with previous work testing sensorimotor coupling to environmental dynamics (Stoffregen et al., 2000, 2006, 2007; Kay and Warren, 2001; Giveans et al., 2011). We have added with the current experiment, explicit evidence that these couplings are robust in the presence of chaotic motion structures of stimulus motion. This opens the way for future research to be conducted into the robustness of these findings, and the expanse of chaotic oscillators to which we are able to couple in an effective fashion. Further, we anticipate the application of this finding in the creation of therapeutic modalities that may seek to positively affect the dynamics of sensorimotor coordination in clinical populations. Lingering questions remain, however. Is attention to chaos a ubiquitous component of the human sensorimotor experience, or is does this propensity develop as we gain experience in the world; i.e., throughout childhood? Children with autism tend to express hyper-rigid behavioral patterns, including movement behaviors (rocking and hopping) and compulsive adherence to daily rituals. It might be interesting to explore if these children express similar flexibility of attention to chaotic motion.

The current work intends to provide an interesting observation for the benefit of the complexity theorist. We have identified not only that persons are sensitive to the dynamics of a chaotic oscillator, but in some ways have a particular preference to their dynamics. Further work will focus on how this approach may be useful in understanding behavioral coordination in a dynamic world rich with complex, and often chaotic, dynamics. This study provides solid ground from which to continue the investigation of sensorimotor coupling in response to a full spectrum of visual stimulus motion structure; from periodic, through chaos, to aperiodic.

DATA AVAILABILITY STATEMENT

The raw data supporting the conclusions of this manuscript will be made available by the authors, without undue reservation, to any qualified researcher.

ETHICS STATEMENT

This study was approved and the protocol was carried out in accordance with the recommendations of the University of Nebraska Medical Center Institutional Review Board. All subjects gave written informed consent in accordance with the Declaration of Helsinki.

AUTHOR CONTRIBUTIONS

JH and NS contributed to the conception and design of the study. JH organized the database, performed the statistical analysis, and wrote the first draft of the manuscript. Both authors contributed to data interpretation, manuscript revision, and approval of the submitted version.

FUNDING

Funding was provided by a Dennis Weatherstone Predoctoral Fellowship (Autism Speaks grant #7070, awarded to author JH), with additional support for materials from the American Society of Biomechanics. Author NS currently receives support from the National Institutes of Health Centers of Biomedical Research Excellence (1P20GM109090-01). The funders had no role in study design, data collection and analysis, decision to publish, or preparation of the manuscript.

REFERENCES

Abarbanel, H. D. I. (1996). *Analysis of Observed Chaotic Data*. New York, NY: Springer-Verlag. doi: 10.1007/978-1-4612-0763-4

Adolph, K. E., and Joh, A. S. (2009). "Multiple learning mechanisms in the development of action," in *Learning and the Infant Mind*, eds A. Woodward and A. Needham (New York, NY: Oxford University Press), 172–207.

Ali, S., Basharat, A., and Shah, M. (2007). *Chaotic Invariants for Human Action Recognition*. Piscataway, NJ: IEEE ICCV.

Bastos, A. M., and Schoffelen, J. M. (2016). A tutorial review of functional connectivity analysis methods and their interpretational pitfalls. *Front. Syst. Neurosci.* 9:175. doi: 10.3389/fnsys.2015.00175

Berthier, N. E., Rosenstein, M. T., and Barto, A. G. (2005). Approximate optimal control as a 359 model for motor learning. *Psychol. Rev.* 112, 329–346. doi: 10.1037/0033-295X.112.2.329

Collins, J. J., and Deluca, C. J. (1994). Random walking during quiet standing. *Phys. Rev. Lett.* 73, 764–767. doi: 10.1103/PhysRevLett.73.764

Dale, R., and Spivey, M. J. (2005). "Categorical recurrence analysis of child language," in *Proceedings of the 27th Annual Meeting of the Cognitive Science Society*. Mahwah, NJ: Lawrence Erlbaum, 530–535.

Dale, R., and Spivey, M. J. (2006). Unraveling the dyad: using recurrence analysis to explore patterns of syntactic coordination between children and caregivers in conversation. *Lang. Learn.* 56, 391–430. doi: 10.1111/j.1467-9922.2006.00372.x

Davis, T. J., Pinto, G. B., and Kiefer, A. W. (2017). The stance leads the dance: the emergence of role in a joint supra-postural task. *Front. Psychol.* 8:718. doi: 10.3389/fpsyg.2017.00718

Duran, B., Kuniyoshi, Y., and Sandini, G. (2008). "Eyes-Neck coordination using chaos," in *Proceedings of the European Robotics Symposium, Springer Tracts in Advanced Robotics*, Napoli, 44, 83–92. doi: 10.1007/978-3-540-78317-6_9

Duran, B., Metta, G., and Sandini, G. (2007a). "Emergence of smooth pursuit using chaos," in *Proceedings of the First International Conference on Self-Adaptive and Self-Organizing Systems*, Boston, MA, doi: 10.1109/SASO.2007.23

Duran, B., Metta, G., and Sandini, G. (2007b). "Towards a "chaotic" smooth pursuit," in *Proceedings of the 7th IEEE-RAS International Conference on Human Robotics*, Birmingham, doi: 10.1109/ICHR.2007.4813901

Fraser, A. M., and Swinney, H. L. (1986). Independent coordinates for strange attractors from mutual information. *Phys. Rev. A* 33, 1134–1140. doi: 10.1103/PhysRevA.33.1134

Fusaroli, R., Konvalinka, I., and Wallot, S. (2014). *Analyzing Social Interactions: The Promises and Challenges of using Cross Recurrence Quantification Analysis*, eds M. Marwan, A. Riley, C. L. Giuliani, and Webber Jr (Cham: Springer), 137–155.

Giveans, M. R., Yoshida, K., Bardy, B., Riley, M., and Stoffregen, T. A. (2011). Postural sway and the amplitude of horizontal eye movements. *Ecol. Psychol.* 23, 247–266. doi: 10.1080/10407413.2011.617215

Haworth, J., Kyvelidou, A., Fisher, W., and Stergiou, N. (2016). Indifference to chaotic motion may be related to social disinterest in children with autism. *J. Motor Learn. Dev.* 4, 219–235. doi: 10.1123/jmld.2015-0031

Haworth, J., Vallabhajosula, S., Tzetzis, G., and Stergiou, N. (2013). "Optimal variability and complexity: a novel approach for management principles," in *Chaos and Complexity Theory for Management: Nonlinear Dynamics*, ed. S. Banerjee (Hershey, PA: IGI Global).

Haworth, J. L., Kyvelidou, A., Fisher, W., and Stergiou, N. (2015). Children's looking preference for biological motion may be related to an affinity for mathematical chaos. *Front. Psychol.* 6:281. doi: 10.3389/fpsyg.2015.00281

Jeka, J. J., and Kiemel, T. (2004). *Noise Associated with the Process of Fusing Multisensory Information. Coordination Dynamics: Issues and Trends*, eds V. K. Jirsa and J. A. S. Kelso (Berlin: Springer).

Kay, B. A., and Warren, W. H. Jr. (2001). Coupling of posture and gait: mode locking and parametric excitation. *Biol. Cybern.* 85, 89–106. doi: 10.1007/PL00008002

King, A. C., Wang, Z., and Newell, K. M. (2012). Asymmetry of recurrent dynamics as a function of postural stance. *Exp. Brain Res.* 220, 239–250. doi: 10.1007/s00221-012-3133-5

Meltzoff, A. N., Kuhl, P. K., Movellan, J., and Sejnowski, T. J. (2009). Foundations for a new science of learning. *Science* 325, 284–288. doi: 10.1126/science.1175626

Paxton, A., and Dale, R. (2017). Interpersonal movement synchrony responds to high-and low-level conversational constraints. *Front. Psychol.* 8:1135. doi: 10.3389/fpsyg.2017.01135

Richardson, D., and Dale, R. (2005). Looking to understand: the coupling between speakers' and listeners' eye movements and its relationship to discourse comprehension. *Cogn. Sci.* 29, 39–54. doi: 10.1207/s15516709cog0000_29

Richardson, D., Dale, R., and Shockley, K. (2008). "Synchrony and swing in conversation: coordination, temporal dynamics and communication," in *Embodied Communication*, eds I. Wachsmuth, M. Lenzen, and G. Knoblich (Oxford: Oxford University Press), 75–93.

Richardson, D. C., Dale, R., and Kirkham, N. Z. (2007). The art of conversation is coordination. *Psychol. Sci.* 18, 407–413. doi: 10.1111/j.1467-9280.2007.01914.x

Schaal, S. (2007). The New Robotics—towards human-centered machines. *HFSP J.* 1, 115–126. doi: 10.2976/1.2748612

Sejnowski, T. J. (2010). "Learning optimal strategies in complex environments," in *Proceedings of the 402 National Academy of Sciences*, Ithaca, NY, 107, 20151–20152. doi: 10.1073/pnas.1014954107

Shinbrot, T., Grebogi, C., Wisdom, J., and Yorke, J. A. (1992). Chaos in a double pendulum. *Am. J. Phys.* 60, 491–499. doi: 10.1119/1.16860

Shockley, K. (2005). "Cross recurrence quantification of interpersonal postural activity," in *Tutorials in Contemporary Nonlinear Methods for the Behavioral Sciences*, eds M. A. Riley and G. C. Van Orden, 142–177.

Shockley, K., Butwill, M., Zbilut, J. P., and Webber, C. L. Jr. (2002). Cross recurrence quantification of coupled oscillators. *Phys. Lett. A* 305, 59–69. doi: 10.1016/S0375-9601(02)01411-1

Shockley, K., Richardson, D. C., and Dale, R. (2009). Conversation and coordinative structures. *Top. Cogn. Sci.* 1, 305–319. doi: 10.1111/j.1756-8765.2009.01021.x

Shockley, K., Santana, M. V., and Fowler, C. A. (2003). Mutual interpersonal postural constraints are involved in cooperative conversation. *J. Exp. Psychol.* 29, 326–332.

Siegler, R. S. (1996). *Emerging Minds: The Process of Change in Children's Thinking*. New York, NY: Oxford University Press.

Siegler, R. S., DeLoache, J., and Eisenberg, N. (2010). *How Children Develop*, 3rd Edn. New York, NY: Worth Publishers.

Spivey, M. J. (2007). *The Continuity of Mind*. New York, NY: Oxford University Press.

Sprott, J. C. (2013). Is chaos good for learning? *Nonlinear Dynam. Psychol. Life Sci.* 17, 223–232.

Stoffregen, T. A., Bardy, B. G., Bonnet, C. T., Hove, P., and Oullier, O. (2007). Postural sway and the frequency of horizontal eye movements. *Motor Control* 11, 86–102.

Stoffregen, T. A., Hove, P., Schmit, J., and Bardy, B. G. (2006). Voluntary and involuntary postural responses to imposed optic flow. *Motor Control* 10, 24–33. doi: 10.1123/mcj.10.1.24

Stoffregen, T. A., Pagulayan, R. J., Bardy, B. G., and Hettinger, L. J. (2000). Modulating postural control to facilitate visual performance. *Hum. Mov. Sci.* 19, 203–220.

Suzuki, Y., Nomura, T., Casadio, M., and Morassa, P. (2012). Intermittent control with ankle, hip, and mixed strategies during quiet standing: a theoretical proposal based on a double inverted pendulum model. *J. Theor. Biol.* 310, 55–79. doi: 10.1016/j.jtbi.2012.06.019

Takens, F. (1981). *Detecting Strange Attractors in Fluid Turbulence*, eds D. Rand and L.-S. Young (NewYork, NY: Springer Verlag).

Theiler, J., Eubank, S., Longtin, A., Galdrikian, B., and Farmer, J. D. (1992). Testing for nonlinearity in time series: the method of surrogate data. *Phys. D* 58, 77–94. doi: 10.1016/0167-2789(92)90102-S

Thelen, E., and Smith, L. (1994). *A Dynamic Systems Approach to the Development of Cognition And action*. Cambridge: The MIT Press Inc.

Todorov, E., and Jordan, M. I. (2002). Optimal feedback control as a theory of motor coordination. *Nat. Neurosci.* 5, 1226–1235. doi: 10.1038/nn963

Ward, L. M., and West, R. L. (1998). Modeling human chaotic behavior: nonlinear forecasting analysis of logistic iteration. *Nonlinear Dynam. Psychol. Life Sci.* 2, 261–282. doi: 10.1023/A:1022957921056

Webber, C. L. Jr., and Zbilut, J. P. (1994). Dynamical assessment of physiological systems and states using recurrence plot strategies. *J. Appl. Physiol.* 76, 965–973. doi: 10.1152/jappl.1994.76.2.965

Zbilut, J. P., Giuliani, A., and Webber, C. L. Jr. (1998). Detecting deterministic signals in exceptionally noisy environments using cross recurrence quantification. *Phys. Lett. A* 246, 122–128. doi: 10.1016/S0375-9601(98)00457-5

Conflict of Interest Statement: The authors declare that the research was conducted in the absence of any commercial or financial relationships that could be construed as a potential conflict of interest.

Copyright © 2018 Haworth and Stergiou. This is an open-access article distributed under the terms of the Creative Commons Attribution License (CC BY). The use, distribution or reproduction in other forums is permitted, provided the original author(s) and the copyright owner(s) are credited and that the original publication in this journal is cited, in accordance with accepted academic practice. No use, distribution or reproduction is permitted which does not comply with these terms.

frontiers in Physiology

ORIGINAL RESEARCH
published: 31 October 2018
doi: 10.3389/fphys.2018.01527

Effects of Kinesiology Tape on Non-linear Center of Mass Dispersion During the Y Balance Test

Pauline Andreo[1], Kinda Khalaf[2], Lainey Heale[3], Herbert F. Jelinek[3]* and Luke Donnan[3]

[1] Department of Pure and Applied Sciences, University of Poitiers, Poitiers, France, [2] Department of Biomedical Engineering, Khalifa University of Science and Technology, Abu Dhabi, United Arab Emirates, [3] School of Community Health, Charles Sturt University, Albury, NSW, Australia

Static taping of the ankle or knee joint is a common method of reducing risk of injury by providing mechanical stability. An alternative taping technique employs kinesiology tape, which has the additional benefit of improving functionality by stimulating proprioception. There is substantial disagreement whether kinesiology tape shows significant differences in proprioception and postural stability as compared to rigid/static tape when applied at the lower limb. The current study investigated the effects of kinesiology tape and static tape during a Y Balance Test on center of mass as an indicator for postural stability. Forty-one individuals, free of injury, performed the Y Balance Test under the three conditions; no tape, kinesiology tape, and static tape applied at the lower limb to the quadriceps, triceps surae and ankle joint. All participants completed the Y Balance Test to determine whether any significant differences could be observed using center of mass movement as a surrogate measure for balance and proprioception. The Minkowski-Bouligand and box-counting fractal dimension analyses were used as measures of the dynamic changes in the center of mass whilst undertaking the Y Balance Test. Statistical analyses included the Kruskal Wallis test to allow for non-normally distributed data and a Bonferroni corrected pairwise T-test as a *post hoc* test to ascertain pairwise differences between the three taping conditions. Significance was set at 0.05. The fractal analyses of the dynamic changes in center of mass showed significant differences between the control and both the static tape and kinesiology tape groups ($p = 0.021$ and 0.009, respectively). The current study developed a novel measure of dynamic changes in the center of mass during a set movement that indicated real-time processing effects during a balance task associated with the type of taping used to enhance postural stability.

Keywords: postural stability, center of mass, balance test, fractal dimension, ankle taping, complex movement

OPEN ACCESS

Edited by:
Sladjana Z. Spasić,
Institute for Multidisciplinary Research,
University of Belgrade, Serbia

Reviewed by:
Nebojša Milošević,
Institute of Biophysics, Faculty of Medicine, University of Belgrade, Serbia
Ian Spence,
University of Sydney, Australia

***Correspondence:**
Herbert F. Jelinek
hjelinek@csu.edu.au

Specialty section:
This article was submitted to Fractal Physiology, a section of the journal Frontiers in Physiology

Received: *08 June 2018*
Accepted: *11 October 2018*
Published: *31 October 2018*

Citation:
Andreo P, Khalaf K, Heale L, Jelinek HF and Donnan L (2018) Effects of Kinesiology Tape on Non-linear Center of Mass Dispersion During the Y Balance Test. Front. Physiol. 9:1527. doi: 10.3389/fphys.2018.01527

INTRODUCTION

Proprioception and Balance

Proprioception is a sensory modality important in monitoring body position in space, balance and movement (Lephart et al., 1997). The somatosensory, vestibular, and visual systems are all involved in proprioception to retain balance and posture and to enable dynamic movements (Woollacott and Shumway-Cook, 2002). The receptors in the skin, muscles, ligaments, and tendons, as well as vestibular and visual information associated with proprioception, provide input to the central nervous system regarding body position. Taping of the lower limb has been used to improve stability using static tape or to enhance proprioception by applying kinesiology tape. The effectiveness of either taping method is best analyzed by measuring the degree of postural control during a balance test. Current measures are based on Euclidean geometry such as area covered by postural sway. Non-Euclidean or complexity measures such as fractal analysis are better suited to determine extent of postural sway and taping effectiveness.

Assessment of Body Balance

Two tests are preferentially used to assess dynamic balance: the Star Excursion Balance Test (SEBT), and the Y Balance Test (YBT). These tests can be used to evaluate physical performance, investigate dynamic postural control, identify athletes at greater risk for injury, and provide quantitative data during rehabilitation. Both tests require reaching of the non-stance leg in set directions from a central standing position. The YBT uses three (anterior, posteromedial, and posterolateral) of the eight SEBT directions. No significant differences in terms of reliability and information gained from the two tests have been reported (Bell et al., 2011; Coughlan et al., 2012). The Balance Error Scoring System (BESS) and the Biodex Balance System are two additional measures of balance (Arnold and Schmitz, 1998). However, these tests do not measure center of mass (CoM) changes during dynamic movement, but rather assess the effect of a movement upon completion. Therefore, a more direct measure of proprioception and balance as key factors influencing the CoM during movement that assesses postural stability is required (Fritschi et al., 2014).

Taping the Lower Limb

Postural stability is important during all types of tasks as part of activities of daily living and sport. The use of tape on the lower limb is often applied to improve dynamic postural control and has been investigated by several researchers (Briem et al., 2011; Nakajima and Baldridge, 2013; Hosp et al., 2015). Static or non-elastic tape (ST) is commonly used to limit the range of motion in a desired direction. This type of tape has been shown to be effective in reducing the prevalence of lower limb injuries (Karlsson et al., 1993; Wilkerson, 2002; Lardenoye et al., 2012; Jackson et al., 2016). However the mechanism responsible for improving postural control has not been clearly elucidated, and may be a function of the reduction in joint flexibility by the rigid tape or due to enhanced proprioceptive input from skin sensory receptors as suggested by the distributors of the kinesiology tape (KT; Corporation, 2017). For three decades KT has been adopted by athletes world-wide, but no clinical study has yet unequivocally shown that KT taping on the lower limb has better outcomes compared to ST for dynamic postural stability. One study reported that application of KT at the knee did not improve knee proprioception in healthy women, yet enhanced proprioception in women with poor proprioceptive ability (Hosp et al., 2015). A further study using the Balance Error Scoring System (BESS) investigated the effects of KT on balance deficits associated with chronic ankle instability. This study concluded that KT improved balance after it had been applied for 48 h, when compared with the pre-test and with the control group results (Jackson et al., 2016). Another study compared taping the ankles with kinesiology tape to rigid tape in male athletes undertaking the SEBT and found no significant effect on muscle activity (Briem et al., 2011). Although rigid tape and not kinesiology tape increased muscle activity when the ankles were taped, no correlation between muscle activation and the influence of either tape on postural stability could be determined. Finally, Nakajima et al. used the SEBT to analyse the effect of KT on dynamic postural control. They concluded that KT had an effect in females only in the posterior-medial and medial directions of the SEBT test (Nakajima and Baldridge, 2013).

Fractal Analysis as a Dynamic Measure

Measures of spatial dispersion of the CoM to investigate the effects of taping on movement have not been investigated using non-linear methods, although they provide means for dynamic assessment of CoM changes during the YBT or other balance tests. Current center of pressure (CoP) or center of mass analyses are based on position time series but also include spatial measures such as sway path length, the area covered by CoP/CoM dispersion, as well as range, maximal sway trajectory and peak velocity (Yamamoto et al., 2015). Thus, CoM can be analyzed as a time series associated with changes in a set direction of movement or as a 2D trajectory or spatial dispersion as a function of postural control during the YBT. Better postural stability is associated with greater variation and dispersion in the CoM trajectory leading to a more complex geometric pattern. Postural stability which is associated with variability in the CoM trajectory and observed during movement is a non-linear phenomenon and is not well described by Euclidean geometry. Fractal geometry may be useful for measuring the CoM trajectory associated with YBT and any changes due to taping (Huang et al., 2013; Gilfriche et al., 2018). The fractal dimension (FD) is a descriptive parameter, which can provide an index of the complexity of a non-linear pattern such as the CoM trajectory. Several fractal analyses methods have been applied to investigate non-linear spatial distributions, among them the box-counting and Minkowski-Bouligand methods are commonly used. The fractal dimension is a useful parameter for classifying complex patterns (Jelinek and Fernandez, 1998) and several studies have described changes in postural stability and balance including the ability of postural adjustments in patients with Prader-Willi Syndrome (Błaszczyk and Klonowski, 2001; Cimolin et al., 2011). The Prader-Willi Syndrome study used the box-counting method to investigate traces of CoP trajectories. The authors demonstrated that the CoP trajectories in Prader-Willi Syndrome were characterized by higher values of FD when compared to a control group. A study investigating ankle sprain injuries, however, indicated a reduction in fractal dimension (Doherty et al., 2015). These two studies suggest that a fractal dimension value that is too small or too large indicates compromised proprioceptive function.

The current study investigated the spatial dispersion of CoM associated with the YBT in a healthy cohort of young adults and used Minkowski-Bouligand and box-counting methods to determine the fractal dimension to evaluate the effect of static vs. kinesiology tape applied to the lower limb compared to no tape.

METHODS

Participants

A total of 41 participants were recruited at Charles Sturt University for the study. The participants completed a questionnaire reporting injuries for the last 5 years. Age, gender, sporting activity, frequency and amount, individual height, and weight for all participants were noted. The Human Research Ethics Committee of Charles Sturt University approved the protocol (protocol number H16113). All participants provided written consent to take part in the research following receipt of an information package.

Taping Procedures

All participants were tested on two separate occasions, using kinesiology tape (Kinesio Tex®) on one occasion, and rigid tape on the other. The order of tape allocation was randomized. Both occasions included a no Tape trial. A single strip of tape was applied without tension to the muscle belly of rectus femoris and the medial head of gastrocnemius while the muscle was under stretch. An anti-inversion ankle strapping was also applied using a single strip of tape without tension starting from the medial lower leg, passing inferiorly over the lateral malleolus (lateral part of the ankle), under the arch of the foot, passing superiorly over the medial malleolus, and finishing at the lateral aspect of the lower leg (Van Den Dries et al., 2013). As the YBT utilizes sagittal plane motion at the knee, and a combination of sagittal and frontal plane motion at the ankle, three strips were applied to potentially influence the three fundamental movements requiring control throughout the task. All strapping was applied following procedures outlined in the guide produced by one KT manufacturer (Capobianco and Van Den Dries, 2013), and applied to the dominant leg (**Figure 1**).

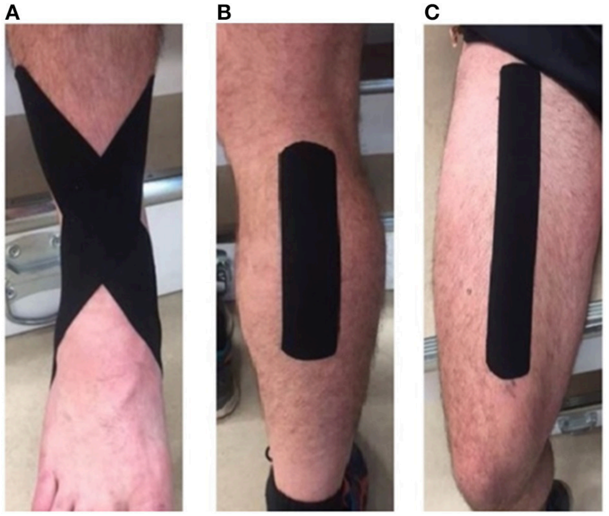

FIGURE 1 | Taping procedures at **(A)** the ankle, **(B)** the calf, and **(C)** the quadriceps.

Y Balance Test

As a method of assessing dynamic postural stability, the Y Balance test (YBT) was used to investigate the effect of taping. The goal of the YBT is to reach as far as possible with one leg in three directions while maintaining balance with the dominant leg. The participant stands at a central point and extends the non-dominant leg anteriorly, posterolaterally, and posteromedially (**Figure 2**). Each participant performed one practice trial to become familiar with the test, before performing five trials with no tape, KT and ST tapes, respectively. On the first testing occasion, the participant performed the YBT untapped and with one of the taping variables (KT or ST). A minimum of 3 days later, the participant performed the YBT again, both untapped and then with either the ST or KT (the tape not used on the first occasion). The minimum 3 days break between testing was used as a washout period to ensure that the results would reflect the taping intervention, not the carry over effects from previous testing (Chow and Liu, 2004). In addition, the 3-day interval also showed whether there was a difference in response to the YBT when no tape was applied. An eight-camera 3D motion capture system (100 Hz, Vicon, Oxford Metrics, UK) was used to obtain kinematic data based on 36 reflective markers applied to the pelvis and lower limb, while an AMTI force plate (1000Hz, AMTI, USA) collected kinetic data (**Figure 2**). Processes specific to Visual3D (Version 6, C-Motion, Germantown, MD) were used to calculate the mass of each segment, which allowed identification of the relative position of the center of mass. A fourth-order Butterworth low-pass filter was used to filter kinematic (18 Hz) and kinetic (50 Hz) data prior to export for statistical analysis. Of the 890 individual trials, the mean duration for the sequence of three reaches was 880.6 (± 314.6) frames (8.81 s). All trials were subsequently normalized to 1,001 frames to allow individual trials to be directly compared. In **Figure 2**, the vertical arrow represents the ground reaction force vector, the circle depicts the relative center of mass. The bottom row represents the CoM dispersion. While movement in the z-axis affects superior and inferior movement of the CoM, movement in the x and y-axis shifts CoM outside the base of support, which requires somatosensory and neuromuscular adaptation to maintain a balanced state. For this reason, the current analysis focused on the CoM dispersion associated with postural adjustment in a 2-dimensional representation in the x and y axis (anterior/posterior and medial/lateral dispersion). The non-linear spatial dispersion characteristics of CoM were determined using fractal analysis and more common linear features including total sway area and maximum/minimum trajectory.

Fractal Analysis

Traditional common features extracted from the spatial dispersion of the center of mass included total path length, maximum and minimum trajectory in each direction and total area (Yamamoto et al., 2015). Fractal analysis was performed on the 2D representation of the CoM trajectory during the YBT from initiation of the reach attempts in the anterior, posterior

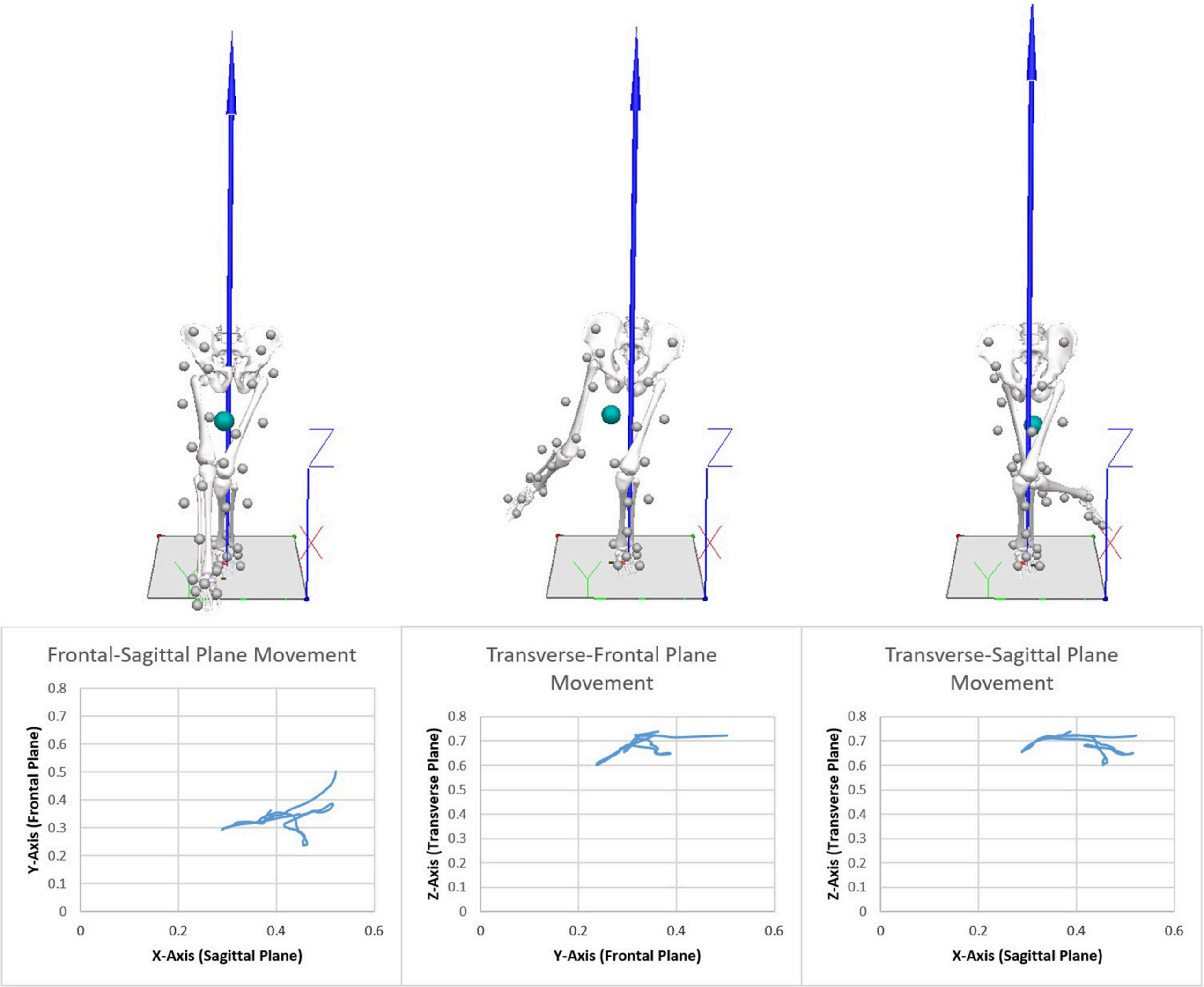

FIGURE 2 | An illustrative example of a Vicon 3D frame.

lateral and posterior medial direction and to return to the central position. The recorded CoM dispersion was then pre-processed by filtering any noise and analyzed.

Minkowski- Bouligand Method

A computer-based approach to measure the fractal dimension was developed by Tom Smith and his colleagues from existing mathematical concepts and implemented applying an in-house Minkowski-Bouligand dimension macro within NIH Image software (Smith and Behar, 1994; Smith et al., 1996; Jelinek and Fernandez, 1998). The Minkowski-Bouligand dimension is determined by replacing each pixel of a line representing the changes in the CoM associated with the YBT with an array of pixels or circles whose diameter increased with each pass (**Figure 3**). The double logarithm of the scale (circle diameter) and length of the line associated with the changes in CoM during the YBT result in a linear relationship (regression line) if the image is fractal over several generations of scales. The slope (S) of the regression line is used to calculate the fractal dimension (Fernández and Jelinek, 2001; Jelinek et al., 2005). The fractal dimension is calculated using the equation: $Df_{MB} = 2–S$.

Box-Counting Method

The box-counting dimension was determined using the FracLac box-counting algorithm in ImageJ (Karperien and Jelinek, 2015). The box-counting method divides the space which contains the image into equal sized boxes of progressively smaller sides. Then, the boxes that include part of the image of interest are counted (**Figure 3**) (Fernández and Jelinek, 2001). The double logarithm of scale vs. the number of filled boxes is an approximate straight line whose gradient is Df_{BC}.

Statistical Analysis

The Shapiro-Wilk Test was used to check for normality as recommended for sample size below 50 and based on

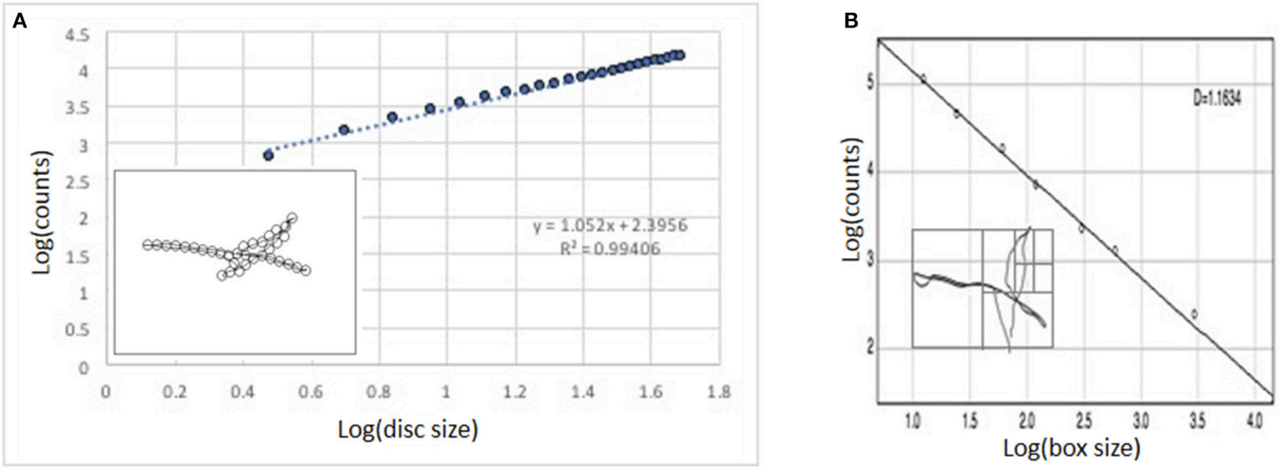

FIGURE 3 | (A) Log-log plot of Minowski dimension analysis. **(B)** Log-log graph of Box counting dimension analysis.

TABLE 1 | Characteristics of participants for gender.

Gender	Age (years)	Height (m)	Weight (kg)	BMI (kg/m^2)
Male	22.91 ± 3.61	1.81 ± 0.07	84.74 ± 10.53	25.67 ± 1.77
Female	21.05 ± 1.82	1.66 ± 0.06	66.57 ± 7.07	24.37 ± 3.35

Mean ± standard deviation.

regression and correlation, whereas the Kolmogorov-Smirnov test is based on the empirical distribution function and only considers the largest discrepancy between observed and hypothesized distributions (Yap and Sim, 2011). The results showed a normal distribution. A repeated measures student t-test was performed to investigate whether significant differences existed between the first trial and the second trial performed without tape 3 days later. Data including fractal dimension, reach distance, and demographic characteristics of the participants were analyzed using a general linear mixed model (Cnaan et al., 1997). Linear mixed-effect models typically combine the components of fixed effects, random effects, and repeated measurements in a single unified approach which was appropriate for the study (Grajeda et al., 2016). The model was followed by a Bonferroni corrected pairwise t-test as a *post hoc* test to ascertain pairwise differences between the three conditions (no tape, KT, rigid tape). Spearman's correlation was determined to investigate whether the fractal dimension was correlated with maximum reach. Descriptive statistics were calculated for male and female groups. Significance was set at $p < 0.05$.

RESULTS

Forty-one participants attended the clinic to assess the effect of taping on balance. Of these, 21 were males and 20 were females. **Table 1** represents the mean and standard deviation of age, height, and weight for each gender.

TABLE 2 | Traditional linear measures of spatial patterns associated with CoM dispersion.

Feature	NoTape	Static tape	Kinesiology tape
AVERAGE TRAJECTORY			
Anterior	63.1 (± 17.3)	65.6 (± 18.9)	66.0 (± 20.7)
Posterior-medial	87.0 (± 13.4)	86.2 (± 16.8)	86.6 (± 13.3)
Posterior-lateral	70.1 (± 14.8)	71.1 (± 19.5)	70.7 (± 19.5)
MAXIMUM TRAJECTORY (FOR ALL PARTICIPANTS)			
Anterior	157.1	150.0	160.5
Posterior-medial	115.0	122.7	115.8
Posterior-lateral	152.0	150.9	147.9
MINIMUM TRAJECTORY (FOR ALL PARTICIPANTS)			
Anterior	36.1	26.9	31.4
Posterior-medial	43.7	47.3	53.8
Posterior-lateral	37.6	39.4	38.6

Mean ± standard deviation. All data in centimeters.

Several variables can affect postural stability including being overweight or obese (Hue et al., 2007). Therefore, body mass index (BMI) was included in the analysis and normal range set at between 20 and 25 kg/m^2. BMI was within the normal range for both genders with females having a slightly lower BMI but not significantly different. No significant difference was noted for age between the genders. The participants also recorded their activity profiles. This indicated that the majority of participants undertook on average 5 h of activity per week.

The change in the CoM dispersion for the no tape condition did not differ between males and females, and therefore male and female data were combined (**Tables 2–4**).

Common features investigated to determine postural stability or sway were analyzed with respect to taping condition and YBT. The results are shown in **Table 2**. No significant effect of taping was observed for total path length, maximum, and minimum trajectory in each direction and total area. **Supplementary File 1** offers a video of a single participant completing the YBT in the

TABLE 3 | Effects of taping measured with the Minkowski-Bouligand method.

	Control	KT	ST
Group	0.957 ± 0.005	0.974 ± 0.007	0.976 ± 0.007*
Males	0.957 ± 0.007	0.979 ± 0.010	0.976 ± 0.010
Females	0.957 ± 0.009	0.969 ± 0.009	0.976 ± 0.009

*Mean ± standard error; *significant finding ($p \leq 0.05$).*

TABLE 4 | Effect of taping measured by the box-counting method.

	Control	KT	ST
Group	1.173 ± 0.006	1.189 ± 0.008	1.197 ± 0.008*
Males	1.167 ± 0.008	1.186 ± 0.010	1.194 ± 0.010
Females	1.179 ± 0.010	1.192 ± 0.010	1.20 ± 0.010

*Mean ± standard error; *significant finding ($p \leq 0.05$).*

no tape condition first and followed by the static tape condition. It should be noted that while no significant effect was observed for common measures of postural stability and sway, an increase in corrective movements can be observed at the femur of the support leg in the static tape condition compared to the no tape condition. Results of the fractal analysis also indicated a significant effect of taping.

A linear mixed effects model was applied to consider the three experimental interventions of no tape, KT and ST tape as well as gender. The *t*-test revealed no significant difference between the first and third day trials. As such, the data was averaged and the effects of KT and ST were compared against this average control condition data. All data were normally distributed (Shapiro-Wilk Test >0.05). **Table 3** shows the results for the Minkowski-Bouligand dimension analysis.

The box-counting results are shown in **Table 4**.

Fractal dimension results close to 1 may reflect a transition phase between Euclidean and fractal forms or are a function of the smoothness of the Minkowski-Bouligand dimension (dilation method) that is more sensitive to linear features.

Significant differences were found when the fixed effects were the Minkowski-Bouligand (Df_{MB}) or box-counting (Df_{BC}) method. The model showed a significant difference for KT and ST groups as compared to control with the Minkowski-Bouligand method ($p = 0.0216$ and $p = 0.0098$ respectively), and for ST with the box-counting method ($p = 0.0048$). The same model was applied for males only and females only. Analysing effects of taping within gender showed that both Df_{MB} and Df_{BC} were significant. A difference was found for KT for males according to the Df_{MB} method ($p = 0.0464$) and for ST according to the box-counting method ($p = 0.0249$) but not for females. A *post hoc* comparison using Bonferroni correction indicated a significant result for no tape vs. rigid tape for both the Minkowski-Bouligand and box-counting methods ($p = 0.052$ and $p = 0.0093$) but no significant difference within gender. The fractal data and maximum reach data showed that a correlation existed for anterior reach and posteromedial reach when using ST taping ($r = 0.65$ and $r = 0.55$, respectively). When maximum reach points in the three directions of the YBT were connected to form a sway area description of maximum reach in the three directions, there was no correlation between the fractal dimension results and the triangle area and perimeter ($r = 0.04$ and $p = 0.9$).

DISCUSSION

The purpose of this study was to investigate the effects of static and kinesiology taping on postural stability during a dynamic movement control test using the Y balance test. Postural control tasks, such as the YBT, allow investigation of movement and balance around a central support base. A change in the CoM trajectory and resulting fractal dimension indicates a change in the postural sensori-motor strategies applied during the YBT. The box-counting and Minkowski-Bouligand methods were used here to investigate changes in the CoM during the YBT. The principal finding of our study was a significant increase in the fractal dimension for rigid tape vs. no tape, when results were corrected for multiple group comparison. However, both taping conditions led to an increase in the Minkowski-Bouligand (Df_{MB}) and box-counting (Df_{BC}) dimensions. Larger fractal dimension values of the CoM trajectory are associated with greater activity of the sensori-motor system in retaining balance during a dynamic movement task. In contrast, in previous studies applying KT did not improve knee or ankle proprioception in a group of healthy young adults, did not decrease or increase performance, and had no effects on muscle activation (Briem et al., 2011; Nakajima and Baldridge, 2013; Hosp et al., 2015. Similar findings were reported when analyzing postural sway using multiscale entropy analysis, where postural sway dynamics of healthy subjects were more complex than that of subjects with a history of falls (Costa et al., 2007). The current data combined with previous data indicates what may seem contradictory results but confirms a physiological adaptation process or adaptive stress response to moderate intermittent stress occurring (Mattson, 2008). Normal physiological phenomena occur within a set range, where activity outside this range is considered pathological. Our results indicate that taping increased complexity of CoM dispersion suggesting an improvement in postural stability. However extensive increases in CoM dispersion has been observed in patients with Prader-Willi Syndrome and in patients prone to falls, which is suggestive of pathology and reduced proprioceptive ability and a reduction in postural control (Costa et al., 2007; Cimolin et al., 2011).

The linear mixed effects model which was used in the current study considers the repeated design nature of the research (no tape, KT, and ST conditions) and gender, and showed a significant difference in males for Df_{MB} when KT was applied and for Df_{BC} when ST was applied. The results suggesting that the fractal analysis method had an effect on the findings. ST led to greater complexity and spread of the CoM trajectory across movement space. In instances where the dynamics of the CoM are within a smaller movement space/envelope, as may be the case with KT, the box-counting method may be more sensitive. Our findings suggest that KT tape may decrease extreme postural sway better to maintain balance due to stimulation of skin receptors and heightened proprioceptive information provided by KT application. This agrees with previous data where KT was shown to improve postural stability in females only in the posterior-medial and medial directions of the SEBT test (Nakajima and Baldridge, 2013). KT also demonstrated significant proprioceptive enhancement at the knee joint after uphill walking in healthy women with poor proprioceptive ability (Hosp et al., 2015). Our results now extend this to a group of healthy young adults. The difference in gender found in the current study may be due to the fact that males and females use different sensori-motor strategies for postural control during movement (Wikstrom et al., 2006; Smith et al., 2012).

The fractal dimension reflects the degree of complexity associated with changes in the CoM trajectory in the anterior-posterior and medial–lateral directions during the YBT. In general, a higher fractal dimension represents more complex movement patterns, possibly reflecting better dynamic control and postural stability (Costa et al., 2007). Conversely, a lower fractal dimension represents reduced dynamic control and less postural stability possibly due to compromised somatosensory feedback. However, fractal analyses results indicating a very much lower or higher fractal dimension are likely indicative of sensori-motor dysfunction and loss of postural stability. A previous study, investigating immediate post-injury movement strategies with SEBT and using the center of pressure to calculate the fractal dimension with a similar method to the dilation method (Katz, 1988) demonstrated a reduction in the fractal dimension for participants with a lateral ankle sprain. The authors interpreted this result as a reduced ability to perform the balance test (Doherty et al., 2015). Pain is known to restrict movement, especially when a maximum reach in any direction is required, and hence the fractal dimension is expected to decrease. Other studies in which control participants were age-matched with patients affected by Prader-Willi Syndrome computed the fractal dimension on the image of the CoP trajectory using the box-counting method and showed that patients with Prader-Willi syndrome were characterized by higher values in the fractal dimension and a poorer balance capacity when compared to the control group (Capodaglio et al., 2011; Cimolin et al., 2011). The higher fractal dimension was interpreted as the inability for these patients to modulate the sensori-motor systems involved in postural control, possibly related to compromised sensori-motor feedback at the spinal cord, brainstem or subcortical/cortical level(s) (Cimolin et al., 2011).

In our study, with a young adult cohort free of injury, the fractal dimension for KT and ST was higher than the control for both methods. This suggests that rigid or kinesiology tapes applied on healthy subjects may improve postural stability. Rigid tape led to slightly higher Df_{MB} and Df_{BC} that could be due to ST decreasing joint movement more than KT. A previous study which investigated the fractal structure of force plate signals suggested that the center of pressure was more useful and sensitive in the evaluation of the age-related decline of postural stability than the CoM (Błaszczyk and Klonowski, 2001). The current study utilized the CoM, and future studies need to investigate the difference between the CoP, which is more sensitive for vertical force distribution through the standing leg, and CoM, which is more sensitive to body sway and movement adjustment. In addition, to determine whether KT does in fact have a significant effect that is different from ST, a larger cohort study is being organized as well as different fractal analysis methods incorporated such as the mass-radius and caliper methods. A future study should include measures of nerve conduction velocity to control for sensory information processing and two-point discrimination assessment in the lower limb as a baseline measure of skin sensation sensitivity.

An association between fractal dimension and maximum leg extension was not found in the current study, suggesting that the CoM is not a function of maximum reach. Consequently, the improved postural stability may not be associated with a shorter reach. According to this result, the fractal dimension represents the dynamics of movement and is not a function of the maximum reach of any movement, which suggests that taping in general does not affect the extent of movement but rather postural stability.

The findings of this study indicate both KT and ST application contribute to increased complexity of CoM movement during a dynamic balance task, however it was only ST that achieved significance when compared to no tape. This is contrary to claims KT has the potential to facilitate changes in proprioception and postural stability. While the findings are of clinical interest, the use of fractal analysis to achieve these findings offers a novel, and potentially more appropriate method for future investigation of movement complexity.

AUTHOR CONTRIBUTIONS

LD and HJ conceived of the study, interpreted the results and finalized the manuscript. KK contributed to interpretation of results and writing the manuscript. LH collected the data, analyzed the data, and contributed to the writing of the manuscript. PA undertook the fractal analysis and contributed to the interpretation of the results and writing of the manuscript.

ACKNOWLEDGMENTS

We wish to acknowledge Simon McDonald from the Spatial Analysis Network (SPAN) at Charles Sturt University for assistance with statistical analysis.

SUPPLEMENTARY MATERIAL

The Supplementary Material for this article can be found online at: https://www.frontiersin.org/articles/10.3389/fphys.2018.01527/full#supplementary-material

REFERENCES

Arnold, B. L., and Schmitz, R. J. (1998). Examination of balance measures produced by the biodex stability system. *J. Athl. Train.* 33, 323–327.

Bell, D. R., Guskiewicz, K. M., Clark, M. A., and Padua, D. A. (2011). Systematic review of the balance error scoring system. *Sports Health* 3, 287–295. doi: 10.1177/1941738111403122

Błaszczyk, J. W., and Klonowski, W. (2001). Postural stability and fractal dynamics. *Acta Neurobiol. Exp.* 61, 105–112.

Briem, K., Eythorsdottir, H., Magnusdottir, R. G., Palmarsson, R., Runarsdottir, T., and Sveinsson, T. (2011). Effects of kinesio tape compared with nonelastic sports tape and the untaped ankle during a sudden inversion perturbation in male athletes. *J. Orthop. Sports Phys. Ther.* 41, 328–335. doi: 10.2519/jospt.2011.3501

Capobianco, S., and Van Den Dries, G. (2013). *Power Taping - Taping Movement, Not Muscles, 3rd Edn.,* Los Gatos, CA: Rocktape Inc.

Capodaglio, P., Menegoni, F., Vismara, L., Cimolin, V., Grugni, G., and Galli, M. (2011). Characterisation of balance capacity in Prader-Willi patients. *Res. Dev. Disabil.* 32, 81–86. doi: 10.1016/j.ridd.2010.09.002

Chow, S. C., and Liu, J. P. (2004). *Design and Analysis of Clinical Trials, 2nd Edn.,* Hoboken, NJ: Wiley.

Cimolin, V., Galli, M., Rigoldi, C., Grugni, G., Vismara, L., Mainardi, L., et al. (2011). Fractal dimension approach in postural control of subjects with Prader-Willi Syndrome. *J. Neuroeng. Rehabil.* 8:45. doi: 10.1186/1743-0003-8-45

Cnaan, A., Laird, N. M., and Slasor, P. (1997). Using the general linear mixed model to analyse unbalanced repeated measures and longitudinal data. *Stat. Med.* 16, 2349–2380.

Corporation, K. H. (2017). *What Makes Kinesio Tape Different?* [Online]. Available online at: https://kinesiotaping.com/about/what-makes-kinesio-different/ [Accessed].

Costa, M., Priplata, A. A., Lipsitz, L. A., Wu, Z., Huang, N. E., Goldberger, A. L., et al. (2007). Noise and poise: Enhancement of postural complexity in the elderly with a stochastic-resonance–based therapy. *EPL* 77:68008. doi: 10.1209/0295-5075/77/68008

Coughlan, G. F., Fullam, K., Delahunt, E., Gissane, C., and Caulfield, B. M. (2012). A comparison between performance on selected directions of the star excursion balance test and the Y balance test. *J. Athl. Train.* 47, 366–371. doi: 10.4085/1062-6050-47.4.03

Doherty, C., Bleakley, C. M., Hertel, J., Caulfield, B., Ryan, J., and Delahunt, E. (2015). Laboratory measures of postural control during the star excursion balance test after acute first-time lateral ankle sprain. *J. Athl. Train.* 50, 651–664. doi: 10.4085/1062-6050-50.1.09

Fernández, E., and Jelinek, H. F. (2001). Use of fractal theory in neuroscience: methods, advantages, and potential problems. *Methods* 24, 309–321. doi: 10.1006/meth.2001.1201

Fritschi, M., Jelinek, H. F., Mcgloughlin, T., Khalaf, K., Khandoker, A. H., and Vallery, H. (2014). Human balance responses to perturbations in the horizontal plane. *Conf. Proc. IEEE Eng. Med. Biol. Soc.* 2014, 4058–4061. doi: 10.1109/EMBC.2014.6944515

Gilfriche, P., Deschodt-Arsac, V., Blons, E., and Arsac, L. M. (2018). Frequency-specific fractal analysis of postural control accounts for control strategies. *Front. Physiol.* 9:293. doi: 10.3389/fphys.2018.00293

Grajeda, L. M., Ivanescu, A., Saito, M., Crainiceanu, C., Jaganath, D., Gilman, R. H., et al. (2016). Modelling subject-specific childhood growth using linear mixed-effect models with cubic regression splines. *Emerg. Themes Epidemiol.* 13:1. doi: 10.1186/s12982-015-0038-3

Hosp, S., Bottoni, G., Heinrich, D., Kofler, P., Hasler, M., and Nachbauer, W. (2015). A pilot study of the effect of kinesiology tape on knee proprioception after physical activity in healthy women. *J. Sci. Med. Sport* 18, 709–713. doi: 10.1016/j.jsams.2014.09.004

Huang, C.-W., Sue, P.-D., Abbod, M. F., Jiang, B. C., and Shieh, J.-S. (2013). Measuring center of pressure signals to quantify human balance using multivariate multiscale entropy by designing a force platform. *Sensors* 13, 10151–10166. doi: 10.3390/s130810151

Hue, O., Simoneau, M., Marcotte, J., Berrigan, F., Doré, J., Marceau, P., et al. (2007). Body weight is a strong predictor of postural stability. *Gait Posture* 26, 32–38. doi: 10.1016/j.gaitpost.2006.07.005

Jackson, K., Simon, J. E., and Docherty, C. L. (2016). Extended use of kinesiology tape and balance in participants with chronic ankle instability. *J. Athl. Train.* 51, 16–21. doi: 10.4085/1062-6050-51.2.03

Jelinek, H., Elston, N., and Zietsch, B. (2005). "Fractal analysis: pitfalls and revelations in neuroscience," in *Fractals in Biology and Medicine, Part 2.1,* eds G. A. Losa, D. Merlini, T. F. Nonnenmacher, and E. R. Weibel (Basel: Birkhauser), 85–94.

Jelinek, H. F., and Fernandez, E. (1998). Neurons and fractals: how reliable and useful are calculations of fractal dimensions? *J. Neurosci. Methods* 81, 9–18.

Karlsson, J., Sward, L., and Andreasson, G. O. (1993). The effect of taping on ankle stability. practical implications. *Sports Med.* 16, 210–215. doi: 10.2165/00007256-199316030-00005

Karperien, A., and Jelinek, H. (2015). Fractal, multifractal, and lacunarity analysis of microglia in tissue engineering. *Front. Bioeng. Biotechnol.* 3:51. doi: 10.3389/fbioe.2015.00051

Katz, M. (1988). Fractals and the analysis of waveforms. *Comput. Biol. Med.* 18, 145–156. doi: 10.1016/0010-4825(88)90041-8

Lardenoye, S., Theunissen, E., Cleffken, B., Brink, P. R., De Bie, R. A., and Poeze, M. (2012). The effect of taping versus semi-rigid bracing on patient outcome and satisfaction in ankle sprains: a prospective, randomized controlled trial. *BMC Musculoskelet. Disord.* 13:81. doi: 10.1186/1471-2474-13-81

Lephart, S. M., Pincivero, D. M., Giraldo, J. L., and Fu, F. H. (1997). The role of proprioception in the management and rehabilitation of athletic injuries. *Am. J. Sports Med.* 25, 130–137. doi: 10.1177/036354659702500126

Mattson, M. P. (2008). Hormesis defined. *Ageing Res. Rev.* 7, 1–7. doi: 10.1016/j.arr.2007.08.007

Nakajima, M. A., and Baldridge, C. (2013). The effect of kinesio(R) tape on vertical jump and dynamic postural control. *Int. J. Sports Phys. Ther.* 8, 393–406.

Smith, A. W., Ulmer, F. F., and Wong, D. P. (2012). Gender differences in postural stability among children. *J. Hum. Kinet.* 33, 25–32. doi: 10.2478/v10078-012-0041-5

Smith, T. G. Jr., and Behar, T. N. (1994). Comparative fractal analysis of cultured glia derived from optic nerve and brain demonstrate different rates of morphological differentiation. *Brain Res.* 634, 181–190. doi: 10.1016/0006-8993(94)91921-6

Smith, T. G. Jr., Lange, G. D., and Marks, W. B. (1996). Fractal methods and results in cellular morphology–dimensions, lacunarity and multifractals. *J. Neurosci. Methods* 69, 123–136. doi: 10.1016/S0165-0270(96)00080-5

Van Den Dries, G., Capobianco, S., Brink, J., Myers, T., and Chu, D. A. (2013). *Power Taping Manual, 3rd Edn: Theories and Practical Applications of Fascial Movement Taping* (Los Gatos, CA: Rocktape Inc.).

Wikstrom, E., D., Tillman, M., J., and Kline, K., and, A., Borsa, P. (2006). Gender and limb differences in dynamic postural stability during landing. *Clin. J. Sport Med.* 16, 311–315. doi: 10.1097/00042752-200607000-00005

Wilkerson, G. B. (2002). Biomechanical and neuromuscular effects of ankle taping and bracing. *J. Athl. Train.* 37, 436–445.

Woollacott, M., and Shumway-Cook, A. (2002). Attention and the control of posture and gait: a review of an emerging area of research. *Gait Posture* 16, 1–14. doi: 10.1016/S0966-6362(01)00156-4

Yamamoto, T., Smith, C. E., Suzuki, Y., Kiyono, K., Tanahashi, T., Sakoda, S., et al. (2015). Universal and individual characteristics of postural sway during quiet standing in healthy young adults. *Physiol. Rep.* 3:e12329. doi: 10.14814/phy2.12329

Yap, B. W., and Sim, C. H. (2011). Comparisons of various types of normality tests. *J. Stat. Comput. Simul.* 81, 2141–2155. doi: 10.1080/00949655.2010.520163

Conflict of Interest Statement: The authors declare that the research was conducted in the absence of any commercial or financial relationships that could be construed as a potential conflict of interest.

Copyright © 2018 Andreo, Khalaf, Heale, Jelinek and Donnan. This is an open-access article distributed under the terms of the Creative Commons Attribution License (CC BY). The use, distribution or reproduction in other forums is permitted, provided the original author(s) and the copyright owner(s) are credited and that the original publication in this journal is cited, in accordance with accepted academic practice. No use, distribution or reproduction is permitted which does not comply with these terms.

frontiers in Physiology

ORIGINAL RESEARCH
published: 20 February 2019
doi: 10.3389/fphys.2019.00131

Improving Precision Force Control With Low-Frequency Error Amplification Feedback: Behavioral and Neurophysiological Mechanisms

Ing-Shiou Hwang[1,2], *Chia-Ling Hu*[2], *Zong-Ru Yang*[1], *Yen-Ting Lin*[3] *and Yi-Ching Chen*[4,5]*

[1] Institute of Allied Health Sciences, College of Medicine, National Cheng Kung University, Tainan, Taiwan, [2] Department of Physical Therapy, College of Medicine, National Cheng Kung University, Tainan, Taiwan, [3] Physical Education Office, Asian University, Taichung, Taiwan, [4] Department of Physical Therapy, College of Medical Science and Technology, Chung Shan Medical University, Taichung, Taiwan, [5] Physical Therapy Room, Chung Shan Medical University Hospital, Taichung, Taiwan

Although error amplification (EA) feedback has been shown to improve performance on visuomotor tasks, the challenge of EA is that it concurrently magnifies task-irrelevant information that may impair visuomotor control. The purpose of this study was to improve the force control in a static task by preclusion of high-oscillatory components in EA feedback that cannot be timely used for error correction by the visuomotor system. Along with motor unit behaviors and corticomuscular coherence, force fluctuations (Fc) were modeled with non-linear SDA to contrast the reliance of the feedback process and underlying neurophysiological mechanisms by using real feedback, EA, and low-frequency error amplification (LF-EA). During the static force task in the experiment, the EA feedback virtually potentiated the size of visual error, whereas the LF-EA did not channel high-frequency errors above 0.8 Hz into the amplification process. The results showed that task accuracy was greater with the LF-EA than with the real and EA feedback modes, and that LF-EA led to smaller and more complex Fc. LF-EA generally led to smaller SDA variables of Fc (critical time points, critical point of Fc, the short-term effective diffusion coefficient, and short-term exponent scaling) than did real feedback and EA. The use of LF-EA feedback increased the irregularity of the ISIs of MUs but decreased the RMS of the mean discharge rate, estimated with pooled MU spike trains. Beta-range EEG–EMG coherence spectra (13–35 Hz) in the LF-EA condition were the greatest among the three feedback conditions. In summary, amplification of low-frequency errors improves force control by shifting the relative significances of the feedforward and feedback processes. The functional benefit arises from the increase in the common descending drive to promote a stable state of MU discharges.

Keywords: force fluctuations, stochastic processes, visuomotor, EMG, EEG

OPEN ACCESS

Edited by:
Srdjan Kesić,
University of Belgrade, Serbia

Reviewed by:
Tara Thiagarajan,
Sapien Labs, United States
Elias Manjarrez,
Benemérita Universidad Autónoma de Puebla, Mexico

****Correspondence:***
Yi-Ching Chen
yiching@csmu.edu.tw

Specialty section:
This article was submitted to Fractal Physiology, a section of the journal Frontiers in Physiology

Received: *20 April 2018*
Accepted: *01 February 2019*
Published: *20 February 2019*

Citation:
Hwang I-S, Hu C-L, Yang Z-R, Lin Y-T and Chen Y-C (2019) Improving Precision Force Control With Low-Frequency Error Amplification Feedback: Behavioral and Neurophysiological Mechanisms. Front. Physiol. 10:131. doi: 10.3389/fphys.2019.00131

INTRODUCTION

A general outcome of motor control is variability (Frank et al., 2006; Bays and Wolpert, 2007). The structures of movement variability [such as force fluctuations (Fc)] are not necessarily a direct consequence of neural noises. Contrary to the whiteness assumption, Fc are colored time series contingent upon environmental contexts and task demands (Miall et al., 1986, 1993). Fc are composed of numerous centrally scaled pulse-like elements that remedy tracking deviations during a visuomotor task (Navas and Stark, 1968; Miall et al., 1986; Slifkin et al., 2000; King and Newell, 2015). The spatial and temporal information in visual feedback determines the transitions of the motor state with respect to target constraints (Hwang et al., 2013; Chen et al., 2017b). Hence, Fc with visual feedback are smaller and have greater complexity as compared to those in a no-vision condition (Baweja et al., 2009). Force tracking results in higher complexity of Fc when the visual display has high spatial resolution than when it has low spatial resolution (Sosnoff et al., 2006). The reason is that high-sensitivity feedback with precise visual information can facilitate richer error correction strategies. A major determinant of Fc is variations in the discharge properties of MUs. In addition, corticomuscular coherence (EEG–EMG coherence) in the beta range (13–35 Hz) plays a critical role in stabilizing corticospinal communication during static contraction (Kristeva et al., 2007; Omlor et al., 2011). Greater beta EEG–EMG coherence represents more effective sensorimotor integration and greater attentional focus being directed toward stabilizing the force output (Witte et al., 2007).

Accurate visual feedback is important to develop a reliable perception–action link. Interestingly, visual display of performance outcomes that are worse than the actual performance can better expedite motor adaptations to novel task constraints than can accurate visual feedback (Patton et al., 2006; Domingo and Ferris, 2010; Reisman et al., 2013). The virtual amplification of task errors, or EA, is frequently used in combination with robotic technology to facilitate motor recovery in patients with neurological disorders (Abdollahi et al., 2014; Kao et al., 2015; Israely and Carmeli, 2016; Bouchard et al., 2017). EA is thought to inflate response conflicts in the error-monitoring network such that participants are more attentive to execution of the motor task (Boussaoud and Kermadi, 1997; Jueptner and Weiller, 1998; Shirzad and Van der Loos, 2012). Alternatively, a model-based study predicted that EA could minimize the effect of overt task fluctuations by reducing the neuromotor noise variance (Hasson et al., 2016). In addition to task improvement, a force-tracking task with EA leads to smaller Fc with higher spectral components and complexity (Williams et al., 2016; Chen et al., 2017b; Hwang et al., 2017). These scenarios support the potential functional benefits of visual EA, including deliberate and richer tuning behaviors with more frequent corrective attempts than with real visual feedback. Physiologically, visually exaggerated mismatches with visual EA favors the use of a feedback process to regulate the MU discharge and the variability of the ISI among those MUs (Chen et al., 2017b). However, the use of visual EA does not always result in behavior success (Wei et al., 2005; Sung and O'Malley, 2011; Bouchard et al., 2015). For instance, EA may add to perceptual conflicts among the visual, proprioceptive, and haptic inputs due to the distortion of real visual consequences (Ogawa and Imamizu, 2013). Moreover, EA may augment the visual information load by proportionately amplifying the full spectrum of execution errors, including functionally irrelevant visual stimuli that could impair the efficacy of corrective behaviors (Lipowski, 1975; Chen et al., 2017a). Hence, to optimize visual EA, it is necessary to focus on the usability of task-related information.

Given the potential positive effects with EA, this study aimed to contrast EA with and without high-frequency error components during low-level static contraction. We argue that not all of the error information, especially the fast-oscillatory components, is helpful to improve visuomotor performance. As a visuomotor task with EA favors the use of a feedback mechanism (Chen et al., 2017b), the amplified fast-oscillatory error components (>0.8 Hz) within visual feedback cannot be effectively used due to a significant delay of 150 ms in the visuomotor loop (Miall et al., 1985, 1986, 1993). The amplification of these high-frequency error components could offset the positive effect of EA on a visuomotor task. Only LF-EA, wherein the error information of rapid fluctuations is excluded, could increase the effectiveness of visual feedback (or a feedback-prone process) for corrections of force-tracking deviations. Employing non-linear Fc dynamics and mathematical decomposition of surface electromyography, this study contrasted the behavior and neural mechanisms of static force-tracking in the real, EA, and LF-EA feedback conditions. Due to potential changes in force gradation strategies, it was hypothesized that (1) the size, complexity, and SDA variables of Fc would be different in the three visual feedback modes (traditional visual feedback, EA, and LF-EA), and (2) the variations in MU discharge and central drive to stabilize corticomuscular communication would vary among the visual feedback modes.

Abbreviations: Δ $\mathrm{MDR}_{\mathrm{RMS}}$, differences in root mean square of mean discharge rate between the EA/LF-EA and control conditions; $\Delta\beta\_\mathrm{Coh}_{\mathrm{EMG-EEG}}$, differences in beta-range EMG-EEG coherence area between the EA/LF-EA and control conditions; $\Delta\mathrm{IR}_{\mathrm{GAV}}$, differences in discharge irregularity between the EA/LF-EA and control conditions; ΔTask Error, difference in task errors between the EA/LF-EA and control conditions; CL, confidence level; CMC, corticomuscular coherence; CV-$\mathrm{ISI}_{\mathrm{mean}}$, coefficient of variance of mean ISI among motor units; $<dF^2>$, mean-squared value of the force fluctuations; $<dF_c{}^2>$, critical point of force fluctuations; D_l, long-term effective diffusion coefficient; DOF, degree of freedom; D_s, short-term effective diffusion coefficient; DSDC, Decomposition-Synthesis-Decomposition-Compare test; dt, time interval; dt_c, critical point of time; EA, error amplification; EEG, electroencephalography; EMG, electromyography; Fc, force fluctuations; FDI, first dorsal interosseus; H_l, long-term scaling exponent; H_s, short-term scaling exponent; IR, irregularity index of inter-spike interval; $\mathrm{IR}_{\mathrm{GAV}}$, global average of irregularity index of inter-spike interval for all motor units; ISI, inter-spike interval; $\mathrm{ISI}_{\mathrm{GAV}}$, global average of mean inter-spike interval for all motor units; $\mathrm{ISI}_{\mathrm{mean}}$, mean value of inter-spike intervals in an individual MUAPT; LF-EA, low-frequency error amplification; MF, mean frequency; MU, motor unit; MUAPT, motor unit action potential train; MVC, maximal voluntary contraction; RE, real error; RF, real force; RMS, root mean square; SampEn, sample entropy; SDA, stabilogram diffusion analysis; T, target signal; VE, visualized error; VF, visualized force.

MATERIALS AND METHODS

Subjects

The participants were 15 healthy adults (8 males and 7 females; mean age: 24.8 ± 0.9 years, range: 21–31 years old) from a university campus or the local community. All were self-reported as being right-handed, and none had symptoms or signs of neuromuscular diseases. The experiments were conducted in accordance with the Declaration of Helsinki and approved by an authorized institutional human research review board (IRB) at the University Hospital of the Chung Shan Medical University, Taiwan. All participants signed a written informed consent form prior to inclusion.

Experimental Procedures

The participants completed a unilateral static force task of isometric index abduction at a low force level (20% MVC) under three error feedback conditions: control, error-amplification (EA), and low-frequency error-amplification (LF-EA). The participants were seated with the palm and forearm of the right hand firmly fixed within a thermoplastic splint on the table. The index finger was held slightly abducted (5 degrees of abduction), and its abduction force was measured using a force transducer (Model: MB-100, Interface Inc., United States) followed by an analog amplifier (gain = 10). The cut-off frequency of the amplifier was 20 Hz so that fast-oscillatory force components such as 8–12 Hz physiological tremor would not be attenuated by the experiment setting. For each individual, the MVC of the FDI was pre-determined from three maximal contraction trials of 3 s separated by 3 min pauses, by averaging the largest force produced in each trial. Interleaved with 3-min pauses, separate experimental trials in the control, EA, and LF-EA conditions commenced in a randomized order, after three practice trials in all conditions. There were four experimental trials for the control, EA, or LF-EA conditions. During the force-tracking in the control condition, the participants were given 2 s to reach the target force (slope: 10% MVC/second) after a latent period of 3 s (**Figure 1A**). Then they coupled isometric force to the target signal (20% MVC) as precisely as possible by pushing their index finger against the force transducer for another 34 s under visual guidance. The force output returned to the resting level in 2 s, followed by a 3-s latency period. The time window of interest was denoted as the 8th to 37th seconds in a total of 44 s for an experimental trial. The resolution of the display of visual feedback on the monitor was 1,920 pixels × 1,080 pixels.

In the EA condition, the VF displayed on the monitor was mathematically transformed to potentiate execution error [mismatches between the real force output (RF) and the target signal (T)] (**Figure 1B**). The VF was equal to the sum of twice the RF minus the target signal (T) (VF = 2RF-T), so the participant would perceive twice the amount of the RE of the static force-tracking task (VE = 2RE). RF in the EA condition was low-pass filtered at 20 Hz, and the VF was relatively noisy, containing enhanced fast-oscillatory force components and tremulous movements. In the LF-EA condition, the RF came from a parallel force channel that pre-conditioned the force output with an analog low-pass filter (cut-off frequency: 0.8 Hz) prior to amplification (**Figure 1B**). The VF was much smoother in the LF-EA condition than in the EA condition. The participants could hardly correct high-frequency errors above 0.8 Hz via visual feedback (Pew, 1974; Miall et al., 1985), because the time period between the pick-up of visual information and its use in producing a required adjustment was at least 150 ms (Miall et al., 1986). For all the feedback conditions, the spatial gain to display the target signal and the force output was roughly 25 pixels per 1% MVC. The inter-trial interval of rest was 2 min. In the LabVIEW platform (LabVIEW v.8.5, National Instruments Inc., United States), the RF conditioned with a low-pass filter at 20 Hz and the target signal were digitalized at 1 kHz by a 16-bit analog-to-digital converter (DAQCard-6024E; National Instruments Inc., United States) in the EA and LF-EA conditions. For the LF-EA condition, the smoother force channel, conditioned with an analog low-pass filter (cut-off frequency: 0.8 Hz), was also recorded.

Electromyographic and Electroencephalographic Recordings

In addition to the force signal, we synchronized multi-electrode surface EMG with 5 surface pin-sensors (0.5 mm diameter at the center and corners of a 5 mm × 5 mm square) (Bagnoli sEMG system, Delsys Inc., United States) to record activities of the FDI muscle. By careful skin preparation and proper sensor application, the peak-to-peak value of baseline noise was controlled under 20 μV to secure the accuracy of EMG decomposition using EMG works v.4.1 (Delsys Inc., United States). The analog EMG signals from each pin-sensor were amplified (gain = 1,000) and filtered with a bandwidth of 20–450 Hz (De Luca et al., 2014). After that, four single differential EMG channels were obtained with pair-wise subtractions of the five pin-detections (voltages of the pin-sensor at the corner minus voltage of the pin-sensor at the center) (De Luca et al., 2006; Nawab et al., 2010; Hu et al., 2013). A high sampling rate of 20 KHz was used to avoid introducing phase skew across channels (De Luca et al., 2006, 2014; Nawab et al., 2010). Two active Ag-AgCl electrodes (3 mm diameter; Model F-E9M-40-5, Grass, United States) were placed 1 cm apart on the C3 area, which was over the hand area of the primary motor cortex. The reference electrodes for the EEG were placed on the bilateral earlobes. After amplification of the recorded signal (gain = 5,000), the EEG signal was hardware-filtered in the frequency range of 0.01–100 Hz and 60 Hz (Model P511, Grass, United States). Synchronized with the EMG system and force data, the EEG signal was sampled at 1,000 Hz.

Stochastic Modeling of Force Fluctuation Dynamics

The force data used for behavior analysis were the RF data low-pass filtered at 20 Hz. To exclude force data irrelevant to visuo-motor processes and error correction (such as 8–12 Hz physiological tremor) (Slifkin et al., 2000; Vaillancourt et al., 2002), the RF was further conditioned with a digital low-pass filter (cut-off frequency: 6 Hz) (Chen et al., 2013; Lin et al., 2014).

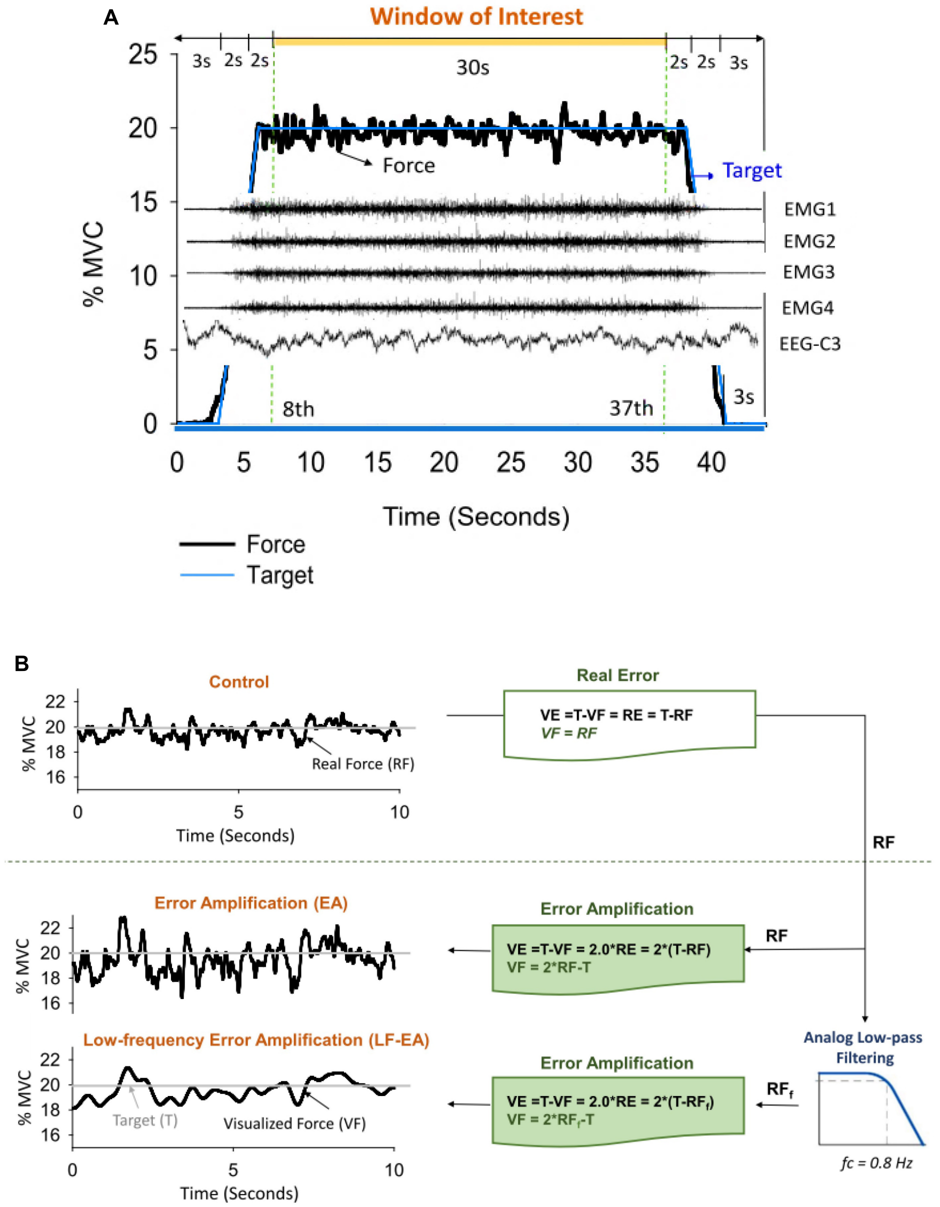

FIGURE 1 | (A) Target signal and representative data. Only force data, EMG, and EEG in the time window of interest were presumably stable for subsequent feature extraction. **(B)** Illustration of manipulation of error augmentation for visual feedback. In the control condition, real force (RF) was shown on the monitor to guide the force task, so that real error (RE) is equivalent to visualized error (VE) during tracking. In the error amplification (EA) and low-frequency error amplification (LF-EA) conditions, the VE of the tracking task were magnified with mathematical transformation. The visualized force outputs (VF) in the EA condition represent on-line force feedback information that doubles the size of the execution error during force-tracking. The LF-EA feedback consists of a low-pass filtering process and an error amplification process during force-tracking. The low-pass filtering process suppresses high-frequency components (>0.8 Hz) of real force. Error amplification process based on the filtered real force (RF_f) magnifies VE that contains only low-frequency components (<0.8 Hz).

Then the conditioned force data in the time window of interest (8th to 37th second) were down-sampled to 100 Hz. The quality of the force-tracking performance was visualized with a return map for the time series of task errors, a graph of the task error E_{i+1} versus the previous task error E_i (Shenker, 1982; Mendez-Balbuena et al., 2012). A poor performance led to a dispersive distribution of error points in the map. In contrast, error points for a good performance concentrated near to the center of the map. The size of the task error was quantified with RMS of mismatch between target and force signal. In the temporal domain, RMS and SampEn were applied to calculate the size and complexity of Fc, defined as force data after removal of a linear trend (Hong and Newell, 2008). Fc characteristics reflect the degree of force steadiness and gradation strategy for force stabilization. SampEn is a popular and reliable entropy measure of the temporal aspects of biological variability

(Richman and Moorman, 2000). The mathematical formula of sample entropy was $SampEn\,(m, r, N) = -\log(\frac{\sum_{\mathrm{i=1}}^{\mathrm{N-m}} A_{\mathrm{i}}}{\sum_{\mathrm{i=1}}^{\mathrm{N-m}} B_{\mathrm{i}}})$, where r = 15% of the standard deviation of the force channel, m is the length of the template (m = 3), and N is the number of data points in the time series. A_{i} is the number of matches of the *i*th template of length $m + 1$ data points, and B_{i} is the number of matches of the *i*th template of length m data points (Pethick et al., 2015). A larger value represents a more complex structure of the low-frequency Fc. In the spectral domain, the MF of Fc was determined based on the spectral profile estimated with a fast Fourier transform and the Welch method (Hanning window; window length: 2.048 s, overlapping time segment: 1/4 × window length) with a spectral resolution of 0.1 Hz. In addition, we quantified the spectral DOF, a statistic to reveal the power dispersion of Fc. Spectral DOF is calculated as $\mathrm{DOF} = \left(\sum_{\mathrm{i}}^{\mathrm{N}} S_{\mathrm{i}}\right)^2 / \sum_{\mathrm{i}}^{\mathrm{N}} S_{\mathrm{i}}^2$. The quantity is unity for a perfect single spectral peak, and a greater value of DOF represents a broader band of Fc (maximal value of N for white noise).

Force fluctuation dynamics were characterized with SDA, a probabilistic tool first proposed by Collins and De Luca (1993). The mathematical concept of the SDA approach was originally designated to resolve the statistical mechanics of a one-dimensional generalized family of Gaussian stochastic processes, such as postural sway (Collins and De Luca, 1993, 1995) and Fc (Chen et al., 2017a). The SDA describes the power-law relationship between the $<dF^2>$ and the dt in which these values occur; i.e., $< dF^2 > \sim dt^{2\mathrm{H}}$. H is the scaling factor, a real number ranging from 0 to 1. For classic Brownian motion, H = 0.5. For the purpose of the present study, SDA was calculated by using the following equation: $\langle dF^2 \rangle = \left\langle \left[x\,(t + dt) - x\,(t)\right]^2 \right\rangle$, where $<\bullet>$ indicates the mean of the time series. The computation of dF^2 was empirically repeated with increasing dt values ranging from 0 to 3 s. The diffusion plot (linear–linear plots or log–log plots) was the mean square of Fc $<dF^2>$ against the time intervals dt (**Figures 2A,B**). Specifically, for biological systems regulated jointly by open-loop and closed-loop processes, the diffusion plots could be best-fitted with piecewise linear regression models, the cross-over phenomenon (Delignières et al., 2011). The dt_{c} was the intersection of the two regression lines of the linear-linear diffusion plot (**Figure 2A**), and variations in the $<dF_{\mathrm{c}}{}^2>$ reflected a paradigm shift in force control (Collins and De Luca, 1993; Toosizadeh et al., 2015). In the linear–linear diffusion plot, the regression slopes (D_{s} and D_{l}) of the short-term and long-term regions were two effective diffusion coefficients, which parameterized the control of the force stochastic activities in those regions, respectively. The H_{s} and H_{l} were linear fits of the log–log plot of the SDA (**Figure 2B**). A scaling exponent greater than 0.5 indicates that the system is governed by the open-loop process (persistence) and that the data series of the past and future are positively correlated (Collins and De Luca, 1993, 1995). Conversely, a scaling exponent smaller than 0.5 indicates that the data series of the past and future are negatively correlated, as regulated by the closed-loop process (anti-persistence). The selection of this model was a matter of physiological concern, due to the underlying shift in feedback and feedforward control for force stabilization with better use of the error information within the visual feedback.

Probability of Motor Unit Discharge

The action potential "templates" of MUs were decomposed from differential EMG channels using a previous proof-of-principle (De Luca et al., 2006; Nawab et al., 2010). Recent studies have shown that the artificial-intelligence-based computation algorithm can produce convincing decomposition results (Nawab et al., 2004; De Luca et al., 2015) via independent verification methods (Hu et al., 2013). The entire data collection period (44 s) was decomposed, resulting in binary spike trains that coded the activations of all MUs with values of 0 or 1 (**Figure 3**). Only discharge patterns of the window of interest were further analyzed. The validity of the EMG decomposition of each MU action potential train (MUAPT) was evaluated with the Decomposition-Synthesis-Decomposition-Compare (DSDC) test (De Luca et al., 1982, 2006). In brief, the DSDC test was used to decompose a synthetic sEMG signal, which was reconstructed by the summation of the predefined MUAPTs (or decomposed results) and Gaussian noise. The decomposed results were compared with the firing instances of predefined MUAPTs, and the percentage of the accuracy and location error of decomposition for each MUAPT was defined as decomposition accuracy. Previous studies have reported that the decomposition accuracy of MUAPTs ranges from 92.5 to 97.6% (De Luca et al., 1982, 2006). In this study, MUs of low decomposition accuracy (<90%) were excluded from the analysis. The discharge variables of MUs were determined in the time window of interest based on the decomposed EMG data of the overall 44 s. Three MU discharge variables were calculated, including global averaged inter-spike interval ($\mathrm{ISI_{GAV}}$), CV-$\mathrm{ISI_{mean}}$, and global averaged irregularity index (IR) of all MUs ($\mathrm{IR_{GAV}}$). In an experimental trial, $\mathrm{ISI_{mean}}$ was the mean value of all ISIs for an individual MUAPT, and the $\mathrm{ISI_{GAV}}$ was the averaged value of the $\mathrm{ISI_{mean}}$ for a group of MUs. Experimentally observed ISI variability among MUs was represented with the CV of the $\mathrm{ISI_{mean}}$ of a group of MUs (CV-$\mathrm{ISI_{mean}}$). Given a series of inter-spike intervals ($\mathrm{ISI_i}$) for a single MU, the irregularity index (IR) (Davies et al., 2006; Witham and Baker, 2007) is mathematically formulated as: $\mathrm{IR} = \frac{1}{N-1} \sum_{\mathrm{i=1}}^{\mathrm{N-1}} \left|\ln\left(\mathrm{ISI_{i+1}}/\mathrm{ISI_i}\right)\right|$. The $\mathrm{IR_{GAV}}$ was the averaged value of the IR for a group of MUs. An increase in force steadiness with LF-EA was likely associated with changes in inter-spike variability. The pooled behaviors of MU discharges were characterized with the mean discharge rate (**Figure 3**). To estimate the mean discharge trace, the global discharge rate was first determined by convolution of the cumulative spike trains of all the MUs with a Hanning window (window duration: 400 ms) (Hwang et al., 2017). The mean discharge rate was the global discharge rate divided by the number of detectable MUs in the experimental trial. The averaging process was used to standardize the amplitude of the global discharge rate across trials. Low-frequency oscillations of the mean discharge rate likely correspond to the common input to the motoneurons, providing a reasonable estimate of the force exerted by the muscle (Farina and Negro, 2015; Farina et al., 2016).

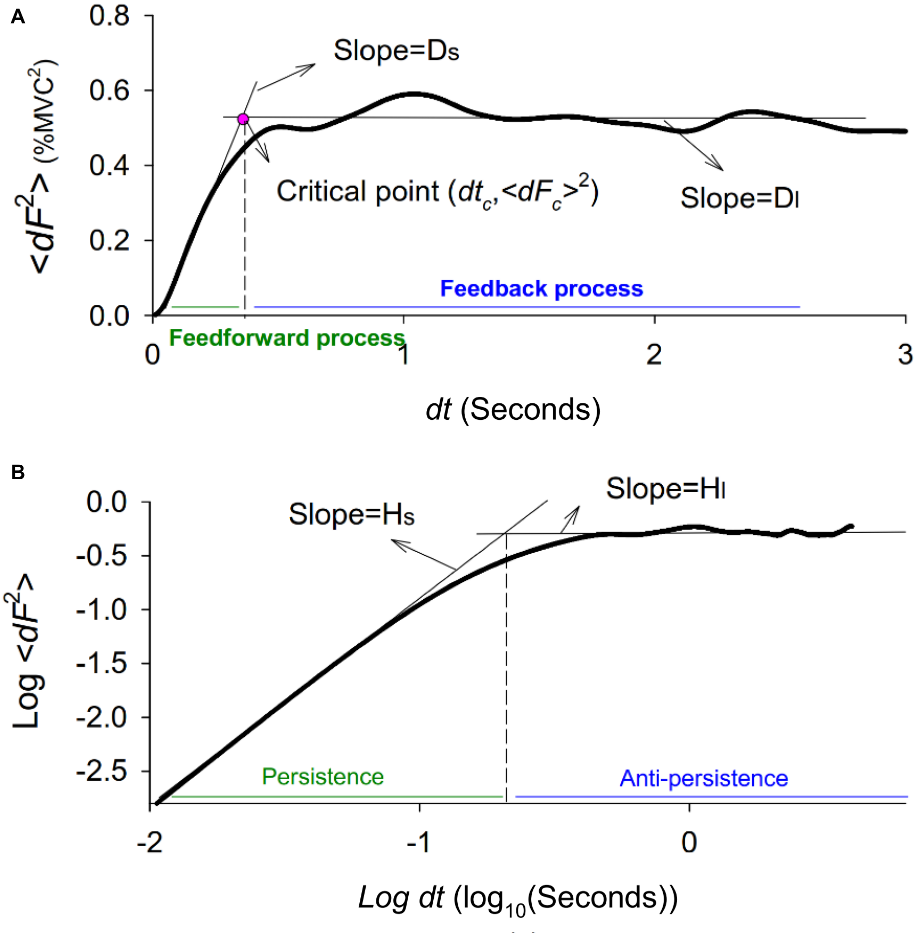

FIGURE 2 | Stabilogram-diffusion plot. **(A)** A typical linear-linear stabilogram-diffusion plot. The short-term effective diffusion coefficient (D_s), and long-term effective diffusion coefficients (D_l) are regression slopes for the short time scale (0–0.5 s) and long time (0.5–3 s) scales. The critical point (dt_c, $<dF_c{}^2>$) is the intersection point of the two regression lines, indexing a shift in open-loop and closed-loop control for the stochastic dynamics of force fluctuations. **(B)** A typical log-log stabilogram-diffusion plot. The computed short-term scaling exponent (H_s) and long-term scaling exponent (H_l) are regression slopes of the short time and long time scales of the log–log stabilogram-diffusion plot.

Corticomuscular Coherence Estimation

Corticomuscular coherence, especially in the spectral range of 13–35 Hz, is known to reflect efferent neural transmission to maintain force steadiness (Kristeva-Feige et al., 2002; Omlor et al., 2011). Four undecomposed EMG signals directly from differential channels were used to calculate CMC. The analog EMG signals were first resampled at 1 KHz, followed by signal conditioning with a band-pass filter (cut-off frequencies: 10 and 400 Hz). The conditioned EMG signal was rectified and high-pass filtered at 5 Hz (Chen et al., 2013). Ocular artifacts in the EEG recordings were removed. The EEG–EMG coherence was determined with EEG C3 and each conditioned EMG signal. The resulting EEG–EMG coherence spectra were averaged to represent the CMC of the experimental trial. The coherence between signals x and y at frequency f, $Coh_{xy}(f)$, was determined according to the following equation: $Coh_{xy}(f) = \frac{|S_{xy}(f)|}{\sqrt{S_{xx}(f) \times S_{yy}(f)}}$. The cross-spectrum between signals x and y at frequency f averaged across N data segments, $S_{xy}(f)$, was calculated as follows: $S_{xy}(f) = \frac{1}{N}\sum_{i=1}^{N} X_i(f) \times Y_i(f)^*$, where $X_i(f)$ denotes the Fourier transform of the data segment i of the channel x at frequency f, and $Y_i(f)^*$ denotes the complex conjugate of the Fourier transform of the data segment i of the channel y at frequency f. To estimate $Coh_{xy}(f)$, EEG, and EMG signals were segmented into artifact-free epochs of 1.024 s without overlapping. Each segmented EEG and four EMG data from the differential channels were Hanning-windowed to minimize spectral leakage, and the $Coh_{xy}(f)$ of a given experimental trial was estimated with a total of 116 epochs (29 epochs/trial × 4 experimental trials). Spectral resolution was 1 Hz. The significance level of EEG–EMG coherence was the 95% CL. The CL was defined as: $\mathrm{CL}(\alpha) = 1 - \left(1 - \frac{\alpha}{100}\right)^{1/N}$. Both the peak coherence and spectral area of the pooled EEG–EMG coherence spectrum in the beta band frequencies (13–35 Hz) were determined for each experimental trial, and those spectral variables of the three experimental trials were averaged

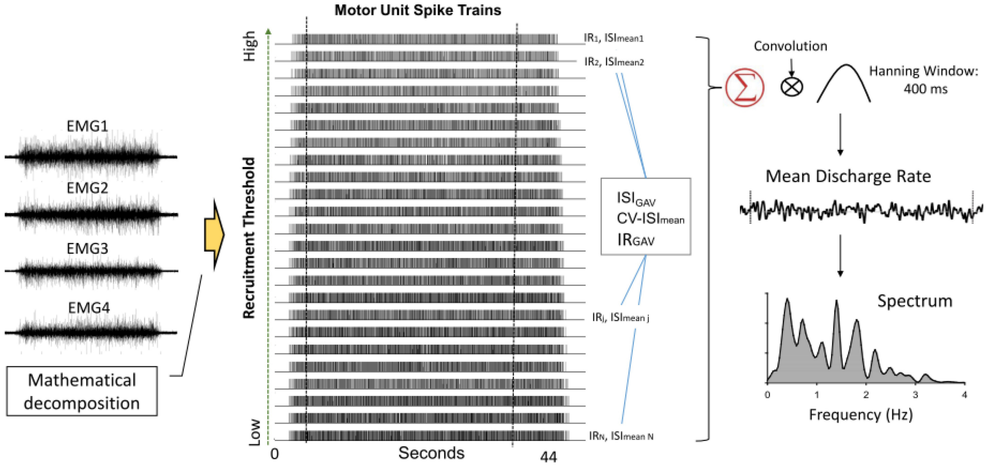

FIGURE 3 | Acquisition of variables of inter-spike interval and mean discharge rate following mathematical decomposition of surface EMG into motor unit spike trains. Mean discharge interval (ISI_{mean}) and irregularity index (IR) of each spike train are determined. The global averages of ISI_{mean} and IR, as well as coefficient of variance of ISI_{mean} (CV-ISI_{mean}) among motor units (MUs). Mean discharge rate is obtained by smoothing the cumulative MU spike trains following convolution with a Hanning window (window length: 400 ms). Spectral distributions of mean discharge rate are estimated.

for all the feedback conditions. All the behavior/physiological variables and their functional implications in this study are briefly summarized in **Figure 4**.

Statistical Analysis

With reference to typical visual feedback to guide force-tracking, the primary research interest of this study was to contrast variations in the stochastic force behaviors and probability structure of MU discharges with the use of EA feedback and LF-EA feedback. On account of the relatively small sample size, the Wilcoxon signed-rank test was used to examine the task error, Fc variables (including SDA variables), inter-spike variables, variables of the mean discharge rate, and EEG–EMG coherence in the beta band in the three feedback conditions. The level of significance was 0.05. In the presence of significant main effects, *post hoc* testing was conducted using the Mann–Whitney *U* test with Bonferroni correction to determine the alpha level of significance ($p = 0.0167$). Spearman rank correlation was used to assess functional linkages between differences in task error between the EA/LF-EA and control conditions with the corresponding changes in those neurophysiological metrics that were sensitive to manipulation of EA. Signal processing and statistical analyses were completed in Matlab R2015b (Mathworks Inc., United States) and the statistical package for IBM SPSS software for Windows v.19.0 (IBM Inc.,

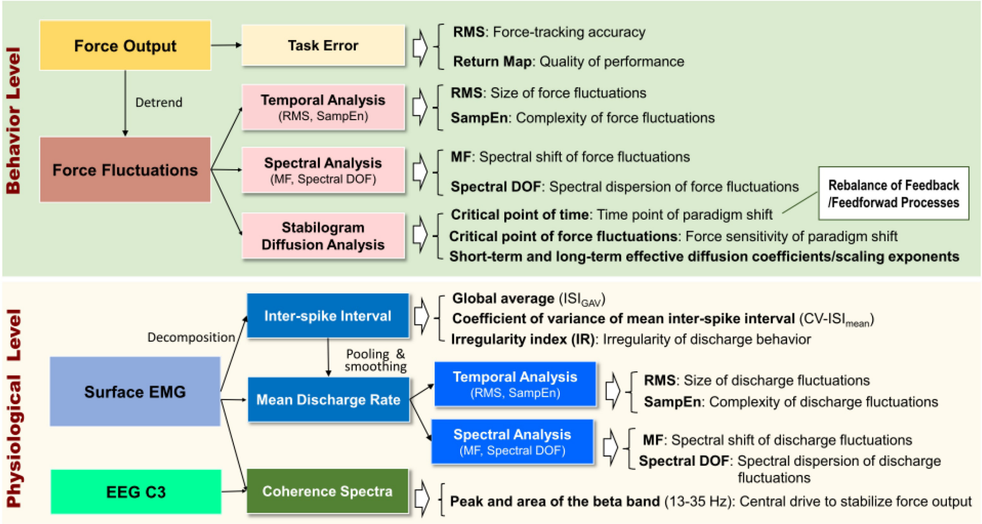

FIGURE 4 | A summary diagram of behavior and physiological variables and their functional implications.

United States), respectively. Data reported in the text and figures without specific notations indicating otherwise are presented as mean ± standard error.

RESULTS

Figure 5A displays the return maps of the task errors from a typical subject in the three conditions: control, EA, and LF-EA. The dispersion of the error points in the maps for the LF-EA condition was smaller than those for the EA and control conditions. This was a qualitative way to characterize stable and accurate force-tracking with LF-EA. **Figure 5B** shows the population means, standard errors, and individual values of force-tracking errors for all three visual conditions. The results of the Wilcoxon signed-rank test revealed that force-tracking errors varied with feedback mode ($\chi_r^2 = 10.13$, $p = 0.006$), with the smallest error for the LF-EA condition ($p \leq 0.006$). **Figure 5C** shows the distribution of differences in tracking error between the EA/LF-EA and control conditions. The majority of the participants exhibited a more positive performance benefit with LF-EA than with EA, as indicated by the smaller mean tracking error relative to that of the control condition. **Table 1** contrasts the differences in the Fc variables among the three visual conditions. The results revealed that all Fc variables were dependent on the feedback mode ($p < 0.05$). *Post hoc* analysis further revealed that the LF-EA condition exhibited the smallest RMS and the largest SampEn of Fc among the three feedback conditions ($p < 0.01$). Both the EA and the LF-EA conditions exhibited mean frequencies and spectral DOF larger than those of the control condition ($p < 0.01$). Functionally, LF-EA led to fine-grained and richer force gradation to rapidly remedy tracking deviations. In addition, the Fc dynamics were characterized with SDA, and all the SDA variables varied with manipulation of the feedback mode ($p \leq 0.006$) (**Table 2**). *Post hoc* test indicated that dt_c was smallest in the LF-EA condition and largest in the control condition ($p < 0.01$). In addition, $\langle dF_c^2 \rangle$ was smaller in the LF-EA condition than in the control and EA conditions ($p < 0.01$). D_s and H_s were smallest in the LF-EA condition ($p < 0.01$), whereas D_l and H_l were largest in the LF-EA condition ($p < 0.01$). The observations indicated that the preclusion of high-frequency feedback components from the EA process led to task improvement during static force-tracking. The functional benefits were associated with the sensible detection of Fc (smallest

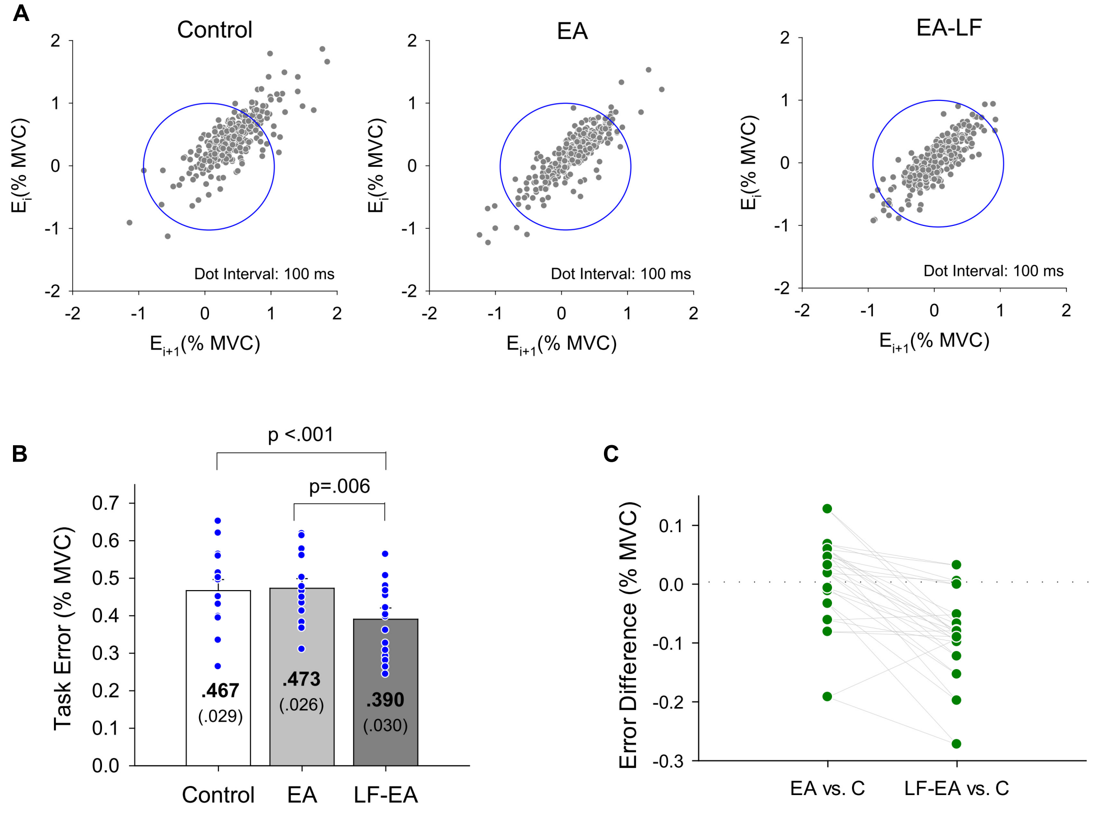

FIGURE 5 | Task error properties. **(A)** Return maps of the force-tracking for a typical subject in the control, EA, and LF-EA condition. Graph of the error E_{i+1} versus previous error E_i where i is the sampling point. For brevity, the interval between two error data is set at 100 ms. Good performance of force-tracking exhibits error points that are concentrated near the center of the blue circle. **(B)** The contrasts of force-tracking error among the three visual feedback conditions. The blue dots represent force-tracking error of all individuals in this study. **(C)** A schematic plot to display scattering of differences in tracking error between the error amplification (EA)/low-frequency error amplification (LF-EA) and control (C) conditions. A more negative value of the error difference indicates a more positive performance benefit, underlying a relatively smaller tracking error in the EA or LF-EA condition. Each green dot represents EA-related differences in tracking error for an individual.

TABLE 1 | Mean and standard errors of task error and force fluctuation variables for the control, error amplification (EA), and low-frequency error amplification (LF-EA).

Behavior variables (n = 15)	Control	EA	LF-EA	*Statistics*
Fc_RMS (% MVC)	0.424 ± 0.029^a	0.424 ± 0.028^a	0.376 ± 0.026^a	$\chi_r^2 = 14.80, p = 0.001$
Fc_SampEn	0.294 ± 0.017^b	0.292 ± 0.016^b	0.336 ± 0.023^b	$\chi_r^2 = 11.02, p = 0.004$
Fc_MF (Hz)	0.832 ± 0.049^c	0.894 ± 0.040^c	0.893 ± 0.045^c	$\chi_r^2 = 12.13, p = 0.002$
Spectra DOF	26.50 ± 1.40^c	29.25 ± 1.05^c	29.67 ± 1.27^c	$\chi_r^2 = 6.40, p = 0.041$

^{a}Control, EA > LF-EA, $p < 0.01$. ^{b}LF-EA > Control, EA, $p < 0.01$. ^{c}LF-EA, EA > Control, $p < 0.01$. (Fc, force fluctuations; RMS, root mean square; SampEn, sample entropy; MF, mean frequency; DOF, degree of freedom).

TABLE 2 | Parameters of stabilogram diffusion analysis (SDA) of static force tracking in the control and error amplification (EA), low-frequency error amplification (LF-EA) conditions.

SDA variables (n = 15)	Control	EA	LF-EA	*Statistics*
dt_c (s)	0.401 ± 0.016^a	0.367 ± 0.015^a	0.329 ± 0.014^a	$\chi_r^2 = 20.93, p < 0.001$
$<dF_c^2>$ (%MVC^2)	0.409 ± 0.063^b	0.442 ± 0.071^b	0.292 ± 0.040^b	$\chi_r^2 = 14.80, p = 0.001$
D_s (%MVC^2/s)	0.601 ± 0.097^b	0.682 ± 0.109^b	0.419 ± 0.064^b	$\chi_r^2 = 14.80, p = 0.001$
D_l (%MVC^2/s)	−0.014 ± 0.006^c	−0.019 ± 0.008^c	0.005 ± 0.002^c	$\chi_r^2 = 14.53, p = 0.001$
H_s (%MVC^2/s)	0.940 ± 0.003^b	0.942 ± 0.003^b	0.937 ± 0.002^b	$\chi_r^2 = 12.13, p = 0.002$
H_l (%MVC^2/s)	−0.088 ± 0.020^c	−0.062 ± 0.014^c	−0.015 ± 0.016^c	$\chi_r^2 = 10.13, p = 0.006$

^{a}Control > EA > LF-EA, $p < 0.01$. ^{b}Control, EA > LF-EA, $p < 0.01$. ^{c}LF-EA > Control, EA, $p < 0.01$. (dt_c, critical point of time; $<dF_c^2>$, critical point of force fluctuations; D_s, short-term effective diffusion coefficients; D_l, long-term effective diffusion coefficients; H_s, short-term scaling exponent; H_l, long-term scaling exponent).

TABLE 3 | Means and standard errors of variables of inter-spike interval **(A)** mean discharge rate **(B)** from all motor units in the control, error amplification (EA), and low-frequency error amplification (LF-EA) conditions.

	Control	EA	LF-EA	*Statistics*
(A) Discharge variables (n = 15)				
ISI_{GAV} (ms)	58.89 ± 3.15	58.78 ± 3.30	59.07 ± 2.99	$\chi_r^2 = 1.20, p = 0.549$
CV-ISI_{mean}	0.238 ± 0.012	0.215 ± 0.012	0.222 ± 0.012	$\chi_r^2 = 5.20, p = 0.072$
IR_{GAV}	0.198 ± 0.007^a	0.194 ± 0.008^a	0.208 ± 0.009^a	$\chi_r^2 = 6.93, p = 0.031$
(B) Mean discharge rate (n = 15)				
RMS (Hz)	0.823 ± 0.067^b	0.785 ± 0.065^b	0.763 ± 0.057^b	$\chi_r^2 = 10.53, p = 0.005$
SampEn	0.319 ± 0.009	0.308 ± 0.007	0.339 ± 0.007	$\chi_r^2 = 1.73, p = 0.420$
MF (Hz)	1.089 ± 0.025	1.074 ± 0.024	1.076 ± 0.017	$\chi_r^2 = 0.40, p = 0.819$
DOF	30.32 ± 0.88	29.88 ± 0.54	31.30 ± 0.85	$\chi_r^2 = 3.73, p = 0.155$

^{a}LF-EA > EA, $p = 0.023$; LF-EA > Control, $p < 0.01$. ^{b}Control > EA > , $p = 0.023$; Control > LF-EA, $p = 0.012$. (ISI_{GAV}, global average of mean discharge interval (ISI_{mean}) of all MUs; IR_{GAV}, global average of irregularity index (IR); CV-ISI_{mean}, Coefficient of variance of ISI_{mean} among motor units; RMS, root mean square; SampEn, sample entropy; MF, mean frequency; DOF, degree of freedom).

dt_c and $<dF_c^2>$ in the LF-EA condition) and a shift in Fc control toward the feedback-prone process.

Under the condition of acceptable decomposition accuracy using the DSDC test (Control: 93.10 ± 0.42%; EA: 93.45 ± 0.42%; LF-EA: 93.76 ± 0.46%), the average numbers of analyzed MUs of an experimental trial did not vary with the feedback conditions (Control: 30.8 ± 1.8; EA: 32.1 ± 2.0; LF-EA: 31.5 ± 1.9; $\chi_r^2 = 1.97$, $p = 0.374$), ($\chi_r^2 = 1.20$, $p = 0.549$). **Table 3A** contrasts the inter-spike (ISI) variables of all MUs among the three feedback conditions. The global averages of the mean inter-spike interval (ISI_{GAV}) and CV-ISI_{mean} were not affected by the feedback mode ($p > 0.05$). Only the discharge irregularity in terms of IR_{GAV} (or global average of IR for all MUs) varied significantly with feedback mode ($p < 0.05$). IR_{GAV} was generally highest in the LF-EA condition ($p < 0.01$). **Table 3B** contrasts the characteristics of the mean discharge rate of the all MUs among the three feedback conditions. Only the RMS of the mean discharge rate was subject to feedback mode ($p = 0.005$). *Post hoc* test revealed that the RMS of the mean discharge rate was significantly smaller in the LF-EA condition than in the control condition ($p = 0.012$). However, the SampEn, MF, and DOF of the mean discharge rate did not significantly vary with feedback mode ($p > 0.05$). **Figure 6A** presents an example of the pooled coherence spectra of the EEG and rectified EMG from a typical participant in the control, EA, and LF-EA conditions. The typical coherence spectra manifested with large power in the beta frequencies (13–35 Hz), exceeding the 95% CL. **Figure 6B** contrasts the population means of the peak coherence and spectral area in the beta frequencies among the three feedback conditions. Both the peak coherence ($\chi_r^2 = 7.60$, $p = 0.022$) and the spectral area in the beta frequencies ($\chi_r^2 = 9.73$, $p = 0.008$) varied significantly with feedback mode.

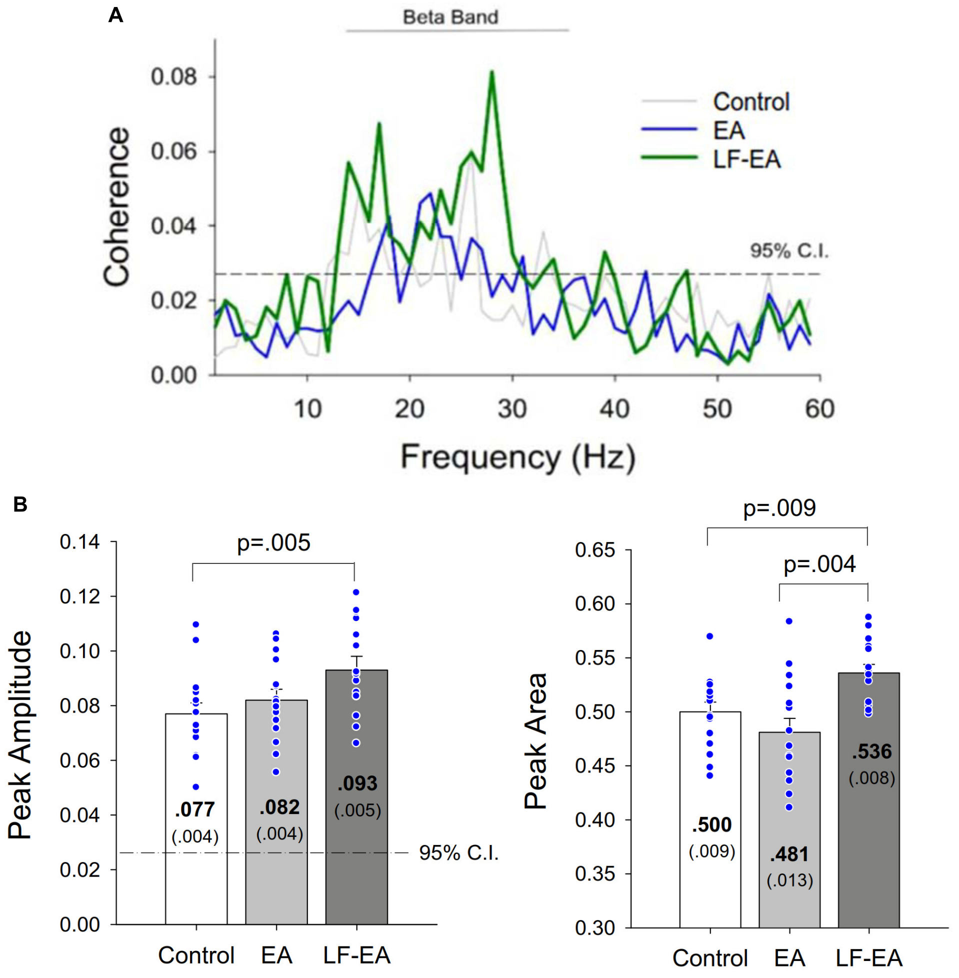

FIGURE 6 | (A) Pooled coherence spectra between the EEG and rectified EMG of a typical participant in the control, error amplification (EA), and low-frequency error amplification (LF-EA) conditions. **(B)** the contrasts of peak coherence and spectral area in the beta band (13–35 Hz) among the three feedback conditions. The blue dots represent coherence values of all individuals in this study.

Beta peak coherence was larger in the LF-EA condition than in the control condition ($p = 0.005$), and the spectral area in the beta frequencies was largest in the LF-EA condition ($p \leq 0.009$). The use of LF-EA appeared to enhance CMC at 13–35 Hz, which might serve to stabilize the motor output and decrease the discharge variability.

Figure 7 presents three scatterplots showing the associations between differences in task error and the neurophysiological metrics (ΔIR_{GAV}, ΔMDR_{RMS}, and $\Delta\beta\text{-}Coh_{EMG-EEG}$) sensitive to manipulation of EA. In terms of Spearman rank correlation (r_s), the change in task error between the LF-EA and control conditions was significantly correlated to ΔMDR_{RMS} and $\Delta\beta\text{-}Coh_{EMG-EEG}$ ($p < 0.05$). In contrast, the change in task error between the EA and control conditions was not significantly correlated to ΔIR_{GAV}, ΔMDR_{RMS}, or $\Delta\beta\text{-}Coh_{EMG-EEG}$ ($p > 0.05$). These facts implied that task improvement in the LF-EA condition relative to that of the control condition could be linked to centrally mediated change in the amplitude of pooled discharges of the MUs.

DISCUSSION

The novel finding of this study was that gating of the high-frequency execution errors prior to virtual amplification (the LF-EA feedback) provided a functional benefit to the stabilization of static force, due to the smaller Fc with higher complexity, MF, and spectral DOF. The LF-EA feedback reduced the perceptual sensitivity to Fc (smaller $<dF_c^2>$) with a greater reliance on the visual feedback process for error corrections (smaller dt_c). Physiologically, the shift in force control was associated with greater global discharge irregularity (IR_{GAV}), smaller fluctuation in the mean discharge rate, and enhanced EMG-EEG coherence in the beta band.

Structural Changes in Force Fluctuations and Implications for Force Control

The time series of Fc modeled with SDA was different from ordinary Brownian motion (un-correlated random-walk), as the

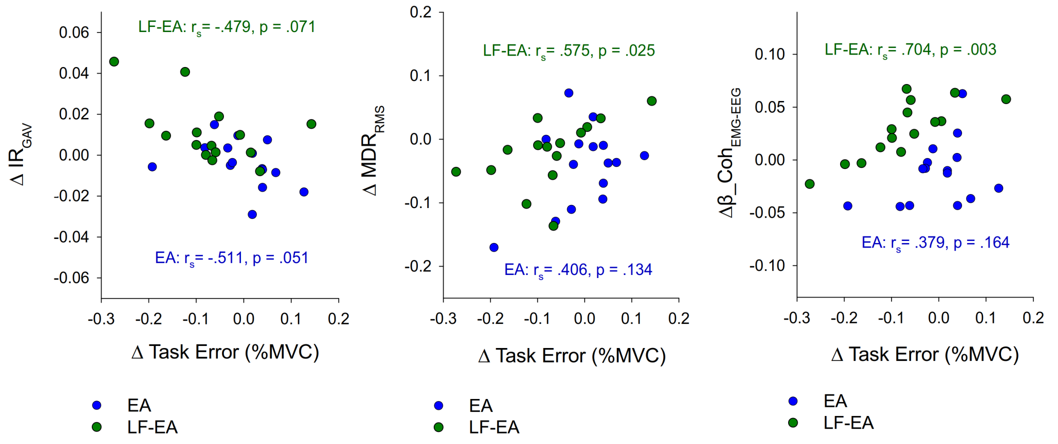

FIGURE 7 | Scatter plots to show the relationships between EA-related changes in task error and neurophysiological metrics. Negative value of ΔTask Error represents task improve with EA or EA-LF feedback. (ΔTask Error, difference in task errors between the EA/LF-EA and control conditions; ΔIR_{GAV}, differences in discharge irregularity between the EA/LF-EA and control conditions; ΔMDR_{RMS}, differences in root mean square of mean discharge rate between the EA/LF-EA and control conditions; $\Delta\beta\_Coh_{EMG-EEG}$, differences in beta-range EMG-EEG coherence area between the EA/LF-EA and control conditions; r_s, Spearman rank correlation).

diffusion curve of Brownian motion is linear and unbounded with the scaling exponent equal to 0.5 (Mandelbrot and van Ness, 1968; Collins and De Luca, 1993). The diffusion curve of the Fc changed slope after the critical point, and the scaling exponents for Fc were, respectively, greater than and less than 0.5 for short-term and long-term intervals (**Figure 2B** and **Table 2**). Hence, like postural sway (Collins and De Luca, 1993, 1995; Delignières et al., 2011), Fc are correlated and bounded random-walk signals, regulated distinctively by two subsystems. An open-loop process predominates Fc control in the short-term region with a scaling exponent greater than 0.5, for the stochastic activity was persistent and Fc data of the past and future were positively correlated. In contrast, a closed-loop process predominates Fc control in the long-term region. The stochastic activity with a scaling exponent smaller than 0.5 was anti-persistent, for Fc data of the past and future were negatively correlated (Collins and De Luca, 1993, 1995). This stochastic model of Fc is reminiscent of a continuum of the control regime of a visuomotor act ranging from feedback (closed-loop) to feedforward (open-loop) (Slifkin et al., 2000). Central to this interpretation is that the SDA variables of Fc in the LF-EA condition indicated a scheme switch of open- and closed-loop controls for static force control, as compared with those of the EA and control feedback modes. The smaller dt_c and $<dF_c^2>$ in the LF-EA condition (**Table 2**) reflected a drift in the equilibrium point of Fc control toward a closed-loop process (Kurz et al., 2013; Coubard et al., 2014; Toosizadeh et al., 2015). The interval of short-term stochastic activity governed by the open-loop regime (dt_c) was significantly shortened, and feedback control was called into play when a smaller degree of Fc ($<dF_c^2>$) took place. The experimental observation was congruent with reductions in the D_s and scaling exponent (H_s). After deconditioning of the feedforward mechanism, force-tracking in the LF-EA condition was more dependent on the feedback mechanism, with a functional benefit of superior task accuracy (**Table 1**). Hence, the prevailing use of the feedback process was conceptually in agreement with the perceptual narrowing (Easterbrook, 1959) and enhanced attentive control (Boussaoud and Kermadi, 1997; Jueptner and Weiller, 1998; Shirzad and Van der Loos, 2012) reported in behavioral studies.

Due to the smaller Fc with greater complexity (**Table 1**), the participants could develop fine-grained force-scaling with a richer correction strategy in the LF-EA condition with the feedback-prone process (Vaillancourt et al., 2002; Chen et al., 2013). Several lines of indirect evidence have shown that modulation of Fc dynamics in the LF-EA condition resembles characteristic changes in Fc after motor practice (Deutsch and Newell, 2004; Hwang et al., 2013). Moreover, the increase in the MF of Fc and flattening of the spectral DOF support of LF-EA indicated that the participants could increase the number of corrective attempts with abundant exploratory efforts to remedy tracking deviations. Gating the high-frequency components brought about these performance benefits because VEs above 0.8 Hz are too fast to be corrected. The interval to accomplish visuomotor correction in humans is at least 1 s (Navas and Stark, 1968; Miall et al., 1985), and primates cannot follow the full excursion of a target higher than 0.9 Hz with the feedback process (Miall et al., 1986). If visual EA contains information that cannot be rapidly responded with the feedback process, lag-induced feedback instability taxes attentional resources with processing visuomotor information that is irrelevant to task success. That is why the task accuracy, Fc properties, and SDA variables between EA and LF-EA were distinct.

Variations in Motor Unit Discharge for Low-Frequency Error Amplification

The adaptation of the Fc dynamic originated from variations in the probability structures of the MU discharges. Physiologically, the decrease in the size of Fc with LF-EA was correspondent with the decrease in RMS of the mean discharge rate (**Table 3B**) rather than CV-ISI$_{\mathrm{mean}}$ (**Table 3A**). It is known that modeling of the mean discharge rate with a pooling process could accentuate synaptic inputs common to a population of active motoneurons but also attenuate the role of independent synaptic inputs to motoneurons (Farina and Negro, 2015; Farina et al., 2016). Therefore, the amplitude modulation of the mean discharge rate implies that LF-EA could effectively reduce the variations in the common input to a muscle. The observed influence of the common input confirms the model-based conjectures, implying a reduction in the intrinsic neuromotor noises at the motoneuronal level with EA (Wei et al., 2005; Hasson et al., 2016; Williams et al., 2016). The modulation of the size of the mean discharge rate was critical to the increase in task precision in the LF-EA condition (**Figure 7**). However, the reduction in the size of Fc with LF-EA is unlikely to have resulted from modulation of independent synaptic inputs to motoneurons because CV-ISI$_{\mathrm{mean}}$, which highlights the influence of synaptic inputs to motoneurons that differ from those that are common, was insensitive to feedback mode. On the other hand, the enhancement of the complexity of Fc in the LF-EA condition (**Table 1**) was nicely compatible with the irregularity of the increases in MU discharge (IR$_{\mathrm{GAV}}$) (**Table 3A**). However, the structures of the mean discharge rate, such as SampEn and DOF (**Table 3B**), did not well index the change in the complexity of Fc in the LF-EA condition. In addition to some unidentified organizational discharge activities, the viscous resistances of the musculotendon system attenuate the transmission of high-frequency neural drive to a muscle (Günther et al., 2007). This non-linearity often complicates the discharge–force relationship.

Variation in Corticospinal Coupling for Low-Frequency Error Amplification

Instead, superior task accuracy and force steadiness in the LF-EA condition were associated with increased EEG–EMG coherence in the beta range (**Figure 4**). An increase in the beta-range EEG–EMG coherence represents greater synchronization of cortical activity to regulate common spinal inputs, a neural marker of steady-state motor output during static contraction (Perez et al., 2006; Kristeva et al., 2007). The beta-range CMC is greatly reduced when a force task is not steady (Salenius et al., 1997; Boonstra et al., 2009). Previous studies have reported that repetitive training can increase the precision of control in a static force task, in association with enhancement of beta-range CMC (Perez et al., 2006; Witte et al., 2007; Larsen et al., 2016). From all the neural sequelae, the enhanced beta-range CMC should contribute to a smaller size of discharge variability with enhanced complexity (**Table 3** and **Figure 7**) and fine-grained force scaling with the feedback-prone process (**Tables 1**, **2**) in the LF-EA condition. Since the beta-range corticomuscular rhythm is modifiable to peripheral sensory afferents (Riddle and Baker, 2005; Lalo et al., 2007), the precise force control in the LF-EA condition might be attributable to the reduction of the cognitive load of processing task-irrelevant error information, which would facilitate rapid integration of the visual and somatosensory information.

Methodological Issues

A contrasting approach to enhance static force control is stochastic resonance (Mendez-Balbuena et al., 2012; Trenado et al., 2014). In addition to an increase in corticomuscular synchronization at 13–35 Hz, a better force precision with a return map of concentrated error points was noted following application of an optimal mechanical Gaussian noise. The task improvement was hypothesized to detect subthreshold sensory signals in the peripheral receptors, pertaining to noise-enhanced sensorimotor integration. However, stochastic resonance differs with the use of LF-EA, which minimizes cognitive load to process functionally irreverent noises. The return map with concentrated error points speaks for additional functional benefits for removal of high-frequency error components (noises) prior to EA (**Figure 5A**). Besides, one matter of concern is the decomposition of multi-electrode surface EMG. Although we cannot deny the likelihood of a small decomposition error (Piotrkiewicz and Türker, 2017), the state-of-the-art decomposition algorithm is a trade-off to capture the discharge variability among MUs and the force–discharge relation, based on a relatively large number of active MUs. To be rigorous, we applied a "reconstruct-and-test" procedure (Nawab et al., 2010; De Luca et al., 2015) to support the accuracy of the obtained identifications (91.2–97.1%) (De Luca et al., 2006; Nawab et al., 2010; Chen et al., 2017a,b; Hwang et al., 2017). The use of multi-channel surface EMG to explore MU behaviors has gained popularity in recent studies (Hu et al., 2014; Laine et al., 2015; Contessa et al., 2016; Chen et al., 2017a,b). In particular, the inconsistent changes in the complexity measures between IR$_{\mathrm{GAV}}$ and the SampEn of the mean discharge rate with LF-EA (**Tables 3A,B**) reinforce the role of decomposition in revealing diverse fractal myoelectric manifestations. A simulated EMG study showed that the fractal characteristic of surface EMG, which accounts for pooled MU behaviors, is jointly subject to variations in the CV of the discharge rate and the degree of MU synchronization (Mesin et al., 2016). Hence, fractal changes in the surface EMG are evident during fatiguing (Ravier et al., 2005) or higher-force ($>$25% MVC) contractions (Beretta-Piccoli et al., 2018). When the CV of the ISI is not expected to change, the discharge irregularity of a single MU such as IR$_{\mathrm{GAV}}$ could be masked by the interference pattern of surface EMG (or the mean discharge rate). Next, a low-pass filtering effect was likely to be effective only in the visual EA condition, though this study did not examine tracking performance in the non-EA condition. According to our preliminary study in healthy adults (n = 14), the task error of the control condition (0.467 ± 0.029% MVC) did not differ significantly from the task error in the condition of low-frequency feedback without EA (0.446 ± 0.039% MVC) (t_{13} = 0.648, p = 0.528) (unpublished data). Therefore, low-frequency error signals without amplification could not facilitate feedback control, and the performance benefit and paradigm shift were evident only in the LF-EA condition. Also, the selection of a low pass threshold of 0.8 Hz for EA was empirically determined. The time period necessary for the detection of visual information and motor adjustments was at least 150 ms

(Miall et al., 1985, 1986), which prevented the participants from timely correcting fast-oscillatory error components. However, on account of the slow tracking response and perceptual motor conflict, the excessive removal of high-frequency error components is disadvantageous to task precision due to the lack of ample information for remedying tracking deviations. The effects of various low-pass thresholds on EA feedback will require further investigation.

CONCLUSION

Virtual potentiation of low-frequency errors below 0.8 Hz for visual feedback more effectively improves task performance than does traditional EA or real visual feedback in a static isometric task. The selective gating of high-frequency error components reduces the task-irrelevant information in the visual feedback that cannot be rapidly processed with a feedback process. This study reveals that the amplification of low-frequency error information could increase the sensitivity to detect Fc and facilitate the state shift to the negative feedback process for force stabilization. The behavior adaptations arise from the promotion of effective corticospinal interactions to enhance discharge irregularity and minimize fluctuations of the common drive to a muscle.

AUTHOR CONTRIBUTIONS

I-SH and Y-CC: conception or design of the work. C-LH and Z-RY: acquisition. I-SH and C-LH: analysis. Y-CC, I-SH, and Y-TL: interpretation of data. I-SH and Y-CC: drafted the work or revised it critically for important intellectual content. Y-CC: final approval of the version to be published. Y-CC and I-SH: agreement to be accountable for all aspects of the work in ensuring that questions related to the accuracy or integrity of any part of the work are appropriately investigated and resolved.

FUNDING

This research was supported by grants from the Ministry of Science and Technology, Taiwan, R.O.C., under grant nos. MOST 105-2410-H-040-009 and MOST 104-2314-B-006 -016 -MY3.

REFERENCES

Abdollahi, F., Case Lazarro, E. D., Listenberger, M., Kenyon, R. V., Kovic, M., Bogey, R. A., et al. (2014). Error augmentation enhancing arm recovery in individuals with chronic stroke: a randomized crossover design. *Neurorehabil. Neural Repair* 28, 120–128. doi: 10.1177/1545968313498649

Baweja, H. S., Patel, B. K., Martinkewiz, J. D., Vu, J., and Christou, E. A. (2009). Removal of visual feedback alters muscle activity and reduces force variability during constant isometric contractions. *Exp. Brain Res.* 197, 35–47. doi: 10.1007/s00221-009-1883-5

Bays, P. M., and Wolpert, D. M. (2007). Computational principles of sensorimotor control that minimize uncertainty and variability. *J. Physiol.* 578, 387–396. doi: 10.1113/jphysiol.2006.120121

Beretta-Piccoli, M., Boccia, G., Ponti, T., Clijsen, R., Barbero, M., and Cescon, C. (2018). Relationship between isometric muscle force and fractal dimension of surface electromyogram. *Biomed. Res. Int.* 2018, 5373846. doi: 10.1155/2018/5373846

Boonstra, T. W., van Wijk, B. C., Praamstra, P., and Daffertshofer, A. (2009). Corticomuscular and bilateral EMG coherence reflect distinct aspects of neural synchronization. *Neurosci. Lett.* 463, 17–21. doi: 10.1016/j.neulet.2009.07.043

Bouchard, A. E., Corriveau, H., and Milot, M. H. (2015). Comparison of haptic guidance and error amplification robotic trainings for the learning of a timing-based motor task by healthy seniors. *Front. Syst. Neurosci.* 9:52. doi: 10.3389/fnsys.2015.00052

Bouchard, A. E., Corriveau, H., and Milot, M. H. (2017). A single robotic session that guides or increases movement error in survivors post-chronic stroke: which intervention is best to boost the learning of a timing task? *Disabil. Rehabil.* 39, 1607–1614. doi: 10.1080/09638288.2016.1205151

Boussaoud, D., and Kermadi, I. (1997). The primate striatum: neuronal activity in relation to spatial attention versus motor preparation. *Eur. J. Neurosci.* 9, 2152–2168.

Chen, Y. C., Lin, L. L., Lin, Y. T., Hu, C. L., and Hwang, I. S. (2017a). Variations in static force control and motor unit behavior with error amplification feedback in the elderly. *Front. Hum. Neurosci.* 11:538. doi: 10.3389/fnhum.2017.00538

Chen, Y. C., Lin, Y. T., Chang, G. C., and Hwang, I. S. (2017b). Paradigm shifts in voluntary force control and motor unit behaviors with the manipulated size of visual error perception. *Front. Physiol.* 8:140. doi: 10.3389/fphys.2017.00140

Chen, Y. C., Lin, Y. T., Huang, C. T., Shih, C. L., Yang, Z. R., and Hwang, I. S. (2013). Trajectory adjustments underlying task-specific intermittent force behaviors and muscular rhythms. *PLoS One* 8:e74273. doi: 10.1371/journal.pone.0074273

Collins, J. J., and De Luca, C. J. (1993). Open-loop and closed-loop control of posture: a random-walk analysis of center-of-pressure trajectories. *Exp. Brain Res.* 95, 308–318. doi: 10.1007/bf00229788

Collins, J. J., and De Luca, C. J. (1995). The effects of visual input on open-loop and closed-loop postural control mechanisms. *Exp. Brain Res.* 103, 151–163. doi: 10.1007/bf00241972

Contessa, P., De Luca, C. J., and Kline, J. C. (2016). The compensatory interaction between motor unit firing behavior and muscle force during fatigue. *J. Neurophysiol.* 116, 1579–1585. doi: 10.1152/jn.00347.2016

Coubard, O. A., Ferrufino, L., Nonaka, T., Zelada, O., Bril, B., and Dietrich, G. (2014). One month of contemporary dance modulates fractal posture in aging. *Front. Aging Neurosci.* 6:17. doi: 10.3389/fnagi.2014.00017

Davies, R. M., Gerstein, G. L., and Baker, S. N. (2006). Measurement of time-dependent changes in the irregularity of neural spiking. *J. Neurophysiol.* 96, 906–918. doi: 10.1152/jn.01030.2005

De Luca, C. J., Adam, A., Wotiz, R., Gilmore, L. D., and Nawab, S. H. (2006). Decomposition of surface EMG signals. *J. Neurophysiol.* 96, 1646–1657. doi: 10.1152/jn.00009.2006

De Luca, C. J., Kline, J. C., and Contessa, P. (2014). Transposed firing activation of motor units. *J. Neurophysiol.* 112, 962–970. doi: 10.1152/jn.00619.2013

De Luca, C. J., LeFever, R. S., McCue, M. P., and Xenakis, A. P. (1982). Control scheme governing concurrently active human motor units during voluntary contractions. *J. Physiol.* 329, 129–142. doi: 10.1113/jphysiol.1982.sp014294

De Luca, C. J., Nawab, S. H., and Kline, J. C. (2015). Clarification of methods used to validate surface EMG decomposition algorithms as described by Farina et al. (2014). *J. Appl. Physiol.* 118:1084. doi: 10.1152/japplphysiol.00061.2015

Delignières, D., Torre, K., and Bernard, P. L. (2011). Transition from persistent to anti-persistent correlations in postural sway indicates velocity-based control. *PLoS Comput. Biol.* 7:e1001089. doi: 10.1371/journal.pcbi.1001089

Deutsch, K. M., and Newell, K. M. (2004). Changes in the structure of children's isometric force variability with practice. *J. Exp. Child Psychol.* 88, 319–333. doi: 10.1016/j.jecp.2004.04.003

Domingo, A., and Ferris, D. P. (2010). The effects of error augmentation on learning to walk on a narrow balance beam. *Exp. Brain Res.* 206, 359–370. doi: 10.1007/s00221-010-2409-x

Easterbrook, J. A. (1959). The effect of emotion on cue utilization and the organization of behavior. *Psychol. Rev.* 66, 183–193. doi: 10.1037/h0047707

Farina, D., and Negro, F. (2015). Common synaptic input to motor neurons, motor unit synchronization, and force control. *Exerc. Sport Sci. Rev.* 43, 23–33. doi: 10.1249/JES.0000000000000032

Farina, D., Negro, F., Muceli, S., and Enoka, R. M. (2016). Principles of motor unit physiology evolve with advances in technology. *Physiology* 31, 83–94. doi: 10.1152/physiol.00040.2015

Frank, T. D., Friedrich, R., and Beek, P. J. (2006). Stochastic order parameter equation of isometric force production revealed by drift-diffusion estimates. *Phys. Rev. E Stat. Nonlin. Soft. Matter Phys.* 74:051905. doi: 10.1103/PhysRevE.74.051905

Günther, M., Schmitt, S., and Wank, V. (2007). High-frequency oscillations as a consequence of neglected serial damping in Hill-type muscle models. *Biol. Cybern.* 97, 63–79. doi: 10.1007/s00422-007-0160-6

Hasson, C. J., Zhang, Z., Abe, M. O., and Sternad, D. (2016). Neuromotor noise is malleable by amplifying perceived errors. *PLoS Comput. Biol.* 12:e1005044. doi: 10.1371/journal.pcbi.1005044

Hong, S. L., and Newell, K. M. (2008). Visual information gain and the regulation of constant force levels. *Exp. Brain Res.* 189, 61–69. doi: 10.1007/s00221-008-1403-z

Hu, X., Rymer, W. Z., and Suresh, N. L. (2013). Assessment of validity of a high-yield surface electromyogram decomposition. *J. Neuroeng. Rehabil.* 10:99. doi: 10.1186/1743-0003-10-99

Hu, X., Rymer, W. Z., and Suresh, N. L. (2014). Accuracy assessment of a surface electromyogram decomposition system in human first dorsal interosseus muscle. *J. Neural Eng.* 11:026007. doi: 10.1088/1741-2560/11/2/026007

Hwang, I. S., Huang, C. T., Yang, J. F., and Guo, M. C. (2013). Characterization of information-based learning benefits with submovement dynamics and muscular rhythmicity. *PLoS One* 8:e82920. doi: 10.1371/journal.pone.0082920

Hwang, I. S., Lin, Y. T., Huang, W. M., Yang, Z. R., Hu, C. L., and Chen, Y. C. (2017). Alterations in neural control of constant isometric contraction with the size of error feedback. *PLoS One* 12:e0170824. doi: 10.1371/journal.pone.0170824

Israely, S., and Carmeli, E. (2016). Error augmentation as a possible technique for improving upper extremity motor performance after a stroke - a systematic review. *Top. Stroke Rehabil.* 23, 116–125. doi: 10.1179/1945511915Y.0000000007

Jueptner, M., and Weiller, C. (1998). A review of differences between basal ganglia and cerebellar control of movements as revealed by functional imaging studies. *Brain* 121, 1437–1449. doi: 10.1093/brain/121.8.1437

Kao, P. C., Srivastava, S., Higginson, J. S., Agrawal, S. K., and Scholz, J. P. (2015). Short-term performance-based error-augmentation versus error-reduction robotic gait training for individuals with chronic stroke: a Pilot Study. *Phys. Med. Rehabil. Int.* 2:1066.

King, A. C., and Newell, K. M. (2015). Selective visual scaling of time-scale processes facilitates broadband learning of isometric force frequency tracking. *Atten. Percept. Psychophys.* 77, 2507–2518. doi: 10.3758/s13414-015-0936-z

Kristeva, R., Patino, L., and Omlor, W. (2007). Beta-range cortical motor spectral power and corticomuscular coherence as a mechanism for effective corticospinal interaction during steady-state motor output. *Neuroimage* 36, 785–792. doi: 10.1016/j.neuroimage.2007.03.025

Kristeva-Feige, R., Fritsch, C., Timmer, J., and Lücking, C. H. (2002). Effects of attention and precision of exerted force on beta range EEG–EMG synchronization during a maintained motor contraction task. *Clin. Neurophysiol.* 113, 124–131. doi: 10.1016/S1388-2457(01)00722-2

Kurz, I., Oddsson, L., and Melzer, I. (2013). Characteristics of balance control in older persons who fall with injury–a prospective study. *J. Electromyogr. Kinesiol.* 23, 814–819. doi: 10.1016/j.jelekin.2013.04.001

Laine, C. M., Martinez-Valdes, E., Falla, D., Mayer, F., and Farina, D. (2015). Motor neuron pools of synergistic thigh muscles share most of their synaptic input. *J. Neurosci.* 35, 12207–12216. doi: 10.1523/JNEUROSCI.0240-15.2015

Lalo, E., Gilbertson, T., Doyle, L., Di Lazzaro, V., Cioni, B., and Brown, P. (2007). Phasic increases in cortical beta activity are associated with alterations in sensory processing in the human. *Exp. Brain Res.* 177, 137–145. doi: 10.1007/s00221-006-0655-8

Larsen, L. H., Jensen, T., Christensen, M. S., Lundbye-Jensen, J., Langberg, H., and Nielsen, J. B. (2016). Changes in corticospinal drive to spinal motoneurones following tablet-based practice of manual dexterity. *Physiol. Rep.* 4:e12684. doi: 10.14814/phy2.12684

Lin, Y. T., Kuo, C. H., and Hwang, I. S. (2014). Fatigue effect on low-frequency force fluctuations and muscular oscillations during rhythmic isometric contraction. *PLoS One* 9:e85578. doi: 10.1371/journal.pone.0085578

Lipowski, Z. J. (1975). Sensory and information inputs overload: behavioral effects. *Compr. Psychiatry* 16, 199–221. doi: 10.1016/0010-440X(75)90047-4

Mandelbrot, B. B., and van Ness, J. W. (1968). Fractional Brownian motions, fractional noises and applications. *SIAM Rev.* 10, 422–437. doi: 10.1137/1010093

Mendez-Balbuena, I., Manjarrez, E., Schulte-Mönting, J., Huethe, F., Tapia, J. A., Hepp-Reymond, M. C., et al. (2012). Improved sensorimotor performance via stochastic resonance. *J. Neurosci.* 32, 12612–12618. doi: 10.1523/JNEUROSCI.0680-12.2012

Mesin, L., Dardanello, D., Rainoldi, A., and Boccia, G. (2016). Motor unit firing rates and synchronisation affect the fractal dimension of simulated surface electromyogram during isometric/isotonic contraction of vastus lateralis muscle. *Med. Eng. Phys.* 38, 1530–1533. doi: 10.1016/j.medengphy.2016.09.022

Miall, R. C., Weir, D. J., and Stein, J. F. (1985). Visuomotor tracking with delayed visual feedback. *Neuroscience* 16, 511–520. doi: 10.1016/0306-4522(85)90189-7

Miall, R. C., Weir, D. J., and Stein, J. F. (1986). Manual tracking of visual targets by trained monkeys. *Behav. Brain Res.* 20, 185–201. doi: 10.1016/0166-4328(86)90003-3

Miall, R. C., Weir, D. J., and Stein, J. F. (1993). Intermittency in human manual tracking tasks. *J. Mot. Behav.* 25, 53–63. doi: 10.1080/00222895.1993.9941639

Navas, F., and Stark, L. (1968). Sampling or intermittency in hand control system dynamics. *Biophys. J.* 8, 252–302. doi: 10.1016/S0006-3495(68)86488-4

Nawab, S. H., Chang, S. S., and De Luca, C. J. (2010). High-yield decomposition of surface EMG signals. *Clin. Neurophysiol.* 121, 1602–1615. doi: 10.1016/j.clinph.2009.11.092

Nawab, S. H., Wotiz, R., and De Luca, C. J. (2004). "Resolving EMG pulse superpositions via utility maximization," in *Proceedings of the 8th World Multiconf. Systemics, Cybernetics, Informatics*, (Orlando, FL), 233–236.

Ogawa, K., and Imamizu, H. (2013). Human sensorimotor cortex represents conflicting visuomotor mappings. *J. Neurosci.* 33, 6412–6422. doi: 10.1523/JNEUROSCI.4661-12.2013

Omlor, W., Patino, L., Mendez-Balbuena, I., Schulte-Mönting, J., and Kristeva, R. (2011). Corticospinal beta-range coherence is highly dependent on the pre-stationary motor state. *J. Neurosci.* 31, 8037–8045. doi: 10.1523/JNEUROSCI.4153-10.2011

Patton, J. L., Stoykov, M. E., Kovic, M., and Mussa-Ivaldi, F. A. (2006). Evaluation of robotic training forces that either enhance or reduce error in chronic hemiparetic stroke survivors. *Exp. Brain Res.* 168, 368–383. doi: 10.1007/s00221-005-0097-8

Perez, M. A., Lundbye-Jensen, J., and Nielsen, J. B. (2006). Changes in corticospinal drive to spinal motoneurones following visuo-motor skill learning in humans. *J. Physiol.* 573, 843–855. doi: 10.1113/jphysiol.2006.105361

Pethick, J., Winter, S. L., and Burnley, M. (2015). Fatigue reduces the complexity of knee extensor torque fluctuations during maximal and submaximal intermittent isometric contractions in man. *J. Physiol.* 593, 2085–2096. doi: 10.1113/jphysiol.2015.284380

Pew, R. W. (1974). "Human perceptual-motor performance," in *Human Information Processing: Tutorials in Performance and Cognition*, ed. B. H. Kantowitz (Hills-dale: Erlbaum), 1–39.

Piotrkiewicz, M., and Türker, K. S. (2017). Onion skin or common drive? *Front. Cell Neurosci.* 11:2. doi: 10.3389/fncel.2017.00002

Ravier, P., Buttelli, O., Jennane, R., and Couratier, P. (2005). An EMG fractal indicator having different sensitivities to changes in force and muscle fatigue during voluntary static muscle contractions. *J. Electromyogr. Kinesiol.* 15, 210–221. doi: 10.1016/j.jelekin.2004.08.008

Reisman, D. S., McLean, H., Keller, J., Danks, K. A., and Bastian, A. J. (2013). Repeated split-belt treadmill training improves poststroke step length asymmetry. *Neurorehabil. Neural Repair* 27, 460–468. doi: 10.1177/1545968312474118

Richman, J. S., and Moorman, J. R. (2000). Physiological time-series analysis using approximate entropy and sample entropy. *Am. J. Physiol. Heart Circ. Physiol.* 278, H2039–H2049. doi: 10.1152/ajpheart.2000.278.6.H2039

Riddle, C. N., and Baker, S. N. (2005). Manipulation of peripheral neural feedback loops alters human corticomuscular coherence. *J. Physiol.* 566, 625–639. doi: 10.1113/jphysiol.2005.089607

Salenius, S., Portin, K., Kajola, M., Salmelin, R., and Hari, R. (1997). Cortical control of human motoneuron firing during isometric contraction. *J. Neurophysiol.* 77, 3401–3405. doi: 10.1152/jn.1997.77.6.3401

Shenker, S. J. (1982). Scaling behavior in a map of a circle onto itself: empirical results. *Physica D* 5, 405–411. doi: 10.1016/0167-2789(82)90033-1

Shirzad, N., and Van der Loos, H. F. (2012). Error amplification to promote motor learning and motivation in therapy robotics. *Conf. Proc. IEEE Eng. Med. Biol. Soc.* 2012, 3907–3910. doi: 10.1109/EMBC.2012.6346821

Slifkin, A. B., Vaillancourt, D. E., and Newell, K. M. (2000). Intermittency in the control of continuous force production. *J. Neurophysiol.* 84, 1708–1718. doi: 10.1152/jn.2000.84.4.1708

Sosnoff, J. J., Valantine, A. D., and Newell, K. M. (2006). Independence between the amount and structure of variability at low force levels. *Neurosci. Lett.* 392, 165–169. doi: 10.1016/j.neulet.2005.09.010

Sung, C., and O'Malley, M. K. (2011). Effect of progressive visual error amplification on human motor adaptation. *IEEE. Int. Conf. Rehabil. Robot.* 2011:5975399. doi: 10.1109/ICORR.2011.5975399

Toosizadeh, N., Mohler, J., Wendel, C., and Najafi, B. (2015). Influences of frailty syndrome on open-loop and closed-loop postural control strategy. *Gerontology* 61, 51–60. doi: 10.1159/000362549

Trenado, C., Mendez-Balbuena, I., Manjarrez, E., Huethe, F., Schulte-Mönting, J., Feige, B., et al. (2014). Enhanced corticomuscular coherence by external stochastic noise. *Front. Hum. Neurosci.* 8:325. doi: 10.3389/fnhum.2014.00325

Vaillancourt, D. E., Larsson, L., and Newell, K. M. (2002). Time-dependent structure in the discharge rate of human motor units. *Clin. Neurophysiol.* 113, 1325–1338. doi: 10.1016/S1388-2457(02)00167-0

Wei, Y., Bajaj, P., Scheidt, R., and Patton, J. L. (2005). "Visual error augmentation for enhancing motor learning and rehabilitative relearning," in *Proceedings of the IEEE International Conf. on Rehabil Robotics*, (Chicago: IEEE), 505–510.

Williams, C. K., Tremblay, L., and Carnahan, H. (2016). It pays to go off-track: practicing with error-augmenting haptic feedback facilitates learning of a curve-tracing task. *Front. Psychol.* 7:2010. doi: 10.3389/fpsyg.2016.02010

Witham, C. L., and Baker, S. N. (2007). Network oscillations and intrinsic spiking rhythmicity do not covary in monkey sensorimotor areas. *J. Physiol.* 580, 801–814. doi: 10.1113/jphysiol.2006.124503

Witte, M., Patino, L., Andrykiewicz, A., Hepp-Reymond, M. C., and Kristeva, R. (2007). Modulation of human corticomuscular beta-range coherence with low-level static forces. *Eur. J. Neurosci.* 26, 3564–3570. doi: 10.1111/j.1460-9568.2007.05942.x

Conflict of Interest Statement: The authors declare that the research was conducted in the absence of any commercial or financial relationships that could be construed as a potential conflict of interest.

Copyright © 2019 Hwang, Hu, Yang, Lin and Chen. This is an open-access article distributed under the terms of the Creative Commons Attribution License (CC BY). The use, distribution or reproduction in other forums is permitted, provided the original author(s) and the copyright owner(s) are credited and that the original publication in this journal is cited, in accordance with accepted academic practice. No use, distribution or reproduction is permitted which does not comply with these terms.

frontiers
in Physiology

ORIGINAL RESEARCH
published: 03 September 2018
doi: 10.3389/fphys.2018.01216

Automated Spatial Pattern Analysis for Identification of Foot Arch Height From 2D Foot Prints

Julien Lucas[1], Kinda Khalaf[2], James Charles[3,4], Jorge J. G. Leandro[5] and Herbert F. Jelinek[6]*

[1] Department of Biology and Computer Science, University of Poitiers, Poitiers, France, [2] Department of Biomedical Engineering, Khalifa University of Science and Technology, Abu Dhabi, United Arab Emirates, [3] Institute of Koorie Education, Deakin University, Waurn Ponds, VIC, Australia, [4] School of Medicine, Deakin University, Waurn Ponds, VIC, Australia, [5] Institute of Mathematics and Statistics, University of São Paulo, São Paulo, Brazil, [6] School of Community Health, Charles Sturt University, Albury, NSW, Australia

Arch height is an important determinant for the risk of foot pathology, especially in an aging population. Current methods for analyzing footprints require substantial manual processing time. The current research investigated automated determination of foot type based on features derived from the Gabor wavelet utilizing digitized footprints to allow timely assessment of foot type and focused intervention. Two hundred and eighty footprints were collected, and area, perimeter, curvature, circularity, 2nd wavelet moment, mean bending energy (MBE), and entropy were determined using in house developed MATLAB codes. The results were compared to the gold standard using Spearman's Correlation coefficient and multiple linear regression models with significance set at 0.05. The proposed approach found MBE combined with foot perimeter to give the best results as shown by ANOVA ($F_{(2,211)} = 10.18$, $p < 0.0001$) with the mean ± *SD* of low, normal, and high arch being, respectively, 0.26 ± 0.025,.24 ± 0.021, and 0.23 ± 0.024. A clinical review of the new cut off values, as set by the first and the third quartiles of our sample, lead to reliability up to 87%. Our results suggest that automated wavelet-based foot type classification of 2D binary images of the plantar surface of the foot is comparable to current state-of-the-art methods providing a cost and time effective tool suitable for clinical diagnostics.

Keywords: non-linear dynamics, complexity, wavelet analysis, bending energy, foot arch height

OPEN ACCESS

Edited by:
Sladjana Z. Spasić,
University of Belgrade, Serbia

Reviewed by:
Carlos D. Maciel,
Universidade de São Paulo, Brazil
Reinaldo Roberto Rosa,
Instituto Nacional de Pesquisas Espaciais (INPE), Brazil

***Correspondence:**
Herbert F. Jelinek
hjelinek@csu.edu.au

Specialty section:
This article was submitted to Fractal Physiology, a section of the journal Frontiers in Physiology

Received: *19 June 2018*
Accepted: *13 August 2018*
Published: *03 September 2018*

Citation:
Lucas J, Khalaf K, Charles J, Leandro JJG and Jelinek HF (2018) Automated Spatial Pattern Analysis for Identification of Foot Arch Height From 2D Foot Prints. Front. Physiol. 9:1216. doi: 10.3389/fphys.2018.01216

INTRODUCTION

The arch height of the foot has long been recognized as a key parameter in foot type classification, and is considered an important prediction and diagnostic tool in lower limb pathology. Some studies have shown that high and low arched foot types can alter plantar pressures as compared to a foot with normal arch height (Van Schie and Boulton, 2000). High arched foot type has also been found to be associated with increased levels of foot discomfort and pain (Burns et al., 2005). Due to differences in repeatability and reliability, as well as ease of use, no single method has been fully accepted for objective foot arch assessment. Various invasive, time consuming, and costly measures exist and have been tested as clinical tools to determine arch height (Hawes et al., 1992), but all require either extensive manual pre-processing or post-processing of the images, before results can be obtained. Several non-invasive methods based on footprint images have also been proposed as useful measures in gait and movement analysis (Johnston, 2014). However, these methods require extensive processing, are very time consuming and largely underutilized by clinicians and researchers. In the current paper, we propose an automated method based on Gabor wavelet results of 2- dimensional footprints and compare these to the current gold standard assessment methodology. Wavelet analysis simplifies the determination of the arch index for clinicians by requiring only the ink foot print without toes to be uploaded to the script. The Gabor-wavelet analysis is a common tool used in 2-dimensional pattern analysis as it allows extraction of a number of features that describe a pattern. In the current research we have determined the circularity, histogram of orientation, and mean bending energy (Costa and Cesar, 2001 #623). These features describe the characteristics of the footprint. For example the circularity feature measures the degree of departure from a circle and is therefore sensitive to the medial part of the footprint, which has a straighter appearance in flatfoot and is more rounded closer to a circle with normal arch height. Arch height is a function of several factors, including a complex foot structure of 26 bones, 16 joints, and more than 100 muscles, tendons, and ligaments. The structure and function of the lower limb ensures support and stability in gait, as well as good posture for balance and movement. The skeletal, musculature, and ligamentous components of the foot lead to the formation of the three plantar arches (Goonetilleke, 2012 #15208), which provide flexibility and weight bearing support (**Figure 1**) (Manley and Solomon, 1979, Parker et al., 2015, Gwani et al., 2017). The foot arch of most importance to function and gait is the medial longitudinal arch (MLA), as this arch provides most of the elasticity and stability during gait. The focus of this paper is the development of new innovative, less time consuming method to calculate the height of this arch to assess pathology.

Medial longitudinal arch height is also important in shock absorption, providing support while walking (Ghasemi et al., 2016). Abnormal arch height such as high arches, flat feet or fallen arches (**Figure 2**) can be responsible for discomfort and more serious pathology, such as, lumbar lordosis, foot eversion, and knees injuries (Nigg et al., 1993), plantar fasciitis, tibialis posterior tendon dysfunction (Johnson and Strom, 1989; Schepsis et al., 1991).

Different methods to evaluate arch height exist and have been verified in several studies. The current gold standard method adopted in clinical practice is the “Arch Index” proposed by Cavanagh and Rodgers (1987). The accuracy of this method has been verified by experts in examining arch height (Menz and Munteanu, 2006). However, the C&R method is difficult to use and time consuming. Clarke’s Arch Angle (Clarke, 1933), Index of Irwin (1937), Truncated Arch Index and the Arch Length Index (Hawes et al., 1992) have been proposed as alternatives but have similar shortcomings and are therefore not used routinely in clinical practice. Automated feature analysis methods with Gabor Wavelet-based feature extraction have been applied in diverse clinical areas and have shown promise in identification of plagiocephaly, proliferative retinopathy, brain tumor detection, and complex image analysis (Jelinek et al., 2003; Jelinek et al., 2014; Nagtode et al., 2016). Therefore, the current paper explores the use of automated images analysis for the classification of footprints within a clinical environment and for research purposes. There is a need to develop a computer-based method to establish arch height which is less time consuming and likely to be used by clinicians and researchers. The new innovative approach developed by the authors is an automated, self-contained computer-based analysis method using digitized 2D footprints. The methodology is based on features derived from geometrical characteristics and the use of the Gabor wavelet.

MATERIALS AND METHODS

Footprints for analysis were collected from 143 volunteers as part of a foot health screening. MLA height index was determined using a pedograph footprint system (Welton, 1992). A sample of two hundred and eighty ink footprints were collected from the volunteers upon informed and written signed consent. The foot ink prints were taken with a standard Ruckgaber Orthopadie ink plate developed by Ruckgaber Bruggemann[1]. Participants volunteered from three different regions of Australia and were included if they could walk unassisted and have no lower limb pathology, footprints were collected with a standard pedograph of the left and right foot. Ethics approval was granted from the Human Research Ethics Committee (HREC) at the University of Newcastle (Protocol Number 2012–0385) and all participants provided written consent following an information session Initially, the arch index proposed by C&R, representing the current gold standard method, was determined. To obtain the Arch Index (AI) requires a line to be drawn from the middle of the heel to the center of the second toe of the foot. Then the toeless footprint is divided into three equal parts by dividing the longitudinal line into three equal parts through drawing two lines perpendicular to the central longitudinal line (**Figure 3**). The footprint image is then imported into the Analyzing Digital Image analyzing program (ADI, University of Massachusetts Amherst, MA, United States) and the outline of the footprint is traced.

The AI is determined by calculating the area of the middle segment (area of section B) and this is divided by the area of the whole foot (area of section A, B, and C), i.e., $B/(A + B + C)$. A low arch is indicated by an AI being equal to or higher than 0.26, whereas a high arch has an AI of equal or lower than 0.21 (Cavanagh and Rodgers, 1987). To calculate the proposed new features, the outline of the footprints was manually traced and then scanned into the computer for further analysis. An Image Editor tool (IrfanView) was used to remove the toes from the image. All prints were analyzed using an in-house algorithm written in MATLAB (MathWorks, MathWorks Inc., New York, NY, United States). Binary images were obtained by applying image thresholding and Sobel operator to the gray scale image. Then the binary images were uploaded as a batch file to the Feature Analysis Algorithm, to determine perimeter, area, curvature, circularity, 2nd moment, entropy, and bending energy

---

[1] http://ruckgaberbrueggemann.de/

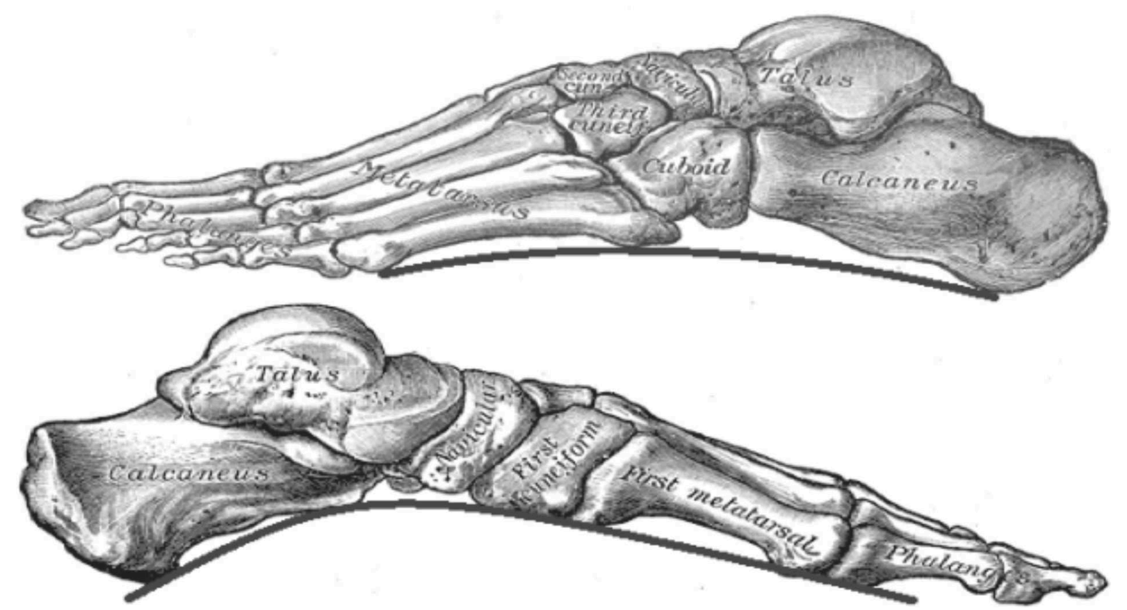

FIGURE 1 | Skeletal structure of the foot. From top to bottom: outline of the lateral arch and medial arch. Adapted from Gray and Lewis (1918).

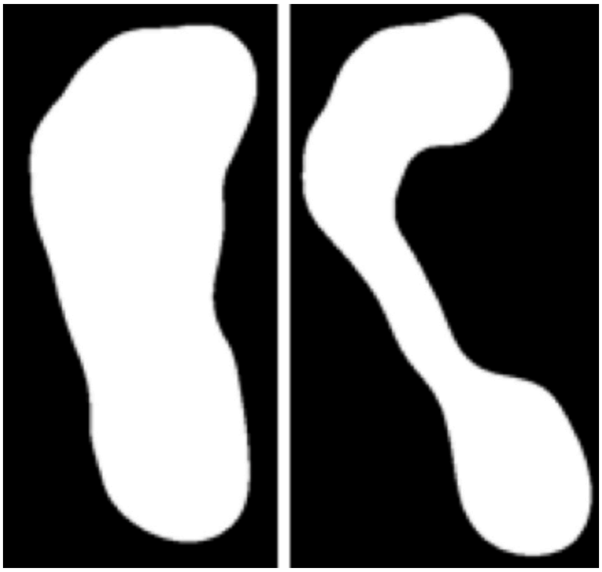

FIGURE 2 | Binary footprint of a flat foot and high arch.

(Van Vliet and Verbeeck, 1993; Costa and Cesar, 2001). Area, perimeter, and circularity features were extracted based on the geometry of the footprint. The wavelet based features, including second moment of the magnitude of the wavelet transform (Arnéodo et al., 2000), entropy-based features of the histogram such as orientation of the wavelet transform and curvature, were consequently determined. Finally, mean bending energy (MBE) and circularity associated with the contour of the footprint were calculated. Using binary images, the perimeter corresponds to the edge between white and black pixels on the image of the foot. The perimeter was calculated by applying an edge detection algorithm, where it was determined by counting the boundary pixels multiplied by $\pi/4$. As for area, each line, and column of the digital footprint corresponded to the sum of foreground pixels. The circularity highlights the relationship between perimeter and area, where P equals perimeter and A corresponds to the area. The circularity is then defined as:

$$C = \frac{P^2}{a} \tag{1}$$

The entropy represents the histogram of the Orientation (angles) of the Wavelet Transform and is a statistical measure of the degree of orientation disorder as follows:

$$E = -\sum_{n=1}^{\infty} p_i \, \mathrm{In}(p_i) \tag{2}$$

where p_i is the frequency of vectors oriented toward a specific direction, and k corresponds to each bin in the histogram. The curvature represents how the direction of a tangent vector varies from point to point on the shape. This feature is given by the following equation:

$$k = \nabla \cdot \frac{\nabla f}{\| \nabla f \|} = \frac{f_{xx} f_y^2 - 2 f_x f_y f_{xy} + f_{yy} f_x^2}{(f_x^2 + f_y^2)^{3/2}} \tag{3}$$

where f_x, f_y, f_{xx}, f_{yy}, *and* f_{xy} denote the first and the second partial derivatives of f with respect to x and y, and the partial derivatives with respect to x and y, respectively. Mean Bending Energy (MBE), also known as boundary energy, is related to the amount of energy necessary to transform the shape of the image

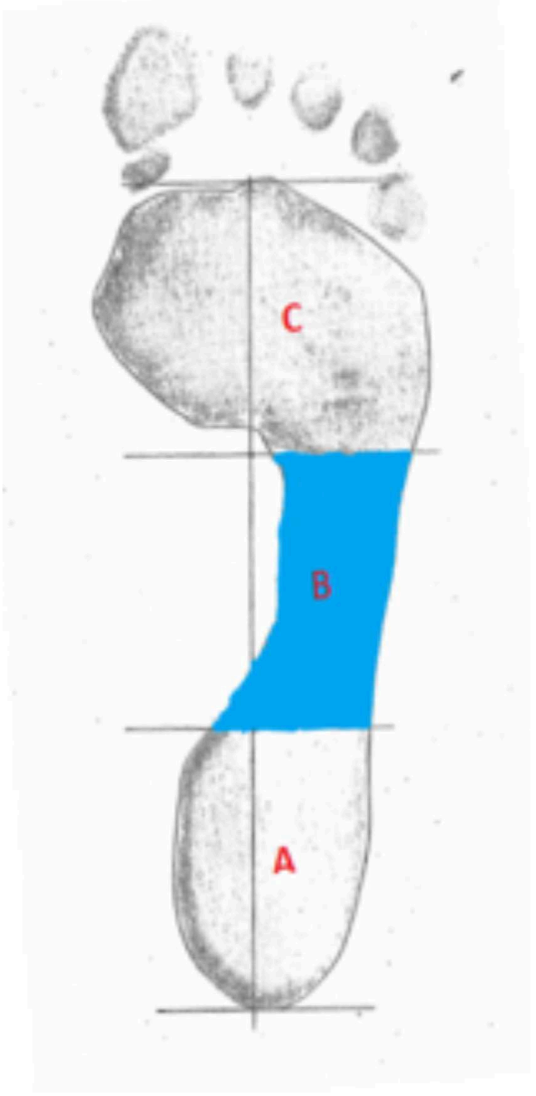

FIGURE 3 | Determination of Arch Index according to Cavanagh and Rogers' method.

into a circle, which would have the same perimeter. This feature is a curvature-based shape descriptor, whose discretised version is defined as:

$$M\widehat{B}E = \frac{1}{N}\sum_{N=0}^{N-1} k\left(n\right)^{2} \tag{4}$$

where N is the number of pixels in the contour and $k(n)$ is the local curvature for the nth pixel in the contour. The Gabor wavelet is defined as:

$$\psi_{G}\left(x\right) = \exp\left(jk_{0}x\right) exp\left(1\frac{1}{2}\left|Ax\right|^{2}\right) \tag{5}$$

Where $j = \sqrt{-1}$, k_0 is a vector, which defines the frequency of the complex exponential, and $A = \mathrm{diag}\left[\varepsilon^{-1/2}, 1\right]$,$\varepsilon \geq 1$is a 2×2 diagonal matrix that defines the anisotropy of the filter, and its elongation in any direction. The Gabor wavelet is a complex exponential modulated by a Gaussian. The above equations were based on the work reported in Costa and Cesar (2001).

Statistical analyses included a correlation analysis using Spearman's correlation coefficient to determine any collinearity between the proposed features and the C&R Arch Index currently used in clinical practice. Simple and multiple linear regression models were also applied to investigate the relationship between the predictor variables. The relative quality of each statistical model consisted of combinations of the proposed features including perimeter, area, curvature, circularity, 2nd moment, entropy, and bending energy (Van Vliet and Verbeeck, 1993; Costa and Cesar, 2001). For example, the corrected Akaike Information Content (AICc) measures the relative quality of the statistical models for the data, with the smallest AICc indicating the best model. The Variance Inflation Factor was applied to ensure that there was no multicollinearity between factors (Zuur et al., 2010). The correlation coefficient (r^2) was used to prove the reliability of the *AHI* linear equation obtained and shown in the results. The model with the lowest AICc and p-value < 0.05 with the least number of features was selected as the best model to describe low, normal and high arch heights and best matched the three groups of C&R (low, normal, and high arches). An Analysis Of Variance (ANOVA) followed by the Tukey HSD *post hoc* (Tukey et al., 1984) test were applied to determine which pairwise groups of models were significantly different. All statistical analyses were carried out in R Studio with significance set at $p < 0.05$.

RESULTS

Spearman's correlation test analysis revealed that several of the proposed features obtained using the Gabor wavelet-based analysis were correlated ($r^2 > 0.7$), including the area

TABLE 1 | Significant result of spearman's correlation for the proposed features.

		Area	**Perimeter**	**Second moment**
Circularity	Correlation coefficient	**–0.892***	**0.692***	
Entropy		0.354	0.014	**–0.683***
Curvature		–0.296	0.089	**0.851***

Correlation is significant at the 0.01 level.

TABLE 2 | Best model regarding cavanagh & rodger classification.

Model	**AICc***
MBE + P	–761.68
MBE + E + P	–760.44
MBE + C + P	–760.31
MBE + SM + P	–759.88

**AICc – corrected akaike information content, MBE – Mean bending energy, P – Perimeter, E – Entropy, C: Circularity, SM: Second moment.*

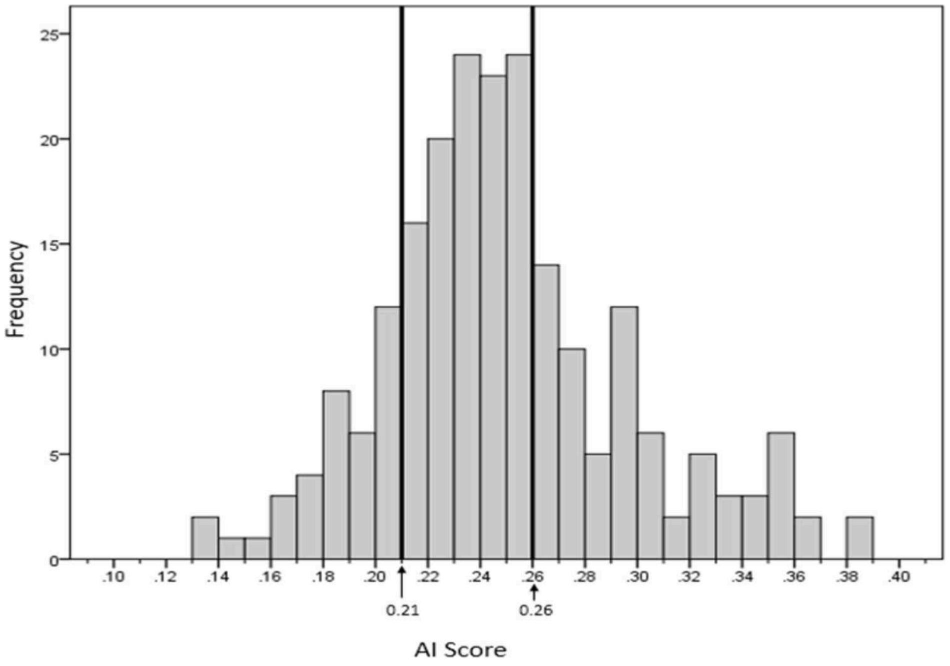

FIGURE 4 | Distribution of arch indices determined with MBE + P using the Cavanagh and Rodgers proposed cut-off values.

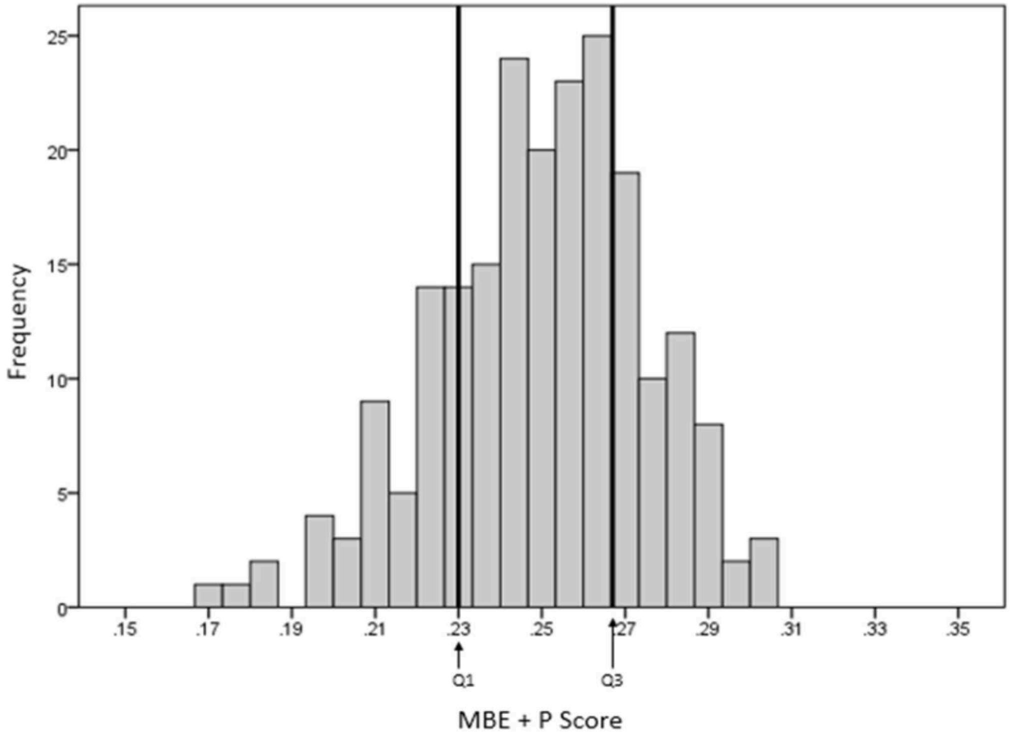

FIGURE 5 | Distribution of scores using the MBE + P equation and cut-offs.

and perimeter with circularity, and the second moment of the Magnitude of the Wavelet transform with entropy and curvature (**Table 1**). Of the correlated pair of features, the feature that had a higher correlation with the dependent variable (arch height) was retained for the regression analysis.

TABLE 3 | Distribution of footprints for each category.

	High arch	Normal	Low arch
Cavanagh and rodgers	37	107	70
MBE + P	53	107	54

From all features, the multiple linear regression models were tested in accordance with the statistical models. Every combination of any model was studied. To avoid multicollinearity issues, any model with a Variance Inflation Factor greater than two was eliminated. Results of this regression tests are shown in the following table. Each one of the four models in **Table 2** is equally valid based on the statistical analyses to model the C&R classification. All models had an R-squared value of 0.28 and were significant ($p < .001$).

The optimal model based on the multiple regression analysis, consisted of the combination of Bending Energy (MBE), and Perimeter (P), with the lowest number of features in the equation. The related equation of this model is the following:

$$AHI = \left(-7.351^{-05} \times P\right) - \left(1050.964 \times M\widehat{BE}\right) + .4597. \quad (6)$$

The ANOVA was further applied to determine any relationship between our best model using two features and the categorized cut-off values defined by C&R at 0.21 and 0.26 with respect to the Arch Index. Results show there is a statistically significant difference between the groups, as set by ANOVA ($F_{(2,211)} = 10.18$, $p < 0.0001$). Tukey's HSD result shows a statistically significant difference in the mean value between the Low Arch and High Arch (0.000113 ± 0.000026 and 0.000135 ± .000026, respectively, $p = .0001$), as well as between the Normal (0.000126 ± 0.000024) and High Arch ($p = 0.002$). However, there were no differences between Normal and Low Arch ($p = 0.191$) for this two feature model. The Mean Bending Energy was the most important feature in this equation with a p-value < 0.001 compared to the Perimeter ($p = 0.05$). Including entropy improved the results and differentiated low arch from normal.

Figures 4 and **5** show the respective AI distribution normalized to the C&R method scores and the MBE + P approach using quartiles to identify the low and high AI. The scores are normally distributed in both situations. The AI mean value for the C&R method was 0.25 and the standard deviation was 0.047. The mean value for the MBE + P approach was 0.25 and the standard deviation 0.025. The arrows indicate the first and the third quartiles of the distribution.

As clinicians typically divide feet into three groups, the distribution of MBE + P scores as shown in **Figure 5** were divided into three quartiles (Q1, Q2, and Q3). Q1 and Q3 are, respectively, showing high arch (low AI) and low arch (high AI).

FIGURE 6 | Visual MBE + P groups of arch height.

The recommended cut-off for low and high AI differed slightly for the MBE + P to that of the C&R approach with high arch and low arch of 0.23 and 0.27 compared to the C&R of 0.21 and 0.26, respectively. The distribution of the footprints for each foot type for both methods from our sample is given in **Table 3**.

A representative example for each footprint category based on the cut-off scores given by the MBE + P equation are shown in **Figure 6**.

DISCUSSION

Automated analysis of foot type using MBE and perimeter is a novel approach, which may give clinicians a powerful, automated tool for timely identification of arch height type and possible risk of foot pathology. Previous methods using MRI, X-ray or CT images have shown good accuracy in Lin et al. (2015) but these methods are expensive, not widely available to clinicians, time consuming and expose participants to radiation. Combining bending energy with perimeter provided a different spatial analysis from the current Cavanagh and Rogers' clinical approach. Our model distinguished the classes proposed by Cavanagh and Rogers providing a reliable tool in determining foot type. However, the mean energy combined with perimeter is more suitable for identification of high arch type, which is more difficult to assess clinically compared to low arch height (being flat footed). The better model based on the AICc in terms of accuracy was the MBE + SM + P model after removing collinearity from the complete model.

Mean Bending Energy plays an important role in the classification of a footprint due to the sensitivity of the measurement that highlights the middle longitudinal arch shape seen in the footprint. However, it depends on how accurately the footprint boundary/outline is presented. The more accurate and clearer the footprint boundary, the better the results. Comparing the two systems indicated that the MBE + P method was more sensitive in highlighting a high arch type as compared to the Cavanagh and Rodgers classification (**Figures 4**, **5**). The results of our approach lead to a greater number of footprints categorized as high arch compared to the C&R categorisation (**Table 3**). However, a review of these mismatched footprints by an experienced clinician indicated that our approach gave an average of 73% reliability for identifying any arch type, with up to 87% reliability in correctly classifying the high arch type. This indicated that the Cavanagh and Rodgers method may under-represent high arch. The C&R method relies on the total footprint area with respect to the area of the midfoot and can lead to some feet being classified as normal, due to the larger total area of the foot, but they may not be high arch foot type. Whereas the Mean Bending Energy + Perimeter relies on the global shape of the foot where the curvature associated with the arch height contributes the most weighting in determining MBE. Therefore, it is less sensitive to the shape of the foot and a better clinical tool that is automated and standardized.

Our automated analysis method utilizing mean bending energy, perimeter and entropy, identified specific frequency content in the footprints associated with specific directions in a localized region around each point of the perimeter of the footprint. This novel, simplified and robust approach provides clinicians a reliable method with faster results for assessment of arch height and a better understanding for predicting injuries associated with foot structure and posture.

AUTHOR CONTRIBUTIONS

JL, KK, JC, JJGL, and HJ contributed to this work. JL and JJGL wrote the scripts and conducted the MATLAB analysis. JC obtained ethical approval and collected the ink foot prints. JC and HJ undertook the statistical analysis and interpretation of the data. All authors contributed to writing main paper. KK gave technical support and conceptual advice. All authors discussed the results and implications and commented on the manuscript at all stages.

ACKNOWLEDGMENTS

The authors wish to acknowledge the assistance by Simon McDonald from the Spatial Analysis Unit at Charles Sturt University with the statistical modeling.

REFERENCES

Arnéodo, A., Decoster, N., and Roux, S. G. (2000). A wavelet-based method for multifractal image analysis. I. methodology and test applications on isotropic and anisotropic random rough surfaces. *Eur. Phys. J. B* 15, 567–600. doi: 10.1007/s100510051161

Burns, J., Crosbie, J., Hunt, A., and Ouvrier, R. (2005). The effect of pes cavus on foot pain and plantar pressure. *Clin. Biomech.* 20, 877–882. doi: 10.1016/j.clinbiomech.2005.03.006

Cavanagh, P. R., and Rodgers, M. M. (1987). The arch index: a useful measure from footprints. *J. Biomech.* 20, 547–551. doi: 10.1016/0021-9290(87)90255-7

Clarke, H. H. (1933). An objective method of measuring the height of the longitudinal arch in foot examinations. *Res. Q.* 4, 99–107.

Costa, L. D. F., and Cesar, R. M. Jr. (2001). *Shape Analysis and Classification : Theory and Practice*. Boca Raton, FL: CRC Press.

Ghasemi, M. S., Koohpayehzadeh, J., Kadkhodaei, H., and Ehsani, A. A. (2016). The effect of foot hyperpronation on spine alignment in standing position. *Med. J. Islam. Repub. Iran* 30, 466.

Goonetilleke, R. S. (2012). *The Science of Footwear*. Boca Raton, FL: CRC Press.

Gray, H., and Lewis, W. H. (1918). *Anatomy of the Human Body*. Philadelphia, PA: Lea & Febiger.

Gwani, A. S., Asari, M. A., and Mohd Ismail, Z. I. (2017). How the three arches of the foot intercorrelate. *Folia Morphol.* doi: 10.5603/FM.a2017.0049 [Epub ahead of print].

Hawes, M. R., Nachbauer, W., Sovak, D., and Nigg, B. M. (1992). Footprint parameters as a measure of arch height. *Foot Ankle* 13, 22–26. doi: 10.1177/107110079201300104

Irwin, L. W. (1937). A study of the tendency of school children to develop flat-footedness. *Res. Q.* 8, 46–53. doi: 10.1080/23267402.1937.10761799

Jelinek, H. F., Cesar, R. M., and Leandro, J. J. G. (2003). Exploring wavelet transforms for morphological differentiation between functionally different cat retinal ganglion cells. *Brain Mind* 4, 67–90. doi: 10.1023/A:1024112215968

Jelinek, H. F., Strachan, B., O'Connor, B., and Khandoker, A. (2014). A continuous point measure for quantifying skull deformation in medical diagnostics. *Health Technol. Lett.* 1, 56–58. doi: 10.1049/htl.2013.0029

Johnson, K. A., and Strom, D. E. (1989). Tibialis posterior tendon dysfunction. *Clin. Orthop. Relat. Res.* 239, 196–206.

Johnston, H. (2014). "The Willandra Lakes Region World Heritage Area, New South Wales, Australia: Land Use Planning and Management of Aboriginal and Archaeological Heritage," in *Archaeological Dimension of World Heritage*, ed. A. Castillo (New York, NY: Springer), 39–55.

Lin, Y. C., Mhuircheartaigh, J. N., Lamb, J., Kung, J. W., Yablon, C. M., and Wu, J. S. (2015). Imaging of adult flatfoot: correlation of radiographic measurements with MRI. *Am. J. Roentgenol.* 204, 354–359. doi: 10.2214/AJR.14.12645

Manley, M. T., and Solomon, E. (1979). The clinical assessment of the normal and abnormal foot during locomotion. *Prosthet. Orthot. Int.* 3, 103–110.

Menz, H. B., and Munteanu, S. E. (2006). Validity of 3 clinical techniques for the measurement of static foot posture in older people. *J. Orthop. Sports Phys. Ther.* 36:179.

Nagtode, S. A., Potdukhe, B. B., and Morey, P. (2016). "Two dimensional discrete wavelet transform and probabilistic neural network used for brain tumor detection and classification," in *Proceedings of the 2016 Fifth International Conference on Eco-friendly Computing and Communication Systems (ICECCS)*, (Bhopal: IEEE), 20–26. doi: 10.1109/Eco-friendly.2016.7893235

Nigg, B. M., Cole, G. K., and Nachbauer, W. (1993). Effects of arch height of the foot on angular motion of the lower extremities in running. *J. Biomech.* 26, 909–916. doi: 10.1016/0021-9290(93)90053-H

Parker, D., Cooper, G., Pearson, S., Crofts, G., Howard, D., Busby, P., et al. (2015). A device for characterising the mechanical properties of the plantar soft tissue of the foot. *Med. Eng. Phys.* 37, 1098–1104. doi: 10.1016/j.medengphy.2015.08.008

Schepsis, A. A., Leach, R. E., and Gorzyca, J. (1991). Plantar fasciitis. Etiology, treatment, surgical results, and review of the literature. *Clin. Orthop. Relat. Res.* 266, 185–196.

Tukey, J. W., Brillinger, D. R., Cox, D. R., and Braun, H. I. (1984). *The Collected Works of John W. Tukey*. Belmont: Wadsworth Advanced Books & Software.

Van Schie, C. H., and Boulton, A. J. (2000). The effect of arch height and body mass on plantar pressure. *WoundsA Comp. Clin. Res. Pract.* 12, 88–95.

Van Vliet, L. J., and Verbeeck, P. W. (1993). "Curvature and bending energy in digitized 2D and 3D images," in *Proceedings of the 8th SCIA*, eds K. A. Hogda, B. Braathen, and K. Heia (Norway: NONIM-Norwegian Soc. Image Process & Pattern Recognition), 1403–1410.

Welton, E. A. (1992). The Harris and Beath footprint: interpretation and clinical value. *Foot Ankle* 13, 462–468. doi: 10.1177/107110079201300806

Zuur, A. F., Ieno, E. N., and Elphick, C. S. (2010). A protocol for data exploration to avoid common statistical problems. *Methods Ecol. Evol.* 1, 3–14. doi: 10.1111/j.2041-210X.2009.00001.x

Conflict of Interest Statement: The authors declare that the research was conducted in the absence of any commercial or financial relationships that could be construed as a potential conflict of interest.

The reviewer CM declared a shared affiliation, with no collaboration, with one of the authors, JL, to the handling editor at the time of the review.

Copyright © 2018 Lucas, Khalaf, Charles, Leandro and Jelinek. This is an open-access article distributed under the terms of the Creative Commons Attribution License (CC BY). The use, distribution or reproduction in other forums is permitted, provided the original author(s) and the copyright owner(s) are credited and that the original publication in this journal is cited, in accordance with accepted academic practice. No use, distribution or reproduction is permitted which does not comply with these terms.

frontiers in Physiology

ORIGINAL RESEARCH
published: 17 January 2019
doi: 10.3389/fphys.2018.01947

Discrete Cosine Transform for the Analysis of Essential Tremor

Jordi Solé-Casals[1,2]*, **Iker Anchustegui-Echearte**[1,3], **Pere Marti-Puig**[1], **Pilar M. Calvo**[4], **Alberto Bergareche**[5,6,7], **José Ignacio Sánchez-Méndez**[4] and **Karmele Lopez-de-Ipina**[2,4]

[1] Data and Signal Processing Research Group, University of Vic-Central University of Catalonia, Barcelona, Spain, [2] Department of Psychiatry, University of Cambridge, Cambridge, United Kingdom, [3] Seidor Labs, Tona, Spain, [4] EleKin Research Group, System Engineering and Automation Department, University of the Basque Country UPV/EHU, Donostia, Spain, [5] Neurodegenerative Disorders Area, Biodonostia Health Research Institute, San Sebastián, Spain, [6] Movement Disorders Unit, Department of Neurology, University Hospital Donostia, San Sebastián, Spain, [7] Biomedical Research Networking Centre Consortium for the area of Neurodegenerative Diseases (CIBERNED), Madrid, Spain

Essential tremor (ET) is the most common movement disorder. In fact, its prevalence is about 20 times higher than that of Parkinson's disease. In addition, studies have shown that a high percentage of cases, between 50 and 70%, are estimated to be of genetic origin. The gold standard test for diagnosis, monitoring and to differentiate between both pathologies is based on the drawing of the Archimedes' spiral. Our major challenge is to develop the simplest system able to correctly classify Archimedes' spirals, therefore we will exclusively use the information of the *x* and *y* coordinates. This is the minimum information provided by any digitizing device. We explore the use of features from drawings related to the Discrete Cosine Transform as part of a wider cross-study for the diagnosis of essential tremor held at Biodonostia. We compare the performance of these features against other classic and already analyzed ones. We outperform previous results using a very simple system and a reduced set of features. Because the system is simple, it will be possible to implement it in a portable device (microcontroller), which will receive the *x* and *y* coordinates and will issue the classification result. This can be done in real time, and therefore without needing any extra job from the medical team. In future works these new drawing-biomarkers will be integrated with the ones obtained in the previous Biodonostia study. Undoubtedly, the use of this technology and user-friendly tools based on indirect measures could provide remarkable social and economic benefits.

Keywords: essential tremor, automatic drawing analysis, archimedes' spiral, discrete cosine features, automatic feature selection

OPEN ACCESS

Edited by:
Sladjana Z. Spasić,
University of Belgrade, Serbia

Reviewed by:
Sergio E. Lew,
Universidad de Buenos Aires,
Argentina
Anna Esposito,
Università degli Studi della Campania
Luigi Vanvitelli Caserta, Italy

***Correspondence:**
Jordi Solé-Casals
jordi.sole@uvic.cat

Specialty section:
This article was submitted to
Fractal Physiology,
a section of the journal
Frontiers in Physiology

Received: 28 June 2018
Accepted: 22 December 2018
Published: 17 January 2019

Citation:
Solé-Casals J,
Anchustegui-Echearte I, Marti-Puig P,
Calvo PM, Bergareche A,
Sánchez-Méndez JI and
Lopez-de-Ipina K (2019) Discrete
Cosine Transform for the Analysis of
Essential Tremor.
Front. Physiol. 9:1947.
doi: 10.3389/fphys.2018.01947

INTRODUCTION

Essential tremor is a neurological disorder 20 times more common than Parkinson's disease that affects individuals worldwide with a prevalence in the western world of about 0.3–4%. With regard to epidemiological analysis, the incidence of ET increases with age, both men and women are affected more or less equally, with an incidence of 23.7 per 100,000 people per year, and may also appear in children. In this scenario, studies suggest that the prevalence among elderly ranges between 3.9 and 14.0%. Moreover, 50 to 70% of essential tremor cases are estimated to be of genetic origin [1] and in these cases an early development of symptoms could appear. In the characterization of this disorder, ET is considered a kinetic rhythmic tremor (4–12 Hz) that only occurs when the affected muscle is exerting an effort, and its amplitude is variable with respect to age, but there is no gender predilection.

The risk of Parkinson's disease in people with essential tremor is higher than in the general population, and stress and fatigue may worsen the tremor. In addition, Parkinson's disease and essential tremor can also occur simultaneously and may appear in individuals of the same family. As far as symptoms of essential tremor are concerned, as in Parkinson's disease, tremor of the hand predominates and occurs in most cases, followed by or at the same time that tremor of the head, voice, neck, face, leg, tongue, trunk and walking difficulties (Louis and Vonsattel, 2007). The symptoms of ET produce a dramatic decline in the performance of daily activities and may lead to disabilities.

Therefore, early treatment of the disorder is essential in order to control and alleviate symptoms and increase the patients' quality of life. In recent years, significant progress has been made in the development of reliable and robust clinical biomarkers. However, despite their utility, some of the tests can be very invasive or involve high cost and technological requirements that make it impossible to apply them to all patients with motor disorders, especially when continuous monitoring is necessary. For these cases, new intelligent non-invasive diagnostic techniques have been developed based on indirect biosignals such as speech, writing or drawing. These developments can become valuable tools for early detection of disorders and friendly monitoring. Additionally, these techniques supervised by health specialists are managed by non-technical staff in the patient's usual environments without introducing stress or altering or blocking their abilities. The systems are very low cost and do not require extensive infrastructures or the availability of medical equipments. The biosignals obtained are simple, natural and easy to process and manage, and the tools are capable of producing information easily, quickly and economically (Lopez-de-Ipiña et al., 2013a,b; Zanuy et al., 2013; Laske et al., 2015). The literature and clinical practice establish that handwritten tasks can be used for the diagnosis of essential tremor and in this sense Archimedes' spiral is the reference test in clinical diagnosis (Pullman , 1998).

In the past, handwriting analysis was performed using an offline test without technological tools. In fact, only the writing or drawing itself (lines on paper) and the perception of the health specialist were available and analyzed. Nowadays, modern capture devices (digitizing tablets and pens) can gather dynamic data with their temporal dimension to include the evolution of the performance and quantitative measurements. Then, the analysis is carried out online with the available spatiotemporal information. The first papers published using digitizing tablets dates back to the 1990s (see Elble et al., 1996; Cameron Riviere et al., 1997; Pullman, 1998 for example), and spread significantly from this century (see Miralles et al., 2006; Zeuner et al., 2007; Haubenberger et al., 2011; Louis et al., 2012 for example), when new and more powerful tablets appeared on the market. These modern digitizing tablets collect not only the x and y coordinate points that describe the hand movement and the evolution of the pattern as it changes position, but can also collect other interesting features, such as the pressure exerted on the writing surface, the azimuth, the angles of the pen with regard to the vertical and horizontal axis, the altitude (Likforman-Sulem et al., 2017), as well as the movement in the air when there is no contact nor pressure between the pen and the paper or device (Sesa-Nogueras et al., 2012). This provides the possibility to analyse both the static characteristics and the dynamics of their evolution (Faundez-Zanuy, 2007):

- Static*:* Also known as "off-line" analysis. In these tests users write their handwriting/drawing on paper and afterwards the strokes are digitized through a camera or an optical scanner. Then, a biometric analysis is carried out.
- Dynamic*:* Also known as "on-line" analysis. In these tests, users write in a digitizing device, which acquires the drawing/handwriting in real time with the whole set of features abovementioned. Not only the strokes but also the spatiotemporal information is available and used.

The present work belongs to a larger cross-sectional study for the characterization of ET by indirect measures, and it is included in the general transversal study conducted at the Biodonostia Health Institute, which focuses on the characterization of genetic ET and is based on families with identified genetic loci. For the detection of ET, Archimedes' spiral has been selected as the reference test for the selection of linear and/or non-linear biomarkers from drawings and writing, bearing in mind that irregularities due to stress may also appear in control persons and patients with ET. A previous work that used the same data (but with other features and classification systems) can be found in (Lopez De Ipina et al. (2015). The main goal of the study is to analyse the capability of a classification system using exclusively the x and y coordinate points of the drawings. This is because we would like to use the handwriting exercise in real time using a tablet or phablet. In the next sections we detail the new proposed features obtained through the discrete cosine transform. Then, several automatic analysis systems, Linear Discriminant Analysis (LDA), k-Nearest Neighborhood (KNN) and Support Vector Machines (SVM), will measure the quality of the selected features. Obtained results will be compared with already available results with the same database in order to check the potential use of these new descriptors.

MATERIALS AND METHODS

Acquisition System

The acquisition system is a digitizing tablet, the Intuos WACOM 4 2017, which is connected to a laptop trough a USB port and captures the spatial coordinates, the azimuth and altitude angles of the pen on the tablet, and the pressure exerted for it on the surface. Sampling frequency is set to 100 Hz. From this data we could infer other variables such as acceleration, speed, etc. (Jain et al., 1999; Sadikov Groznik et al., 2014).

Database

In this paper we use the database named BIODARW, first presented in (Lopez De Ipina et al., 2015; López-de-Ipiña et al., 2016). We have a total of 21 control people (CP) and 29 ET people. The test consists of, among other exercises, drawing the Archimedes' spiral (**Figure 1**) with both the dominant and non-dominant hands. Therefore, originally the database contains 100 handwriting samples. In order to compare our results with the ones in Lopez De Ipina et al. (2015) and López-de-Ipiña et al.

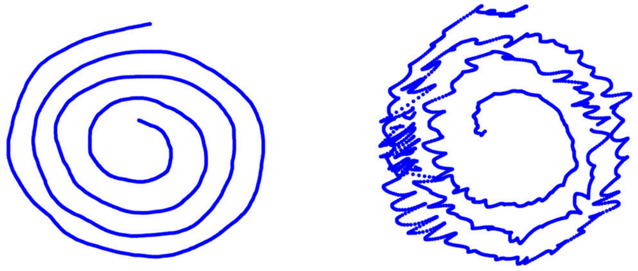

FIGURE 1 | Example of the original drawing of Archimedes' spiral, performed by a control individual (**Left**) and an individual with essential tremor (**Right**).

(2016), we will proceed as done in these works and will only use the BIODARWO subset, which consists of 51 samples: 24 samples for the ET group and 27 samples for the control group. The selection of these samples was as follows:

a. For the ET group, only the sample with the best quality is chosen (one hand), but 5 subjects are discarded due to the poor quality of the samples.
b. For the control group, the best sample (habitually the dominant hand) is kept, but in 6 cases, also the non-dominant hand is included

The medical team carried out this selection. Detailed information of recruitment acquisition procedure and selection of this subset can be found in López-de-Ipiña,(2016). **Table 1** summarizes the features of the group with ET with regard to test features, diagnosis and demography. Due to lack of space, only the first 9 subjects are presented.

Discrete Cosine Transform of Type II, Partial Reconstructions and Residues

Considering the set of N points x_n where n goes from 0 to $N-1$, and N transformed coefficients X_k, where k goes also from 0 to $N-1$, the forward and backward expressions of the type II Discrete cosine transform take the form:

$$X_k = \sum_{n=0}^{N-1} c_k x_n \cos\left(\frac{\pi}{N}\left(n+\frac{1}{2}\right)k\right); \quad k = 0, \cdots, N-1 \quad (1)$$

and,

$$x_n = \sum_{k=0}^{N-1} c_k X_k \cos\left(\frac{\pi}{N}\left(n+\frac{1}{2}\right)k\right); \quad n = 0, \cdots, N-1 \quad (2)$$

and, Where c_k is defined as:

$$c_k = \begin{cases} \sqrt{\frac{1}{N}}; & k = 0 \\ \sqrt{\frac{2}{N}}; & k \neq 0 \end{cases} \quad (3)$$

Equations (1) and (2) show that, from all the coefficients X_k, the N samples of the original x_n sequence is perfectly recovered.

Let us consider only the first L coefficients of X_k to reconstruct the original sequence x_n, in order to obtain an approximation $\tilde{x}_n$ as follows:

$$\tilde{x}_n = \sum_{k=0}^{L-1} c_k X_k \cos\left(\frac{\pi}{N}\left(n+\frac{1}{2}\right)k\right); \quad n = 0, \cdots, N-1 \; and \; (L < N) \quad (4)$$

And the remaining X_k, to form the residue $\hat{x}_n$ as:

$$\hat{x}_n = \sum_{k=L}^{N-1} c_k X_k \cos\left(\frac{\pi}{N}\left(n+\frac{1}{2}\right)k\right); \quad n = 0, \cdots, N-1 \quad (5)$$

It comes directly from (4) and (5) that the original sequence x_n is $x_n = \tilde{x}_n + \hat{x}_n$. As commonly $L \ll N$, the calculus of $\tilde{x}_n$ involves fewer coefficients than the one for $\hat{x}_n$, therefore the residue $\hat{x}_n$ is obtained more efficiently from $\tilde{x}_n$ as:

$$\hat{x}_n = x_n - \tilde{x}_n \quad (6)$$

We propose the use of the DCT because this transformation is often used in lossy data compression applications. The property of the DCT that makes it suitable for compression is its high degree of spectral compaction; this means that the DCT representation of a signal tends to concentrate more of its energy in a small number of coefficients, the first ones, compared to other transformations such as DFT. Therefore, this characteristics will allow us to keep a small number of coefficients containing the fundamental information about the drawings.

Extracted Features

The digitalizing tablet used was an Intuos Wacom 4. The pen tablet captures the spatial coordinates (x_n, y_n), the pressure, and the azimuth and altitude angles of drawing. In this study only the spatial coordinates (x_n, y_n) were used.

To characterize each spiral by means of a single real sequence the spatial coordinates (x_n, y_n) can be combined in several ways. We investigate two options: (i) calculating the radius of the polar coordinates and (ii) estimating a distance. **Figure 2** shows a block diagram of the two processes:

- The radius method: in this case, the radius was calculated by transforming the Cartesian coordinates to Polar coordinates. Therefore, the new sequence r_n was obtained as $r_n = \sqrt{{x_n}^2 + {y_n}^2}$. An example of the radius sequence r_n for a healthy subject and a patient is shown in **Figure 3**.
- The residue method: in this case, the Cosine transform was applied to each coordinate $x_n$and y_n separately, and then the inverse Cosine transform was calculated using a predefined number of coefficients, obtaining the estimated sets $\tilde{x}_n$ and $\tilde{y}_n$. The inverse Cosine Transform of each axis was subtracted from the original signal and we obtained the residue calculated as the distance between the two signals. Finally, we characterize each spiral with a single real sequence rd_n obtained from de residues $\hat{x}_n$ and $\hat{y}_n$ of (x_n, y_n) as follows:

$$rd_n = \sqrt{(x_n - \tilde{x}_n)^2 + (y_n - \tilde{y}_n)^2} = \sqrt{(\hat{x}_n)^2 + (\hat{y}_n)^2} \quad (7)$$

TABLE 1 | Some examples of the database, together with electrophysiological test features and diagnosis using Fahn–Tolosa–Marin (FTM) scale values for the selected individuals with ET (ET_*x*).

ET_*x*	Electrophysiological test features			Diagnosis	Demography	
	Frequency (Hz)	**Amplitude (V)**	**Pattern**	**FTM Scale**	**Age**	**Gender**
ET_01	8.5	20	Synchronous	1	48	Female
ET_02	6.5	variable	Alternating	8	72	Male
ET_03	10.5	200	Synchronous	1	46	Male
ET_04	4.5	503.6	Synchronous	3	80	Female
ET_05	6.6	298	Synchronous	22	68	Female
ET_06	9.5	46	Synchronous	2	46	Female
ET_07	5	173	Synchronous	50	75	Male
ET_08	6.5	159	Synchronous	40	75	Male
ET_09	8	128	Synchronous	9	75	Female

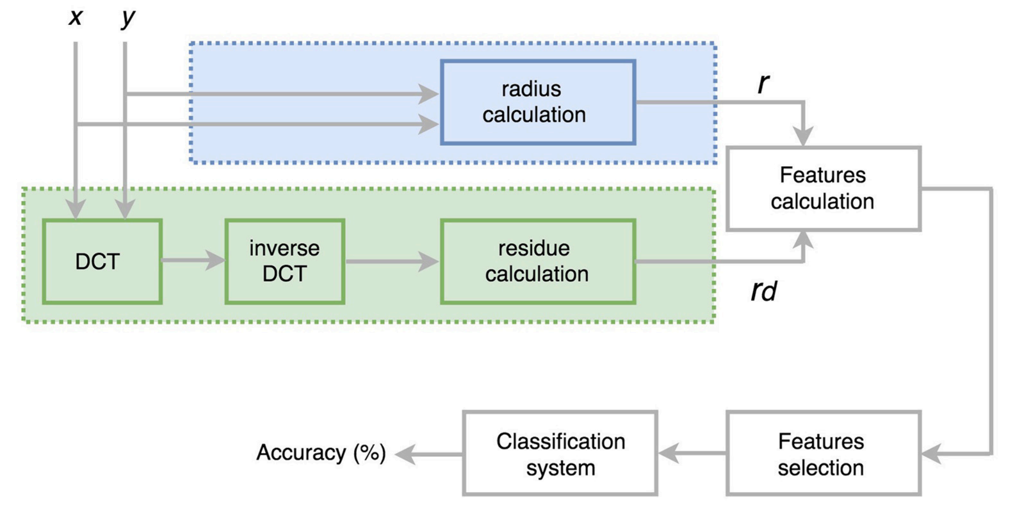

FIGURE 2 | Block diagram of the experimental part.

- An example of the sequences rd_n is shown in **Figure 4**. In order to evaluate the effect of the number of coefficients, several number of coefficients have been considered in the experiments.

By visual observation, comparing **Figures 3**, **4**, we notice that the irregularity of the signal is, as expected, bigger for the ET subjects compared to controls, and more notorious in residue than in the radius signal.

From these two signals, the radius and the residue, we extract a set of temporal and frequency features. The temporal features are, for example, the root mean square, standard deviation, maximum fractal length, or zero crossing. Frequency features, obtained from the Welch periodogram transform, are, for example, the mean frequency and its amplitude, median frequency, total power, 1st, 2nd, and 3rd spectral moments, kurtosis, or autocorrelation. The complete list of features is shown in **Table 2** (temporal domain features) and **Table 3** (frequency domain features). We refer the reader to Shair et al. (2017) for details on the features and how to calculate them. The total number of extracted features is 34 and we will use feature selection algorithm to keep the most discriminative ones.

Classification Systems

Linear Discriminant analysis (LDA), k-nearest neighbors (k-NN) and support vector machine (SVM) with radial basis kernel have been used as classification algorithm to discriminate between ET and control subjects. To evaluate the performance of these algorithms we implemented the leave-one-out technique. Although all the drawing samples have been done with a template and the same pen tablet, the number of drawing points acquired was different for each sample. In order to ensure the same number of points in each sequence, we resampled all the exercises to enforce 4096 points in all of them. Establishing the same number of points is mandatory in order to be able to compare the different Cosine transforms. Normalization was also applied in order to have a unit norm in all the features. Results were evaluated by means of the Accuracy (%). In the training and validation steps we use a *k*-fold cross validation strategy with

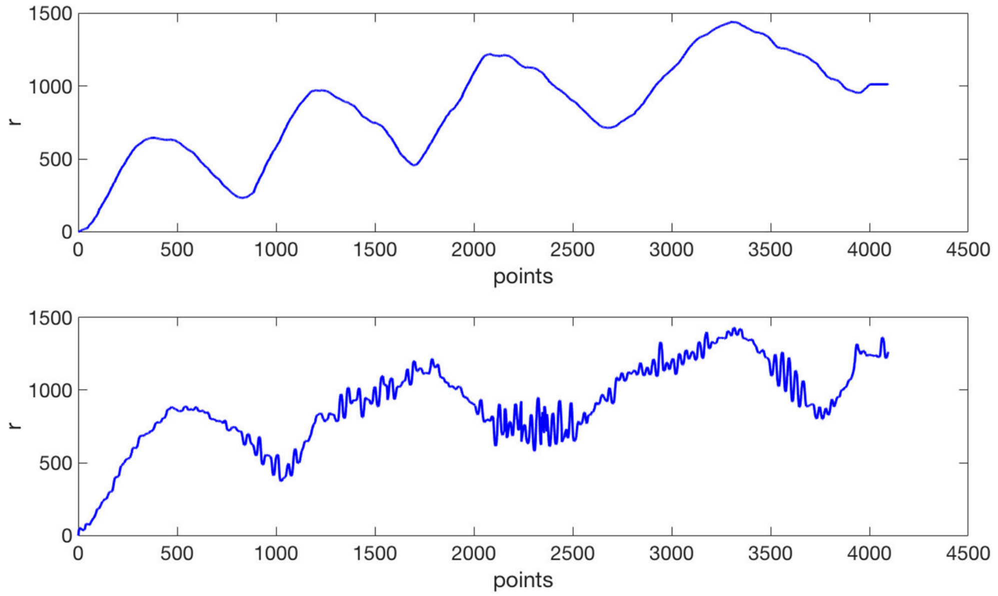

FIGURE 3 | An example of Archimedes' spirals radius *r* performed by the same subjects of **Figure 1**. At the top for the control subject; at the bottom for the ET patient.

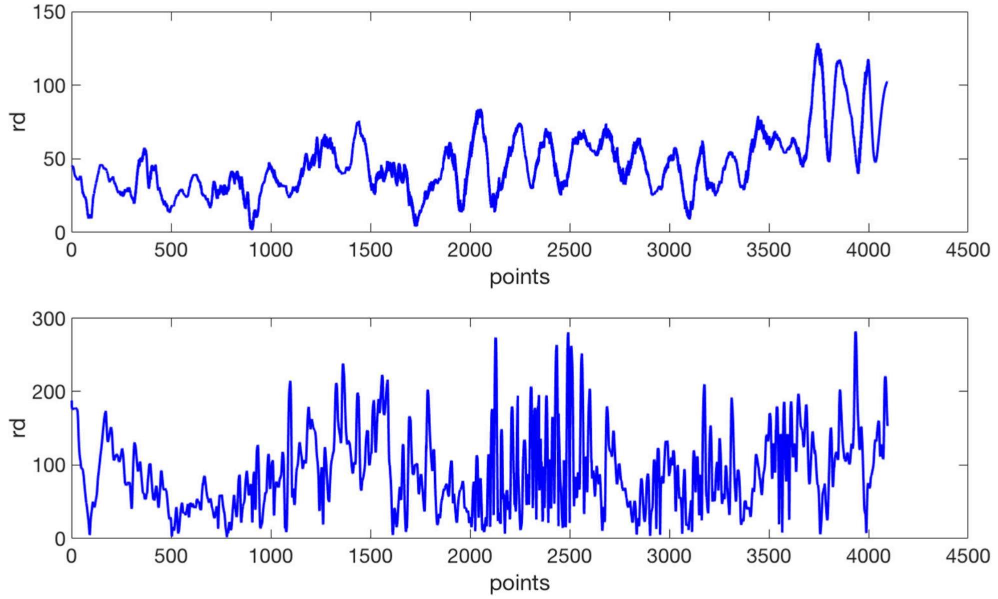

FIGURE 4 | An example of the residue *rd* performed by the same subjects of **Figure 1**. At the top for the control subject; at the bottom for the ET patient.

$k = 10$. Cross-validation is a robust technique for the selection of variables and widely used to obtain realistic results reducing overfitting.

Experiments

Experiments where carried on the BIODARWO dataset. A feature selection algorithm was applied in order to improve the classification rate removing the similarities and dependencies between features. Relieff algorithm (Kononenko et al., 1997) was selected for its well performance in binary classification problems. This method is one of the best enabling the classifiers to achieve the highest classification accuracy while reducing the number of unnecessary attributes. Also, and very important for us, Relieff gives as output an ordered list of features according to their importance, which will allow us to select the first of them (Molina et al., 2002; Cehovin and Zoran, 2010). In this study the Relieff algorithm implementation from MATLAB.

The feature selection algorithm was applied to the residue and radius features in order to obtain the best performance in both

TABLE 2 | List of the extracted features from the temporal domain.

Temporal Features	Descriptor
Sample entropy (SENT)	$m = 3, r = 0.2$
Mean absolute value (MAV)	$\frac{1}{N}\sum_{i=1}^{N} \lvert X_i \rvert$
Variance (VAR)	$\frac{1}{N-1}\sum_{i=1}^{N} \lvert X_i - \mu \rvert^2$
Root mean square (RMS)	$\sum_{i=1}^{N} \frac{1}{N} X_i^2$
Log detector (LOG)	$e^{\frac{1}{N}\sum_{i=1}^{N} log(\lvert X_i \rvert)}$
Waveform length (WL)	$\sum_{i=1}^{N-1} \lvert X_{i+1} - X_i \rvert$
Standard deviation (STD)	$\sqrt{\frac{1}{N-1}\sum_{i=1}^{N} \lvert X_i - \mu \rvert^2}$
Difference Absolute standard deviation (AAC)	$\sqrt{\frac{1}{N-1}\sum_{i=1}^{N-1} (X_{i+1} - X_l)^2}$
Fractal dimension (FD)	Higuchi's algorithms with $m = 5$
Maximum fractal length (MFL)	$log(\sum_{i=1}^{N-1} \lvert X_{i+1} - X_i \rvert)$
Myopulse percentage rate (MYO)	Percentage of time where the signal is bigger than two times the mean
Integrated EMG (IEMG)	$\sum_{i=1}^{N} \lvert X_i \rvert$
Simple square EMG (SSI)	$\sum_{i=1}^{N} X_i^2$
Zero crossing (ZC)	The number of times in which the signal crosses its mean
Slope sign change (SSC)	The number of times in which the slope of the sign changes
Wilson amplitude (WAMP)	$\sum_{i=1}^{N-1} \lvert X_i - X_{i+1} \rvert > \epsilon$ where ϵ is the mean of the signal
Autoregressive coefficients (AR, 4 coefficients)	AR parameter estimation via Yule-Walker method

The descriptor includes the values of the parameters (when needed) and/or the mathematical definition. Details on all the features can be found in Shair et al. (2017).

TABLE 3 | List of the extracted features from the frequency domain.

Frequency Features	Descriptor
Main peak amplitude (Pmax)	Maximum peak
Main peak frequency (Fmax)	Frequency of the max peak
Mean power (MP)	$\frac{1}{N}\sum_{i=1}^{N} \lvert P_i \rvert$
Total power (TP)	$\sum_{i=1}^{N} P_i$
Mean frequency (MNF)	Estimates the mean normalized frequency of the power spectrum
Median frequency (MDF)	Estimates the median normalized frequency of the power spectrum
Standard deviation (STD)	$\sqrt{\frac{1}{N-1}\sum_{i=1}^{N} \lvert P_i - \mu \rvert^2}$
1st spectral moment (SM1)	Spectral moments
2nd spectral moment (SM2)	Spectral moments
3rd spectral moment (SM3)	Spectral moments
Kurtosis (KUR)	Kurtosis of the power spectrum
Skewness (SKW)	Skewness of the power spectrum
Autocorrelation (Auto, 3 coefficients)	3 firsts coefficients of the autocorrelation

The descriptor includes the values of the parameters (when needed) and/or the mathematical definition. Details on all the features can be found in Shair et al. (2017).

cases. Several numbers of features were tested and experimentally we obtained the best performance using the top 5-predictor rank features. The 5 characteristics selected in each case are the following, sorted according to their importance:

Residue method:

1. Mean frequency (MNF)
2. Wilson amplitude (WAMP)
3. Mean absolute value (MAV)
4. Maximum fractal length (MFL)
5. Fractal dimension (FD)

Radius method:

1. Maximum fractal length (MFL)
2. Fractal dimension (FD)
3. Myopulse percentage rate (MYO)
4. Mean absolute value (MAV)
5. Standard deviation (STD)

RESULTS AND DISCUSSION

Three different classification algorithms have been used to compare the performance of the residue method and the radius method. For the residue method, several coefficients for the inverse cosine transform were considered in order to establish the optimal value.

First, a LDA was used. As can be seen in **Table 4**, the maximum accuracy was 85.71% obtained for the residue method with 17 coefficients, while for the radius method the best accuracy was 75.51%. An improvement of 10% was achieved using the cosine transform apporach, instead of working directly with the radius. This emphasizes the importance of using the residue as a time series rather than working directly with the radius, as the residue contains more information regarding the tremor. We can see the results of the LDA as a reference results, and the other systems will try to improve these ones.

Next, the k-NN method was used. In this case, different number of neighbors were tested. Results are shown in **Table 5** for the residue method, and in **Table 6** for the radius method. The maximum accuracy was 83.67% obtained for the residue method with 17 coefficients and 3 neighbors, while for the radius method the best accuracy was 81.63% with 3, 4, and 5 neigbors. We note that results are worst than the ones obtained using LDA, but again, the residue method outperforms the radius method, even if that now the difference is smaller. The number of neighbors can be kept small (in both cases 3 was enough), which is interesting from the point of view of simplicity. The number of coefficients for the inverse cosine transform was again 17.

Then, we used explored a non-linear classification system. Specifically we used an SVM with RBF kernel. The number of coefficients of the inverse cosine transform was explored and, as in the other two cases, we found that 17 was the best case. Therefore, we established 17 coefficients and then we performed a tunning for the kernel scale and penalty cost of missclassifaction in order to achieve the best classification rate (accuracy). Results for the residue method with 17 coefficients are presented in **Table 7**. The maximum accuracy achieved with this approcah was 95.92%, for the scale of 0.2 and costs 10^3 and 10^4. Several

TABLE 4 | Accuracy (%) for the LDA classifier for the residue of the cosine transform (as a function of the number of coefficients considered) and for the radius.

	Coefficients											
	10	**15**	**16**	**17**	**18**	**20**	**21**	**22**	**23**	**25**	**30**	**50**
Residue of the CT	75.51	79.59	81.63	**85.71**	79.59	71.43	77.55	79.59	77.55	79.59	77.55	77.55
Radius	75.51											

The best result is highligted in bold

TABLE 5 | Accuracy (%) from k-NN classifier and residue method, where k stands for the number of neighbors used in the classification algorithm.

	Coefficients											
k	**10**	**15**	**16**	**17**	**18**	**20**	**21**	**22**	**23**	**25**	**30**	**50**
1	75.51	75.51	77.55	79.59	77.55	67.34	75.51	75.51	77.55	73.46	73.46	77.55
3	69.38	77.55	73.46	**83.67**	77.55	65.30	71.42	73.46	67.34	65.30	69.38	63.26
5	69.38	79.59	71.42	77.55	73.46	59.18	77.55	71.42	69.38	65.30	69.38	67.34
7	73.46	73.46	73.46	79.59	81.63	63.26	69.38	67.34	71.42	71.42	67.34	69.38
9	77.55	75.51	73.46	73.46	69.38	73.46	67.34	65.30	69.38	69.38	67.34	73.46
11	77.55	77.55	77.55	77.55	75.51	69.38	71.42	63.26	67.34	63.26	59.18	79.59
13	77.55	77.55	73.46	73.46	67.34	65.30	71.42	61.22	65.30	65.30	69.38	79.59
15	77.55	75.51	71.42	73.46	69.38	69.38	71.42	67.34	67.34	67.34	69.38	77.55
17	71.42	75.51	69.38	79.59	73.46	69.38	71.42	63.26	65.30	69.38	69.38	73.46
19	71.42	75.51	71.42	81.63	77.55	67.34	71.42	63.26	61.22	65.30	63.26	67.34
21	69.38	75.51	73.46	79.59	75.51	71.42	71.42	75.51	65.30	~~61.22~~	~~61.22~~	~~71.42~~
23	73.46	75.51	73.46	79.59	73.46	75.51	71.42	73.46	75.51	71.42	67.34	69.38
25	67.34	77.55	69.38	77.55	77.55	69.38	73.46	73.46	65.30	67.34	71.42	73.46
27	67.34	77.55	71.42	73.46	73.46	67.34	73.46	75.51	67.34	73.46	73.46	75.51
29	69.38	67.34	73.46	75.51	73.46	71.42	73.46	71.42	69.38	69.38	71.42	73.46
31	71.42	67.34	71.42	75.51	73.46	71.42	73.46	71.42	71.42	67.34	69.38	69.38
33	71.42	73.46	67.34	71.42	71.42	67.34	71.42	71.42	73.46	69.38	69.38	75.51

The best result is highligted in bold.

other combinations reached accuracies over 90%, which is a very good result. For the radius method, results are shown in **Table 8**. In this case the maximum accuracy was 85.71%, for the cost 10^4 and scales 0.7–1. This result outperforms the ones obtained previously with LDA and k-NN.

In order to demonstrate the capability of the system, **Table 9** (left) presents the confusion matrix obtained with the residue method, for 5 features and the SVM classifier. From these values we can calculate the sensitivity (SEN) and specificity (SPE) of the system, which results in the following values:

$$
\begin{aligned}
SEN &= \frac{TP}{TP+FN} = \frac{20}{21} = 95.24\ \% \\
SPE &= \frac{TN}{TN+FP} = \frac{26}{28} = 92,86\ \%
\end{aligned}
\tag{8}
$$

where TP, TN, FP, and FN stands for the true positive, true negative, false positive and false negative values of the confusion matrix.

Finally, we explore the combination of both methods (residue and radius features). For that, we started from the best previous case (SVM with RBF, using the 5 features of the residue method) and adding 1 feature of the radius method; then adding 2 features; then 3 features; then 4 features and finally the 5 features. When adding new features, we followed the ranking presented in section 2.6. For the case of 5 (residue) + 2 (radius) features (see **Table 10**) we achieved an accuracy of 97.96%, outperforming the best result obtained before. The radius features added that contributed to increase the accuracy were the Maximum fractal length and the Fractal dimension. In that case, the confusion matrix (see **Table 9**) contains only one missclassified sample, which corresponds to a control subject that the system classifies as ET. Therefore, sensitivity and specificity are increased to the following values: $SEN = 100\%$; $SPE = 96.42\%$, see (9). The exact same result whas obtained for 5(residue) + 3(radius), in that case adding also the Myopulse percentage ratio.

$$
\begin{aligned}
SEN &= \frac{TP}{TP+FN} = \frac{21}{21} = 100\ \% \\
SPE &= \frac{TN}{TN+FP} = \frac{27}{28} = 96,42\ \%
\end{aligned}
\tag{9}
$$

We can see that for the three classification systems the residue method always obtained the best accuracies. In particular, the SVM classifier was the best choice for both methods, and the results obtained with the residue method clearly outperforms the results obtained with the radius method. The best results, using only one of the methods is close to 96% of accuracy, clearly exceeding the best results obtained in (Lopez De Ipina et al., 2015) and (López-de-Ipiña et al., 2018) and similar to those obtained in (López-de-Ipiña et al., 2016), in all the cases using the same database. But the combination of both methods allowed to increase up to almost 98% of accuracy. This is interesting because it means that some information is complementary and therefore useful for the classifier.

It is important to emphasize that while all the possible characteristics captured by the Intuos device (including pressure, air time, surface time, azimuth and elevation angles, speed, acceleration, etc.), were used in the previous works, now only the *x* and *y* coordinate points are used. For example, comparing our results with those presented in our recently publiched work (López-de-Ipiña et al., 2018), we can see that we propose a new set of extremely reduced features derived directly from the *x* and *y* coordinate points, which allows us to obtain better results (97.96% against 91%) than those in (López-de-Ipiña et al., 2018). We combined *x* and *y* coordinate values in two ways: (i) calculating the radius and (ii) calculating the residue after reconstructing the coordinate points using the cosine and inverse cosine transforms. With only this information we were able to outperform the best accuracy obtained in previous results, with a very simple method and using only 7 features, instead of 70 to 198 features used in (López-de-Ipiña et al., 2016), for example.

TABLE 6 | Accuracy (%) from k-NN classifier and radius features, where k stands for the number of neighbors used in the algorithm.

k	CR(%)
1	77.55
3	**81.63**
5	**81.63**
7	**81.63**
9	79.59
11	77.55
13	77.55
15	73.46
17	69.38
19	69.38
21	69.38
23	67.34
25	67.34
27	65.30
29	65.30
31	63.26
33	61.22

The best results is highligted in bold

The results of our study will allow its implementation in real time by means of a validation study to confirm its usefulness in the differential diagnosis of essential tremor with respect to other entities with which it can be confused such as physiological tremor, tremor in Parkinson's disease and dystonia, as well as in the evolutionary monitoring of essential tremor after the start of any of the specific treatments already available.

There are several reasons to explore only these features. Among them, the simplicity to obtain them, because this is the traditional available information of any acquiring system. This can make it easier and allow the use of other simpler acquisition systems by tracking only the *x* and *y* coordinate values, rather than, for example, the pencil angles or the pressure exerted during the drawing process. Then, using fewer phisical variables will lead to a small number of features and therefore also simple clasification methods. Finally, the computational time is also affected by the simplicity or complexity of the data to acquire, the features to extract and the clasification system to implement. Using only information of the *x* and *y* coordinates allowed us to reduce complexity and hence also computational time. This is important if we want to work in real time in autonomous

TABLE 7 | Accuracy (%) from SVM RBF classifier and residue features with 17 coefficients, where cost stands for the penalty cost of missclassification and scale is the kernel scale applied.

	Scale										
Cost	0.1	0.2	0.3	0.4	0.5	0.6	0.7	0.8	0.9	1	1.1
10^{-5}	55.10	55.10	55.10	55.10	55.10	55.10	55.10	55.10	55.10	55.10	55.10
10^{-4}	55.10	55.10	55.10	55.10	55.10	55.10	55.10	55.10	55.10	55.10	55.10
10^{-3}	55.10	55.10	55.10	55.10	55.10	55.10	55.10	55.10	55.10	55.10	55.10
10^{-2}	55.10	55.10	55.10	55.10	55.10	55.10	55.10	55.10	55.10	55.10	55.10
10^{-1}	55.10	65.31	55.10	55.10	55.10	55.10	55.10	55.10	55.10	55.10	55.10
1	85.71	81.63	77.55	77.55	77.55	79.59	77.55	75.51	73.47	69.39	61.22
10^{1}	89.80	87.76	87.76	89.80	81.63	81.63	81.63	79.59	79.59	79.59	79.59
10^{2}	91.84	93.88	89.80	87.76	87.76	89.80	89.80	89.80	89.80	89.80	89.80
10^{3}	91.84	**95.92**	91.84	83.67	87.76	89.80	85.71	89.80	87.76	87.76	87.76
10^{4}	91.84	**95.92**	91.84	91.84	91.84	87.76	83.67	85.71	87.76	87.76	87.76

The best result is highligted in bold.

TABLE 8 | Accuracy (%) from SVM with RBF kernel classifier and radius features, where cost stands for the penalty cost of missclassification and scale is the kernel scale applied.

	Scale										
Cost	0.1	0.2	0.3	0.4	0.5	0.6	0.7	0.8	0.9	1	1.1
10^{-5}	55.10	55.10	55.10	55.10	55.10	55.10	55.10	55.10	55.10	55.10	55.10
10^{-4}	55.10	55.10	55.10	55.10	55.10	55.10	55.10	55.10	55.10	55.10	55.10
10^{-3}	55.10	55.10	55.10	55.10	55.10	55.10	55.10	55.10	55.10	55.10	55.10
10^{-2}	55.10	55.10	55.10	55.10	55.10	55.10	55.10	55.10	55.10	55.10	55.10
10^{-1}	67.35	63.27	55.10	55.10	55.10	55.10	55.10	55.10	55.10	55.10	55.10
1	77.55	79.59	77.55	77.55	77.55	75.51	73.47	73.47	69.39	63.27	61.22
10^{1}	75.51	77.55	79.59	81.63	79.59	79.59	77.55	77.55	77.55	77.55	77.55
10^{2}	71.43	73.47	81.63	77.55	77.55	81.63	79.59	79.59	79.59	79.59	79.59
10^{3}	67.35	71.43	79.59	83.67	83.67	81.63	79.59	77.55	75.51	75.51	77.55
10^{4}	63.27	75.51	75.51	79.59	81.63	83.67	**85.71**	**85.71**	**85.71**	**85.71**	83.67

The best result is highligted in bold.

TABLE 9 | Confusion matrix obtained when using a SVM classifier.

		Predicted	
		ET	**Control**
Actual	ET	20	1
	Control	2	26
Actual	ET	21	0
	Control	1	27

On the top, with the residue method (5 features); on the bottom with the residue method plus 2 features of the radius method: Maximum fractal length and Fractal dimension.

systems, which is one of the goals of the abovementioned project.

Working with the residue is clearly a good option, outperforming in all the cases the results obtained directly with the radius, and the small set of features, all of them that can be interpreted by health specialists in order to investigate the relevance and usefulness of the biomarkers for early diagnosis of ET.

CONCLUSIONS

Nowadays, a large number of models of wireless triaxial accelerometers and gyroscopes that allow clinical assessment of postural and kinetic tremor are In addition, there are new techniques in development such as the measurement of the components of recovery of the blinking reflex, kinematic measurements, analysis of accelerometry data and computerized measurements of the ocular movement whose objective is to be able to objectively distinguish the physiological tremor from the essential tremor, mainly when it is of mild severity. Unfortunately, the advantages of high sensitivity and accuracy in the linear register of portable motion transducers are mitigated by the large variability in the random amplitude of the tremor.

This work analyzed the capability of the cosine transform as a technique to be used for obtaining relevant biomarkers from drawings and handwriting. This is part of a wider cross study on the diagnosis of essential tremor, which is developed in the Biodonostia Health Institute. Specifically, the main goal was to obtain good results using simple information provided by the x and y coordinates of the Archimedes' spiral drawing. The collection of a standardized writing sample is a method used in clinical practice and research to assess the severity of tremor. The method has many practical advantages. It is easy to obtain and takes little time to implement. In fact, the samples can even be collected remotely using different devices, allowing them to be studied in different real-life situations and saving time and resources when it comes to evaluating a large number of people. Surprisingly, there are virtually no published data to address a methodological problem that arises: the validity of the method. The performance of the hand-drawn spiral as a screening tool for Essential Tremor depends to some extent on the sample of case studies and the cut-off points used for sensitivity and specificity.

We investigated two possibilities, the first one using the radius derived directly by transforming the Cartesian coordinates to Polar coordinates, and the second one using the residue calculated as the distance between the coordinates and its reconstruction by means of the pair cosine transform / inverse cosine transform at a given number of the coefficients. Classical features, both temporal and frequential, were derived for both cases and the Relieff method was used to reduce the set to the top 5-predictor rank features. Interestingly, 3 of the 5 features are common in both cases. Also, notice that for the radius method all the features are from time domain while for the residue method, one is from frequency domain and the others from time domain. This seems to point out that time domain features are very relevant. The results using only one of the methods are optimal for the residue method, with accuracy up to almost 96% using only 5 features using a SVM classification system. But the results are even better (only one misclassified sample) when adding the first two features of the radius method (fractal related), reaching an accuracy of almost 98% with 7 features.

Louis (2015) demonstrated that the hand-drawn spiral is a sensitive and specific screening method as a measure of tremor severity for those tremors of mild to moderate amplitude or greater according to the WHIGET Tremor Rating Scale. This scale allows to rate postural and kinetic tremor during each test, including the four hand-drawn spirals: 0 (none), 1 (mild),

TABLE 10 | Accuracy (%) from SVM with RBF kernel classifier, residue features plus the following radius features: Maximum fractal length and Fractal dimension.

	Scale										
Cost	**0.1**	**0.2**	**0.3**	**0.4**	**0.5**	**0.6**	**0.7**	**0.8**	**0.9**	**1**	**1.1**
10^{-5}	55.1	55.1	55.1	55.1	55.1	55.1	55.1	55.1	55.1	55.1	55.1
10^{-4}	55.1	55.1	55.1	55.1	55.1	55.1	55.1	55.1	55.1	55.1	55.1
10^{-3}	55.1	55.1	55.1	55.1	55.1	55.1	55.1	55.1	55.1	55.1	55.1
10^{-2}	55.1	55.1	55.1	55.1	55.1	55.1	55.1	55.1	55.1	55.1	55.1
10^{-1}	55.1	65.31	55.1	55.1	55.1	55.1	55.1	55.1	55.1	55.1	55.1
1	87.76	81.63	81.63	79.59	79.59	77.55	79.59	79.59	73.47	67.35	67.35
10^1	**97.96**	89.8	89.8	83.67	83.67	83.67	81.63	81.63	81.63	81.63	81.63
10^2	**97.96**	95.92	93.88	91.84	91.84	89.8	91.84	89.8	89.8	89.8	83.67
10^3	**97.96**	95.92	93.88	91.84	93.88	91.84	91.84	91.84	93.88	93.88	93.88
10^4	**97.96**	95.92	93.88	91.84	93.88	91.84	91.84	91.84	89.8	89.8	89.8

The best result is highligted in bold. Cost stands for the penalty cost of missclassification and scale is the kernel scale applied.

2 (moderate), 3 (severe). In his study, when the tremor ratio was ≥ 1.5 (i.e., a mild to moderate tremor) the spiral analysis obtained a sensitivity between 78.8 and 97.0% depending on the samples and a specificity of 95.3%. The analysis proposed in our work achieves 100% sensitivity and 96.42% specificity even when the severity cut-off point is reduced to mild amplitude tremors (which would correspond to 1 on the WHIGET scale). In fact, the only badly classified case of our sample corresponds to a control without TE that has oscillations in the trace and that corresponds to a case of exaggerated physiological tremor (due to stress, drug consumption, etc.) and that can be classified as <1 in the scale. At present, these cases can only be adequately discriminated by means of more sophisticated tests such as the electromyographic register. Therefore, our method significantly improves the analysis of drawing results as a tremor screening tool because it allows for the proper classification of almost all tremor cases, even those of slight amplitude. This is interesting for real-time applications, because the computational cost is very low. Given the interesting results obtained by the cosine transform applied to the x and y coordinates, in future works we will evaluate this transform on the pressure and other direct characteristics measured by the digitation tablet.

ETHICS STATEMENT

This study was carried out in accordance with the recommendations of the Ethics Committee of the Donostia University Hospital (San Sebastian, Spain), which approved the protocol. All subjects gave written informed consent in accordance with the Declaration of Helsinki.

AUTHOR CONTRIBUTIONS

JS-C, PM-P, and KL conceived the algorithm. IA-E, PM-P, and JS-C implemented the feature selection algorithm and the classification algorithm and performed the data analysis. PC and IS-M collected the experimental data, and contributed to the signal processing section. KL and AB had theoretical contributions on the analysis of the results. JS-C, IA-E, KL, and PC wrote the first draft of the paper. All authors reviewed the draft of the paper and approved the final manuscript.

ACKNOWLEDGMENTS

We thank the Ministry of Business and Knowledge of the Government of Catalonia that partially supported this study through the Industrial Doctorates Plan to IA-E. We also thank the grant of DomusVi Foundation “Kms para recordar,” the programs of Basque Government, ETORTEK and IT115-16, the Gipuzkoa Goverment, Red Guipuzcoana de Ciencia, Tecnología e Innovación, and the Ministry of Science and Innovation for the TEC2016-77791-C04-R grant, which partially supported the study. Finally we would like to thank reviewers for their detailed and helpful comments to the manuscript.

REFERENCES

Cameron Riviere, N., Stephen Reich, G., and Nitish Thakor, V. (1997). Adaptive Fourier modeling for quantification of tremor. *J. Neurosci. Methods* 74, 77–87.

Cehovin, L., and Zoran, B. (2010). Empirical evaluation of feature selection methods in classification. *Intellig. Data Anal.* 14, 265–281. doi: 10.3233/IDA-2010-0421

Elble, R. J., Brilliant, M., Leffler, K., and Higgins, C. (1996). Quantification of essential tremor in writing and drawing. *Mov. Disord.* 11, 70–78.

Faundez-Zanuy, M. (2007). On-line signature recognition based on VQ-DTW. *J. Pattern Recog.* 40. 981–982. doi: 10.1016/j.patcog.2006.06.007

Haubenberger, D., Kalowitz, D., Nahab, F. B., Toro, C., Ippolito, D., Luckenbaugh, D. A., et al. (2011). Validation of digital spiral analysis as outcome parameter for clinical trials in essential tremor. *Mov. Disord.* 26, 2073–2080. doi: 10.1002/mds.23808

Jain, A., Bolle, R., and Pankanti, S. (1999). *Biometrics. Personal Identification in a Networked Society*. Norwell, MA: Kluwer Academic Publishers.

Kononenko, I., Simec, E., and Robnik-Sikonja, M. (1997). *Overcoming the myopia of inductive learning algorithms with Relieff. Appl. Intelli.* 7, 39–55.

Laske, C., Sohrabi, H. R., Frost, S. M., López-de-Ipiña, K., Garrard, P., Buscem, M., et al. (2015). Innovative diagnostic tools for early detection of Alzheimer's disease. *Alzheimer Dement*. 11, 561–578. doi: 10.1016/j.jalz.2014.06.004

Likforman-Sulem, L., Esposito, A., Faundez-Zanuy, M., Clemencon, S., and Cordasco, G. (2017). EMOTHAW: A novel database for emotional state recognition from handwriting and drawing. *IEEE Trans. on Human-Mach. Syst*. 47, 273–284. doi: 10.1109/THMS.2016.2635441

Lopez De Ipina, K., Iturrate, M., Calvo, P. M., Beitia, B., Garcia-Melero, J., Bergareche A., et al. (2015). "Selection of Entropy Based Features for the Analysis of the Archimedes' spiral applied to essential tremor," in *2015 4th InternationalWork Conference on Bioinspired Intelligence (IWOBI)* (San Sebastián).

Lopez-de-Ipiña, K., Alonso, J. B., Solé-Casals, J., Barroso, N., Faundez-Zanuy, M., and Travieso, C. (2013a). *On Automatic Diagnosis of Alzheimer's Disease based on Spontaneous, Speech Analysis and Emotional Temperature, Cognitive Computation*. Berlin: Springer.

Lopez-de-Ipiña, K., Alonso, J. B., Travieso, C. M., Solé-Casals, J., Egiraun, H., and Faundez-Zanuy, M. (2013b). On the selection of non-invasive methods based on speech analysis oriented to automatic alzheimer disease diagnosis. *Sensors* 13, 6730–6745. doi: 10.3390/s130506730

López-de-Ipiña, K., Solé-Casals, J., Faundez-Zanuy, M., Calvo, P. M., Sesa, E., Martinez de Lizarduy, U. et al. (2016). Selection of entropy based features for automatic analysis of essential tremor. *Entropy* 18:184. doi: 10.3390/e18050184

López-de-Ipiña, K., Solé-Casals, J., Faundez-Zanuy, M., Calvo, P. M., Sesa, E., Roure, J., et al. (2018). Automatic analysis of archimedes' spiral for characterization of genetic essential tremor based on shannon's entropy and fractal dimension. *Entropy* 20:531. doi: 10.3390/e20070531

Louis, E. D. (2015). Utility of the hand-drawn spiral as a tool in clinical-epidemiological research on essential tremor: data from four essential tremor cohorts. *Neuroepidemiology* 44, 45–50. doi: 10.1159/000371850

Louis, E. D., Gillman, A., Boschung, S., Hess, C. W., Yu, Q., and Pullman, S. L. (2012). High width variability during spiral drawing: further evidence of cerebellar dysfunction in essential tremor. *Cerebellum* 11, 872–9. doi: 10.1007/s12311-011-0352-4

Louis, E. D., and Vonsattel, J. P. (2007). The emerging neuropathology of essential tremor. *Movement Dis*. 23, 174–181. doi: 10.1002/mds.21731

Miralles, F., Tarongí, S., and Espino, A. (2006). Quantification of the drawing of an Archimedes spiral through the analysis of its digitized picture. *J. Neurosci. Methods* 152, 18–31. doi: 10.1016/j.jneumeth.2005.08.007

Molina, L., C., Belanche, L., and Nebot, A. (2002). "Feature selection algorithms: a survey and experimental evaluation,"*2002 IEEE International Conference on Data Mining 2002 Proceedings*. (Maebashi), 306–313.

Pullman, S. L. (1998). Spiral analysis: a new technique for measuring tremor with digitizing tablet. *Mov. Disord*. 3, 85–89. doi: 10.1002/mds.870131315

Sadikov Groznik, A., V., Žabkar, J., Mozina, M., Georgiev, D., Pirtosek, Z., et al. (2014). "Parkinson Check smart phone app. frontiers in artificial intelligence and applications," in *Proceedings of ECAI 2014* (Amsterdam: IOS Press), 1213–1214.

Sesa-Nogueras, E., Faundez-Zanuy,M., and Mekyska, J. (2012). An information analysis of in-air and on-surface trajectories in online handwriting. *Cogn. Comput*. 4, 195–205. doi: 10.1007/s12559-011-9119-y

Shair, E., F., Ahmad, S., A., Marhaban, M., H., et al. (2017). EMG processing based measures of fatigue assessment during manual lifting, *BioMed. Res. Int.* 2017:3937254. doi: 10.1155/2017/3937254

Zanuy, M., Hussain, A., Mekyska, J., Sesa-Nogueras, E., Monte-Moreno, E., Esposito, A., et al. (2013). Biometric applications related to human beings: there is life beyond security. *Cogn. Comput.* 5, 136–151. doi: 10.1007/s12559-012-9169-9

Zeuner, K. E., Peller, M., Knutzen, A., Holler, I., Münchau, A., Hallett, M., Deuschl, G., and Siebner, H. (2007). How to assess motor impairment in writer's cramp. *Mov. Disord*. 22, 1102–1109. doi: 10.1002/mds.21294

Conflict of Interest Statement: IA-E was employed by company Seidor Labs as a PhD student.

The remaining authors declare that the research was conducted in the absence of any commercial or financial relationships that could be construed as a potential conflict of interest.

Copyright © 2019 Solé-Casals, Anchustegui-Echearte, Marti-Puig, Calvo, Bergareche, Sánchez-Méndez and Lopez-de-Ipina. This is an open-access article distributed under the terms of the Creative Commons Attribution License (CC BY). The use, distribution or reproduction in other forums is permitted, provided the original author(s) and the copyright owner(s) are credited and that the original publication in this journal is cited, in accordance with accepted academic practice. No use, distribution or reproduction is permitted which does not comply with these terms.

ORIGINAL RESEARCH
published: 06 December 2018
doi: 10.3389/fphys.2018.01721

Investigating Multimodal Diagnostic Eye Biomarkers of Cognitive Impairment by Measuring Vascular and Neurogenic Changes in the Retina

Delia Cabrera DeBuc[1]*, Gabor Mark Somfai[2,3], Edmund Arthur[1], Maja Kostic[1], Susel Oropesa[1] and Carlos Mendoza Santiesteban[1]

[1] Department of Ophthalmology, Bascom Palmer Eye Institute, University of Miami, Miami, FL, United States, [2] Retinology Unit, Pallas Kliniken, Olten, Switzerland, [3] Department of Ophthalmology, Semmelweis University, Budapest, Hungary

OPEN ACCESS

Edited by:
Sladjana Z. Spasić,
University of Belgrade, Serbia

Reviewed by:
Alessandro Giuliani,
Istituto Superiore di Sanità (ISS), Italy
Stefan Talu,
Technical University of Cluj-Napoca, Romania

***Correspondence:**
Delia Cabrera DeBuc
dcabrera2@med.miami.edu

Specialty section:
This article was submitted to Fractal Physiology, a section of the journal Frontiers in Physiology

Received: *30 June 2018*
Accepted: *15 November 2018*
Published: *06 December 2018*

Citation:
Cabrera DeBuc D, Somfai GM, Arthur E, Kostic M, Oropesa S and Mendoza Santiesteban C (2018) Investigating Multimodal Diagnostic Eye Biomarkers of Cognitive Impairment by Measuring Vascular and Neurogenic Changes in the Retina. Front. Physiol. 9:1721. doi: 10.3389/fphys.2018.01721

Previous studies have demonstrated that cognitive impairment (CI) is not limited to the brain but also affects the retina. In this pilot study, we investigated the correlation between the retinal vascular complexity and neurodegenerative changes in patients with CI using a low-cost multimodal approach. Quantification of the retinal structure and function were conducted for every subject ($n = 69$) using advanced retinal imaging, full-field electroretinogram (ERG) and visual performance exams. The retinal vascular parameters were calculated using the Singapore Institute Vessel Assessment software. The Montreal Cognitive Assessment was used to measure CI. Pearson product moment correlation was performed between variables. Of the 69 participants, 32 had CI (46%). We found significantly altered microvascular network in individuals with CI (larger venular-asymmetry factor: 0.7 ± 0.2) compared with controls (0.6 ± 0.2). The vascular fractal dimension was lower in individuals with CI (capacity, information and correlation dimensions: D_0, D_1, and D_2 (mean ± SD): 1.57 ± 0.06; 1.56 ± 0.06; 1.55 ± 0.06; age 81 ± 6years) vs. controls (1.61 ± 0.03; 1.59 ± 0.03; 1.58 ± 0.03; age: 80 ± 7 years). Also, drusen-like regions in the peripheral retina along with pigment dispersion were noted in subjects with mild CI. Functional loss in color vision as well as smaller ERG amplitudes and larger peak times were observed in the subjects with CI. Pearson product moment correlation showed significant associations between the vascular parameters (artery-vein ratio, total length-diameter ratio, D_0, D_1, D_2 and the implicit time (IT) of the flicker response but these associations were not significant in the partial correlations. This study illustrates that there are multimodal retinal markers that may be sensitive to CI decline, and adds to the evidence that there is a statistical trend pointing to the correlation between retinal neuronal dysfunction and microvasculature changes suggesting that retinal geometric vascular and functional parameters might be associated with physiological changes in the retina due to CI. We suspect our analysis of combined structural-functional parameters, instead of individual biomarkers, may provide a useful clinical marker of CI that could also provide increased sensitivity and specificity for the differential diagnosis of CI. However, because of our study sample was small, the full extent of clinical applicability of our approach is provocative and still to be determined.

Keywords: eye biomarkers, retinal vascular complexity, Alzheimer's disease, cognitive impairment, fractal dimension, neurodegeneration, electroretinography

INTRODUCTION

According to the 2015 World Alzheimer Report, there are approximately 46 million dementia patients worldwide (Prince et al., 2015). This number will almost double every 20 years, and it is estimated to increase to 131.5 million by 2050. It has been estimated that the total worldwide dementia-related healthcare cost is $818 billion, rising to $2 trillion by 2030 (Prince et al., 2015).

Alzheimer's disease (AD) is the most common, progressive cause of dementia in the elderly, and a severe burden on the aging society worldwide (Prince et al., 2015). Also, dementia is most common among older patients with longer Parkinson's disease (PD) duration, and least common in individuals with multiple sclerosis (MS). Previous studies have suggested that AD initiates decades before it is clinically expressed (La Rue and Jarvik, 1987; Linn et al., 1995; Snowdon et al., 1996; Braak and Braak, 1997; Elias et al., 2000; Kawas et al., 2003). Therefore, it would be possible to identify persons who will ultimately express the disorder long before the early symptoms appear as well as to target potential interventions to prevent disease expression in such individuals at high risk.

As an anatomically integral part of the brain, the retina shares important structural and pathogenic pathways with the central nervous system (Cabrera DeBuc et al., 2017). The link between eye pathology and AD, PD and MS has been established in multiple studies (Katz and Rimmer, 1989; London et al., 2012; Cabrera DeBuc et al., 2017; Hampel et al., 2018). In particular, neuronal loss in AD associated with optic nerve parameters include retinal ganglion cells which are similar to neurons in the cerebral cortex, and have been correlated to neurodegeneration in AD (Katz and Rimmer, 1989; Hampel et al., 2018). Recently, advances in neuro-electrophysiological and optical imaging technologies have facilitated non-invasive morphological and functional measurements in the eye using electroretinography and advanced retinal imaging. Specifically, retinal microvascular changes as well as the abnormal bioelectrical activity of retinal ganglion cells, photoreceptors and the optic nerve have been associated with cognitive decline and brain changes in relation to aging and early AD (Moschos et al., 2012; Ong et al., 2014; Hampel et al., 2018). Moreover, it has been hypothesized that if an association can be made between the amyloid in the brain and the amyloid in the eye, then it would be feasible to diagnose AD by looking into the eye (Koronyo-Hamaoui et al., 2011; Koronyo et al., 2012; Hampel et al., 2018). Therefore, the vast research exploring cognitive impairment non-invasively in the brain through the easily accessible retina warrants further investigation to support the use of retinal biomarkers in the detection of cognitive decline even during the asymptomatic period.

The discovery of biomarkers is a complicated process that demands considering multiple factors and approaches to obtain reliable markers that allow us to predict risk or response to treatment very early and with low false positive and false negative rates. Unfortunately, the critical barriers to primary prevention of cognitive decline are the lack of rapid, non-invasive, sensitive and low-cost biomarkers. In this pilot study, we investigated the extent to which measures of vascular complexity and neurodegenerative changes in the retinal tissue contribute to differences in cognitive function using a low-cost multimodal approach. Our central hypothesis is that multivariate eye biomarkers reflect distinctive eye-brain signatures of cognitive impairment that might be associated with the onset and progression of cognitive decline. Therefore, quantification of the retinal vascular network complexity and its neural function was performed for each study participant using advanced retinal imaging, full-field electroretinogram (ERG) as well as visual performance exams. Our preliminary findings show that our multimodal approach to evaluating visual capacities in elderly individuals may add predictive value of early visual pathway injury associated with cognitive decline and facilitate the introduction of novel multimodal eye biomarkers for early detection of cognitive impairment at a low-cost.

MATERIALS AND METHODS

The Human Research Ethics Committee of the University of Miami, Miami, FL, United States approved all protocols and methods described in this study. The research adhered to the tenets outlined in the Declaration of Helsinki. Informed consent was obtained from all participants following a thorough explanation of all test procedures. All study subjects underwent cognitive function assessment and ERG followed by advanced retinal imaging, color vision test and visual performance exams of both eyes.

Study Participants

Prospective subjects with cognitive impairment were identified in a non-systematic fashion as they appeared in the clinic or identified from a population attending adult care centers and community clinics with a diagnosis of AD. Study subjects were recruited in numerous ways using flyers, a university press release that generated interest in the community of Miami-Dade and Broward counties in Florida, and by giving talks to AD caregiver support groups in the nearby regions. Study subjects (or for the patients with cognitive decline, reliable caregivers/informants) were interrogated about subjective changes in vision that may have occurred in the recent past or over the progression of their disease. The exclusion criteria were age under 55 years and the presence of any ophthalmic history before recruitment. Participants who were not capable of comprehending information, and making decisions about participation in the study due to cognitive impairments that affect decision-making to make informed choices, had informed consent obtained through a proxy. The macular and optic disk regions were scrutinized for abnormalities and subjects without any ocular history except for cataract surgery were included in the analyses. All subjects wore their own best optical correction for the visual performance tests. Both hypertension and diabetes mellitus as well as cardiovascular disease were considered comorbid medical conditions related to retinal vascular alterations. Also, current or history of study subject-reported smoking categorized as current, past, or never, was considered because of earlier reports linking smoking with potential vascular changes in the retina (Sun et al., 2009).

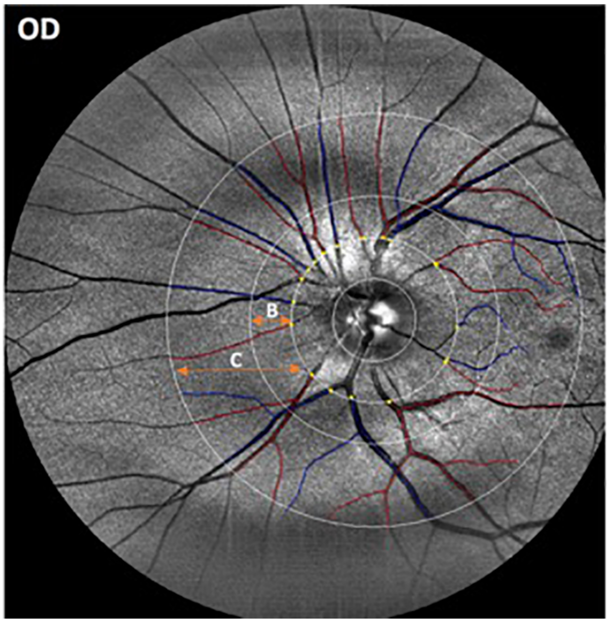

FIGURE 1 | Representative image obtained with the EasyScan unit (i-Optics Corporation, Netherlands) and analyzed with the SIVA program that measured the caliber of the vessels emerging from the optic disk. Arterioles are in red and venules are in blue. The SIVA software automatically detects the optic disk and traces vessels in a zone 0.5 to 2.0-disk diameter from the disk margin. The different circular ROIs with various radii around the optic disk center are labeled as B (0.5 – 1.0 disk diameters away from the disk margin) and C (0.5- 2.0 disk diameters away from the disk).

Fundus Imaging and Quantitative Analysis of the Retinal Vascular Network

Retinal fundus photographs were taken of each eye with a non-mydriatic digital camera (EasyScan, iOptics, Netherlands) based on scanning laser ophthalmoscopy (SLO) technology that has better penetration of media opacities such as cataract (Webb et al., 1987). Its high-resolution images reveal what cannot be seen with a traditional fundus camera, thanks to its multiple plane principle (**Figure 1**). This low-cost camera with a FOV of 45° and image size of 1024 × 1024 requires minimal operator training, and it is conceived to maximize patient flow. Also, its compact, ergonomic design and low power flash help ensure patient comfort. Moreover, taking a high-contrast, detailed retinal image is easy and intuitive. With one push of a button, it can be operated anywhere and captures the image in both eyes in less than 5 min.

Retinal images from all participants were masked and collected for further analysis. The right eye was imaged first followed by the left eye. Optic-disk centered images of a selected eye from each participant were analyzed with a semi-automated computer-assisted program, Singapore I Vessel Assessment (software version 3.0, National University of Singapore) (Cheung et al., 2011). Images with poor quality were removed from the analysis. The investigation was performed using a standardized protocol by a trained grader after the retinal arterioles and venules were identified automatically by the SIVA program (**Figure 1**). The circular retinal region of interest (ROI) for the overall analyses were 0.5 – 1.0 disk diameters away from the disk margin (zone B in **Figure 1**) or 0.5–2.0 disk diameters away from the disk margin (zone C in **Figure 1**). This particular ROI selection to measuring the geometric vascular parameters warranted that the retinal vessels had reached arteriolar status. All artifacts traced as vessels were removed by comparing the automated vessel tracing with the fundus images obtained with the EasyScan unit. Two experienced retinal specialists revised the vessel classification (i.e., arteries/veins) automatically generated by the SIVA software, and assessed all fundus photographs to identify and rule out retinal pathological features related to age-related macular degeneration (AMD), diabetic retinopathy and glaucoma. Then, all misclassifications of the retinal vessels were corrected by the grader, and images showing signs of AMD and other pathological features related to diabetic retinopathy (e.g., exudates, edema, cotton wool spots, hemorrhages, microaneurysms) and glaucoma (suspicious optic disk cupping) were discarded. Moreover, the resulting geometric vascular parameters of the retina were obtained and used for further analysis: retinal vascular caliber, summarized as central retinal artery/vein equivalent (CRAE, CRVE), curvature tortuosity (cTORTa, cTORTv), branching coefficient (BCa, BCv), branching asymmetry factor (AFa, AFv), length diameter ratio (LDRa, LDRv), and artery-vein ratio (AVR) as described in earlier studies (Cheung et al., 2011). The reliability assessment and detailed characterization of these vascular parameters have been described elsewhere (Liew et al., 2008; Cheung et al., 2011). The SIVA program calculates the CRAE and CRVE parameters, based on the revised Knudtson–Parr–Hubbard formula. These parameters represent the average width of the central retinal vessels. The AVR consists of a ratio of the caliber of arterioles to venules, and it is not affected by magnification differences caused by refractive errors and camera lens adjustments (Cosatto et al., 2010). The BC is an estimate of the ratio between the diameters of the main vessel and the diameters of its branches, which is also known as daughter vessels (Zamir et al., 1979). Therefore, a vascular network with comparably sized vessel diameters between the main vessel and its branch is characterized by a higher BC, while a reduction in the branches' diameters compared to the main vessel is related to a lower BC. Also, cTORT is a tortuosity index defined as the integral of curvature squared along the path of the vessel normalized by the total arc length (Hart et al., 1999). Therefore, cTORT considers the bowing and points of inflection. Straighter vessels are characterized by a lower tortuosity index. The LDR is a measure of the vessel width defined as the length of the vessel from the midpoint of one bifurcation to the midpoint of the next bifurcation. It is expressed as a ratio to the diameter of the parent vessel at the first bifurcation (Cheung et al., 2011). The ratio of the squares of the two branching vessel widths is used to calculate AFa and AFv.

Fractal Dimension of the Retinal Vascular Network

Fractal analysis, a mathematical method used to measure complexity in natural phenomenon (Mandelbrot, 1982), is a well proved and reliable methodology used to characterize the retinal vasculature (Liew et al., 2008; Cosatto et al., 2010; Thomas et al., 2014). This method was introduced in ophthalmology by Family et al. (1989), and since then, interest in investigating the association between the fractal dimension (FD) of the retinal vasculature and disease severity and progression has dramatically increased. The retinal vasculature tree could be quantified with various methods of fractal analysis (Stosic and Stosic, 2006; Macgillivray et al., 2007; Ţălu, 2013a,b). The vascular FD, characterizes a "global" measure that includes the whole branching pattern of the retinal vascular tree. Therefore, a more complex branching pattern indicates a larger FD value. Self-similarity over different scales is an important property of the fractal structures. This self-similar property means that at different magnifications or scales, a similar pattern with different sizes can be perceived. This property can be described by the following equation:

$$N(r) = \text{const}\, r^{-D} \qquad (1)$$

where N(r) is certain measurements applied on the complex pattern of the fractal structure at a scale or magnification r; D is the FD that implies how many new similar patterns are observed as the resolution magnification (scale) increases or decreases.

Because the human retinal vessel structures have been shown to be geometrical multifractals (Family et al., 1989; Mainster, 1990; Kyriacos et al., 1997; Stosic and Stosic, 2006; Ţălu, 2013b), the vascular FD was calculated from the skeletonized vascular network (**Figure 2**) using both a monofractal and multifractal approach (Vehel and Legrand, 2003). In contrast to most studies, our approach did not use different circular regions of interest with various radii around the optic disk centers. Instead, to obtain comparable FD values, the skeleton comprised the whole branching pattern observable in the full 45° FOV.

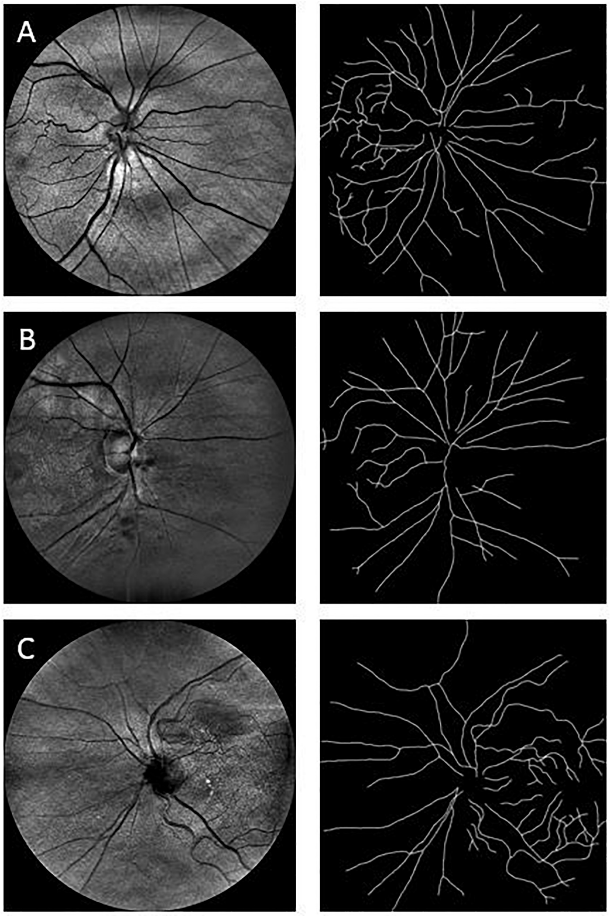

FIGURE 2 | Sample images used in the fractal analysis. Images in the left column are the raw images obtained with the EasyScan system, while those in the right are their respective skeleton images that were used in the fractal analysis. Row **(A)** is from a healthy cognitively individual (MoCA score range: 29.6–25.2), Row **(B)** is from an MCI subject (MoCA score range: 25.2–19), and Row **(C)** is from a participant with more cognitive deterioration than MCI (MoCA score range: 21 to 11.4). MoCA, Montreal Cognitive Assessment.

The box-counting method, proposed by Liebovitch and Toth (1989), is the most popular monofractal approach for estimating the FD of fractal objects. This method generates data by covering the object with a rectangular coordinate grid and breaking the data into boxes and then analyzing the subsets by counting the number of boxes. Therefore, the measurement N(r) in (1) is the number of boxes with side-length r that overlap with the vessel segmentation or skeleton, and the box dimension (D_B) can be calculated as the absolute value of the slope of N(r) plotted against r in a log-log plot.

The multifractal approach was used to investigate the effect of the scale on the multifractal dimension (Stosic and Stosic, 2006; Gould et al., 2011). In this approach, the multifractal behavior in the structure is described by finding the generalized dimension Dq, which is associated to a value of q that expresses the fractal properties in different scales. The plot of Dq vs. q is usually sigmoidal and decreasing to a multifractal configuration. This method has been employed effectively to prove geometric multifractality of the diffusion limited aggregation (DLA) fractal dimension (Vicsek et al., 1990). Certain studies consider determined values of Dq (e.g., D_0, $D_{1,}$ and D_2), which describe the multifractal characteristics of an object when condition $D_0 \geq D_1 \geq D_2$ is satisfied. Particularly, the capacity dimension D_o (or box counting), has been reported to be constantly larger than the information (or Shannon or entropy) dimension D_1, which was in turn always larger than the correlation dimension D_2 (i.e., all satisfying $D_o > D_1 > D_2$). In all studies, all the three generalized dimensions (D_o, $D_{1,}$ and D_2) are being significantly lower than the DLA fractal dimension ($D \approx 1.7$) (Witten and Sander, 1981; Family et al., 1989; Mainster, 1990; Kyriacos et al., 1997; Stosic and Stosic, 2006). The D_1 measures the uncertainty or entropy of a random event, being lower or less informative for events that happen very often while larger or more informative for events that might happen less likely (Stosic and Stosic, 2006). The D_2 estimates the FD via the association between two pixels inside a region (Stosic and Stosic, 2006). Therefore, in our study, the multifractal behavior in the retinal images was analyzed using the generalized dimension spectrum for *q* values ranging between −10 and +10, where all dimensions were statistically examined. Accordingly, $D_{o,}$ $D_{1,}$ and D_2 were computed and compared to check for consistency where $D_o > D_1 > D_2$.

The public domain Java image-processing program ImageJ together with the FracLac plug-in was used to calculate the multifractal properties of the retinal vasculature network (Karperien, 1993). A total of 12 different grid positions was defined in the grid design pane of the FracLac environment. This arrangement facilitated multiple scans by changing the starting position of the sampling grid each time to capture the variation attributable to the grid orientations or positions. The recommend setting for this parameter is 4 – 12 grid positions or orientations as sampling tends to be unaffected beyond 12 positions. We optimized this parameter by using 3 different number of grid positions (9, 12, and 15) to test whether the different number of grid positions may result in different slopes (D_0) and R^2 values in the double log plots. As shown in **Figures 3**, **4**, the slopes and R^2 values remained the same. Hence, we used the recommended number of 12 grid positions. A linear scaling method was also used to set 20 varying box sizes from a minimum box size of 10 pixels to a maximum box size of approximately 60% of the image size. The FracLac software computes the constant linear scale as the difference between the minimum and maximum box sizes divided by the number of different box sizes. The "greater dim" and "check pix" check-boxes were selected to make sure the longer side of the bounding box was used as the image dimension and that only boxes containing meaningful pixels were used in the computations of FD, respectively. No sub sampling was selected in the sub scan options. The generalized dimension spectrum was set from −10 to 10 with an increment of 1 and a graph of Dq vs. q was chosen in the MF (multifractal) Graphs options. In the data processing option, we selected "show optimal sample only" for the multifractal optimizer option and "no filter" for the multifractal filters. Regression for the double log plots and "draw grids" (to show whether grids used in the FD calculation contained meaningful pixels) options were selected in the graphics option.

Electroretinography

Several ERG changes have been recorded in patients with AD (Sadun et al., 1987; Armstrong, 1996). Earlier studies have reported that the involvement of the visual cortex may be the cause for dysfunction of the elementary visual sensation that may be involved in the development of visual cognitive deficits and vision-related behavioral symptoms (Strenn et al., 1991; Granholm et al., 2003). Moreover, flash ERG was used to demonstrate dysfunction of the retina under photopic and scotopic conditions in patients with dementia with Lewy bodies (Devos et al., 2005). The use of the full-field ERG was also suggested to find whether dysfunction of preganglionic elements may also occur in AD (Parisi et al., 2001). Intriguingly, it has been also suggested that the ERG could be possibly used as a marker of central dopamine and serotonin levels (Lavoie et al., 2014).

Evaluation of the bioelectrical activity of the retina was performed with a full-field ERG (RETeval^{TM}, LKC Technologies, Inc., Gaithersburg, MD, United States) according to the International Society for Clinical Electrophysiology of Vision (ISCEV) protocol (Marmor et al., 2004; Holder et al., 2007; Hood et al., 2008). The RETeval^{TM} system is a full-field flicker ERG recording device designed as a low-cost handheld alternative to traditional ERG screening without the need for mydriasis (Kato et al., 2015). It can perform measurements in both eyes in about 3 min without any eye contact. Also, various flicker-based or single-flash based protocols are available through a protocol chooser that enables other ERG/VEP tests (Sadun et al., 1987). The intensity of the flash source of this device is calibrated consistently with the light-adapted 3.0 flicker ERG protocol of the ISCEV standard. The ERG examination was performed by an experienced examiner trained in the use of the RETeval^{TM} unit. As per the manufacturer's recommendations, a disposable, self-adhering skin contact electrode array (Sensor Strip; LKC Technologies) was placed on the cheek inferior to the lateral half of the lower eyelid (∼2 mm from the eyelid margin) and the lead was connected to this strip to initiate the ERG recordings. Participants were seated in an upright position and with the fellow eye covered were asked to focus on the red beam projected from the device. The right eye was tested first followed by the left eye. The skin contact electrode strips were disposed of to prevent rescreening of other study subjects using the used strips. ERG amplitudes and implicit time values were measured consistent with the recommendations by the ISCEV (McCulloch et al., 2015). The protocol used was the ISCEV 6 step, light-adapted first. Assessments consisted of light-adapted ERG (stimulus strength, 3.0 cd·s/m^2; frequency, 28.3 Hz flicker response); and dark-adapted ERG including rod, maximal dark-adapted and cone responses. Implicit times and amplitude values of the ERGs

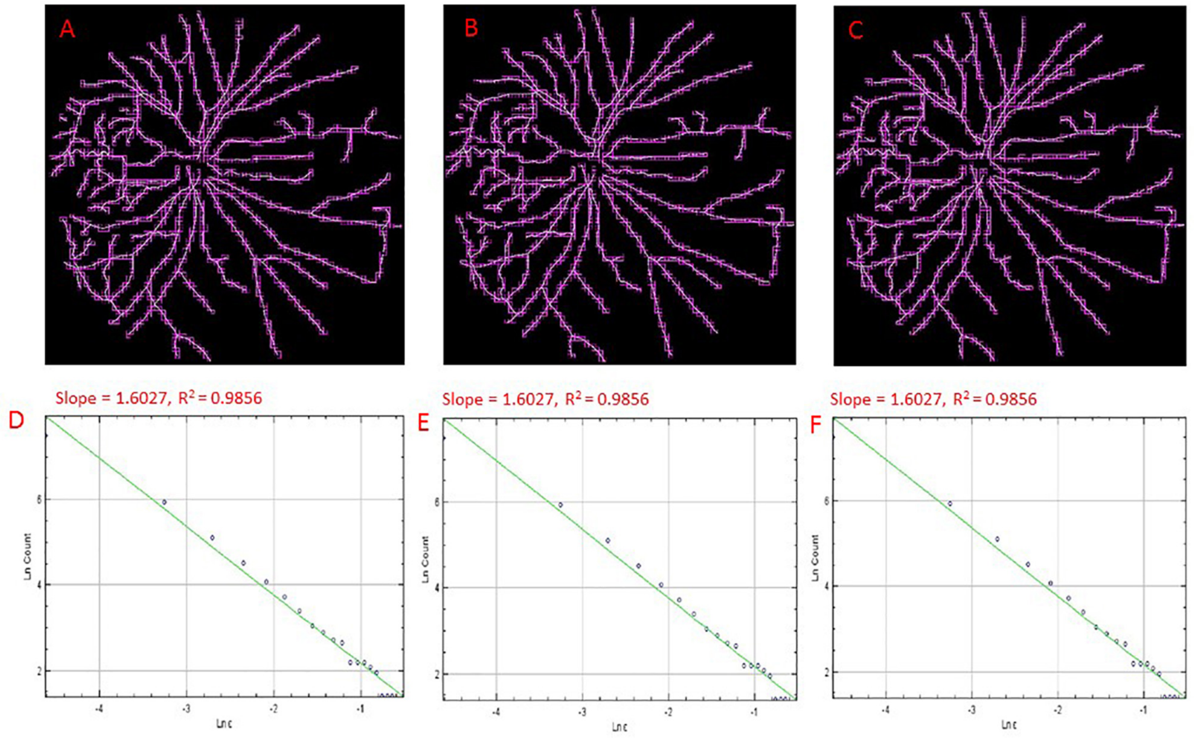

FIGURE 3 | Skeletons of vessels obtained from an cSLO image of a cognitively healthy individual with overlaid boxes at different number (i.e., 9, 12, and15) of grid positions, 9 **(A)**, 12 **(B)**, and 15 **(C)** with their corresponding double-log plots **(D–F)** of the count of boxes containing meaningful pixels vs. box size showing the slope (D_0) and the R^2 values of the regression lines. Overlaid boxes on the skeletonized images are shown to indicate that only boxes containing meaningful pixels were counted and used in the computation of the fractal dimension (D_0 or the slope). Different number of grid positions are shown in **(A–C)** from the FracLac settings to show that these parameters were optimized and that a change in the number of grid positions did not result in a change in the slope (D_0) or the R^2 values **(D–F)**. Hence the recommended number of 12 grid positions was used.

elicited by 141 to 424 flashes were processed separately for each eye.

Also, all comparisons were established by using our ERG data collected along with the reference data provided by the manufacturer of the RETeval^{TM} device. Specifically, the ERG norm in the RETeval^{TM} system is based on reference data collected from 244 individuals aged 4–85 who were carefully examined to have normal vision. The criteria followed to classify the eyes as normal were a BCVA of 20/25 (0.1 logMAR) or better, optic nerve cupping $< 50\%$, no glaucoma or retinal diseases, no prior intraocular surgery (excepting non-complicated cataract or refractive surgery performed more than 1 year before), IOP ≤ 20 mmHg, no diabetes, and no diabetic retinopathy as determined by the ophthalmologist or optometrist.

Color Vision Quantification

Alzheimer's disease is one of the chronic illnesses that can lead to acquired color vision deficiencies and ultimately, to color blindness (Pache et al., 2003; Cabrera DeBuc et al., 2017). For example, it has been reported that the cone contrast test scores in elderly individuals may be affected by cognitive decline (Simunovic, 2016). Therefore, study subjects were tested for acquired color vision deficiencies considering that the loss in cone function could be caused by neurological, systemic, ocular disorders and trauma to the eye or brain (Simunovic, 2016). A commercially available tablet-based Cone Contrast Test unit (CCT, Provideo CCT Plus System, Innova Systems Inc., Burr Ridge, IL, United States) was used to test the type and severity of color vision deficiency (Rabin et al., 2011). The tablet-based CCT scores, expressed in the range from 0 to 100, were measured on a portable tablet display (10.1″, 1366 × 768 pixels, Windows 8) with a touchscreen interface and the system firmware version 14.2.6. The color vision examination was conducted from the right eye to the left eye in a dark room with the tablet's display parallel to the individual's face plane and positioned at near distance (75 cm). The liquid crystal display of the tablet-based CCT was calibrated before the examination. The score results from the left eyes were used when both eyes met the inclusion criteria to lessen potential errors due to inexperience with the CCT test.

The stimulus displayed by the tablet-based CCT system consisted of a randomized series of colored letters on a gray background which are visible only to Red (R), Green (G), or Blue (B) cones in decreasing steps of cone contrast (**Figure 5**). During the exam, a single letter is displayed in the center of the screen, and the observer had to use a mouse to select the letter seen from an adjacent 10-letter matching display. Then, based on the observer' s correct or incorrect responses, color contrast is

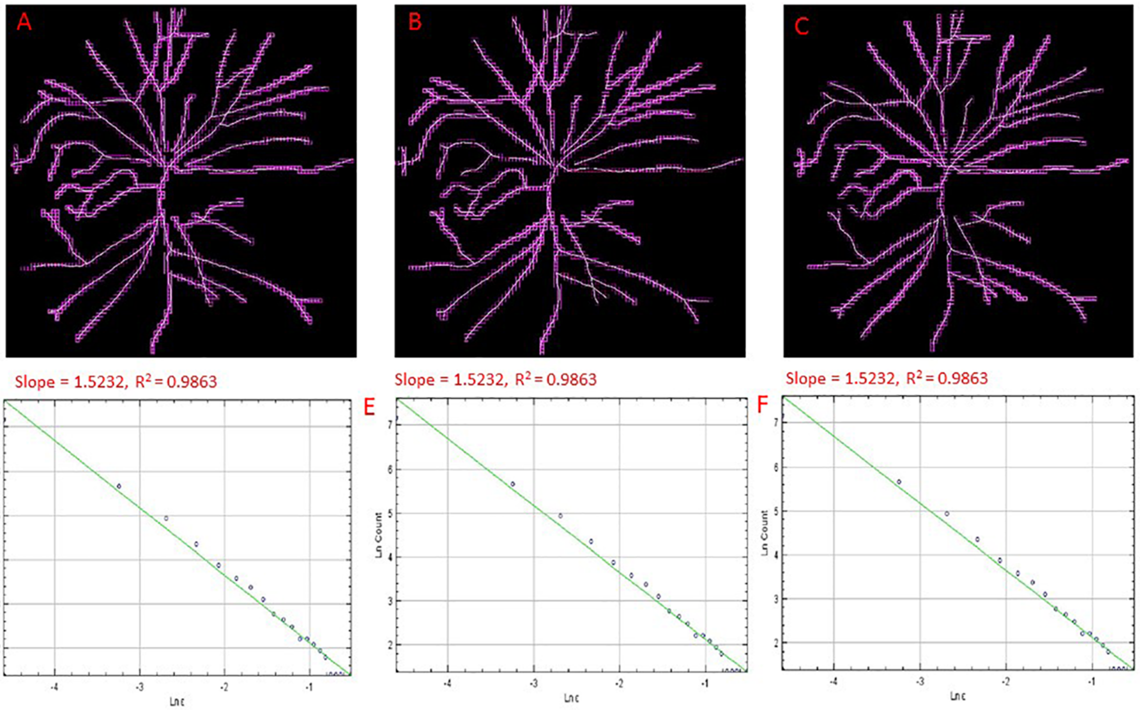

FIGURE 4 | Skeletons of vessels from an cSLO image of a MCI participant with overlaid boxes at different number of grid positions, 9 **(A)**, 12 **(B)**, and 15 **(C)** with their corresponding double-log plots **(D–F)** of the count of boxes containing meaningful pixels vs. box size showing the slope (D_0) and the R^2 values of the regression lines. Overlaid boxes on the skeletonized images are shown to indicate that only boxes containing meaningful pixels were counted and used in the computation of the fractal dimension (D_0 or the slope). Different number of grid positions are shown in **(A–C)** from the FracLac settings to show that these parameters were optimized and that a change in the number of grid positions did not result in a change in the slope (D_0) or the R^2 values **(D–F)**. Hence the recommended number of 12 grid positions was used. For all double log pots of the remaining cognitively impaired and healthy controls, see **Supplementary Information**.

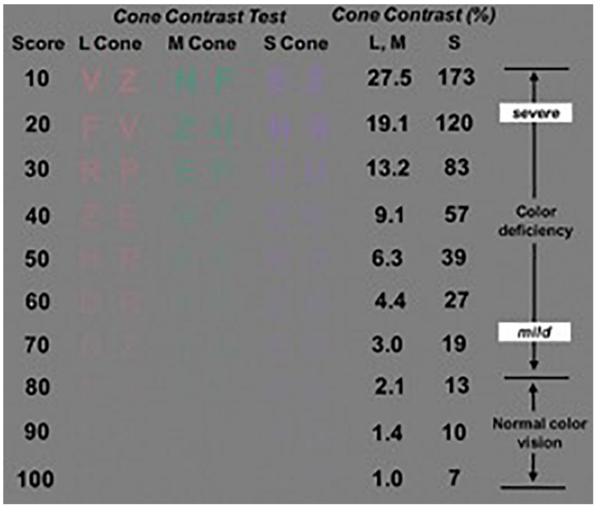

	Cone Contrast Test			Cone Contrast (%)		
Score	L Cone	M Cone	S Cone	L, M	S	
10	V Z	N F		27.5	173	
20	F V			19.1	120	severe
30	R P	E P		13.2	83	
40	Z E			9.1	57	Color deficiency
50				6.3	39	
60				4.4	27	
70				3.0	19	mild
80				2.1	13	
90				1.4	10	Normal color vision
100				1.0	7	

FIGURE 5 | The cone contrast test (CCT) design principles showing the Long, Middle, and Short- CCT scores (i.e., Red, Green and Blue CCT scores, respectively). Image modified from Rabin et al. (2011).

adjusted up and down using a staircase program, to establish the lowest (least visible) R, G, and B cone contrast that the individual can see. The R, G, and B cone CCT scores are expressed on a scale of 0–100 based on the number of letters identified correctly. As previously reported, Cone contrast test (CCT) scores of 75 or greater were defined as normal (Rabin et al., 2011). Also, the CCT can be used after cataract surgery in elderly patients (Fujikawa et al., 2018).

Visual Performance Test

The Ceeable Visual Field Analyzer (CVFA) is a cloud-based digital platform used to detect and diagnose retinal disease, and as an aid in monitoring progression of visual disease (Fink, 2004). The CVFA delivers rapid, accurate and low-cost visual testing to patient populations that may not have access to traditional visual testing services. The system is based on the 3D Computer Automated Threshold Amsler Grid (3D-CTAG) test. With one eye covered, the subject is positioned in front of a touch-sensitive computer screen on a head-chin rest and finger-traces the areas of an Amsler grid that are missing from his field of vision. Various degrees of contrast of the Amsler grid are presented by repeating the test at different grayscale levels. The resulting 3D data represent the measured contrast sensitivity across the tested visual field and are stored in a relational MySQL database. The platform includes an automated and integrated artifact removal, analysis, and characterization system, which analyzes 3DCTAG visual field data and objectively identifies and characterizes the occurring visual field defects (scotomas) within according to visual field data transforms and scotoma data transforms. Following each test, a topographical contour map, a 3D depiction of the central hill-of-vision, and the comprehensive visual field and scotoma characterization are automatically generated and displayed onscreen, using the freely available Gnuplot© plotting package.

Assessment of Cognitive Function

Cognitive function was assessed using the Montreal Cognitive Assessment (MoCA), a widely-used screening test for detecting cognitive impairment (Nasreddine et al., 2005). This brief assessment is a one-page 30-point test administered in about 10–12 min. An experienced examiner performed the test. It focuses on several cognitive domains: short-term memory, visuospatial abilities, executive functions, language abilities, orientation to time and place as well as attention, concentration, and working memory. The MoCA total score range is from 0–30, with lower scores (<26 points) indicating poorer cognitive ability. Patients with a score of $\geq$ 26 points are generally considered as having normal cognition with an average score of 27.4, compared with 22.1 in people with mild cognitive impairment (MCI) and 16.2 in people with AD (Folstein et al., 1975; Smith et al., 2007). One of the advantages of the MoCA test is that it measures an essential component of dementia (i.e., executive function) that is not measured by the mini-mental state examination (MMSE). It also allows cognitive testing for those who are visually impaired.

Statistical Analysis

All statistical analyses were performed using IBM SPSS Statistics for Windows, Version 24.0 (IBM Corporation, Armonk, NY, United States). All values are presented as per mean and standard deviation (SD). A p value < 0.05 was considered statistically significant. The Shapiro–Wilk test of normality was used to test the normal distribution of the covariates used in our statistical analysis. The Shapiro–Wilk test did not come out significant for the covariates used in our statistical analysis, hence parametric tests were used. Independent sample *t*-tests were used to compare the means of the variables between the cognitively healthy and the cognitively impaired groups. Pearson product moment correlation was used to find the associations between vascular and functional parameters. Partial correlations were then performed to assess the unique associations between each vascular parameter and the functional parameter while controlling for the other covariates.

RESULTS

Of the 69 initially recruited participants, 32 had cognitive impairment (46%). We excluded data from individuals that had eyes with poor image quality, AMD, glaucoma, diabetic retinopathy, along with data from a subject with a cardiac pacemaker implanted. Six subjects were pseudophakic but without any ocular history except for cataract surgery. All participants with diabetes mellitus (n = 9) and hypertension (n = 10) were well controlled and did not exhibit retinopathy signs. After applying all exclusion criteria, a total of 20 subjects with cognitive impairment were included in the final analyses. **Table 1** shows the baseline characteristics of these participants. Furthermore, we found that some participants (n = 17) with no cognitive impairment had some illnesses (e.g., pre-diabetes, diabetic retinopathy, glaucoma, cataract, AMD, hypothyroidism, controlled HIV, childhood's eye injury, uncontrolled hypertension, uncontrolled diabetes, and cardiovascular disease) that may share a risk factor with the outcome (i.e., cognitive impairment) under study. Also, although quality of the retinal image was acceptable, an image from one of the cognitively healthy subjects couldn't be read by the SIVA software for further analysis. Therefore, a total of 19 healthy participants with no cognitive impairment was integrated into a data group after removing the above participants with risk factors and individuals that did not fulfill the age-matching criterion needed for establishing rigorous comparisons with the group of patients with cognitive impairment (**Table 1**).

Only 6 out of 22 associations were found to be significant. These parameters were the AVR, LDRt, D_0, D_1, D_2 and the IT. The Pearson product moment correlation found significant associations between the vascular parameters and IT (**Table 2**)

TABLE 1 | Baseline characteristics of participants with cognitive impairment and cognitively healthy individuals after applying the inclusion/exclusion criteria.

Characteristic	Cognitive impairment (*n* = 20)	Cognitively healthy (*n* = 19)
Mean age, years (*SD*)	81(6)	80(7)
Mean MoCA (*SD*)	17(5)	27(1)
Mean HR [beats per minute, (*SD*)]	72(12)	76(2)
S_pO_2	96(2)	98(1)
Male, n (%)	4(20)	3(16)
Ever smoked, n (%)	4(20)	2(10)
Current smoker, n (%)	0(0)	0(0)
Hypertension, n (%)	6(30)	4(20)
Diabetes, n (%)	6(30)	3(16)
Pseudophakic, n (%)	2(10)	4(21)
Dyslipidemia, n (%)	3(15)	0(0)

MoCA, Montreal Cognitive Assessment.

TABLE 2 | Statistical significant associations between retinal vascular and functional parameters.

Parameters correlated	Pearson coefficients	*p*-value
AVR vs. IT	0.75	< 0.001
LDRt vs. IT	0.48	0.03
D_o vs. IT	0.64	0.002
D_1 vs. IT	0.67	0.001
D_2 vs. IT	0.69	0.001

AVR, arteriole–venular ratio; IT, implicit time; LDRt, total length-to-diameter ratio (i.e., arteriolar+venular); D_o, capacity dimension; D_1, information dimension; D_2, correlation dimension. For full correlations between all variables, see ***Supplementary Tables 1–7*** *in the* ***Supplementary Materials****.*

TABLE 3 | Associations between retinal vascular and functional parameters after partial correlation analyses.

Parameters correlated	Partial correlation coefficient	*p*-value	Control variables
AVR vs. IT	0.39	0.13	D_0, D_1, D_2, LDRt
LDRt vs. IT	0.15	0.57	D_0, D_1, D_2, AVR
D_0 vs. IT	0.005	0.98	D_1, D_2, AVR, LDRt
D_1 vs. IT	−0.045	0.87	D_0, D_2, AVR, LDRt
D_2 vs. IT	0.091	0.74	D_0, D_1, AVR, LDRt

For the abbreviations see ***Table 2****.*

but these associations were not significant in the partial correlations when other covariates were controlled for. Partial correlation analysis results are shown in **Table 3**.

The fractal analysis was optimized to detect subtle changes in the examined vascular structures (Stosic and Stosic, 2006). Specifically, for all the two sets of images obtained for both the cognitively healthy (*n* = 19) and impaired individuals (*n* = 20), the generalized dimension D_q was extracted for different values of q ($-10 < q < 10$) using the skeletons. **Figure 6** shows the generalized dimension spectrum D_q vs. independent variable q. As expected, the retinal vascular tree displayed multifractal properties revealed by the descending sigmoid curve **Figure 6**, giving distinctive FD as the scale was changed. Also, we observed a trend with lower standard deviation (i.e., less oscillation) in cognitively healthy subjects compared to the individuals with cognitively impairment (**Figure 7**). The calculated mean and standard deviations of generalized dimensions D_0, D_1, and D_2 for both groups are shown in **Table 4**. Our results also demonstrate that the overall FD is lower that of the DLA ($D_{q\,=\,2} \sim 1.71$) (Vicsek et al., 1990). The generalized dimensions corresponding to both groups showed a statistically significance difference (**Table 4**).

We found that the complexity of the branching pattern (FD) of retinal vessels was significantly lower in patients with cognitive impairment in comparison to age-matched controls (see **Table 4**). As expected the MoCA scores were significantly lower ($p < 0.001$) in the group of cognitive impairment cases compared with the age-matched controls. Although individuals with cognitive impairment showed a trend toward a higher length diameter ratio (LDRa, LDRv, and LDRt), this difference was not statistically significant. We observed that the asymmetry factor was significantly higher in patients with cognitive impairment than in age-matched controls (see **Table 4**). Also, peripheral drusen-like regions and retinal pigment dispersion were noted in some elderly subjects with MCI (see **Figure 7**). Geometric vascular parameters and functional measures did not significantly correlate with the MoCA score. For all full-field ERG measurements, smaller amplitudes and larger peak times were observed in the subjects with cognitive impairment (see **Table 5**). Also, there was a statistical significant ($p < 0.001$) difference in the amplitudes and implicit times between the cognitively healthy group and the one with cognitive deterioration. It is also evident that the implicit time was less variable than the amplitude. Furthermore, the implicit time's increase that is perceived with the manifestation of pathologic changes of the retina was highly consistent in all patients with cognitive deterioration, and showed practically no overlap between control data and pathologic values: the range of variation seen for control data is between 29.4 and 29.8 ms, while for patients with cognitive impairment it is between 29.6 and 32.8 ms.

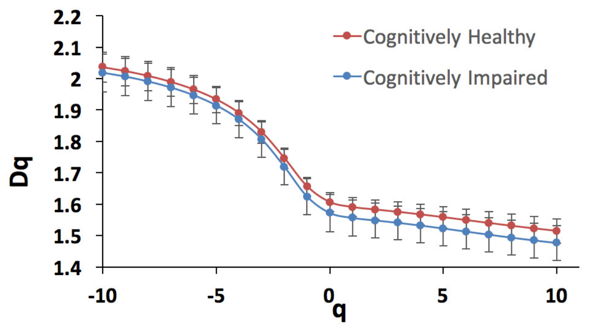

FIGURE 6 | Generalized dimension spectrum D_q vs. q for the cognitively healthy individuals (*n* = 19, blue trace) and cognitively impaired (*n* = 20, red trace).

Visual performance test with the three-dimensional computer-automated version of the threshold Amsler grid test (Ceeable Inc.) demonstrated that this method is subject to variability in the observer's judgment of the grid threshold for most of the elderly subjects with cognitive impairment. Therefore, because of variability may be exacerbated in these individuals characterized by a pervasive inability to follow detailed task instructions, the visual performance results obtained with the Ceeable platform were not used in the overall analysis. The visual performance test with the computerized Cone Contrast test (CCT, Innova Systems Inc.) revealed functional loss in color vision (see **Table 6**). There were more patients with more green deficiency than red or blue deficiency. The scores corresponding to both groups showed a statistically significance difference.

DISCUSSION

In this study, multimodal parameters characterizing the structure and function of the retina were compared to evaluate the retinal vascular alterations regarding the retinal function in patients with cognitive impairment. The study was designed to obtain multiple retinal measures, such as structural and functional indicators of the retina. This specific design provided an opportunity to find and study the relationship between various pieces of information, such as the caliber, tortuosity, and network complexity of the retinal microvasculature (arteries and veins) with respect to functional features (e.g., contrast sensitivity, electrical response through ERGs), concomitant with both fractal- vascular and neural analysis.

Retinal vascular attenuation is a well-recognized indicator in patients with cognitive impairment. However, it has not been

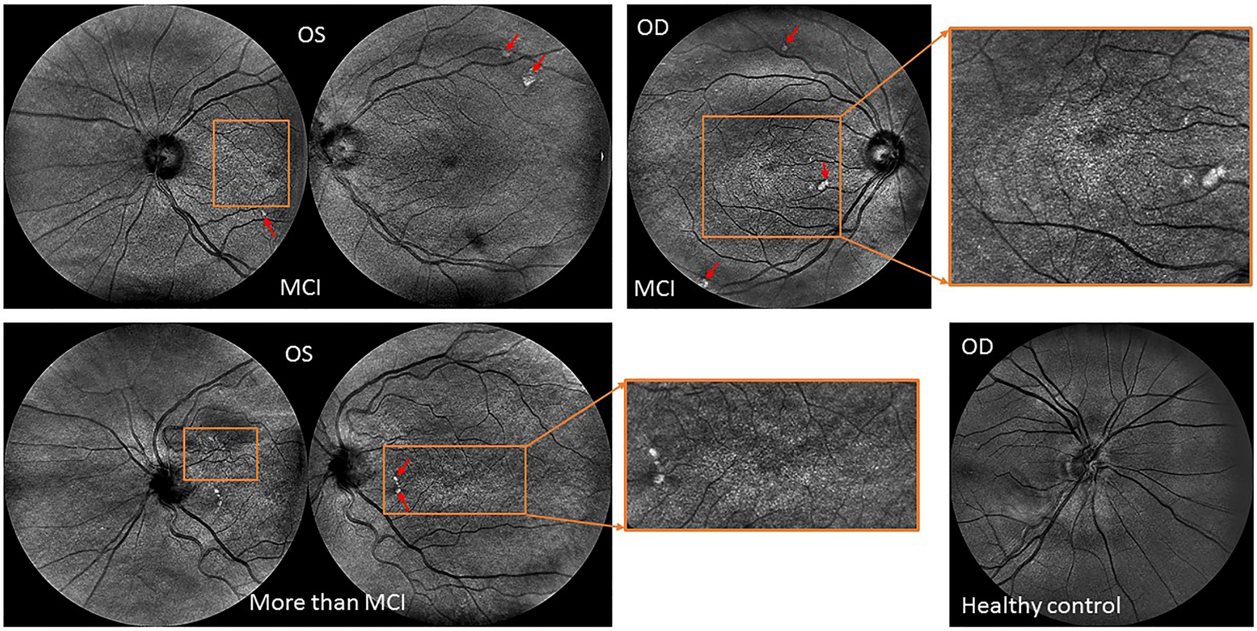

FIGURE 7 | Retinal topographical features observed in individuals with mild cognitive impairment. **(Top row)** Central and nasal infrared light-images obtained from a female subject (79 years old) with MCI showing extramacular features such as drusen-like regions depicted by irregularly shaped bright spots in the periphery of the superior quadrant as well as with pigment dispersion in both eyes. **(Bottom image: Left)** Central and nasal infrared light-images obtained from a female subject (81 years old) with MCI showing tortuous vessels, extramacular features such as drusen-like regions along with pigment dispersion in the left eye. **(Right)** Nasal infrared-light image obtained from a healthy control (71 years old). All images were acquired with the EasyScan Unit (i-Optics Corporation, The Netherlands). The EasyScan camera is a dual color confocal SLO: Infrared (785 nm) and pure green (532 nm). The different colors are related to different penetration depth. ?The red arrows indicate the location of the drusen and white spots observed at extramacular locations. The ROIs enclosed by the orange rectangles indicate the locations where pigment dispersion was observed. The green light-image (see fundus image shown in **Figure 1**) is reflected at the retinal nerve fiber layer showing the vascular structure up to the 4th bifurcation. The infrared light-image is reaching the choroidal vessel layer.

studied yet in relation to the retinal function, measured by using a low-cost full-field ERG technique. The finding of a significant correlation between the 30 Hz flicker ERG implicit time of the b-wave and AVR, D_0, D_1, $D_{2,}$ and LDRt in patients with cognitive decline is intriguing and requires further studies to clarify the underlying pathophysiology and validate its clinical usefulness in predicting the development of cognitive decline using the eye as a surrogate marker. A decrease in amplitude and an increase of the 30 Hz flicker ERG implicit time of the b-wave are usually observed in all retinal pathologies that comprise the photoreceptors when the flicker ERG method has been used to assess photoreceptor function (Meyer et al., 1978; Kondo and Sieving, 2002; Alexander et al., 2006; Verma and Pianta, 2009). Also, previous studies suggest only modest decreases in photopigment optical density with age (Keunen et al., 1987; Elsner et al., 1988; Renner et al., 2004). Therefore, it may be possible that the significant correlations between the ERG parameters and vascular measures could be more related to cognitive decline than aging.

The lack of significant "unique" associations between the vascular parameters and the 30 Hz flicker ERG implicit time may be due to the small sample size in our data as significant trends are seen in the Pearson correlations and these trends may remain significant in the partial correlations in a larger sample size. Secondly, vascular parameters are associated physiologically – for example the vessel branching, artery-vein ratio, and vessel caliber may be related to the complexity of the branching network (FD). Therefore, finding a unique association between these parameters and functional parameters as it was performed with the partial correlations analysis may be statistically robust but in practice, may not follow how the retina is physiologically wired. However, the associations between multiple vascular parameters and functional parameters as shown with the Pearson product moment correlations (**Table 2**) might describe how the retinal is physiologically wired. Nevertheless, we provide both correlations (**Tables 2**, 3) to show the statistically significant trend and how this trend changes in the partial correlations.

The CCT scores have been reported to be affected in the elderly due to cognitive decline (Simunovic, 2016). In our study, not only were most patients with cognitive decline found with more green deficiency than red or blue deficiency, but also all CCT scores were severely reduced below the normal decline level (i.e., below a CCT score of 75) associated with aging and reported for the elderly in the eighth and ninth decades of life (i.e., in the 70–79 and 80–89-year age group) (Fujikawa et al., 2018). Although cataract formation may affect the CCT score in phakic eyes of patients in the eighth and ninth decades of life (Fujikawa et al., 2018), the 6 pseudophakic patients in our study were reported to have undergone uneventful cataract surgery with the implantation of a posterior chamber intraocular lens

TABLE 4 | Geometric vascular parameters obtained for patients with cognitive impairment in comparison with the cognitively normal individuals.

Vascular Parameters	**Cognitive Impairment Cases *n* = 20 Mean (*SD*)**	**Cognitively Healthy Cases *n* = 19 Mean (*SD*)**	***p*-Value**
Fractal dimension			
D_0	1.57 (0.06)	1.61 (0.03)	**0.03***
D_1	1.56 (0.06)	1.59 (0.03)	**0.03***
D_2	1.55 (0.06)	1.58 (0.03)	**0.02***
Caliber (μm)			
CRAE	65.88 (7.39)	66.73 (6.46)	0.707
CRVE	92.54 (7.15)	92.49 (9.02)	0.984
Bifurcation			
BCa	1.65 (0.46)	1.47 (0.35)	0.169
BCv	1.30 (0.48)	1.34 (0.49)	0.812
BCt	1.55 (0.36)	1.50 (0.28)	0.631
AFa	0.75 (0.11)	0.74 (0.16)	0.765
AFv	0.74 (0.22)	0.61 (0.19)	**0.042***
AFt	0.77 (0.05)	0.71 (0.10)	**0.018***
Tortuosity			
cTORTa (10^{-4})	4.30 (7.04)	4.13 (0.83)	0.485
cTORTv (10^{-4})	4.06 (1.06)	3.82 (0.80)	0.433
cTORTt (10^{-4})	4.17 (0.71)	3.97 (0.64)	0.374
Ratio measures			
AVR	0.92 (0.25)	0.86 (0.20)	0.427
LDRa	8.98 (7.46)	7.35 (5.86)	0.456
LDRv	4.52 (6.06)	2.58 (3.77)	0.240
LDRt	9.7 (6.8)	7.13 (4.56)	0.173

The data reported was measured in the region C (i.e., area between 0.5 and 2.0 disc diameters away from the disc margin, see ***Figure 1****) for all parameters except for the fractal parameters that were calculated in the whole area occupied by the branching pattern (FOV = 45°). The P-values were calculated by independent sample t-test. AVR, arteriole–venular ratio; BCa, arteriolar branching coefficient; BCv, venular branching coefficient; BCt total branching coefficient (i.e., arteriolar+venular); CRAE, central retinal arteriolar equivalent; CRVE, central retinal venular equivalent; LDRa, arteriolar length-to-diameter ratio; LDRv, venular length-to-diameter ratio; LDRt, total length-to-diameter ratio (i.e., arteriolar + venular); cTORTa, curvature arteriolar tortuosity cTORTv, curvature venular tortuosity; cTORTt, total tortuosity (i.e., arteriolar+venular); AFa, asymmetry arteriolar factor; AFv, asymmetry venular factor; Aft, total asymmetry factor (i.e., arteriolar+venular).* D_o*: capacity dimension,* D_1*: information dimension,* D_2*: correlation dimension. *Significant (*$p < 0.05$*).*

TABLE 5 | Light-adapted 3.0 flicker ERG (28.3 Hz) measurements recorded from patients with cognitive impairment in comparison with the normative data of the RETeval system.

Light Adapted Test(flicker cone–3.0 cd.s/m^2, 30 cd/m^2, 28.3 Hz)	**ERG reference data *n* = 244 median [90% CI] Age: [76 – 86]**	**Cognitive Impairment Cases *n* = 20 median [90% CI] Age: [69 – 90]**	**Cognitively Healthy Cases *n* = 19 median [90% CI] Age: [60 – 88]**	***p*-value**
Amplitude(μV)	**2.5% limit** 19.6 [18–22.1] **97.5% limit** 39.4 [35.5–43.1]	12.6 [10.9 – 14.4]	37.4 [36.6 – 38.2]	**<0.001****
Implicit Time(ms)	**2.5% limit** 25.6 [25.1–26.3] **97.5% limit** 29.6 [29.2–29.9]	31.2 [29.6–32.8]	29.6 [29.4 –29.8]	**<0.001****

*Amplitude (μV) and implicit time (ms) are denoted along with the medians and 90% confidence intervals of the 2.5 and 97.5% reference limits. The P-values comparing cognitive impairment vs. cognitively healthy cases were calculated by independent sample t test. **Significant (*$p < 0.01$*).*

TABLE 6 | Long, Middle, and Short- CCT scores (i.e., Red, Green, and Blue CCT scores) for the cognitive impairment group.

Rabin CCT scores	Cognitive Impairment Cases *n* = 20 Mean (*SD*)	Cognitively Healthy Cases *n* = 19 Mean (*SD*)	*p*-value
L-CCT (red)	56 (12)	91 (8)	**<0.001****
M-CCT (green)	47 (18)	89 (8)	**<0.001****
S-CCT (blue)	63 (12)	91 (7)	**<0.001****

*CCT scores of 75 or greater are defined as normal (Rabin et al., 2011). The visual performance test with the computerized CCT, revealed functional loss in color vision. The P-values were calculated by an independent sample t-test. **Significant ($p < 0.01$).*

(IOL). Therefore, we believe that these patients with IOL had clear optical media that could not significantly influence our CCT results. Interestingly, it has been reported that individuals with cognitive deterioration due to AD struggle discriminating between green and blue stimuli on the Stroop test which relies on a cognitive measure that requires intact color vision (Cohen et al., 1988; Fisher et al., 1990). These results add to the evidence that extrastriate lesions could result in tritanomalous color deficits (Meadows, 1974; Pearlman et al., 1979), and that the extrastriate cortex is severely disturbed neuropathologically in AD (Lewis et al., 1987). Therefore, pathological changes due to cognitive decline observed in the striate area (IVcß) of the brain that receives color information from the lateral geniculate nucleus, suggest additional basis for deficits in color vision in the brain as described here (Beach and McGeer, 1988).

As in previous studies, we found reduction of vascular branching complexity (FD) in the patients with cognitive decline (Berisha et al., 2007; Frost et al., 2013; Cheung et al., 2014a,b; Ong et al., 2014; Williams et al., 2015). However, compared to these studies, our study used a more robust approach considering the actual multifractal properties of the retinal microvasculature network. Of note, since the findings of AMD and cognitive deterioration due to AD commonalities suggest a degree of overlap (Williams et al., 2014), we assessed all retinal images to identify and rule out retinal pathological features related to AMD. Interestingly, in our patients with cognitive impairment, we observed extramacular drusen in the superior quadrant for some MCI individuals. This trend has been reported previously as to be significantly related with cognitive deterioration due to AD in patients with peripheral drusen (Csincsik et al., 2018). Two earlier studies that may add to this evidence have described the presence of amyloid beta in retinal drusen deposits (Ding et al., 2008; Zhao et al., 2015). Also, abundant amyloid beta pathology has been detected in AD patients in the periphery of the superior quadrant (Koronyo et al., 2017).

Several ERG changes have also been recorded in patients with cognitive deterioration due to AD (Sadun et al., 1987; Armstrong, 1996). Earlier studies have reported that the involvement of the visual cortex may be the cause for dysfunction of the elementary visual sensation that may be involved in the development of visual cognitive deficits and vision-related behavioral symptoms (Strenn et al., 1991; Granholm et al., 2003). The use of the full-field ERG has been suggested to find whether dysfunction of preganglionic elements may also occur in cognitive deterioration due to AD (Parisi et al., 2001). Possible dysfunction of preganglionic elements could explain the increase in P50 implicit time observed in AD patients and this is supported by data obtained in glaucoma or in multiple sclerosis in which the delay of the P50 implicit time could be ascribed to a dysfunction of both ganglionic and preganglionic elements (Katz and Rimmer, 1989; Tobimatsu et al., 1989; Holder, 1997; Porciatti et al., 1997). Moreover, flash ERG was used to demonstrate dysfunction of the retina under photopic and scotopic conditions in patients with dementia with Lewy bodies (Devos et al., 2005). This study outlined that the retinal dysfunction may be related to slight alteration of the photoreceptors and numerous pale inclusions in the outer plexiform layer found at the post-mortem examination, suggesting specific retinopathy (Devos et al., 2005). In our study, we also found a significant reduced a-wave amplitude indicating abnormal photoreceptor function associated to a longer response of the rods under scotopic conditions (Tzekov and Mullan, 2014). The association between the retinal vascular attenuation and the severity of the scotopic full-field alteration have been previously reported in patients with cone degeneration (e.g. retinitis pigmentosa) for which oxidative stress has been suggested to play a potential pathogenic role like in AD (Mecocci et al., 1994; Sandberg et al., 1996; Markesbery, 1997; Wang et al., 2005; Ma et al., 2012). Also, a recent study reported that subretinal injection of amyloid β in C57/BL6 mice yields declined scotopic response (Liu et al., 2015). Interestingly, as in our study, the infrared SLO images revealed drusen-like regions depicted by irregularly shaped bright areas. Moreover, a substantial decrease in mixed rod-cone responses (i.e., decreased a- and b-wave amplitudes) has been noted in mice carrying ApoE-ε 4 allele of apolipoproteine E4 which is the most prevalent genetic risk factor for the late-onset AD that acts in synergy with Aβ (Antes et al., 2013). Consequently, these recent studies on animal models and our preliminary results suggest that evaluation of the bioelectric activity of the retina with ERG may add significant value to the retinal biomarker exploration in cognitive impairment at the early stage. Also, the fact that the 90% confidence intervals of the averages of the cognitively healthy and cognitively impaired groups are not overlapping (**Table 5**) supports the opportunity to define distinctive domains for the values of the implicit time that can be correlated with the presence and, respectively, the non-existence of cognitive impairment in the individuals analyzed.

A thorough search of the relevant literature yielded no related article reporting retinal vascular and functional abnormalities in cognitive impairment using a multimodal approach that requires an instrumentation cost of less than $45,000. The primary strength of this study is the low-cost multimodal approach implemented to measure combined structural-functional parameters, instead of individual markers. The portability and low-cost of our approach will facilitate to further extend the collection of data in community settings for population health management. Another strength is the multifractal analysis conducted considering that most studies have relied on monofractal analysis; a scheme which has largely attained limited success (Stosic and Stosic, 2006; Azemin et al., 2012).

This study has some important limitations. The exclusion of eyes due to poor image quality because of opacities in the ocular media (e.g., cataracts and floaters in some elderly subjects), and the presence of confounding factors limited the sample size. Also, we found some challenges in achieving both structural and functional data with high quality, mainly in elderly patients with cognitive impairment who are easily fatigued. These challenges can be more complex if the study subject has poor vision. Also, we did not examine the relationship between the vast number of parameters in the SIVA platform and the functional parameters because of small sample size. Besides the complexity of the branching pattern of retinal vessels, AVR, asymmetry ratios, LDR, branching coefficients, tortuosity and vessel caliber, it is possible that other geometric vascular parameters (e.g., other bifurcation parameters, branching coefficient angle, etc.) are associated with physiological changes in the retina due to cognitive decline and that the functional parameters are sensitive to these changes. Another limitation could be that the cognitive function of the study patients was only assessed by the MoCA test. Therefore, differential diagnosis of cognitive impairment was not possible, and detailed evaluations of cognitive functions including pathological examinations and neuroimaging of the brain will be needed to confirm the existence of cognitive deterioration due to AD. However, although AD is the most common, progressive cause of dementia in the elderly, our study recruited subjects independently of their cognitive impairment's causation which helped us to assess the collection of data in community settings for population health management. It has been reported that amyloid deposition can be identified among cognitively normal elderly persons during life and the prevalence of asymptomatic amyloid deposition may be like that of symptomatic amyloid deposition. An early study has shown that in a group of participants without clinically significant impairment, amyloid deposition was not associated with worse cognitive function, suggesting that an elderly person with a significant amyloid burden can remain cognitively normal (Aizenstein et al., 2008). Pagani et al. (2016) has also shown that there is no deterministic relation between cognitive impairment and AD severity. Nevertheless, a longitudinal follow-up of study subjects would be required to support the potential of amyloid imaging to identify preclinical Alzheimer disease or alternatively, to show that amyloid deposition is not sufficient to cause Alzheimer disease within some specified period. Therefore, our multivariate and multimodal approach using an agnostic-cognitive impairment assessment could be a starting point for expanding the methodology in community settings to assess the eye-brain conditions of individuals under the risk of cognitive deterioration.

Although significant correlations between the functional and vascular parameters did not survive after the partial correlations analyses, that does not imply the statistical trends found in this study are not revealing of alteration and disease of the neurovascular component in general. Also, the cross-sectional setting of our study couldn't facilitate the investigation of temporal and causal relationships between the retinal functional and structural features with cognitive impairment. However, due to the strict exclusion criteria used in our study, we only analyzed very good quality data that makes our results more robust. Despite the above limitations, the retinal vascular attenuation and reduced complexity of the vascular branching network is comparable to those observed in earlier studies (Berisha et al., 2007; Frost et al., 2013; Cheung et al., 2014a,b). We continue collecting data under this study and expect to explore the multiple relationships and statistical trends further with larger sample size.

CONCLUSION

The difficulty in detecting cognitive impairment in its early stages poses a limitation on the onset of cognitive decline diagnosis. Unfortunately, there is no successful treatment once early cognitive impairment or dementia becomes clinically apparent (Hampel et al., 2018). This study illustrates that there are multimodal retinal markers that may be sensitive to cognitive impairment decline, and adds to the evidence that there is a statistical trend pointing to the correlation between retinal neuronal dysfunction and microvasculature changes. This trend suggests that retinal geometric vascular and functional parameters might be associated with physiological changes in the retina due to cognitive decline. We suspect our analysis of combined structural-functional parameters, instead of individual biomarkers, may serve as a useful clinical marker of cognitive decline that could also provide increased sensitivity and specificity for the differential diagnosis of cognitive impairment. However, because of our study sample was small, the full extent of clinical applicability of our approach is provocative and still to be determined. This study also adds support to the use of a multimodal diagnostic biomarker approach of cognitive impairment based on the retinal structure-function relationship which also has the advantage of a low-cost implementation in community settings to detect cognitive decline-specific pathology in the retina, which could enable the early diagnosis and monitoring of disease progression. Provided a clinical correlation between the eye and brain measures can be confirmed, screening of eyes in people being considered at risk of cognitive impairment could help in the development of an alternative low-cost approach for early diagnosis as well as potentially serve to monitor the effectiveness of emerging therapies.

AUTHOR CONTRIBUTIONS

DCD conceived and designed the study. DCD, GS, EA, MK, SO, and CMS performed the study. DCD, GS, EA, and SO analyzed the data. DCD and GS contributed to reagents, materials, and analysis tools. DCD, GS, and EA contributed to the writing of the manuscript.

FUNDING

This study was supported in part by the Finker Frenkel Legacy Foundation, a NIH Center Grant No. P30-EY014801 to the University of Miami, by an unrestricted grant to the University of Miami from Research to Prevent Blindness, Inc., and the Alzheimer's Association (AARGD-17-531255, DCD).

ACKNOWLEDGMENTS

We gratefully acknowledge the support of this work by the Finker Frenkel Legacy Foundation in Florida and the Alzheimer's Association. We are very grateful to the researchers and community leaders (Gloria Orlandi-Kass from the Alzheimer's Association Southeast Florida Chapter also, Angela Aracena, Anselma M. Moody, Lilian Moreno, Martha Castilleja, and Antonina Gaynor from the Easter Seals in South Florida) who took out time from their busy schedules to help us with the recruitment in this study. We thank all reviewers for their critical reading of the manuscript and insightful comments on the earlier drafts of the paper, as these comments led us to an improvement of the work.

SUPPLEMENTARY MATERIAL

The Supplementary Material for this article can be found online at: https://www.frontiersin.org/articles/10.3389/fphys.2018.01721/full#supplementary-material

REFERENCES

Aizenstein, H. J., Nebes, R. D., Saxton, J. A., Price, J. C., Mathis, C. A., Tsopelas, N. D., et al. (2008). Frequent amyloid deposition without significant cognitive impairment among the elderly. *Arch. Neurol.* 65, 1509–1517. doi: 10.1001/archneur.65.11.1509

Alexander, K. R., Rajagopalan, A. S., Raghuram, A., and Fishman, G. A. (2006). Activation phase of cone phototransduction and the flicker electroretinogram in retinitis pigmentosa. *Vision Res.* 46, 2773–2785. doi: 10.1016/j.visres.2006.01.007

Antes, R., Ezra-Elia, R., Weinberger, D., Solomon, A., Ofri, R., and Michaelson, D. M. (2013). ApoE4 induces synaptic and ERG impairments in the retina of young targeted replacement apoE4 mice. *PLoS One* 8:e64949. doi: 10.1371/journal.pone.0064949

Armstrong, R. A. (1996). Visual field defects in Alzheimer's disease patients may reflect differential pathology in the primary visual cortex. *Optom. Vis. Sci.* 73, 677–682. doi: 10.1097/00006324-199611000-00001

Azemin, M. Z., Kumar, D. K., Wong, T. Y., Wang, J. J., Mitchell, P., Kawasaki, R., et al. (2012). Age-related rarefaction in the fractal dimension of retinal vessel. *Neurobiol. Aging.* 33, 194.e1–194.e4. doi: 10.1016/j.neurobiolaging.2010.04.010

Beach, T. G., and McGeer, E. G. (1988). Lamina-specific arrangement of astrocytic gliosis and senile plaques in Alzheimer's disease visual cortex. *Brain Res.* 463, 357–361. doi: 10.1016/0006-8993(88)90410-6

Berisha, F., Feke, G. T., Trempe, C. L., Mcmeel, J. W., and Schepens, C. L. (2007). Retinal abnormalities in early Alzheimer's disease. *Invest. Ophthalmol. Vis. Sci.* 48, 2285–2289. doi: 10.1167/iovs.06-1029

Braak, H., and Braak, E. (1997). Frequency of stages of Alzheimer-related lesions in different age categories. *Neurobiol. Aging.* 18, 351–357. doi: 10.1016/S0197-4580(97)00056-0

Cabrera DeBuc, D., Somfai, G. M., and Koller, A. (2017). Retinal microvascular network alterations: potential biomarkers of cerebrovascular and neural diseases. *Am. J. Physiol. Heart. Circ. Physiol.* 312, H201–H212. doi: 10.1152/ajpheart.00201.2016

Cheung, C. Y., Ong, S., Ikram, M. K., Ong, Y. T., Chen, C. P., Venketasubramanian, N., et al. (2014a). Retinal vascular fractal dimension is associated with cognitive dysfunction. *J. Stroke Cerebrovasc. Dis.* 23, 43–50. doi: 10.1016/j.jstrokecerebrovasdis.2012.09.002

Cheung, C. Y., Ong, Y. T., Ikram, M. K., Ong, S. Y., Li, X., Hilal, S., et al. (2014b). Microvascular network alterations in the retina of patients with Alzheimer's disease. *Alzheimers Dement.* 10, 135–142. doi: 10.1016/j.jalz.2013.06.009

Cheung, C. Y., Tay, W. T., Mitchell, P., Wang, J. J., Hsu, W., Lee, M. L., et al. (2011). Quantitative and qualitative retinal microvascular characteristics and blood pressure. *J. Hypertens.* 29, 1380–1391. doi: 10.1097/HJH.0b013e328347266c

Cohen, J., Cronin-Golomb, A., Growdon, J. H., and Corkin, S. (1988). Colour vision deficits in Alzheimer's disease. *Soc. Neurosci. Abstr.* 14:219.

Cosatto, V. F., Liew, G., Rochtchina, E., Wainwright, A., Zhang, Y., Hsu, W., et al. (2010). Retinal vascular fractal dimension measurement and its influence from imaging variation: results of two segmentation methods. *Curr. Eye Res.* 35, 850–856. doi: 10.3109/02713683.2010.490628

Csincsik, L., Macgillivray, T. J., Flynn, E., Pellegrini, E., Papanastasiou, G., Barzegar-Befroei, N., et al. (2018). Peripheral retinal imaging biomarkers for Alzheimer's disease: a pilot study. *Ophthalmic Res.* 59, 182–192. doi: 10.1159/000487053

Devos, D., Tir, M., Maurage, C. A., Waucquier, N., Defebvre, L., Defoort-Dhellemmes, S., et al. (2005). ERG and anatomical abnormalities suggesting retinopathy in dementia with Lewy bodies. *Neurology* 65, 1107–1110. doi: 10.1212/01.wnl.0000178896.44905.33

Ding, J. D., Lin, J., Mace, B. E., Herrmann, R., Sullivan, P., and Bowes Rickman, C. (2008). Targeting age-related macular degeneration with Alzheimer's disease based immunotherapies: anti-amyloid-beta antibody attenuates pathologies in an age-related macular degeneration mouse model. *Vision Res.* 48, 339–345. doi: 10.1016/j.visres.2007.07.025

Elias, M. F., Beiser, A., Wolf, P. A., Au, R., White, R. F., and D'agostino, R. B. (2000). The preclinical phase of alzheimer disease: a 22-year prospective study of the Framingham Cohort. *Arch. Neurol.* 57, 808–813. doi: 10.1001/archneur.57.6.808

Elsner, A. E., Berk, L., Burns, S. A., and Rosenberg, P. R. (1988). Aging and human cone photopigments. *J. Opt. Soc. Am. A.* 5, 2106–2112. doi: 10.1364/JOSAA.5.002106

Family, F., Masters, B. R., and Platt, D. E. (1989). Fractal pattern formation in human retinal vessels. *Phys. D Nonlinear Phenom.* 38, 98–103. doi: 10.1016/0167-2789(89)90178-4

Fink, W. (2004). Neural attractor network for application in visual field data classification. *Phys. Med. Biol.* 49, 2799–2809. doi: 10.1088/0031-9155/49/13/003

Fisher, L. M., Freed, D. M., and Corkin, S. (1990). Stroop color-word test performance in patients with Alzheimer's disease. *J. Clin. Exp. Neuropsychol.* 12, 745–758. doi: 10.1080/01688639008401016

Folstein, M. F., Folstein, S. E., and Mchugh, P. R. (1975). "Mini-mental state". A practical method for grading the cognitive state of patients for the clinician. *J. Psychiatr. Res.* 12, 189–198. doi: 10.1016/0022-3956(75)90026-6

Frost, S., Kanagasingam, Y., Sohrabi, H., Vignarajan, J., Bourgeat, P., Salvado, O., et al. (2013). Retinal vascular biomarkers for early detection and monitoring of Alzheimer's disease. *Transl. Psychiatry* 3:e233. doi: 10.1038/tp.2012.150

Fujikawa, M., Muraki, S., Niwa, Y., and Ohji, M. (2018). Evaluation of clinical validity of the Rabin cone contrast test in normal phakic or pseudophakic eyes and severely dichromatic eyes. *Acta Ophthalmol.* 96, e164–e167. doi: 10.1111/aos.13495

Gould, D. J., Vadakkan, T. J., Poché, R. A., and Dickinson, M. E. (2011). Multifractal and lacunarity analysis of microvascular morphology and remodeling. *Microcirculation* 18, 136–151. doi: 10.1111/j.1549-8719.2010.00075.x

Granholm, E., Morris, S., Galasko, D., Shults, C., Rogers, E., and Vukov, B. (2003). Tropicamide effects on pupil size and pupillary light reflexes in Alzheimer's and Parkinson's disease. *Int. J. Psychophysiol.* 47, 95–115. doi: 10.1016/S0167-8760(02)00122-8

Hampel, H., Toschi, N., Babiloni, C., Baldacci, F., Black, K. L., Bokde, A. L. W., et al. (2018). Revolution of Alzheimer precision neurology. Passageway of systems biology and neurophysiology. *J. Alzheimers Dis.* 64, S47–S105. doi: 10.3233/JAD-179932

Hart, W. E., Goldbaum, M., Cote, B., Kube, P., and Nelson, M. R. (1999). Measurement and classification of retinal vascular tortuosity. *Int. J. Med. Inform.* 53, 239–252. doi: 10.1016/S1386-5056(98)00163-4

Holder, G. E. (1997). The pattern electroretinogram in anterior visual pathway dysfunction and its relationship to the pattern visual evoked potential: a personal clinical review of 743 eyes. *Eye (Lond.)* 11, 924–934. doi: 10.1038/eye.1997.231

Holder, G. E., Brigell, M. G., Hawlina, M., Meigen, T., Vaegan, Bach, M., International Society for Clinical Electrophysiology of Vision (2007). ISCEV standard for clinical pattern electroretinography–2007 update. *Doc. Ophthalmol.* 114, 111–116. doi: 10.1007/s10633-007-9053-1

Hood, D. C., Bach, M., Brigell, M., Keating, D., Kondo, M., Lyons, J. S., et al. (2008). ISCEV guidelines for clinical multifocal electroretinography (2007 edition). *Doc. Ophthalmol.* 116, 1–11. doi: 10.1007/s10633-007-9089-2

Karperien, A. (1993). FracLac for ImageJ— FracLac Advanced User's Manual. Bethesda, MD: National Institutes of Health. Available: http://rsb.info.nih.gov/ij/plugins/fraclac/fraclac-manual.pdf (accessed August 20, 2018).

Kato, K., Kondo, M., Sugimoto, M., Ikesugi, K., and Matsubara, H. (2015). Effect of pupil size on flicker ERGs recorded with RETeval system: new mydriasis-free full-field ERG system. *Invest. Ophthalmol. Vis. Sci.* 56, 3684–3690. doi: 10.1167/iovs.14-16349

Katz, B., and Rimmer, S. (1989). Ophthalmologic manifestations of Alzheimer's disease. *Surv. Ophthalmol.* 34, 31–43. doi: 10.1016/0039-6257(89)90127-6

Kawas, C. H., Corrada, M. M., Brookmeyer, R., Morrison, A., Resnick, S. M., Zonderman, A. B., et al. (2003). Visual memory predicts Alzheimer's disease more than a decade before diagnosis. *Neurology* 60, 1089–1093. doi: 10.1212/01.WNL.0000055813.36504.BF

Keunen, J. E., Van Norren, D., and Van Meel, G. J. (1987). Density of foveal cone pigments at older age. *Invest. Ophthalmol. Vis. Sci.* 28, 985–991.

Kondo, M., and Sieving, P. A. (2002). Post-photoreceptoral activity dominates primate photopic 32-Hz ERG for sine-, square-, and pulsed stimuli. *Invest. Ophthalmol. Vis. Sci.* 43, 2500–2507.

Koronyo, Y., Biggs, D., Barron, E., Boyer, D. S., Pearlman, J. A., Au, W. J., et al. (2017). Retinal amyloid pathology and proof-of-concept imaging trial in Alzheimer's disease. *JCI Insight* 2:93621. doi: 10.1172/jci.insight.93621

Koronyo, Y., Salumbides, B. C., Black, K. L., and Koronyo-Hamaoui, M. (2012). Alzheimer's disease in the retina: imaging retinal abeta plaques for early diagnosis and therapy assessment. *Neurodegener. Dis.* 10, 285–293. doi: 10.1159/000335154

Koronyo-Hamaoui, M., Koronyo, Y., Ljubimov, A. V., Miller, C. A., Ko, M. K., Black, K. L., et al. (2011). Identification of amyloid plaques in retinas from Alzheimer's patients and noninvasive in vivo optical imaging of retinal plaques in a mouse model. *Neuroimage* 54, S204–S217. doi: 10.1016/j.neuroimage.2010.06.020

Kyriacos, S., Nekka, F., Vicco, P., and Cartilier, L. (1997). "The retinal vasculature: towards an understanding of the formation process," in *Fractals in Engineering*, eds L. J. Vehel, E. Lutton, and C. Tricot (London: Springer), 383–397.

La Rue, A., and Jarvik, L. F. (1987). Cognitive function and prediction of dementia in old age. *Int. J. Aging Hum. Dev.* 25, 79–89. doi: 10.2190/DV3R-PBJQ-E0FT-7W2B

Lavoie, J., Illiano, P., Sotnikova, T. D., Gainetdinov, R. R., Beaulieu, J. M., and Hebert, M. (2014). The electroretinogram as a biomarker of central dopamine and serotonin: potential relevance to psychiatric disorders. *Biol. Psychiatry* 75, 479–486. doi: 10.1016/j.biopsych.2012

Lewis, D. A., Campbell, M. J., Terry, R. D., and Morrison, J. H. (1987). Laminar and regional distributions of neurofibrillary tangles and neuritic plaques in Alzheimer's disease: a quantitative study of visual and auditory cortices. *J. Neurosci.* 7, 1799–1808. doi: 10.1523/JNEUROSCI.07-06-01799.1987

Liebovitch, L. S., and Toth, T. (1989). A fast algorithm to determine fractal dimensions by box counting. *Phys. Lett. A* 141, 386–390. doi: 10.1016/0375-9601(89)90854-2

Liew, G., Wang, J. J., Cheung, N., Zhang, Y. P., Hsu, W., Lee, M. L., et al. (2008). The retinal vasculature as a fractal: methodology, reliability, and relationship to blood pressure. *Ophthalmology* 115, 1951–1956. doi: 10.1016/j.ophtha.2008.05.029

Linn, R. T., Wolf, P. A., Bachman, D. L., Knoefel, J. E., Cobb, J. L., Belanger, A. J., et al. (1995). The 'preclinical phase' of probable Alzheimer's disease. A 13-year prospective study of the Framingham cohort. *Arch. Neurol.* 52, 485–490. doi: 10.1001/archneur.1995.00540290075020

Liu, C., Cao, L., Yang, S., Xu, L., Liu, P., Wang, F., et al. (2015). Subretinal injection of amyloid-beta peptide accelerates RPE cell senescence and retinal degeneration. *Int. J. Mol. Med.* 35, 169–176. doi: 10.3892/ijmm.2014.1993

London, A., Benhar, I., and Schwar, M. (2012). The retina as a window to the brain-from eye research to CNS disorders. *Nat. Rev. Neurol.* 9, 44–53. doi: 10.1038/nrneurol.2012.227

Ma, Y., Kawasaki, R., Dobson, L. P., Ruddle, J. B., Kearns, L. S., Wong, T. Y., et al. (2012). Quantitative analysis of retinal vessel attenuation in eyes with retinitis pigmentosa. *Invest. Ophthalmol. Vis. Sci.* 53, 4306–4314. doi: 10.1167/iovs.11-8596

Macgillivray, T. J., Patton, N., Doubal, F. N., Graham, C., and Wardlaw, J. M. (2007). Fractal analysis of the retinal vascular network in fundus images. *Conf. Proc. IEEE. Eng. Med. Biol. Soc.* 2007, 6456–6459. doi: 10.1109/IEMBS.2007.4353837

Mainster, M. A. (1990). The fratal properties of retinal vessels: embryological and clinical implications. *Eye (Lond.)* 4, 235–241. doi: 10.1038/eye.1990.33

Mandelbrot, B. B. (1982). *The Fractal Geometry of Nature*. New York, NY: W.H. Freeman.

Markesbery, W. R. (1997). Oxidative stress hypothesis in Alzheimer's disease. *Free Radic. Biol. Med.* 23, 134–147. doi: 10.1016/S0891-5849(96)00629-6

Marmor, M. F., Holder, G. E., Seeliger, M. W., and Yamamoto, S., International Society for Clinical Electrophysiology Of Vision (2004). Standard for clinical electroretinography (2004 update). *Doc. Ophthalmol.* 108, 107–114. doi: 10.1023/B:DOOP.0000036793.44912.45

McCulloch, D. L., Marmor, M. F., Brigell, M. G., Hamilton, R., Holder, G. E., Tzekov, R., et al. (2015). ISCEV standard for full-field clinical electroretinography (2015 update). *Doc. Ophthalmol.* 130, 1–12. doi: 10.1007/s10633-014-9473-7

Meadows, J. C. (1974). Disturbed perception of colours associated with localized cerebral lesions. *Brain* 97, 615–632. doi: 10.1093/brain/97.1.615

Mecocci, P., Macgarvey, U., and Beal, M. F. (1994). Oxidative damage to mitochondrial DNA is increased in Alzheimer's disease. *Ann. Neurol.* 36, 747–751. doi: 10.1002/ana.410360510

Meyer, J. J., Korol, S., Gramoni, R., and Tupling, R. (1978). Psychophysical flicker thresholds and ERG flicker responses in congenital and acquired vision deficiencies. *Mod. Probl. Ophthalmol.* 19, 33–49.

Moschos, M. M., Markopoulos, I., Chatziralli, I., Rouvas, A., Papageorgiou, S. G., Ladas, I., et al. (2012). Structural and functional impairment of the retina and optic nerve in Alzheimer's disease. *Curr. Alzheimer Res.* 9, 782–788. doi: 10.2174/156720512802455340

Nasreddine, Z. S., Phillips, N. A., Bedirian, V., Charbonneau, S., Whitehead, V., Collin, I., et al. (2005). The montreal cognitive assessment, MoCA: a brief screening tool for mild cognitive impairment. *J. Am. Geriatr. Soc.* 53, 695–699. doi: 10.1111/j.1532-5415.2005.53221.x

Ong, Y. T., Hilal, S., Cheung, C. Y., Xu, X., Chen, C., Venketasubramanian, N., et al. (2014). Retinal vascular fractals and cognitive impairment. *Dement. Geriatr. Cogn. Dis. Extra* 4, 305–313. doi: 10.1159/000363286

Pache, M., Smeets, C. H., Gasio, P. F., Savaskan, E., Flammer, J., Wirz-Justice, A., et al. (2003). Colour vision deficiencies in Alzheimer's disease. *Age Ageing* 32, 422–426. doi: 10.1093/ageing/32.4.422

Pagani, M., Giuliani, A., Oberg, J., Chincarini, A., Morbelli, S., Brugnolo, A., et al. (2016). Predicting the transition from normal aging to Alzheimer's disease: a statistical mechanistic evaluation of FDG-PET data. *Neuroimage* 141, 282–290. doi: 10.1016/j.neuroimage.2016.07.043

Parisi, V., Restuccia, R., Fattapposta, F., Mina, C., Bucci, M. G., and Pierelli, F. (2001). Morphological and functional retinal impairment in Alzheimer's disease patients. *Clin. Neurophysiol.* 112, 1860–1867. doi: 10.1016/S1388-2457(01)00620-4

Pearlman, A. L., Birch, J., and Meadows, J. C. (1979). Cerebral color blindness: an acquired defect in hue discrimination. *Ann. Neurol.* 5, 253–261. doi: 10.1002/ana.410050307

Prince, M., Wimo, A., Guerchet, M., Ali, G. C., Wu, Y. T., and Prina, M. (2015). *World Alzheimer Report 2015. The Global Impact of Dementia*. London: Alzheimer's Disease International (ADI).

Porciatti, V., Di Bartolo, E., Nardi, M., and Fiorentini, A. (1997). Responses to chromatic and luminance contrast in glaucoma: a psychophysical and electrophysiological study. *Vision. Res.* 37, 1975–1987. doi: 10.1016/S0042-6989(97)00018-7

Rabin, J., Gooch, J., and Ivan, D. (2011). Rapid quantification of color vision: the cone contrast test. *Invest. Ophthalmol. Vis. Sci.* 52, 816–820. doi: 10.1167/iovs.10-6283

Renner, A. B., Knau, H., Neitz, M., Neitz, J., and Werner, J. S. (2004). Photopigment optical density of the human foveola and a paradoxical senescent increase outside the fovea. *Vis. Neurosci.* 21, 827–834. doi: 10.1017/S0952523804216030

Sadun, A. A., Borchert, M., Devita, E., Hinton, D. R., and Bassi, C. J. (1987). Assessment of visual impairment in patients with Alzheimer's disease. *Am. J. Ophthalmol.* 104, 113–120. doi: 10.1016/0002-9394(87)90001-8

Sandberg, M. A., Weigel-Difranco, C., Rosner, B., and Berson, E. L. (1996). The relationship between visual field size and electroretinogram amplitude in retinitis pigmentosa. *Invest. Ophthalmol. Vis. Sci.* 37, 1693–1698.

Simunovic, M. P. (2016). Acquired color vision deficiency. *Surv. Ophthalmol.* 61, 132–155. doi: 10.1016/j.survophthal.2015.11.004

Smith, T., Gildeh, N., and Holmes, C. (2007). The montreal cognitive assessment: validity and utility in a memory clinic setting. *Can. J. Psychiatry* 52, 329–332. doi: 10.1177/070674370705200508

Snowdon, D. A., Kemper, S. J., Mortimer, J. A., Greiner, L. H., Wekstein, D. R., and Markesbery, W. R. (1996). Linguistic ability in early life and cognitive function and Alzheimer's disease in late life. Findings from the Nun Study. *JAMA* 275, 528–532. doi: 10.1001/jama.1996.03530310034029

Stosic, T., and Stosic, B. D. (2006). Multifractal analysis of human retinal vessels. *IEEE. Trans. Med. Imaging* 25, 1101–1107. doi: 10.1109/TMI.2006.879316

Strenn, K., Dal-Bianco, P., Weghaupt, H., Koch, G., Vass, C., and Gottlob, I. (1991). Pattern electroretinogram and luminance electroretinogram in Alzheimer's disease. *J. Neural. Transm. Suppl.* 33, 73–80. doi: 10.1007/978-3-7091-9135-4_12

Sun, C., Wang, J. J., Mackey, D. A., and Wong, T. Y. (2009). Retinal vascular caliber: systemic, environmental, and genetic associations. *Surv. Ophthalmol.* 54, 74–95. doi: 10.1016/j.survophthal.2008.10.003

Ţălu, Ş. (2013a). Characterization of retinal vessel networks in human retinal imagery using quantitative descriptors. *Hum. Vet. Med. Bioflux* 5, 52–57.

Ţălu, Ş. (2013b). Multifractal geometry in analysis and processing of digital retinal photographs for early diagnosis of human diabetic macular edema. *Curr. Eye Res.* 38, 781–792. doi: 10.3109/02713683.2013.779722

Thomas, G. N., Ong, S. Y., Tham, Y. C., Hsu, W., Lee, M. L., Lau, Q. P., et al. (2014). Measurement of macular fractal dimension using a computer-assisted program. *Invest. Ophthalmol. Vis. Sci.* 55, 2237–2243. doi: 10.1167/iovs.13-13315

Tobimatsu, S., Celesia, G. G., Cone, S., and Gujrati, M. (1989). Electroretinograms to checkerboard pattern reversal in cats: physiological characteristics and effect of retrograde degeneration of ganglion cells. *Electroencephalogr. Clin. Neurophysiol.* 73, 341–352. doi: 10.1016/0013-4694(89)90112-0

Tzekov, R., and Mullan, M. (2014). Vision function abnormalities in Alzheimer disease. *Surv. Ophthalmol.* 59, 414–433. doi: 10.1016/j.survophthal.2013.10.002

Vehel, J. L, and Legrand, P. (2003). "Bayesian multifractal signal denoising. IEEE 6, VI-177," in *IEEE International Conference on Acoustics, Speech, and Signal Processing* (Accession No. 7816409), Brighton. doi: 10.1109/ICASSP.2003.1201647

Verma, R., and Pianta, M. J. (2009). The contribution of human cone photoreceptors to the photopic flicker electroretinogram. *J. Vis.* 9, 9.1–12.

Vicsek, T., Family, F., and Meakin, P. (1990). Multifractal geometry of diffusion-limited aggregates. *Europhys. Lett.* 12, 217–222. doi: 10.1209/0295-5075/12/3/005

Wang, J., Xiong, S., Xie, C., Markesbery, W. R., and Lovell, M. A. (2005). Increased oxidative damage in nuclear and mitochondrial DNA in Alzheimer's disease. *J. Neurochem.* 93, 953–962. doi: 10.1111/j.1471-4159.2005.03053.x

Webb, R. H., Hughes, G. W., and Delori, F. C. (1987). Confocal scanning laser ophthalmoscope. *Appl. Opt.* 26, 1492–1499. doi: 10.1364/AO.26.001492

Williams, M. A., Mcgowan, A. J., Cardwell, C. R., Cheung, C. Y., Craig, D., Passmore, P., et al. (2015). Retinal microvascular network attenuation in Alzheimer's disease. *Alzheimers Dement. (Amst).* 1, 229–235. doi: 10.1016/j.dadm.2015.04.001

Williams, M. A., Silvestri, V., Craig, D., Passmore, A. P., and Silvestri, G. (2014). The prevalence of age-related macular degeneration in Alzheimer's disease. *J. Alzheimers Dis.* 42, 909–914. doi: 10.3233/JAD-140243

Witten, T. A., and Sander, L. M. (1981). Diffusion-limited aggregation: a kinetic critical phenomenon. *Phys. Rev. Lett.* 47, 1400–1403. doi: 10.1103/PhysRevLett.47.1400

Zamir, M., Medeiros, J. A., and Cunningham, T. K. (1979). Arterial bifurcations in the human retina. *J. Gen. Physiol.* 74, 537–548. doi: 10.1085/jgp.74.4.537

Zhao, Y., Bhattacharjee, S., Jones, B. M., Hill, J. M., Clement, C., Sambamurti, K., et al. (2015). Beta-amyloid precursor protein (betaAPP) processing in Alzheimer's disease (AD) and age-related macular degeneration (AMD). *Mol. Neurobiol.* 52, 533–544. doi: 10.1007/s12035-014-8886-3

Conflict of Interest Statement: The authors declare that the research was conducted in the absence of any commercial or financial relationships that could be construed as a potential conflict of interest.

Copyright © 2018 Cabrera DeBuc, Somfai, Arthur, Kostic, Oropesa and Mendoza Santiesteban. This is an open-access article distributed under the terms of the Creative Commons Attribution License (CC BY). The use, distribution or reproduction in other forums is permitted, provided the original author(s) and the copyright owner(s) are credited and that the original publication in this journal is cited, in accordance with accepted academic practice. No use, distribution or reproduction is permitted which does not comply with these terms.

frontiers in Physiology

ORIGINAL RESEARCH
published: 05 September 2018
doi: 10.3389/fphys.2018.01233

Investigating the Fractal Dimension of the Foveal Microvasculature in Relation to the Morphology of the Foveal Avascular Zone and to the Macular Circulation in Patients With Type 2 Diabetes Mellitus

Maja Kostic[1†], Nathan M. Bates[1†], Nebojsa T. Milosevic[2], Jing Tian[1], William E. Smiddy[1], Wen-Hsiang Lee[1], Gabor M. Somfai[3,4], William J. Feuer[1], Joyce C. Shiffman[1], Ajay E. Kuriyan[1], Ninel Z. Gregori[1], Sandra Pineda[1] and Delia Cabrera DeBuc[1*]

[1] Miller School of Medicine, Bascom Palmer Eye Institute, University of Miami, Miami, FL, United States, [2] Department of Biophysics, University of Belgrade, Belgrade, Serbia, [3] Retinology Unit, Pallas Kliniken, Olten, Switzerland, [4] Department of Ophthalmology, Semmelweis University, Budapest, Hungary

OPEN ACCESS

Edited by:
Sladjana Z. Spasić,
Institute for Multidisciplinary Research,
University of Belgrade, Serbia

Reviewed by:
Daniel Goldman,
University of Western Ontario, Canada
Josephine Louise Vaughan,
University of Newcastle, Australia

***Correspondence:**
Delia Cabrera DeBuc
dcabrera2@med.miami.edu

†These authors have contributed equally to this work

Specialty section:
This article was submitted to Fractal Physiology, a section of the journal Frontiers in Physiology

Received: 30 June 2018
Accepted: 15 August 2018
Published: 05 September 2018

Citation:
Kostic M, Bates NM, Milosevic NT, Tian J, Smiddy WE, Lee W-H, Somfai GM, Feuer WJ, Shiffman JC, Kuriyan AE, Gregori NZ, Pineda S and Cabrera DeBuc D (2018) Investigating the Fractal Dimension of the Foveal Microvasculature in Relation to the Morphology of the Foveal Avascular Zone and to the Macular Circulation in Patients With Type 2 Diabetes Mellitus. Front. Physiol. 9:1233. doi: 10.3389/fphys.2018.01233

In this study, we examined the relationship between the fractal dimension (FD), the morphology of the foveal avascular zone (FAZ) and the macular circulation in healthy controls and patients with type 2 diabetes mellitus (T2DM) with and with no diabetic retinopathy (DR). Cross-sectional data of 47 subjects were analyzed from a 5-year longitudinal study using a multimodal optical imaging approach. Healthy eyes from nondiabetic volunteers ($n = 12$) were selected as controls. Eyes from patients with T2DM were selected and divided into two groups: diabetic subjects with mild DR (MDR group, $n = 15$) and subjects with DM but without DR (DM group, $n = 20$). Our results demonstrated a higher FD in the healthy group (mean, 1.42 ± 0.03) than in the DM and MDR groups (1.39 ± 0.02 and 1.35 ± 0.03, respectively). Also, a bigger perimeter, area, and roundness of the FAZ were found in MDR eyes. A significant difference in area and perimeter ($p \leq 0.005$) was observed for the MDR group supporting the enlargement of the FAZ due to diabetic complications in the eye. A moderate positive correlation ($p = 0.014$, $R^2 = 43.8\%$) between the FD and blood flow rate (BFR) was only found in the healthy control group. The BFR calculations revealed the lowest values in the MDR group (0.98 ± 0.27 μl/s vs. 1.36 ± 0.86 μl/s and 1.36 ± 0.57 μl/sec in the MDR, DM, and healthy groups, respectively, $p = 0.2$). Our study suggests that the FD of the foveal vessel arborization could provide useful information to identify early morphological changes in the retina of patients with T2DM. Our results also indicate that the enlargement and asymmetry of the FAZ might be related to a lower BFR because of the DR onset and progression. Interestingly, due to the lack of FAZ symmetry observed in the DM and MDR eyes, it appears that the distribution of flow within the retinal vessels loses complexity as the vascular structures distributing the flow are not well described by fractal branching. Further research could determine how our approach may be used to aid the diagnosis of retinal neurodegeneration and vascular impairment at the early stage of DR.

Keywords: diabetic retinopathy, fractal analysis, foveal avascular zone, blood flow rate, fractal dimension

INTRODUCTION

Diabetes mellitus is one of the leading causes of vision loss (Diabetes Fact Sheet, 2017). Central vision loss, which is the most common impairment related to diabetic macular edema (DME), has a big impact on quality of life (Bourne et al., 2013; Korobelnik et al., 2014). The worldwide prevalence of DM is predicted to grow to 430 million patients by 2030, according to the World Health Organization (Korobelnik et al., 2014). Diabetes prevalence has also increased at a faster rate in lower income countries when compared to wealthier nations countries (Diabetes Fact Sheet, 2017). Also, rates of retinopathy are higher among people with type 1 diabetes mellitus (T1DM), individuals with longer duration of diabetes, and Caucasian populations (Yau et al., 2012; Bourne et al., 2013; Korobelnik et al., 2014). There is also a correlation between lower socioeconomic status and higher rates of retinopathy (Yau et al., 2012; Bourne et al., 2013).

Microaneurysms, capillary nonperfusion, and ischemia within the retina are the characteristic pathological features of DR (Elman et al., 2010; Hwang et al., 2015, 2016; Ishibazawa et al., 2015). These pathophysiologic changes can be associated with several complications, such as DME and diabetic macular ischemia (Beltramo and Porta, 2013; American Academy of Ophthalmology., 2014; Varma et al., 2014; Couturier et al., 2015; Das et al., 2015; Bradley et al., 2016). These complications compound impaired blood and oxygen supply of the neuroglial tissues of the retina. The expression of vascular endothelial growth factor (VEGF), which acts as an angiogenic agent and increases vascular permeability, is enhanced in the hypoxic environment (Choi et al., 2013). Diabetic maculopathy is caused by a combination of both VEGF-mediated factors and mediators (Agemy et al., 2015; Mastropasqua et al., 2015; Gorczynska et al., 2016). High glucose levels lead to microvasculopathy with alterations in the blood-retinal barrier, causing pericyte loss and endothelial cell-cell junction breakdown (Kaur et al., 2008). This capillary disruption increases vascular permeability and the pooling of fluid within the plexiform layers of the retina and the subretinal space (Ishibazawa et al., 2015). These pathophysiological changes can result in a gradual loss of visual acuity.

The FAZ is the macular region that is most susceptible to retinal changes in individuals with diabetes (Choi et al., 2013; Varma et al., 2014). The FAZ is the central part of the macula and is surrounded by interconnected capillary beds. This vascular network terminates in the central macula forming a vascular ring-shaped border with an average diameter of 500–600 μm (de Carlo et al., 2015a,c). In some patients with DME, central visual loss may be due to edema as well as ischemia occurring due to capillary dropout sufficient to increase the FAZ area (Choi et al., 2013). Most DR patients will not experience vision changes until late-stage disease, therefore, early detection and immediate intervention may better preserve vision (Aiello, 2003). Consequently, early detection and accurate staging are critical for determining optimal management. DME treatments have been developed, including focal or grid photocoagulation and anti-VEGF therapy, both of which have been demonstrated to be effective (American Academy of Ophthalmology., 2014; Couturier et al., 2015; Wiley et al., 2016). Anti-VEGF therapy has also been shown recently to slow the progression and, in some cases, reverse the degree of ophthalmoscopically observed nonproliferative retinopathy (Ip et al., 2012, 2015). However, the pathology involved in the retinal hemodynamics throughout the course of DR is not completely understood (Pemp and Schmetterer, 2008; Kur et al., 2012; Stitt et al., 2016).

Various diagnostic techniques exist to assess the structure and function of the retina. Ophthalmoscopy and fundus photographs are standard techniques used in DR, with the fundus photographs being comparable to ophthalmoscopy under dilated pupils while remaining cost effective for screening in diabetes clinics (Lee et al., 1993). Fluoroscein angiography is also recognized as a useful tool for healthcare professionals diagnosing and treating DR (Agemy et al., 2015). However, it requires venipuncture which may lead to allergic reactions and, in rare cases, death due to anaphylaxis (Yannuzzi et al., 1986). In addition, the technique is costly and time-consuming, requiring up to 30 min only for image acquisition itself (Matsunaga et al., 2014; Sim et al., 2014; Di et al., 2016). Nevertheless, it has historically been the standard in the assessment of DR and DME. Retinal hemodynamic abnormalities and retinal oxygen metabolism have also been investigated in patients with DR (Kohner et al., 1995; Bursell et al., 1996; Calles-Escandon and Cipolla, 2001; Schram et al., 2005). For example, the retinal function imager (RFI) (Optical Imaging Ltd, Rehovot, Israel) is a noninvasive imaging technique that has been used to investigate the microcirculation in the retina of patients with DM (Grinvald et al., 2004; Nelson et al., 2005).

Research in different areas of complications associated to DM is constantly evolving (Campagnoli et al., 2017; Somfai et al., 2018). The search for risk biomarkers characterizing preclinical abnormalities is fundamental to fast-track the discovery of novel treatments. For example, FD is one of the vascular architectural parameters commonly used to quantify changes in the retinal branching pattern and vascular density due to disease progression (Lim et al., 2009; Cosatto et al., 2010). Fractal geometry studies of the retinal vasculature can be performed by fractal analysis, a mathematical method used to measure complexity in natural phenomenon (Mandelbrot, 1982). The concept of fractal geometry was first described by Mandelbrot in 1989 (Smith et al., 1996; Fernández and Jelinek, 2001; Di Ieva et al., 2015). Later, Family et al. introduced this method in ophthalmology and since then, interest in studying the association between the FD of the retinal vasculature and disease severity and progression has dramatically increased (Family et al., 1989; Fractals medicine., 1991; Cheung et al., 2009; Grauslund et al., 2010; Yau et al., 2010; Aliahmad et al., 2014; Broe et al., 2014). Although, the retinal vasculature tree could be quantified with various methods of fractal analysis (Stosic and Stosic, 2006; Macgillivray et al., 2007), the digital retinal images could be investigated through complexity, space-filling, shape, and tortuosity of retinal blood vessels. These characteristics could be quantified by the box-counting method of fractal analysis (Milošević, 2015).

In this study, we examined the relationship between the fractal dimension (FD), the morphology of the foveal avascular zone (FAZ) and the macular circulation in healthy controls and patients with type 2 diabetes mellitus (T2DM) with and with no diabetic retinopathy (DR). Our results suggest that the FD of the foveal vessel arborization could provide useful information to identify early morphological changes in the retina of patients with T2DM.

METHODS

Study Population

The study was approved by the Institutional Review Board (University of Miami, Miami, FL, USA). The research adhered to the tenets outlined in the Declaration of Helsinki and written informed consent was obtained from each study subject. In this prospective study, enrollment was offered to patients with DM referred to the comprehensive ophthalmology clinic that had DR up to early treatment diabetic retinopathy study (ETDRS) level 35 and without macular edema, as well as diabetic patients with no retinopathy and healthy individuals (Group ETDRSR, 1981).

Patients with proliferative disease, clinically significant macular edema (CSME), and anatomic abnormalities that might confound the evaluation of macular architecture (such as glaucoma, vitreoretinal traction, and epiretinal membranes) were excluded. Patients with medical conditions that might affect visual function, those taking medications that might affect retinal thickness (e.g., chloroquine or anti-cholesterol agents containing niacin), recent cataract surgery, previous vitrectomy, or unstable blood sugars were also excluded.

The routine ophthalmic examination was carried out with dilated fundoscopy and patients were divided into two groups based on the absence of DR (DM group) and presence of mild DR (MDR group). Any eyes with more severe DR (i.e., greater than ETDRS level 35) were excluded from the study. Study subjects (age-matched) were selected from a 5-year longitudinal study based on the quality of the overall imaging data required to perform all analyses. **Table 1** shows the demographics of the study population. A total of 47 study participants (58 eyes) were identified with good quality images from the RFI system.

TABLE 1 | Study Participant Demographics.

Descriptor	Healthy	DM	MDR
Number of patients (Male/Female)	12 (3/9)	20 (6/14)	15 (8/7)
Number of Eyes (OD/OS)	13 (5/8)	28 (10/18)	17 (9/8)
Mean age ± SD, years	54.08 ± 7.71	52.64 ± 7.79	52.63 ± 5.79

Hemodynamic Analysis

This analysis was performed by the RFI system, which is based on a standard fundus camera extended by a customized stroboscopic flash lamp system. A green ("red-free") light with a spectrum of 548 ± 75 nm is used for illumination and the interval between consecutive flashes is typically 17.5 ms. One session of RFI data consists of 8 images with a resolution of 1,024 × 1,024 pixels in an area of 4.3 × 4.3 mm or 7.2 × 7.2 depending on the choice of field of view (20° or 35°) during the imaging acquisition. In this study, all the images were captured with the setting of 20° field of view (FOV) at a resolution of 4.3 microns/pixel. The heartbeats of the patient were monitored with a finger probe sensor and the image acquisition was synchronized with the cardiac cycle to neutralize the effects of pulsation on arterial blood flow velocity (BFV) (Grinvald et al., 2004; Nelson et al., 2005; Tian et al., 2016).

Once the image was acquired, the RFI built-in software generated (a) the flow movie (a.k.a. "ratio video") through differential processing so that the motion of individual clusters of red blood cells can be followed by the human eye; and (b) a non-invasive capillary perfusion map (nCPM) was generated through analyzing the difference of pixel intensities in adjacent frames (Nelson et al., 2005; Izhaky et al., 2009). A good quality scanning session is characterized by sharp vessel borders on the raw fundus images, clear red blood cell movement along the vessels on ratio videos and a visible capillary network on the nCPM. Therefore, images were evaluated for optical quality, exposure and focus. We obtained 3 or more good-quality sessions for each eye by the same experienced photographer with at least 5 good images per session that were selected for further analysis using a custom-built software (Tian et al., 2016). In our method, the BFV is calculated by maximizing cross-correlation of intensity profiles between adjacent frames and the BFR is computed by multiplying the BFV with the cross-sectional area (Tian et al., 2016). All BFR measurements were obtained for the overall arteries, overall veins and overall vessels (i.e., arteries and veins) for each study group.

Fractal Analysis

The fractal analysis of the retinal vascular network was performed using the box-counting method (Smith et al., 1996; Fernández and Jelinek, 2001; Milošević, 2015, 2016; Rajkovic et al., 2017). The RFI images were imported in Image J (National Institutes of Health, Bethesda, MD) and used to calculate the FD after grayscale format conversion (**Figure 1**). The box counting method generates data by "covering" the object with a rectangular coordinate grid and breaking the data into boxes and then analyzing the subsets by counting the number of boxes (Smith et al., 1996; Fernández and Jelinek, 2001). The lower and upper box-dimensions of a subset $F \subset R^n$ are respectively defined by

$$\dim_B(F) = \lim_{\delta \to 0} \frac{\log N_\delta(F)}{-\log \delta}, \dim_B(F) = \lim_{\delta \to 0} \frac{\log N_\delta(F)}{-\log \delta} \qquad (1)$$

and if lower and upper values are equal, then the common value is referred to as the box-counting dimension of F and is denoted by

$$\dim_B(F) = \lim_{\delta \to 0} \frac{\log N_\delta(F)}{-\log \delta} \qquad (2)$$

Where $N_\delta(F)$ can be the smallest number of cubes of side δ (naturally, in 3D) that covers F or the largest number of disjoint cubes of side δ with centers in F (Falconer, 1989).

When plane-projection of the object is analyzed, this method measures FD by covering the image with a rectangular coordinate grid with cell size r and counts the number of boxes, where the cell size is expressed as the number of foreground pixels. The number of squares $N(r)$ needed to cover the image is given by a power law

$$N(r) = const \cdot r^{-D} \tag{3}$$

Where D is the box dimension, calculated as an absolute value of the slope of the log-log relationship between $N(r)$ and r as previously described in detail (Milošević, 2015).

Morphology Analysis of the FAZ

The foveal morphology analysis was performed on the nCPM composite images, which were generated from the individual scans taken with the RFI (Tian et al., 2016). These capillary maps were then used to gather information regarding the FAZ, which can be identified in the image as the central area where no vasculature is present. An active contouring model was used to identify and outline the FAZ (Nikolay, 2016; Bates et al., 2018). The active contouring program is run by constant user supervision; therefore, each run was reviewed ensuring that it accurately represented the FAZ. If it appeared to be inaccurate, the simulation was rerun with different parameters, specifically with a different region of interest drawn to capture the area better. If it was still not representative of the actual FAZ, the image was excluded from the analysis due to poor quality. This process was done blindly, in that the group of the patient was unknown. Following identification of the FAZ using active contouring, the images were analyzed using ImageJ (National Institutes of Health, Bethesda, MD) (Smith et al., 1996; Schneider et al., 2012). This software allows for the easy acquisition of data regarding the region of interest, including area, circumference, perimeter, and the maximum/minimum Feret diameter. Area, perimeter, and roundness are parameters that we used for this study.

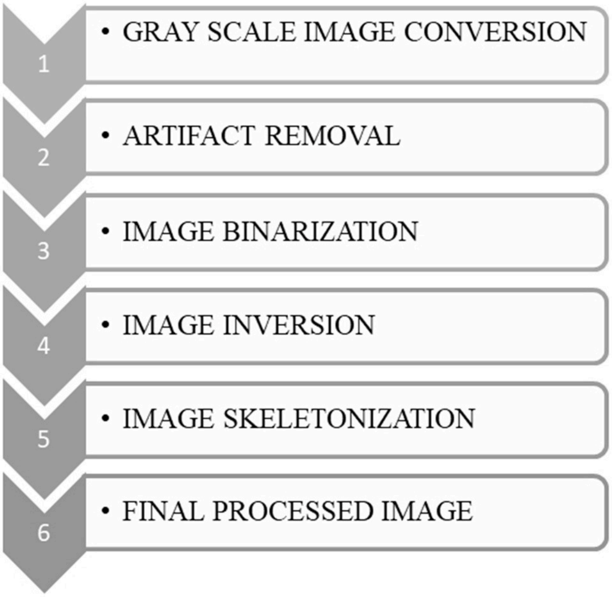

FIGURE 1 | Sketch diagram of skeletonized box dimension (D_{skel}) obtained by the box-counting method.

Ethics Approval

The Human Research Ethics Committee of the University of Miami, Miami, FL, USA approved all protocols and methods described in this study. The research adhered to the tenets outlined in the Declaration of Helsinki. Informed consent was obtained from all participants following a thorough explanation of all test procedures.

Statistical Analysis

Linear regression was used to determine the relationship between the BFR, FD, and FAZ parameters among the three groups. A one-way ANOVA test was used to determine if there was a difference present in any group, and then a *post hoc* Kruskal-Wallis test was used to identify these individual group differences. In all cases, a p-value of 0.05 was used to define significance (Katz and McSweeney, 1980; Armstrong et al., 2000).

RESULTS

Fractal Dimension

FD was calculated for the three study groups. ANOVA showed a statistically significant difference ($p < 0.001$) between all study groups. The highest FD values were obtained for the healthy group (1.42 ± 0.03) compared to those calculated for the DM and MDR groups (1.39 ± 0.02 and 1.35 ± 0.03, respectively) (see **Figure 2**). An example of the nCPM and corresponding skeleton images used in the fractal analysis is shown in **Figure 3**.

The intergroup differences measured with the Kruskal-Wallis analysis revealed a statistically significantly larger FD in the healthy group compared to the one obtained from the DM and MDR groups ($p = 0.002$). Also, a statistically significant difference ($p < 0.001$) was found between the healthy and the MDR group, as well as between the DM and MDR groups ($p < 0.001$).

FAZ Dimensions

The area, perimeter and roundness of the FAZ were calculated to characterize the morphology of the FAZ region (Bates et al., 2018)

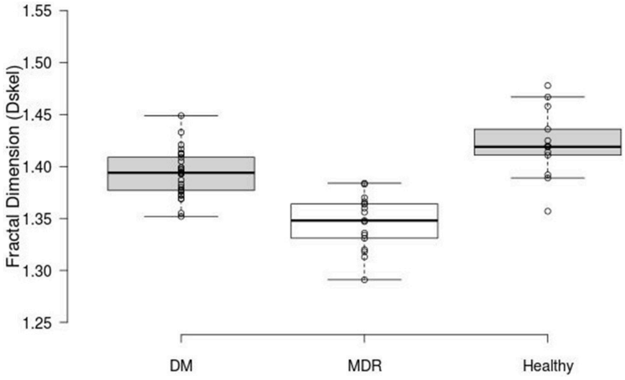

FIGURE 2 | Box plots displaying the FD results. The middle 50% *(mean and 95% CI)* of the data groups are as follows: DM (1.3765–1.4105), MDR (1.3255–1.365), and Healthy (1.4015–1.447).

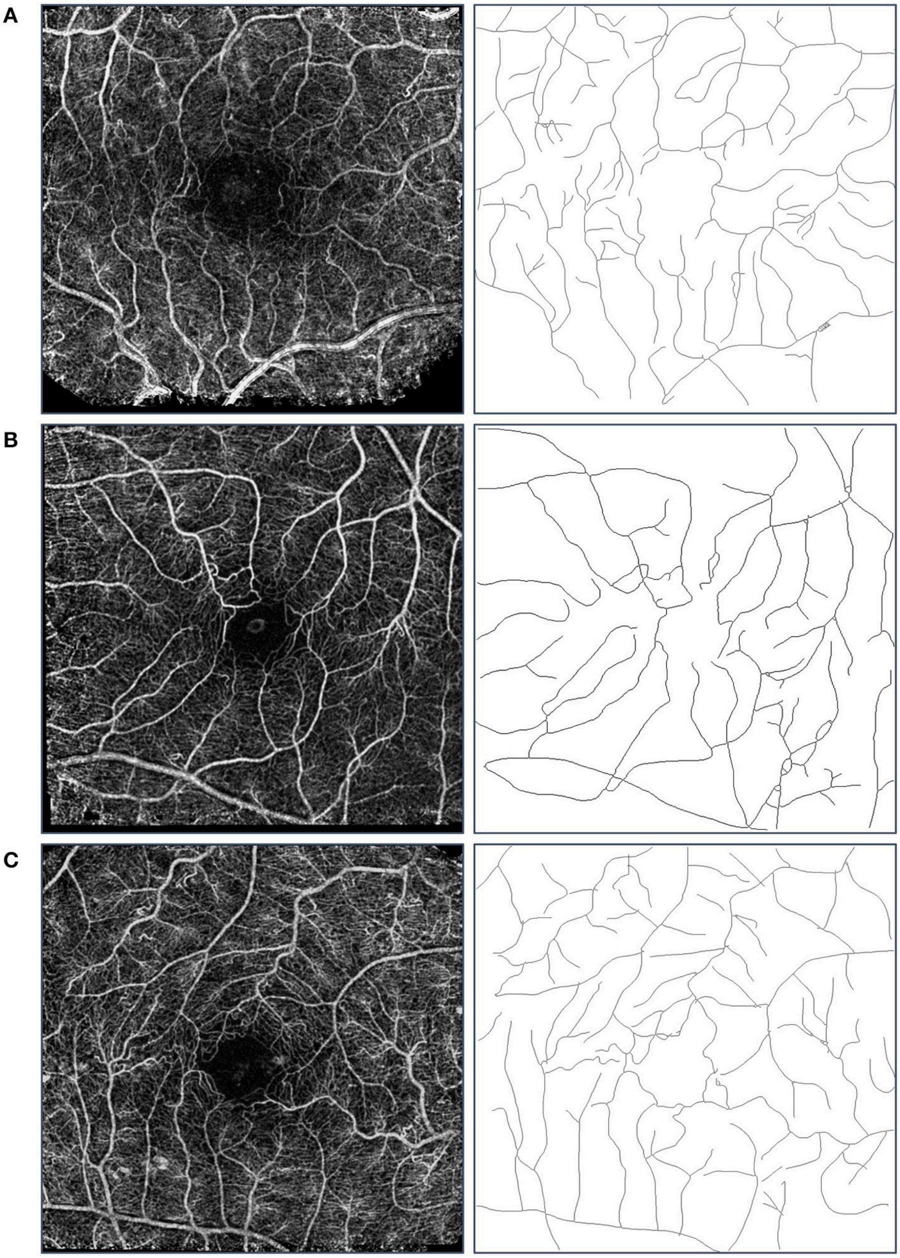

FIGURE 3 | Sample images used in the fractal analysis. Images in the left column are the composite nCPM images generated from the RFI system, while those in the right are their respective skeleton images that were used in the fractal analysis. Row **(A)** is from the healthy group, Row **(B)** from the DM group, and Row **(C)** from the MDR group. We note that the blood vessel types used in the analysis were the major arterial and venous trees.

A summary of the results for the three study groups is presented in **Table 2**. ANOVA showed significance in all parameters with multiple significant differences in the pairwise comparisons as seen in **Table 2**.

Blood Flow Rate

Figure 4 shows the BFR results obtained for the overall blood vessels (i.e., both arteries and veins) per study group. Our results showed 0.98 ± 0.27 μl/s, 1.36 ± 0.86 μl/s, and 1.36 ± 0.57 μl/s in the MDR, DM, and healthy groups, respectively. No significant difference ($p = 0.2$) was found in the ANOVA analysis.

Relationship Between the Vascular FD, the Morphology of the FAZ, and Macular Circulation

Linear regression results showed significant differences for the healthy group when analyzing the correlations between the vascular FD and BFR parameters (see **Table 3**). For all three

TABLE 2 | Results of the FAZ characterization for all three groups (first three columns show the morphological parameters).

Descriptor	Healthy mean(±SD)	DM mean(±SD)	MDR mean(±SD)	Healthy vs. DM	Healthy vs. MDR	DM vs. MDR
Area (mm²)	0.19 ± 0.05	0.21 ± 0.06	0.25 ± 0.06	0.26	**<0.01**	**0.02**
Perimeter (mm)	2.03 ± 0.24	2.16 ± 0.39	2.50 ± 0.41	0.29	**<0.01**	**<0.01**
Roundness	0.87 ± 0.07	0.84 ± 0.09	0.90 ± 0.06	0.21	0.31	**0.02**

The p-values of the Kruskal-Walls test are shown in the last three columns) with significant results in bold. Note that roundness as defined by Image J – represents how closely a region conforms to a circle.

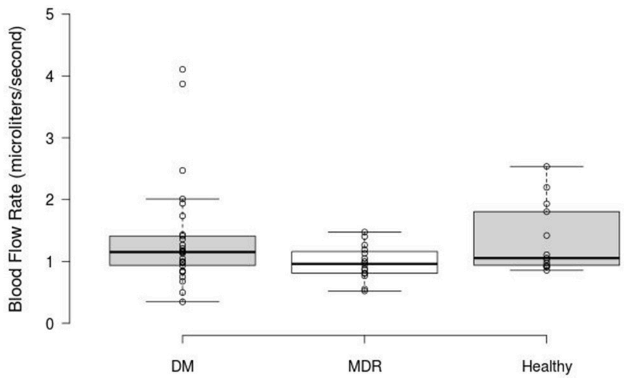

FIGURE 4 | Box Plot displaying the BFR results obtained for the overall blood vessels in the three study groups. The middle 50% of the data groups are as follows: DM (0.89–1.42), MDR (0.809–1.17), and Healthy (0.85–1.868).

groups of patients, FD was calculated and compared with BFR data for overall arteries, veins, and vessels. A summary of the results for all three study groups is presented in **Table 3**. Only the healthy control group showed a significant linear correlation between the FD and BFR parameters.

In comparing the BFR with the FAZ characteristics, only the DM group showed a statistically significant linear relationship. These relationships are shown in **Figure 5**, where the R^2 value and the equation of the line of best fit is displayed on their respective graphs.

DISCUSSION

In this study, we investigated the FD of the foveal vessel arborization in relation to the morphology of the FAZ and the macular circulation in patients with T2DM. Our results demonstrated the highest FD in the healthy group compared to the DM and MDR groups, with a significant difference between the three groups. Our results are similar to the outcomes presented by Grauslund et al., where the FD of 94 patients with T1DM without proliferative retinopathy were compared with 79 T1DM patients with proliferative retinopathy and found that the group with the most severe disease had lower FD (Grauslund et al., 2010). Similarly, Aliahmad et al. found that the healthy group had higher FD compared with the diabetic group and suggested that a low FD could be a result of the retina being less effective, which may lead to an increased risk of complications like proliferative retinopathy (Mainster, 1990; Aliahmad et al., 2014).

Numerous studies have assessed the vascular complexity (FD) in patients with different types of DM and stages of DR with contradicting findings. A 16-years study that monitored 180 patients with T1DM found that FD of the retinal vasculature generally decreased in these population. It was also found that lower FD could predict neuropathy (Broe et al., 2014). On the other hand, Cheung et al. and Yau et al. found that an increase in vascular FD was associated with an increased incidence of retinopathy (Cheung et al., 2009; Yau et al., 2010). However, all these studies had different study designs and used fundus machines with different resolutions and illumination settings. The quality of the images acquired from the study subjects was also dissimilar. Also, the region of interest for the FD calculation was not the same for all studies. For example, our study analyzed the FD in a 20° FOV while the other studies looked at the vessels at a larger scale. This difference in methodologies may cause contradicting findings among studies. Huang et al. found that the FD must be calculated under very rigorous settings after investigating the reliability of the vascular FD calculated from retinal images acquired with 5 different fundus cameras (Huang et al., 2016). Therefore, when comparing different studies, it is of great importance to consider the study design, the settings used for the analysis of the acquired images and image resolution among other key factors.

The results of our study showed that there were significant differences in FAZ parameters that describe different morphology characteristics between all 3 groups. Results of the FAZ characterization showed no significant differences in the DM group in comparison to the healthy group, while the MDR group had significantly higher FAZ area and perimeter in comparison to the healthy and DM groups. Also, a significant difference in roundness was only observed between DM and MDR groups. These findings might indicate that the FAZ roundness might be a good indicator of DR onset and progression. Intriguingly, as reported in our previous study, the fact that the FAZ area was larger in the MDR group but more asymmetric in the DM group suggest a possible anisotropy in the mechanical properties of the diabetic retina with no retinopathy. This anisotropy may trigger the FAZ elongation in a preferred direction as probably a result of autoregulation (Bates et al., 2018).

The findings in the current study support the loss of symmetry in the FAZ expansion with worsening of the retinopathy condition. Our results are in accordance with the fact that the enlargement of the FAZ area is an indicator of DR onset and progression besides being an indicator of visual prognosis in patients with DME (Bates et al., 2018). It is well known that larger FAZ area is associated with

TABLE 3 | Linear regression results obtained for all three groups after analyzing the correlations between the FD and BFR. Significant results ($p < 0.05$) are highlighted in bold.

Group	Overall Arteries	Overall Veins	Overall Blood Vessels						
	Slope	R^2	p	**Slope**	R^2	p	**Slope**	R^2	p
Healthy	0.04	0.45	**0.01**	0.03	0.31	**0.04**	0.04	0.44	**0.01**
DM	∼0	<0.01	0.8	∼0	<0.01	0.65	∼0	<0.01	0.75
MDR	0.01	0.02	0.58	0.03	0.14	0.16	0.03	0.10	0.24

Results are presented as: Slope of linear regression, R^2 value, and p-value. Slope listed as ∼0 refers to a slope of less than 0.001.

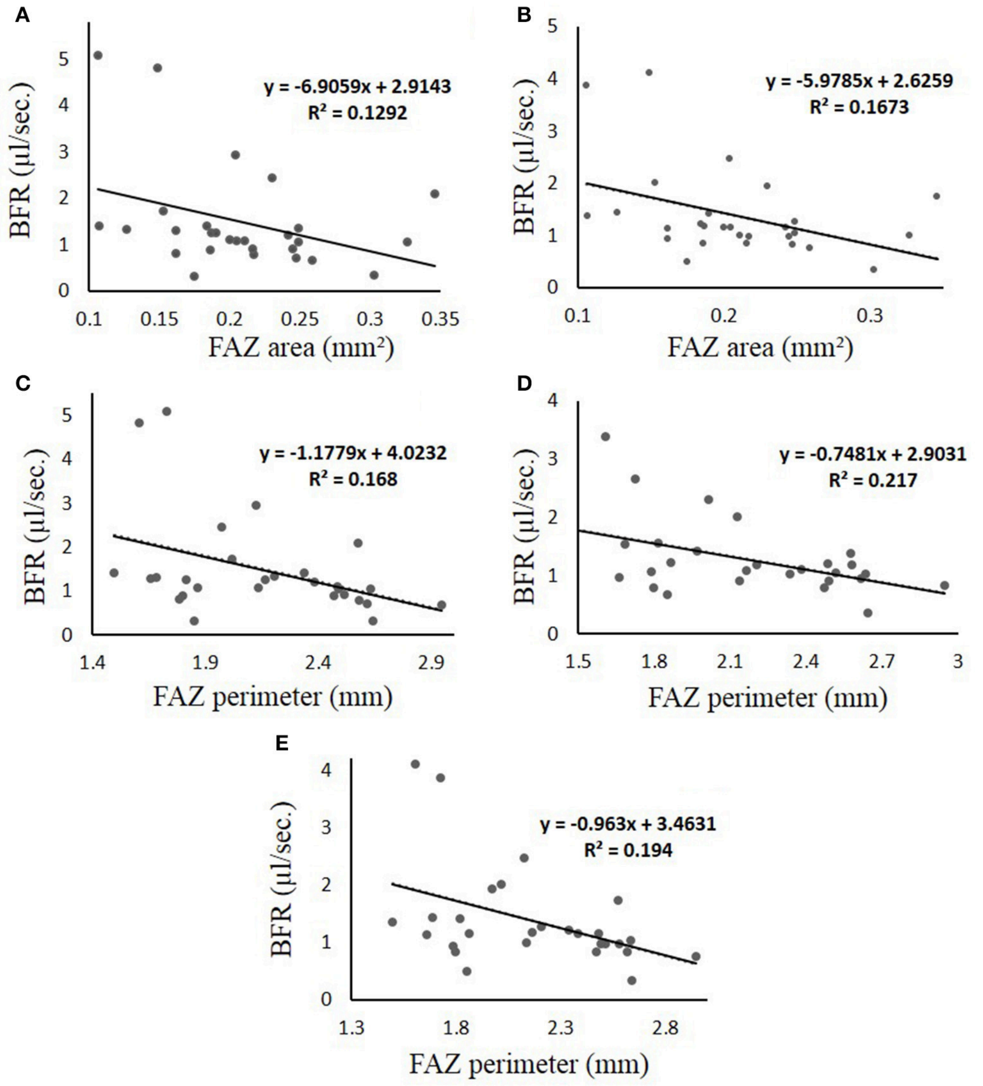

FIGURE 5 | (A–E) Linear regression results obtained for the DM group of patients, which is the only group that displayed significance when comparing the BFR to the FAZ characteristics. Each figure is labeled with measured parameters. The line represents thel ine of best fit, of which the equation is displayed in the graph region. In all cases, the "y-axis" represents BFR in µl/s and the "x-axis" represents FAZ area in mm^2. **(A)** BFR vs. FAZ area in veins **(B)** BFR vs. FAZ area in all vessels **(C–E)** BFR vs. FAZ Perimeter for arteries, veins, and all vessels, respectively. The R^2 is the coefficient of determination, which compares the ratio of the average difference of the data point and the line of the best fit with that of the data point and the average "y" value.

progression of DR, compared to healthy individuals, as reported after using FA (Sakata et al., 2006). Additionally, Optical Coherence Tomography-Angiography (OCTA) studies have found a negative correlation between FAZ area and visual acuity. However, FAZ size is not fixed among individuals; therefore, its normal variation makes assessment of retinal pathology in terms of FAZ size very difficult (de Carlo et al., 2015b; Freiberg et al., 2015; Mammo et al., 2015; Spaide et al., 2015; Takase et al., 2015; Al-Sheikh et al., 2016; Bhanushali et al., 2016; Samara et al., 2016; Tan et al., 2016).

There are many discrepancies in studies targeting retinal blood flow, mainly due to differences in the device used and in the study design. Particularly, the variability in these studies is affected by factors including the recruitment of patients with T1DM diabetes vs. T2DM, controlled vs. poorly controlled diabetes, age, presence or absence of other co-morbidities such as systemic hypertension (Kohner, 1975; Grunwald et al., 1993, 1996; Schmetterer and Wolzt, 1999; Pournaras et al., 2008). Our study population consisted of age-matched groups composed by healthy controls and T2DM subjects with and with no mild DR. The diabetes disease condition in T2DM patients was in control but most of the T2DM patients were hypertensive (under control). The fastest BFR for overall vessels (that is, arteries and veins taken together) was found in healthy subjects, compared with the DM and MDR groups, whereas the slowest BFR was observed in the MDR group. This is in correlation with previous investigations where reduced retinal blood flow and vessel stiffness seemed to be associated with nonperfusion in the vasculature network (Kohner, 1975; Grunwald et al., 1996; Schmetterer and Wolzt, 1999; Sakata et al., 2006; Pournaras et al., 2008).

In comparing the correlation of the BFR and FD for the three groups, a significant correlation between FD and BFR was obtained for the healthy group in all three groupings of the vessels (overall arteries, overall veins and overall vessels). Nevertheless, we did not find any significant correlation for the DM and MDR groups. Also, the BFR and vascular FD among healthy subjects and diabetic patients with and with no DR have not been compared in previous studies. According to our findings, it seems that the flow distribution of the retinal vessels loses complexity while fractal branching does not adequately describe the vascular structures involved in this process.

Although the BFR was lower in the MDR group than in the DM and healthy groups, intriguingly, the correlation between BFR and FAZ was statistically significant with low R-squared values only for the DM group. It is possible that our data contain an intrinsically higher amount of unexplainable variability. Also, there was a negative correlation between FAZ perimeter and BFR for the DM group when compared in overall arteries, overall veins and overall vessels. As well as there was a negative correlation between FAZ area and BFR for overall veins and overall vessels. Interestingly, we saw no statistically significant correlation between BFR and FAZ roundness in the DM group. Also, there was no statistically significant correlation between BFR and FAZ in the MDR and healthy groups.

The reduction in BFR in patients with DM may be due to morphological changes of the vascular bed in combination with lack of capability of vascular autoregulation and the decrease of blood fluidity (Ashton, 1974; Sinclair et al., 1982; McMillan, 1989). Our results could be explained by the fact that an increase in FAZ area and perimeter can result in decreased BFV, and consequently a decreased BFR, as demonstrated by the negative correlation observed between BFR and FAZ size. However, our study does not have the full power to prove this outcome as there are many factors that have an influence on microcirculation in diabetic patients with DR, such as duration of disease, changes in ocular biomechanics, and the presence of other concomitant systemic diseases (e.g., controlled hypertension in our diabetic groups) that can contribute to a slower BFR in patients with DR. A statistically significant negative correlation between capillary BFV and FAZ size in T2DM was found in a previous study that used FA as the measurement method (Sakata et al., 2006). However, a correlation between FAZ parameters and BFR in patients with DR or a healthy control group seems to be unavailable in the current literature. Our fractal dimension results also revealed the potential use of this method to quantify the progressive change in DR between the increased and decreased vessel complexity stages. The complexity index of the retinal vascular pattern characterized by fractal analysis may uncover potential regulation of specific markers of disease status.

There are important limitations to the present study that need to be addressed. There was a different sample size for each one of the 3 groups due to the exclusion of eyes because of the poor image quality obtained with the RFI unit in some eyes with media opacities. Also, only subjects with T2DM were included. Consequently, the degree to which our outcomes can be generalized to individuals with Type 1 diabetes is uncertain. Especially, retinal structure and function may be affected by factors such as hyperlipidemia, older age, and hypertension in Type 2 diabetes. Furthermore, we conducted our study in a relatively small sample of patients. A better understanding of the correlation between BFR, FD, and FAZ measurements in a bigger number of subjects and longitudinal studies is devised as a future study.

CONCLUSION

There are many structural and hemodynamic parameters that can play a role in the development of DR. Particularly, the development of advanced imaging will facilitate that these quantitative measurements can help with the identification of changes in the retinal structure affected by various diseases with greater precision and detail (Tian et al., 2016). Our results suggest that the FD of the foveal vessel arborization in conjunction with other functional and structural parameters could provide useful information to identify early morphological changes in the retinal tissue of patients with T2DM. The data also lead us to believe that the enlargement and asymmetry of the FAZ area might be related to a lower BFR associated with the onset and progression of DR (Krawitz et al., 2017). Notably, due to the lack of FAZ symmetry observed in DM and MDR eyes, it appears that the distribution of flow within the retinal vessels loses complexity as the vascular structures distributing the flow are not well described by fractal branching. In addition, despite the availability of many different studies about FAZ and DM or FD and FAZ, to our knowledge, there are no known studies that correlate FD with hemodynamic and structural parameters. However, further longitudinal research is warranted to determine how our approach may be used to aid diagnosis of retinal neurodegeneration and vascular impairment at the early stage of DR. There is no doubt that there is a need for a better understanding of structural and hemodynamic parameters which are integrally interdependent. Specifically, the multimodal measurements in our future work would not only provide details of retinal pathophysiology but could possibly contribute as a biomarker in disease staging.

AUTHOR CONTRIBUTIONS

DC conceived and designed the study. DC, JT, GS, WS, W-HL, AK, NG, SP, and MK performed the study; NB, NM, JT, GS, WF, JS, DC, and MK analyzed the data. JT, DC, WF, JS, SP, and NM: contributed reagents, materials, and analysis tools. MK, NB, NM, JT, DC, WS, and GS contributed to the writing of the manuscript.

FUNDING

This study was supported in part by a NIH Grant No. NIH R01EY020607, a NIH Center Grant No. P30-EY014801, by an unrestricted grant to the University of Miami from Research to Prevent Blindness, Inc., and by an Eotvos Scholarship of the Hungarian Scholarship Fund.

REFERENCES

Agemy, S. A., Scripsema, N. K., Chirag, M. S., Chui, T., Garcia, P. M., Lee, J. G., et al. (2015). Retinal vascular perfusion density mapping using optical coherence tomography angiography in normals and diabetic retinopathy patients. *Retina* 35, 2253–2263. doi: 10.1097/IAE.0000000000000862

Aiello, L. M. (2003). Perspective on diabetic retinopathy. *Am. J. Ophthalmol.* 136, 122–135. doi: 10.1016/S0002-9394(03)00219-8

Aliahmad, B., Kumar, D. K., Sarossy, M. G., and Jain, R. (2014). Relationship between diabetes and grayscale fractal dimensions of retinal vasculature in the Indian population. *BMC Ophthalmol.* 14:152 doi: 10.1186/1471-2415-14-152

Al-Sheikh, M., Akil, H., Pfau, M., and Sadda, S. R. (2016). Swept-source OCT angiography imaging of the foveal avascular zone and macular capillary network density in diabetic retinopathy. *Invest. Ophthalmol. Vis. Sci.* 57:3907–3913. doi: 10.1167/iovs.16-19570

American Academy of Ophthalmology. (2014). *American Academy of Ophthalmology Retina and Vitreous Panel. Preferred Practice Pattern® guidelines. Diabetic retinopathy*. San Francisco, CA: American Academy of Ophthalmology. Available online at: http://www.aao.org/ppp

Armstrong, R. A., Slade, S. V., and Esperjesi, F. (2000). An introduction to analysis of variance (ANOVA) with special reference to data from clinical experiments in optometry. *Ophthalmic Physiol. Opt.* 20, 235–241. doi: 10.1016/S0275-5408(99)00064-2

Ashton, N. (1974). Vascular basement membrane changes in diabetic retinopathy. *Br. J. Ophthalmol.* 58, 344–366. doi: 10.1136/bjo.58.4.344

Bates, N. M., Tian, J., Smiddy, W., Lee, W. H., Somfai, G., Feuer, W., et al. (2018). Relationship between the morphology of the foveal avascular zone, retinal structure, and macular circulation in patients with diabetes mellitus. *Sci. Rep.* 8:5355. doi: 10.1038/s41598-018-23604-y

Beltramo, E., and Porta, M. (2013). Pericyte loss in diabetic retinopathy: mechanisms and consequences. *Curr. Med. Chem.* 20, 3218–3225. doi: 10.2174/09298673113209990022

Bhanushali, D., Anegondi, N., Gadde, S. G., Srinivasan, P., Chidambara, L., Yadav, N. K., et al. (2016). Linking retinal microvasculature features with severity of diabetic retinopathy using optical coherence tomography angiography. *Invest. Ophthalmol. Vis. Sci.* 57, 519–525. doi: 10.1167/iovs.15-18901

Bourne, R. R., Stevens, G. A., White, R. A., Smith, J. L., Flaxman, S. R., Price, H., et al. (2013). Causes of vision loss worldwide, 1990–2010: a systematic analysis. *Lancet Global Health* 1:e339-49. doi: 10.1016/S2214-109X(13)70113-X

Bradley, P. D., Sim, D. A., Keane, P. A., Cardoso, J., Agrawal, R., Tufail, A., et al. (2016). The evaluation of diabetic macular ischemia using optical coherence tomography angiography. *Invest. Ophthalmol. Vis. Sci.* 57, 626–631. doi: 10.1167/iovs.15-18034

Broe, R., Rasmussen, M. L., Frydkjaer-Olsen, U., Olsen, B. S., Mortensen, H. B., Peto, T., et al. (2014). Retinal vascular fractals predict long-term microvascular complications in type 1 diabetes mellitus: the Danish Cohort of Pediatric Diabetes (DCPD1987). *Diabetologia* 57, 2215–2221. doi: 10.1007/s00125-014-3317-6

Bursell, S. E., Clermont, A. C., Kinsley, B. T., Simonson, D. C., Aiello, L. M., and Wolpert, H. A. (1996). Retinal blood flow changes in patients with insulin-dependent diabetes mellitus and no diabetic retinopathy. *Invest. Ophthalmol. Vis. Sci.* 37, 886–897.

Calles-Escandon, J., and Cipolla, M. (2001). Diabetes and endothelial dysfunction: a clinical perspective. *Endocr. Rev.* 22, 36–52. doi: 10.1210/edrv.22.1.0417

Campagnoli, T. R., Somfai, G. M., Tian, J., DeBuc, D. C., and Smiddy, W. E. (2017). Noninvasive, high-resolution functional macular imaging in subjects with retinal vein occlusion. *Ophthalmic Surg. Lasers Imag. Retina* 48, 799–809. doi: 10.3928/23258160-20170928-04

Cheung, N., Donaghue, K. C., Liew, G., Rogers, S. L., Wang, J. J., Lim, S. W., et al. (2009). Quantitative assessment of early diabetic retinopathy using fractal analysis. *Diabetes Care* 32, 106–110. doi: 10.2337/dc08-1233

Choi, W., Mohler, K. J., Potsaid, B., Lu, C. D., Liu, J. J., Jayaraman, V., et al. (2013). Choriocapillaris and choroidal microvasculature imaging with ultrahigh speed OCT angiography. *PLoS ONE* 8:e0081499. doi: 10.1371/journal.pone.0081499

Cosatto, V. F., Liew, G., Rochtchina, E., Wainwright, A., Zhang, Y., Hsu, W., et al. (2010). Retinal vascular fractal dimension measurement and its influence from imaging variation: results of two segmentation methods. *Curr. Eye Res.* 35, 850–856. doi: 10.3109/02713683.2010.490628

Couturier, A., Mané, V., Bonnin, S., Erginay, A., Massin, P., Gaudric, A., et al. (2015). Capillary plexus anomalies in diabetic retinopathy on optical coherence tomography angiography. *Retina* 35, 2384–2391. doi: 10.1097/IAE.0000000000000859

Das, A., McGuire, P. G., and Rangasamy, S. (2015). Diabetic macular edema: pathophysiology and novel therapeutic targets. *Ophthalmol* 122, 1375–1394. doi: 10.1016/j.ophtha.2015.03.024

de Carlo, T. E., Bonini Filho, M. A., Chin, A. T., Adhi, M., Ferrara, D., Baumal, C. R., et al. (2015a). Spectral-domain optical coherence tomography angiography of choroidal neovascularization. *Ophthalmol* 122, 1228–1238. doi: 10.1016/j.ophtha.2015.01.029

de Carlo, T. E., Chin, A. T., Bonini Filho, M. A., Adhi, M., Branchini, L., Salz, D. A., et al. (2015b). Detection of microvascular changes in eyes of patients with diabetes but not clinical diabetic retinopathy using optical coherence tomography angiography. *Retina* 35, 2364–2370. doi: 10.1097/IAE.0000000000000882

de Carlo, T. E., Romano, A., Waheed, N. K., and Duker, J. S. (2015c). A review of optical coherence tomography angiography (OCTA). *Int J Retina Vitr.* 1:5. doi: 10.1186/s40942-015-0005-8

Di Ieva, A., Esteban, F. J., Grizzi, F., Klonowski, W., and Martin-Landrove, M. (2015). Fractals in the neurosciences, part II: clinical applications and future perspectives. *Neuroscientist* 21, 30–43. doi: 10.1177/1073858413513928

Di, G., Weihong, Y., Xiao, Z., Zhikun, Y., Xuan, Z., Yi, Q., et al. (2016). A morphological study of the foveal avascular zone in patients with diabetes mellitus using optical coherence tomography angiography. *Graefes Arch. Clin. Exp. Ophthalmol.* 254, 873–879. doi: 10.1007/s00417-015-3143-7

Diabetes Fact Sheet (2017). *World Health Organization*. Available online at: http://www.who.int/mediacentre/factsheets/fs312/en/

Elman, M. J., Aiello, L. P., Beck, R. W., Bressler, N. M., Bressler, S. B., Edwards, A. R., et al. (2010). Randomized trial evaluating ranibizumab plus prompt or deferred laser or triamcinolone plus prompt laser for diabetic macular edema. *Ophthalmology* 117, 1064–1077. doi: 10.1016/j.ophtha.2010.02.031

Falconer, K. (1989). *Fractal Geometry: Mathematical Foundation and Applications*. New York, NY: John Wiley and Sons.

Family, F., Masters, B. R., and Platt, D. E. (1989). Fractal pattern formation in human retinal vessels. *Physica D* 38, 98–103. doi: 10.1016/0167-2789(89)90178-4

Fernández, E., and Jelinek, H. F. (2001). Use of fractal theory in neuroscience: methods, advantages, and potential problems. *Methods* 24, 309–321. doi: 10.1006/meth.2001.1201

Fractals and medicine. (1991). Fractals and medicine. *Lancet*. 338, 1425–1426. doi: 10.1016/0140-6736(91)92726-I

Freiberg, F. J., Pfau, M., Wons, J., Wirth, M. A., Becker, M. D., and Michels, S. (2015). Optical coherence tomography angiography of the foveal avascular zone in diabetic retinopathy. *Graefes Arch. Clin. Exp. Ophthalmol.* 254, 1051–1058. doi: 10.1007/s00417-015-3148-2

Gorczynska, I., Migacz, J. V., Zawadzki, R. J., Capps, A. G., and Werner, J. S. (2016). Comparison of amplitude-decorrelation, speckle-variance and phase-variance OCT angiography methods for imaging the human retina and choroid. *Biomed. Opt. Express* 7, 911–942. doi: 10.1364/BOE.7.000911

Grauslund, J., Green, A., Kawasaki, R., Hodgson, L., Sjølie, A. K., and Wong, T. Y. (2010). Retinal vascular fractals and microvascular and macrovascular complications in type 1 diabetes. *Ophthalmol* 117, 1400–1405. doi: 10.1016/j.ophtha.2009.10.047

Grinvald, A., Bonhoeffer, T., Vanzetta, I., Pollack, A., Aloni, E., Ofri, R., et al. (2004). High-resolution functional optical imaging: from the neocortex to the eye. *Opthalmol. Clin. North Am.* 17, 53–67. doi: 10.1016/j.ohc.2003.12.003

Group ETDRSR (1981). Diabetic retinopathy study. report number 6. design, methods, and baseline results. report number 7. a modification of the airlie house classification of diabetic retinopathy. *Invest. Ophthalmol. Vis. Sci.* 21, 1–226.

Grunwald, J. E., Brucker, A. J., Grunwald, S. E., and Riva, C. E. (1993). Retinal hemodynamics in proliferative diabetic retinopathy. a laser Doppler velocimetry study. *Invest. Ophthalmol. Vis. Sci.* 34, 66–71.

Grunwald, J. E., DuPont, J., and Riva, C. E. (1996). Retinal haemodynamics in patients with early diabetes mellitus. *Br. J. Ophthalmol.* 80, 327–331. doi: 10.1136/bjo.80.4.327

Huang, F., Dashtbozorg, B., Zhang, J., Bekkers, E., Abbasi-Sureshjani, S., Berendenschot, T. T., et al. (2016). Reliability of using retinal vascular fractal dimension as a biomarker in the diabetic retinopathy detection. *J. Ophthalmol.* 2016:6259047. doi: 10.1155/2016/6259047

Hwang, T. S., Gao, S. S., Liu, L., Lauer, A. K., Bailey, S. T., Flaxel, C. J., et al. (2016). Automated quantification of capillary nonperfusion using optical coherence tomography angiography in diabetic retinopathy. *JAMA Ophthalmol.* 134, 367–373. doi: 10.1001/jamaophthalmol.2015.5658

Hwang, T. S., Jia, Y., Gao, S. S., Bailey, S. T., Lauer, A. K., Flaxel, C. J., et al. (2015). Optical coherence tomography angiography features of diabetic retinopathy. *Retina* 35, 2371–2376. doi: 10.1097/IAE.0000000000000716

Ip, M. S., Domalpally, A., Hopkins, J. J., Wong, P., and Ehrlich, J. (2012). Long-term effects of ranibizumad on diabetic retinopathy severity and progression. *Arch. Ophthalmol.* 130, 1145–1152. doi: 10.1001/archophthalmol.2012.1043

Ip, M. S., Domalpally, A., Sun, J. K., and Ehrlich, J. S. (2015). Long-term effects of therapy with ranibizumab on diabetic retinopathy severity and baseline risk factors for worsening retinopathy. *Ophthalmol* 122, 367–374. doi: 10.1016/j.ophtha.2014.08.048

Ishibazawa, A., Nagaoka, T., Takahashi, A., Omae, T., Tani, T., Sogawa, K., et al. (2015). Optical coherence tomography angiography in diabetic retinopathy: a prospective pilot study. *Am. J. Ophthalmol.* 160, 35–44. doi: 10.1016/j.ajo.2015.04.021

Izhaky, D., Nelson, D. A., Burgansky-Eliash, Z., and Grinvald, A. (2009). Functional imaging using the retinal function imager: direct imaging of blood velocity, achieving fluorescein angiography-like images without any contrast agent, qualitative oximetry, and functional metabolic signs. *Jpn. J. Ophthalmol.* 53, 345–351. doi: 10.1007/s10384-009-0689-0

Katz, B. M., and McSweeney, M. (1980). A multivariate kruskal-wallis test with post hoc procedures. *Multivariate Behav. Res.* 15, 281–297. doi: 10.1207/s15327906mbr1503_4

Kaur, C., Foulds, W. S., and Ling, E. A. (2008). Blood-retinal barrier in hypoxic ischaemic conditions: Basic concepts, clinical features and management. *Prog. Retin. Eye Res.* 27, 622–647. doi: 10.1016/j.preteyeres.2008.09.003

Kohner, E. M. (1975). Dynamic changes in the microcirculation of diabetes as related to diabetic microangiopathy. *Acta Med. Scand. Suppl.* 578, 41–47.

Kohner, E. M., Patel, V., and Rassam, S. M. (1995). Role of blood flow and impaired autoregulation in the pathogenesis of diabetic retinopathy. *Diabetes* 44, 603–607. doi: 10.2337/diab.44.6.603

Korobelnik, J. F., Do, D. V., Schmidt-Erfurth, U., Boyer, D. S., Holz, F. G., Heier, J. S., et al. (2014). Intravitreal aflibercept for diabetic macular edema. *Ophthalmol* 121, 2247–2254. doi: 10.1016/j.ophtha.2014.05.006

Krawitz, B. D., Mo, S., Geyman, L. S., Agemy, S. A., Scripsema, N. K., Garcia, P. M., et al. (2017). Acircularity index and axis ratio of the foveal avascular zone in diabetic eyes and healthy controls measured by optical coherence tomography angiography. *Vision Res.* 139, 177–186. doi: 10.1016/j.visres.2016.09.019

Kur, J., Newman, E. A., and Chan-Ling, T. (2012). Cellular and physiological mechanisms underlying blood flow regulation in the retina and choroid in health and disease. *Prog. Retin. Eye Res.* 31, 377–406. doi: 10.1016/j.preteyeres.2012.04.004

Lee, V. S., Kingsley, R. M., Lee, E. T., Lu, M., Russell, D., Asal, N., et al. (1993). The diagnosis of diabetic retinopathy. ophthalmoscopy versus fundus photography. *Ophthalmol* 100, 1504–1512. doi: 10.1016/S0161-6420(93)31449-1

Lim, S. W., Cheung, N., Wang, J. J., Donaghue, K. C., Liew, G., Amirul Islam, D. M., et al. (2009). Retinal vascular fractal dimension and risk of early diabetic retinopathy: a prospective study of children and adolescents with type 1 diabetes. *Diabetes Care* 32, 2081–2083. doi: 10.2337/dc09-0719

Macgillivray, T. J., Patton, N., Doubal, F. N., Graham, C., and Wardlaw, J. M. (2007). Fractal analysis of the retinal vascular network in fundus images. *Conf. Proc. IEEE Eng. Med. Biol. Soc.* 1, 6455–6458. doi: 10.1109/IEMBS.2007.4353837

Mainster, M. A. (1990). The fractal properties of retinal vessels: embryological and clinical implications. *Eye* 4, 235–241. doi: 10.1038/eye.1990.33

Mammo, Z., Balaratnasingam, C., Yu, P., Xu, J., Heisler, M., Mackenzie, P., et al. (2015). Quantitative noninvasive angiography of the fovea centralis using speckle variance optical coherence tomography. *Invest. Ophthalmol. Vis. Sci.* 56, 5074–5086. doi: 10.1167/iovs.15-16773

Mandelbrot, B. B. (1982). *The Fractal Geometry of Nature*. New York, NY: W.H. Freeman.

Mastropasqua, R., Di Antonio, L., Di Staso, S., Agnifili, L., Di Gregorio, A., Ciancaglini, M., et al. (2015). Optical coherence tomography angiography in retinal vascular diseases and choroidal neovascularization. *J. Ophthalmol.* 2015:343515. doi: 10.1155/2015/343515

Matsunaga, D., Yi, J., Puliafito, C. A., and Kashani, A. H. (2014). OCT angiography in healthy human subjects. *Ophthalmic Surg. Lasers Imaging Retina* 45, 510–515. doi: 10.3928/23258160-20141118-04

McMillan, D. E. (1989). The blood viscosity problem in diabetes. *Proc. Am. Diabetes Assoc.* 7, 66–71.

Milošević N. T. (2015). "Fractal analysis of two dimensional images: parameters of the space-filling and shape," in *Proceedings of 20th International Conference on Control Systems and Computer Science* Vol. 2 (Bucharest), 539–544.

Milošević N. T. (2016). "The morphology of the brain neurons: box-counting method in quantitative analysis of 2D image," in The Fractal Geometry of the Brain, ed Di A. Ieva (New York, NY: Springer), 109–126.

Nelson, D. A., Krupsky, S., Pollack, A., Aloni, E., Belkin, M., Vanzetta, I., et al. (2005). Special report: noninvasive multi-parametric functional optical imaging of the eye. *Ophthalmic Surg. Lasers Imaging* 36, 57–66.

Nikolay, S. (2016). *Active Contours Implementation and Test Platform GUI. Mathworks File Exchange*. Available online at: https://www.mathworks.com/matlabcentral/fileexchange/30284-active-contours-implementation---test-platform-gui?

Pemp, B., and Schmetterer, L. (2008). Ocular blood flow in diabetes and age-related macular degeneration. *Can. J. Ophthalmol.* 43, 295–301. doi: 10.3129/i08-049

Pournaras, C. J., Rungger-Brändle, E., Riva, C. E., Hardarson, S. H., and Stefansson, E. (2008). Regulation of retinal blood flow in health and disease. *Prog. Retin. Eye Res.* 27, 284–330. doi: 10.1016/j.preteyeres.2008.02.002

Rajkovic, N., Krstonošic, B., and Milošević N. T. (2017). Box-counting method of 2D neuronal image: method modification and quantitiative analysis demonstrated on images from the monkey and human brain. *Comput. Math. Methods Med.* 2017:8967902. doi: 10.1155/2017/8967902

Sakata, K., Funatsu, H., Harino, S., Noma, H., and Hori, S. (2006). Relationship between macular microcirculation and progression of diabetic macular edema. *Ophthalmol* 113, 1385–1391. doi: 10.1016/j.ophtha.2006.04.023

Samara, W. A., Shahlaee, A., Adam, M. K., Khan, M. A., Chiang, A., Maguire, J. I., et al. (2016). Quantification of diabetic macular ischemia using optical coherence tomography angiography and its relationship with visual acuity. *Ophthalmology* 124, 235–244. doi: 10.1016/j.ophtha.2016.10.008

Schmetterer, L., and Wolzt, M. (1999). Ocular blood flow and associated functional deviations in diabetic retinopathy. *Diabetologia* 42, 387–405. doi: 10.1007/s001250051171

Schneider, C. A., Rasband, W. S., and Eliceiri, K. W. (2012). NIH to ImageJ: 25 years of image analysis. *Nat. Methods* 9, 671–675. doi: 10.1038/nmeth.2089

Schram, M. T., Chaturverdi, N., Schalwijk, C. G., Fuller, J. H., and Stehouwer, C. D. (2005). Markers of inflammation are cross-sectionally associated with microvaacular complications and cardiovascular disease in type 1 diabetes – the EURODIAB prospective complications study. *Diabetologia* 48, 370–378. doi: 10.1007/s00125-004-1628-8

Sim, D. A., Keane, P. A., Fung, S., Karampelas, M., Sadda, S. R., Fruttiger, M., et al. (2014). Quantitative analysis of diabetic macular ischemia using optical coherence tomography. *Invest. Ophthalmol. Vis. Sci.* 55, 417–423. doi: 10.1167/iovs.13-12677

Sinclair, S. H., Grunwald, J. E., Riva, C. E., Braunstein, S. N., Nichols, C. W., and Schwarz, S. S. (1982). Retinal vascular autoregulation in diabetes mellitus. *Ophthalmology* 89, 748–750. doi: 10.1016/S0161-6420(82)34720-X

Smith, T. G. Jr., Lange, G. D., and Marks, W. B. (1996). Fractal methods and results in cellular morphology – dimensions, lacunarity, and multifractals. *J. Neurosci. Methods* 69, 123–136. doi: 10.1016/S0165-0270(96)00080-5

Somfai, G. M., Gerding, H., and DeBuc, D. C. (2018). The use of optical coherence tomography for detection of early diabetic retinopathy. *Klin Monatsbl Augenheilkd* 234, 1–8. doi: 10.1055/s-0044-101827

Spaide, R. F., Fujimoto, J. G., and Waheed, N. K. (2015). Image artifacts in optical coherence tomography angiography. *Retina* 35, 2163–2180. doi: 10.1097/IAE.0000000000000765

Stitt, A. W., Curtis, T. M., Chen, M., Medina, R. J., McKay, G. J., Jenkins, A., et al. (2016). The progress in understanding and treatment of diabetic retinopathy. *Prog. Retin Eye Res.* 51, 156–186. doi: 10.1016/j.preteyeres.2015.08.001

Stosić, T., and Stosić, B. D. (2006). Multifractal analysis of human retinal vessels. *IEEE Trans. Med. Imaging* 25, 1101–1107. doi: 10.1109/TMI.2006.879316

Takase, N., Nozaki, M., Kato, A., Ozeki, H., Yoshida, M., and Ogura, Y. (2015). Enlargement of foveal avascular zone in diabetic eyes evaluated by en face optical coherence tomography angiography. *Retina* 35, 2377–2383. doi: 10.1097/IAE.0000000000000849

Tan, C. S., Lim, L. W., Chow, V. S., Chay, I. W., Tan, S., and Cheong, K. X. (2016). Optical coherence tomography angiography evaluation of the parafoveal vasculature and its relationship with ocular factors. *Invest. Ophthalmol. Vis. Sci.* 57, 224–234. doi: 10.1167/iovs.15-18869

Tian, J., Somfai, G. M., Campagnoli, T. R., Smiddy, W. E., and DeBuc, D. C. (2016). Interactive retinal blood flow analysis of the macular region. *Microvasc. Res.* 104, 1–10. doi: 10.1016/j.mvr.2015.11.003

Varma, R., Bressler, N. M., Doan, Q. V., Gleeson, M., Danese, M., Bower, J. K., et al. (2014). Prevalence of and risk factors for diabetic macular edema in the United States. *JAMA Ophthalmol.* 132, 1334–1340. doi: 10.1001/jamaophthalmol.2014.2854

Wiley, H. E., Thompson, D. J., Bailey, C., Chew, E. Y., Cukras, C. A., Jaffe, G. J., et al. (2016). A crossover design for comparative efficacy: a 36-week randomized trial of bevacizumab and ranibizumab for diabetic macular edema. *Ophthalmology* 123, 841–849. doi: 10.1016/j.ophtha.2015.11.021

Yannuzzi, L. A., Rohrer, K. T., Tindel, L. J., Sobel, R. S., Costanza, M. A., Shields, W., et al. (1986). Fluorescein angiography complication survey. *Ophthalmology* 93, 611–617. doi: 10.1016/S0161-6420(86)33697-2

Yau, J. W., Kawasaki, R., Islam, F. M., Shaw, J., Zimmet, P., Wang, J. J., et al. (2010). Retinal fractal dimension is increased in persons with diabetes but not impaired glucose metabolism: the Australian Diabetes, Obesity and Lifestyle (AusDiab) study. *Diabetologia* 53, 2042–2045. doi: 10.1007/s00125-010-1811-z

Yau, J. W., Rogers, S. L., Kawasaki, R., Lamoureux, E. L., Kowalski, J. W., Bek, T., et al. (2012). Global prevalence and major risk factors of diabetic retinopathy. *Diabetes Care* 35, 556–564. doi: 10.2337/dc11-1909

Conflict of Interest Statement: The authors declare that the research was conducted in the absence of any commercial or financial relationships that could be construed as a potential conflict of interest.

Copyright © 2018 Kostic, Bates, Milosevic, Tian, Smiddy, Lee, Somfai, Feuer, Shiffman, Kuriyan, Gregori, Pineda and Cabrera DeBuc. This is an open-access article distributed under the terms of the Creative Commons Attribution License (CC BY). The use, distribution or reproduction in other forums is permitted, provided the original author(s) and the copyright owner(s) are credited and that the original publication in this journal is cited, in accordance with accepted academic practice. No use, distribution or reproduction is permitted which does not comply with these terms.

frontiers in Physiology

ORIGINAL RESEARCH
published: 18 June 2018
doi: 10.3389/fphys.2018.00711

Quantitative Analysis of the Antiepileptogenic Effects of Low Frequency Stimulation Applied Prior or After Kindling Stimulation in Rats

Mostafa Jalilifar[1], *Ali Yadollahpour*[1]*, *Ahmad Ali Moazedi*[2] *and Zohreh Ghotbeddin*[3]

[1] Department of Medical Physics, Faculty of Medicine, Ahvaz Jundishapur University of Medical Sciences, Ahvaz, Iran, [2] Department of Biology, Faculty of Science, Shahid Chamran University of Ahvaz, Ahvaz, Iran, [3] Department of Physiology, Faculty of Veterinary Medicine, Shahid Chamran University of Ahvaz, Ahvaz, Iran

Background and Objective: Developing quantitative measures based on spectral analysis of electroencephalograph (EEG) recordings of neural activities plays an important role in developing efficient treatments for epilepsy. Such biomarkers can be used for developing open or closed loop approaches for seizure prediction or prevention. This study aims to quantitatively evaluate antiepileptogenic effects of low frequency stimulation (LFS) applied immediately before or after kindling stimulations using spectral power analysis of extracellular EEG in rat.

Methods: Nineteen adult rats were used: seven for kindle, six for LFS+Kindle (LFSK) and six for Kindle+LFS (KLFS). Four packages of LFS (1Hz) were applied immediately before or after rapid kindling stimulations. The power spectral densities of afterdischarge (AD) sections of EEG corresponding to different stages of kindling for delta (0–4 Hz), theta (4–8 Hz), alpha (8–12 Hz), beta (12–28 Hz), gamma (28–40 Hz) sub-bands, and theta/alpha ratio were comparatively investigated. Moreover, correlation between AD duration (ADD) and its different frequency components was calculated.

Results: Both LFSK and KLFS significantly increased delta and reduced beta and gamma oscillations, compared with kindle group. However, just the reduction in LFSK group was significant. Both protocols increased theta/alpha ratio, but just LFSK showed significant increase ($p < 0.05$). Although LFSK enhanced theta/alpha ratio more than KLFS, the difference was not statistically significant. Furthermore, strong correlation between each frequency sub band and ADD was not observed in kindle and LFS treated groups (both LFSK and KLFS).

Conclusion: Although behavioral assessments showed relatively the same level of antiepileptogenic effects for KLFS and LFSK, quantitative assessments showed more significant differences in the quantitative measures between the two protocols. Developing more quantitative EEG based measures correlated with LFS-induced effects can facilitate developing open or closed loop seizure prevention modalities.

Keywords: kindling, low frequency stimulation, spectral power, extracellular EEG, quantitative assessment

OPEN ACCESS

Edited by:
Sladjana Z. Spasić,
University of Belgrade, Serbia

Reviewed by:
Ali Jahanshahi,
Maastricht University Medical Centre, Netherlands
Tifei Yuan,
Shanghai Mental Health Center, China

****Correspondence:***
Ali Yadollahpour
yadollahpour.a@gmail.com

Specialty section:
This article was submitted to Fractal Physiology, a section of the journal Frontiers in Physiology

Received: *03 March 2018*
Accepted: *23 May 2018*
Published: *18 June 2018*

Citation:
Jalilifar M, Yadollahpour A, Moazedi AA and Ghotbeddin Z (2018) Quantitative Analysis of the Antiepileptogenic Effects of Low Frequency Stimulation Applied Prior or After Kindling Stimulation in Rats. Front. Physiol. 9:711. doi: 10.3389/fphys.2018.00711

INTRODUCTION

Epilepsy is a chronic neurological disorder with 1.5% world population prevalence (Demos, 2005). It is characterized by recurrent seizures which disruptively propagate from the seizure origin to other regions of the brain. Cortical excitability of different areas of the brain is increased in epileptic patients (Lerchl et al., 1990; de Boer et al., 2008). Temporal lobe epilepsy (TLE) is the most common type of epilepsy in adults that originates in medial or lateral temporal lobe and spreads rapidly to other regions (Pritchard, 1986; Devinsky, 1991). Electrical kindling is a reliable experimental model to study TLE where repetitive electrical stimulations with a threshold intensity at particular sites of the brain induce progressive, generalized seizures through long term potentiation (LTP) mechanism (Goddard et al., 1969; Lothman et al., 1985). During the kindling process, afterdischarge (AD) waves appear in the electroencephalogram (EEG) baseline. ADs are electroencephalographic responses to seizures and they stem from the collective activity of neurons and produce consecutive large spikes in the baseline of EEG signals (Peterson and Albertson, 1982).

Animal studies have demonstrated that electrical stimulation of the epileptic focus, particularly in low frequency stimulation (LFS) may be an appropriate alternative treatment for intractable epilepsy (Velišek, Velišková and Stanton, 2002; Ozen et al., 2008; Jalilifar et al., 2017a). LFS can inhibit epileptic seizures through increasing the threshold for evoking neuronal action potentials (Albensi et al., 2004; Schrader et al., 2006). Moreover, administration of LFS especially in hippocampus and amygdala induces long term depression (LTD) as well as prevents kindling-induced LTP (Fujii et al., 1999; Albensi et al., 2004). Studies are ongoing to determine effective protocols of LFS for seizure inhibition (Shahpari et al., 2012). Time of LFS administrations is one of the main factors influencing the amount of antiepileptic effects of LSF. The behavioral data of our previous study showed that LFS application either before or after termination of kindling stimulation significantly increased AD threshold, inhibited kindling acquisition, and also increased the number of stimulations required to achieve kindling stages, compared with the control animals that received only kindling stimulation. Although administration of LFS prior to kindling stimulation produced a more inhibitory effect than the post kindling protocol, the difference was not statistically significant. To determine effective LFS parameters, efficient biomarkers should be developed for quantitative assessments of epileptogenesis process as well as the LFS induced effects. Most of the studies on kindling have used the behavioral assessments based on kindling stages and duration of AD to evaluate the LFS efficacy. However, behavioral assessments suffer subjective and objective errors since the identification of start and end of each stage, its duration, as well as duration of AD are determined manually. EEG signals have a high temporal and good spatial resolution making them appropriate measures to identify efficient LFS parameters as well as to determine the antiepileptic mechanisms of LFS (Yadollahpour and Jalilifar, 2014). However, visual assessments of EEG signals to identify and quantify the oscillatory activities and their behavioral correlates yield no valuable information. Using different spectral analysis methods of EEG enable researchers to identify, quantify, and characterize the oscillatory components in the EEG signals as well as to develop quantitative measures which are correlates of different behavioral features (Kleinfeld, 2008). The two main advantages of using spectral analysis in electrophysiological studies are determination of the number of degree of freedom for calculation of confidence of interval is more convenient in frequency domain than the time domain and two the most of biological phenomena have simpler representation in the frequency domain (Kleinfeld, 2008). In this regard, the goal of quantitative EEG is to identify different measures in frequency domain and consequently investigate the brain functions. Fourier analysis is a main group of spectral analyses where time series signals, namely EEG, are decomposed into sinusoidal functions.

This study focuses on the frequency domain features of the epileptic activities from the AD of the EEG signals that could provide more clear understanding of the intrinsic neural network involved in kindling process. Developing quantitative and objective assessments of LFS effects on epileptogenesis using EEG signals can reduce the objective and subjective errors present in the behavioral assessments. In our previous studies we determined the main spectral features of EEG signals in different stages of kindling and also assessed the variations of different EEG based measures during progression of kindling (Jalilifar et al., 2016, 2017b). Our findings along with the findings of previous studies showed significant correlations between variations of specific sub-bands of EEG with different phases of epileptogenesis: We classified EEG signal into different sub-bands whose powers are considered as a synchronization of neural discharge index. These sub-bands include delta (1–4 Hz), theta (4–8 Hz), alpha (8–12), beta (12–28 Hz) and gamma (28–40 Hz). Delta frequencies are synchronized in deep sleep state, associated with seizure-like activities in the brain (Walter, 1936). Theta waves are usually recorded from Medial Septum area of hippocampus and they are related with voluntary movements of rats. Alpha oscillations originate from occipital and other sensory areas. Several studies have demonstrated that alpha waves are affected by thalamus and sensorimotor cortex in rats (Hughes and Crunelli, 2005; Shaker, 2006). Beta and gamma rhythms are predominant in the neocortex and hippocampus of consciousness humans and animals (Haenschel et al., 2000). Theses waves are also augmented in generalization of epileptic seizures. Moreover, suppression of beta and gamma frequencies can inhibit the progression of epileptogenesis process (Tsuchiya and Kogure, 2011). In addition to the above sub-bands, alterations of theta/alpha ratio have shown a significant correlation with the level of alertness in cognitive studies (Sadighi Alvandi et al., 2015) because theta sub-bands are usually correlated with learning and alertness disorders, and they are often emerged with high amplitude in the epileptic patients while alpha frequencies are generally the most stable brain waves. In line with our previous studies, this study aims to quantitatively investigate the antiepileptogenic effects of LFS applied either immediately prior or after daily kindling stimulation in amygdale rapid kindling model in rats.

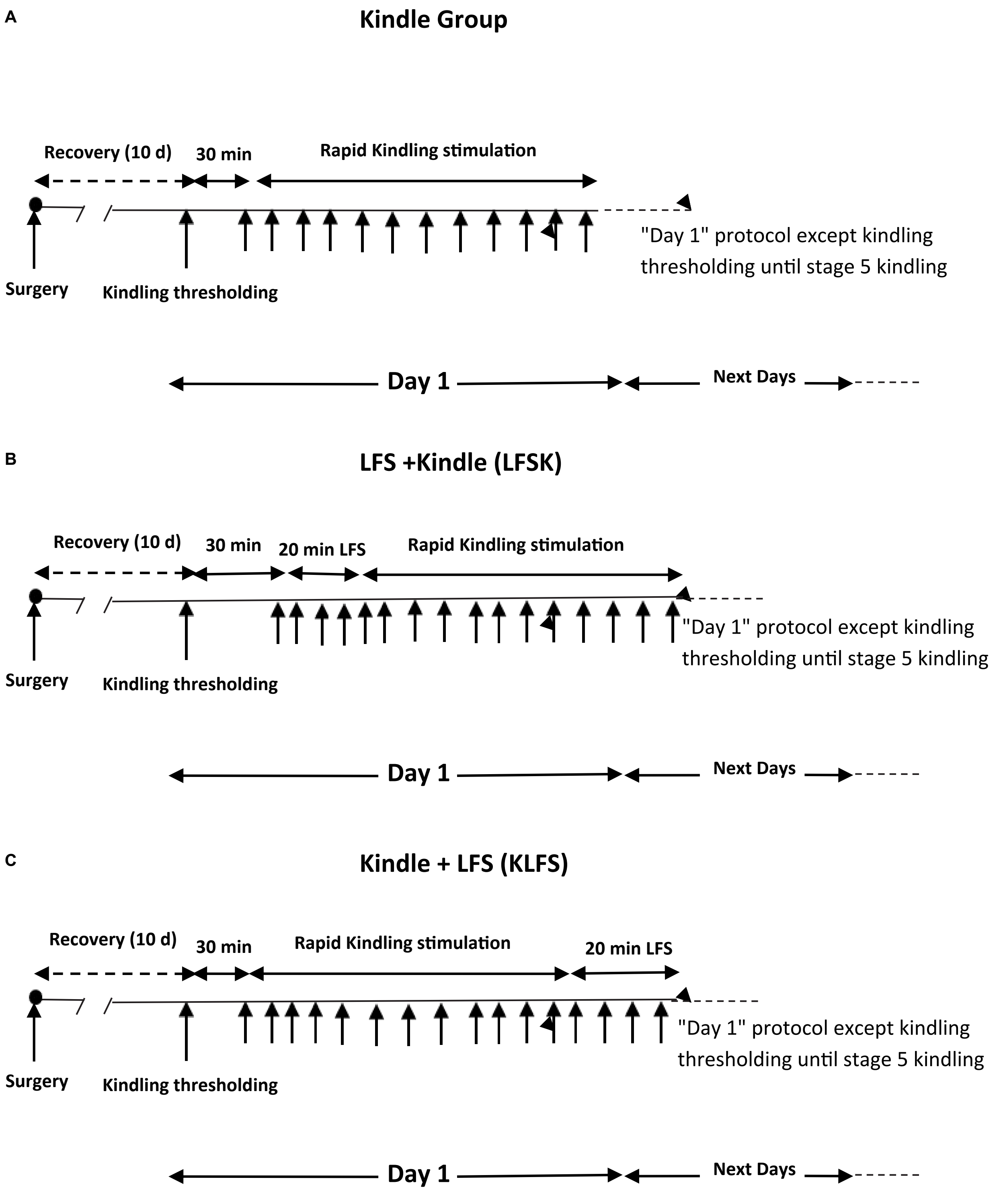

FIGURE 1 | Schematic diagram of experimental groups. **(A)** Kindle group. **(B)** LFS + kindle (LFSK) group, **(C)** kindle + LFS (KLFS) group.

In addition, the time dependent effects of LFS on kindling induced epileptogenesis are investigated using EEG spectral power analyses. To do so, the effects of LFS in the two protocols on the spectral powers of delta (1–4 Hz), theta (4–8 Hz), alpha (8–12 Hz), beta (12–28 Hz), gamma (28–40 Hz), and theta/alpha ratio are comparatively assessed.

MATERIALS AND METHODS

Animals and Surgery

All of the experimental procedures of this study were approved by local ethics committee of AJUMS which were in complete accordance with the guide for the care and use of laboratory animals set by the National Academy of Sciences (National Institutes of Health Publication No. 86-23). Adult male Wistar rats (weighing 190–210 g at the time of surgery) were obtained from the animal house of Ahvaz Jundishapur University of Medical Sciences (AJUMS) (Ahvaz, Iran). They were accommodated individually in a colony room with an ambient temperature (25 ± 2°C) and artificial 12:12-h light-dark cycle (light on at 6.30–18.30).

The rats were anesthetized with intraperitoneal injection of the mixture of Ketamine (100 mg/kg) and Xylazine (10 mg/kg) (Esmaeilpour et al., 2013). and underwent surgery process: four holes were drilled stereotaxically on the skull two holes for anchor screws, one for implantation of a monopolar stainless steel electrode used as ground and another for placement of a tripolar stainless steel electrode (two poles for stimulation and one for recording) in the right amygdala according to the Paxinos and Watson atlas coordinates: anteroposterior: −2.5 mm; lateral: 4.8 mm; vertical: 7.2 and 0.2 mm below the skull (Paxinos et al., 2009). After the placement in the coordinates, the electrodes were attached into a socket and maintained with dental acrylic cement.

Kindling and LFS

Nineteen rats were randomly divided into 3 groups including one kindle ($n = 7$) as control group and two treatment groups of LFS + kindle (LFSK) ($n = 6$) and kindle + LFS (KLFS) ($n = 6$). Following a 10-day recovery period after surgery, the threshold intensity for kindling stimulation was determined as the minimum intensity required to evoke at least 6 s ADs with the amplitude of at least 2.5 times higher than the baseline EEG (Yadollahpour et al., 2014). It was determined by a 3 s of monophasic square wave of 50 Hz applied initially at 30 μA and increased in increment of 15 μA at minimum of 30 min intervals. The rats that represented no AD with maximum 350 μA current intensity were excluded from the experiment. Moreover, the animals that entered in deep inhibitory state and those animals showed unusual response including severe reactions at the kindling threshold intensity were excluded from the study. All rats were subjected to kindling stimulation consisting of a 3 s of monophasic square wave (1 ms duration) of 50 Hz with the threshold intensity applied 12 times per day at 5 min intervals (Shahpari et al., 2012). The kindling stages for the further assessments were recorded by the researchers based on the following behavioral characteristics: stage 1 characterized by mouth and facial movements, stage 2 by head nodding, stage 3 by Forelimb clonus, stage 4 by rearing, and stage 5 characterized by falling and loss of balance (Racine, 1972). Kindling stimulations in the kindle group were continued until the observation of the stage 5 of kindling. The average days in the control group to reach the stage 5 was 4.42 ± 0.53 days. Therefore, to compare the behavioral data between the control and LFSK and KLFS groups on a standard basis, the animals of these groups were stimulated for 5 days. In the LFSK group, four packages of LFS with 5 min interval were applied immediately before the start of 12 daily kindling stimulations, while in the KLFS group these packages were applied immediately after termination of 12 daily kindling stimulations (**Figure 1**). Each LFS package consisted of 200 monophasic square pulses, 0.1 ms pulse duration at 1 Hz with the threshold intensity (Yadollahpour et al., 2014). After the completion of the experiments the animals were sacrificed using Co2 in a euthanizing chamber. All efforts were made to minimize animal suffering and reduce the number of animals used in this study.

Spectral Analysis of afterdischarge

Electroencephalograph signals were recorded through the electrode implanted in the amygdale and monitored with the Electromodule system (ScienceBeam Co, Iran). Data were digitized at a sampling rate of 10 KHz. During the kindling acquisition, the time and duration of each kindling stage were saved as an event file which should be considered in extracting each stage. It should be noted that only the AD parts of EEG were selected and treated with Hann window function with an overlap of 50% and then were transferred into the frequency function by Fast Fourier Transform (FFT) and their power spectrum and the power of each sub band including delta (1–4 Hz), theta (4–8 Hz), alpha (8–12 Hz), beta (12–28 Hz), gamma (28–40 Hz), and theta/alpha ratio were determined using MATLAB version 2013b for Windows.

Statistical Analysis

Data were represented as the mean ± standard error of mean (SEM). The normality of the data was evaluated using Kolmogorov–Smirnov test. A one-way analysis of variance (ANOVA) following Bonferroni's *post hoc* was used to compare different sub bands power of baseline periods between the experimental groups. A two-way ANOVA following a *post hoc* Bonferroni's test was performed to compare different sub bands power of AD related to Racine stages and also theta/alpha ratio of EEG between kindle ($n = 7$), LFSK ($n = 6$), and KLFS ($n = 6$) groups. The correlation between AD duration (ADD) and the spectral powers of different EEG sub bands were assessed using Pearson's correlation coefficient. All Statistical analyses were performed with IBM SPSS 21 for windows. For all analyses, the tests were carried out two-sided and significance was set at $p < 0.05$.

RESULTS

Kindling Induced EEG Features

In the recently published papers, we identified the main quantitative features of different kindling stages during epileptogenesis (Jalilifar et al., 2016) and then for the main phases of seizure acquisition initial, localized and generalized seizure stages in the amygdale rapid kindling model (Jalilifar et al., 2017b) (detailed data not provided here). The main features of kindling were as follows: The kindling acquisition process was accompanied by increase in delta (1–4 Hz) and theta (4–8 Hz) waves in the stages of 3, 4, and 5, compared with the control group. Moreover, with the progression of the kindling process, high beta (20–28 Hz) and gamma (28–40 Hz) oscillations were reduced. Delta sub-band power significantly increased during generalized seizure stages (GSSs) (stages 4 and 5). Furthermore, the theta/alpha ratio in the localized seizure stage (stage 3) (LSS) was higher than GSSs and the sham group.

General EEG Features of the Experimental Groups

Afterdischarge duration was significantly decreased following application of LFS either before or after the kindling stimulation as compared with the kindle group ($F[2,78] = 19.682$, $p < 0.05$) (Jalilifar et al., 2017b). LFS could also significantly prevent the generalization of behavioral stages during the kindling procedure in a way that all animals in the kindle group represented GSSs of the kindling process within 5 stimulation days while only one animal in the LFSK group (16%) and two animals (32%) in the KLFS showed GSSs at the end of the experiment. The animals in both LFSK and KLFS groups received higher numbers of numbers to exhibit LSS and GSSs of the kindling in comparison with the kindle group (for stage 2: $H[2] = 6.725$, $p > 0.05$, stage 3: $H[2] = 8.498$, $p < 0.05$, stage 4–5: $H[2] = 13.658$, $p < 0.05$). Animals in the LFSK group showed LSS and GSSs of the kindling process with higher numbers of stimulation than the KLFS; however, the difference was not significant ($p > 0.05$) (Jalilifar et al., 2017a). Moreover, the daily stages represented in the LFSK and KLFS groups were significantly decreased compared with the kindle group (for day 2: $H[2] = 10.191$, $p < 0.05$, day 3: $H[2] = 13.696$, $p < 0.05$, day 4: $H[2] = 12.003$, $p < 0.05$, day 5: $H[2] = 10.667$, $p < 0.05$) (Jalilifar et al., 2017a).

Animals in the experimental groups showed different number of main phases of seizures. However, in the kindle group all animals achieved 61 times initial seizure stages (stages 1 and 2) (ISSs), 42 LSS, and 35 times GSSs, whereas the LFSK animals showed 38 times ISSs, 13 LSS, and 4 times GSSs. Besides, the KLFS rats showed 39, 14, and 6 times ISSs, LSS, and GSSs, respectively which were registered for further analyses (Jalilifar et al., 2017a).

Figures 2A,B respectively show the baseline and the epileptic (AD section) EEG records in the kindle group. **Figures 3A,B** respectively show examples of baseline and AD section EEGs in the LFS treated group. We recorded a 7 s length EEG of baseline neural activities prior to kindling stimulation and performed the FFT analyses on the 7 s length EEGs of baseline and epileptic activities in different groups. **Figure 3** represents a baseline EEG and epileptic EEG in the LFSK group (**Figure 3**). The FFT analyses for the baseline and epileptic activities of the LFSK and KLFS did not significantly differ; therefore, we presented one example from the LFSK. In the all experimental groups, delta and theta components [Low Frequency Band (LFB) (0–8 Hz)] were dominant bands during baseline activity, while Mid Frequency Band (8–12 Hz) (MFB) and High Frequency Band (12–40)

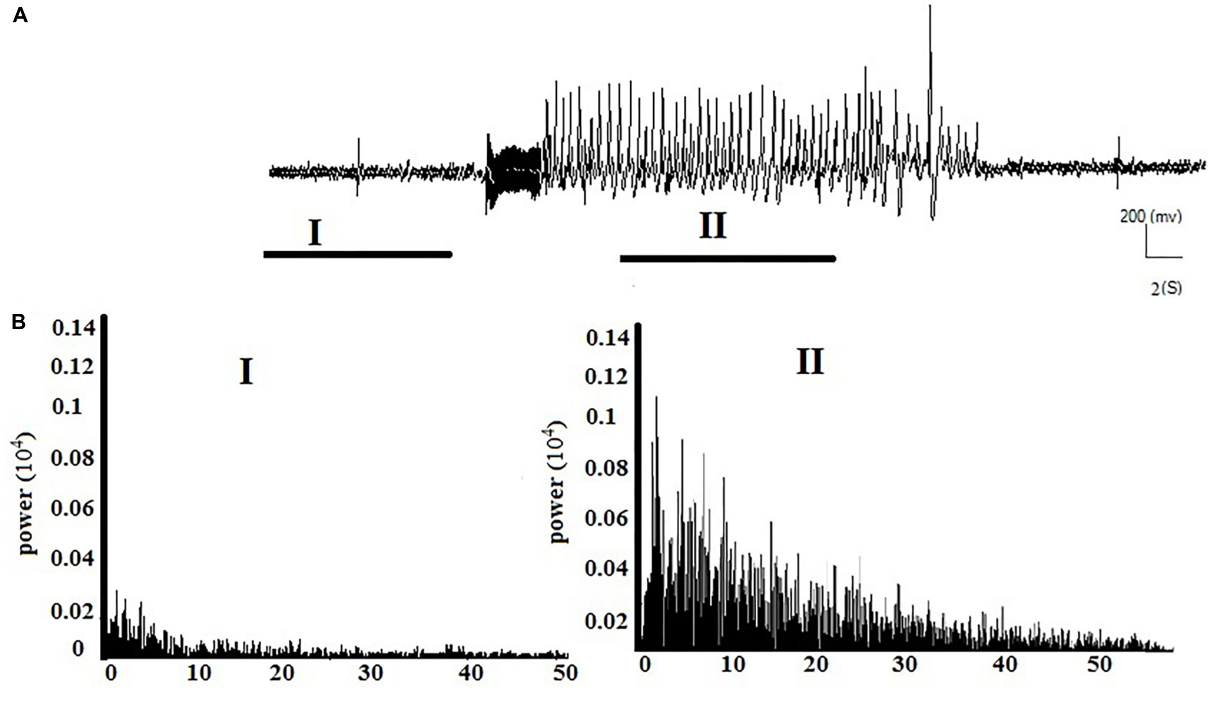

FIGURE 2 | Example of the EEG record and corresponding FFT analysis in the kindle group. **(A)** A continuous baseline EEG record from the baseline period (I) to the AD duration (II). **(B)** The power spectrum corresponding to each phase of the EEG using FFT analysis.

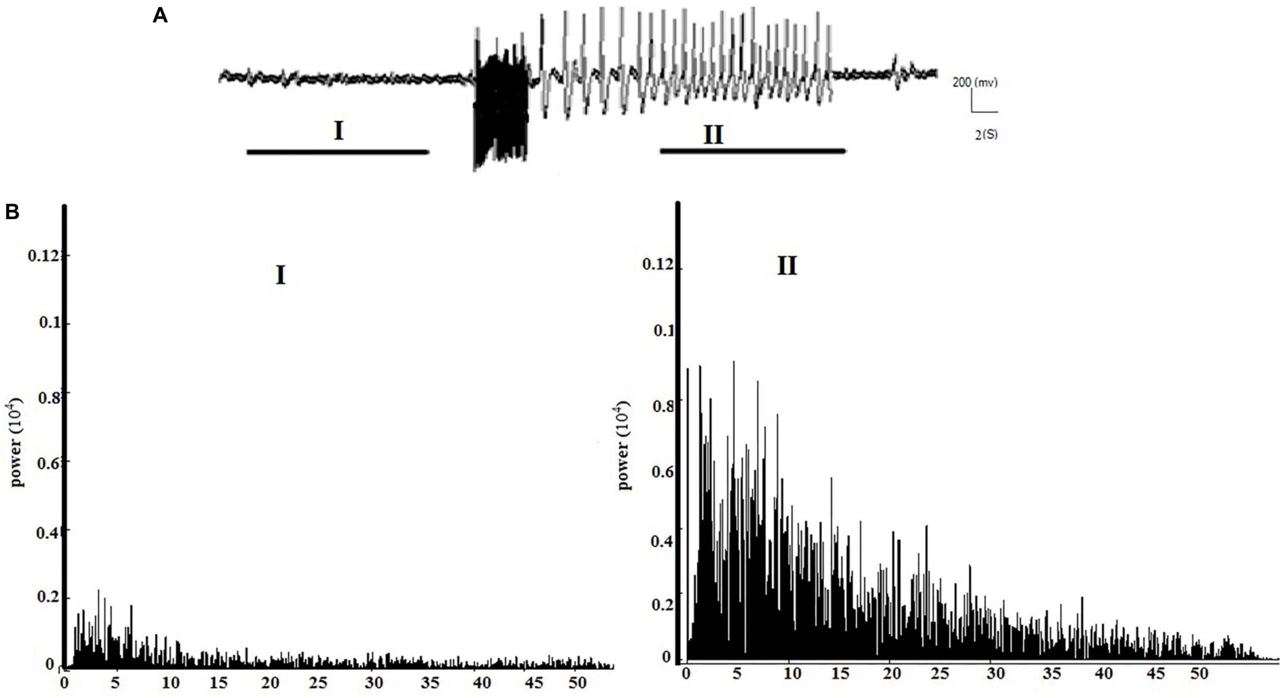

FIGURE 3 | The spectral powers of the baseline and AD section of EEGs and the corresponding FFT analysis in the LFSK group. The LFSK and KLFS groups showed no significant differences in spectral powers. **(A)** A continuous baseline EEG (I) to the AD section EEG (II). **(B)** The spectral powers corresponding to baseline EEG and epileptic activities of the EEG signals.

(HFB) activities were enhanced along with the spreading epileptic activities (emerging AD waves). Moreover, during the AD period, larger spikes occurred at higher frequencies in the power spectrum of the EEG, compared with the baseline periods (**Figures 2**, **3**).

The power spectral density percentages of LFB, MFB, and HFB of the baseline EEG were compared between the three experimental groups. A one-way ANOVA test showed no significant difference in the LFB power [$F(2,16) = 1.778$, $p > 0.05$], MFB [$F(2,16) = 2.053$, $p > 0.05$], and HFB [$F(2,16) = 1.372$, $p > 0.05$] between the Kindle, LFSK and KLFS groups (**Figure 4**).

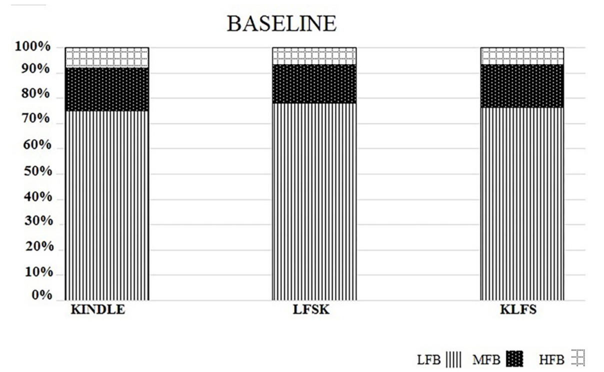

FIGURE 4 | The spectral power density percentage of the three experimental groups for the baseline activities. There was no significant difference in the low (LFB), mid (MFB), and high frequency band (HFB) powers between the experimental groups ($p > 0.05$).

Spectral Analysis of AD

To clarify the effect of LFS on the frequency components of AD, the power spectrums of the kindling stages were compared between the experimental groups. **Figures 5A,B** are representative EEG signals of ISSs of the kindling acquisition in the kindle and also in the LFSK or KLFS groups, respectively. Since the induced changes in the power spectrum of both the LFSK and the KLFS in ISSs were relatively similar, we only demonstrated an example of the LFSK in **Figure 5**. There was no significant difference in the power spectrum of ISSs between the kindle and LFS treated animals (**Figures 5A,B**). According to **Figure 5C**, the LFB was dominant in ISSs of all the experimental groups. However, there was no significant difference in the LFB [$F(2,18) = 0.2$, $p > 0.05$], MFB [$F(2,18) = 0.613$, $p > 0.05$], and HFB [$F(2,18) = 0.164$, $p > 0.05$] power between the experimental groups (**Table 1**). It should be noticed that the animals in the kindle group showed totally 61 times ISSs while the LFSK and KLFS animals represented totally 38 and 39 times ISSs respectively which were included in this part of the analysis.

Figures 6A–C show examples of the power spectrum of LSS of the kindling acquisition in the kindle, LFSK, and KLFS groups, respectively. Application of LFS immediately either before or after the kindling stimulation reduced mid frequency (8–12 Hz) and high frequency (12–40 Hz) oscillations induced in LSS

TABLE 1 | The raw values and descriptive statistics of the LFB, MFB, and HFB in ISSs between the experimental groups.

Stage	Group	Sub band	Mean	Standard deviation (*SD*)	Statistics	*P*-value
ISSs	LFB	Kindle	0.828	0.088	*F*(2,18) = 0.2	*P* = 0.821
		LFSK	0.845	0.043		
		KLFS	0.851	0.057		
	MFB	Kindle	0.082	0.041	*F*(2,18) = 0.613	*P* = 0.554
		LFSK	0.065	0.032		
		KLFS	0.065	0.019		
	HFB	Kindle	0.088	0.046	*F*(2,18) = 0.164	*P* = 0.851
		LFSK	0.081	0.035		
		KLFS	0.074	0.047		

There was no significant difference in the power of different sub-bands between the experimental groups.

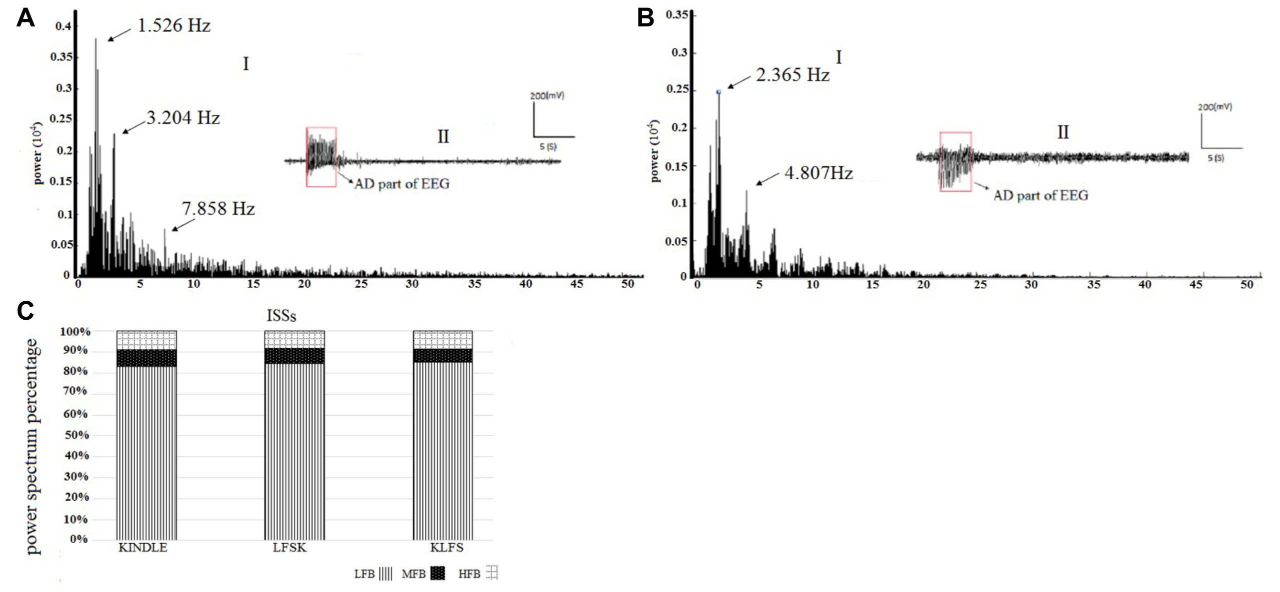

FIGURE 5 | (A-I) An example of EEG power spectrum and **(A-II)** corresponding EEG signal of the ISS in the kindle group. Spectral power of only AD section or epileptic waves is performed. **(B-I)** The power spectrum of the ISS in the LFSK group. The LFSK and KLFS groups showed no significant differences in spectral powers. **(B-II)** An example EEG signal of ISS in the LFSK group. There was no significant difference between the control and intervention groups. **(C)** The power spectrum density percentage of the ISS sections of the EEG signals in the experimental groups. There was no significant difference in the power of different sub-bands between all groups ($p > 0.05$).

than the kindle group. We compared the power spectrum density percentages of LSS in the kindle, LFSK, and KLFS groups (**Figure 6D**). A One-Way ANOVA indicated a significant difference in the LFB power between the experimental groups [$F(2,12) = 8.788$, $p < 0.05$]. In this regard, application of the LFS either before or after the kindling stimulation significantly increased the LFB power, compared with the kindle group ($p < 0.05$).

In addition, there was a significant difference in the MFB [$F(2,12) = 5.543$, $p < 0.05$] and HFB [$F(2,12) = 7.417$, $p < 0.05$] power between the experimental groups (**Table 2**). In fact, MFB and HFB powers were significantly decreased in LSS of the LFSK, compared with the kindle group ($p < 0.05$). Although the MFB and HFB powers in the KLFS group were lower than the kindle, the difference was not significant ($p > 0.05$) (**Table 2**). Moreover, there was no significant difference in different sub-bands power of the EEG signals between the LFSK and KLFS groups ($p > 0.05$) (**Table 2**).

In the kindle group, the mid frequency (12–40 Hz) oscillations in LSS are more than the ISSs (**Figures 5A** and **6A**). Interestingly, not only did these figures confirm our result, but other power spectrum figures related to LSS of the experimental animals also supported the above idea and our results convinced us to only show one figure as a representative. It is worth noting that all animals in the kindle group demonstrated 42 times LSS which took on average 12.4285 s, and animals in the LFSK and KLFS showed 13 times LSS with an average of 9.373 s and 14 times with an average of 10.064 s, respectively.

Figures 7A–C are respectively examples of the power spectrum of the GSSs in the kindle and LFS treated groups. There were large peaks at mid (8–12 Hz) and high (12–40 Hz) frequencies in the kindle group (**Figure 7A**). Moreover, fewer

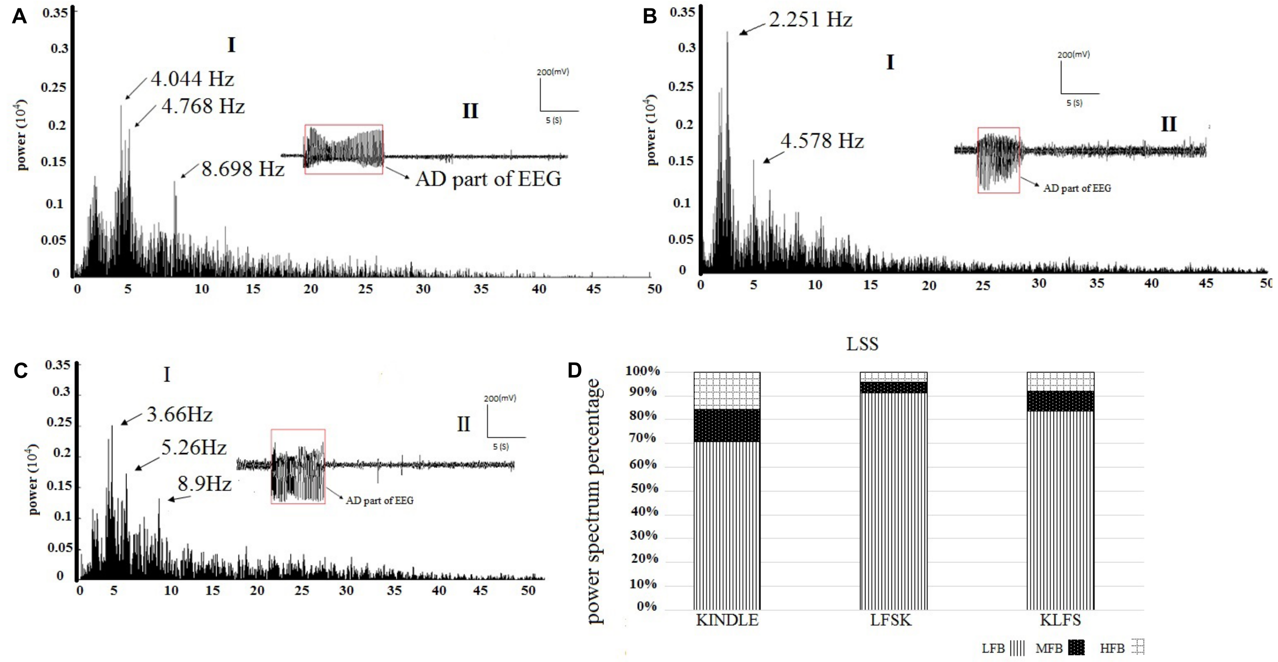

FIGURE 6 | (A-I) An example of EEG power spectrum of the LSS and **(A-II)** corresponding EEG signal in the kindle group. The mid frequency (8–12 Hz) oscillations were evident in this stage. The peaks occurred at higher frequencies compared with ISSs of the kindle group. Furthermore, high frequency activities were more than ISSs of the kindle group. **(B-I)** The power spectrum of the LSS in the LFSK group. **(B-II)** An EEG signal example of LSS in the LFSK group. There were two peaks at 2.25 Hz and 4.58 Hz in the low frequency range (0–8 Hz). **(C-I)** The power spectrum of LSS in the KLFS. C-II: An EEG signal example of LSS in the KLFS group. **(D)** The power spectrum density percentage of LSS sections of the EEG signals in the experimental groups.

TABLE 2 | The raw values and descriptive statistics of the LFB, MFB, and HFB in LSS between the experimental groups.

Stage	Group	Sub band	Mean	*SD*	Statistics	*P*-value
LSS	LFB	Kindle	0.7091	0.1005	*F*(2,12) = 8.788	
		LFSK	0.9124	0.0223		*P* = 0.014
		KLFS	0.8825	0.0465		*P* = 0.034
	MFB	Kindle	0.1323	0.0556	*F*(2,12) = 5.543	
		LFSK	0.0451	0.0058		*P* = 0.049
		KLFS	0.0582	0.0172		*P* = 0.1
	HFB	Kindle	0.1557	0.0595	*F*(2,12) = 7.417	
		LFSK	0.042	0.0219		*P* = 0.023
		KLFS	0.0592	0.0330		*P* = 0.053

There was no significant difference in the power of different sub-bands between the experimental groups. The p-value represented the level of significance against the kindle group. LFSK and KLFS groups showed no significant difference in the power of different sub-bands in the LSS phase ($p > 0.05$).

peaks occurred at MFB and HFB in the GSSs in the LFSK and KLFS groups, compared with the Kindle (**Figures 7B,C**). The MFB and HFB components in the kindle group exceeded both LFS and KLFS groups (**Figures 7A–D**).

There were three peaks in the power spectrum of GSSs in the kindle group. These peaks were much larger and occurred at higher frequencies as compared with LSS of the kindle group. In addition, high frequency activities (12–40 Hz) were much higher than the LSS in the kindling group.

Only one rat in the LFSK and two rats in the KLFS group showed GSSs. Animals in the kindle group showed 35 times GSSs with an average length of 22.28 s, whereas animals in the LFSK and KLFS groups exhibited 4 and 6 times GSSs with length of 16.9 and 17.82 s, respectively. Therefore, to determine the power spectrum density percentage, we compiled these two groups into one LFS treated group (**Figure 7D**). Due to the imbalanced nature of the sample and fewer animals in both LFSK and KLFS groups showed GSSs than the kindle group, the statistical results were hardly reliable hence not reported here.

Comparisons of ADD Frequency Components

The power of different sub bands of EEG in the Racine stages was compared between different groups. A two-way ANOVA

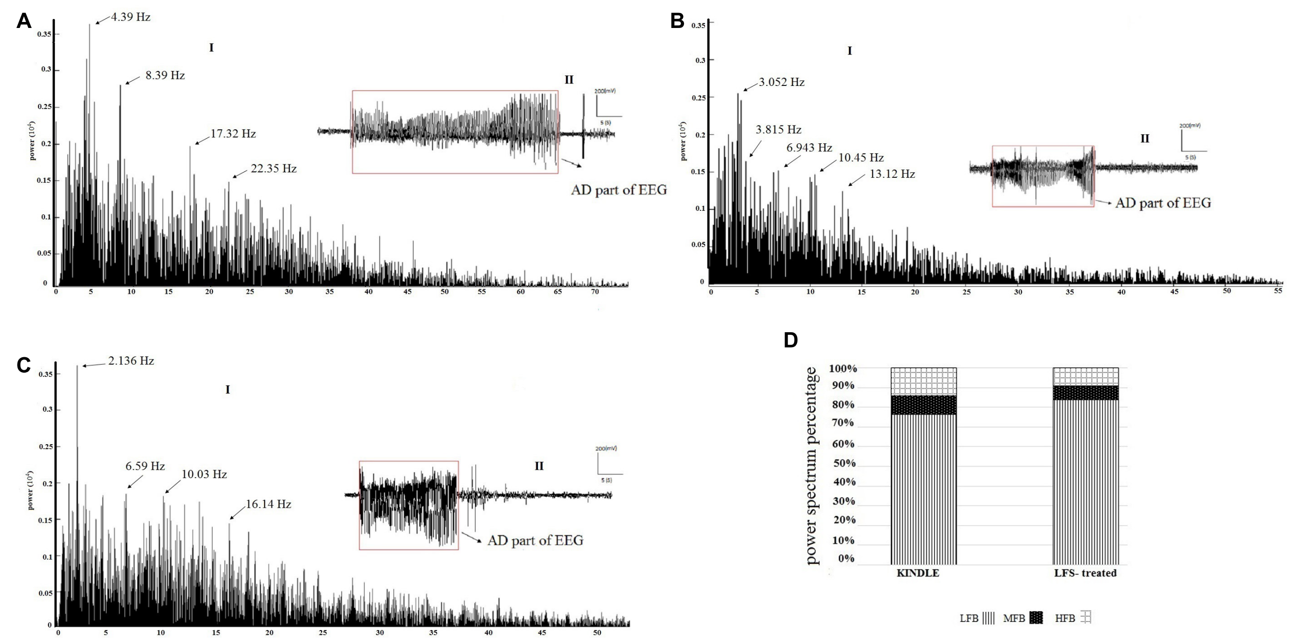

FIGURE 7 | (A-I) An example of EEG power spectrum and **(A-II)** corresponding EEG signal of the GSSs in the kindle group. The mid (8–12 Hz) and high frequency (12–40 Hz) oscillations increased during epileptogenesis. **(B-I)** The power spectrum and **(B-II)** corresponding EEG signal of the GSSs in LFSK group. High frequency activities (12–40 Hz) were lower than the GSSs of the kindle group. **(C-I)** The power spectrum and **(C-II)** corresponding EEG of GSSs in the KLFS group. **(D)** The power spectrum density percentage of the GSSs in the kindle and intervention groups. Contribution of MFB and HFB in the LFS treated animals decreased.

test showed a significant difference in the power of delta, beta and gamma sub bands between the groups ($p < 0.05$) (**Table 3**). A significant increase of delta power was observed in LFS treated groups compared with the kindle group ($p < 0.05$) (**Figure 8A**). However, there was no significant difference between the KLFS and LFSK groups ($p > 0.05$). In addition, administration of LFS only before kindling significantly reduced beta and gamma powers compared with the kindle group ($p < 0.05$), however these reductions were not significant in the KLFS group (**Figures 8D,E**). The LFSK protocol reduced the high frequency (12–40 Hz) power much more than the KLFS which likely lead to more inhibitory effects. The theta/alpha ratio increased in both LFSK and KLFS groups, compared with the kindle group; however, only the LFSK group was significantly different than the kindle group ($p < 0.05$). Moreover, the LFSK protocol increased the theta/alpha ratio more than KLFS protocol, whereas the difference was not statistically significant ($p > 0.05$).

TABLE 3 | Results of a two-way ANOVA.

Sub band	*F*(2, 33)	*P*-value
Delta	5.974	0.006
Theta	1.261	0.297
Alpha	0.91	0.412
Beta	6.282	0.005
Gamma	4.373	0.021
Theta/Alpha	7.84	0.002

According to the Table, there was a significant difference between the experimental groups in delta, beta, gamma power, and theta/alpha ratio (p < 0.05).

Comparison of Theta/Alpha Ratio

Due to the emergence of theta waves in the epileptic seizures and the association of alpha waves with alertness disturbances, in recent years the theta/alpha ratio has been considered as an important index to analyze the level of alertness as well as epileptic depolarization. In this regard, the theta/alpha ratio was evaluated in different stages of kindling and also it was compared between the kindle, the LFSK, and the KLFS groups. Seven animals in the kindle group, 6 in the LFSK, and 6 in the KLFS contributed to these analyses.

According to **Figure 8F**, application of LFS caused an increase of the theta/alpha ratio either before or after termination of kindling stimulation as compared with the Kindle group. However, the increase only in the LFSK group was significant ($p < 0.05$) (**Figure 8F**) (**Table 3**). Although application of LFSK could enhance theta/alpha ratio more than KLFS, the difference was not statistically significant.

Correlation Between Frequency Contents and Duration of Epileptic Activities

The correlation analysis of ADD and powers of different EEG sub bands was determined. We aimed to quantitatively analyze the inhibition effect of LFS and only describe the difference between the Kindle and the LFS treated groups. Three rats

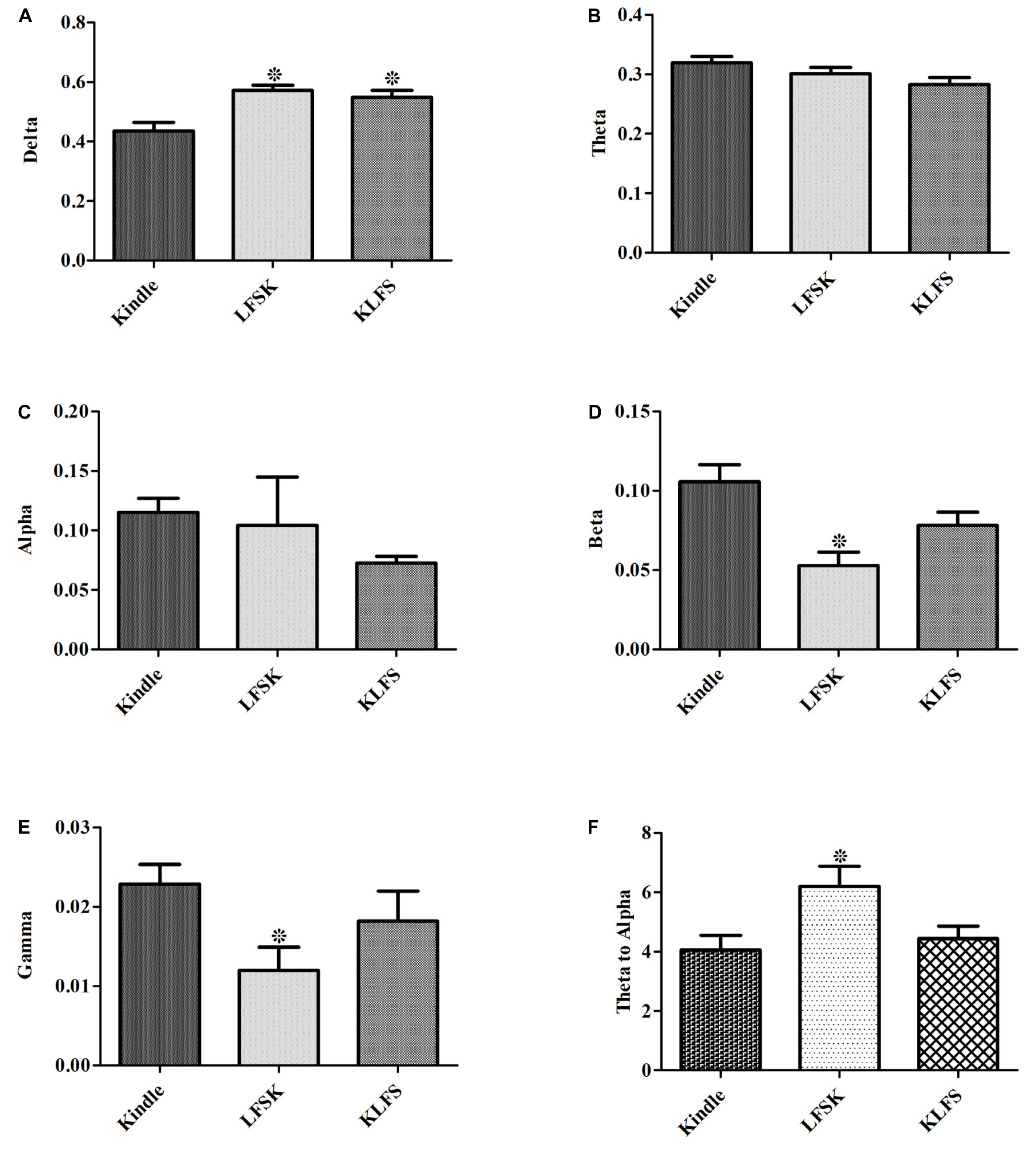

FIGURE 8 | Contribution of each sub band to different groups. **(A–E)** Showed the power of Delta, Theta, Alpha, Beta, and Gamma for the kindle, LFSK, and KLFS, respectively. **(F)** Comparison of the Theta/alpha ratio in the experimental groups. The data were represented as Mean ± SEM. *: significant difference compared with kindle group ($P < 0.05$).

in each LFSK and KLFS group showed LSS and one rat in the LFSK and 2 in the KLFS showed GSSs. Therefore, we combined the LFSK and KLFS animals into one LFS treated group to use the correlation test. To perform correlation analysis, EEG signals in each stage of Racine were divided into 3 sub bands including LFB (0–8 Hz), MFB (8–12), and HFB (12–40). We then determined the Pearson's correlation coefficients between each of three sub bands and ADD for different kindling stages.

In the kindle group, no significant correlation observed between each frequency band and the different seizure stages. There was a low negative correlation between MFB and ADD in ISSs ($r = -0.4$, $p > 0.05$). In addition, a small correlation was observed between ADD and different frequency bands in GSSs (**Table 4**).

In the LFS treated animals, a significant or strong correlation was not observed between each frequency band and ADD in ISSs and LSS of the kindling. There was a low positive correlation

TABLE 4 | Statistical data of the correlation test between EEG sub-bands and ADD in ISSs, LSS, and GSSs in the kindle group.

Stage		*R*	*P*-value
1&2 (ISSs)	ADD & LFB	0.38	0.4
	ADD & MFB	−4.0	0.364
	ADD & HFB	−233.0	0.466
3 (LSS)	ADD & LFB	−172.0	0.557
	ADD & MFB	0.2	0.667
	ADD & HFB	0.282	0.54
4&5 (GSSs)	ADD & LFB	−851.0	0.735
	ADD & MFB	0.168	0.718
	ADD & HFB	0.124	0.791

between ADD and LFB in LSS ($r = 0.427$, $r > 0.05$) whereas a low negative correlation was witnessed between ADD and HFB ($r = -0.448$, $p > 0.05$) (**Table 5**). Since only three animals in the LFS treated groups developed GSSs, we cannot rely on the correlation test in GSSs in this group.

DISCUSSION

The results of this study demonstrated that LFS administration either immediately before or after the kindling stimulation significantly inhibited kindling progression. Our behavioral results showed LFS immediately before kindling stimulation induced greater inhibition effects than the LFS applied immediately after kindling. However, the difference was not statistically significant. Wu et al. (2008) reported that therapeutic application of LFS was strongly time dependent in such a way that applying daily LFS immediately after kindling stimulations produced an antiepileptogenesis effect while delayed LFS applied after the cessation of AD not only could not retard kindling acquisition, but it also accelerated kindling progression (Wu et al., 2008). In addition, Sun et al. (2010) showed that LFS administration immediately after daily kindling stimulation could suppress the epileptogenesis process, whereas LFS administration before the termination of daily kindling stimulation, did not result in inhibitory effect (Sun et al., 2010). However, the findings of the previous studies on the time dependency of LFS effects were controversial necessitating further studies in this regard (Kile et al., 2010; Lucas et al., 2012; Shahpari et al., 2012; Ghotbedin et al., 2013; Jalilifar et al., 2017a,b). Therefore, the present study aimed to investigate the time-dependent effects of LFS using kindling signal processing. In this regard, we comparatively evaluated the quantitative features of kindle group, and LFS-induced changes in two protocols of LFSK and KLFS with spectral assessments using FFT analysis.

TABLE 5 | Statistical data of the correlation test between EEG sub-bands and ADD in ISSs, LSSs, and GSSs in LFS treated groups.

Stage	LFSK-KLFS	*R*	*P*-value
1&2 (ISSs)	ADD & LFB	−123.0	0.536
	ADD & MFB	0.25	0.962
	ADD & HFB	0.4	0.432
3	ADD & LFB	0.427	0.399
	ADD & MFB	0.2	0.704
	ADD & HFB	−844.0	0.373
4&5 (GSSs)	ADD & LFB	0.721	0.488
	ADD & MFB	−557.0	0.456
	ADD & HFB	−927.0	0.48

Quantitative assessments of EEG signals demonstrated that administration of LFS reduced beta and gamma oscillations as well as increased delta sub band power. Moreover, alpha power decreased following application of LFS, but the reduction was not statistically significant (**Figures 5–7**). Application of LFS prior the kindling stimulation (LFSK) reduced beta and gamma sub bands power more than KLFS but the difference remained insignificant (**Figure 8**).

Since we aimed to quantitatively analyze EEG signals related to the Racine stages, we only focused on the part of the AD that occurred with emerging different seizure stages. Therefore, other parts of the AD which corresponded to other behavioral states were excluded from the analysis. According to the power spectrum figures (**Figures 5–7**), with progression of the kindling acquisition, larger peaks occurred in the mid (8–12 Hz) and high (12–40 Hz) frequencies and also a remarkable shift toward higher frequencies was evident at higher frequencies. However, there was no significant difference in the power spectrum figures between the LFSK and KLFS groups.

Our results showed no significant difference in the power of LFB, MFB, and HFB components in ISSs, LSS, and GSSs between the experimental groups. MFB and HFB components were considerably higher in the kindle group than the LFSK and KLFS animals, whereas LFB increased in both LFSK and KLFS groups (**Figure 6D**). Moreover, our findings demonstrated that high frequency components were increased at GSSs in all the experimental groups vis-a-vis LSS of the kindling (**Figures 6** and **7**).

We have analyzed the background EEG of the experimental groups for 7 s before the start of the kindling stimulation to clarify whether LFS only changed seizure activities or whether it also affected the background EEG. Since the results confirmed no significant differences in LFB, MFB, and HFB powers of the baseline EEG signals between the experimental groups, it is claimed that the group differences can only account for the seizure activity but not the background EEG. We previously reported increase of delta and theta oscillations with generalization of the kindling process (Jalilifar et al., 2016). In this regard, power spectrum results confirmed that the LFB (delta and theta sub-bands) is dominant with the progression of the kindling acquisition. We also found increase of HFB components in the GSSs. It can be observed that application of LFS especially in LSS and GSSs of the kindling acquisition reduced HFB components. Besides, more peaks occurred in the power spectrum figures of GSSs at higher frequencies as compared with LFS treated animals. In fact, there were larger peaks in GSSs of kindle animals at frequencies above 15 Hz whereas in the GSSs of the LFS treated group these picks were located at lower frequencies. To prove the above mentioned idea, application of LFS either before or after the kindling stimulation significantly increased delta power (**Figure 8A**). Moreover, the results showed that HFB power was increased in both LFSK and KLFS groups but the difference in the LFSK was only significant (**Figure 8**). Our behavioral data showed that ADD in the kindle group was significantly higher than the LFSK and KLFS ($p < 0.05$). However, to determine power spectrum figures and also EEG signal processing, we only focused on the part of AD that includes Racine stages and the parts of ADD related to other behavioral states were excluded from the signals. Therefore, we only quantitatively analyzed the duration of different stages of the kindling. Different studies have offered the ratio of theta/alpha as an important index for analyzing epileptic seizures (Fernández et al., 2003; Sadighi Alvandi et al., 2015). Our data indicated increase of theta/alpha ratio following the application of LFS. However, this increase would be much higher if LFS was applied before the kindling stimulation, compared with the application of LFS after the termination of kindling stimulation. The difference may be related to greater inhibitory effect of LFS when it was applied before the kindling stimulation than KLFS.

The results showed no significant correlation between each frequency sub band and ADD in different stages of Racine in the kindle group. There was a low negative correlation between ADD and MFB and also low positive correlation between ADD and LFB in ISSs in the kindle group. In addition, a weak correlation between ADD and different frequency sub bands was observed in the LFS treated animals.

The exact mechanisms of the antiepileptogenesis effects of LFS are not clearly determined, but two main theories have been proposed on the mechanism of action of LFS or more widely electromagnetic modulations on neural activities: dispersion theory and LTD. In the dispersion theory, the main idea is that injecting an external energy, usually in the form of electrical or electromagnetic fields can disturb or disperse the ongoing intrinsic neural activities. The impaired ongoing neural activities can be disturbed by an external electric field in appropriate frequencies.

Tsuchiya and Kogure (2011) found a strong positive correlation between an increase of high frequency components (12–30 Hz) and the behavioral progression of kindling, whereas decrement of these high frequency activities was associated with incomplete kindling stages which cannot support our findings (Tsuchiya and Kogure, 2011). Similar to our results, Musto et al. (2009) demonstrated that electrical kindling development could be suppressed by reducing gamma oscillations (21–40 Hz) indicating that the beta (12–20 Hz) and gamma waves in hippocampus were involved in the propagation of kindling seizures (Musto et al., 2009). Likewise, Dugladze et al. (2007) surveyed chemical kindling using kainic acid and they found suppressing theta waves meanwhile increasing gamma oscillations with behavioral progression of kindling (Dugladze et al., 2007). In this regard, application of LFS before the kindling stimulation, though not considerable, reduced beta and gamma power more than the KLFS group which confirmed more inhibitory effect of LFS when applied immediately before the kindling stimulation (**Figure 7B**).

Low frequency stimulation can also inhibit epileptogenesis process through LTD phenomenon (Goodman et al., 2005; Ozen et al., 2008). In this regard, application of LFS seems to suppress the release of glutamate and increase of inhibitory receptor activity and consequently leads to decrease of beta and gamma frequencies.

Furthermore, alteration in the glutaminergic neural activity following amygdala kindling may happen in CA1 neurons of hippocampus. In this regard, Ueda and Tsuru (1995) reported increase of the amount of NMDA receptors and release of glutamate during amygdala kindling which might be involved in generalization of kindling seizures (Ueda and Tsuru, 1995). Thus, reducing NMDA receptors can be another antiepileptogenesis mechanism of LFS and the reason for decrease of high frequency components (12–40 Hz). There are many reports that the disappearance of high frequency activities causes a relative increase of low frequency oscillations of the targeted neurons, which in turn inhibit the development of epileptogenesis. Delta and theta frequencies are implicated in maintenance of inhibitory system of hippocampus and amygdala regions (Miller et al., 1994). Moreover, increase of LFB contribution including delta band following application of LFS occurred due to decrease of the excitatory neural network activity (Dugladze et al., 2007).

Our findings showed that LFS immediately before or after kindling stimulations significantly inhibit kindling-induced epileptogenesis where the LFSK showed greater inhibiting effects than KLFS. It indicates that time of LFS application does not result in significantly different antiepileptic effects. However, some of the previous studies have reported the time of LFS application is an important factor in exerting the antiepileptic effects. In a similar study, Shahpari et al. (2012) compared the antiepileptic effects of LFS with the same protocol of our study immediately before kindling and 5 min after the termination of kindling and reported that LFS immediately before kindling stimulation induced more inhibiting effects (Shahpari et al., 2012). Considering the non-significant difference between LFSK and KLFS in antiepileptic effects, it seems that LFS partly exerts its inhibiting effects through the dispersion mechanism. This can be concluded that time of LFS application However, the difference resulted from the different studies conducted in two separate laboratories should be accounted. It can be concluded that a combination of wide dispersion and LTD might be the main responsible mechanism of action of LFS antiepileptic effects.

Administration of the same LFS protocol immediately before or after kindling stimulations significantly inhibit the kindling induced epileptogenesis in a way that LFS before the kindling stimulations exerts greater inhibiting effects than the KLFS protocol but the difference was not significant. Similarly, the quantitative measures including delta, beta and gamma oscillations, and theta/alpha ratio showed the greater changes in the LFSK than the KLFS group.

One of the main limitations of the present study is that the number of rats that reached the GSSs in the LFSK and KLFS groups was low. Investigating the effects of LFS alone on the baseline EEG signals of the amygdala could result in usefull information on determining markers for treatment response monitoring. Moreover, it is recommended to study the effects of kindling and LFS on the other regions in the brain to identify the associated measures and the spatial distribution of the effects. In our studies due to technical limits in the recording system we did not investigate these effects. Further studies are needed with bigger sample sizes and with more rats showing stages 4–5 to reach more reliable results.

CONCLUSION

The LFS in both protocols can inhibit the kindling induced epileptogenesis. Our findings showed that application of LFS can increase the delta power while decreasing beta and gamma oscillations. It seems that LFS can provide antiepileptogenic effect through increasing LFB, meanwhile decreasing high frequency components which can be a helpful index for identifying LFS-induced antiepileptogenesis. Moreover, application of LFS before the kindling stimulation decreased beta and gamma oscillations and theta/alpha ratio more than the KLFS protocol which may be related to more inhibitory effects of the LFSK protocol compared with the KLFS. Behavioral assessments showed relatively the same level of antiepileptogenic effects for KLFS and LFSK, quantitative assessments showed more significant differences in the quantitative measures between the two protocols. Developing more quantitative EEG based measures correlated with LFS-induced effects can facilitate developing open or closed loop seizure prevention modalities.

AUTHOR CONTRIBUTIONS

MJ and AY contributed in study design and methodology, data collection and analyses, and manuscript preparation. AM and ZG contributed in the methodology and data collection and reviewed the manuscript.

FUNDING

This study a part of the M.Sc. thesis registered in the Medical Physics department, School of Medicine, Ahvaz Jundishapur University of Medical Sciences (AJUMS) and was financially supported by AJUMS (Grant No. U-94174). This work was partially presented in the 2nd International Brain Stimulation Conference, 5–8 March 2017 (Jalilifar et al., 2017c).

REFERENCES

Albensi, B. C., Ata, G., Schmidt, E., Waterman, J. D., and Janigro, D. (2004). Activation of long-term synaptic plasticity causes suppression of epileptiform activity in rat hippocampal slices. *Brain Res.* 998, 56–64. doi: 10.1016/j.brainres.2003.11.010

de Boer, H. M., Mula, M., and Sander, J. W. (2008). The global burden and stigma of epilepsy. *Epilepsy Behav*. 12, 540–546. doi: 10.1016/j.yebeh.2007.12.019

Demos, J. N. (2005). *Getting Started with Neurofeedback*. New York, NY: WW Norton & Company.

Devinsky, O. (1991). Interictal behavioral changes in epilepsy. *Front. Clin. Neurosci.* 12, 1–21.

Dugladze, T., Vida, I., Tort, A. B., Gross, A., Otahal, J., Heinemann, U., et al. (2007). Impaired hippocampal rhythmogenesis in a mouse model of mesial temporal lobe epilepsy. *Proc. Natl. Acad. Sci. U.S.A*. 104, 17530–17535. doi: 10.1073/pnas.0708301104

Esmaeilpour, K., Masoumi-Ardakani, Y., Sheibani, V., Shojaei, A., Harandi, S., and Mirnajafi-Zadeh, J. (2013). Comparing the anticonvulsant effects of low frequency stimulation of different brain sites on the amygdala kindling acquisition in rats. *Basic Clin. Neurosci.* 4, 250–256.

Fernández, T., Herrera, W., Harmony, T., Díaz-Comas, L., Santiago, E., Sánchez, L., et al. (2003). EEG and behavioral changes following neurofeedback treatment in learning disabled children. *Clin. EEG Neurosci.* 34, 145–152. doi: 10.1177/155005940303400308

Fujii, S., Kuroda, Y., Ito, K. I., Kaneko, K., and Kato, H. (1999). Effects of adenosine receptors on the synaptic and EPSP−spike components of long−term potentiation and depotentiation in the guinea−pig hippocampus. *J. Physiol*. 521, 451–466. doi: 10.1111/j.1469-7793.1999.00451.x

Ghotbedin, Z., Janahmadi, M., Mirnajafi-Zadeh, J., Behzadi, G., and Semnanian, S. (2013). Electrical Low frequency stimulation of the kindling site preserves the electrophysiological properties of the rat hippocampal CA1 pyramidal neurons from the destructive effects of amygdala kindling: the basis for a possible promising epilepsy therapy. *Brain Stimulat.* 6, 515–523. doi: 10.1016/j.brs.2012.11.001

Goddard, G. V., McIntyre, D. C., and Leech, C. K. (1969). A permanent change in brain function resulting from daily electrical stimulation. *Exp. Neurol*. 25, 295–330. doi: 10.1016/0014-4886(69)90128-9

Goodman, J. H., Berger, R. E., and Tcheng, T. K. (2005). Preemptive low−frequency stimulation decreases the incidence of amygdala−kindled seizures. *Epilepsia* 46, 1–7. doi: 10.1111/j.0013-9580.2005.03804.x

Haenschel, C., Baldeweg, T., Croft, R. J., Whittington, M., and Gruzelier, J. (2000). Gamma and beta frequency oscillations in response to novel auditory stimuli: a comparison of human electroencephalogram (EEG) data with in vitro models. *Proc. Natl. Acad. Sci. U.S.A*. 97, 7645–7650. doi: 10.1073/pnas.120162397

Hughes, S. W., and Crunelli, V. (2005). Thalamic mechanisms of EEG alpha rhythms and their pathological implications. *Neuroscientist* 11, 357–372. doi: 10.1177/1073858405277450

Jalilifar, M., Yadollahpour, A., Moazedi, A. A., and Ghotbeddin, Z. (2016). Classifying amygdala kindling stages using quantitative assessments of extracellular recording of EEG in rats. *Brain Res. Bull.* 127, 148–155. doi: 10.1016/j.brainresbull.2016.09.012

Jalilifar, M., Yadollahpour, A., Moazedi, A. A., and Ghotbeddin, Z. (2017a). Low frequency electrical stimulation either prior to or after rapid kindling stimulation inhibits the kindling-induced epileptogenesis. *Biomed. Res. Int*. 2017:8623743. doi: 10.1155/2017/8623743

Jalilifar, M., Yadollahpour, A., Moazedi, A. A., and Ghotbeddin, Z. (2017b). Quantitative assessments of extracellular EEG to classify specific features of main phases of seizure acquisition based on kindling model in Rat. *Neurosci. Lett*. 656, 144–151. doi: 10.1016/j.neulet.2017.07.034

Jalilifar, M., Yadollahpour, A., Moazedi, A. A., and Ghotbeddin, Z. (2017c). Quantitative evaluation of antiepileptogenic effects of LFS either before or after kindling stimulation using spectral power analysis of extracellular EEG in rats. *Brain Stimulat.* 10, 504–506. doi: 10.1016/j.brs.2017.01.476

Kile, K. B., Tian, N., and Durand, D. M. (2010). Low frequency stimulation decreases seizure activity in a mutation model of epilepsy. *Epilepsia* 51, 1745–1753. doi: 10.1111/j.1528-1167.2010.02679.x

Kleinfeld, D. (2008). Application of spectral methods to representative data sets in electrophysiology and functional neuroimaging. *Soc. Neurosci.* 3, 21–34.

Lerchl, A., Nonaka, K. O., Stokkan, K. A., and Reiter, R. J. (1990). Marked rapid alterations in nocturnal pineal serotonin metabolism in mice and rats exposed to weak intermittent magnetic fields. *Biochem. Biophys. Res. Commun*. 169, 102–108. doi: 10.1016/0006-291X(90)91439-Y

Lothman, E., Hatlelid, J. M., Zorumski, C. F., Conry, J. A., and Moon, P. F. (1985). Kindling with rapidly recurring hippocampal seizures. *Brain Res.* 360, 83–91. doi: 10.1016/0006-8993(85)91223-5

Lucas, T., Pereyra, J., Pastorino, A., Smigliani, F., Ocariz, G., Ortmann, M., et al. (2012). Effect of unilateral low-frequency stimulation of hippocampus on rapid kindling—induced seizure development in rats. *Neurosci. Med.* 3, 174–180. doi: 10.4236/nm.2012.32022

Miller, J. W., Turner, G. M., and Gray, B. C. (1994). Anticonvulsant effects of the experimental induction of hippocampal theta activity. *Epilepsy Res.* 18, 195–204. doi: 10.1016/0920-1211(94)90040-X

Musto, A. E., Samii, M. S., and Hayes, J. F. (2009). Different phases of afterdischarge during rapid kindling procedure in mice. *Epilepsy Res.* 85, 199–205. doi: 10.1016/j.eplepsyres.2009.02.020

Ozen, L. J., Young, N. A., Koshimori, Y., and Teskey, G. C. (2008). Low-frequency stimulation reverses kindling-induced neocortical motor map expansion. *Neuroscience* 153, 300–307. doi: 10.1016/j.neuroscience.2008.01.051

Paxinos, G., Watson, C., Carrive, P., Kirkcaldie, M., and Ashwell, K. W. S. (2009). *Chemoarchitectonic Atlas of the Rat Brain.* Cambridge, MA: Academic Press.

Peterson, S. L., and Albertson, T. E. (1982). Neurotransmitter and neuromodulator function in the kindled seizure and state. *Prog. Neurobiol.* 19, 237–270. doi: 10.1016/0301-0082(82)90008-9

Pritchard, W. S. (1986). Cognitive event-related potential correlates of schizophrenia. *Psychol. Bull.* 100:43. doi: 10.1037/0033-2909.100.1.43

Racine, R. J. (1972). Modification of seizure activity by electrical stimulation: II. Motor seizure. *Electroencephalogr. Clin. Neurophysiol.* 32, 281–294. doi: 10.1016/0013-4694(72)90177-0

Sadighi Alvandi, M., Shahabi, M. P., Nejad, G. G., and Foolad, F. (2015). The effects of verapamil and ethosuximide on the brain bioelectrical activity of WAG/Rij rats. *Neurosci. J.* 3, 11–18. doi: 10.18869/acadpub.shefa.3.2.11

Schrader, L. M., Stern, J. M., Wilson, C. L., Fields, T. A., Salamon, N., Nuwer, M. R., et al. (2006). Low frequency electrical stimulation through subdural electrodes in a case of refractory status epilepticus. *Clin. Neurophysiol.* 117, 781–788. doi: 10.1016/j.clinph.2005.12.010

Shahpari, M., Mirnajafi-Zadeh, J., Firoozabadi, S. M., and Yadollahpour, A. (2012). Effect of low-frequency electrical stimulation parameters on its anticonvulsant action during rapid perforant path kindling in rat. *Epilepsy Res.* 99, 69–77. doi: 10.1016/j.eplepsyres.2011.10.023

Shaker, M. M. (2006). EEG waves classifier using wavelet transform and Fourier transform. *Brain* 2:3.

Sun, H. L., Zhang, S. H., Zhong, K., Xu, Z. H., Zhu, W., Fang, Q., et al. (2010). Mode-dependent effect of low-frequency stimulation targeting the hippocampal CA3 subfield on amygdala-kindled seizures in rats. *Epilepsy Res.* 90, 83–90. doi: 10.1016/j.eplepsyres.2010.03.011

Tsuchiya, K., and Kogure, S. (2011). Fast Fourier transformation analysis of kindling-induced afterdischarge in the rabbit hippocampus. *Epilepsy Res.* 95, 144–151. doi: 10.1016/j.eplepsyres.2011.03.015

Ueda, Y., and Tsuru, N. (1995). Simultaneous monitoring of the seizure-related changes in extracellular glutamate and γ-aminobutyric acid concentration in bilateral hippocampi following development of amygdaloid kindling. *Epilepsy Res.* 20, 213–219. doi: 10.1016/0920-1211(94)00081-7

Velìšek, L., Velìšková, J., and Stanton, P. K. (2002). Low-frequency stimulation of the kindling focus delays basolateral amygdala kindling in immature rats. *Neurosci. Lett.* 326, 61–63. doi: 10.1016/S0304-3940(02)00294-X

Walter, W. G. (1936). The location of cerebral tumours by electro-encephalography. *Lancet* 228, 305–308. doi: 10.1016/S0140-6736(01)05173-X

Wu, D. C., Xu, Z. H., Wang, S., Fang, Q., Hu, D. Q., Li, Q., et al. (2008). Time-dependent effect of low-frequency stimulation on amygdaloid-kindling seizures in rats. *Neurobiol. Dis.* 31, 74–79. doi: 10.1016/j.nbd.2008.03.007

Yadollahpour, A., Firouzabadi, S. M., Shahpari, M., and Mirnajafi-Zadeh, J. (2014). Repetitive transcranial magnetic stimulation decreases the kindling induced synaptic potentiation: effects of frequency and coil shape. *Epilepsy Res.* 108, 190–201. doi: 10.1016/j.eplepsyres.2013.11.023

Yadollahpour, A., and Jalilifar, M. (2014). Seizure prediction methods: a review of the current predicting techniques. *Biomed. Pharmacol. J.* 7, 153–162. doi: 10.13005/bpj/466

Conflict of Interest Statement: The authors declare that the research was conducted in the absence of any commercial or financial relationships that could be construed as a potential conflict of interest.

Copyright © 2018 Jalilifar, Yadollahpour, Moazedi and Ghotbeddin. This is an open-access article distributed under the terms of the Creative Commons Attribution License (CC BY). The use, distribution or reproduction in other forums is permitted, provided the original author(s) and the copyright owner are credited and that the original publication in this journal is cited, in accordance with accepted academic practice. No use, distribution or reproduction is permitted which does not comply with these terms.

frontiers in Physiology

ORIGINAL RESEARCH
published: 06 December 2018
doi: 10.3389/fphys.2018.01753

Designing and Implementing an ANFIS Based Medical Decision Support System to Predict Chronic Kidney Disease Progression

Ali Yadollahpour[1], Jamshid Nourozi[2], Seyed Ahmad Mirbagheri[3], Eric Simancas-Acevedo[4] and Francisco R. Trejo-Macotela[5]*

[1] Department of Medical Physics, School of Medicine, Ahvaz Jundishapur University of Medical Sciences, Ahvaz, Iran, [2] Department of Environmental and Energy, Science and Research Branch, Islamic Azad University, Tehran, Iran, [3] Department of Civil and Environmental Engineering, K. N. Toosi University of Technology, Tehran, Iran, [4] Telematics Engineering Department, Polytechnic University of Pachuca, Zempoala, Mexico, [5] Graduate and Research Department, Polytechnic University of Pachuca, Zempoala, Mexico

Background and objective: Chronic kidney disease (CKD) has a covert nature in its early stages that could postpone its diagnosis. Early diagnosis can reduce or prevent the progression of renal damage. The present study introduces an expert medical decision support system (MDSS) based on adaptive neuro-fuzzy inference system (ANFIS) to predict the timeframe of renal failure.

Methods: The core system of the MDSS is a Takagi-Sugeno type ANFIS model that predicts the glomerular filtration rate (GFR) values as the biological marker of the renal failure. The model uses 10-year clinical records of newly diagnosed CKD patients and considers the threshold value of 15 cc/kg/min/1.73 m^2 of GFR as the marker of renal failure. Following the evaluation of 10 variables, the ANFIS model uses the weight, diastolic blood pressure, and diabetes mellitus as underlying disease, and current $GFR_{(t)}$ as the inputs of the predicting model to predict the GFR values at future intervals. Then, a user-friendly graphical user interface of the model was built in MATLAB, in which the user can enter the physiological parameters obtained from patient recordings to determine the renal failure time as the output.

Results: Assessing the performance of the MDSS against the real data of male and female CKD patients showed that this decision support model could accurately estimate GFR variations in all sequential periods of 6, 12, and 18 months, with a normalized mean absolute error lower than 5%. Despite the high uncertainties of the human body and the dynamic nature of CKD progression, our model can accurately predict the GFR variations at long future periods.

Conclusions: The MDSS GUI could be useful in medical centers and used by experts to predict renal failure progression and, through taking effective actions, CKD can be prevented or effectively delayed.

Keywords: chronic kidney disease, adaptive neuro fuzzy inference system, medical decision support system, renal failure progression, prediction

OPEN ACCESS

Edited by:
Srdjan Kesić,
University of Belgrade, Serbia

Reviewed by:
Ingrid Inge Prkacin,
University of Zagreb School of Medicine, Croatia
Gonzalo Marcelo Ramírez-Avila,
Universidad Mayor de San Andrés, Bolivia

****Correspondence:***
Ali Yadollahpour
yadollahpour.a@gmail.com

Specialty section:
This article was submitted to Fractal Physiology, a section of the journal Frontiers in Physiology

Received: *24 July 2018*
Accepted: *20 November 2018*
Published: *06 December 2018*

Citation:
Yadollahpour A, Nourozi J, Mirbagheri SA, Simancas-Acevedo E and Trejo-Macotela FR (2018) Designing and Implementing an ANFIS Based Medical Decision Support System to Predict Chronic Kidney Disease Progression. Front. Physiol. 9:1753. doi: 10.3389/fphys.2018.01753

INTRODUCTION

Early and differential diagnosis or prediction of disease progression and improving diagnosis reliability are today becoming prerequisite needs in medicine and health systems (Anagnostou et al., 2003; Al-Shayea et al., 2013). In this regard, developing expert and intelligent systems based on machine learning approaches for efficient diagnosis, prediction, and effective management of diseases has drawn considerable research attention among physicians and researchers (Anagnostou et al., 2003; Ohlsson, 2004; Ubeyli and Güler, 2005; Parthiban and Subramanian, 2008; Pandey and Mishra, 2009; Lee and Wang, 2011; Al-Shayea et al., 2013). Decision support systems (DSSs) taking advantages of recent advances in software and computational knowledge in medicine can reduce or even prevent the adverse effects of diseases (Hunt et al., 1998; Montgomery et al., 2000; Garg et al., 2005; Pandey and Mishra, 2009; Lee and Wang, 2011). Medical decision support systems (MDSSs) are intelligent and expert systems used in medicine to help medical experts make appropriate decisions in different fields (Smith et al., 2003). Physicians and health experts could use these systems to eliminate the biases associated with humans, such as tiredness, and environmental interfering factors and to make knowledge-based decisions (Ohlsson, 2004; Garg et al., 2005). Artificial intelligence has gained considerable research interest and has been utilized in different domains of modern medicine such as alarm producing, reminders, and approving diagnostic decisions. In medicine, there is an integrated relationship between data and knowledge, in which knowledge of detection, diagnosis, interpretation, and treatment of a disease is influenced by the data of that disease (Miller, 1994). The level of this relation varies depending on the disease type and interfering and biasing factors. In this regard, intelligent computing models as a category of artificial intelligence prefer to work with data rather than knowledge (Pandey and Mishra, 2009). The artificial intelligence-based MDSSs compared with other MDSSs are more robust and rigorous systems (Ohlsson, 2004; Hayward et al., 2010). The MDSSs can reduce uncertainties and processing time, and produce the knowledge extracted from raw data to be used by medical experts. Computer-based MDSSs can be implemented in web-based frameworks with full time online access in healthcare systems (Hunt et al., 1998; Ohlsson, 2004; Garg et al., 2005). The adaptive neuro-fuzzy inference system (ANFIS) integrates neural networks and fuzzy logic principles into a single framework with learning capability to approximate non-linear functions and works as a universal estimator (Jang, 1992, 1993). ANFIS is a type of neural network, based on the Takagi–Sugeno fuzzy inference system, developed in the early 1990s. The learning networks in this model are based on mathematical computations capable of solving complex problems. ANFIS-based predicting models resembling human brain functions can accurately predict diseases (Jang and Sun, 1997; Ubeyli and Güler, 2005). This system has been used for predicting the onset, classification or differential diagnosis of different disorders including heart failure, cognitive disorders, Alzheimer disease, ischemia, multiple sclerosis, etc. (Brier et al., 2003; Lauer et al., 2005; Ubeyli and Güler, 2005; Ercelebi and Subasi, 2006; Krug et al., 2008; Emam et al., 2010; Al-Kasasbeh et al., 2011; Yadollahpour and Jalilifar, 2014; Norouzi et al., 2016; Zhao et al., 2017). Clinical decisions based on fuzzy logic models are cost effective and beneficial in improving healthcare systems. One of the significant features of fuzzy logic approaches is removing uncertainties of dynamic systems. Uncertainties can be represented and controlled effectively (Parthiban and Subramanian, 2008). Fuzzy logic models were used in predicting appendicitis with high accuracy (Pandey and Mishra, 2009; Al-Shayea et al., 2013). Different expert systems have been used in medicine (Buchanan and Shortliffe, 1984; Ohlsson, 2004; Lee and Wang, 2011; Ma, 2012). MYCIN is one of the early clinical decision systems developed at Stanford University in the early 1970s. This DSS was an expert system based on artificial intelligence to identify bacteria causing severe infections in order to recommend specific antibiotics for patients (Buchanan and Shortliffe, 1984). This DSS used the results of physical and laboratory tests of subjects to diagnose blood infections. Chronic kidney disease (CKD) is a global health problem with 8 to 16 percent worldwide prevalence (Nugent et al., 2011). The prevalence of the disease has dramatically increased worldwide (Meguid El Nahas and Bello, 2005). Variations in population censuses, different diagnoses in different racial populations, a lack of diagnosis in early stages and risk factors contribute to the rapid increase of the disease (Coresh et al., 2002; Bello et al., 2005; El Nahas, 2005). Annual costs of CKD patients are high, and so the disease imposes high costs on each country. Annual costs of CKD patients in the USA exceeded 39.46 million US$ for 2008, equaling 23 percent of healthcare expenditures (Coresh et al., 2002). Despite the high medical costs and advances in dialysis treatments for CKD patients, mortality and morbidity rates of the disease are still high and the patients have a low quality of life (Pickle et al., 1996).

Reviewing the recent literature in MDSSs showed that fuzzy intelligent systems, especially neuro-fuzzy inference systems, have been widely used in predicting the state and progression of various diseases (Ubeyli and Güler, 2005; Parthiban and Subramanian, 2008; Lee and Wang, 2011). Findings of these studies showed that utilizing these expert systems in combination with the knowledge and diagnosis of clinical specialists can significantly reduce diagnostic errors. Such systems yield more accuracy compared with machine learning techniques.

Early diagnosis of CKD disease is a necessary step to reduce or even prevent the progression of renal damage. Because of the covert nature of the disease in early stages, the uncertainties governing the disease's status, and progression resulting from dynamic features of the human body, we need a robust model to accurately predict the disease's progression. To our knowledge there has not been any study using fuzzy intelligent systems to build a DSS to predict the time of renal failure. In this study we propose a MDSS based on the ANFIS system to predict renal failure progression. We first designed three models to predict the worsening time frame of CKD, including linear regression, multilayer perceptron neural network, and ANFIS models to assess their accuracy (data not presented). Among the three predicting models, ANFIS showed the greatest accuracy (more than 95%) in predicting GFR (Norouzi et al., 2016). Therefore, in this study, we used the ANFIS as the core computing model to build an MDSS for predicting renal failure in CKD patients with a user-friendly interface.

In computerized MDSSs different techniques and algorithms can be used, including rule based reasoning, case based reasoning and machine learning techniques (Pandey and Mishra, 2009). Among these methods, various machine learning-based methods have been used in medicine and healthcare, such as decision trees, artificial intelligence network support vector machines, and Bayesian networks. However, fuzzy intelligent techniques have not yet been used to predict worsening renal function. Furthermore, no MDSS is available to monitor kidney disease progression or to predict the appropriate time for renal replacement therapy (RRT) in CKD patients. ANFIS systems have significant potential for predicting systems high in uncertainty and with a highly dynamic nature, such as CKD progression in the human body as the modeled environment (Parthiban and Subramanian, 2008; Ghumbre and Ghatol, 2010).

EXPERIMENTAL SECTION

Patients and Data Collection

All the data of the present study were comprised of the clinical records of a cohort study of newly diagnosed CKD patients who were serially admitted to the Clinic of Nephrology, Imam Khomeini Hospital (Tehran, Iran) during October 2002-October 2011. All the procedures of the present study were approved by the ethics committee of the Tehran University of Medical Sciences, which coincide completely with the Declaration of Helsinki Ethical Principles for Medical Research Involving Human Subjects (General Assembly of the World Medical Association, 2014). Written consent was obtained from all patients who participated in the study. The inclusion criteria for CKD were small-sized kidneys in ultrasound images or GFR <60 cc/kg/min/1.73 m^2 for more than 3 months. All the patients whose records were used for the analysis had visited the clinic for at least 6 months. A total of 465 CKD patients participated in the study. They were divided into two groups according to their adherence patterns to the follow-up schedule in the clinic. The test group consisted of 389 patients who continuously (at least every 6 months) were visited in the clinic. The control group consisted of 76 patients who did not regularly follow their visit schedule in the clinic. The patients whose visits postponed for at least 1 year were categorized as control group.

At each visit, a set of clinical and physiological parameters was recorded and monitored for each patient. The variables included the patient's weight, diastolic and systolic blood pressure, serum creatinine level, fasting plasma glucose, lipid profile, calcium, phosphorus, hemoglobin, uric acid, and GFR. Then, the patients were administered suitable treatments for blood pressure, bone mineral metabolism indices, and hemoglobin control. The GFR was estimated using the Modification of Diet in Renal Disease (MDRD) equation. The end point for the patient's follow-up was a GFR value <15 cc/kg/min/1.73 m^2 or start of RRT or patient death. The MDRD is a formula for estimating GFR based on creatinine and patient characteristics (Levey et al., 1999). This equation is used only for CKD patients, so for acute kidney failure it may result in an inaccurate estimation. All quantitative variables were considered as continuous to have a better training of the model. The recorded clinical and physiological variables along with the demographic data were used to create a dataset. We initially selected 10 variables that were expected to influence the CKD status and progression based on the previous studies and the viewpoints of nephrology specialists (**Figure 1**). These variables were then used as the input of the predicting models to calculate GFR values at future intervals. The variables included age, sex, weight, underlying diseases, diastolic blood pressure, creatinine, calcium, phosphorus, uric acid, and GFR. In next

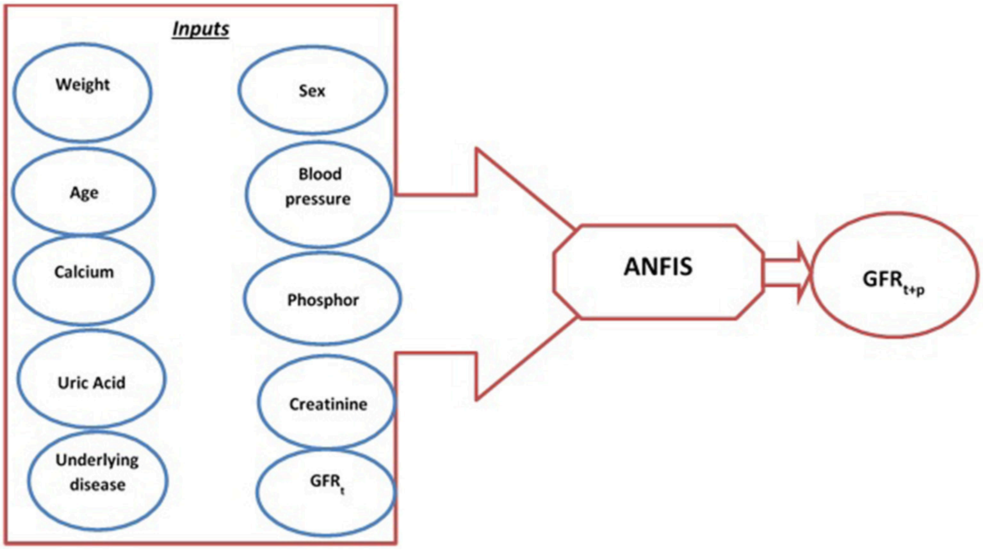

FIGURE 1 | Schematic diagram of predicting model and input variables.

step, Pearson's correlation coefficient test was used to determine the variables that significantly influence the GFR values. The four variables weight, diastolic blood pressure, diabetes mellitus as underlying disease, and current GFR showed significant correlation with GFR values and were selected as the inputs of the GFR predicting models.

To develop an MDSS for predicting renal failure we first should develop a predicting model to forecast the renal failure time and the time frame where kidney disease worsens. According to the clinical measurements (independent physiological parameters) and clinical outcomes, when GFR reaches <15cc/kg/min/1.73 m^2, RRT including dialysis or transplant is necessary for the patient's survival (Gaspari et al., 2004). Regarding the previous studies and clinical data, GFR is the only reliable parameter of renal function and progression of CKD (Gaspari et al., 2004). Therefore, to predict renal failure, GFR values should be predicted over time. Predicting the variations of GFR values, we can predict the time at which the GFR reaches the threshold value of 15 cc/kg/min/1.73 m^2 indicating the time for RRT. The real data recorded during a 10-year period were recorded at 6-month intervals. Therefore, the GFR values were predicted for three sequential 6-month intervals at 6-, 12-, and 18-month intervals. The $GFR_{(t+p)}$ with $p = 1,2,3$ represents the GFR values at 6-, 12-, and 18-month intervals.

We used three predicting models, including improved linear regression, ANFIS, and multilayer perceptron neural networks, to predict the GFR in future time intervals (data not presented). Among the three predicting models, ANFIS was capable of accurately predicting GFR with more than 95% precision (Norouzi et al., 2016). Therefore, ANFIS was used as a core predicting model in building the MDSS.

Model Description

The ANFIS model used in the present study (**Figure 2**) is based on the model proposed by Jang (Jang, 1992), which is a learner network equivalent to the Takagi-Sugeno fuzzy inference system. Learning in this network is a continuous update of the network parameters. Factors of layer I and layer IV are of the learner type. Factors of the first layer determine membership functions. Factors of layer IV determine the first-order estimated function. The ANFIS training algorithm is a hybrid algorithm, which uses the ordinary least squares algorithm to update coefficients of output functions (fi), while the error back propagation algorithm is used to update fundamental factors of the system (Jang, 1992; Jang and Sun, 1997).

The results of our predicting models support the previous findings, which showed a higher predicting efficacy from ANFIS compared to the linear regression and multilayer perceptron neural network (Norouzi et al., 2016). The ANFIS model could predict the GFR values for future 6-month intervals with normalized mean square error lower than 5%. Therefore, the ANFIS model was used to build the MDSS system. The detailed features of the predicting model can be found in Norouzi et al. (2016). In brief, the ANFIS model works as below: Data of 465 CKD patients were divided into training and test datasets. Training data were used to optimize the weights and other parameters in the model. The test data were used to evaluate the quality of estimates and forecasts. In all further processing and modeling, the test dataset was not used for training models. The test data were randomly selected so that all data had an equal chance to participate in the selection process. The test dataset is usually selected from 30 to 40% of the available data. In this study, 30 and 70% of the data were selected as the test and the

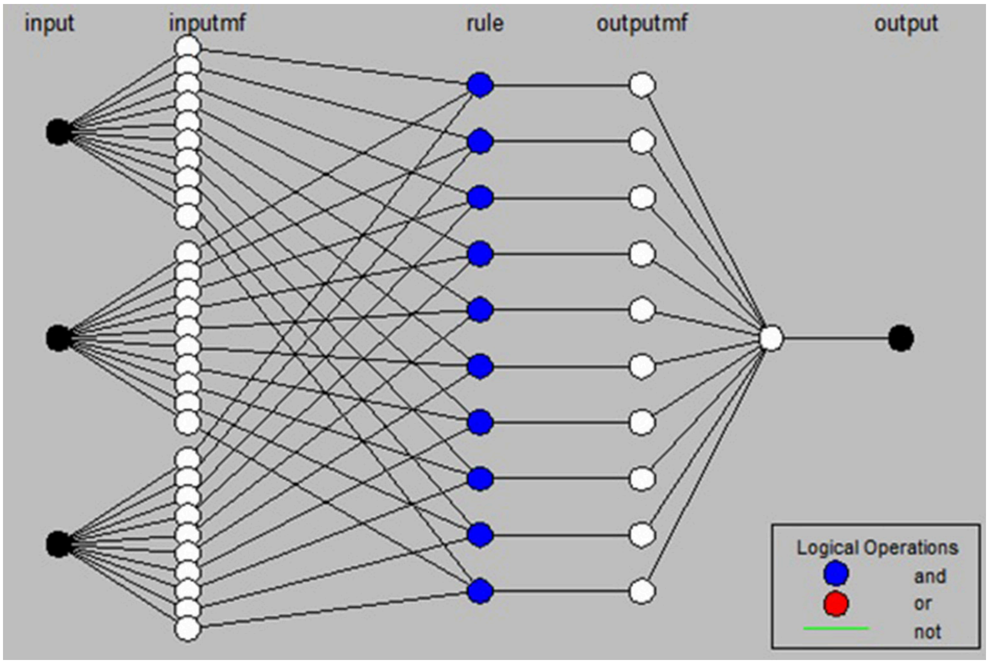

FIGURE 2 | Structure of the ANFIS model used in the present study.

training datasets, respectively. The input variables were fuzzified with Genfis3 code in MATLAB and then a fuzzy rule base was established using the Fuzzy C-Means (FCM) clustering approach. The membership functions of the input variable were created. The resulting fuzzy rules in the rule base were used to estimate GFR values. The membership functions were Gaussian. The fuzzy rules in the rule base build a fuzzy inference system and after training, which was converted to an ANFIS model. The trained ANFIS was used for predicting the GFR values at a 6-month interval and the predicting performance of ANFIS model for training dataset for the 6, 12, and 18-month future intervals was evaluated against the real measured GFR values.

RESULTS

Implementing the MDSS

Regarding the framework and nature of neuro-fuzzy based DSS, whose functions are based on learning, the data of all patients in this study were divided into training and test datasets. The data from the test dataset were used to evaluate the predicting performance of accuracy of the predicting model.

Three criteria were selected to evaluate and compare the accuracy of the two neural network models: Mean Square Error (MSE), Mean Absolute Error (MAE), and Normalized MSE (NMSE). Of them, the NMSE is preferred since it provides the normalized error ranged from 0 to 100 percent. The formula for error criteria is expressed by Equations (1) to (3) as follows:

$$MSE = \frac{\sum_{i=1}^{N} (y_i - \hat{y}_i)^2}{N} \tag{1}$$

$$MAE = \frac{\sum_{i=1}^{N} \left| y_i - \hat{y}_i \right|}{N} \tag{2}$$

$$NMSE = \frac{\sum_{i=1}^{N} (y_i - \hat{y}_i)^2}{\sum_{i=1}^{N} (y_i)^2} \times 100 \tag{3}$$

Table 1 shows the ANFIS predictions of GFR values at sequential $\mathrm{GFR}_{(t+1,\,2,\,3)}$ for the training and test datasets based on the error criteria. The results show that the ANFIS neural network can accurately predict the GFR values for both training and test datasets at all three periods of 6, 12, and 18 months (**Figures 3**, **4**). Despite increasing the predicting interval to 12 and 18 months, the ANFIS was still able to accurately predict the GFR values. Given the low error rate of the test data, the proposed ANFIS could be generalized to predict GFR values in new patients.

Assessment of the MDSS Performance

In addition to GFR prediction, the model produces a fuzzy rule base. The fuzzy rule base converts the complex relationships between experimental inputs and GFR as simple linear models in different modeling environments. The transparency of the GFR membership function in the ANFIS is the advantage of ANFIS compared to other predicting models such as linear regression and multilayer perceptron neural network. The trained ANFIS system could effectively predict the GFR values at sequential 6-, 12-, and 18-month intervals. In assessing the performance of the model, we evaluated the modeling results for different patients through assessing the effects of underlying disease, gender, and initial GFR values. The predicting results showed a different disease progression between male and female CKD patients when the underlying disease was diabetes mellitus + urologic disease (**Figure 5**). The predicted GFR values for male patients reached 7 during the 18-month interval, $\mathrm{GFR}_{(t+3)}$, indicating a failure of renal function (**Figure 5A**). However, female CKD patients showed a $\mathrm{GFR}_{(t+3)}$ value of about 37, indicating the improvement of kidney function (**Figure 5B**). The predicted data followed the real measurements well.

TABLE 1 | Error criteria for the training/test datasets for 6, 12, and 18-month periods i.e., GFR $(_{t+1,2,\text{and}3})$.

		Training dataset	Test dataset
6-month	MSE	58.6253	58.6253
	MAE	4.7654	4.7654
	NMSE	4.7676%	4.7676%
12-month	MSE	54.885	54.885
	MAE	5.5010	5.5010
	NMSE	4.3019%	4.3019%
18-month	MSE	64.0022	64.0022
	MAE	5.9302	5.9302
	NMSE	4.8787%	4.8787%

MSE, Mean Square Error; MAE, Mean Absolute Error; NMSE, Normalized MSE.

Following the performance assessment of the predicting model, we designed a friendly-use graphical user interface (Meguid El Nahas and Bello, 2005) in MATLAB to build an MDSS for predicting the GFR values of CKD patients (**Figures 6A,B**). The MDSS uses the ANFIS model as its core computing model with appropriate topological structure. This system can be used by personnel with no programming or computer knowledge. The user defines the input variables, which are the results of laboratory and clinical assessments, and the system predicts the GFR values at three sequential 6-month intervals. The error of each computation is also represented by the model that helps the physicians to take appropriate decisions on the treatment options for each CKD patient. The model gives the minimum and maximum range of GFR at each interval. The average predicting error of the model, obtained through different comparisons with the real test data, was lower than 5%. The error range of our proposed model is sufficiently low to effectively support medical decisions in CKD management.

DISCUSSION

The present study introduces a new MDSS for monitoring and predicting renal failure progression in CKD patients. We

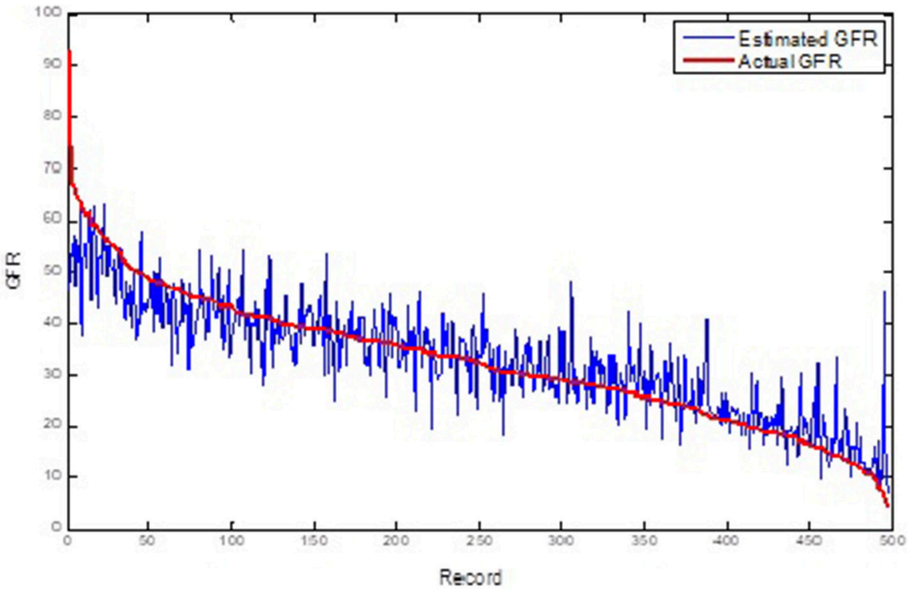

FIGURE 3 | Comparison of the ANFIS prediction and real GFR$_{(}t + 1)$ values for the training dataset.

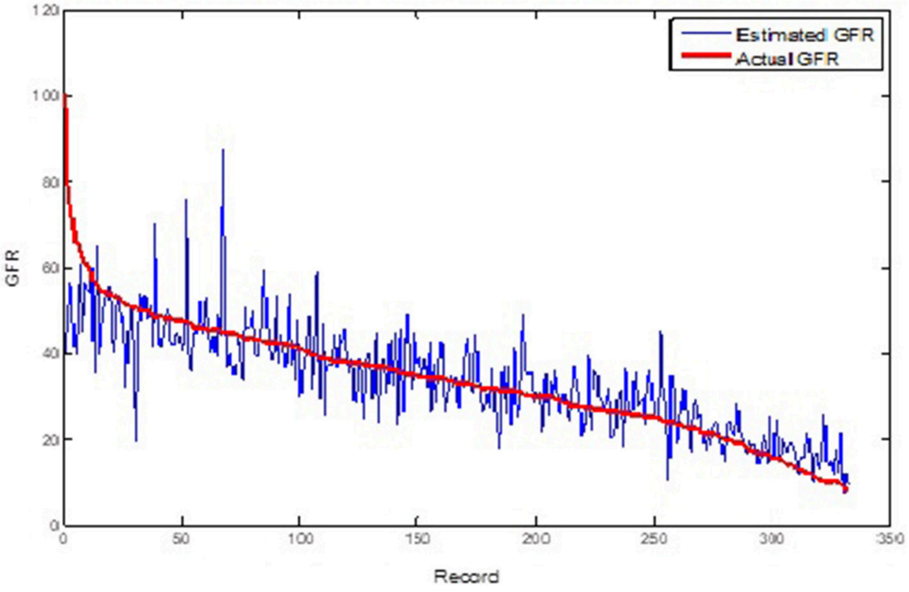

FIGURE 4 | Comparison of the ANFIS prediction and real GFR$_{(}t + 1)$ values for the test dataset.

evaluated the performance of three predicting models: improved linear regression model, MLP, and ANFIS neural networks. Of these, the latter showed the highest accuracy. The user-friendly MDSS was then built based on the predicting model. The MDSS showed high efficiency in predicting the GFR values. This DSS can reduce the cost of CKD management as well as reducing the mortality rate of the disease. In combination with the experience and knowledge of expert nephrologists, the proposed MDSS can significantly improve the quality of life of CKD patients. It is possible to use this system more in practice to help the management team to support patients effectively.

Several authors have attempted to predict the survival time of hemodialysis patients. Among them, Ma (Ma, 2012) worked with artificial neural and neuro-fuzzy models while other authors used machine learning based methods (Brier et al., 2003; Gaspari et al., 2004; Sengur, 2008; Hussain et al., 2011). A comparison of the results mentioned above, alongside ours, allowed us to

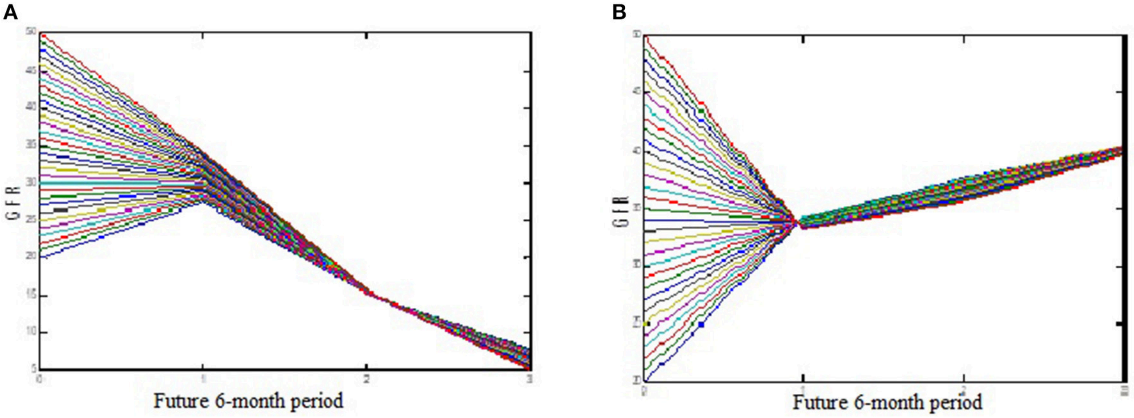

FIGURE 5 | Predicted GFR variation among CKD patients with underlying disease of diabetes mellitus + urologic disease for sequential three 6-month interval. **(A)** Male patient; **(B)** female parient.

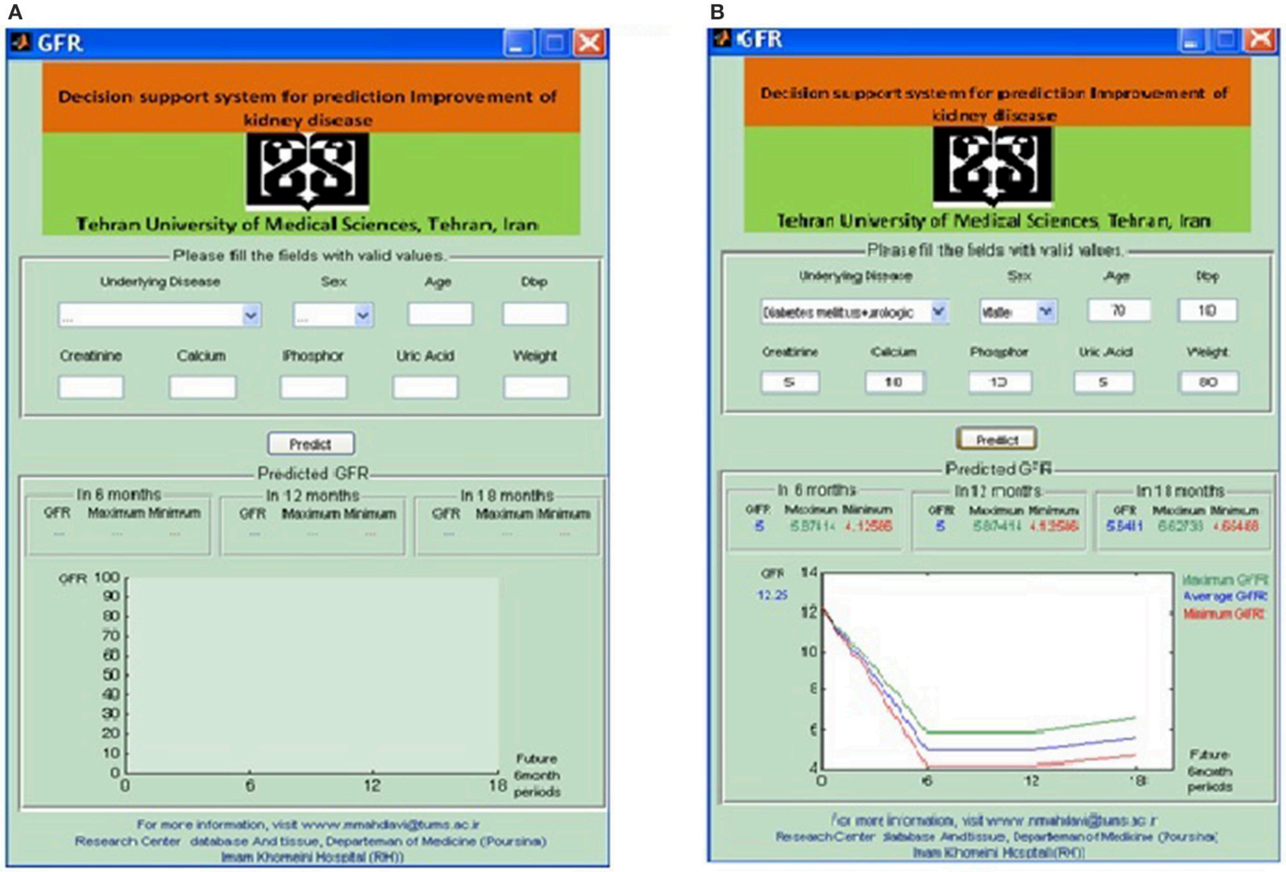

Underlying Disease: Diabetes mellitus+urologic
Sex: Male
Age: 70
Dbp: 10
Creatinine: 5
Calcium: 10
Phosphor: 10
Uric Acid: 5
Weight: 80

	In 6 months			In 12 months			In 18 months	
GFR	Maximum	Minimum	GFR	Maximum	Minimum	GFR	Maximum	Minimum
5	5.87114	4.12586	5	5.87411	4.13586	5.5411	6.62738	4.65488

GFR 12.25

FIGURE 6 | (A) Graphical user interface of the proposed MDSS based in ANFIS predicting model. **(B)** The output of GUI in a test patient.

affirm that our predicting models provide a reliable method to foresee the timeframe of worsening renal function in CKD patients. The strong point of our proposed MDSS was its high reliability in the prediction of GFR. This reliability comes from incorporating sequential measurements of GFR in CKD patients for an extended period of follow up (mean: 37.6 months). However, our DSS needs further improvement to include all influential parameters on CKD progression as well as to improve its ability to predict GFR variations in shorter intervals.

ETHICS STATEMENT

This study was carried out in accordance with the recommendations of Declaration of Helsinki, Ethics committee of Tehran University of Medical Sciences, Tehran, Iran with written informed consent from all subjects. All subjects gave written informed consent in accordance with the Declaration of Helsinki. The protocol was approved by the ethics committee of Tehran University of Medical Sciences, Tehran, Iran.

AUTHOR CONTRIBUTIONS

JN and SM conceptualized the study and provided the resources. JN, SM, and AY performed the methodology and curated the data. JN and AY contributed to the software. JN, SM, AY, ES-A, and FT-M did the validation, investigation and the visualization. JN, AY, ES-A, and FT-M executed the formal analysis, the writing of the manuscript and prepared the original draft. SM, AY, ES-A, and FT-M wrote, reviewed and edited the manuscript. SM provided supervision. JN were responsible for the project administration and the funding acquisition.

FUNDING

This research was funded by Tehran University of Medical Sciences, Tehran, Iran [Grant No.: 18325].

ACKNOWLEDGMENTS

The authors would like to thank Dr. Asadzadeh for his cooperation and technical assistance during the different stages of the present study. This study was financially supported by a grant from Tehran University of Medical Sciences.

REFERENCES

Al-Kasasbeh, R., Korenevskiy, N., Ionescou, F., Alshamasin, M., and Kuzmin, A. (2011). Synthesis of fuzzy logic for prediction and medical diagnostics by energy characteristics of acupuncture points. *J. Acupunct. Meridian Stud.* 4, 175–182. doi: 10.1016/j.jams.2011.09.005

Al-Shayea, Q., El-Refae, G., and Yaseen, S. (2013). Artificial neural networks for medical diagnosis using biomedical dataset. *Int. J. Behav. Healthc. Res.* 4, 45–63. doi: 10.1504/IJBHR.2013.054519

Anagnostou, T., Remzi, M., Lykourinas, M., and Djavan B. (2003). Artificial neural networks for decision-making in urologic oncology. *Eur. Urol.* 43, 596–603. doi: 10.1016/S0302-2838(03)00133-7

Bello, A. K., Nwankwo, E., and El Nahas, A. M. (2005). Prevention of chronic kidney disease: a global challenge. *Kidney Int. Suppl.* 98, S11–7. doi: 10.1111/j.1523-1755.2005.09802.x

Brier, M. E., Ray, P. C., and Klein, J. B. (2003). Prediction of delayed renal allograft function using an artificial neural network. *Nephrol. Dial. Transplant.* 18, 2655–2659. doi: 10.1093/ndt/gfg439

Buchanan, B. G., and Shortliffe, E. H. (1984). *Rule-Based Expert Systems : The MYCIN Experiments of the Stanford Heuristic Programming Project.* Addison-Wesley, University of Michigan.

Coresh, J., Astor, B. C., McQuillan, G., Kusek, J., Greene, T., Van Lente, F., et al. (2002). Calibration and random variation of the serum creatinine assay as critical elements of using equations to estimate glomerular filtration rate. *Am. J. Kidney Dis.* 39, 920–929. doi: 10.1053/ajkd.2002.32765

El Nahas, M. (2005). The global challenge of chronic kidney disease. *Kidney Int*. 68, 2918–2929. doi: 10.1111/j.1523-1755.2005.00774.x

Emam, A., Tonekabonipour, H., Teshnelab, M., and Aliyari Shoorehdeli, M. (2010). "Ischemia prediction using ANFIS," in *2010 IEEE International Conference on Systems, Man and Cybernetics* (Istanbul: IEEE), 4041–4044. doi: 10.1109/ICSMC.2010.5642197

Ercelebi, E., and Subasi, A. (2006). "Classification of EEG for epilepsy diagnosis in wavelet domain using artifical neural network and multi linear regression," in *2006 IEEE 14th Signal Processing and Communications Applications* (Antalya), 1–4. doi: 10.1109/SIU.2006.1659852

Garg, A. X., Adhikari, N. K., McDonald, H., Rosas-Arellano, M. P., Devereaux, P. J., Beyene, J., et al. (2005). Effects of computerized clinical decision support systems on practitioner performance and patient outcomes: a systematic review. *JAMA* 293, 1223–1238. doi: 10.1001/jama.293.10.1223

Gaspari, F., Ferrari, S., Stucchi, N., Centemeri, E., Carrara, F., Pellegrino, M., et al. (2004). Performance of different prediction equations for estimating renal function in kidney transplantation. *Am. J. Transplant.* 4, 1826–1835. doi: 10.1111/j.1600-6143.2004.00579.x

General Assembly of the World Medical Association (2014). World Medical Association Declaration of Helsinki: ethical principles for medical research involving human subjects. *J. Am. Coll. Dent.* 81, 14–8.

Ghumbre, S. U., and Ghatol, A. A. (2010). An intelligent system for hepatitis b disease diagnosis. *Int. J. Comput. Appl.* 32, 455–460. doi: 10.2316/Journal.202.2010.4.202-2874

Hayward, J., Alvarez, S. A., Ruiz, C., Sullivan, M., Tseng, J., and Whalen, G. (2010). Machine learning of clinical performance in a pancreatic cancer database. *Artif. Intell. Med.* 49, 187–195. doi: 10.1016/j.artmed.2010.04.009

Hunt, D. L., Haynes, R. B., Hanna, S. E., and Smith, K. (1998). Effects of computer-based clinical decision support systems on physician performance and patient outcomes: a systematic review. *JAMA* 280, 1339–1346. doi: 10.1001/jama.280.15.1339

Hussain, M., Wajid, S. K., Elzaart, A., and Berbar, M. (2011). "A comparison of SVM kernel functions for breast cancer detection," in *Computer Graphics, Imaging and Visualization (CGIV), 2011 Eighth International Conference on* (Singapore: IEEE), 145–150. doi: 10.1109/CGIV.2011.31

Jang, J.-S. (1992). *Neuro-Fuzzy Modeling: Architectures, Analyses, and Applications.* Berkeley: University of California.

Jang, J.-S. R. (1993). ANFIS: adaptive-network-based fuzzy inference system. *IEEE Trans. Syst. Man. Cybern.* 23, 665–685. doi: 10.1109/21.256541

Jang, J.-S. R., and Sun, C.-T. (1997). *Neuro-fuzzy and Soft Computing: A Computational Approach to Learning and Machine Intelligence.* Upper Saddle River, NJ: Prentice-Hall, Inc.

Krug, D., Elger, C. E., and Lehnertz, K. (2008). "A CNN-based synchronization analysis for epileptic seizure prediction: Inter- and intraindividual generalization properties," in *Proc. IEEE International* Workshop on *Cellular Neural Networks and their Applications* (Santiago de Compostela), 92–95. doi: 10.1109/CNNA.2008.4588656

Lauer, R. T., Smith, B. T., and Betz, R. R. (2005). Application of a neuro-fuzzy network for gait event detection using electromyography in the child with cerebral palsy. *IEEE Trans. Biomed. Eng.* 52, 1532–1540. doi: 10.1109/TBME.2005.851527

Lee, C. S., and Wang, M. H. (2011). A fuzzy expert system for diabetes decision support application. *IEEE Trans. Syst. Man, Cybern. Part B* 41, 139–153. doi: 10.1109/TSMCB.2010.2048899

Levey, A. S., Bosch, J. P., Lewis, J. B., Greene, T., Rogers, N., and Roth, D. (1999). A more accurate method to estimate glomerular filtration rate from serum creatinine: a new prediction equation. Modification of diet in renal disease study group. *Ann. Intern. Med.* 130, 461–70. doi: 10.7326/0003-4819-130-6-199903160-00002

Ma, T. M. (2012). *Local and Personalised Modelling for Renal Medical Decision Support System*. Available online at: http://aut.researchgateway.ac.nz/handle/10292/4472.

Meguid El Nahas, A. M., and Bello, A. K. (2005). Chronic kidney disease: the global challenge. *Lancet* 365, 331–340. doi: 10.1016/S0140-6736(05)17789-7

Miller, R. A. (1994). Medical diagnostic decision support systems–past, present, and future: a threaded bibliography and brief commentary. *J. Am. Med. Inform. Assoc*. 1, 8–27.

Montgomery, A. A., Fahey, T., Peters, T. J., MacIntosh, C., and Sharp, D. J. (2000). Evaluation of computer based clinical decision support system and risk chart for management of hypertension in primary care: randomised controlled trial. *BMJ* 320, 686–90. doi: 10.1136/bmj.320.7236.686

Norouzi, J., Yadollahpour, A., Mirbagheri, S. A., Mazdeh, M. M., and Hosseini, S. A. (2016). Predicting renal failure progression in chronic kidney disease using integrated intelligent fuzzy expert system. *Comput. Math. Methods Med.* 2016:6080814. doi: 10.1155/2016/6080814

Nugent, R. A., Fathima, S. F., Feigl, A. B., and Chyung, D. (2011). The burden of chronic kidney disease on developing nations: a 21st century challenge in global health. *Nephron Clin. Pract.* 118, c269–c277. doi: 10.1159/000321382

Ohlsson, M. (2004). WeAidU-a decision support system for myocardial perfusion images using artificial neural networks. *Artif. Intell. Med.* 30, 49–60. doi: 10.1016/S0933-3657(03)00050-2

Pandey, B., and Mishra, R. B. (2009). Knowledge and intelligent computing system in medicine. *Comput. Biol. Med.* 39, 215–230. doi: 10.1016/j.compbiomed.2008.12.008

Parthiban, L., and Subramanian, R. (2008). Intelligent heart disease prediction system using CANFIS and genetic algorithm. *Citeseer*. Available online at: http://citeseerx.ist.psu.edu/viewdoc/download?doi=10.1.1.451.9421&rep=rep1&type=pdf (Accessed July 20, 2018).

Pickle, L. W., Mungiole, M., Jones, G. K., and White, A. A. (1996). Atlas of United States Mortality. Available onlie at: https://www.cdc.gov/nchs/data/misc/atlasmet.pdf (Accessed July 20, 2018).

Sengur, A. (2008). An expert system based on principal component analysis, artificial immune system and fuzzy k-NN for diagnosis of valvular heart diseases. *Comput. Biol. Med.* 38, 329–338. doi: 10.1016/j.compbiomed.2007.11.004

Smith, A. E., Nugent, C. D., and McClean, S. I. (2003). Evaluation of inherent performance of intelligent medical decision support systems: utilising neural networks as an example. *Artif. Intell. Med.* 27, 1–27. doi: 10.1016/S0933-3657(02)00088-X

Ubeyli, E. D., and Güler, I. (2005). Automatic detection of erthemato-squamous diseases using adaptive neuro- fuzzy inference systems. *Comput. Biol. Med.* 35, 421–433. doi: 10.1016/j.compbiomed.2004.03.003

Yadollahpour, A., and Jalilifar, M. (2014). Seizure prediction methods: a review of the current predicting techniques. *Biomed. Pharmacol. J.* 7, 153–162. doi: 10.13005/bpj/466

Zhao, Y., Healy, B. C., Rotstein, D., Guttmann, C. R., Bakshi, R., Weiner, H. L., et al. (2017). Exploration of machine learning techniques in predicting multiple sclerosis disease course. *PLoS ONE* 12: e0174866. doi: 10.1371/journal.pone.0174866

Conflict of Interest Statement: The authors declare that the research was conducted in the absence of any relationships that could be construed as a potential conflict of interest.

Copyright © 2018 Yadollahpour, Nourozi, Mirbagheri, Simancas-Acevedo and Trejo-Macotela. This is an open-access article distributed under the terms of the Creative Commons Attribution License (CC BY). The use, distribution or reproduction in other forums is permitted, provided the original author(s) and the copyright owner(s) are credited and that the original publication in this journal is cited, in accordance with accepted academic practice. No use, distribution or reproduction is permitted which does not comply with these terms.

frontiers
in Physiology

ORIGINAL RESEARCH
published: 08 May 2018
doi: 10.3389/fphys.2018.00493

Check for updates

Reducing the Number of Individuals to Monitor Shoaling Fish Systems – Application of the Shannon Entropy to Construct a Biological Warning System Model

Harkaitz Eguiraun[1,2]*, Oskar Casquero[3], Asgeir J. Sørensen[4] and Iciar Martinez[2,5,6]

[1] Department of Graphic Design & Engineering Projects, Faculty of Engineering in Bilbao, University of the Basque Country UPV/EHU, Bilbao, Spain, [2] Research Centre for Experimental Marine Biology and Biotechnology – Plentziako Itsas Estazioa, University of the Basque Country UPV/EHU, Plentzia, Spain, [3] Department of Systems Engineering and Automatic Control, Faculty of Engineering in Bilbao, University of the Basque Country UPV/EHU, Bilbao, Spain, [4] Centre for Autonomous Marine Operations and Systems, Department of Marine Technology, Norwegian University of Science and Technology, Trondheim, Norway, [5] IKERBASQUE Basque Foundation for Science, Bilbao, Spain, [6] Norwegian College of Fishery Science, Faculty of Biosciences, Fisheries and Economics, University of Tromsø, Tromsø, Norway

OPEN ACCESS

Edited by:
Sladjana Z. Spasić,
University of Belgrade, Serbia

Reviewed by:
Gonzalo Marcelo Ramírez-Avila,
Universidad Mayor de San Andrés, Bolivia
Hector Zenil,
Karolinska Institute (KI), Sweden

***Correspondence:**
Harkaitz Eguiraun
harkaitz.eguiraun@ehu.eus

Specialty section:
This article was submitted to Fractal Physiology, a section of the journal Frontiers in Physiology

Received: 28 February 2018
Accepted: 18 April 2018
Published: 08 May 2018

Citation:
Eguiraun H, Casquero O, Sørensen AJ and Martinez I (2018) Reducing the Number of Individuals to Monitor Shoaling Fish Systems – Application of the Shannon Entropy to Construct a Biological Warning System Model. Front. Physiol. 9:493. doi: 10.3389/fphys.2018.00493

The present study aims at identifying the lowest number of fish (European seabass) that could be used for monitoring and/or experimental purposes in small-scale fish facilities by quantifying the effect that the number of individuals has on the Shannon entropy (SE) of the trajectory followed by the shoal's centroid. Two different experiments were performed: (i) one starting with 50 fish and decreasing to 25, 13, and 1 fish, and (ii) a second experiment starting with one fish, adding one new fish per day during 5 days, ending up with five fish in the tank. The fish were recorded for 1h daily, during which time a stochastic event (a hit in the tank) was introduced. The SE values were calculated from the images corresponding to three arbitrary basal (shoaling) periods of 3.5 min prior to the event, and to the 3.5 min period immediately after the event (schooling response). Taking both experiments together, the coefficient of variation (CV) of the SE among measurements was largest for one fish systems (CV 37.12 and 17.94% for the daily average basal and response SE, respectively) and decreased concomitantly with the number of fish (CV 8.6–10% for the basal SE of 2 to 5 fish systems and 5.86, 2.69, and 2.31% for the basal SE of 13, 25, and 50 fish, respectively). The SE of the systems kept a power relationship with the number of fish (basal: R^2 = 0.93 and response: R^2 = 0.92). Thus, 5–13 individuals should be the lowest number for a compromise between acceptable variability (<10%) in the data and reduction in the number of fish. We believe this to be the first scientific work made to estimate the minimum number of individuals to be used in subsequent experimental (including behavioral) studies using shoaling fish species that reaches a compromise between the reduction in number demanded by animal welfare guidelines and a low variability in the fish system's response.

Keywords: fish monitoring, biological warning systems, fish welfare, the 3Rs, Shannon entropy, non-linear signal processing, non-invasive monitoring, intelligent aquaculture

INTRODUCTION

Large scale production aquaculture platforms, such as offshore exploitations, alone or within offshore multipurpose structures, are considered to hold the key to solve some of the challenges that must be addressed in order to increase the total production and the efficiency of fish farming to provide food for the exponentially growing human population (Bostock et al., 2010; Anon, 2011; European Aquaculture Technology and Innovation Platform-Eatip, 2012; Kalogerakis et al., 2015; FAO, 2016). One requisite for the optimal functionality of such production platforms is the implementation of intelligent structures that should be able to identify, register and respond to changing external and internal environments. In answer to this need and to improve the farmer's ability to monitor, control and document biological processes in fish farms by applying control-engineering principles, the concept of precision fish farming (PFF) has been introduced (Føre et al., 2018). Unfortunately, in contrast to the increasing amount of works devoted to the study of the physical and intelligent design of the farming structures, there are few published works devoted to the automatic monitoring of the real fish being farmed and to the integration of that information into the whole intelligent system (Eguiraun et al., 2015). Monitoring of the fish behavior is important for at least three main reasons: (i) to avoid escapes, (ii) for the early detection of abnormalities in their behavior that may be an indication of disease, parasites or the presence of contaminants that may compromise their health and wholesomeness, and (iii) to document the fish welfare during the production.

Fish cognition and behavior is a well-established research field (Vila Pouca and Brown, 2017 and references therein), and the characterisation of fish model systems' behavior, using behavioral measurable changes, has found several practical applications, such as the detection of leaders in a group (Mwaffo et al., 2017), the identification of information flows within a school of fish (Crosato et al., 2018), the presence in the aquatic environment of contaminants including caffeine (Ladu et al., 2015), drugs (Liu et al., 2011), hypochlorite (Magalhães et al., 2007; Nimkerdphol and Nakagawa, 2008; Teles et al., 2015), methyl-mercury (Eguiraun et al., 2014, 2016), the Se:Hg molar ratio in their feeds (Eguiraun et al., 2018) and alterations in environmental parameters such as hypoxia, feeding regime (Polonschii et al., 2013), and high fish density (Papoutsoglou et al., 1998; Di Marco et al., 2008).

Consequently, and following Hellou's (2011) recommendations to assess the environmental quality of water, Eguiraun et al. (2015) recommended the implementation of biological warning system (BWS) into aquaculture by using fish of the same species being cultivated as the system's sensor. The working hypothesis was that undesirable agents capable of altering biochemical and/or physiological processes of the fish would also alter the Shannon entropy (SE) of the system in a quantifiable manner (as shown by Eguiraun et al., 2014), and that this alteration could be used as an indicator of a deviation from the desired working point established by the fish farmer. Once the farmer detects a deviation, a series of pre-established rules included in the obligatory Hazard Analysis and Critical Control Point plan of each facility must be followed.

Each cage may hold several hundred thousand fish in intensive farming, i.e., up to several million fish per farm (Føre et al., 2018), which complicates the monitoring of all fish for control purposes. Therefore, to implement the BWS in an effective manner, one alternative is to construct a small-scale facility with fish of the same characteristics and subject to the same conditions as those in the commercial farming cages. Such a small-scale monitoring set-up would resemble and impose similar demands to the set-up for experimental studies with fish. These demands include respecting the ethical principles (Russell and Burch, 1959) and legal framework (European Commission, 2010) concerning the 3Rs. These three Rs (3Rs), necessary for a more ethical use of animals in testing, were initially mentioned by Russell and Burch (1959). They stand for Replacement: the adoption of methods which avoid or replace the use of animals in research (for example the use of mathematical models to study animal behavior instead of using live organisms); Reduction: the application of methods to obtain adequate information from fewer animals, or to obtain more information from the same number of animals and Refinement: the use of methods to eliminate or minimize potential pain, suffering or distress, and enhance animal welfare for the animals used. The present work can only contribute to the Reduction in the number of individuals for procedures that demand the use of live fish. To identify this lowest possible number is in itself a challenge, since there is usually no explanation regarding the criteria used to select the number of fish in physiological and toxicological experiments. The studies published on the effect of perturbations on fish systems, as well as behavioral studies, use different numbers of fish: some use only one fish (Magalhães et al., 2007; Brodin et al., 2013), while others use three fish (Teles et al., 2015), five fish (Crosato et al., 2018), fewer than 15 fish (Krause, 1993; Huth and Wissel, 1994; Krause and Tegeder, 1994; Ladu et al., 2015), 18–40 fish (Sadoul et al., 2014), 19–26 fish (Eguiraun et al., 2016), 30–300 fish (Tunstrøm et al., 2013), and 81 fish (Eguiraun et al., 2014). However, we have not been able to find any publication providing any scientific explanation about the reasons that led the authors to use those particular numbers of individuals.

In order to select the number of fish to test, the shoaling nature of the species must be taken into consideration. Studies on the collective behavior of different species have indicated that many observed features of social interactions can be predicted assuming that the individuals follow behavioral rules that maximize their entropy (Mann and Garnett, 2015) and that the collective behavior is determined by the number of topologically interacting neighbors, as proposed by Ballerini et al. (2008). These authors reconstructed 3D positions of airborne birds in flocks of thousands of individuals and showed that their interactions were based on their topological, and not metrical, distance, i.e., each bird interacted on average with a fixed number of neighbors (6–7), and not with all the neighbors within a fixed metric distance. Examples of interactions are orientation toward other fish, collective swarming, schooling, or flocking behaviors. Thus, in flocking starlings, each individual topologically interacts with 6–8 neighbors and the interaction with about 10 neighbors speeds up the rate of convergence (both speed and time to initiate the flocking behavior) irrespective of the total size of the swarm (Shang and Bouffanais, 2014). Studies on the social behavior of fish (Hemelrijk, 2002) indicate that fish schooling behavior emerge from the interaction of at least four neighbors (Huth and Wissel, 1994) and Crosato et al. (2018) used five fish to examine their interactions during the performance of U-turns in a circular tank of water. Consequently, considering the shoaling nature of the European seabass (*Dicentrarchus labrax*), our hypothesis was that there would be critical differences between the SE of, on one hand, the basal (shoaling) behavior of the systems of only one fish and those of more than one fish, and, on the other, the SE of the response to the event (schooling) of systems with fewer than five fish and systems with five or more fish (Huth and Wissel, 1994).

Accordingly, and given that previous studies (Kadota et al., 2011; Liu et al., 2011; Spasic et al., 2011; Quach et al., 2013; Bae and Park, 2014; Eguiraun et al., 2014, 2016, 2018; Forlim and Pinto, 2014) have identified the SE of the system as a variable with the potential to serve for fish health and welfare monitoring, the present work was designed to understand how the variation in the fish number affects the system dynamics in order to answer the following research questions: (i) Does the SE of a fish system vary according to the number of fish? (ii) if it does vary, how is this relationship? and, finally (iii) is it possible to identify the lowest number of individuals which could be used in monitoring and/or experimental settings? To answer these questions two different experiments were performed: (i) one experiment starting with 50 fish and decreasing the number to 25, 13, and finally one fish, and (ii) a second experiment, studying the system with initially one fish, then adding one new fish per day during 5 days, and ending with five fish in the tank.

Based on the experimental results, the main scientific contribution of the present work is to provide a key piece of information to set up a BWS, namely the minimum number of fish necessary to be monitored. The last part of this study presents a theoretical BWS model that integrates all the empirical knowledge obtained in order to provide results, in a non-invasive manner, about the health status of monitored or experimental fish.

MATERIALS AND METHODS

Ethics Statement

The experimental protocols and procedures conducted in the present experiment had been approved by The Ethical Committee of the University of the Basque Country UPV/EHU for Animal Welfare No. CEBA/285/2013MG.

Animals and Acclimation Conditions

European sea bass (*Dicentrarchus labrax*) generously provided by Grupo Tinamenor (Cantabria, Spain) had been acclimated in the Research Centre for Experimental Marine Biology and Biotechnology – Plentzia Marine Station of University of the Basque Country UPV/EHU for 3 months in two flow-through 1,800 L epoxy-coated fiberglass tanks containing aerated, naturally sand filtered seawater pumped from the Cantabric Sea in the North of the Iberian Peninsula (43°24′49.5′′N 2°57′06.5′′W). During this period, the seawater conditions oscillated according to the natural environmental variation, and they were always within the values for optimal growth for the species. The fish were fed INICIO Plus feed from BioMar (56% crude protein, 18% crude fat) following the manufacturer specifications for fish size, biomass and water temperature.

The length and weight of the fish used in Experiment A are shown in **Table 1** and the approximate total biomass for Experiment B is shown in **Table 2**. Fish of this size are considered sexually immature (Pickett and Pawson, 1994; Fishbase.org, 2015).

Experimental Conditions

The salinity was measured using a multiparametric meter HANNA HI98192 and the O_2 saturation with the JBL O_2 kit. Water temperature, pH, and ammonium were monitored daily in both tanks using a thermometer (±0.5°C), a CRISOM pH-meter Basic 20+ and Sera NH_4-NH_3 ammonium kit, respectively. The values are shown in **Table 3**. Water flow (fixed at 0.54 m^3/h) and additional air supply diffused by stone were kept constant and were interrupted, in order to avoid artifacts in the images, only during the time necessary to record the fish. The experiments were performed in the period November-December during which only small variations were detected in the seawater temperature and pH following the usual seasonal changes.

Two identical fiberglass tanks were used (100 cm × 100 cm × 90 cm) under direct white artificial light (2 × 58 W

TABLE 1 | Experiment A.

***n* = 50 fish**	**Tank 1**		**Tank 2**	
	Size [mm]	**Weight [g]**	**Size [mm]**	**Weight [g]**
Avg	159.5	36.02	158.1	35.28
Max	200.0	60.00	197.0	64.00
Min	135.0	18.00	130.0	17.00
Median	154.5	33.50	156.0	33.00
Total biomass		1,801		1,764

Biomass at the beginning of the experiment. Tanks 1 and 2 were filled with 50 fish each. Data on individual fish are shown in Supplementary Data Sheet S1.

TABLE 2 | Experiment B.

Day number	**Tank 1**		**Tank 2**	
	Fish name	**Total biomass [g]**	**Fish names**	**Total biomass [g]**
1	*a*	77	*b*	78
2	*c*	51	*a,b*	155
3	*d*	53	*a,b,c*	206
4	*e*	58	*a,b,c,d*	259
5	*f*	53	*a,b,c,d,e*	312

Daily biomass in Tank 1. The biomass in Tank 2 is an approximation estimated by adding the weights of the fish coming from Tank 1, but the individual fish were not taken out of the Tank 2 and weighted every day.

TABLE 3 | Water/environmental conditions.

	Min	Max
Temperature [°C]	16.9	18.5
pH	7.76	7.93
Ammonium	0.0	0.0
Water flow [m^3/h]	0.54	0.54
Salinity [g/l]	33	33
O_2 Saturation	>80%	>80%

Minimum and maximum values in relevant seawater parameters during the experimental period (November–December). Daily values are listed in Supplementary Data Sheet S2.

and 5,200 lm), avoiding the formation of shadows into the tanks and using the same light conditions in both. The tanks, equipped with a flow through system, were filled up to 81 cm from the upper border with 810 L of naturally sand filtered seawater. One camera was placed in each tank and exactly in the same position in both tanks, obtaining in both situations the same visual angle. The photoperiod was fixed at 12h/12h dark/light.

Experimental Set-Up

Experiment A was performed reducing the number of fish to imitate the usual procedure in many physiological and toxicological experiments. The fish are exposed to a given condition or contaminant and every x-days a certain number of fish (usually between 10 and 20, depending on the type of analyses to be performed, their cost and the expected variability of the parameter measured) are removed and sacrificed to perform biochemical and histological analyses, while the rest remains in the tank. After a new period of x-days the same number of fish is removed and so on. This is usually done to examine the effect of the contaminant, or the treatment, along time. In addition, we were interested in having more replicates of the measurements in tanks with only one fish, because, if it was a reliable system, that would be the most convenient from the point of view of reducing costs and animal suffering, and because many protocols use only one-fish to perform diverse studies, as mentioned in the introduction. Therefore, Experiment B was designed with two purposes: firstly, to obtain more replicates from one-fish system, but using different individual fish, and, secondly, to study the behavior of the system for 1–5 individuals, since Experiment A did not cover than range. In both, A and B Experiments, however, the individuals came from a larger group of fish and had been acclimated for at least 23 h to the identical settings as those used for this study.

Experiment A – Systems With 1 to 50 Fish

Each of the two replicate groups consisted of 50 fish with a biomass as similar to each other as possible (**Table 1**). The fish were acclimated for 12 days to the new conditions, and they were monitored and recorded during the next 5 days following the procedure described below. After that, both groups were reduced to 25 fish, trying to maintain a similar biomass in both groups. The remaining 25 fish per group were acclimated for another 2.5 days and subsequently monitored and recorded for 5 days. Past those 5 days both groups were reduced to 13 fish per group, acclimated for 2.5 days and recorded for 5 days. Finally, the groups were reduced to only one fish. Again, after 2.5 days of acclimation, they were recorded for the final 5 days of the experiment (**Figure 1**).

Experiment B – Systems With 1–5 Fish

The experimental schedule is shown in **Figure 2**. In this particular case and during the 5 days the experiment lasted, tank 1 had only one fish and every day the fish that had been 1 day in tank 1 was transferred to tank 2, and a new fish was placed in tank 1. The new fish introduced every day in the experimental tank was taken from the acclimation tank not used for the experiments. All fish had an acclimation period of 23 h to the new experimental conditions. For a better understanding of the procedure, each fish has been named with a letter from *a* to *f* in **Figure 2** and **Table 2**. The approximate biomass is summarized in **Table 2**.

Data Acquisition

Data acquisition was done by video camera as described in Eguiraun et al. (2014). In short, recording was performed using a GoProHero3 camera with underwater housing inside each tank. Raw data were recorded in 1080p high definition format, 24 frames per second (fps) and 16:9 video size and it was stored in SanDisk 32Gb UltraMicroSDHCTM (Class 10) secure cards.

As already mentioned, the water flow and air intake were halted during the recording period to avoid bubbles and disturbances in the images. Recording was set to 1 h per day and

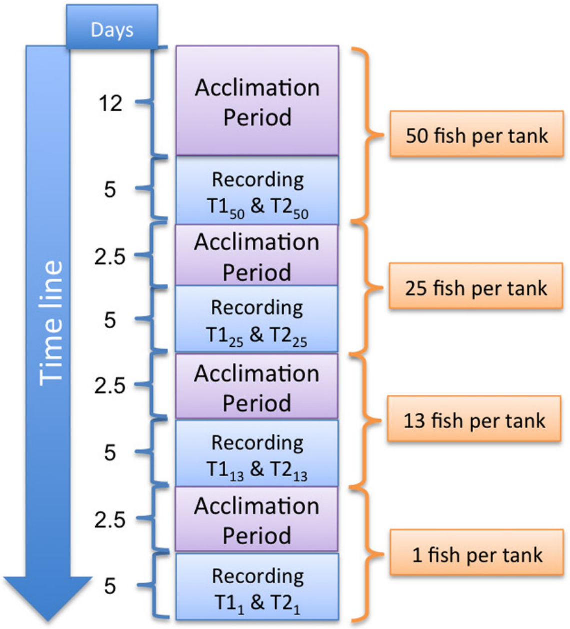

FIGURE 1 | Description of Experiment A. The fish number is halved in each step except the last one, when it was reduced from 5 to 1 individual. T1 and T2 indicate tank 1 and 2, respectively, and the sub-index the number of fish. The number of days the activities lasted is shown under "Days" on the left.

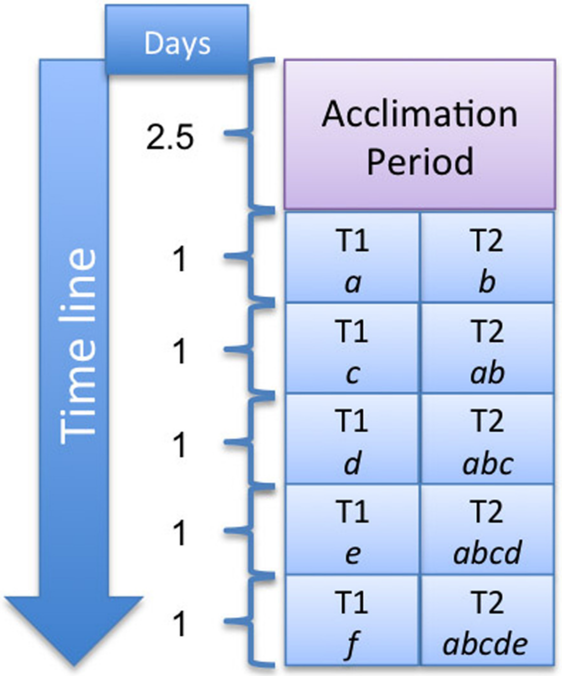

FIGURE 2 | Description of Experiment B. The fish number is kept constant, only one fish, in tank 1. Each day the fish that had been for 1 day in tank 1 was transferred to tank 2. Thus, the number of fish in tank 2 increased by one individual every day. T1 and T2 indicate tank 1 and 2, respectively. The number of days the activity lasted is shown under "Days" on the left; each letter within the tanks, *a*, *b*, *c*, *d*, *e,* and *f* refer to an individual fish.

approximately in the middle of that period a stochastic event (a disturbance) consisting of a hit in the tank was introduced. The disturbance is a stochastic event, because it is meant to occur in a random manner, i.e., the fish must not be able to predict when it will take place The images to be processed consisted of three measures of the basal state, of 3.5 min each, and the 3.5 min after the disturbance, as described in Eguiraun et al. (2014) and in **Figure 3**.

Image Post-processing

It was performed as described by Eguiraun et al. (2014). Once the four video clips (three arbitrary clips of the basal state and one clip containing the system's response to the event) per tank and per day were located in the 1 h recording, they were transformed into a 640 pixel × 480 pixel format image sequences per video clip at 24 fps using the iMovie commercial software and MPEG Streamclip free software. Subsequent image and feature extraction were carried out with MATLAB R2014a (MathWorks Inc.) running on a MacBookPro 2,6 GHz Intel Core i7 laptop with a SSD storage disk and 16 Gb of RAM. The procedure used for image and feature extraction is detailed in Supplementary Data Sheet S3.

Trajectory Estimation

The methodology used from image acquisition to fish group centroid trajectory estimation is depicted in **Figure 4** and was based on that described in Eguiraun et al. (2014) with the modifications detailed in Supplementary Data Sheet S4 and already used in Eguiraun et al. (2016). It was performed using MATLAB R2014a (MathWorks Inc.). Firstly, the trajectory of the cluster's centroid was built computing the elements center's in every single frame, which led to a very noisy signal unsuitable for the subsequent non-linear signal analysis. Thus, the noise of the signal was reduced calculating the cluster's centroid applying the K-means algorithm to the number of elements in each frame using the centers of the elements in the first frame as input coordinates. Secondly, the trajectories in X and Y were analyzed in the same format they were obtained although they have different scale dimensions. X trajectories have dimension from 0 to 640 and Y trajectories have dimension from 0 to 480 due to the 640 × 480 pixel image size. The results indicated that analyzing those raw trajectories leads to satisfactory results and differences were not found between the results obtained analyzing the raw and the normalized trajectories. However, and with the purpose of building a more robust algorithm for future applications, the X and Y trajectories presented in the current work were normalized using Z-score technique. Supplementary Data sheet S5 contains the data for each of the 200 calculated trajectories.

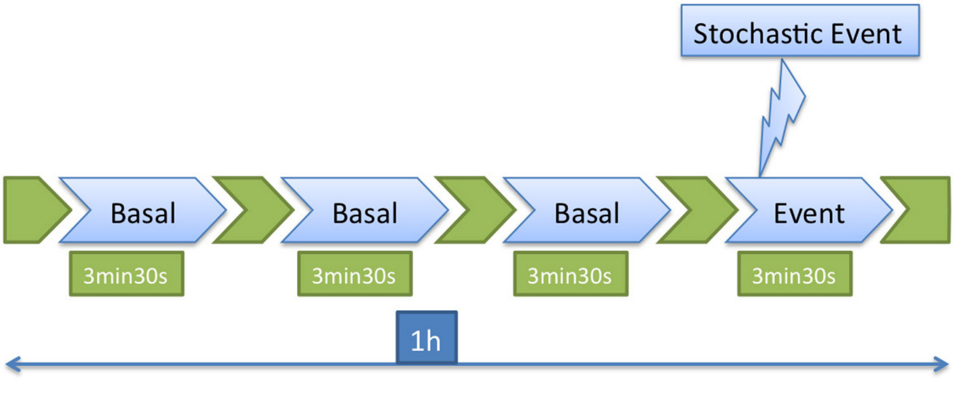

FIGURE 3 | Recording procedure. Three basal and one event response measurements were processed from the total recorded period of 1 h.

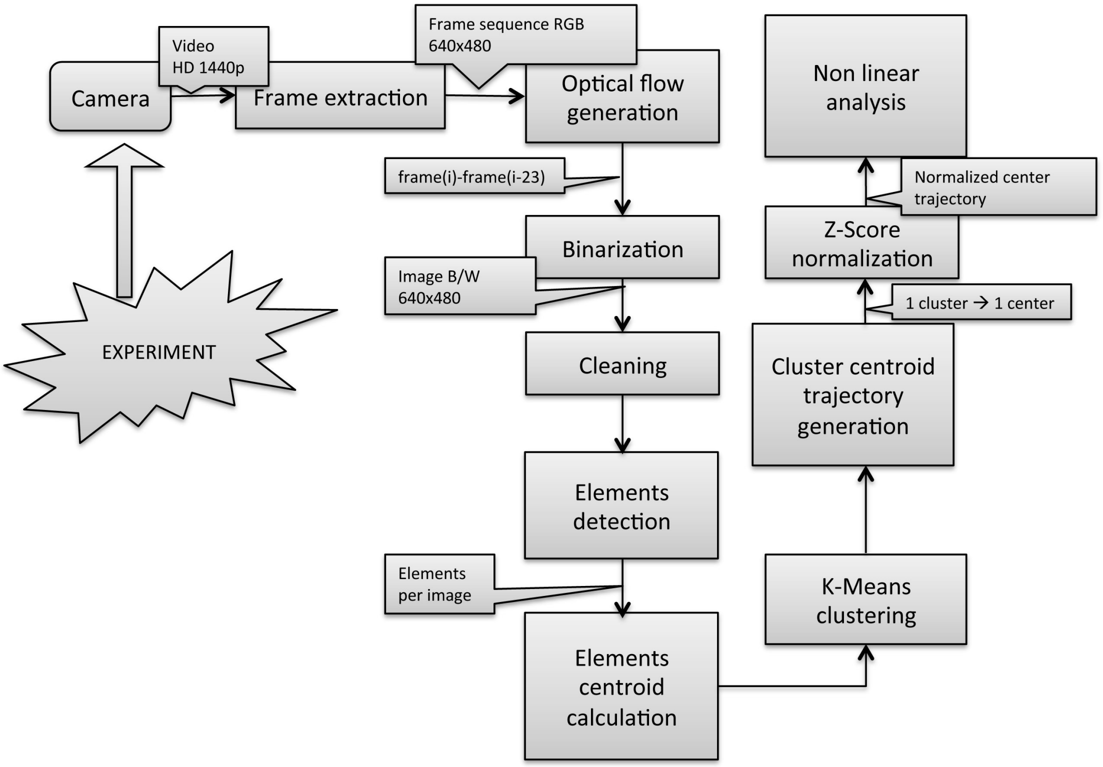

FIGURE 4 | Data acquisition and processing workflow. Taken from Eguiraun et al. (2016).

Non-linear Trajectory Analysis

Shannon entropy has been used because our previous work (Eguiraun et al., 2014) showed it to be the most sensitive among five algorithms tested, namely: Shannon and permutation entropies, and Katz, Higuchi, and Katz-Castiglioni's fractal dimensions, to serve as a tool for the non-invasive quantification of fish responses and has subsequently been successfully applied to the study of the effect of certain chemicals (methylmercury and sodium selenite) on the complexity of the seabass centroid trajectories (Eguiraun et al., 2014, 2016, 2018). The Shannon entropy was initially described as an expression of the amount of missing information within a message, since the concept of entropy, within this particular context, was developed by Shannon in his works on a mathematical theory of communication (Shannon, 1948, 1951). Thus, the SE is a measure of the predictability of the value of a variable. The variable in our case is a time series consisting of samples constructed as successive positions of the fishes' cluster's centroid (x_i,y_i) in the frame of the image (640 pixels × 480 pixels; i.e., $0 < x_i < 640$ and $0 < y_i < 480$). If the predictability of the value of variables (x and y) is high, then the SE is low (i.e., if, knowing the values of x_{i-1} and y_{i-1}, then it is easy to predict x_i and y_i, respectively). On the other hand, the higher the difficulty to predict x_i and y_i, the higher the SE. Thus, the highest SE will correspond to a system whose centroid may jump from any one position to any other one from frame to frame (i.e., all the pixels will have the same probability (1/640 will be the probability for every x_i and 1/480 for every y_i). The lowest SE will correspond to a system whose centroid moves in a completely predictable manner: the centroid will occupy some few positions with a very high probability and the probability of occupying any other position will be practically zero. A real-life system will be somewhere between these two extremes.

We are aware of the fact that SE is not the optimal algorithm to explain sophisticated mental or behavioral processes, but we wish to stress that it is not our aim to study complex behavioral characteristics, as may be the orientation of the individuals, their interactions, how the shoal is formed, the presence of leaders, how the information flows among the individuals initiation and characteristics of collective behavior, etc. That kind of complex studies requires a completely different technical set up regarding image acquisition, data extraction, and analysis (see all the above mentioned papers on collective behavior and Gauvrit et al. (2017) for a recently published method of analysis for complex human behavior). We use the SE because we aim at implementing a system as simple and robust as possible and with the sole purpose of characterizing the trajectory signals of different experimental cases to perform comparisons among them. This very same simplicity, already described in our previous work (Eguiraun et al., 2014) and particularly regarding the 2D analysis of a 3D event together with the image segmentation method, makes our approach not suitable for complex behavioral studies, but adequate for routine monitoring of normal/not normal behaviors of the fish system, not of individual fish.

As already mentioned, the SE was first described by Shannon (1948, 1951) and it is calculated by the equation:

$$H(X) = -\sum_{x_i \in \Theta} p(x_i)\log p(x_i) = -E[\log p(x_i)]$$

Where X represents a random variable with a set of values Θ and probability mass function $p(x_i) = P_r\{X = x_i\}$, $x_i \in \Theta$, and E represents the expectation operator. Note that $p \log p = 0$ if $p = 0$. The implementation in MATLAB R2014a (MathWorks Inc.) of the SE function is described in Supplementary Data Sheet S6.

Statistical Parameters

The coefficients of variation (CV), defined as the ratio of the standard deviation to the mean, were calculated in Microsoft Office Excel 2007 and the curve fittings were performed using the Curve Fitting Toolbox 3.4.1 that is included in MATLAB R2014a (MathWorks Inc.).

RESULTS

Table 4 and **Figure 5** show the daily evolution in both tanks of the SE corresponding to the basal trajectories (T1-b and T2-b in **Figure 5**) and to the trajectories followed in response to the stochastic event (T1-e and T2-e in **Figure 5**) of Experiment A. The responses obtained in both tanks were very similar and the SE of the system kept a power relationship with the number of fish (**Table 5**). In addition, the SE of the basal and response trajectories in tanks with 13 or more fish had always values higher than 3.97, while the in one-fish systems they were lower than 2.79. The coefficient of variation (CV) of the basal SE values also kept a relationship with the number of fish, being largest in the 1 fish systems (60.8% vs. about 4–8% for 50–13 fish, see **Table 6**). The raw data are listed in Supplementary Data Sheet S7.

The results of Experiment B are shown in **Figure 6**. As in Experiment A, the SE of one-fish systems always kept similarly low values (lower than 2.2 for the basal and 2.7 for the response) and the SE of both the basal and response trajectories increased with increasing number of fish (**Figure 6**) following a power function (**Table 5**). Also as in Experiment A, the CV of the SE in the one-fish systems was much larger than in any of the other ones: 43.7% vs. about 10% for the 2–5 fish systems (**Table 6**). The raw data are listed in Supplementary Data Sheet S8.

Taken the results of both experiments together improved the goodness of the fit of the power relationship between the SE and number of fish (R^2 = 0.93 for the basal and R^2 = 0.92 for the response) and confirmed the higher variability in the SE of low-fish number systems, particularly those with only one-fish (**Tables 5, 6** and **Figure 7**).

BWS Model

The purpose of measuring the SE of the basal and of the disturbed states was to obtain information on two relevant statuses (i.e., shoaling and schooling) in a healthy system in order to be integrated in a BWS. Since we found that both SE values kept a similar relationship with the number of fish, but they were not identical (**Figure 7**), we considered that the inclusion of both might strengthen a potential model that would ultimately permit their integration into a BWS monitoring tool, an example of which is described below. As already mentioned, our hypothesis, supported by previous works on the alteration of the SE in seabass systems contaminated with MeHg (Eguiraun et al., 2014, 2018), is that those SE values would be different in a healthy system than in an unhealthy one, and that this information may make possible to construct a model for a BWS.

The first step in the construction of the model would be the collection of data corresponding to the healthy system under the same conditions in which the monitoring is going to be performed. These data include the size and number of the fish, and all the other environmental parameters. From these data, the SE of both the basal and disturbed states of both the control (healthy) system and of the system being monitored should be estimated. Using these four measurements, three sub-models would be constructed whose combination would provide the integrated or "overall" model, as shown in **Figure 8**. The three sub-models are: (i) Basal reference sub-model: built using the entropy generated by the fish system in its basal state; (ii) Event

TABLE 4 | Daily evolution of the Shannon entropy in Experiment A in tanks 1 (T1) and 2 (T2).

		Day 1		Day 2		Day 3		Day 4		Day 5	
# fish	Tank #	Basal	Event	Basal	Event	Basal	Event	Basal	Event	Basal	Event
50	T_1	4.92 ± 0.14	5.16	4.98 ± 0.15	5.23	4.73 ± 0.11	5.00	4.79 ± 0.04	4.77	5.09 ± 0.28	4.82
	T_2	4.62 ± 0.07	4.62	4.66 ± 0.09	5.68	4.60 ± 0.04	4.89	4.63 ± 0.08	4.84	4.68 ± 0.10	4.81
25	T_1	4.71 ± 0.01	4.85	4.47 ± 0.10	4.53	4.50 ± 0.14	4.41	4.30 ± 0.05	4.75	4.46 ± 0.11	5.46
	T_2	4.76 ± 0.04	4.98	4.78 ± 0.22	4.76	4.67 ± 0.11	4.73	4.67 ± 0.10	4.58	4.69 ± 0.36	5.41
13	T_1	4.11 ± 0.23	4.27	4.05 ± 0.11	3.88	4.75 ± 0.45	4.43	4.20 ± 0.34	4.05	4.34 ± 0.55	4.40
	T_2	3.97 ± 0.17	4.47	3.99 ± 0.20	4.40	4.21 ± 0.27	4.16	3.99 ± 0.08	4.02	3.97 ± 0.08	4.06
1	T_1	0.59 ± 0.39	2.79	1.84 ± 0.63	2.63	0.97 ± 0.77	2.26	1.34 ± 0.34	2.15	0.87 ± 0.03	1.49
	T_2	0.52 ± 0.23	2.79	0.73 ± 0.19	1.63	0.38 ± 0.13	2.07	1.40 ± 0.47	1.50	2.01 ± 0.49	2.31

Shannon entropy (SE) of the basal (average of six different measurements; two tanks and three measurements per tank) and event responses are shown. The raw data are listed in Supplementary Data Sheet S7.

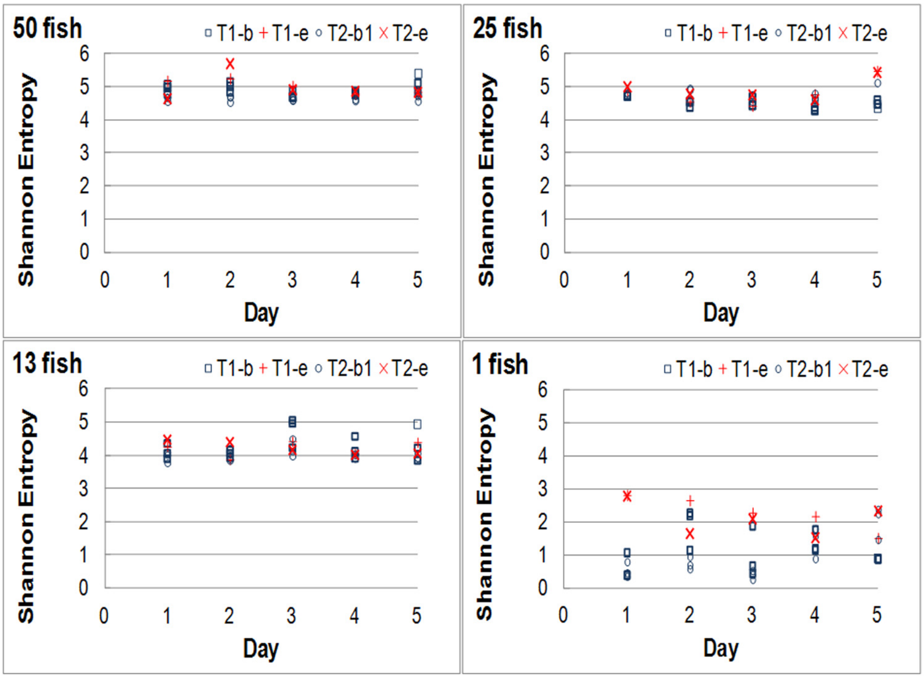

FIGURE 5 | Daily evolution of the Shannon entropy (SE) for Experiment A showing the SE values obtained in tanks 1 and 2 for the basal state (T1-b and T2-b) and in response to the stochastic event (T1-e and T2-e). The number of individuals is indicated on the Top-Left of each plot.

TABLE 5 | Curve fitting parameters and goodness of the fit of the Shannon entropy (SE) vs. fish number.

$y = a.x^b + c$		Basal	95% confidence bounds	Response	95% confidence bounds
For 1–5 fish systems					
Coefficients	a	−143.6	−22700, 22400	−0.92	−11.77, −0.06
	b	−0.01	−1.48, 1.47	−1.89	−7.80, 4.01
	c	145.10	−22400, 22700	3.42	2.60, 4.23
Goodness of the fit	SSE	8.07		0.42	
	R^2	0.72		0.79	
	Adjusted R^2	0.70		0.73	
	RMSE	0.55		0.24	
For 1–50 fish systems					
Coefficients	a	−4.17	−4.70, −3.64	−5.92	−11.77, −0.06
	b	−0.49	−0.64, −0.34	−0.16	−0.38, 0.05
	c	5.40	4.87, 5.94	8.21	2.31, 14.10
Goodness of the fit	SSE	28.24		5.90	
	R^2	0.93		0.92	
	Adjusted R^2	0.92		0.91	
	RMSE	0.44		0.35	

The SE values (y) of the basal state and of the response to the event were fitted as a function of the fish number (x). a, b, and c are the coefficients of the curve. The goodness of the fit was estimated by the sum of squares due to error (SSE), R-square, adjusted R-square, and root mean squared error (RMSE).

reference sub-model: built using the entropy of the fish system in response to a disturbance; (iii) Basal/Event relationship reference sub-model: built using the ratio between the "basal" and the "event" SE values.

The difference between the expected SE of the healthy system and the online signals measured by the monitoring tool detecting the actual SE of the system (for both the basal and disturbed statuses) will be called "error signal." These error signals are the outputs of the proposed "overall" model and they should be integrated in knowledge models of higher order, i.e., as inputs to the "Model Integration" block in **Figure 8**. Error signals larger than the previously estimated normal variation in a healthy system should be interpreted as a deviation from the norm in the system (i.e., the introduction of a possibly undesirable agent) and the supervisor in charge of the monitoring operation should proceed to identify the cause of such deviation and follow the

TABLE 6 | Coefficients of variation (CV) of the measured SE values for Experiments A and B.

		Number of fish							
	SE	**50**	**25**	**13**	**5**	**4**	**3**	**2**	**1**
Experiment A, all measurements	Basal	4,19	4,34	8,10					60.83
Experiment B, all measurements	Basal				9,90	10,03	8,63	9,85	43.66
Experiments A+B									
All measurements	Basal	4,19	4,34	8,10	9,90	10,03	8,63	9,85	55,15
AVG of three replicates	Basal	2,31	2,69	5,86					37,12
All measurements	Response	6,12	7,20	4,93					19,51

The CV of "All measurements" were calculated including all the SE values obtained, i.e., three basal and one response for each day. The "AVG of 3 replicates" were calculated including only the average of the three basal replicates obtained each day. There were no replicates of the responses to the event.

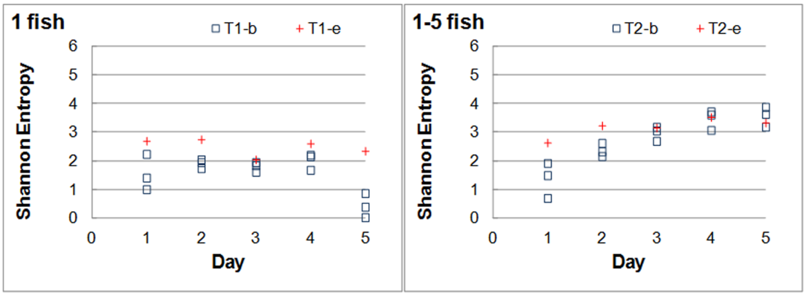

FIGURE 6 | Daily evolution of the Shannon entropy in Experiment B. Tank 1 (Left plot) contained only one fish, but a different fish every day, during the 5 experimental days. The number of fish in Tank 2 (Right plot) increased by one individual daily. The number of fish is indicated on the Top-Left of the panels. The square markers correspond to the SE values for the basal states and the crosses to the SE in response to the event.

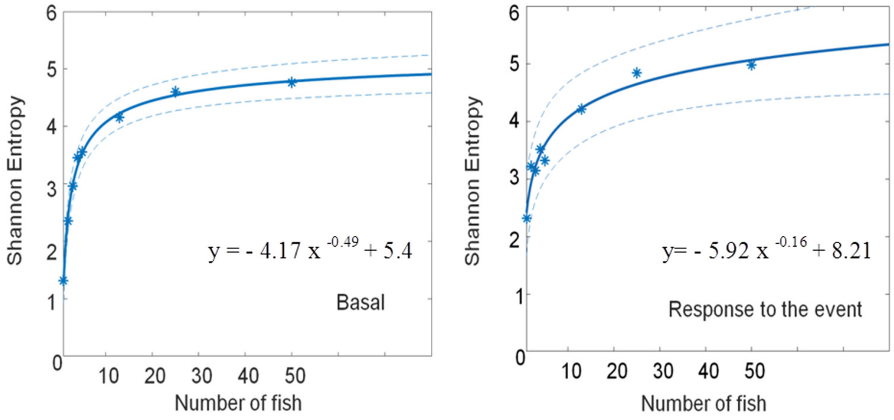

FIGURE 7 | Curve fitting of the Shannon entropy as a function of the fish number. The basal state (Left) and the response to the event (Right) are shown together with the 95% confidence bounds. The parameters of the curve fitting are shown in **Table 5**.

previously established corrective actions. Since it is desirable that the normal variation is a low as possible, one-fish systems (with CV of up to 60%) should be avoided.

DISCUSSION

The aim of the present work was to obtain an essential piece of information for BWS design purposes and for physiological research: to elucidate whether the number of fish affected the SE of the system in a known shoaling fish species (European seabass) and, if so, what type of relationship these two variables kept. As we have already mentioned, it must be noted that we did not aim at mapping behavioral characteristics such as time swimming or resting, aggressive behavior, the kind of shoaling and schooling itself or inter-individual interactions which would require a different methodological approach and algorithms more sophisticated than the SE to analyze the data (see for example the works by Tunstrøm et al., 2013; Teles et al., 2015; Gauvrit et al., 2017; Crosato et al., 2018).

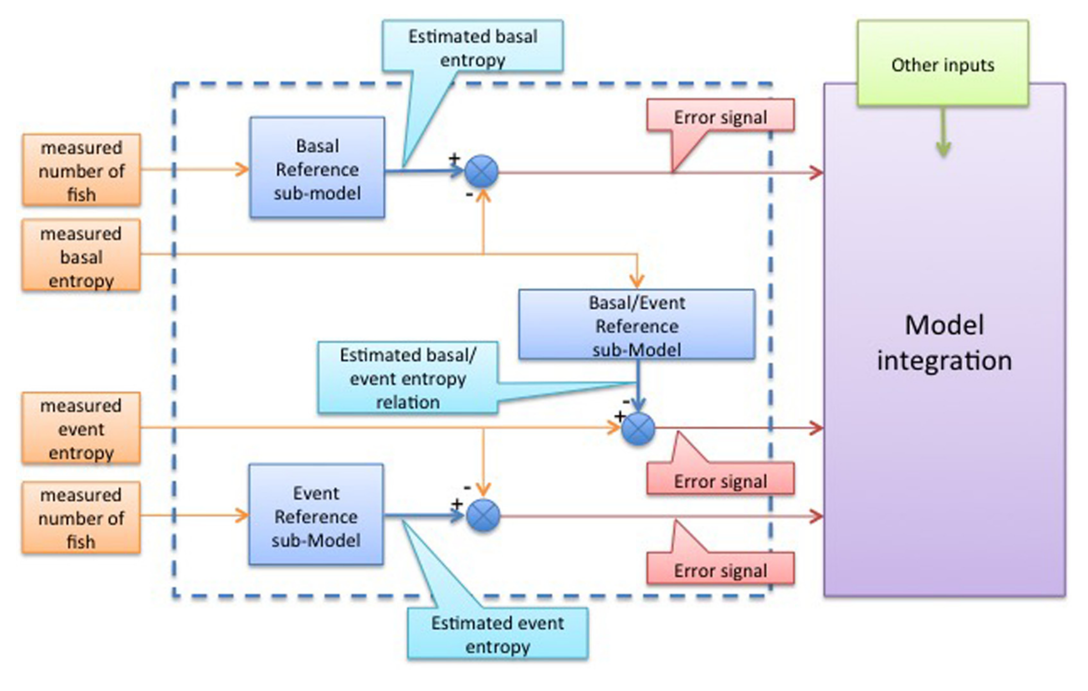

FIGURE 8 | Schematic representation of the model defining inputs, generated outputs due to error signals, internal variables, and sub-model interactions. The output error signals should feed the subsequent phase of the model where all this information is integrated in the Model Integration box.

The two experiments performed, A and B, are considered to contribute equally to the study of the system's behavior with different number of fish, and whether the experiment was performed by decreasing or by increasing the number of fish in the tank should not have a bearing on the results because the fish had been acclimated for a long enough period of time prior to the recordings. The acclimation periods we have used (12 and 2.5 days and 23 h) are longer or similar to most of those reported in the literature, for example Stienessen and Parrish (2013) used only 1 day and Melvin et al. (2017) indicated that these kind of studies should be preceded by an acclimation period of at least several hours to evaluate normal baseline behaviors. For the freshwater species they used, mosquitofish (*Gambusia affinis*), this period was 8 h. Moreover, in both Melvin et al. (2017) and our present work, the fish had been acclimated to the laboratory tanks for 3 months prior to the initiation of the experiment, which was carried out in similar tanks and conditions to those to which they had been acclimated to.

Implementation of a BWS, or establishment of an experimental fish system, requires the characterization of the "normal" or "healthy" biological system, in order to be able to detect alterations provoked by the introduction of undesirable agents (such as predators, infectious or parasitic agents, contaminants or others) that would make the system become unbalanced, stressed or unhealthy. The healthy system will have a basal and a disturbed state, each with their corresponding SE values that will be "normal," meaning that those will represent the shoaling basal state and the schooling reaction to a stochastic stimulus. The introduction of a detrimental agent (chronic stress, a toxicant, pathogen, parasite, etc.) should initiate the transformation of the "healthy" system into an "unhealthy" one and, consequently, induce alterations in the SE of both the basal and altered statuses. We initially thought that the SE in the response to a disturbance (i.e., the schooling reaction) might reflect better the health status of the system, so that if the fish had been affected for example, by a contaminant, its reflexes might have been altered and hence the initiation of the schooling should be different from the response of a healthy one (Eguiraun et al., 2014). On the other hand, it was also possible that the SE of the shoaling basal state itself might be different in healthy than in contaminated fish-systems and, in any case, it was likely that the information obtained from both measurements would be more robust than the information provided by any one of them. Therefore, we decided to include the analysis of both, the basal and disturbed states, in the present work and in the proposed model.

The number of fish is a characteristic intrinsic to the system and it should, a priori, not have a bearing on its health status. However, in the mid to long-term it may affect the health of the system if the number is too high or too low. Thus, in order to save costs, animal suffering and to respect the legal framework, it is desirable to select the lowest number that affects as little as possible the health status of the system, i.e., the lowest number of fish that provides results according to the variables being tested, such as contaminant concentration, and not to the composition of the system itself.

The one-fish systems had unusually low SE values, which may be explained by the shoaling nature of the species: when placed alone, we observed that fish moved very little, and this will translate in a low SE value due to the fact that it would be easier to predict the positions x_i and y_i (knowing x_{i-1} and y_{i-1}) of a one-fish system that is hardly moving (we hypothesize that this is probably due to fear, as explained in the next paragraph), than the centroid of a cluster of fishes feeling safer within a shoal of increasing size that will probably display increased unpredictability of movements due to either free, random swimming, or to schooling to escape predators. The increased difficulty in predicting the trajectory of the shoal would result in concomitantly increasing SE values, as shown in Tank 2 of Experiment B and in Experiment A.

To explain the above hypothesis, we would like to introduce the selfish herd theory proposed by Hamilton (1971), according to which individuals in a herd will try to avoid the periphery where the risk of predation is greatest. This theory was empirically proven in a situation of stress for the minnow (*Phoxinus phoxinus*) (Krause, 1993) and for sticklebacks (*Gasterosteus aculeatus*) (Krause and Tegeder, 1994). Applying this theory, it is reasonable to assume: (i) that a fish which would naturally shoal, being alone in a clean tank where it cannot even exhibit full mimicry, will feel exposed and stressed, and will try to move as little as possible to avoid attracting undesired attention from potential predators, (ii) that the intensity of the response to this stress will vary according to the individual genotype, stock of origin and possibly life history of the individual, as shown by Herbert-Read et al. (2017), and (iii) that those factors will, in turn, contribute to the large CV of individual SE values of 1-fish systems, which must necessarily reflect the variability in the responses from each different individual.

Consequently, we would not recommend performing physiological or toxicological experiments, nor set up a BWS, with only one fish, given that the set up itself will likely influence the well being of the individual. Rather, it should be selected a system with the lowest number of fish that allows the individuals to feel safe, i.e., the lowest number that allow the fish feel that they are in a shoal and with possibilities to school and escape predators if necessary. For our fish and experimental conditions, somewhere between 5 and 13 fish would be acceptable. It is interesting to note that this number agrees with the 6–10 number of interacting neighbors to initiate convergence to swarming in birds (Shang and Bouffanais, 2014) and with the "at least four neighbors" necessary to achieve schooling behavior in fish (Huth and Wissel, 1994) previously mentioned.

The concepts and results shown here may apply not only to European seabass, but also to other similarly shoaling species. Although the behavior and response of the system will likely be species-specific, this approach might be applied with few modifications to monitoring species such as salmon, seabream, charr, cod, trout, and others of high relevance to the aquaculture industry. Furthermore, once the number of fish to be used in live systems has been scientifically selected, complex behavioral studies may be carried out using some of the more sophisticated analytical methods described by different authors and software (see references from the section "Introduction," "Material and Methods," and the free available software[1]). The main use of the present work would be to contribute to animal welfare and to scientifically justify the selection of the lowest possible number of individuals to be experimented upon when applying for the permit to perform experiments to the respective Animal Welfare Committees.

CONCLUSIONS

We believe this to be the first scientific work designed to estimate the minimum number of individuals to be used in studies of shoaling fish species (albeit not of the shoaling itself) that reaches a compromise between the Reduction in number demanded by animal welfare guidelines and a low (or as low as possible) variability in the fish system's response. This work also presents for the first time a potential model using the SE of the biological system, for the robust and practical implementation of a small-scale BW-monitoring system (to monitor the health and welfare of the fish) into an intelligent aquaculture platform.

Several conclusions can be drawn from the present study. One is that to set-up a monitoring BWS or an experiment using a shoaling species such as the European seabass, one should avoid using 1-fish systems. The second is that the minimum number of fish to monitor should be between five and 13 fish since that number is a good compromise between acceptable variability in the results and the concept of Reduction to satisfy the criteria for animal welfare in experimental settings. A third conclusion is that one should use both the basal SE and the SE in response to an event in the design of the practical model, since they give complementary information and both parameters are relevant. Finally, there is still a significant amount of work that needs to be done, as described in the next section, in order to further develop the BWS approach in practical aquaculture settings and, in particular, in Intelligent Aquaculture structures.

Future Work

Further work within this line of research should include the validation of the present results using individuals of different size and species, as well as the development and validation of an early response model (such as the one presented above) of the system integrating all the relevant information needed to establish the "normal" response of the system. Once the monitoring system is defined, the next step will be its integration within the intelligent aquaculture structure. Additionally, it must be borne in mind that data on the system's SE can be obtained by processing images, as we have done here, but infrared images, echo signals and labels carried by the fish are also methods with potential to provide such relevant information that have been tested and offer great promise (Føre et al., 2011, 2017). Last, but not least, the use of more complex methods for the acquisition of behavioral data and of algorithms for their analysis may provide further evidence as to the type of disturbance that may affect the system, when such disturbance takes place. The current procedure is only designed to identify a normal operating system from a deviated

---

[1] http://complexitycalculator.com

one, which may be enough for the farmer or the researcher to identify the presence of an agent causing an alteration into the system but, as mentioned above, more fine analyses might help to elucidate the type of alteration suffered and/or the type of external agent introduced that one should look for. The latter may be particularly interesting in the case of novel or unexpected contaminants.

It is a challenge to speculate on how a very large fish system, for example with several hundred thousand fish, may behave. This question, however, is very important if one wishes to optimize, in a rational manner, the building of large off-shore fish aquaculture structures. Whether it is the SE or some other better suited algorithm the one that may help us to understand the dynamics of such large systems and optimize them and the welfare of the fish, we cannot say at this time, but it is with no doubt a very interesting and challenging field of research that will contribute practical data to fish farmers. Future works in this field will require the contribution from experts with wide and very different fields of expertise.

AUTHOR CONTRIBUTIONS

HE conceived and designed the experiments, analyzed and interpreted the data, and wrote the manuscript. OC and AS interpreted the data and wrote the manuscript. IM contributed to the experimental design, analysis and interpretation of the data, and writing of the manuscript.

FUNDING

The work was financed through grant nos. CTM2012-40203-C02-01 (project *BMW*) and RTC-2014-2837-2 (project *Selatún*), both from the Spanish Ministry of Economy and Competitiveness (http://www.mineco.gob.es) and by grant no. KK-2016/00057 (project *Maromega*) Elkartek, from the Basque Government-Eusko Jaurlaritza.

ACKNOWLEDGMENTS

The fish were provided by Tinamenor (Cantabria Spain) and the experiment was performed with the technical assistance of Dr. Urtzi Izagirre.

SUPPLEMENTARY MATERIAL

The Supplementary Material for this article can be found online at: https://www.frontiersin.org/articles/10.3389/fphys.2018.00493/full#supplementary-material

REFERENCES

Anon (2011). *The European Bioeconomy in 2030 – Delivering Sustainable Growth by Addressing the Grand Societal Challenges*. Available at: http://www.epsoweb.org/file/560 [accessed April 27, 2018].

Bae, M. J., and Park, Y. S. (2014). Biological early warning system based on the responses of aquatic organisms to disturbances: a review. *Sci. Total Environ.* 466–467, 635–649. doi: 10.1016/j.scitotenv.2013.07.075

Ballerini, M., Cabibbo, N., Candelier, R., Cavagna, A., Cisbani, E., Giardina, I., et al. (2008). Interaction ruling animal collective behavior depends on topological rather than metric distance: evidence from a field study. *Proc. Natl. Acad. Sci. U.S.A.* 105, 1232–1237. doi: 10.1073/pnas.0711437105

Bostock, J., McAndrew, B., Richards, R., Jauncey, K., Telfer, T., Lorenzen, K., et al. (2010). Aquaculture: global status and trends. *Philos. Trans. R. Soc. Lond. B Biol. Sci.* 365, 2897–2912. doi: 10.1098/rstb.2010.0170

Brodin, T., Fick, J., Jonssom, M., and Klaminder, J. (2013). Dilute concentrations of a psychiatric drug alter behavior of fish from natural populations. *Science* 339, 814–815. doi: 10.1126/science.1226850

Crosato, E., Jiang, L., Lecheval, V., Lizier, J. T., Wang, X. R., Tichit, P., et al. (2018). Informative and misinformative interactions in a school of fish. *Swarm Intell.* 1–23. doi: 10.1007/s11721-018-0157-x

Di Marco, P., Priori, A., Finoia, M. G., Massari, A., Mandich, A., and Marino, G. (2008). Physiological responses of European sea bass *Dicentrarchus labrax* to different stocking densities and acute stress challenge. *Aquaculture* 275, 319–328. doi: 10.1016/j.aquaculture.2007.12.012

Eguiraun, H., Casquero, O., and Martinez, I. (2018). The Shannon entropy trend of a fish system estimated by a machine vision approach seems to reflect the molar Se:Hg ratio of its feed. *Entropy* 20:90. doi: 10.3390/e20020090

Eguiraun, H., Izagirre, U., and Martinez, I. (2015). A paradigm shift in safe seafood production: from contaminant detection to fish monitoring - Application of biological warning systems to aquaculture. *Trends Food Sci. Technol.* 43, 104–113. doi: 10.1016/j.tifs.2015.01.007

Eguiraun, H., Lopez-de-Ipina, K., and Martinez, I. (2014). Application of entropy and fractal dimension analyses to the pattern recognition of contaminated fish responses in aquaculture. *Entropy* 16, 6133–6151. doi: 10.3390/e16116133

Eguiraun, H., López-de-ipiña, K., and Martinez, I. (2016). Shannon entropy in a European seabass (*Dicentrarchus labrax*) system during the initial recovery period after a short-term exposure to methylmercury. *Entropy* 18, 1–10. doi: 10.3390/e18060209

European Aquaculture Technology and Innovation Platform-Eatip (2012). *The Future of European Aquaculture Our Vision: A Strategic Agenda for The Future of European Aquaculture*. Available at: www.eatip.eu

European Commission (2010). Directive 2010/63/EU of the European Parliament and of The Council of 22 September 2010 on the protection of animals used for scientific purposes (Text with EEA relevance). *Off. J. Eur. Union* 276, 33–79.

FAO (2016). *The State of World Fisheries and Aquaculture 2016. Contributing to Food Security and Nutrition for All. Rome, Italy*. Available at: http://www.fao.org/3/a-i3720e.pdf [accessed December 12, 2017].

Fishbase.org (2015). *A Global Information System on Fishes*. Available at: www.fishbase.org [accessed December 12, 2017].

Føre, M., Alfredsen, J. A., and Gronningsater, A. (2011). Development of two telemetry-based systems for monitoring the feeding behaviour of Atlantic salmon (*Salmo salar* L.) in aquaculture sea-cages. *Comput. Electron. Agric.* 76, 240–251. doi: 10.1016/j.compag.2011.02.003

Føre, M., Frank, K., Dempster, T., Alfredsen, J. A., and Høy, E. (2017). Biomonitoring using tagged sentinel fish and acoustic telemetry in commercial salmon aquaculture: a feasibility study. *Aquac. Eng.* 78, 163–172. doi: 10.1016/j.aquaeng.2017.07.004

Føre, M., Frank, K., Norton, T., Svendsen, E., Alfredsen, J. A., Dempster, T., et al. (2018). Precision fish farming: a new framework to improve production in aquaculture. *Biosyst. Eng.* doi: 10.1016/j.biosystemseng.2017.10.014

Forlim, C. G., and Pinto, R. D. (2014). Automatic realistic real time stimulation/recording in weakly electric fish: long time behavior characterization in freely swimming fish and stimuli discrimination. *PLoS One* 9:e84885. doi: 10.1371/journal.pone.0084885

Gauvrit, N., Zenil, H., Soler-Toscano, F., Delahaye, J. P., and Brugger, P. (2017). Human behavioral complexity peaks at age 25. *PLoS Comput. Biol.* 13:e1005408. doi: 10.1371/journal.pcbi.1005408

Hamilton, W. D. (1971). Geometry for the selfish herd. *J. Theor. Biol.* 31, 295–311. doi: 10.1016/0022-5193(71)90189-5

Hellou, J. (2011). Behavioral ecotoxicology, an "early warning" signal to assess environmental quality. *Environ. Sci. Pollut. Res.* 18, 1–11. doi: 10.1007/s11356-010-0367-2

Hemelrijk, C. K. (2002). Understanding social behavior with the help of complexity science (Invited Article). *Ethology* 108, 655–671. doi: 10.1046/j.1439-0310.2002.00812.x

Herbert-Read, J. E., Rosén, E., Szorkovszky, A., Ioannou, C. C., Rogell, B., Perna, A., et al. (2017). How predation shapes the social interaction rules of shoaling fish. *Proc. R. Soc. B Biol. Sci.* 284:20171126. doi: 10.1098/rspb.2017.1126

Huth, W., and Wissel, C. (1994). The simulation of fish schools in comparison with experimental data. *Ecol. Modell.* 75, 135–145. doi: 10.1016/0304-3800(94)90013-2

Kadota, M., White, E. J., Torisawa, S., Komeyama, K., and Takagi, T. (2011). Employing relative entropy techniques for assessing modifications in animal behavior. *PLoS One* 6:e28241. doi: 10.1371/journal.pone.0028241

Kalogerakis, N., Arff, J., Banat, I. M., Broch, O. J., Daffonchio, D., Edvardsen, T., et al. (2015). The role of environmental biotechnology in exploring, exploiting, monitoring, preserving, protecting and decontaminating the marine environment. *New Biotechnol.* 32, 157–167. doi: 10.1016/j.nbt.2014.03.007

Krause, J. (1993). The effect of "Schreckstoff" on the shoaling behavior of the minnow: a test of Hamilton's selfish herd theory. *Anim. Behav.* 45, 1019–1024. doi: 10.1006/anbe.1993.1119

Krause, J., and Tegeder, R. W. (1994). The mechanism of aggregation behavior in fish shoals: individuals minimize approach time to neighbours. *Anim. Behav.* 48, 353–359. doi: 10.1006/anbe.1994.1248

Ladu, F., Mwaffo, V., Li, J., Macrì, S., and Porfiri, M. (2015). Acute caffeine administration affects zebrafish response to a robotic stimulus. *Behav. Brain Res.* 289, 48–54. doi: 10.1016/j.bbr.2015.04.020

Liu, Y., Chon, T.-S., Baek, H., Do, Y., Choi, J. H., and Chung, Y. D. (2011). Permutation entropy applied to movement behaviors of *Drosophila melanogaster*. *Mod. Phys. Lett. B* 25, 1133–1142. doi: 10.1142/S021798491102684X

Magalhães, D. D. P., Armando da Cunha, R., Albuquerque dos Santos, J. A., Buss, D. F., and Baptista, D. F. (2007). Behavioral response of zebrafish Danio rerio Hamilton 1822 to sublethal stress by sodium hypochlorite: ecotoxicological assay using an image analysis biomonitoring system. *Ecotoxicology* 16, 417–422. doi: 10.1007/s10646-007-0144-2

Mann, R. P., and Garnett, R. (2015). The entropic basis of collective behavior. *J. R. Soc. Interface* 12:20150037. doi: 10.1098/rsif.2015.0037

Melvin, S. D., Petit, M. A., Duvignacq, M. C., and Sumpter, J. P. (2017). Towards improved behavioral testing in aquatic toxicology: acclimation and observation times are important factors when designing behavioral tests with fish. *Chemosphere* 180, 430–436. doi: 10.1016/j.chemosphere.2017.04.058

Mwaffo, V., Butail, S., and Porfiri, M. (2017). Analysis of pairwise interactions in a maximum likelihood sense to identify leaders in a group. *Front. Robot. AI* 4:35. doi: 10.3389/frobt.2017.00035

Nimkerdphol, K., and Nakagawa, M. (2008). Effect of sodium hypochlorite on zebrafish swimming behavior estimated by fractal dimension analysis. *J. Biosci. Bioeng.* 105, 486–492. doi: 10.1263/jbb.105.486

Papoutsoglou, S., Tziha, G., Vrettos, X., and Athanasiou, A. (1998). Effects of stocking density on behavior and growth rate of European sea bass (*Dicentrarchus labrax*) juveniles reared in a closed circulated system. *Aquac. Eng.* 18, 135–144. doi: 10.1016/S0144-8609(98)00027-2

Pickett, G. D., and Pawson, M. (1994). "Sea bass biology," in *Fish & Fisheries Series*, ed. D. L. Noakes (Berlin: Springer).

Polonschii, C., Bratu, D., and Gheorghiu, E. (2013). Appraisal of fish behavior based on time series of fish positions issued by a 3D array of ultrasound transducers. *Aquac. Eng.* 55, 37–45. doi: 10.1016/j.aquaeng.2013.03.001

Quach, Q. K., Chon, T.-S., Kim, H., and Van Nguyen, T. (2013). One and two-individual movements of fish after chemical exposure. *J. Korean Phys. Soc.* 63, 18–27. doi: 10.3938/jkps.63.18

Russell, W. M. S., and Burch, R. (1959). *The Principles of Humane Experimental Technique*. London: Methuen & Co.

Sadoul, B., Mengues, P. E., Friggens, N. C., Prunet, P., and Colson, V. (2014). A new method for measuring group behaviours of fish shoals from recorded videos taken in near aquaculture conditions. *Aquaculture* 430, 179–187. doi: 10.1016/j.aquaculture.2014.04.008

Shang, Y., and Bouffanais, R. (2014). Influence of the number of topologically interacting neighbors on swarm dynamics. *Sci. Rep.* 4:4184. doi: 10.1038/srep04184

Shannon, C. E. (1948). A mathematical theory of communication. *Bell Syst. Tech. J.* 27, 379–423. doi: 10.1002/j.1538-7305.1948.tb01338.x

Shannon, C. E. (1951). Prediction and entropy of printed English. *Bell Syst. Tech. J.* 30, 50–64. doi: 10.1002/j.1538-7305.1951.tb01366.x

Spasic, S., Kesic, S., Kalauzi, A., and Saponjic, J. (2011). Different anesthesia in rat induces distinct inter-structure brain dynamic detected by Higuchi fractal dimension. *Fractals* 11, 113–123. doi: 10.1142/S0218348X1100521X

Stienessen, S. C., and Parrish, J. K. (2013). The effect of disparate information on individual fish movements and emergent group behavior. *Behav. Ecol.* 24, 1150–1160. doi: 10.1093/beheco/art042

Teles, L. O., Fernandes, M., Amorim, J., and Vasconcelos, V. (2015). Video-tracking of zebrafish (*Danio rerio*) as a biological early warning system using two distinct artificial neural networks: probabilistic neural network (PNN) and self-organizing map (SOM). *Aquat. Toxicol.* 165, 241–248. doi: 10.1016/j.aquatox.2015.06.008

Tunstrøm, K., Katz, Y., Ioannou, C. C., Huepe, C., Lutz, M. J., and Couzin, I. D. (2013). Collective states, multistability and transitional behavior in schooling fish. *PLoS Comput. Biol.* 9:e1002915. doi: 10.1371/journal.pcbi.1002915

Vila Pouca, C., and Brown, C. (2017). Contemporary topics in fish cognition and behavior. *Curr. Opin. Behav. Sci.* 16, 46–52. doi: 10.1016/j.cobeha.2017.03.002

Conflict of Interest Statement: The authors declare that the research was conducted in the absence of any commercial or financial relationships that could be construed as a potential conflict of interest.

Copyright © 2018 Eguiraun, Casquero, Sørensen and Martinez. This is an open-access article distributed under the terms of the Creative Commons Attribution License (CC BY). The use, distribution or reproduction in other forums is permitted, provided the original author(s) and the copyright owner are credited and that the original publication in this journal is cited, in accordance with accepted academic practice. No use, distribution or reproduction is permitted which does not comply with these terms.

Advantages of publishing in Frontiers

OPEN ACCESS
Articles are free to read
for greatest visibility
and readership

FAST PUBLICATION
Around 90 days
from submission
to decision

HIGH QUALITY PEER-REVIEW
Rigorous, collaborative,
and constructive
peer-review

TRANSPARENT PEER-REVIEW
Editors and reviewers
acknowledged by name
on published articles

Frontiers
Avenue du Tribunal-Fédéral 34
1005 Lausanne | Switzerland

Visit us: www.frontiersin.org
Contact us: info@frontiersin.org | +41 21 510 17 00

REPRODUCIBILITY OF RESEARCH
Support open data
and methods to enhance
research reproducibility

DIGITAL PUBLISHING
Articles designed
for optimal readership
across devices

FOLLOW US
@frontiersin

IMPACT METRICS
Advanced article metrics
track visibility across
digital media

EXTENSIVE PROMOTION
Marketing
and promotion
of impactful research

LOOP RESEARCH NETWORK
Our network
increases your
article's readership